

Dissertation
submitted to the
Combined Faculties for the Natural Science and for Mathematics
of the Ruperto Carola University Heidelberg, Germany
for the degree of
Doctor of Natural Science

presented by:

Sebastian Trick
born in Heilbronn

oral examination: 21.07.2004

Formation of Nitrous Acid on Urban Surfaces
-
a physical-chemical perspective

Referees:

Prof. Dr. Ulrich Platt

Prof. Dr. Ulrich Schurath

Abstract

Nitrous acid (HONO) has been observed in the nocturnal urban atmosphere for decades. During daylight hours, the rapid photolysis of HONO is a significant source of OH-radicals, which drive tropospheric chemistry and ozone-formation. Recently, unexpected high values of HONO have been detected during the day. Despite its importance, sources of HONO are still poorly understood. Direct emission of HONO or homogeneous chemical formation alone cannot explain the high HONO-to-NO₂ ratios often measured in the boundary layer. Today it is thus generally accepted that HONO is formed by heterogeneous hydrolysis of NO₂. However, large uncertainties about the nature of the surfaces and the chemical conversion mechanism remain.

Here, we present direct measurements from three field campaigns detecting daytime HONO mixing ratios of ~200 ppt using DOAS. A chemical transport model (RCAT 8.1.2) was modified to quantify the individual contribution of the vertical transport effects and chemical processes for different times of the day. While aerosols were found to be of minor importance under all circumstances, vertical transport and heterogeneous HONO production on the ground surface (at ~5%) and on canopies (at ~45%) were found to be of major influence on the daytime production of atmospheric HONO.

The heterogeneous interactions of HONO with real urban surfaces were further investigated in a smog chamber using a White-type DOAS multi-reflection system. The NO₂ uptake coefficients on these surfaces were calculated to be $\gamma_{\text{NO}_2} \sim 10^{-8}$ on Teflon, $\sim 10^{-7}$ on PE foil, $\sim 10^{-5}$ on asphalt and concrete, $\sim 3 \times 10^{-6}$ on roof-tiles and flagstone-tiles, and $\sim 2 \times 10^{-5}$ on grass. The higher values were found to be well correlated to an enhanced BET surface. The HONO concentrations were found to scale with the relative humidity, and thus the HONO uptake coefficient is not independently determinable. Therefore, a model (HeCSI) was developed using Langmuir adsorption-desorption isotherms to describe the concentration-time series of all trace gases. Based on this new model approach, HONO uptake coefficients, the amount of HONO adsorbed on the surfaces of the smog chamber, and the out-gassing frequency could be determined. It was found that the physical-chemical equilibrium underlying the model describes the chemical NO_x - system at all times

Zusammenfassung

Salpetrige Säure (HONO) wird seit Jahrzehnten in der nächtlichen urbanen Atmosphäre beobachtet. Am Tage stellt ihre rasche Photolyse eine bedeutende Quelle des OH-Radikals dar, das die troposphärische Chemie und Ozonbildung katalysiert. In jüngster Zeit werden hohe HONO - Messwerte auch am Tage gefunden. Neben dieser atmosphärischen Bedeutung der HONO, sind ihre Quellen nur wenig verstanden. Direkte Emissionen und homogene Reaktionen können für sich nicht die häufig in der PBL gemessenen HONO-zu-NO₂ Verhältnisse erklären. Es gilt heute als gesichert, dass HONO aus der heterogenen Hydrolyse von NO₂ entsteht. Jedoch bestehen dabei enorme Unsicherheiten betreff der Beschaffenheit der Oberfläche und des Mechanismus der chemischen Umwandlung.

In dieser Arbeit wurden während dreier Feldmesskampagnen HONO - Tageswerte ~200 ppt mit DOAS gemessen. Ein Chemie-Transport Model (RCAT 8.1.2) wurde modifiziert, um die einzelnen Beiträge von Vertikaltransport und chemischen Prozessen tageszeitabhängig zu quantifizieren. Während danach Aerosole nur einen vernachlässigbaren Einfluss auf die atmosphärischen HONO Konzentrationen unter nahezu allen Bedingungen auszuüben scheinen, beeinflussen die vertikale Mischung, die heterogenen Reaktionen am Boden (dort zu ~5%) und besonders an Hauswänden (zu ~45%) enorm die Bilanz von HONO am Tage.

Die heterogenen Wechselwirkungen von HONO mit realen urbanen Oberflächen wurden in einer Smogkammer mittels eines DOAS White-Vielfachreflexionssystem untersucht. Die NO₂ uptake Koeffizienten für verschiedene Oberflächenarten wurden berechnet: $\gamma_{\text{NO}_2} \sim 10^{-8}$ auf Teflon, $\sim 10^{-7}$ auf PE Folie, $\sim 10^{-5}$ auf Asphalt und Beton, $\sim 3 \times 10^{-6}$ auf Dach- und Keramikfließen und $\sim 2 \times 10^{-5}$ auf Gras. Diese erhöhten Werte konnten durch eine vergrößerte BET Oberfläche erklärt werden. Die HONO - Konzentrationen wurden korreliert mit der relativen Luftfeuchte beobachtet, so dass HONO uptake Koeffizienten nicht analytisch bestimmbar sind. Daher wurde ein Model (HeCSI) entwickelt, das die Langmuir Absorptions-Desorptions-Isotherme nutzt, um die Konzentrationszeitreihen aller Spurenstoffe gleichzeitig zu beschreiben. Mit diesem neuen Modellansatz konnten die HONO uptake Koeffizienten, die Menge der an den Wänden der Smogkammer absorbierten HONO und dessen Ausgasrate ermittelt werden. Weiter konnte gezeigt werden, dass mittels dieses physikalischen-chemischen Gleichgewichts, das dem Model zugrunde liegt, das chemische NO_x-Reaktionssystem zu jeder Zeit beschreibbar ist.

Table of content

1	Introduction	1
2	Theoretical Background: Chemistry and Physics of the Lower Troposphere	5
2.1	Tropospheric Nitrogen Oxides	6
2.1.1	Sources and Sinks of Tropospheric Nitrogen Oxides	6
2.1.2	Overview of Tropospheric NO _y Chemistry	11
2.2	Photochemical Reactions	13
2.2.1	The Photo-Stationary Steady State & Leighton Ratio	13
2.2.2	Deviations from the Leighton Ratio & the Formation of Photosmog	14
2.2.3	The Origin of the Tropospheric OH Radicals	15
2.3	Nitrous Acid (HONO)	18
2.3.1	Importance of Atmospheric HONO	18
2.3.2	Diurnal Variation of HONO in the Troposphere	19
2.3.3	Direct Emission Sources of Nitrous Acid	21
2.3.4	Homogeneous Formation of Nitrous Acid	23
2.3.5	Heterogeneous Formation of Nitrous Acid	25
2.3.5.1	<i>The Disproportionation of NO_x</i>	25
2.3.5.2	<i>Direct Reduction on Fresh Soot</i>	26
2.3.5.3	<i>Further Heterogeneous Reactions yielding HONO</i>	26
2.3.5.4	<i>Photolytic Enhancement of HONO Formation</i>	27
2.3.6	HONO Formation by Heterogeneous Disproportionation of NO ₂	28
2.3.6.1	<i>Formation of Nitrous Acid on Airborne Particles (Aerosols)</i>	28
2.3.6.2	<i>Formation of Nitrous Acid on Macroscopic Surfaces & on the Ground</i>	30
2.3.6.3	<i>Evidence for a ground-near Source by Vertical Gradients of HONO</i>	31
2.3.6.4	<i>Kinetics & Water Dependence of HONO Formation</i>	33
2.3.6.5	<i>Mechanistic Sequences of Heterogeneous HONO Formation</i>	35
2.3.7	Sinks of Atmospheric Nitrous Acid	38
2.4	Heterogeneous Reactions and Catalysis	40
2.4.1	Heterogeneous Catalysis	40
2.4.2	Adsorption and Desorption of Gases on a Solid Surface	42
2.4.2.1	<i>Possibilities of Gas-Phase to Solid-Surface Interactions</i>	42
2.4.2.2	<i>Energetic Aspects of Adsorption and Desorption</i>	44
2.4.3	Thermodynamic and Kinetic Considerations	46
2.4.3.1	<i>Empirical Aspects on Thermodynamics</i>	46
2.4.3.2	<i>Mathematical Description of Adsorption</i>	47
2.4.3.3	<i>Description of Kinetic of Desorption</i>	49
2.4.4	Derivation and Applications of Adsorption Isotherms	49
2.4.4.1	<i>The Langmuir Adsorption-Desorption Isotherms</i>	49
2.4.4.2	<i>Kinetic of Heterogeneously (Catalyzed) Reactions</i>	50
2.4.4.3	<i>Other Adsorption Isotherms: BET Theory</i>	51

2.5	Basics of Atmospheric Dynamics of the Boundary Layer	54
2.5.1	The Structure of the Planetary Boundary Layer	54
2.5.1.1	<i>The Laminar Surface Layer</i>	54
2.5.1.2	<i>The Prandtl Layer</i>	55
2.5.1.3	<i>The Ekman Layer</i>	55
2.5.1.4	<i>The Height of the PBL</i>	55
2.5.2	Diurnal Variations of the PBL: Micrometeorological Description	56
2.5.3	Transport Processes in the PBL: The Friction Velocity	58
2.5.3.1	<i>Neutral Layering</i>	59
2.5.3.2	<i>Labile and Stable Layering</i>	60
2.5.4	Radon as a Tracer for Mixing in and the Height of the PBL	62
3	Measurement Methods	65
3.1	Overview of Detection Techniques for Nitrous Acid	65
3.1.1	Chemical Surface Collection Techniques	65
3.1.1.1	<i>The Denuder Technique</i>	66
3.1.1.2	<i>Chemiluminescence Detection</i>	68
3.1.1.3	<i>The DNPH-HPLC Method</i>	69
3.1.1.4	<i>The LOPAP Instrument</i>	69
3.1.2	Mass Spectrometry	70
3.1.3	Spectroscopic Methods	71
3.1.3.1	<i>UV – PF / LIF - Sensor</i>	71
3.1.3.2	<i>IR – Spectroscopy</i>	71
3.2	Differential Optical Absorption Spectroscopy	72
3.2.1	An Overview of DOAS Applications	72
3.2.2	Theoretical Description of DOAS	73
3.2.2.1	<i>Basic Theory of Absorption Spectroscopy & Lambert-Beers Law</i>	73
3.2.2.2	<i>DOAS for Atmospheric Measurements: Numerical Description</i>	77
3.2.2.3	<i>The Analysis Procedure</i>	79
3.2.2.4	<i>Error Estimation</i>	81
3.2.2.5	<i>Effects of Residual Structures: X-Absorber and Detection Limit</i>	81
3.2.3	Instrumental Setup of a DOAS System	82
3.2.3.1	<i>The Long Path (LP) DOAS System</i>	82
3.2.3.2	<i>The DOAS White Multi-Reflection System</i>	84
3.2.3.3	<i>The Light Source</i>	87
3.2.3.4	<i>The Spectrograph</i>	87
3.2.3.5	<i>The Detector</i>	88
3.2.3.6	<i>Characterization of the Detector Unit</i>	89
3.2.3.7	<i>The Quartz Fiber Mode Mixer</i>	91
3.2.4	Performing HONO Measurements by DOAS	91
3.2.4.1	<i>The Measurement Algorithm for HONO</i>	91
3.2.4.2	<i>Reference Spectra for the DOAS Evaluations</i>	93
3.2.4.3	<i>Evaluation of LP-DOAS Data</i>	94
3.2.4.4	<i>Evaluation of White-DOAS Data</i>	96
4	Field Studies and Results	99
4.1	The Rome 2001 field campaign: Detection of Daytime HONO	99
4.1.1	The Area of Rome	99

4.1.2	Measurements in the City Center of Rome	101
4.1.2.1	<i>Instrumental Setup of the LP-DOAS</i>	101
4.1.2.2	<i>Trace Gas Measurements in the City Center of Rome</i>	102
4.1.2.3	<i>Radiance Data</i>	104
4.1.2.4	<i>Aerosol Particles</i>	105
4.1.3	The Villa Ada Background Measurement Station	107
4.1.3.1	<i>The HONO Measurements at Villa Ada</i>	107
4.1.3.2	<i>Intercomparison of HONO Measurement Techniques</i>	108
4.1.3.3	<i>Additional Trace Gases measured at Villa Ada</i>	109
4.1.3.4	<i>Natural Radioactivity Measurements and Meteorology</i>	109
4.1.4	The Measurements in Montelibretti	110
4.1.4.1	<i>Setup of the LP-DOAS System</i>	111
4.1.4.2	<i>Trace Gas Measurements in Montelibretti</i>	111
4.1.4.3	<i>Additional Measurements in Montelibretti</i>	113
4.1.5	Intercomparison between Rome and Montelibretti Trace Gas Data	114
4.1.6	Photochemical Smog Events	114
4.1.6.1	<i>The Smog Event on 31.05.2001</i>	115
4.1.6.2	<i>Pollution Event on 24.05.2001</i>	116
4.1.7	Qualitative Correlations of HONO and Radon Data	117
4.1.7.1	<i>HONO-Time-Derivative by Vertical Mixing of the PBL</i>	118
4.1.7.2	<i>Influence of Atmospheric Stability on Daytime HONO Values</i>	121
4.2	The Format 2002 campaign: Intercomparison of Trace Gas Measurements	123
4.2.1	The Measurement Location	123
4.2.2	DOAS Measurements at Bresso	124
4.2.2.1	<i>Setup of the DOAS White-Multi-Reflection System</i>	124
4.2.2.2	<i>Measurement of Trace Gases in Bresso</i>	125
4.2.3	Additional Equipment at Bresso	127
4.2.3.1	<i>In-situ Trace Gas Measurements</i>	127
4.2.3.2	<i>Radiance Data</i>	127
4.2.3.3	<i>Aerosol Particles</i>	128
4.2.3.4	<i>Meteorological Data at Bresso</i>	128
4.2.4	Intercomparison of HONO Measurements	129
4.3	The Turm 2003 campaign: Vertical Profiles of HONO	131
4.3.1	The Area of the FZ Karlsruhe and the Meteorological Tower	131
4.3.1.1	<i>The location of the Forschungszentrum Karlsruhe</i>	131
4.3.1.2	<i>The Meteorological Tower</i>	131
4.3.2	The Active Long Path DOAS System	133
4.3.3	Retrieval of trace gas profiles from LP-DOAS data	135
4.3.3.1	<i>Deconvolution of Temporal and Spatial Information</i>	135
4.3.3.2	<i>Error Estimation and Limitations of the DOAS Vertical Profiles</i>	136
4.3.3.3	<i>Calculation of Vertical Gradients</i>	137
4.3.4	Additional Equipment and cooperating groups	138
4.3.4.1	<i>Ozone Measurements</i>	138
4.3.4.2	<i>The Radiance Data</i>	138
4.3.4.3	<i>Natural Radon Activity and Atmospheric Dynamic</i>	138
4.3.4.4	<i>In-situ Instruments of cooperating groups at the Tower</i>	139
4.3.5	Time Series of Traces Gases	140
4.3.5.1	<i>Temporal Trends of O₃ and HCHO</i>	140
4.3.5.2	<i>Time Series of HONO, and NO₂ in Different Altitudes</i>	140
4.3.5.3	<i>The Altitude Dependent HONO-toNO₂ ratio</i>	142

4.3.6	Nighttime Vertical Gradients of the Trace Gases	144
4.3.6.1	<i>NO₂ Gradients</i>	144
4.3.6.2	<i>HONO Gradients</i>	146
4.3.6.3	<i>The HONO-to-NO₂ Ratio</i>	146
4.3.6.4	<i>O₃ and NO Gradients</i>	148
4.3.7	Influence of Vertical Transport in the PBL on Gradients	148
4.3.8	Temporal Trends of Vertical Gradients	149
4.3.9	Daytime Gradients of the Trace Gases	152
5	<i>The Smog Chamber Studies: Heterogeneous HONO Formation</i>	153
5.1	Experimental Setups	154
5.1.1	The Smog Chamber	154
5.1.1.1	<i>Characteristics of the Gas Supply</i>	155
5.1.1.2	<i>The Leakage of the Smog Chamber</i>	156
5.1.1.3	<i>Mixing and Homogeneity of the Smog Chamber</i>	156
5.1.1.4	<i>Humidification of the Smog Chamber</i>	157
5.1.2	Generation of the Injected NO ₂	157
5.1.3	The Investigated Surfaces	157
5.1.4	The Measurement Techniques	159
5.1.4.1	<i>The DOAS White System inside the Smog Chamber</i>	159
5.1.4.2	<i>Additional Measurements during the IUP 2002 campaign</i>	160
5.1.4.3	<i>Measurement Equipment during the KIP 2003 campaign</i>	160
5.2	Results of the Experiments	161
5.2.1	Experiments on Teflon and PE Surface	164
5.2.2	Experiments on Real Urban Surfaces	166
5.2.3	Experiment of HONO Formation on Grass	168
5.3	Analysis of NO₂ Decays	169
5.3.1	Calculation of the NO ₂ Uptake Coefficients	169
5.3.2	Dependence of the NO ₂ Uptake Coefficients on R.H.	172
5.4	Analysis of HONO in the Smog Chamber	174
5.4.1	Dependence of HONO Yield on NO ₂	174
5.4.2	Dependence of HONO on Relative Humidity	176
5.5	Analysis of NO_x Chemistry in the Smog Chamber: Modeling Studies	179
5.5.1	Modifications of Langmuir Theory for HONO	179
5.5.2	Description of the Model	181
5.5.3	The Mechanism of the NO _x Chemistry in the Smog Chamber	183
5.5.3.1	<i>Modeled NO₂ Chemistry</i>	183
5.5.3.2	<i>Chemistry of Surface Adsorbed Species</i>	184
5.5.3.3	<i>Modeled Time Series of HONO</i>	186
5.5.3.4	<i>Secondary Reactions yielding NO</i>	187
5.5.4	Sensitivity Studies of the HeCSI Model	189
5.5.5	Model Results for the different Surface Types	191

5.6	Atmospheric Relevance	193
5.6.1	Discussion of NO ₂ Uptakes & Comparison to Literature	193
5.6.2	Influence of Enhanced NO ₂ Uptakes on HONO Formation	194
5.6.3	Importance R.H. Independence of NO ₂ Uptake Coefficients	195
5.6.4	Influence of a Constant R.H. on HONO Formation	195
5.6.5	Limitations of the HeCSI Mechanism	197
6	Modeling Studies: Analysis of Atmospheric Daytime HONO	199
6.1	The Diurnal Variation of HONO Chemistry in Urban Areas	199
6.1.1	HONO Accumulation in the Nocturnal Boundary Layer (Stage 1)	201
6.1.2	HONO Photolysis and Dilution after Sunrise (Stage 2)	204
6.1.3	The OH-NO-HONO Steady State during Daytime (Stage 3)	208
6.2	Modeling Daytime HONO and Vertical Transport	210
6.2.1	Description of the RCAT 8.1.2 Model	210
6.2.1.1	<i>Calculations of Vertical Transport</i>	210
6.2.1.2	<i>Chemical Mechanisms</i>	212
6.2.1.3	<i>Extension of the Model to Daytime Urban Scenarios</i>	213
6.2.2	Setup of Parameters & Model Sensitivity Studies	214
6.2.2.1	<i>Model Parameters for Scenarios</i>	214
6.2.2.2	<i>Reproduction of the Time Series of Trace Gases</i>	216
6.2.2.3	<i>Influence of Starting Parameters</i>	222
6.2.3	Results of the Model	223
6.2.3.1	<i>The Vertical Profiles of NO, O₃ and VOCs</i>	223
6.2.3.2	<i>Vertical Distribution, Sources and Sinks of NO₂</i>	225
6.2.3.3	<i>Vertical Distribution, Sources and Sinks of HONO</i>	226
6.2.3.4	<i>Contribution of the Different Sources and Sinks to Daytime HONO Values</i>	231
6.2.4	Comparison to previous Models in Literature	237
6.2.5	Contribution of HONO to the Daytime OH Budget	237
7	Conclusions and Outlook	243
7.1	Conclusions from the Field and Modeling Studies: Daytime HONO Levels, Explanation and Consequences	243
7.2	Conclusions from Laboratory Studies: Interactions of HONO with Real Urban Surfaces	245
7.3	Final Conclusions, Summary and Outlook	247
	Literature	249
	Appendix	263
	A. The HeCSI Model Source Code	263
	B. The Chemical Mechanism of the RACM Model	267
	Acknowledgement	277

1 Introduction

The study of atmospheric chemistry and atmospheric physics became a scientific discipline in the 18th century, focusing at that time on the identification and quantification of the major chemical constituents of our atmosphere: nitrogen, oxygen, water vapor, carbon dioxide, and the noble gases. By developing more sophisticated instruments in the late 19th and early 20th century, the so-called trace gases were detected at mixing ratios of the order of less than 1 molecule per million air molecules (1 part per million, ppm). Since then, we have found a myriad of these trace gas species, some detected in mixing ratios as low as 1 part per trillion (ppt) or less [Finlayson-Pitts and Pitts, 2000].

Despite their low atmospheric concentrations, these species are known to directly impact human and biosphere health, as well as cause well-known phenomena such as urban photochemical (summer) smog, acid (rain) deposition, and stratospheric¹ ozone depletion. The striking increase in the long-lived greenhouse gases carbon dioxide (CO₂), methane (CH₄), and nitrous oxide (N₂O) since 1850, is held to be responsible for global warming and climate change in general. There is strong evidence that the composition of the atmosphere is not only changing on a global scale, but also the basic chemistry of the lower atmosphere (the troposphere) seems to be altered due to enhanced levels of trace gases. It is generally accepted today that the emission of these trace species into the atmosphere has dramatically increased since the beginning of industrialization in the 19th century. The concentrations of tropospheric ozone (O₃), nitrogen oxides (NO_x), sulfate (SO₄), and (carbonaceous) aerosol particles were especially enhanced in the northern hemisphere due these significant anthropogenic causes.

The first air pollution events were reported from London in the 1840's, and were caused by the widespread use of coal containing sulfuric compounds for industrial and domestic heating purposes. The so-called "London Smog"² was characterized by enhanced levels of SO₂ and particulate matter in the presence of dense fog and low inversion layers [Wilkins, 1954]. The special meteorological conditions concentrated the pollutants in a relatively small volume in the lowermost 50 – 100 m of the atmosphere, inhibiting propagation to higher altitudes by vertical mixing. In the following years, episodes of this London-smog air pollution were reported regularly, directly affecting public health and responsible for the death of thousands of people [Wilkins, 1954]. Consequently, the reduction of these pollutants in industrial and domestic exhaust was addressed, and technical and chemical process engineering made exhaust desulphurization and particle filtering possible. However, NO_x emissions have increased during the past decades.

In the late 1940's, a remarkable new air pollution phenomenon began to impact the urban area of the mega-city of Los Angeles. In contrast to the previous smog events, the so-called "Los Angeles smog" occurred despite low sulfur emissions, at higher temperatures, and under conditions of bright sunshine during summer days. It contained high concentrations of strongly oxidizing, plant killing pollutants, and irritated the respiratory tract and the eyes of

¹ The stratosphere extends from the tropopause, which is located at ~ 10 - 15 km altitude, to ~ 45 - 55 km. Both altitude values are depending on latitude and time of year.

² The composite word "smog" is a combination of smoke and fog, which already characterizes this air pollution phenomenon.

animals and humans [Middleton *et al.*, 1950], attributed to high levels of ozone by successive research. This new type of summertime smog (or photosmog) is now recognized to be a worldwide problem in many cities and surrounding areas with high emissions of organic species and nitrogen oxides irradiated by sunlight (photochemical air pollution). The primary pollutants, NO_x (NO + NO₂) and VOCs (volatile organic compounds), undergo several photochemical reactions in sunlight forming secondary pollutant species, in particular ozone. To reduce photosmog, a reduction of automobile traffic by law was considered, as the source of NO_x is mainly combustion processes from on-road automobile traffic. On the other hand, VOCs are emitted also by natural sources, e.g. trees and other plants.

The complex physical and chemical mechanisms in the atmosphere causing this photosmog have been the focus of atmospheric research ever since. Several authors [Levy, 1973; Stedman *et al.*, 1970; Weinstock, 1969] proposed that daytime chemistry of both the clean and polluted troposphere is driven by reactions of a catalyst, the hydroxyl radical OH, which plays a key role by initiating a chain reaction by attacking VOCs. The removal of the VOCs by this reaction cycle produces secondary radicals like organic peroxy radicals (RO₂), which convert NO to NO₂. The subsequent photolysis of NO₂ finally generates ozone in the lower atmosphere.

For a long time, the dominant source of the OH radicals was believed to be the photodissociation of ozone and formaldehyde by actinic UV radiation in sunlight, in both clean and polluted air. In the late 1970's, new aspects of atmospheric chemistry, especially the photo-oxidative daytime formation of ozone and other photo-oxidants from VOCs, were discovered, and night-time chemistry was shown to be important as well in both the polluted and clean atmosphere [Platt *et al.*, 1979]. Nitrous acid (HONO) was detected for the first time in the ambient air by [Perner and Platt, 1979; Platt and Perner, 1980; Platt *et al.*, 1980] as a reactive intermediate of the NO_x chemistry in the troposphere. Its amounts depend on the degree of pollution, and thus HONO is often referred to as a typical product of the polluted urban air. The mixing ratios of HONO show a typical diurnal variation dominated by its photolysis. It could be shown that HONO photo-dissociates directly at low-energy wavelengths into NO and OH radicals [Stockwell and Calvert, 1978], thus presenting a further source of the hydroxyl radical, especially in the early morning, when the formation of OH from other mechanisms is still slow [Alicke, 2000; Alicke *et al.*, 2003; Alicke *et al.*, 2002; Harris *et al.*, 1982; Harrison *et al.*, 1996; Jenkin *et al.*, 1988; Platt, 1986; Sjödin, 1988; Staffelbach *et al.*, 1997a; Staffelbach *et al.*, 1997b]. Consequently, research activity focused on the detection of HONO in urban and rural areas, and several atmospheric measurements have been reported with accumulated night-time HONO mixing ratios up to 15 ppb in heavily polluted areas (see e.g. [Alicke, 2000; Appel *et al.*, 1990; Febo *et al.*, 1996; Harrison *et al.*, 1996; Lammel and Cape, 1996; Notholt *et al.*, 1992; Reisinger, 2000; Veitel, 2002; Winer and Biermann, 1994]).

The contribution of HONO to the OH budget during the day was initially considered as an boost to the early morning OH-peak, while recent studies show that up to 35 % of the total OH is produced by HONO photolysis over the entire 24-hour period [Alicke *et al.*, 2003; Alicke *et al.*, 2002]. A modeling study showed that HONO could even become the dominant OH source throughout the entire day in winter [Aumont *et al.*, 2003]. Recently, more and more field measurements using multiple detection techniques show increased HONO daytime mixing ratios of about 200 ppt in polluted urban [Kleffmann *et al.*, 2003; Veitel, 2002; Zhou *et al.*, 2002a], as well as remote areas [Nefel *et al.*, 1996; Staffelbach *et al.*, 1997a; Zhou *et al.*, 2001]. This is more than twice the amount expected thus far [Finlayson-Pitts and Pitts, 2000; Lammel and Cape, 1996; Stutz *et al.*, 2002]. Obviously, this would have an enormous impact on the atmosphere's OH budget, and therefore directly affect the daytime chemistry in the troposphere.

Consequently, one of the main goals of this thesis was the detection and the quality assurance of these elevated daytime HONO mixing ratios, as previous studies often used rather

questionable measurement techniques, which were known to have inferences producing artificial amounts of nitrous acid. A long-path setup of the well-proven Differential Optical Absorption Spectroscopy (DOAS) was therefore used in this thesis during three field campaigns: in the urban areas of Rome in 2001 in the framework of the European NITROCAT (NITRous acid and its influence on the Oxidation Capacity of the ATmosphere) project, during the European FORMAT (formaldehyde as a tracer of oxidation in the troposphere) field studies in Milan in 2002, and also at the rural site of the Forschungszentrum Karlsruhe in 2003 (Turm, 2003). Here, the question of the type of surface responsible for the nitrous acid formation was addressed by performing trace gas gradient measurements at the instrumentally well-equipped meteorological tower. A large number of simultaneous measurements of several trace gases and meteorological parameters were performed during these campaigns, and further techniques for the detection of atmospheric nitrous acid were implemented in order to carry out intercomparisons of the different techniques. A quantification of the different mechanisms contributing to these daytime HONO values is subsequently required. However, in the complex physical and chemical system of the lowest part of the troposphere (the Planetary Boundary Layer), i.e. vertical and horizontal transport and mixing, chemical production and removal, no analytical solutions can be given. Instead, a computer simulation (model) needs to be developed to describe these terms simultaneously.

Despite the importance of HONO as a direct precursor of the OH-radical and its potential health impact, the production processes, particularly during daytime, are not well understood. Direct emissions of HONO by traffic related combustion processes, heating, and industrial burn have been identified and quantified [Ackermann, 2000; Kessler and Platt, 1984; Kirchstetter *et al.*, 1996; Kurtenbach *et al.*, 2001; Pitts *et al.*, 1984a], but cannot solely explain the observed atmospheric concentrations. Several HONO producing reactions in the gas phase have been suggested [Chan *et al.*, 1976b; Howard, 1977; Kaiser and Wu, 1977a; Stockwell and Calvert, 1983; Tyndall *et al.*, 1995; Wayne and Yost, 1951], but all homogeneous productions pathways have been reported to be of minor importance, since they are much too slow under atmospheric conditions. Among them, only the homogeneous recombination of the NO and OH radicals may contribute to significant amounts of nitrous acid under conditions of elevated NO concentrations, particularly during daytime [Nguyen *et al.*, 1998; Pagsberg *et al.*, 1997; Stuhl and Niki, 1972; Westenberg and DeHaas, 1972; Zabarnick, 1993], but this process competes with photolysis. Thus, the net production of new OH radicals by HONO photolysis depends on the amount of NO present.

As nitrous acid concentrations were generally found to scale with NO₂ mixing ratios, and depend on the ratio of the surface to air volume, HONO is believed to be formed by the heterogeneous conversion of nitrogen oxides (e.g. [Ammann *et al.*, 1998; Calvert *et al.*, 1994; Finlayson-Pitts *et al.*, 2003; Goodman *et al.*, 1999; Jenkin *et al.*, 1988; Kalberer *et al.*, 1999; Kleffmann *et al.*, 1998; Pitts *et al.*, 1984b; Platt, 1986; Sakamaki *et al.*, 1983; Svensson *et al.*, 1987]). The exact mechanism of the HONO formation was thus far poorly understood. Only the first order dependence of the heterogeneous NO₂ hydrolysis could be derived from laboratory studies and field measurements. Even under assumption of favorable conditions, the rate coefficient for this HONO formation lies about four orders of magnitude lower than observed [Platt, 1986]. Thus, it is most commonly thought that this production of nitrous acid is catalytically accelerated or proceeds at the ground surface [Chan *et al.*, 1976b; Kaiser and Wu, 1977b; Platt, 1986], while other studies derived the surface of buildings in urban environments as possible sources of HONO [Andres-Hernandez *et al.*, 1996; Febo *et al.*, 1996; Harris *et al.*, 1982; Harrison and Kitto, 1994]. However, the exact location, i.e. the surface of the production of atmospheric HONO remains unclear.

To the present, only HONO formation measurements on “laboratory surfaces” such as glass or Teflon were performed. Real urban surfaces, for example asphalt roads, are more complex, and have not been considered in model calculations thus far. Therefore, it was also one of the

main goals of this thesis to investigate the rate coefficient for heterogeneous HONO formation on these real urban surfaces. These measurements took place under atmospheric conditions in an isolated smog chamber in order to exclude non-controllable influences of the environment on the experiments. The trace gas concentrations were measured by an optical multi-reflection system, applying the Differential Optical Absorption Spectroscopy (DOAS) technique. The dependence of the formation of HONO on the concentration of NO_2 , its precursor, and on the variable relative humidity, was studied.

The overall question is whether the enhanced and unambiguous daytime concentrations of nitrous acid can be explained by either enhanced or catalyzed chemical production on these real urban surfaces, or by the stronger influence of vertical transport in the daytime planetary boundary layer, or whether an additional daytime source mechanism of HONO is required, as suggested by several groups [Dibb *et al.*, 2002; Kleffmann *et al.*, 2003; Vogel *et al.*, 2003; Zhou *et al.*, 2001].

Therefore, the current state of knowledge of NO_x and HONO chemistry will be described in detail in chapter 2. This includes its sources and sinks in the troposphere, as well as the different formation mechanisms and source quantification for the hydroxyl radical. A special focus will be on the different heterogeneous formation pathways yielding HONO at various surfaces. A general description of heterogeneous interactions of gases with solid surfaces will be given as well in chapter 2.4. As some knowledge of the dynamics and transport processes in the lower atmosphere (the Planetary Boundary Layer) is urgently required to distinguish between chemical and purely physical source ascertainment, we will also give a brief introduction to these topics in chapter 2.5.

In the experimental section of chapter 3, we will present the different measurement techniques used to date for the detection of HONO in the ambient air, which will justify the use of the DOAS technique for our studies. The specific setup of the DOAS long path and multi-reflection White system will be explained, along with the details of the evaluation procedure for deriving nitrous acid concentrations from the raw spectra.

An in-detail description of the field campaigns of this thesis will be addressed in chapter 4. This includes qualitative discussions of the trace gas time series, meteorological parameters, and further accompanying in-situ measurements. For the Rome 2001 campaign, the quality assurance for detected daytime HONO, its dependence on the vertical transport in the PBL, and its contribution to the photochemical smog events will be shown. An intercomparison of in situ monitors with the DOAS system was performed during the Milan 2002 field studies. HONO and NO_2 gradients were measured during the Turm 2003 project. A qualitative discussion including chemical formation, removal, and physical transport effects will finally be presented in chapter 4.

The setup and the characterization of the smog chamber, as well of the different real urban surfaces analyzed in these laboratory studies, will be described in chapter 5. We will present the basic analysis thus far applied to these types of experiments, and also show their limitations with respect to the performance of our experimental procedure. This will lead to the new "HeCSI" model, developed in this thesis, which describes the time series of trace gases in the smog chamber, based on simple physical-chemical assumptions.

The therein derived new description of interaction of gaseous species with a heterogeneous surface and the corresponding rate constants will be implemented in the discussion of the daytime HONO levels in chapter 6. A recently developed model, combining effects of vertical transport as well as boundary layer chemistry in a new approach, will be applied to our data. We will show that its description of the atmosphere is valid to quantify the contribution of different sources and removal processes yielding or destroying HONO during the day.

The results of this thesis will be summarized in chapter 7, after which an outlook to further required work will finally be given.

2 Theoretical Background: Chemistry and Physics of the Lower Troposphere

Scientific research on atmospheric chemistry, and especially such key words as “Acid Rain”, “Ozone Hole”, “Greenhouse Effect”, “Global Warming”, and “Summer Smog” became more and more well known, even to public interest, during the past years. These processes are all either directly or even indirectly linked to the oxides of nitrogen (for an overview see e.g. [Finlayson-Pitts and Pitts, 2000; Seinfeld and Pandis, 1998]).

The explanation of the huge ozone loss occurring in polar spring in the Arctic and the Antarctic regions (known as the “Ozone Hole”) was even honored by a Nobel Prize. It could be shown that in the stratosphere, NO and NO₂, formed by reactions of N₂O [Crutzen, 1970] or NO_x emitted directly into the stratosphere, [Johnston, 1971] both directly destroy the earth's stratospheric UV protection shield of ozone. However, the nitrogen compounds also act as a reservoir for ozone-destroying halogeneous compounds [Farman *et al.*, 1985], which get released from chlorofluorocarbons (CFCs).

In the troposphere, the lower part of the atmosphere, nitrogen oxides play a central role in essentially all facets of atmospheric chemistry as well. From the beginning of the industrial revolution and thus man-made (anthropogenic) emissions of trace gases to the atmosphere, acid rain was observed in both rural as well as urban areas. It could be shown that e.g. the forest dieback or the damage to historic monuments are a direct consequence of these emissions. At this time, the acid rain was mainly caused by sulfuric acid generated from SO₂ in industrial emissions, and organic acids. The so-called “London” smog as a consequence of high concentrations of SO₂ and particulate matter (“smoke”) in the presence of dense fog and low inversions was also observed. However, emissions characteristics have changed since that time especially in Europe and nowadays, acid deposition is mainly due to nitric acid (HNO₃), the final oxidized form of all nitrogen oxides (see chapter 2.1.1, and 2.1.2).

Additionally, in the late 1940's, a new type of air pollution phenomenon was observed in the area of Los Angeles / USA. Here, the ambient air contained strongly oxidizing, eye-watering and plant-killing pollutants – especially on hot days with bright sunshine. Plant pathologists at the University of California, Riverside, observed a unique type of damage to agricultural crops in areas of the Los Angeles basin impacted by this “plague” and reported it to be an entirely new form of air pollution: the so-called “Los Angeles smog” or photosmog [Middleton *et al.*, 1950]. By the performance of studies in laboratory environments shortly thereafter in the early 1950's, these plant damage symptoms were ascribed to high concentrations of ozone. It was shown that this ozone formation is caused by nitrogen oxides, which undergo several reactions on the oxidizing troposphere. Their photolysis in the presence of hydrocarbons (HC) or other volatile organic compounds (VOCs), which occur in polluted air originating from e.g. auto exhaust, underwent a complex reaction system and finally formed the high concentrations of ozone as well as other atmospheric pollutants (see chapter 2.2.1, and 2.2.2).

Since then, high ozone levels have been measured throughout the world, e.g. Athens (Greece), Sydney (Australia), and Mexico City (Mexico) with ozone mixing ratios of up to 400 ppb.

Although photochemical air pollution was first recognized in the Los Angeles area, it is now known as a world wide problem in areas where volatile organic compounds (VOC) and NO_x emissions from major mobile and stationary sources are "trapped" by thermal inversions and irradiated by sunlight during transport to downwind regions.

In ozone formation, the key role is played by the so-called hydroxyl radical (OH), which is the most important oxidizing species in the daytime atmosphere (see chapter 2.2.3 and reviews e.g. by [Crutzen and Zimmermann, 1991; Logan, 1983; Logan *et al.*, 1981]). One oxide of nitrogen is nitrous acid (see chapter 2.3); an important and under some circumstances even the dominant [Alicke, 2000; Alicke *et al.*, 2003; Alicke *et al.*, 2002] precursor of these OH-radicals.

Despite the fact that the impact of nitrous acid (HONO) on these phenomenons is well known to impact (see chapter 2.3.7), its origin in tropospheric air masses, especially the contribution of the different possible sources (see chapters 2.3.3, 2.3.4, and 2.3.5) of HONO is still not clear. As a heterogeneous formation is accepted to be the most likely source (see chapter 2.3.5), we will also give a brief overview of possible heterogeneous interactions of gases with surfaces (see chapter 2.4). However atmospheric transport processes might also strongly influence both the distribution of HONO in the Planetary Boundary Layer (see chapter 2.5) as well as its observed concentrations (see chapter 4, and 6), and thus will be briefly described in chapters 2.5.1, 2.5.2, 2.5.3, and 2.5.4.

2.1 Tropospheric Nitrogen Oxides

Nitrogen oxides generally all belong to the group of substrates with a nitrogen-oxygen bonding summarized by the formula of N_nO_m (whereas n and m respectively are natural numbers). The most important atmospheric nitrogen oxides are merged to NO_x = NO + NO₂. Finally, all reactive atmospheric trace gases are often referred to as nitrogen oxides NO_y where NO_y = (NO + NO₂ + HNO₃ + PAN³ + HONO + NO₃ + N₂O₅ + organic nitrates etc.). These atmospheric NO_y all mainly originate in NO, which is primarily emitted into the atmosphere from biogenic but also anthropogenic sources. By the tropospheric oxidation processes, NO is then converted into higher oxidized nitrogen oxide forms. However NO can also be recycled by photolytic decomposition of the higher oxides (e.g. NO₂) during the day, yielding a photo-stationary steady state between NO, NO₂ and ozone. This so-called Leighton ratio, which can be established quickly during daytime, is further influenced by the oxidation of VOCs (volatile organic compounds), and by free radicals (mainly the hydroxyl radical OH). Especially during meteorological situations typical for summer conditions with high solar radiation and small vertical mixing (inversion), this system becomes self-amplifying. Thus high mixing ratios of ozone and other pollutants might occur. Above a certain threshold, this is called summer smog.

2.1.1 Sources and Sinks of Tropospheric Nitrogen Oxides

The discussion of atmospheric nitrogen oxide chemistry needs to include factors such as location, magnitude and type of emission. Several reviews have been published on the balancing of sources and sinks of tropospheric NO_x since e.g. [Logan, 1983]. However, to extrapolate emission data, which were achieved from a ground-based measurement network, to global scale requires great effort and statistical uncertainties remain large. Nowadays, satellite measurements [Beierle *et al.*, 2003; Leue *et al.*, 2001; Wagner *et al.*, 2002b] allow an

³ PAN = peroxyacetyl nitrate = CH₃C(O)OONO₂

independent approach to determine trace gas emissions directly on a global scale. The entire globe is monitored with a single instrument under the same conditions and over long periods of time. A six-year mean (1996 - 2001) of tropospheric NO₂ is shown in figure 2.1 (adapted from [Beierle *et al.*, 2003]). The locations of enhanced NO₂ levels are often correlated with industrial areas, and therefore, anthropogenic sources.

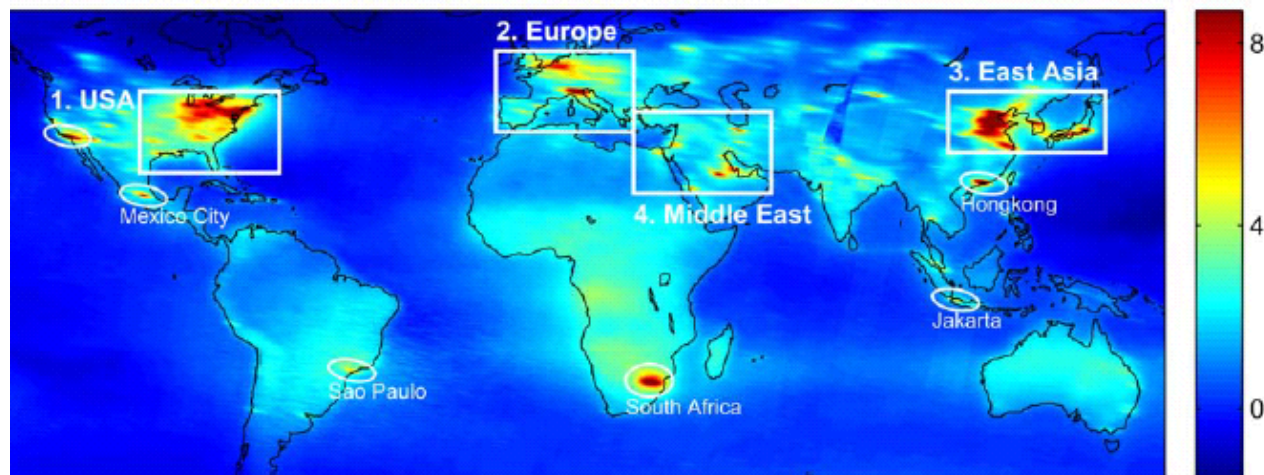


figure 2.1: Six years mean (1996 - 2001) of global tropospheric NO₂ Vertical Column Density in 10^{15} molecules cm^{-2} (see scale on the right). The cycle of the framed areas correspond to the heavily pollute areas of 1. US East Coast, 2. Europe, 3. East Asia and 4. Middle East, and 5. some individual metropolises (taken from [Beierle *et al.*, 2003]).

However, a distinctive source quantification of tropospheric trace gas emissions is thus far only possible from ground-based measurements. For the USA as the country with the highest pollution among all western-industrial countries (see figure 2.1), the trends of increase of emissions of NO_x can be seen in table 2.1, recently published by the Environmental Protection Agency [EPA, 2002]. These data (see also figure 2.2) confirm results by [Hammeed and Dignon, 1992], who found an increase of the anthropogenic sources of nitrogen oxides by about 350 % since 1983. However, other species, such as particle matters (PM 10 and PM 2.5) and VOCs remain at constant levels. SO₂ and CO even decrease since the introduction of catalytic converters to industrial engineering processes [EPA, 2002].

As can be seen in table 2.1 and figure 2.2, about three-quarters of the tropospheric nitrogen oxides are generated anthropogenically, mainly by fossil fuel burning. The figure 2.3 quantifies the different anthropogenic NO_x sources: the largest sources are road traffic and electrical utility fuel combustion, each with a contribution to the total anthropogenic NO_x of nearly one third. It is noteworthy in this context that heavy trucks and vehicles without a catalytic converter have the strongest influence on traffic emissions [Kessler, 1984]. Laboratory studies indicate that the ratio of 0.6 % NO_x in these exhaust gases directly correspond to the chemical balance between N₂, O₂ and NO at a typical combustion temperature of 2500 K [Zeldovich *et al.*, 1946]:



However, a three-way catalytic converter of the EURO II norm is known to reduce the emissions of nitrogen oxides to one tenth [BMBF, 1996].

It is important to mention that the largest contribution to anthropogenic NO_x (typically > 90 %) is emitted as NO. The direct contribution of NO_2 can vary between 1 and 30 % [Lenner, 1987; Lenner *et al.*, 1983].

Source Category	1940	1950	1960	1970	1980	1990	1996	1998
FUEL COMB. ELEC. UTIL.	660	1,316	2,538	4,000	7,024	6,663	6,057	6,103
Coal	467	1,118	2,038	3,888	6,123	5,642	5,542	5,306
Oil	256	584	1,154	2,112	3,439	4,532	3,748	3,622
Gas	198	198	498	1,012	901	221	103	208
residual	6	29	9	40	39	207	101	206
distillate	187	175	489	972	862	14	2	2
natural	NA	NA	NA	NA	NA	565	265	344
natural gas	NA	NA	NA	NA	NA	565	264	342
FUEL COMB. INDUSTRIAL	2,543	3,192	4,075	4,325	3,555	3,075	3,072	2,969
Coal	2,012	1,076	762	771	444	585	567	548
Oil	122	297	239	352	266	265	231	216
Gas	365	1,756	2,954	3,060	2,619	1,182	1,164	1,154
natural	337	1,692	2,945	3,053	2,469	957	978	943
Internal Combustion	NA	NA	NA	NA	NA	874	967	932
FUEL COMB. OTHER	529	647	760	836	741	1,196	1,224	1,117
Commercial/Institutional Gas	7	18	55	120	131	200	238	234
Residential Other	177	227	362	439	356	790	763	700
natural gas	20	50	149	242	239	449	481	410
CHEMICAL & ALLIED PRODUCT MFG	6	63	110	271	213	168	146	152
METALS PROCESSING	4	110	110	77	65	97	87	88
PETROLEUM & RELATED INDUSTRIES	105	110	220	240	72	153	134	178
OTHER INDUSTRIAL PROCESSES	107	93	131	187	205	378	386	408
Mineral Products	106	89	123	169	181	270	286	303
cement mfg	32	55	79	97	99	151	172	182
SOLVENT UTILIZATION	NA	NA	NA	NA	NA	1	2	2
STORAGE & TRANSPORT	NA	NA	NA	NA	NA	3	7	7
WASTE DISPOSAL & RECYCLING	110	215	331	440	111	91	95	97
ON-ROAD VEHICLES	1,330	2,143	3,982	7,300	8,621	7,099	7,949	7,765
Light-Duty Gas Vehicles & Motorcycles	970	1,415	2,607	4,158	4,421	3,220	2,979	2,849
light-duty gas vehicles	970	1,415	2,606	4,156	4,416	3,208	2,967	2,857
Light-Duty Gas Trucks	204	339	525	1,278	1,408	1,256	1,950	1,917
light-duty gas trucks 1	132	219	339	725	864	754	1,156	1,132
light-duty gas trucks 2	73	120	186	553	544	472	794	785
Heavy-Duty Gas Vehicles	156	295	363	278	300	326	329	323
Diesels	NA	93	467	1,676	2,493	2,287	2,591	2,676
heavy-duty diesel vehicles	NA	93	467	1,676	2,463	2,240	2,544	2,630
NON-ROAD ENGINES AND VEHICLES	991	1,538	1,443	1,971	3,529	4,804	5,167	5,280
Non-Road Gasoline	122	249	312	85	101	120	132	159
Non-Road Diesel	103	187	247	1,109	2,125	2,513	2,786	2,806
construction	70	158	157	436	843	1,102	1,218	1,230
farm	33	29	50	350	926	898	1,001	999
Aircraft	NA	2	4	72	106	158	167	168
Marine Vessels	109	108	106	171	467	943	985	1,008
Railroads	657	992	772	495	731	929	922	947
MISCELLANEOUS	990	665	441	330	248	369	452	328
TOTAL ALL SOURCES	7,374	10,093	14,140	20,025	24,384	24,049	24,876	24,454

Notes: NA = not available. For several source categories, emissions either prior to or beginning with 1995 are not available at the more detailed level but are contained in the more aggregate estimate.
 Other categories may contain emissions that could not be accurately allocated to specific source categories.
 In order to convert emissions to gigagrams (thousand metric tons), multiply the above values by 0.0072.

table 2.1: National emission trends in the USA for nitrogen oxides 1940 through 1998 in thousand short tons [EPA, 2002].

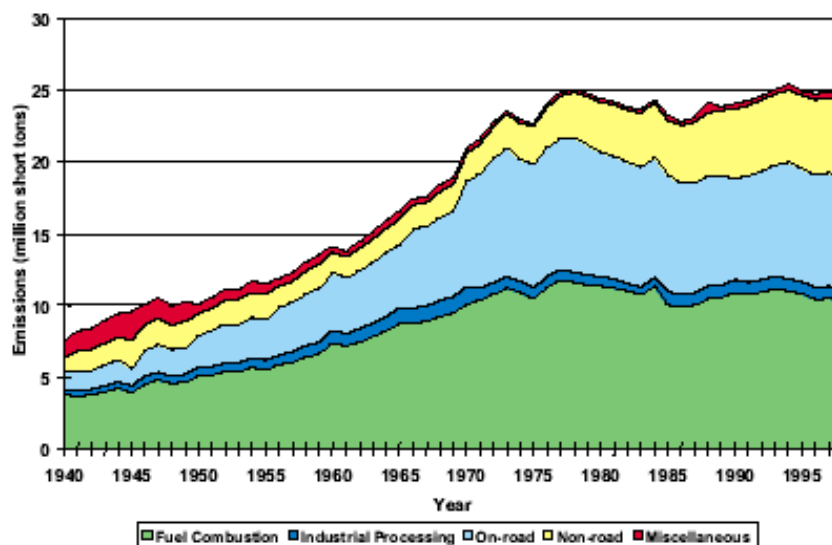


figure 2.2: Trend of anthropogenic emissions of nitrogen oxides in the USA from 1940 through 1996 in million short tons [EPA, 2002].

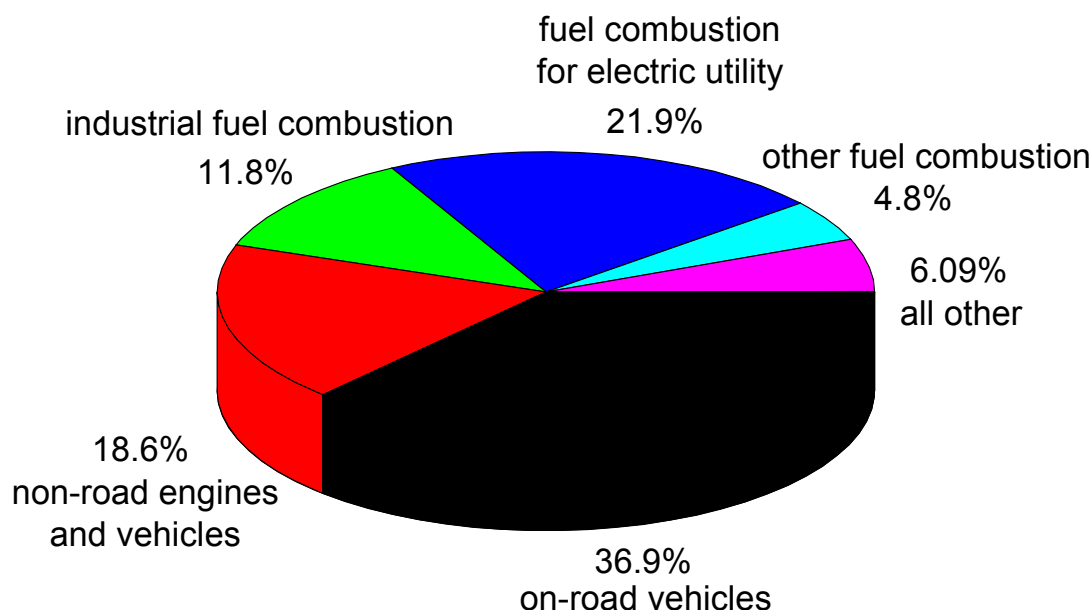


figure 2.3: Contribution of various sources to total anthropogenic NO_x emissions in the United States in 2002 [EPA, 2002].

Sources of nitrogen oxides are not only located in urban and suburban areas, but also e.g. in the tropics, where biomass burning as well as the soils themselves are the main sources of NO_x , and also nitric acid. Biomass burning is either anthropogenic or a natural source. Thereby, nitrification, denitrification, and the decomposition of nitrite (NO_2^-) contribute to NO production [EPA, 2002].

Several further natural sources of NO_x exist. Among them, the production by lightning contributes most, approximately 10 – 33 Tg / yr [Flatoy and Hov, 1997; Levy et al., 1996; Price et al., 1997a; Price et al., 1997b]. Some bacteria in the ground are also known to produce NO_x in significant amounts. As yet, this source has not been well quantified, but estimations are in the order of ~ 18 % of the total NO_x emissions. Finally, the oxidation of NH_3 by photochemical processes in oceans and by some terrestrial plants also yields small amounts of NO [Wayne et al., 2002; Wild et al., 1997]. To illustrate this close link between ammonia and NO source distribution, the total emission density of NO , its biogenic sources, as well as precursors, such as biogenic emitted VOCs and biogenic emitted ammonia are plotted in figure 2.4 by the [EPA, 2002] for emissions in 1998 in the USA in million short tons per country.

Finally, oxygen atoms $\text{O}^1(\text{D})$, which were produced photolytically ($\lambda \leq 310$ nm, [DeMore et al., 1997]) in the stratosphere, can directly yield NO by the reaction with N_2O (“laughing gas”). Its main sources are biological and, to a lesser extent, anthropogenic processes. While biomass burning is the major anthropogenic source, there are a variety of smaller sources, including motor vehicles. Interestingly, N_2O emissions from current cars with catalytic converters appear to be higher than from vehicles that are not equipped with a catalyst [Berges et al., 1993], while total NO_x emissions of catalyst-equipped cars are much lower. N_2O is inert in the troposphere and is ultimately transported to the stratosphere, where it acts as a major source of NO_x . Model calculations by [Levy and Mahlman, 1980; Levy et al., 1980], including the stratosphere-troposphere exchange, showed that this source contributes to only about 0.5 % of the total tropospheric NO source strength, but it is nevertheless the most important NO source for the stratosphere.

The sinks of nitrogen are primarily dry or wet deposition of nitric acid (HNO_3 or HONO_2). As a consequence of several chemical reactions in the atmosphere (see chapter 2.1.2), NO_x is

transformed to water-soluble species like nitric acid or nitrous acid (HONO), which are washed out of the atmosphere by rain (wet deposition) and are therefore a major constituent of acid rain. The dry deposition consists of agglomeration on aerosols and the ground, and possibly some chemical reactions. The dry deposition of the “sticky” HNO₃ molecule by adsorption on aerosols and the ground has been quantified to be responsible for between 16 % and 40 % of the total nitrogen flux to the surface by [Russell *et al.*, 1993] and [Nielsen *et al.*, 1996], respectively.

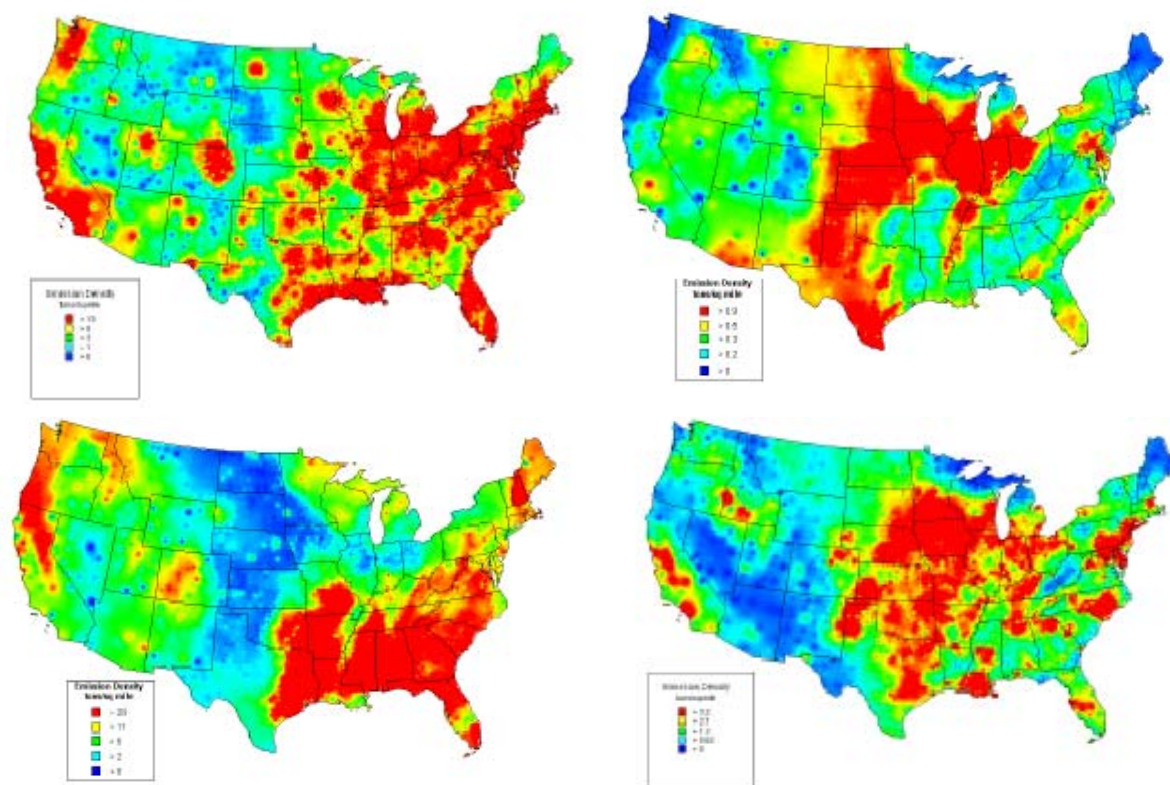


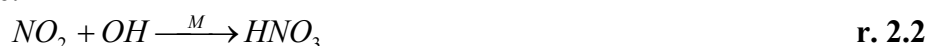
figure 2.4: Emission density in 1998 in the USA [EPA, 2002]: Upper left map: total NO emissions, upper right: biogenic NO emissions. Lower left: biogenic VOC emissions, lower right: biogenic ammonia emissions.

However, several chemical reactions are needed to transform the NO_x into the higher oxidized form of nitric acid for all the physical removal processes described above.

Nitric acid is formed in most of the reactions yielding HONO (as will be described in chapter 2.3) in equal stoichiometric amounts. Thus, for an exact quantitative analysis of the atmospheric formation of nitrous acid, it is necessary to take nitric acid into account as well. Unfortunately, HNO₃ is not only rapidly removed from the gas phase, but also difficult to measure. Usually the denuder technique, chromatography, FTIR spectroscopy or IR-diode-lasers are used to measure HNO₃ (see chapter 3). In contrast to HONO, HNO₃ is not only observed in urban areas, but also in the clean atmosphere. Nitric acid is more stable with respect to chemical decomposition and photolysis is weaker: resulting in a high lifetime of approx. 16-17 d at SZA = 0°. HNO₃ is removed from the atmosphere highly efficiently and faster than calculated from photolysis [Shaw, 1984] due to dry and especially wet deposition, or agglomeration on aerosols, which are subsequent deposits.

Except for reactions of HONO formation (these will be discussed in detail in chapter 2.3), two main reactions yield HNO₃. Among these, the homogeneous recombination of nitrogen

dioxide with the hydroxyl radical is the most important, and directly yields nitric acid in the atmospheric gas phase:



$$\text{with } k_{r.2.2} = 8.7 \times 10^{-12} \text{ cm}^3 \text{ molec}^{-1} \text{ s}^{-1} \text{ [DeMore et al., 2003]}^4$$

Assuming an average OH concentration of $2 \times 10^6 \text{ molec cm}^{-3}$ [Ehhalt et al., 1994], the lifetime of NO_2 results only in approx. 8 hours during daytime. Other reactions occur, especially during the night via the anhydride of the nitric acid, N_2O_5 , which is believed to play a significant role in tropospheric chemistry [Finlayson-Pitts and Pitts, 2000]. N_2O_5 is produced by NO_2 and NO_3 . We will not discuss the NO_3 chemistry in this thesis (for a summary refer to e.g. [Geyer, 2000]), but only introduce its formation of NO_3 from NO_2 and O_3 , representing another possible NO_2 (and thereby NO_x) sink:



$$\text{with } k_{r.2.3} = 3.2 \times 10^{-17} \text{ cm}^3 \text{ molec}^{-1} \text{ s}^{-1} \text{ [DeMore et al., 2003]}^4$$

Even though the rate coefficient of this reaction at 298 K is relatively small, reaction r. 2.3 cannot be neglected in areas featuring high O_3 concentrations in the evening hours and at night. Assuming 100 ppb of O_3 , which is still near or below the air quality standards of most countries, the lifetime of NO_2 with respect to O_3 is only 3.5 h [Finlayson-Pitts and Pitts, 2000]. Further, the NO_3 reacts with NO_2 in a temperature dependent equilibrium forming N_2O_5 via:



The temperature dependence for this equilibrium was suggested as $K_{\text{eq}}(T) = \exp(-60.46 + 10724 / T)$ [Wängberg et al., 1997]. Using the measured concentrations of NO_2 and NO_3 and the equilibrium constant for the N_2O_5 source reaction r. 2.4 of $K_{\text{eq}} = 2.9 \times 10^{-11} \text{ cm}^3 \text{ molec}^{-1}$, peak mixing ratios of N_2O_5 up to about 10 – 15 ppb in a polluted atmosphere have been calculated [Atkinson et al., 1986].

Beside the deposition onto surfaces, the major sink of N_2O_5 in the troposphere appears to be homogeneous or heterogeneous hydrolysis and subsequent dry or wet deposition.:



[Mentel et al., 1996; Wahner et al., 1998b] suggest that this reaction is both first and a second order in water. There are currently some uncertainty concerning the value of the rate constant and its order with respect to water [DeMore et al., 2003].

[Dentener and Crutzen, 1993] predicted that in the northern hemisphere, more than a half and up to 90 % of the HNO_3 formation occurs by reaction r. 2.5, and r. 2.6 and the adsorption of NO_3 on wet surfaces. Therefore, N_2O_5 has to be seen as a major sink of nitrogen oxides in the polluted troposphere as discussed in detail by [Geyer et al., 2001a; Geyer et al., 2003b].

Further HNO_3 formation reactions e.g. the reaction of NO_3 and aldehydes [Morris and Niki, 1974] or alkenes [Hoshino et al., 1978] or with Dimethylsulfide (DMS) in the marine boundary layer are discussed by [Geyer, 2000; Geyer et al., 2001a; Geyer et al., 2003b].

2.1.2 Overview of Tropospheric NO_y Chemistry

Before we discuss the sources and sinks as well as the atmospheric reactions of nitrous acid, in detail, a brief overview of NO_y -chemistry in the troposphere is given by figure 2.5.

⁴ The following rate constants are upper limits, since they are temperature and pressure dependent. This dependence will be explained in detail in chapter 2.4, and with respect to HONO reactions in chapter 2.3.4.

It can easily be seen that the central role is played by NO_x , which is primarily emitted in the form of NO (see chapter 2.1.1), and represents the “basic material” for most other nitrogen oxides. A small part of NO_y is directly emitted as nitrous acid. The N_2O was already mentioned to be inert with respect to tropospheric oxidation chemistry. It undergoes no further reactions, but is completely transported into the stratosphere. Nitrogen monoxide is in a photo-stationary steady state with NO_2 via ozone (see chapter 2.2). The reaction of NO_2 and O_3 forms the most important nighttime radical NO_3 (see [Geyer, 2000]). The nitrate radical further forms N_2O_5 in the presence of NO_2 very quickly. N_2O_5 subsequently reacts on wet surfaces to form HNO_3 . Almost 90 % of the nitrogen oxides are deposited from the troposphere by these production pathways (see chapter 2.1.1). Wet deposition of nitric acid is the most important sink for NO_x and is part of the acidic rain phenomenon. Recently, a review of the atmospheric chemistry of NO_x with special respect to its interactions with VOCs has been carried out [Atkinson, 2000].

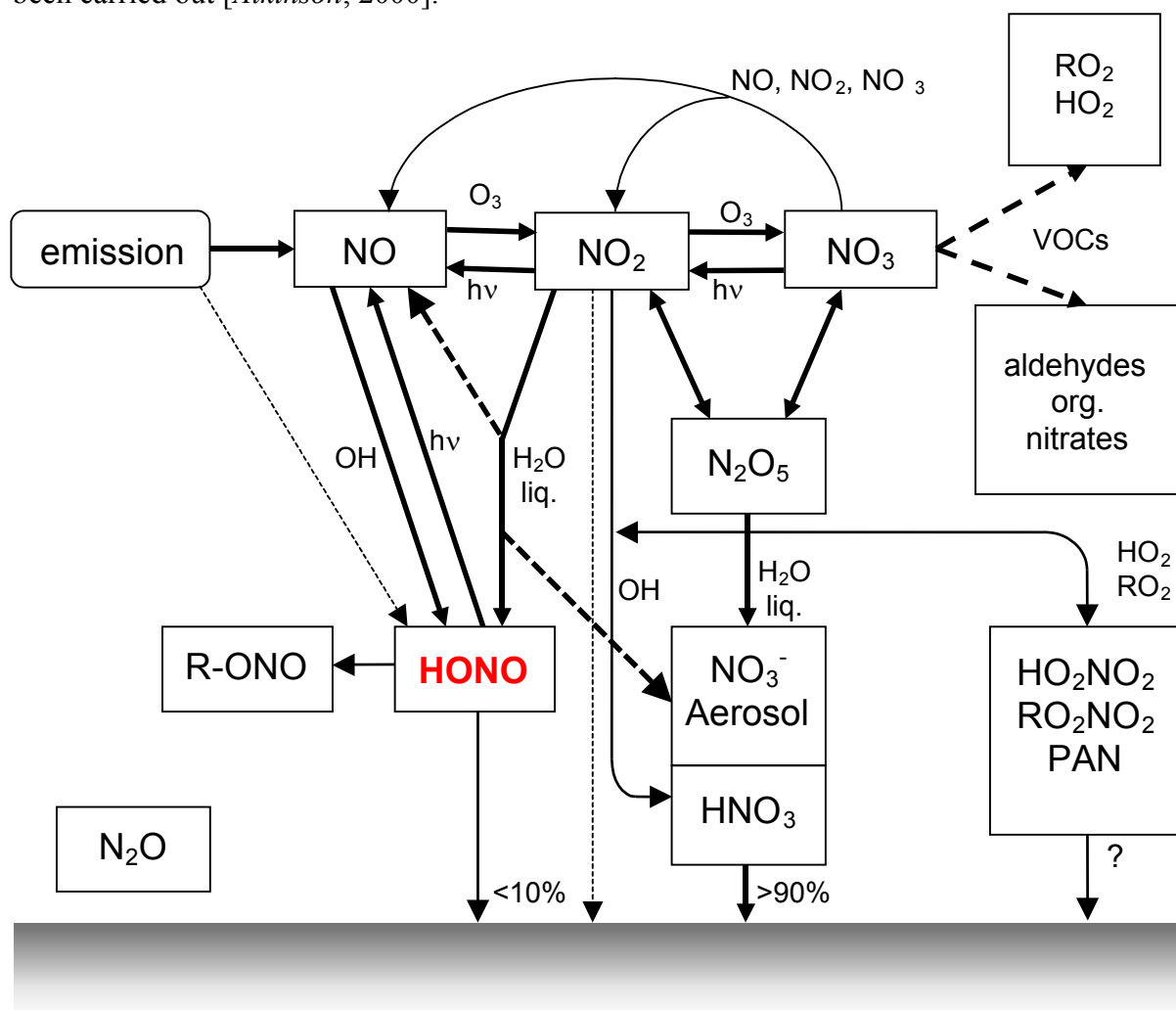


figure 2.5: Overview of the tropospheric nitrogen oxides chemistry.

Nitrous acid (HONO) is mainly formed by the reaction of NO_2 with (liquid) water (see 2.3). HONO is then photolyzed during the day to form NO and the hydroxyl radical OH , which is part of virtually all reactions in daytime chemistry of polluted air masses.

2.2 Photochemical Reactions

2.2.1 The Photo-Stationary Steady State & Leighton Ratio

We have already mentioned in chapter 2.1.2 (see also figure 2.5) that the primary emitted NO is in a steady state with NO₂ involving O₃ as well. This is true for a hypothetical “free” atmosphere containing only those components but no organics (VOCs). Under these circumstances, the concentration ratio of O₃, NO and NO₂ should be a constant as described by the self-contained reaction cycle⁵ of:



Thus a so-called photo-stationary steady state of the NO_x is established, referred to as Leighton ratio [Leighton, 1961] (named after Philip Leighton, who wrote the first definitive monograph on air pollution in 1961). Using the rate constants of $k_{r.2.7} = 1.8 \times 10^{-14} \text{ cm}^3 \text{ molec}^{-1} \text{ s}^{-1}$ for the reaction of NO with O₃ and J_1 for photolysis of NO₂ respectively this ratio can be quantified to be:

$$\frac{[O_3] \cdot [NO_2]}{[NO]} = \frac{k_3}{J_1} \quad \text{resp.} \quad \frac{[NO_2]}{[NO]} = [O_3] \cdot \frac{k_3}{J_1} \quad \text{eq. 2.1}$$

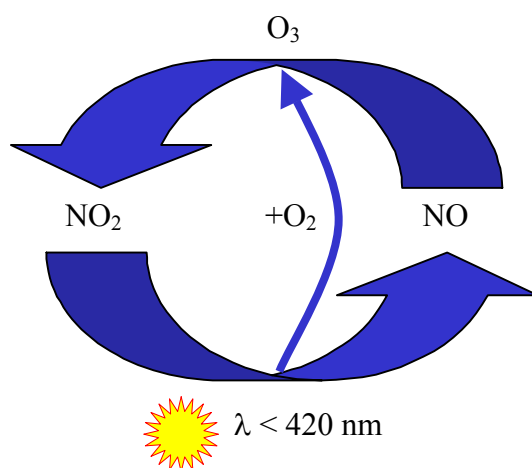


figure 2.6: Schematic summary of the reactions r. 2.7, r. 2.8, and r. 2.9 yielding the photo-stationary steady state of NO_x in the absence of VOCs.

We have already mentioned that the net ozone production by the reactions r. 2.7, r. 2.8, and r. 2.9 above is zero. However the sum of both concentrations, O₃ and NO₂, should be constant as long as the concentrations of NO, NO₂ and O₃ are well-described by the Leighton ratio:

$$O_x = [NO_2] + [O_3] = \text{const.} \quad \text{eq. 2.2}$$

Any deviations from the zero cycle, and especially periods of enhanced photochemistry yielding the photosmog phenomenon can be identified as an increase in the O_x sum.

⁵ In such a reaction cycle net production and net loss of any species are zero

2.2.2 Deviations from the Leighton Ratio & the Formation of Photosmog

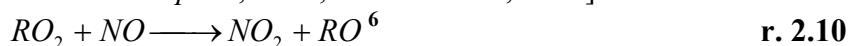
In general, the Leighton relationship is only valid when reactions r. 2.7, r. 2.8, and r. 2.9 are the major loss processes for NO₂ and O₃, respectively (reaction r. 2.8 is essentially always the loss process for O(³P)). In addition to deviations of the Leighton ratio due to VOCs (see below), further parameters disturb the Leighton relationship or limit its applications.

First, the photolysis frequency of NO₂ obviously changes due to the solar zenith angle (SZA), thus the ratio varies during the day. At sunset and sunrise, the rate of photolysis of NO₂ via r. 2.7 is sufficiently small. Under these circumstances, steady-state assumptions are not valid [Calvert and Stockwell, 1983].

Next, non-chemical loss processes as well as fluxes of NO from the surface and micrometeorological effects also perturb the Leighton ratio [Carroll and Thompson, 1995].

Further, derivations of the pure Leighton ratio can also occur when sinks of O₃ other than reaction r. 2.9 become significant. These additional loss processes may include photolysis of ozone, which again increases with the SZA during daytime, as well as reactions with NO₂, alkenes, and the radicals HO₂ and OH.

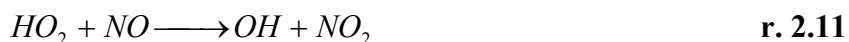
Finally, in the presence of further oxidizing species, NO can be converted to NO₂ by reactions other than r. 2.9 [Carroll and Thompson, 1995; Parrish et al., 1986]:



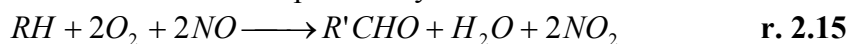
Consequently, no ozone is consumed for the NO oxidation and the O_x is no longer constant, but increases. The photolysis of these NO₂ molecules gained by the reactions r. 2.10, and r. 2.11 yields a net production of O₃. Taking into account the reactions r. 2.10, and r. 2.11 of NO with RO₂ and HO₂ producing NO₂, the description of the balance of NO, NO₂ and O₃ by eq. 2.1 becomes:

$$\frac{[NO_2]}{[NO]} = \frac{1}{J_{(R,1)}} \cdot \left\{ k_{(R,3)} \cdot [O_3] + k_{(R,11)} \cdot [HO_2] + \sum_{RO_2} k_{(R,9)} \cdot [RO_2] \right\} \quad \text{eq. 2.3}$$

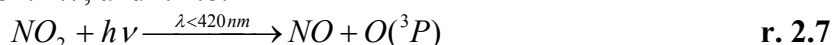
The peroxy-radicals (RO₂) and hydroxyl-radicals (HO₂) originate in the oxidation of the volatile organic compounds (VOCs). Therefore, the most likely oxidant is the prominent OH radical and the common scheme of the oxidation of one hydrocarbon (RH) in the troposphere can now be described as:



The overall scheme for reactions above is expressed by:



This scheme can be applied until the initial VOC is transformed to CO₂ (or CO and H₂O), finally followed by the photolysis of NO₂ yielding a NO and the recombination of O(³P) described by reactions r. 2.7, and r. 2.8:



Thus, a net ozone production is observed finally as described by the over-all scheme:



⁶ Here, "R" represents an organic (VOC) molecule without its functional group.

This reaction scheme is illustrated by figure 2.7. The lower cycle depicts the undisturbed stationary state without O_3 net production as already presented by figure 2.6: by the oxidation of “combustible” VOCs (green half-cycle on top), a second cycle (red cycle in the middle) is initialized. Within, oxidizing radicals undergo the reactions summarized by r. 2.15, but feed back to the lowest (blue) cycle and convert NO to NO_2 without O_3 consumption. Thus, a net source of ozone is finally established.

However, especially in summer, with high solar radiation and a simultaneous ground inversion, a self-amplification of the system can occur, yielding high concentrations of ozone and other pollutants. The final remaining question is the origin of the introduced OH radicals, which initialize the oxidation of the VOCs, as shown above.

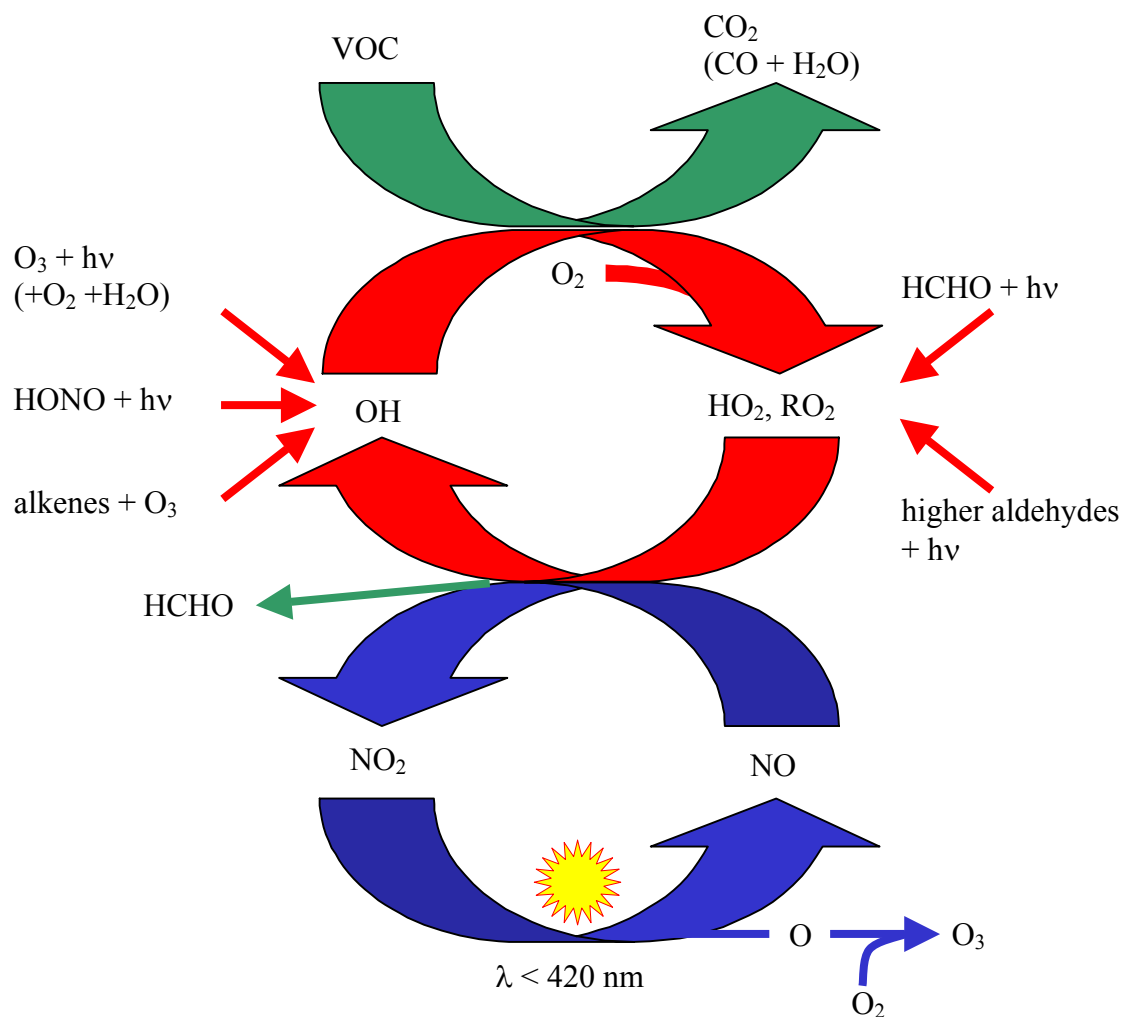


figure 2.7: Reaction cycles of tropospheric nitrogen oxides and ozone with the impact of RO_x . Ozone is formed in the presence of RO_x , NO_x and sunlight. Note that $HONO$ photolysis is one of the pathways forming OH and thereby O_3 .

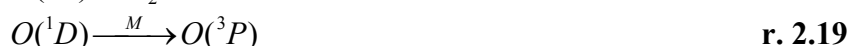
2.2.3 The Origin of the Tropospheric OH Radicals

The OH -radical is accepted to be the most important oxidizing species in the daytime atmosphere (see e.g. review by [Crutzen and Zimmermann, 1991]), and often referred to as “detergent of the atmosphere”. Ozone formation in both polluted and clean areas is based on this central compound. Peak daytime hydroxyl radical concentrations in the range of $(2 - 10) \cdot 10^6 \text{ molec cm}^{-3}$ have been measured at ground levels at mid-latitudes during summer

[*Brauers et al.*, 1996; *Eisele et al.*, 1997; *Hofzumahaus et al.*, 1998; *Holland et al.*, 1998; *Holland et al.*, 1995; *Holland et al.*, 2001]. A diurnally and annually averaged global mean tropospheric OH concentration of $0.7 - 1.0 \times 10^6$ molec cm^{-3} has been estimated [*Crutzen and Zimmermann*, 1991; *Prinn et al.*, 1995].

A summary, comparison, but also a quantification of different OH-radical production mechanisms was recently carried out by [*Alicke*, 2000] in detail. Here we will give a brief overview of the major tropospheric formation pathways, as their quantification is essential for the understanding of tropospheric chemistry, the ozone budget, and especially the impact of daytime nitrous acid on both.

For a long time, the production from excited $\text{O}(^1\text{D})$ atoms via the photolysis of O_3 at wavelengths below 320 nm (reaction r. 2.17) was believed to be not only the major but also the only relevant source of OH-radicals. This is still essentially true on a global scale [*Crutzen and Zimmermann*, 1991; *Logan et al.*, 1981]. The $\text{O}(^1\text{D})$ atoms subsequently react with water vapor to produce OH radicals directly (r. 2.18) or be quenched by air molecules



The branching ratio of reactions r. 2.18, and r. 2.19 depends on the concentration of H_2O in ambient air and therefore also on the temperature. For example, at 50 % relative humidity and 300 K at the earth's surface, about 10 % of the $\text{O}(^1\text{D})$ generates OH. The over-all efficiency of this reaction was found to be about 5 to 20 %. Generally, photolysis of ozone starts late in the morning reaching a maximum around noon. [*Alicke*, 2000] quantified the contributions of the different OH-radical production mechanisms: depending on the composition of the atmosphere, ozone photolysis was found to be a dominant source, responsible for 45 – 55 % of the daily OH production in remote or even semi-polluted regions with low NO_x and VOC, while only 15 – 30 % of the OH-radicals originated from the ozone photolysis in polluted areas [*Alicke*, 2000].

Especially in highly polluted (urban) areas, the photolysis of formaldehyde contributes to approx. 30 % to the total OH-production [*Alicke*, 2000]. The HCHO photolysis at wavelengths below 370 nm [*Ehhalt et al.*, 1998; *Fried et al.*, 1997; *Kleinman et al.*, 1995; *Meller and Moortgat*, 2000] yields HO_2 , which is rapidly converted to OH in the presence of NO:



Higher aldehydes produce OH and HO_2 radicals as well by analogous decomposition channels as described above. Due to the small photolysis frequencies, this mechanism only becomes important in heavily polluted areas with high concentrations of the corresponding aldehyde [*Alicke*, 2000].

Obviously, the importance of the OH-production mechanism also depends on solar radiation and therefore the time of day. The photolysis of other species yielding OH-radicals, such as HCHO and HONO, starts earlier in the morning, due to their lower dissociation energy thresholds.

We will discuss the nitrous acid and its atmospheric trends in detail in chapter 2.3. Generally, HONO accumulates during the night and high values are often reached before sunrise. Due to photolysis starting at 405 nm the raised HONO concentrations are rapidly converted into NO and OH-radicals [*Stockwell and Calvert*, 1978; *Stutz et al.*, 2000]:



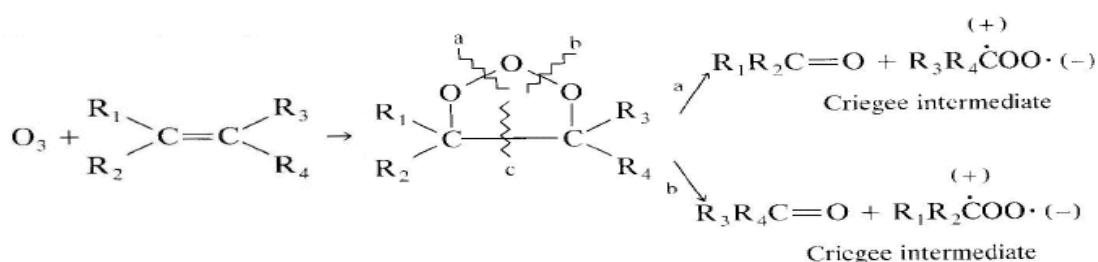
r. 2.24

The combination of high HONO concentrations at sunrise and the fast photolysis are expected to result in a peak in the production of OH, which can surpass the other sources.

Several studies, but mostly calculations about the impact of HONO photolysis on ozone production were carried out in the last decades. OH production rates were estimated in the range of $(0.1 - 3) \times 10^7$ molec $\text{cm}^{-3}\text{s}^{-1}$ for up to 8 ppb of nitrous acid in Los Angeles in the morning hours [Harris *et al.*, 1982; Sjödin, 1988]. Model studies showed strong evidence of an increase of OH-radicals and thus O_3 of approx. 10 and 10 – 55 %, respectively earlier in the morning due to HONO photolysis [Harris *et al.*, 1982; Harrison *et al.*, 1996; Jenkin *et al.*, 1988; Staffelbach *et al.*, 1997a; Staffelbach *et al.*, 1997b]. [Staffelbach *et al.*, 1997b] also showed that a constant HONO mixing ratio of 200 ppt in the whole boundary layer (formed at the surface or directly emitted) enhances the daily ozone maximum by 25 ppb.

However, an accurate experimental determination of the OH production due to HONO photolysis was first reported by [Alicke, 2000]. It was observed that the HONO photolysis in the morning could yield OH formation rates that are comparable to the total OH formation rates at noon. During the first 4 to 6 hours after sunrise HONO photolysis was by far the most important OH source in the lowest part of the troposphere. Contributions of 17 – 34% of the total OH formation, for the heavily polluted Milan / Italy region, but also 14 – 20% in the rural area of Pabstthum / Germany, and 22% at the semi-rural Nashville / USA were observed. Therefore, HONO photolysis is one of the most important, under certain conditions even the dominant, source of OH radicals in the polluted urban environment, and even in semi polluted areas its contribution is not negligible.

Another reaction involving ozone and yielding OH-radicals is the so-called ozonolysis of alkenes reacting with ozone [Atkinson and Aschmann, 1993; Atkinson *et al.*, 1992; Paulson *et al.*, 1997]. The mechanism of the ozonolysis is well known for liquid-phase chemistry, but the gas-phase reaction pathways are only poorly understood yet. However, the initial step in the reaction chain is accepted to be the addition of O_3 to the π -electrons system of the alkenes double bond. Via the so-called primary ozonoid (molooid), which is unstable, an aldehyde or ketone and an bi-radical intermediate called the Criegee zwitterion intermediate is formed by cleaving of a peroxy O-O-bond:



Within further reaction steps, this intermediate containing excess energy might either be stabilized or decompose in a variety of ways whereas it then represents a direct source of hydroxyl radicals. The OH production yields of these reactions vary from 7 to 100 % depending on the structure and size of the alkene [Paulson *et al.*, 1999], but become especially important at night in the absence of the photolytic sources of OH, as it does not require sunlight. It therefore proceeds during the night, but its rate still depends on the presence of ozone as well as large ($\geq \text{C } 5$) alkenes, for example biogenic VOCs or anthropogenic emissions.

Finally, further reactions were listed by [Alicke, 2000], such as the reaction of RO_2 with NO , or the nighttime reaction of NO_3 with alkenes (recently quantified by [Geyer, 2000; Geyer *et al.*, 2003a; Geyer *et al.*, 2003b]). Despite the fact that these contribute largely to the nighttime radical budget, all were found to be of minor importance compared to the daytime OH-radical

production (0 – 3 %), especially in urban areas with higher nitrogen monoxide concentrations during the night, which prevent higher NO₃ concentrations.

2.3 Nitrous Acid (HONO)

Nitrous acid was first identified in the atmosphere by [Nash, 1974; Perner and Platt, 1979; Platt and Perner, 1980; Platt *et al.*, 1980]. Since then many atmospheric measurements at various sites have been reported (see [Lammel and Cape, 1996] or [Calvert *et al.*, 1994] for recent reviews). Maximum mixing ratios in urban regions of up to 15 ppb [Winer and Biermann, 1994] in Los Angeles / USA or 10 ppb in Milan / Italy [Febo *et al.*, 1996] are reported. Generally, the HONO concentrations are higher in (polluted) urban areas than those in rural (see e.g. [Andres-Hernandez *et al.*, 1996; Harrison and Kitto, 1994; Neftel *et al.*, 1996]) and remote areas. Nitrous acid concentrations were found to scale with NO₂ concentrations and the ratio HONO / NO₂ is generally less than 10 %. Its amount depends on the degree of pollution and thus HONO is often named a typical product of the polluted urban air. However, recent measurements indicate that HONO plays a much larger role for the reactive nitrogen budget than previously expected for a rural site.

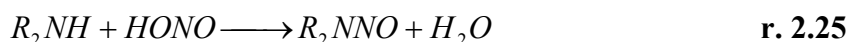
2.3.1 Importance of Atmospheric HONO

Since the mid 1970` s [Cox, 1974; Nash, 1974; Perner and Platt, 1979] it is well-known that HONO is of major significance for tropospheric chemistry by its photolysis (as also already mentioned in chapter 2.2.3) yielding NO at wavelengths of 300 nm < λ < 405 nm and thus representing a direct source of OH-radicals [Stockwell and Calvert, 1978; Stutz *et al.*, 2000]:



The contribution of HONO to the total OH budget during the day was underestimated for a long time. However, more recent measurements show that up to 30 % of the total OH is produced by HONO photolysis in a 24-hour period under various conditions [Alicke *et al.*, 2003; Alicke *et al.*, 2002; Stutz *et al.*, 2002; Stutz and Geyer, 2003]. This role of nitrous acid in atmospheric chemistry has been underestimated for a long time and has therefore been neglected in many models.

In contrast, the health impact of HONO, such as lowering the human lung functionality [Beckett *et al.*, 1995; Rasmussen *et al.*, 1995] has been accepted for several years already. Further, it is well known that nitrous acid undergoes several reactions in both the atmosphere as well as in the biosphere. Here, it is a precursor of different carcinogenic species [Hanst, 1978; Pitts *et al.*, 1978] accumulating e.g. in the human lung. Thereby, HONO reacts in the dark with secondary amines (dimethylamine (DMA) and diethylamine (DEA) yielding the carcinogenic nitrosamine and water:



Amines are emitted into the air as a result of a wide variety of sources like leather tanneries, rocket fuels, tire and amine factories, and tobacco smoke (see e.g. [Fine, 1980]). Although little is known about the concentrations of amines in urban air, the levels to which the general public is exposed are presumably quite low [Pitts *et al.*, 1978].

Despite the importance of HONO as direct OH-radical precursor for the atmospheric chemistry and its potential health impact, the production processes are not well understood, as reviewed by [Calvert *et al.*, 1994; Lammel and Cape, 1996]. Generally, three different types of sources or reactions of formation of the atmospheric HONO can be distinguished: direct emission (discussed in chapter 2.3.3), gas-phase (homogeneous) reactions (in chapter 2.3.4), and finally formation in a thin layer of water on a surface (heterogeneous reactions as

discussed in detail in chapter 2.3.5). These different formation pathways are illustrated by different colors in the first cycle of figure 2.8. The second shows the impact of HONO on photochemistry in the troposphere.

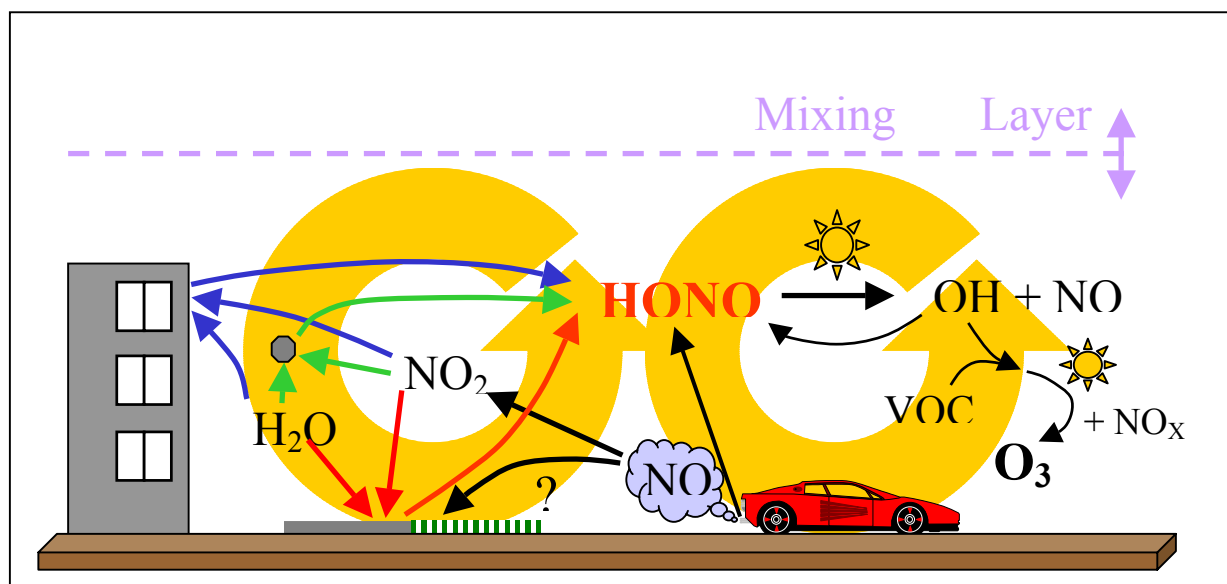


figure 2.8: The atmospheric chemistry of HONO [Stutz et al., 2000].

2.3.2 Diurnal Variation of HONO in the Troposphere

The mixing ratios of HONO show a typical diurnal variation dominated by its photolysis. During the night, the mixing ratios increase to levels of some 100 ppt in rural areas and up to several ppb in polluted air until midnight, but also in the second half of the night, when NO_2 mixing ratios play an as important role as meteorological parameters (for a tabular summary refer to [Alicke, 2000; Trick, 2000]). A peak in the HONO mixing ratio is often observed before sunrise (up to 14 ppb were reported by [Appel et al., 1990; Febo et al., 1996; Harrison et al., 1996; Notholt et al., 1992]), but nearly constant values [Alicke, 2000] or slight decrease with a second HONO maximum just before dawn [Alicke, 2000; Notholt et al., 1992; Reisinger, 2000] have been reported. However, after sunrise, decay within approx. 2 hours is caused by photolysis. The time derivative of the HONO mixing ratio during sunrise depends on the intensity of solar radiation (e.g. on latitude and degree of cloud cover) but also on dilution by convective mixing. In mid-latitudes during summer, for example, its lifetime is ~ 2 h one hour after sunrise and ~ 8 minutes at noon (under clear skies). The lifetime can essentially be longer under cloudy skies [Stutz et al., 2000]. Typically, this leads to low values during the day. About 5 to 150 ppt were observed in rural and medium polluted areas up to date (see e.g. [Alicke, 2000; Alicke et al., 1999; Reisinger, 2000]). Recently, measurements using multiple measurement techniques show HONO daytime mixing ratios of about 200 ppt in polluted areas [Harrison et al., 1996; Kleffmann et al., 2003; Zhou et al., 2002a] as well as in remote areas [Nefel et al., 1996; Staffelbach et al., 1997a; Zhou et al., 2001] (see table 2.2). The seasonal pattern of HONO concentrations during daytime and night were studied by denuder techniques [Baria et al., 2003] as well as by DOAS [Veitel, 2002]. Due to higher solar radiation and thus photolysis, lower values of HONO concentrations are generally observed in summertime.

location	conditions	[HONO]	[HONO]/[NO ₂]	[NO]/[NO ₂]	instrument	reference
Birmingham, UK	urban, clear sky, winter	100 - 200 ppt	1 - 1.5 %	0.5	Denuder	[Harrison et al., 1996]
Merenschwand, Switzerland	rural, summer, no emissions from cars	100 ppt	n.a.	n.a.	Denuder	[Nefitel et al., 1996]
Chiasso, Switzerland	rural, summer, no emissions from cars, in plume of Po valley	200 ppt	10 %	0.1	Denuder	[Staffelbach et al., 1997a]
Rome, Italy	urban area, high building density, hot, summer, 50 m above streets	200 ppt	2 - 3 %	0.1	DOAS	this thesis, see chapter 4.1.2.2
Montelibretti, Italy	rural area, above valley with highway, summer, in plume of Rome	< 90 ppt	< 5 %	n.a.	DOAS	this thesis, see chapter 4.1.4.2
Arctic snow pack	remote, cold, spring	10 ppt	n.a.	n.a.	HPLC	[Zhou et al., 2001]
Pinnacle, NY	rural, summer, no direct emissions	60 ppt	5 % to NO _x	n.a.	HPLC	[Zhou et al., 2002a]
Milan, Italy	suburban	< detection limit	< 1 %	0.2	DOAS	[Stutz et al., 2002]
Houston, TX	suburban, summer, 2-50 m above grassland	< 50 ppt	< 1 %	0.1	DOAS	[Stutz et al., 2004a]
Boston, MA	urban, summer, 20 m above streets	200 ppt	4 %	n.a.	DOAS	[Wang et al., 2003]
Phoenix, AZ	urban, summer	up to 500 ppt	2 %	n.a.	DOAS	[Wang et al., 2003]
Pabstthum, Germany	rural, summer, no traffic nearby	< 100 ppt	< 5 %	0.1	DOAS	[Alicke et al., 2003]
Karlsruhe, Germany	suburban, fall, small urban area in research center	210 ppt	2 %	2	LOPAP II	[Vogel et al., 2003], resp. [Kleffmann et al., 2003]
New York City	urban, summer	250 ppt	n.a.	n.a.	HPLC	[Ren et al., 2003]

table 2.2: Summary of observed daytime levels of HONO at different locations and under different conditions. The listed HONO mixing ratios as well as the HONO-to-NO₂ and the NO-to-NO₂ ratios are mean values averaged over the whole period of observation during the corresponding measurement campaigns.

The height of the boundary layer should majorly influence these effects on nitrous acid concentrations: a very low inversion height during the night should lead to a much higher HONO concentration assuming that the precursors are emitted in the same amount. The effects of the boundary layer height have been studied for a long time [Appel *et al.*, 1990; Febo *et al.*, 1993; Harrison *et al.*, 1996; Sjödin and Ferm, 1985], but measurements were performed with instruments of 0.5 - 24-hour time resolution, too slow to follow the decrease of HONO at sunrise. However, further investigations have recently been published [Alicke, 2000; Alicke *et al.*, 1999; Kleffmann *et al.*, 2003; Perrino *et al.*, 2001; Stutz *et al.*, 2004a; Veitel, 2002; Vogel *et al.*, 2003] indicating the strong influence of the boundary layer height to both the accumulation of nighttime HONO mixing ratios as well as the presence of high daytime HONO values.

2.3.3 Direct Emission Sources of Nitrous Acid

Due to the fact that nitrous acid is very closely linked to NO_x chemistry, sources of NO_x are potential sources for HONO as well. However, the thermodynamics as well as the kinetics of combustion processes, which form the most prominent NO_x source, are unfavorable for HONO formation. Nevertheless, HONO may be formed as combustion gases cool down immediately after exiting from the combustion chamber, for example in a car tailpipe. Several studies have been carried out to estimate the source strength of nitrous acid from direct emissions such as combustion engines (see table 2.3 below).

system	$\frac{HONO}{NO_x}$ ^{combustion} [%]	reference
Diesel engine	1.0	[Kessler and Platt, 1984]
gasoline engine (rich operation conditions)	< 0.01	[Kessler and Platt, 1984]
gasoline engine (lean operation conditions)	0.15	[Kessler and Platt, 1984]
highway variety of vehicles (gasoline engine)	0.5	[Kessler and Platt, 1984]
gasoline engine (catalyst-equipped)	0.1 – 1.8	[Pitts <i>et al.</i> , 1984a]
ambient air	< 0.1	[Calvert <i>et al.</i> , 1994]
traffic tunnel	0.8	[Winer and Biermann, 1994]
traffic tunnel	0.29 ± 0.05	[Kirchstetter <i>et al.</i> , 1996]
traffic tunnel	0.8 ± 0.1	[Kurtenbach <i>et al.</i> , 2001] and [Ackermann, 2000]
Diesel engine (truck)	0.53 ± 0.08	[Kurtenbach <i>et al.</i> , 2001] and [Ackermann, 2000]
Diesel engine (car)	0.66 ± 0.2	[Kurtenbach <i>et al.</i> , 2001] and [Ackermann, 2000]
gasoline engine (car, catalyst-equipped)	0.65 ± 0.24	[Kurtenbach <i>et al.</i> , 2001] and [Ackermann, 2000]

table 2.3: HONO emitted as a fraction of NO_x in vehicle exhaust.

Up to 1.8 % of the total NO_x emitted from combustion processes was observed to be direct nitrous acid emission. Thus, only in heavily polluted areas and mainly in areas of high traffic, this source becomes significant. In table 2.3, different measurements of the ratio of HONO to total NO_x are listed for various combustion engine types. Generally, the HONO / NO_x ratio is lower for modern cars with catalytic converters ([HONO]:[NO_x] < 0.15 % [Kessler and Platt,

1984] resp. 0.65 % [Ackermann, 2000]) compared to cars or heavy trucks with Diesel engines ([HONO]:[NO_x] 1 % [Kessler and Platt, 1984] resp. 0.55 - 0.66 % [Ackermann, 2000]).

Since the concentration of total NO_x is much larger in Diesel exhaust compared to normal gas engines, higher concentrations of HONO are found in Diesel exhaust as well. These higher amounts of HONO in Diesel exhaust are suspected to be caused by the higher aerosol concentration in Diesel exhaust and thus the fast formation of nitrous acid on particles in the exhaust pipe. Thereby, fresh soot particles showing a high reaction probability might operate as oxidizing surfaces as indicated by [Ammann *et al.*, 1998] and described in detail later in chapter 2.3.5.2.

The state of engine operation also influences the amount of HONO directly emitted by traffic. In figure 2.9 the mixing ratios for the different nitrogen oxides are shown depending on the engine rotary speed and torque. As can be seen for the diesel engine the HONO emissions have a maximum at low engine rotary speed. [Pitts *et al.*, 1984a] indicated that cold engine operation as well as poor maintenance or ageing of the catalyst increase HONO tailpipe emissions. The very low HONO / NO₂ ratios for catalyst-equipped, well-maintained gasoline automobile engines were confirmed by studies of [Calvert *et al.*, 1994]. The experiments by [Ackermann, 2000; Kurtenbach *et al.*, 2001] were performed in a different manner than the previous laboratory measurements: in a traffic tunnel, where the engines of all cars and trucks passing had been running for a minimum of 15 minutes. Thus, emissions of a large amount of traffic in the controllable tunnel were measured and one car with a possibly old gasoline engine, which might not be representative for the entire fleet, could not skew the measurements. They observed equal HONO / NO₂ ratios for both Diesel as well as gasoline engines in automobiles. On average, an emission ratio of 0.8 ± 0.1 % was observed (75 % gasoline engines, 12 % trucks, 13 % diesel driven passenger cars). A traffic study in the USA indicates a lower emission ratio of 0.3 % [Kirchstetter *et al.*, 1996]. The difference may be attributed to differences in fleet composition and engine technology in Europe and the USA.

Without measuring the direct emission exhaust, further evidence for the possible significance of this direct emission source of HONO is shown by a report by [Winer and Biermann, 1994]. Between sunset and midnight during six periods in the fall of 1987 in Los Angeles, HONO and NO₂ data was obtained. No correlation between HONO and NO₂ concentrations or the square of the NO₂ concentration were observed, but during these periods with CO and NO. Since both, CO and NO, are primarily emitted from combustion sources, direct HONO emission from combustion processes was deduced to be about 0.8 % of the total NO_x emissions. Additionally, a rate of conversion of NO₂ to HONO of about 1 % per hour was calculated. This is in agreement with the HONO production rate from heterogeneous NO₂ reactions analogous to those observed in smog chambers.

However, none the HONO-to-NO₂ ratios derived from these measurements cannot explain the observed HONO concentrations in the atmosphere. A recent study by [Gutzwiller *et al.*, 2002] found strong evidence for semivolatile and / or water-soluble species contained in diesel exhaust being significantly involved in secondary HONO formation. Consequently, a fraction of 2.3 % of NO_x emitted was heterogeneously converted to HONO, which may be sufficient to explain atmospheric concentrations of HONO.

Combustion processes are not only limited to traffic, but also indoor gas heating and gas cooking also represent strong in-door combustion processes. Peak levels (15 min) of up to 100 ppb of HONO and 24 h averages as high as 40 ppb were measured by [Brauer *et al.*, 1990; Febo and Perrino, 1991]. Generally, indoor-HONO levels are strictly correlated to indoor NO_x levels and inversely correlated to indoor O₃ values. Up to 17 % of indoor NO₂ was observed as HONO by [Lee *et al.*, 2002]. Indoor measurements of elevated levels of nitrous acid were also performed in cars by [Febo and Perrino, 1995]. Mixing ratios of up to 30 ppb were observed during transit through polluted areas (urban sites), where 1.4 ppb only were

detected outdoors at the same time. This high concentration persisted for many hours even when the cars are moved to an unpolluted site.

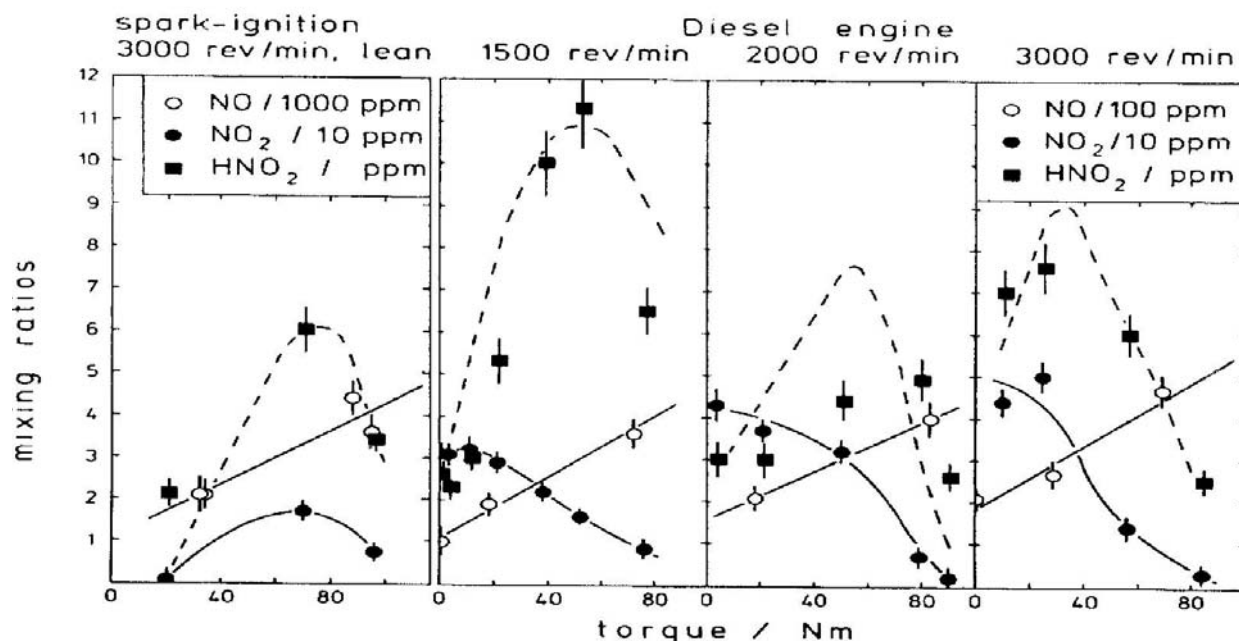


figure 2.9: The dependence of HONO, NO₂ and NO in diesel and gasoline exhaust on the engine rotary speed and torque [Perner et al., 1985].

A biogenic source of HONO was suggested as well by [Rondon and Sanhueza, 1988]. In the absence of anthropogenic sources and with respect to transport limitations for nitrous acid, they concluded that the HONO observed was generated in fires in the Venezuelan savannah during the biomass-burning season.

2.3.4 Homogeneous Formation of Nitrous Acid

Among the various reactions occurring in the atmosphere, several occurring only in the gas-phase (homogeneous) have been examined for their formation potential of nitrous acid. Most of them were found to be of minor relevance as a source of tropospheric HONO. Significant amounts of HONO are only obtained from the inverse of the photolysis r. 2.20, the recombination of the hydroxyl radicals with nitrogen monoxide [Nguyen et al., 1998; Pagsberg et al., 1997; Stuhl and Niki, 1972; Westenberg and DeHaas, 1972; Zabarnick, 1993]:



Thereby [M] represents a third molecule for this three-body collision (most likely oxygen O₂ or nitrogen N₂), which is necessary to reduce the excess energy of the molecules to form a stable product and thus guarantees the conservation of energy and momentum. It was shown by [Ahmed et al., 1997] that the efficiency of oxygen as collision partner is about 70 %, compared to 30 % for nitrogen. In general, rate constants k are temperature and pressure dependent. For a three-body gas-phase reactions, the rate constants can be calculated from their low and high-pressure limits given for a specific temperature [DeMore et al., 2003]:

$$k_0(T) = k_0^{300} (T/300)^{-n} \quad \text{and} \quad k_\infty(T) = k_\infty^{300} (T/300)^{-m} \quad \text{eq. 2.4}$$

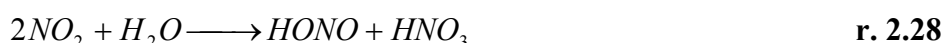
For reaction r. 2.26 these are reported to be $k_0(T) = (7 \pm 1) \cdot 10^{-31}$; $k_\infty(t) = (3.6 \pm 1.0) \cdot 10^{-11}$, $n = (2.6 \pm 0.3)$, $m = (0.1 \pm 0.5)$ [DeMore et al., 2003]. Combining both and using:

$$k(M, T) = \left(\frac{k_0(T)[M]}{1 + (k_0(T)[M]/k_\infty(T))} \right) \cdot 0.6^{\{1 + [\log_{10}(k_0(T)[M]/k_\infty(T))]^2\}^{1/2}} \quad \text{eq. 2.5}$$

the rate constant for reaction r. 2.26 at 290 K and sea level pressure becomes $k = 7.78 \times 10^{-12} \text{ cm}^3 \text{ molec}^{-1} \text{ s}^{-1}$. Including the efficiencies described above, we finally get $k = 3.89 \times 10^{-12} \text{ cm}^3 \text{ molec}^{-1} \text{ s}^{-1}$.

During daytime, under conditions of high amounts of NO (e.g. close to main traffic roads), this reaction might become an important HONO source. Since both radicals, NO and OH are produced by photolysis of HONO, reaction r. 2.26 only represent a secondary source of HONO in the atmosphere. Considering the photolysis of HONO back to NO and OH, a steady state between these three species is established within about 10 min and can therefore not be assumed as a net HONO source. Assuming high mixing ratios of NO of 50 ppb, and an OH concentration of $2 \times 10^6 \text{ molec cm}^{-3}$, the maximum HONO level formed by reaction r. 2.26 can be calculated to be in the range of 27.5 ppt for a photolysis frequency of $2 \times 10^{-3} \text{ s}^{-1}$. However, this reaction pathway cannot explain the night-time production of HONO, because both NO and OH levels are generally very low during the night [Geyer *et al.*, 2003b]. Even if assuming a night-time hydroxyl radical concentration of $1 \times 10^5 \text{ molec cm}^{-3}$ and a NO night-time mixing ratio like those measured for the highly polluted environment during the Rome 2001 campaign of 70 ppb (see chapter 4.1), only 90 ppt h⁻¹ are formed by reaction r. 2.26.

It is known that the bulk of urban HONO is formed via other pathways already suggested by [Chan *et al.*, 1976b; Kaiser and Wu, 1977a; Wayne and Yost, 1951]. These reactions are the disproportionation of NO_x involving water vapor:

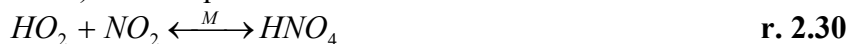


Therefore, the photolysis of HONO formed via these reactions represents a net OH source that is important for the creation of photosmog [Alicke, 2000; Alicke *et al.*, 2003; Alicke *et al.*, 2002]. However, both of these homogeneous reactions represent three-body collisions in the gas-phase, which seem rather unlikely. The rate constants for these reactions, determined to be of second order kinetic with respect to NO_x, were reported by [Wayne and Yost, 1951] to be $k_{r. 2.27} = 1.2 \times 10^{-34} \text{ cm}^6 \text{ molec}^{-2} \text{ s}^{-1}$ and by [Chan *et al.*, 1976b] and [Kaiser and Wu, 1977a] in the order of 10^{-34} to 10^{-40} for these homogeneous reactions r. 2.27, and r. 2.28. Thus, both are much too slow at atmospheric NO_x levels to explain the HONO production.

[Stockwell and Calvert, 1983] suggested the most important nighttime radical NO₃ to initiate further homogeneous formation of HONO in the nocturnal urban atmosphere. The peroxy-radical, which is the product of its reaction with e.g. formaldehyde or acetaldehyde, reacts with nitrogen dioxide forming HONO by:



Taking into account the upper limit of $k_{r. 2.29} < 3 \times 10^{-15} \text{ cm}^3 \text{ molec}^{-1} \text{ s}^{-1}$ [Howard, 1977] for this reaction only, the time dependence of ambient NO₃, O₃ and NO₂ data from [Harris *et al.*, 1982] could be fitted reasonably well by [Stockwell and Calvert, 1983]. However, both [Pitts *et al.*, 1984d], who measured NO₃, NO₂ and O₃ in the same air mass, as well as [Killus and Whitten, 1985] could not satisfactorily explain the observations of [Harris *et al.*, 1982] applying the mechanism suggested by [Stockwell and Calvert, 1983]. Further, recent measurements by [Tyndall *et al.*, 1995] have not only reduced the upper limit for the rate coefficient to $k_{r. 2.29} < 5 \times 10^{-16} \text{ cm}^3 \text{ molec}^{-1} \text{ s}^{-1}$, but also observed pernitric acid (HNO₄) to be the primary product (> 99%) of the equilibrium reaction r. 2.29 of HO₂ and NO₂:



HNO₄ is not stable under conditions of polluted urban atmospheres and decomposes within seconds via reaction r. 2.30. Subsequently, the HO₂ self reaction forms H₂O₂, which reacts in the gas-phase mainly with OH, dissolves in water or on wet surfaces or is photolyzed.

The similar reaction of alkoxy radicals might yield nitrous acid as well as the corresponding aldehyde:



However, the rate constant of $k_{r, 2.31} \approx 1.5 \times 10^{-15} \text{ cm}^3 \text{ molec}^{-1} \text{ s}^{-1}$ [DeMore *et al.*, 2003] is again obviously too small to explain the observed night time HONO mixing ratios, especially since the atmospheric lifetime of peroxy radicals is very short.

2.3.5 Heterogeneous Formation of Nitrous Acid

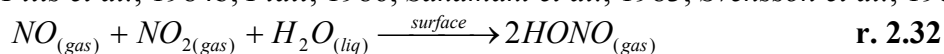
We have shown in the previous chapter 2.3.3 that direct emission sources of nitrous acid exist, but cannot explain the observed HONO / NO₂ ratios [Platt, 1986]. None of the homogeneous reactions described above in chapter 2.3.4 are of significance for formation of HONO in the troposphere either.

However, the assumption that some of the reactions presented above proceed heterogeneously, for example on wet surfaces like aerosol, buildings or the ground, has been confirmed by several authors [Ammann *et al.*, 1998; Becker *et al.*, 1995; Calvert *et al.*, 1994; Chan *et al.*, 1976b; Febo *et al.*, 1987; Goodman *et al.*, 1999; Jenkin *et al.*, 1988; Junkermann and Ibusuki, 1992; Kaiser and Wu, 1977b; Kalberer *et al.*, 1999; Kleffmann *et al.*, 1998; Lammel and Perner, 1988; Longfellow *et al.*, 1998; Pitts *et al.*, 1984b; Platt, 1986; Sakamaki *et al.*, 1983; Svensson *et al.*, 1987].

In this chapter, we will first give a brief overview of several heterogeneous reactions investigated for their potential of atmospheric production of HONO. The most prominent reaction, the heterogeneous hydrolysis of NO₂ will be discussed in more detail in the next chapter with special respect to its favor location of occurrence, its kinetics and mechanistic sequences.

2.3.5.1 The Disproportionation of NO_x

HONO is nowadays suspected to be formed by the reactions r. 2.27, or r. 2.28 heterogeneously, further involving only NO_x, as an increase of the reactivity with the surface-to-volume ratio is generally observed [Calvert *et al.*, 1994; Chan *et al.*, 1976b; Febo *et al.*, 1987; Kaiser and Wu, 1977b; Kleffmann *et al.*, 1998; Lammel and Cape, 1996; Lammel and Perner, 1988; Pitts *et al.*, 1984b; Platt, 1986; Sakamaki *et al.*, 1983; Svensson *et al.*, 1987]:



Modeling studies [Aumont *et al.*, 2003; Moussiopoulos *et al.*, 2000; Vogel *et al.*, 2003] also predict the importance of these heterogeneous reaction pathways forming HONO as well.

A number of laboratory and field studies [Alicke, 2000; Jenkin *et al.*, 1988; Kleffmann *et al.*, 1998; Pitts *et al.*, 1984b; Sakamaki *et al.*, 1983; Svensson *et al.*, 1987] have suggested that reaction r. 2.32 is not significant for the atmospheric formation of HONO, as it is found to be independent from NO. Several field observations, where the presence of high ozone at night or low NO was documented, confirm this result [Harrison and Kitto, 1994; Kessler and Platt, 1984; Zellweger *et al.*, 1999]. However, the reaction r. 2.32 may become important in polluted air masses containing huge amounts of NO, as observed by [Notholt *et al.*, 1992] for foggy episodes of high NO, NO₂ and aerosol concentrations.

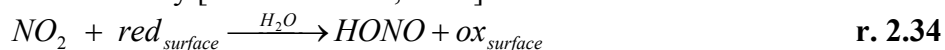
Thus, it is currently believed that the primary production pathway of nitrous acid formation is the heterogeneous reaction of nitrogen dioxide with water on a surface by reaction r. 2.32 [Ammann *et al.*, 1998; Becker *et al.*, 1995; Calvert *et al.*, 1994; Goodman *et al.*, 1999; Jenkin *et al.*, 1988; Junkermann and Ibusuki, 1992; Kalberer *et al.*, 1999; Kleffmann *et al.*, 1998;

Lammel and Perner, 1988; Longfellow *et al.*, 1998; Sakamaki *et al.*, 1983; Svensson *et al.*, 1987].

The location of the formation, the exact reaction mechanism, and the rate coefficient of the HONO production are still the most uncertain properties, since it is apparent that its formation not only depends on the available surface area but also on the composition of the surface.

2.3.5.2 Direct Reduction on Fresh Soot

It was mentioned in the discussion of direct emission sources of HONO that it may be formed heterogeneously from NO₂ suspended on a reducing soot surface (e.g. in the automobile exhaust pipe) as indicated by [Ammann *et al.*, 1998]:



In this reaction r. 2.34, which proceeds 10⁵ to 10⁷ times faster than on other particle surfaces, nitrous acid can be produced above the theoretical thermodynamic equilibrium concentration, as long as the HONO destruction is slow enough. However, only a very small fraction of the surface of fresh soot particles acts reducing (a few per cent of a monolayer) with a high reaction probability. [Ammann *et al.*, 1998] observed a HONO production of 3.3·10¹³ molecules per s per cm² aerosol surface within the first seconds. The rate constantly decreases afterwards towards zero within a total measurement time of 155 seconds.

[Kalberer *et al.*, 1999] also investigated the formation of nitrous acid on soot particles, but a production of HNO₃ corresponding to reaction r. 2.33 was not observed. Thus, the direct reduction of NO₂ to HONO on the soot particle surface according to reaction r. 2.34 was postulated. Due to the limited amount of reactants on the particle surface, a very fast termination of the reaction at a few ppb NO₂ was found and a HONO formation potential of the soot used of about 1 x 10¹⁵ HONO molecules per cm² particle surface at 30 % relative humidity (R.H.). Further, a non-linear behavior as a function of the R.H. in the range from 2 % to 70 % could be derived for the HONO production: increasing from 2 % up to 40 %, and returning to a decrease until 70 %, where it is again as low as at 2 % R.H. Thus it was suggested that H₂O is either directly involved in the chemical reaction of NO₂ to HONO or builds up a precursor (e.g. by hydrolysis) which acts as the reaction partner for NO₂. At high humidity, the increasing amount of adsorbed water makes the reactive surface less accessible or less reactive to NO₂. The strong oxidant O₃ was also found to impact on the HONO formation, causing an aging of the soot aerosol surface, resulting in a lower HONO formation potential [Kalberer *et al.*, 1999]. The exposure of the surface to an ozone dose of only 105 ppb x min, had a yield of 10 % less HONO formed on the particle surface, compared to a fresh aerosol surface.

It was finally concluded that the direct reduction reaction of NO₂ to HONO on soot particles saturates and is not the main source of HONO in the polluted boundary layer. This was confirmed by modeling studies of [Aumont *et al.*, 1999] showing that the general consequences for the NO_x chemistry in the troposphere are small, especially due to the fast saturation of the surface within less than one minute. However, by a mechanism recycling the particle surface reactivity with respect to the NO₂ to HONO conversion, reaction r. 2.34 would become an important atmospheric source of HONO on soot aerosol particles. First evidence for such a procedure was observed by [Gerecke *et al.*, 1998] by irradiating soot particles with light.

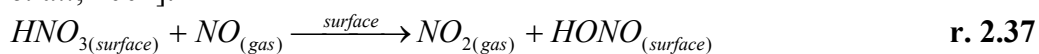
2.3.5.3 Further Heterogeneous Reactions yielding HONO

Further reactions have been reported to produce HONO as well. [Svensson *et al.*, 1987] have suggested the reaction of NO_x with sulfur compounds, especially sulfuric acid H₂SO₄:



However, [Kleffmann, 1998; Kleffmann *et al.*, 1998] excluded any evidence for the tropospheric formation of HONO due to these reactions, as both proceed much too slow even in highly polluted urban areas.

Several laboratory studies by the group of Finlayson-Pitts [Mochida and Finlayson-Pitts, 2000; Rivera-Figueroa *et al.*, 2003; Saliba *et al.*, 2000; Saliba *et al.*, 2001] indicated the so-called renoxification being possibly relevant for the formation of nitrous acid in the polluted urban troposphere. Laboratory studies of heterogeneous reaction of HNO₃ in thin water films on silica surfaces with gaseous NO, CO, CH₄ and SO₂ were studied by [Rivera-Figueroa *et al.*, 2003], but significant reaction probabilities were only observed for the reaction with NO. This reaction of gaseous NO with HNO₃ on borosilicate glass (the chemistry was found insensitive to whether the substrate is pure silica or borosilicate glass) in the presence of water was studied as a function of surface water coverage and the loss of gaseous NO and the formation of NO₂ were measured in a long path cell using FTIR spectroscopy. A reaction scheme illustrated below was observed. Thereby, the first step is believed to be the reaction of gaseous NO with surface adsorbed HNO₃. The lower limit for the reaction probability is believed to be $\gamma_{NO} = (6 \pm 2) \times 10^{-9}$, and is generally larger under conditions of higher R.H. Within the decrease of nitric acid, NO₂ is rapidly formed and instantaneously emitted into the gas-phase. Additionally, surface adsorbed HONO is formed in this reaction. There are different possibilities of subsequent steps for this surface-bound HONO. It may either react with HNO₃ or with another HONO at the surface, generating NO₂ and NO respectively [Mochida and Finlayson-Pitts, 2000], but a formation of solvated N₂O₄ was also reported [Saliba *et al.*, 2001]:



or:



A significant production of HONO from this reaction scheme was reported [Saliba *et al.*, 2000]. Therefore, HONO may be released in reaction r. 2.37 back into the gas-phase as we will show in detail by the analysis of our studies in chapter 5.5.

However, the renoxification chemistry may become especially important under highly polluted conditions with huge amounts of NO present, and in the boundary layer of polluted urban atmospheres, where silica surfaces are plentiful in particles, soils and building materials, as well as globally in the free troposphere, where dust particles are present. Consequently, HNO₃ may be converted back to photochemically active NO_x in the atmosphere.

2.3.5.4 Photolytic Enhancement of HONO Formation

In the last few years, more and more evidence for high daytime levels of nitrous acid were reported (see table 2.2, and chapter 4 of this thesis). Those elevated daytime levels in the HONO concentration were measured by different techniques at various sites: highly polluted urban areas [Ren *et al.*, 2003; Wang *et al.*, 2003; Zhou *et al.*, 2002a], as well as in rural,

suburban [Harrison *et al.*, 1996; Kleffmann *et al.*, 2003; Nefel *et al.*, 1996; Staffelbach *et al.*, 1997a] or remote [Dibb *et al.*, 2002; Zhou *et al.*, 2001] areas, or above snow-pack. However, no satisfactory explanation is given in any measurements reported so far, nor can models simulate these observed daytime HONO values [Vogel *et al.*, 2003]. Thus it is expected that there either has to be taken into account an additional and new source of HONO, which is especially efficient during daytime, or an enhancement (e.g. of any mechanism influencing atmospheric dynamics) may be the cause (see chapter 2.5). We will discuss this in more detail in chapter 6.

However, recently suggested mechanisms of HONO production during daytime are controversial. [Dibb *et al.*, 2002; Zhou *et al.*, 2001; Zhou *et al.*, 2002b] observed a significant production of HONO on a glass sample manifold wall surface when exposed to sunlight in summer. It was concluded that HONO was produced by photolysis of adsorbed nitric acid / nitrate on the manifold wall surfaces, followed by the subsequent reaction of produced NO₂ and adsorbed H₂O on surface. This was already indicated by [Akimoto *et al.*, 1987] in laboratory studies, which observed an enhancement of the NO₂ to HONO conversion in air, when irradiated by light. Combining measurement observations and modeling studies on HONO gradients, a similar conclusion was drawn by [Kleffmann *et al.*, 2003; Vogel *et al.*, 2003]. Contrastingly, [Ramazan *et al.*, 2003] found a photodepression of the NO₂ hydrolysis on wet surfaces.

2.3.6 HONO Formation by Heterogeneous Disproportionation of NO₂

In the chapters above and especially chapter 2.3.5.1, we have shown the importance of the heterogeneous hydrolysis of NO₂, yielding HONO and HNO₃ according to reaction r. 2.33 as the only atmospheric source of significant amounts of nitrous acid other than direct emission. For more than two decades, research on HONO production has been addressed to this heterogeneous formation pathway, but still the mechanistic sequences summarized by reaction r. 2.33 are only poorly understood. Thus in the following chapters, we will discuss this reaction in more detail, including the possible surfaces (airborne particles such as aerosols in chapter 2.3.6.1, or the ground surface in chapter 2.3.6.2, and 2.3.6.3), where this reaction r. 2.33 could take place in the atmosphere, the kinetic law description (chapter 2.3.6.4) for reaction r. 2.33, and finally its mechanistic sequences (chapter 2.3.6.5).

2.3.6.1 Formation of Nitrous Acid on Airborne Particles (Aerosols)

Various types of airborne surfaces, i.e. aerosol particles (see [Grassian, 2001] for a recent review) or cloud droplets were identified as possible substrates for HONO formation by r. 2.33. Some prominent examples are: cloud droplets [Acker *et al.*, 2002; Acker *et al.*, 2001a; Harrison and Collins, 1998; Lammel and Perner, 1988; Li, 1994; Notholt *et al.*, 1992], soot aerosol particles [Ammann *et al.*, 1998; Kalberer *et al.*, 1999; Kirchner *et al.*, 2000; Kotamarthi *et al.*, 2001], wetted SiO₂ and soot particles [Grassian, 2001], sulfuric acid droplets [Kleffmann *et al.*, 1998; Longfellow *et al.*, 1998], different carbonaceous surfaces [Kalberer *et al.*, 1999; Kleffmann *et al.*, 1998; Preszler-Princea *et al.*, 2002], and secondary organic aerosols (SOAs) [Bröske *et al.*, 2003]. Contrasting results were obtained by these studies as summarized by [Grassian, 2001].

Kinetic studies on these surfaces require a lot of effort and depend especially on the preparation and conditioning of the airborne particles. The rate-limiting step of the heterogeneous reaction r. 2.33 is the uptake into the differing phase, involving several, partly reversible, processes that are illustrated in figure 2.10. Before the reaction r. 2.33 proceeds at the surface, the gaseous species has to be transported towards the surface, i.e. the aerosol

particle. After the reaction took place, the trace gas needs to be transported apart from the surface. The physical theory of molecular diffusion will be described in chapter 2.5.

The net uptake of a gas molecule into a fluid can be described by the uptake coefficient γ , which can be measured in the laboratory. γ_{exp} can be written as the inverse sum of the different single transfer resistances, the gas (Γ_{gas}) and liquid diffusion (Γ_{liq}), and the reaction in the liquid phase (Γ_r):

$$\frac{1}{\gamma_{\text{exp}}} = \frac{1}{\Gamma_{\text{gas}}} + \frac{1}{\alpha} + \frac{1}{\Gamma_{\text{liq}} + \Gamma_r} \quad \text{eq. 2.6}$$

The actual transition into the gas-phase or the boundary layer is described by the accommodation coefficient α , which can be studied by different laboratory techniques, and is defined as:

$$\alpha = \frac{\text{number of molecules lost to the surface}}{\text{number of gas - surface collisions}} \quad \text{eq. 2.7}$$

Now, the total flux j into the liquid phase can be calculated using $\langle v \rangle$ as the Boltzmann distributed average velocity of the gas molecule:

$$j = \frac{\gamma_{\text{exp}} \cdot [\text{gas}] \cdot \langle v \rangle}{4} \quad \text{eq. 2.8}$$

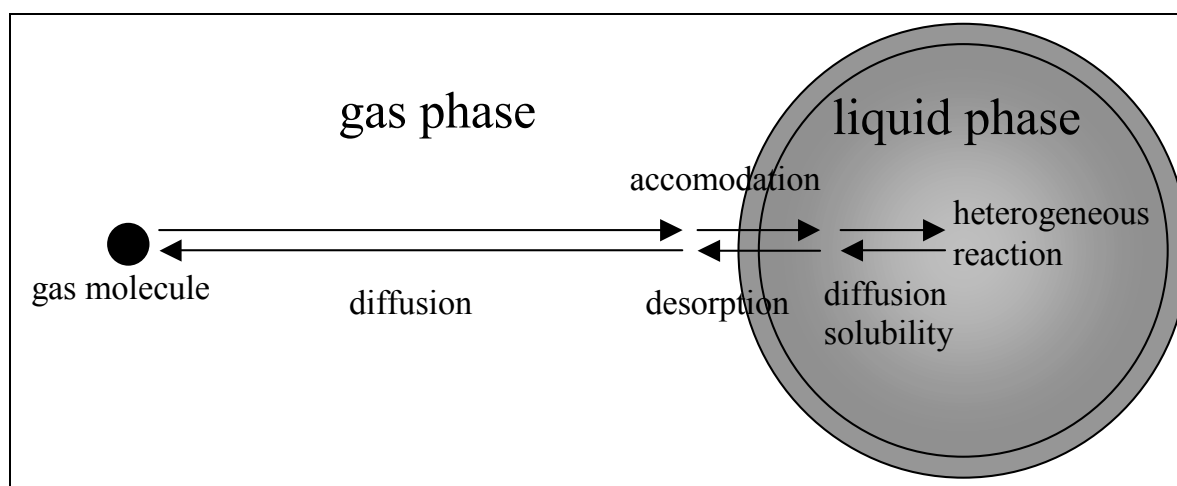


figure 2.10: Schematic view of the different processes occurring during the uptake of a species from the gas-phase in the liquid phase of an aerosol particle [Kleffmann et al., 1998].

We will use this γ -description for calculating production rates of nitrous acid in the troposphere. According to [Kleffmann et al., 1998], we assume the uptake coefficient γ varies only between 3×10^{-7} for a sulfuric acid / water solution with more than 60 weight % H_2SO_4 and 10^{-6} for pure H_2O . In the case of such a small uptake coefficient, a possible limitation by gas-phase diffusion can be neglected for atmospheric conditions [Lee and Tang, 1988]. Most aerosols are only weakly acidic, so the accommodation coefficient for pure water ($\alpha = 10^{-6}$) can be used [Kleffmann et al., 1998]. Considering equations eq. 2.6, and eq. 2.8 above, we can finally calculate the NO_2 conversion rates:

$$\frac{\% \text{NO}_2}{h} = \frac{1}{4} \cdot \langle v_{\text{NO}_2} \rangle \cdot \frac{S}{V} \cdot \alpha \cdot 3600 \cdot 100 \quad \text{eq. 2.9}$$

Taking further into account the stoichiometry of reaction r. 2.33, the calculated values have to be divided by a factor of 2 to obtain the HONO formation rate as summarized for three different scenarios in table 2.4 below.

Usually, HONO production rates in the range between 0.5 % / h and 1.5 % / h are observed in the troposphere (see e.g. [Kessler and Platt, 1984; Stutz et al., 2002; Winer and Biermann, 1994]). Thus, a significant amount of the observed HONO formation can be explained by the heterogeneous reaction of NO₂ on wet surfaces, for the case of the high aerosol load, or meadow surfaces. Its importance may even increase, as S / V values of aerosols are usually calculated based on the assumption of a spherical shape. However, the real surface area can be much larger if one takes into account a possible irregular shape of the aerosol with pores. Thus it is most likely to be underestimated. [Keyser et al., 1991] have shown that molecules can diffuse deeply into porous surfaces, especially for small uptake coefficients.

pollution scenario	S / V [$\mu\text{m}^2 \text{cm}^{-3}$]	yield of % HONO / h
normally polluted	900	0.015
heavily polluted	30,000	0.5
grass meadow ⁷ :	100,000	1.6

table 2.4: Yield of HONO in % per hour for three different pollution scenarios resulting from different surface to volume ratios. (according to [Kleffmann et al., 1998]).

For the scenarios calculated above, an atmospheric HONO formation on cloud droplets and fog [Lammel and Cape, 1996] and on the ground [Harrison and Kitto, 1994; Trick, 2000] was not considered.

In general, the measured values for the uptake of NO₂ onto the aerosol particles were reported in a range of 10⁻³ to 10⁻⁹, spanning 6 orders of magnitude. Depending on their individual observations, contrasting conclusions were drawn by these authors and some scenarios were shown, where airborne particles become crucially important for the atmospheric formation of HONO. However, in the last few years, it became clear that the determined HONO formation rates lead, even under assumption of favorable conditions for the aerosols, to a HONO formation rate, which is about two up to four orders of magnitude lower than observed in the atmosphere [Bröske et al., 2003; Kirchner et al., 2000; Kleffmann et al., 1998; Platt, 1986].

2.3.6.2 Formation of Nitrous Acid on Macroscopic Surfaces & on the Ground

It is also possible that reactions r. 2.32 and r. 2.33 proceed on the ground surface as suggested by [Chan et al., 1976b; Kaiser and Wu, 1977b; Platt, 1986]. Other studies suggested the surface of buildings in urban environments as possible sources of HONO [Andres-Hernandez et al., 1996; Febo et al., 1996; Harris et al., 1982; Harrison and Kitto, 1994; Neftel et al., 1996]. However, all of these surfaces are macroscopic ones, and differ from the airborne particles (see chapter 2.3.6.1) only by the transport towards and apart from the surface: an additional turbulent transport has to be taken into account. A description of turbulent transport will be given in chapter 2.5.

Kinetic studies of the HONO formation on macroscopic surfaces, which seem to be more favorable than aerosols [Platt, 1986], were only performed on Teflon and quartz glass in laboratory experiments so far (e.g. [Kleffmann et al., 1998; Pitts et al., 1984b; Sakamaki et al., 1983; Svensson et al., 1987]). Their values for the HONO formation rate coefficient cannot explain the atmospheric HONO concentrations (see also table 2.5).

However, real urban surfaces, for example high-frequented asphalt roads, are more complex. They are exposed to the weather, consist of several pores and cracks, they contain several inclusions (e.g. silica stones, tarmac, or even grass), abrasions (e.g. from car tires) and they do

⁷ Assumptions: Mixing height during the night 100 m; 10 times larger surface with grass compared to flat even ground.

not consist of a pure chemical substance, but of a mixture of various organic and inorganic compounds. These additional substances in a real urban surface may accelerate catalytically the HONO formation by reaction r. 2.33 as indicated by [Andres-Hernandez *et al.*, 1996; Febo *et al.*, 1996; Goodman *et al.*, 1999; Harris *et al.*, 1982; Harrison and Kitto, 1994; Neftel *et al.*, 1996].

The inner surface of macroscopic surfaces is also much higher than that of aerosols due to the “fractal” structure, pores and cracks. Even assuming a large aerosol surface size of $1000 \mu\text{m}^2\text{cm}^{-3}$ with a boundary layer height of 200 m over a ground surface of 1 cm^2 , the total aerosol surface is only 0.2 cm^2 (excluding the ground). This calculation is based on the spherical shape of the aerosols, but the “real” aerosol surface is much rougher and as discussed in the next chapter, soot particles can have a very high HONO reactive uptake coefficient [Ammann *et al.*, 1998; Kalberer *et al.*, 1999; Notholt *et al.*, 1992]. However, even a higher surface of the aerosol is comparably small to the real surface of the ground.

2.3.6.3 Evidence for a ground-near Source by Vertical Gradients of HONO

As the formation of HONO in the troposphere is strongly coupled to the area and nature of the surface in the boundary layer involved (airborne aerosols or macroscopic ground surface), we need a measure to identify and characterize these surfaces. Laboratory studies are too specific and thus limited with respect to the composition of surfaces in the real atmosphere and their impact on HONO formation. The field measurements of the vertical fluxes and resulting gradients of any trace gas are known to be a useful tool to clarify this important task.

Mainly due to lower emissions, the ground seems to be the surface with largest surface-to-volume ratios at night, but aerosols can also be important if they feature a higher reactive uptake coefficient. During the day, the aerosol surface to volume ratio can increase to a value comparable to the S/V ratio of the ground.

Evidence for formation of nitrous acid on grass ground surface under certain circumstances was shown by measurements of vertical gradients between 0.25 and 2 m in a field study by [Harrison and Kitto, 1994; Harrison *et al.*, 1996]. Depending on the ambient concentration of NO_2 , HONO fluxes pointing upwards ($[\text{NO}_2] > 10 \text{ ppb}$) and downwards ($[\text{NO}_2] < 10 \text{ ppb}$) to the surface were observed. [Harrison and Kitto, 1994; Harrison *et al.*, 1996] concluded that the net effect consists of two contributing processes: formation of HONO from NO_2 on the ground surface concurring with dry deposition of HONO on the ground. By a modeling study of [Harrison *et al.*, 1996], the NO_2 -to-HONO conversion rate was determined to be $5.6 \times 10^{-6} \text{ s}^{-1}$ per mixing height (m) and the HONO dry deposition rate to be 0.02 s^{-1} per mixing height (m). However, the denuder (see chapter 3.1.1.1) system used by [Harrison and Kitto, 1994] is known for artificial production of nitrite in the sampling tube. Consequently, the daytime values of $\sim 1 \text{ ppb}$ at noon seem at least questionable. A comparison of the denuder system used by [Harrison and Kitto, 1994] with a long path DOAS instrument showed no agreement for the measured HONO (see [Stutz, 1996]).

Further measurements using advanced denuder techniques over grassland were performed by [Spindler *et al.*, 1998] and [Neftel *et al.*, 1996]. While [Spindler *et al.*, 1998] generally observed higher HONO concentrations at a height of 4.5 m compared to the concentrations measured at a height of 0.8 m at NO_2 mixing ratios constantly below 10 ppb, no evidence for a negative gradient of HONO at NO_2 levels exceeding 10 ppb in the height range of 3.20 m to 1.60 m was found by [Neftel *et al.*, 1996]. Instead, the concentration in this range was constant.

Measurements of vertical gradients of HONO over a grass meadow surface in a height interval of 0.5 to 4 m were performed by [Alicke, 2000; Stutz *et al.*, 2002] using the DOAS technique (see chapter 3.2). A homogeneous distribution of the HONO concentration over the whole height interval was mostly measured at high NO_2 concentrations well above 10 ppb, in

contrast to results by [Harrison and Kitto, 1994]. Significant HONO gradients were measured only on a few occasions, yielding a net HONO flux towards the ground. This was explained by [Stutz *et al.*, 2002] assuming a steady state between HONO production and deposition on the ground with NO₂-to-HONO conversion rate coefficients much less efficient (about a factor of 10 lower) than found in the laboratory on artificial surfaces. In this study, no evidence for significant production on aerosols was found, even under medium to heavily polluted conditions, excluding soot aerosol in or near exhaust pipes. Consequently, HONO formation is believed to proceed mainly on ground surfaces.

Upward fluxes of NO_x and HONO were also observed by [Honrath *et al.*, 2002], by vertical gradient measurements of NO_x, HONO, and HNO₃ in the lower 1 – 2 m above the snow-pack at Summit, Greenland, during summer 2000. Simultaneous measurements of atmospheric turbulence using eddy covariance systems were performed. Those fluxes, which were highly correlated with diurnally varying sunlight intensity, were not balanced by the HNO₃ flux, which was found smaller in magnitude but towards the ground. Slow NO_x export from the snow towards the atmospheric boundary layer due to nitrate photolysis in the snow-pack was further suspected to alter NO_x and (through HONO photolysis) OH levels in remote snow-covered regions [Honrath *et al.*, 2002].

A larger height interval, up to ~ 450 m, was chosen by [Veitel, 2002] for DOAS measurements. These long-term gradient field studies were not performed over grass surfaces, but over the city of Heidelberg, a typical mix of urban surfaces (asphalt, concrete and other artificial materials as well as grass- and woodland of parks). In contrast to previous measurements, the concentration of HONO as well as the ratio HONO / NO₂ was found to decrease with altitude under virtually all atmospheric circumstances by day and night [Veitel, 2002]. Seasonal as well as diurnal variations were analyzed and a HONO formation rate of ≈ 0.25 % (HONO / NO₂) h⁻¹ was observed in the lower PBL. In the middle and upper PBL, however, the formation rates are substantially smaller (approx. a factor of 2). However, a distinct correlation to the aerosol concentration was not observed [Veitel, 2002]. Influences of transport processes in the PBL (see chapter 2.5.3) were qualified, yielding the result that the HONO / NO₂ ratio always decreased with height, but showed a much larger absolute gradient under stable atmospheric conditions, with less effective vertical mixing.

Recent measurements of vertical gradients of HONO by [Kleffmann *et al.*, 2003], using the in-situ technique of the LOPAP instrument (see chapter 3.1.1.4), and the analysis by modeling studies of [Vogel *et al.*, 2003] confirm these findings, i.e. higher concentrations of HONO closer to the ground surface. Additionally, the performance of the measurements at the 200 m high well-equipped meteorological tower of the IMK, FZ Karlsruhe, where our field studies of vertical gradients took place as well (see chapter 4.3), further allowed to quantify these influences of transport processes in the PBL discussed by [Veitel, 2002]. However, the modeling results and the values of HONO observed by the measurements in different heights disagree. Due to this, an additional HONO source in the atmosphere was postulated by [Kleffmann *et al.*, 2003; Vogel *et al.*, 2003] and will be discussed in detail in chapter 2.3.5.4, and chapter 6.2.

Another model approach with an essentially higher influence of vertical mixing processes in the PBL was used by [Geyer and Stutz, 2003; Stutz *et al.*, 2004a] for their analysis of NO₃ and corresponding species gradient measurements. This so-called NCAT model was also applied to the HONO gradient data of [Wang *et al.*, 2003], showing good agreement between the measured nighttime values and the modeling based on the K-theory (see chapter 2.5.3, and chapter 6.2).

However, we will show in chapter 6.2 that this model approach is also valid in explaining our observed daytime gradients of nitrous acid during the Turm 2003 campaign at the meteorological tower of the IMK, FZ Karlsruhe. Therefore, daytime chemistry, i.e. mainly

photolysis (see chapter 2.3.1, and 2.3.7), and labile layering in the PBL, which usually occurs during the day (see chapter 2.5.2, 2.5.3.2), was needed to be included in the NCAT model.

2.3.6.4 Kinetics & Water Dependence of HONO Formation

In this section, we will show some empirical findings about the heterogeneous HONO formation, which were combined to an equation, which describes the kinetics.

A square dependence of the HONO production on NO_2 [Cheung *et al.*, 2000] would be expected for reaction r. 2.33, but measurements in smog chambers⁸ and the atmosphere show a remarkably linear correlation between the HONO formation rate and the NO_2 concentration [Ackermann, 2000; Finlayson-Pitts *et al.*, 2003; Jenkin *et al.*, 1988; Kessler and Platt, 1984; Kleffmann *et al.*, 1998; Pitts *et al.*, 1984b; Sakamaki *et al.*, 1983; Svensson *et al.*, 1987]. Other groups observed a reaction order between one and two [Mertes and Wahner, 1995]. Possible explanations for this observed linear dependence of the HONO formation on NO_2 will be discussed in chapter 2.3.6.5.

The heterogeneous nature of the reaction r. 2.33 was proven by observing an increase of the HONO formation with the surface to volume ratio in smog chambers (see e.g. [Kleffmann *et al.*, 1998; Pitts *et al.*, 1984b; Sakamaki *et al.*, 1983; Svensson *et al.*, 1987]).

Concerning the yield of HONO from reaction r. 2.33, it was found that 50% of the adsorbed NO_2 is released as HONO [Goodman *et al.*, 1999; Kleffmann *et al.*, 1998; Svensson *et al.*, 1987]. NO and N_2O have also been reported [Finlayson-Pitts *et al.*, 2003; Kleffmann *et al.*, 1998] as gas-phase products of secondary reactions in minor amounts. The other 50 % of the nitrogen were observed to remain as HNO_3 at the surface [Finlayson-Pitts *et al.*, 2003; Goodman *et al.*, 1999; Svensson *et al.*, 1987]. In contrast, [Stutz *et al.*, 2002] observed only one HONO molecule being released from a grass surface for every 33 NO_2 molecules deposited.

Combining an observed first order kinetic with respect to the precursor NO_2 for the heterogeneous HONO formation, the rate constant k of reaction r. 2.33 was derived empirically from smog chamber data [Kessler, 1984; Svensson *et al.*, 1987; Winer and Biermann, 1994] as:

$$\frac{d[\text{HONO}]}{dt} = [\text{H}_2\text{O}] \cdot \frac{S}{V} \cdot k \cdot [\text{NO}_2] \quad \text{eq. 2.10}$$

Here, the concentrations are given in molec cm^{-3} , the surface S (e.g. smog chamber) in m^2 and its volume V in m^3 . The kinetic law further depends on the amount of water [H_2O] (given in ppm) present (this will be discussed below).

publication	k [$\text{s}^{-1} \text{ppm}^{-1} \text{m}$]	surface studied
[Pitts <i>et al.</i> , 1984b]	$4.2 \cdot 10^{11}$	Teflon
[Svensson <i>et al.</i> , 1987]	$4.6 \cdot 10^{11}$	Teflon / glass
[Kleffmann <i>et al.</i> , 1998]	$3.7 \cdot 10^{10}$	quartz glass
[Ackermann, 2000]	$3.2 \cdot 10^9$	traffic tube (coated metal plates, tarmac)
[Trick, 2000]	$6.0 \cdot 10^9$	PE foil and asphalt

table 2.5: HONO production rates on different types of surfaces (standardized).

⁸ Measurements in smog chambers generally show lower production rates compared to the atmosphere, whereas experiments in a smog chamber by [Kleffmann *et al.*, 1998] showed a parallel formation of NO and N_2O as well.

Different values of the rate coefficient k were reported in literature as can be seen from table 2.7. In particular, the measurements by [Ackermann, 2000] show that high HONO production rates may be caused by high aerosol concentrations and the strongly enlarged⁹ surfaces of a road tunnel. This again indicates the strong influence of the surface type on the HONO formation.

As expressed by equation eq. 2.10., [Jenkin *et al.*, 1988; Pitts *et al.*, 1984b; Sakamaki *et al.*, 1983; Svensson *et al.*, 1987] observed an increase of the heterogeneous HONO formation proportional to the gas phase water concentration. Due to the high amounts of water present under tropospheric conditions and consequently the coverage of surfaces by at least one or more layers of water, it seems to be more likely that an adsorbed water molecule is involved in the formation of HONO. This is indicated e.g. by [Finlayson-Pitts *et al.*, 2003; Kleffmann *et al.*, 1998] who did not observe any dependence of the heterogeneous HONO formation on gas-phase water concentration. It was suggested that an uniform water coverage on the walls of the reaction vessel exists. Based on this finding, a modified approach deals with the uptake coefficient of the gaseous molecule into the liquid phase as performed e.g. by [Kleffmann *et al.*, 1998]. The rate-limiting step of the heterogeneous reaction r. 2.33 is thereby the uptake into the differing phase, involving several, partly reversible, processes that are illustrated in figure 2.10.

So far only few studies have focused on the water dependence of the HONO formation in more detail. From laboratory studies and testing in the atmosphere, [Lammel, 1999] classified surfaces as “dry” (below ~ 50 % R.H.), “wet” (above that, but below ~ 95 % R.H.), and “aqueous” ($> \sim 95$ % R.H.). With the exception of the soot particles, the R.H. dependence of the HONO formation by reaction r. 2.33 was further described by [Lammel, 1999] as a pseudo-first order behavior for “dry” and “aqueous” surfaces (consequently the HONO formation was independent of the concentration of H_2O), but dependent on the water concentration with a second order rate constant for a “wet” surface. This parameterization is based on the arguments that the amount of chemisorbed (see chapter 2.4.2) water at very dry conditions becomes approximately independent of the water vapor levels, while in a “wet” case the amount of adsorbed water is dependent on water vapor.

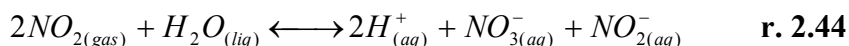
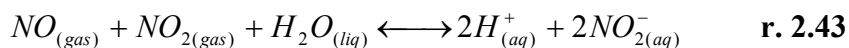
The dependence on the R.H. of the surface adsorbed water was also studied e.g. by [Saliba *et al.*, 2001]. A linear increase of the surface adsorbed water was observed in the range of 10 to 70 % R.H., with derivations above and below, respectively, but in general following the shape of a BET isotherm (see chapter 2.4.4.3). However, the qualitative comparison of the studies by [Saliba *et al.*, 2001] with those by [Lammel, 1999], showed a steady increase of the number of water mono-layers (see chapter 2.4.2), adsorbed at various surfaces of atmospheric relevance, with the R.H.

A recent field study by [Stutz *et al.*, 2004b] measured the concentrations of NO_2 , HONO and R.H. at different locations and the data was analyzed, indicating the ratio of the concentrations of nitrous acid and nitrogen dioxide to be strongly dependent on the relative humidity. According to [Stutz *et al.*, 2002], a pseudo steady state was assumed between the heterogeneous conversion of NO_2 towards HONO and the loss of HONO on the surface, characterized by the ratio of the reactive uptake coefficients for each process. It was observed by [Stutz *et al.*, 2004b] that the reaction probability for the NO_2 to HONO conversion is more dependent on R.H. than the loss of HONO. Only if the reaction probability for this loss is independent from R.H., [Stutz *et al.*, 2004b] achieved a linear dependence of the HONO formation on R.H., which is in agreement with laboratory studies.

⁹ Due to the agglomeration of dust and dirt on all surfaces caused by the traffic in the tunnel.

2.3.6.5 Mechanistic Sequences of Heterogeneous HONO Formation

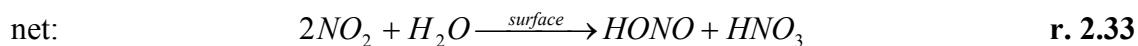
Due to the high amounts of water present in the troposphere and possible multi-layering, an aqueous phase may be established on surfaces (see chapter 2.4.4.3). Consequently, HONO was believed to be formed in the multiphase chemistry of the nitrogen oxides for a long time. [Schwartz and White, 1981b] reviewed this and considered the possible role of the following equilibria:



The formation rates of HONO and HNO₃ in cloud water through these reactions were found to be dependent on the partial pressures of all reaction educts [Schwartz and White, 1981b], thus reflecting higher-order rate expressions. Consequently, a second order rate coefficient for reactions r. 2.43, and r. 2.44 in the liquid phase was observed by several groups, which essentially agree [Komiyama and Inoue, 1978; Komiyama and Inoue, 1980; Lee and Schwartz, 1981a; Lee and Schwartz, 1981b]. However, these values lead, even under assumption of favorable conditions to a rate of HONO formation of about four orders of magnitude lower than observed [Lammel and Cape, 1996; Platt, 1986]. Additionally, [Schwartz and White, 1981b] found the solubility of NO and NO₂ expressed in terms of a Henry equilibrium to have a rate constant in the order of 1.93 x 10⁻³ mol L⁻¹atm⁻¹ for NO and 1.0 x 10⁻² mol L⁻¹atm⁻¹ for NO₂. Both rate constants are at the lower limit of solubilities. Thus, it seems unlikely that the disproportionation of NO_x proceeds via r. 2.43 or r. 2.44.

At high NO_x partial pressures (ppm region), these reaction pathways r. 2.43, and r. 2.44 may become more important, but in the moderately polluted atmosphere, they are slow, even in the presence of 1g of H₂O (liq.) per m³ of air. Thus it was concluded by [Schwartz and White, 1981b] that the heterogeneous formation of HONO cannot proceed via r. 2.43, and r. 2.44 unless high partial pressures (> 0.1 ppm) of NO_x are maintained in contact with liquid water for substantial periods of time (tens of hours).

Besides, the measured second order kinetic of HONO formation with respect to NO_x is controversy to other observations (see chapter 2.3.6.4). The linear dependence of the heterogeneous HONO formation on NO₂ was explained by [Jenkin *et al.*, 1988] using the following reaction scheme:



Here, reaction r. 2.47 is the step determining the overall reaction rate. This is expected to be first order with respect to NO₂ by basic theory.

However, the results published by [Ahmed *et al.*, 1997] imply that adsorption of NO₂ on water seems unlikely. Thus a different explanation for the HONO formation was given by [Mertes and Wahner, 1995]. They suggested that the anhydrides of nitrous and nitric acid (N₂O₃ and N₂O₄) are intermediates in the HONO formation reaction:



The anhydrides show a high solubility in water, so the rate-limiting step proceeds in the condensed phase. Afterwards, the pH dependent Henry-equilibrium¹⁰ adjusts for HONO and HNO₃ and subsequently the nitrous acid escapes from the liquid phase to the gaseous phase [Barney and Finlayson-Pitts, 2000]. With this mechanism, a much higher nitrous acid formation efficiency is reached compared to the formation via reaction r. 2.33, but it includes NO, which was thought to play only a minor role in the formation process of nitrous acid. According to [Schurath, 2000] an alternative mechanism may be proposed, without any involvement of NO:



The formation on e.g. aerosols may therefore be written as:

$$\frac{d[HONO]}{dt} = \gamma \cdot [N_2O_4] \cdot \frac{\langle v \rangle}{4} \cdot S_{aerosol} = \gamma \cdot K_{dim} \cdot [NO_2]^2 \cdot Z_{surf} \quad \text{eq. 2.11}$$

where γ is the probability for the corresponding reaction, and $S_{aerosol}$ is the specific surface of the atmospheric aerosol [cm^{-1}]. Further, $\langle v \rangle$ is the average velocity of the NO_2 molecules according to a Maxwell-Boltzmann statistics yielding a collision frequency $Z_{surf} < 1 \text{ s}^{-1}$ in combination with typical aerosol surfaces of $1000 \mu\text{m}^2 \text{cm}^{-3}$. Taking the equilibrium constant K_{dim} of the NO_2 to N_2O_4 dimerisation (r. 2.50) into account, which is $\sim 10^{-18} \text{ cm}^3 \text{molec}^{-1}$ at a temperature of 283 K, the HONO production rate can be calculated as:

$$\frac{d[HONO]}{dt} = \gamma \cdot 10^{-18} \text{ cm}^3 \cdot [NO_2]^2 \cdot 1 \text{ s}^{-1} \quad \text{eq. 2.12}$$

Thus, even for a small production rate of 0.05 ppb HONO / h at an NO_2 mixing ratio of 20 ppb, the probability of the reaction γ has to be larger than one, and the adsorption of NO_2 on the water surface of aerosols has to be assumed as contrasting [Ahmed et al., 1997].

However, evidence for an important role of the anhydrides N_2O_4 and N_2O_3 in the formation of atmospheric formation of nitrous acid was given by several publications during the last few years.

The reaction pathways for the hydrolysis of NO_2 producing HONO were calculated by [Chou et al., 1999] based on density-functional theory. It could be shown that by the homogeneous hydrolysis of NO_2 or N_2O_4 , the OH radical is a reaction intermediate, which combines with a second NO_2 to form HNO_3 in the next reaction step. The number of H_2O molecules was varied and the bimolecular reaction ($NO_2 + H_2O$) could be excluded due to the reversibility (with no energy barrier) of the reaction forming HONO [Chou et al., 1999]. Thus, additional H_2O molecules are needed to stabilize the transition state or the intermediate that contains the OH radical. However, the energy barrier is too high, and this reaction is insignificant. A high energetic barrier was calculated for N_2O_4 , indicating that all homogeneous hydrolysis of NO_2 is practically insignificant also in the formation of HONO regardless of water vapor pressure, and that a heterogeneous process is most likely responsible [Chou et al., 1999].

[Barney and Finlayson-Pitts, 2000] considered N_2O_4 as a key intermediate in the heterogeneous hydrolysis of NO_2 to form HONO in the atmosphere. The uptake of 2.9 Torr of NO_2 in N_2 at a total pressure of 508 Torr on a porous glass surface was studied using FTIR under conditions of varying amounts of surface-adsorbed water. The water uptake on silicate type surfaces was shown to be relevant for the further proceeding of the heterogeneous reactions forming HONO [Sumner and Finlayson-Pitts, 2003]. It was found that the ratio of N_2O_4 to NO_2 was enhanced on the glass surface relative to the gas phase. Even under relatively dry surface conditions, the formation of gas-phase NO and N_2O , as well as surface-

¹⁰ Henry's law coefficients are a quantitative measure to describe the equilibrium between X (gas) \leftrightarrow X (aq). They are calculated by $H_x [\text{mol l}^{-1} \text{atm}^{-1}] = [X(\text{aq})]/P_x$, with the partial pressure P_x of [X] in the gas phase. Some Henry's law coefficients for NO_2 can be found in [Cheung et al., 2000; Finlayson-Pitts and Pitts, 2000].

adsorbed HNO_3 was observed due to the presence of small amounts of water at the surfaces. When increasing the initial R.H., surface-adsorbed HNO_3 was formed immediately, as well as gas-phase NO , N_2O , and HONO .

An integrated mechanism was recently proposed by [Finlayson-Pitts *et al.*, 2003; Wingen *et al.*, 2003] and is illustrated by figure 2.11.

Here, the N_2O_4 is the key-precursor surface species. By isomerization, the adsorbed dinitrogen tetroxide forms its asymmetric form of ONONO_2 . This species autoionizes generating NO^+NO_3^- in competition with the back reaction with gas-phase NO_2 yielding N_2O_4 . In a complex reaction with water, HONO is finally formed, which escapes into the gas-phase, while the equal amount of HNO_3 remains at the surface. The surface nitric acid generates NO_2^+ , which is well known for concentrated solutions of HNO_3 [Finlayson-Pitts *et al.*, 2003]. Secondary reactions of nitrous acid with HNO_3 at the surface yield NO^+ . Reactions with NO_2^+ , which finally escapes into the gas phase as NO (see figure 2.11) are also observed.

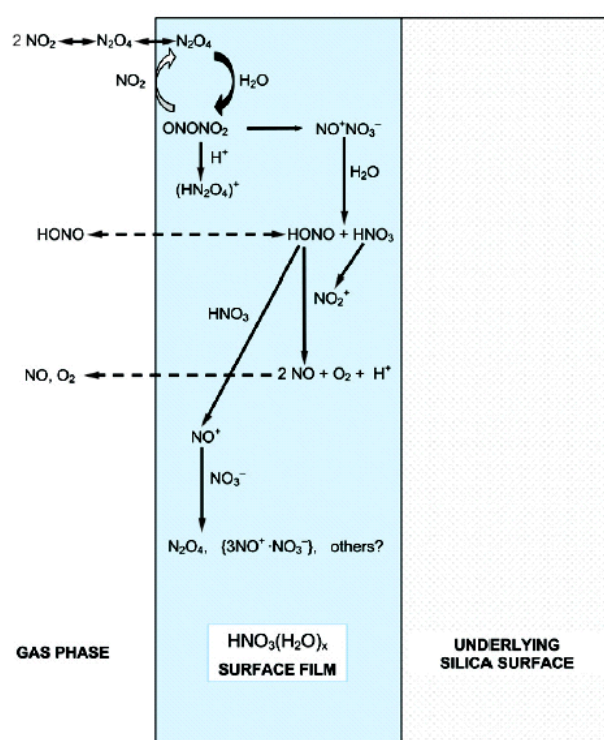


figure 2.11: Reaction scheme of HONO formations proposed by [Finlayson-Pitts *et al.*, 2003; Wingen *et al.*, 2003].

The mechanism was tested for mass balance, gas-phase products, intermediates, but also kinetics and essentially agrees with all previous work (see chapters above), as reported by [Finlayson-Pitts *et al.*, 2003]. It was concluded that the NO observed in the gas-phase (beside HONO) originated in secondary reactions of HONO at the surface, which has become acidic due to simultaneous generation of HNO_3 , which remains at the surface. The production of NO by bimolecular secondary reactions of HONO at the surface is thereby highly sensitive to HONO and has an induction time [Finlayson-Pitts *et al.*, 2003]. The yield of HONO in the gas-phase is much less than 50 % of the NO_2 loss, but including products, such as NO , from secondary reactions, 50 % were found. For longer reaction times and higher R.H., small amounts of N_2O were observed in the gas-phase as well.

Taking into account the low Henry's law coefficients (see above) for NO_2 [Finlayson-Pitts and Pitts, 2000; Schwartz and White, 1981a; Schwartz and White, 1981b], and no evidence

for a reactive uptake of NO₂ from ab-initio calculations by [Cheung *et al.*, 2000], [Finlayson-Pitts, 2004] concluded that there is no evidence for NO₂ adsorbed at the surface. However, N₂O₄ showing a high affinity to the wet surface was suggested to interact with HNO₃ or HNO₃-(H₂O)_n complexes. It could be shown that significant amounts of non-dissociated HNO₃ are present at the surface and that the water stabilizes these complexes or even the hydrates. Due to this fact, a contamination with acid of the smog chamber was observed [Finlayson-Pitts, 2004]. The kinetic order of the HONO formation with respect to water was observed to increase with water vapor concentration. This increase was much larger than expected for a linear behavior, but followed the shape of the isotherm (see chapter 2.4.4) for water uptake on the surface. Of crucial importance is the reaction order with respect to NO₂, as is the dimerization towards N₂O₄. However, [Finlayson-Pitts *et al.*, 2003] suggest the back reaction of the asymmetric ONONO₂ with gas-phase NO₂ regenerating N₂O₄ is faster than its reaction with water. Consequently, the rate of HONO formation becomes first order in NO₂. We will show, however, in the modeling studies carried out for the smog chamber measurements (see chapter 5.5) that this mechanism is applicable to our data. It was chosen therefore as basic theory for the analysis of our data of heterogeneous HONO formation.

2.3.7 Sinks of Atmospheric Nitrous Acid

We have already mentioned the photolysis of HONO [Stockwell and Calvert, 1978; Stutz *et al.*, 2000] yielding NO and the OH-radical directly to be the dominant sink for atmospheric nitrous acid:



This yields lifetimes of approx. 8 min for HONO at noon under clear-sky conditions. Thus, a steady state for daytime nitrous acid is suspected, resulting in the observed HONO daytime mixing ratios given above. The importance of HONO photolysis for the primary production of OH radicals was recently carried out by modeling studies of [Aumont *et al.*, 2003]. The three different HONO sources (direct emission, heterogeneous production on the ground surface and heterogeneous production on the aerosol surface) to the NO_x / HO_x / O₃ chemistry and budgets in the polluted boundary layer were investigated for different scenarios. Major relevance of HONO photolysis was found for the evolution of photosmog episodes for summertime conditions, but for wintertime conditions, HONO sources were found to be major contributors to the primary OH production, leading to major changes in the HO_x and NO_x budget all day long.

Nevertheless, a few percent of HONO is also expected to be destroyed by OH radicals:



$$\text{with } k_{r. 2.53} = 4.5 \times 10^{-12} \text{ cm}^3 \text{ molec}^{-1} \text{ s}^{-1} \text{ [DeMore et al., 2003].}$$

Using a typical nighttime OH concentration of (1 – 7) × 10⁵ molec cm⁻³, the resulting lifetime of nitrous acid by this reaction r. 2.53 can be calculated to be between 610 and 88 hours [Holland *et al.*, 2001]. Thus this mechanism only becomes important at high OH concentrations during the day.

HONO is a fairly stable compound in the nocturnal boundary layer. However, both reverse-reactions of nitrous acid corresponding to reactions r. 2.27, and r. 2.28, the self-reaction of HONO [Chan *et al.*, 1976b; Mebel *et al.*, 1998] as well as the reaction of nitrous acid with nitric acid [Kaiser and Wu, 1977b], were found to be too slow in the gas-phase to be significant in the atmosphere:



$$k_{r. 2.54}(300\text{K}) = 1.4 \cdot 10^{-24} - 1.2 \cdot 10^{-27} \text{ cm}^3 \text{ molec}^{-1} \text{ s}^{-1} \text{ [Mebel et al., 1998]}$$



$$k_{r. 2.55}(300\text{K}) = 1.55 \cdot 10^{-17} \text{ cm}^3 \text{ molec}^{-1} \text{ s}^{-1} \text{ [Kaiser and Wu, 1977b]}$$

It is currently unclear whether these reactions r. 2.54, and r. 2.55 can become important, if proceeding heterogeneously, but it is thought to be of minor importance in the atmosphere due to the low binding affinity of NO_2 [Ahmed *et al.*, 1997].

The HONO self-reaction r. 2.54 was observed by the groups [Mertes and Wahner, 1995; Svensson *et al.*, 1987; TenBrink and Spoelstra, 1998] to occur heterogeneously on surfaces (e.g. of the reaction vessels, see r. 2.39). According to their laboratory results, a second order rate of reaction for the HONO loss was proposed by [Svensson *et al.*, 1987]. Due to a modified HONO removal from their smog chamber after preparations on the reactors walls, the HONO sink reaction was suspected to proceed heterogeneously by a rate constant of $10^{-22} \text{ cm}^3 \text{ molec}^{-1} \text{ s}^{-1}$ on a “passivated” surface. [TenBrink and Spoelstra, 1998] quantified this heterogeneous second order loss of HONO to occur via a rate constant of $1.5 \cdot 10^{-19} \text{ cm}^3 \text{ molec}^{-1} \text{ s}^{-1}$. Lifetimes of HONO in the nocturnal boundary layer are of the order of several hours [Spindler *et al.*, 1998], if layer removed by dry deposition onto the ground surface followed by the heterogeneous self-reaction of HONO.

However, in a combined equilibrium of all, the HONO formation reactions r. 2.32, and r. 2.33 as well as the different loss processes for nitrous acid (r. 2.54, and r. 2.55) are likely to establish themselves as surface-reactions during the night [Schurath, 2000; Syomin *et al.*, 2002]. This was also observed by [Trick, 2000; Trick *et al.*, 2003] in a smog chamber, when the rate of reaction for HONO decomposition changed from an order of 2 to an order of 1 with decreasing HONO concentrations in the chamber.

[Kleffmann *et al.*, 1998; Kleffmann *et al.*, 1994] observed the formation of nitrous oxide during the decay of HONO in a laboratory system, which seems to occur on the reactor surface. The overall reaction is suggested to be



but the exact mechanism still remains unclear.

Gas-phase reactions of HONO with NO_2 , O_3 , and HCl , were studied by [Lu *et al.*, 2000], who calculated means of ab-initio molecular-orbital and examined transition-state theory. For the formation of HNO_3 and NO from the reaction of $\text{HONO} + \text{NO}_2$ via the abstraction of OH in HONO by NO_2 , an activation energy in the range of $\sim 32 \text{ kcal mol}^{-1}$ and a rate constant of $1.2 \times 10^{-14} \text{ cm}^3 \text{ mol}^{-1} \text{ s}^{-1}$ were calculated [Lu *et al.*, 2000]. Lower activation of $\sim 14 \text{ kcal mol}^{-1}$ were calculated for the $\text{HONO} + \text{O}_3$ and the $\text{HONO} + \text{HCl}$ reaction respectively; rate coefficients of $5.7 \times 10^{-2} \text{ cm}^3 \text{ mol}^{-1} \text{ s}^{-1}$ and $0.13 \times 10^2 \text{ cm}^3 \text{ mol}^{-1} \text{ s}^{-1}$ at 300 K were obtained. It was concluded [Lu *et al.*, 2000] that the three gas-phase reactions are too slow be significant under the stratospheric and tropospheric conditions.

Further chemical sink reactions of HONO occur especially at temperatures below 0°C on freezing cloud or fog droplets or ice surfaces. These reactions include the oxidation of nitrous acid / nitrite in the aqueous solutions of these particles yielding nitrate or hydroxyl anions. However, this HONO sink is not well quantified and is only thought to be of importance in Polar Regions, the upper troposphere and lower stratosphere (see [Finlayson-Pitts and Pitts, 2000]).

Finally, as a water-soluble acid, HONO can be removed from the atmosphere via wash out by rain (wet deposition), where it contributes to acid rain, or obviously by dry deposition, consisting of agglomeration on aerosols and the ground [Stutz *et al.*, 2002] and chemical reactions. [Stutz *et al.*, 2002] also observed HONO formation and deposition on the ground balancing each other. Thus, highest HONO values can be found at the compensation point between both processes. For a grass meadow surface, this compensation point was found at a HONO / NO_2 ratio of $3 \pm 1 \%$. However, deposition of HONO on rough surfaces plays a key role for the HONO gradient measured in the lower PBL [Stutz *et al.*, 2002].

2.4 Heterogeneous Reactions and Catalysis

Catalysts¹¹ were already introduced to chemistry in the 19th century. Nowadays, more than 90 % of all chemical manufacturing processes in use throughout the world utilize a catalyst in one form or another. Prominent examples are e.g. the steam-reform-cracking in the petroleum refineries, the Fischer-Tropsch catalysis on hydrocarbons, the Haber-Bosch ammonia synthesis, the Ostwaldt nitrogen oxidation, and last but not least the (three-way) automobile exhaust catalyst as already presented in chapters 2.1.1, and 2.3.3. The science and technology of catalysis are therefore of central practical importance for any chemical engineering, as well as environmental-related techniques.

Some reactions (e.g. oscillating reactions) are known to occur autocatalytic, i.e. the reaction is catalyzed by its products. However, the addition of a further species operating as a catalyst is more likely. Different types of addition of this catalyst are possible. In laboratories, a homogeneous catalysis is often performed, where the catalyst is in the same phase as the reaction mixture (e.g. an acid or base added to an aqueous solution). In industrial processes and even in environmental practice, the heterogeneous catalysis, where the catalyst is in a different phase than the reaction mixture (e.g. a solid for a gas-phase reaction), is used more often. In the following, we will only refer to the heterogeneous catalysis of gas-phase reactions proceeding heterogeneously via the surface of a solid.

In general, a catalyst is known to lower a reactions activation energy, mostly by providing an alternative reaction path that avoids the slow, rate-determining step of the un-catalyzed reaction (valid for all kinds of catalysis). The catalyst may actively participate in the reaction (or some steps of the reaction), e.g. as bonding partner, but in general remains un-consumed and does not appear in the overall net reaction equation. At the same temperature and pressure, chemical reactions proceed faster towards its products, if they are catalyzed. In chemical balance-reactions, the catalyst enhances both the reactions towards the products as well as the back-reaction towards the educts. The free reaction enthalpies ΔG are reduced by an equal amount and thus only the time until the equilibrium is reached is changed, but the balance equilibrium composition is not altered. Further, the catalytic substances enhance the efficiency of a chemical reaction and are often marked by a enormous selectivity.

To describe this in a more quantitative way, it is essential, to define the term “catalytic activity” first. For heterogeneous catalysis, this requires quite some experimental effort, especially to distinguish between catalytic or surface-related effects. Often, this distinction cannot be well defined and both aspects have to be taken into account.

2.4.1 Heterogeneous Catalysis

As we will show in chapter 2.4.3, any gas-solid or liquid-solid-catalyzed reaction can be expressed as the product of a rate coefficient k and a pressure (or concentration) dependent term of the reactant i :

$$rate = k \cdot p_i \quad \text{eq. 2.13}$$

The rate constant of the overall catalytic reactions usually includes several elementary reaction steps, of which one is rate determining. All of these rate constants are known by basic theory of physical chemistry to further be dependent on external parameters, such as temperature, pressure, but in the case of heterogeneous or catalytic reactions also on the surface material and condition of the solid. This is expressed by the Arrhenius equation:

¹¹ The originally meaning by Berzelius in 1836 was “loosening down” in Greek.

$$k = A \cdot \exp\left(\frac{-E_a^*}{R \cdot T}\right) \quad \text{eq. 2.14}$$

Here, A is the so-called pre-exponential factor including e.g. the temperature dependence. The apparent activation energy E_a^* of the catalytic reaction is not the true activation energy E_a , as the concentration of the reactant at the catalyst is generally temperature dependent (even if the catalysts structure remains unchanged). Thus, the long-time used definition of a catalytic reaction acceleration caused by lowering the overall activation energy is generally not valid.

Far more convenient is the concept of turnover frequency (TOF) or turnover number. Here, the number of times n that the overall catalytic reaction in question takes place per catalytic site S per unit time t for a fixed set of reaction conditions (temperature, pressure or concentration, reactant ratio, extent of reaction) is defined:

$$TOF = \frac{1}{S} \cdot \frac{dn}{dt} \quad \text{eq. 2.15}$$

The number of active surface sites on a surface S is usually easy to determine for enzymatic processes, but difficult for heterogeneous reactions. Thus, S is often replaced by the total, readily measurable area A of the exposed catalyst (obviously corresponding to lower values of the TOF), or it is expressed per mass or per volume of the catalyst. To link both, the reaction rate coefficients and the turnover frequency, the TOF is often divided by the flux of reactant incident upon the catalyst, yielding the so-called overall reaction probability R_p defined by:

$$\gamma = \frac{\text{rate of formation of product}}{\text{rate of incidence of reactant}} \quad \text{eq. 2.16}$$

Another possibility to define catalytic activity is via the temperature required for the reaction in order to attain a certain (arbitrary) rate of conversion. Plots of the catalytic activity (the temperature at a fixed conversion rate for a series of catalysts versus the enthalpy reduction by these catalysts) yield the so-called volcano-plots. Highest catalytic activity is obtained at the peak of that curve, corresponding to the highest stability of the so-called transitory state (see below) at the catalysts surface. However, this approach may be misleading due to the optimized temperatures of different catalysts.

With these TOF or R_p , we have now a measure for deciding, if a reaction proceeds catalytically or not. The question remains, why the heterogeneous phase, the solid, may act as a catalyst. First, this might be caused by surface-related effects only, i.e. the fact that for a bimolecular reaction, the concentrations of the reactants are much higher than in the gas phase. Consequently, the catalytic reaction mechanism is not different in character from a homogeneous one, but due to the concentration factors.

For many cases, such as uni-molecular reactions, the concept of surface concentration effect is not applicable, but catalysis occurs anyway. This is due to the fact that an intrinsically different reaction path is provided by the catalyst and the specific nature of the well-designed catalyst becomes quite important. Here, the geometric surface type (e.g. lattice type, pores, etc.) of the solid as well as its electronic structure (e.g. π -electron bonding, valence-bond of metals, etc) is of essential importance. The bond between the adsorbed species and the atoms on the surface of the solid established by chemisorption may be described by linear combination of the molecular orbitals (LCAO, resp. LCMO method). As known e.g. from organo-metallic catalysis, this requires a highest occupied molecular orbital (HOMO) as well as a lowest unoccupied molecular orbital (LUMO). Both have further restrictions to be combined, such as comparable energetic levels, but also their symmetry and this directly impacts on the transitory state yielding a high stereo-selectivity of the products in both isotopic as well as isomeric respect. The transition states or even ensembles of atoms (clusters) are formed in the reactions of the species adsorbed at the heterogeneous surface. These adsorbed intermediates may have a lifetime of some few μs or even ns, but enable the overall-reaction to proceed via reaction coordinates not possible in the gas-phase.

2.4.2 Adsorption and Desorption of Gases on a Solid Surface

In all heterogeneous processes at least one of the reactants must be attached to the exterior surface of the solid for a significant period of time, no matter if catalysis occurs or not. Within the heterogeneous transformation of two gas-phase species A and B forming e.g. C on a surface, mainly two different mechanisms of adsorption can occur [Thomas and Thomas, 1997]: only one of them is bound and converted to the products, while the other impacts upon it from the gas phase (Eley-Rideal mechanism); or both species are attached to the surface, and the reaction takes place in the resulting adsorbed layer (Langmuir-Hinshelwood mechanism - as illustrated by figure 2.12):

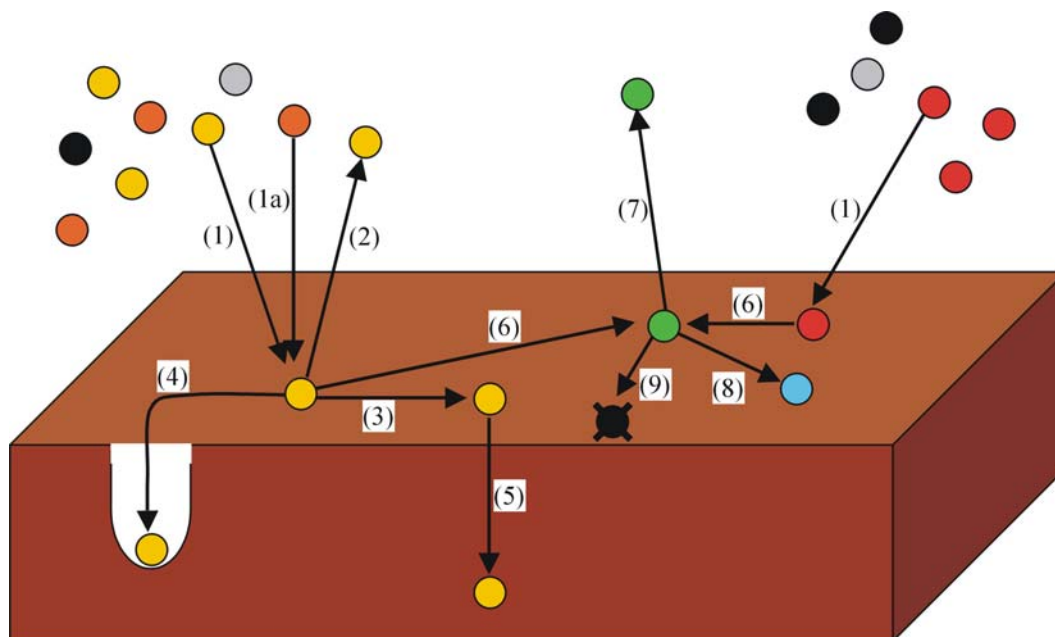


figure 2.12: Langmuir-Hinshelwood mechanism of heterogeneous catalysis: A species is molecularly adsorbed from the gas-phase (1) at a surface site. Another trace gas with equal bonding enthalpy might compete for the same surface site (1a). The species can be desorbed (2) again or undergo surface diffusion / migration (3), pore diffusion (4), bulk diffusion (5) or surface poisoning (9). However, also heterogeneous reactions (6) with another species adsorbed at the surface can occur. The reaction product is finally desorbed (7) again into the gas-phase or involved in further (secondary) reactions on the surface (8).

Thus in the Langmuir-Hinshelwood mechanism, the rate of a heterogeneous reaction is controlled by the reaction rate coefficient of the adsorbed molecules and all adsorption and desorption processes are in an equilibrium. In the Eley-Rideal mechanism, the heterogeneous reaction taking place between strongly adsorbed atoms (chemisorbed) and kept weakly by physical adsorption species is most likely limited due to the rate of chemisorption itself.

2.4.2.1 Possibilities of Gas-Phase to Solid-Surface Interactions

Corresponding to [Thomas and Thomas, 1997], we will distinguish *absorption*, which is a bulk phenomenon, from *adsorption* referred to as the accumulation of material at a surface and thus proportional to the surfaces area but not to its volume. This distinction is impossible, however, if the solids are capable of intercalating guest species or if they are highly microporous. In both cases, the surface area inside the solid is dominant.

Further, we need to distinguish between physical adsorption and chemisorption [Thomas and Thomas, 1997]. The main differences are summarized by table 2.6:

	physical adsorption	chemisorption
bond structure	permanent dipole, induced dipole, or quadrupole („van-der-Waals adsorption“)	chemical bonding of valence-electrons
enthalpy changes	$\Delta H \sim -10$ to -40 kJ mol^{-1}	$ \Delta H > 80 \text{ kJ mol}^{-1}$ (often exceed 400 kJ mol^{-1})
temperatures	close to the boiling point of the adsorbent, often low	no restriction
multi-layering	often	rare
surface site selectivity	low (only at low coverage)	very high

table 2.6: Distinction between physical adsorption and chemisorption by some parameters.

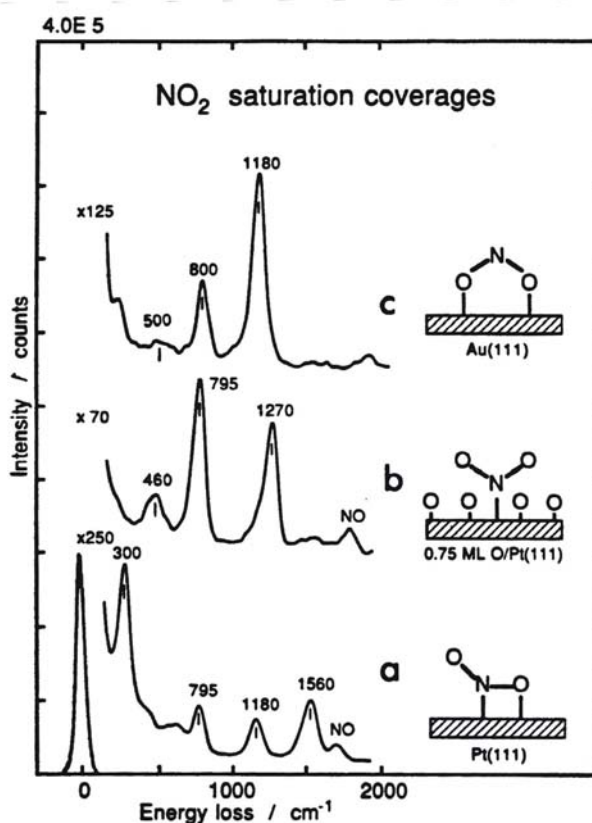


figure 2.13: High-resolution electron energy-loss spectroscopy (HREELS) spectra for the chemisorption of NO_2 on $\text{Pt}(111)$ in different bonding geometries (adapted from [Bartram and Koel, 1988]).

These main differences are all due to the bonding-structure: chemical bonds by the chemisorption, but van-der-Waals attraction by electric forces of dipoles, induced dipoles or quadrupole moments by the physical adsorption. Consequently, they differ in their enthalpy changes as well as the temperatures at which they occur. Generally, adsorption is

characteristic for a given temperature, and (equilibrium) pressure, but also the surface area available.

Since chemisorptions are chemical reactions confined to the surface of solids, they are very site-specifically selective, even in the same solid. Chemisorption can occur via molecular (non-dissociated adsorption) or dissociative adsorption (into fragments of the original molecule) at the surface. However, a new bond is established between the adsorbed species and the surface of the solid. The chemisorption was for a long time not distinguished from catalysis, as both appear intertwined: chemisorption as the mode of adsorption and heterogeneous reaction or catalysis as the consequence.

At low coverage, a certain degree of selectivity is observed for some processes of physical adsorption as well, but multi-layering adsorption within becomes almost indistinguishable from condensation or liquefaction at higher coverage.

Possible structures of surface-bound NO_2 are shown in figure 2.13 for adsorption on Pt(111) as solid surface.

2.4.2.2 Energetic Aspects of Adsorption and Desorption

From the energetic point of view, the events occurring within chemisorption or physical adsorption can be approximated by a Lennard-Jones potential energy diagram [*Lennard-Jones and Devonshire*, 1936] (figure 2.14).

First, the gas molecule may be elastically scattered (i.e. without loss of energy) back into the gas-phase. However, it may also lose sufficient translational energy to the solid and thus become trapped in a physically adsorbed state (the first shallow potential minimum in figure 2.14). In this state, the molecule may either be inelastically (i.e. with loss of energy) scattered back into the gas-phase or hop or migrate¹² to a neighboring site at the surface, or at least it may be chemisorbed, if it is proceeding nearer to the surface from that precursor state of physical adsorption. However, in chemisorption, the molecule is either directly bound by losing chemical energy released to the surface by exothermic transfer¹³ or undergoes further hops or migrations on the surface to dissipate excess energy. Finally, the molecule or its dissociated is bound to the solid of the surface. It should be mentioned that chemisorption might also occur without prior trapping by physical adsorption. However, there is evidence for the physical adsorption as a precursor state, as often chemisorption is observed as a non-activated process (becomes true, whenever the crossover x in figure 2.14 is below the potential energy zero) [*Thomas and Thomas*, 1997].

Using experimental techniques, it can be ascertained which state is taken up by a molecule, when it collides with a particular solid surface. The experimental techniques for characterizing surfaces are described in detail e.g. by [*Adamson and Gast*, 1997; *Thomas and Thomas*, 1997]. The most commonly used techniques are X-ray emission spectroscopy (XRE), X-ray adsorption spectroscopy (XANES, EXAFS), X-ray fluorescence (XRF), X-ray diffraction (XRD), nuclear magnetic resonance (NMR) spectroscopy, electron-spin resonance (ESR) spectroscopy, Mössbauer spectroscopy (Moss.S, CEMS), Raman spectroscopy (RS), Auger electron spectroscopy (AES), UV-photoelectron-induced spectroscopy (UPS, XPD, XPS, ESCA), scanning transmission or scanning tunneling microscopy (EELS, SEM, TEM, ED, HREM, STEM, STM), but also ion-scattering (ISS), secondary-ion mass spectroscopy

¹² Surface migration occurs, when its activation energy is lower than the thermal kinetic energy (kT) of the adsorbate. Thus the adsorbed species is freely mobile across the surface and its behavior is that of a gas molecule restricted to two dimensions.

¹³ Since entropy decreases by adsorption, the enthalpy ΔH must be negative (exothermic) due to spontaneous events expressed by the Gibbs-Helmholtz potential $\Delta G = \Delta H - T\Delta S < 0$.

surface is thus assumed to be a rigid matrix of discrete sites for adsorbed species. It leads to a convenient method [Adamson and Gast, 1997; Thomas and Thomas, 1997] of defining surface coverage Θ as:

$$\Theta = \frac{\text{number of absorbed species}}{\text{number of atoms in the outermost layer of the substratum}} \quad \text{eq. 2.18}$$

Experiments showed that well-defined super-mesh (supper-lattice) structures are adopted as the surface is gradually populated [Thomas and Thomas, 1997]. The limits of stability of these various structures are often illustrated by simple phase diagrams (temperature-surface coverage plots). The equation eq. 2.18 is thus identical to the description of the surface coverage Θ as the ratio of the numbers of surface sites occupied to the total number of surface sites available.

2.4.3 Thermodynamic and Kinetic Considerations

Some thermodynamic and kinetic considerations can easily be performed. We will present them in the next chapter. Before we do so, we will mathematically deduce equations to describe the processes involved in adsorption and desorption. However, several further aspects of adsorption and desorption will remain unmentioned in this thesis, such as hysteresis of adsorption-desorption, characterizations of the structure of the surface itself, the experimental techniques to quantify this, the significance of pore structure and surface area, the theory of poisoning, but also promotion, deactivation and selectivity of catalysts. These topics are explained in detail in other literature (see e.g. [Adamson and Gast, 1997; Thomas and Thomas, 1997]).

2.4.3.1 Empirical Aspects on Thermodynamics

Experiments showed that the equilibrium distribution of adsorbent molecules between the surface (adsorbent) and the gas-phase depends on the pressure, temperature, the type of surface of the adsorbent, and the type of the adsorbate. Illustration of experimental results is usually presented by an adsorption isotherm, which shows the amount adsorbed as a function of the equilibrium pressure of the gas at a constant temperature. Empirically, the Brunauer classification [Brunauer *et al.*, 1938] (see figure 2.15) describes five types of adsorption isotherms and can be applied to for all kinds of solids and adsorbates.

Type I isotherms are most likely observed in heterogeneous reactions. The amount of a gas adsorbed saturates at certain coverage of the surface. However, all refer to different scenarios of adsorption, desorption and surface coverage and, essentially, one has to distinguish. When measuring adsorption isotherms for coverage Θ at different temperatures T , the adsorption heat ($-\Delta H_a$) can be obtained by the Clausius-Clapeyron equation:

$$\left. \frac{d \ln p}{d(1/T)} \right|_{\Theta=\text{const}} = -\frac{\Delta H_a}{R} \quad \text{eq. 2.19}$$

A plot of $\ln p$ versus $1/T$ at constant coverage yields the isosteric adsorption heat at the respective coverage. The effective size of adsorbed species can be determined by performing this procedure for a set of adsorption isotherms, (if derivations in the plot of isosteric heat of adsorption occur) and conclusions about the nature of adsorption link [Thomas and Thomas, 1997] can be reached.

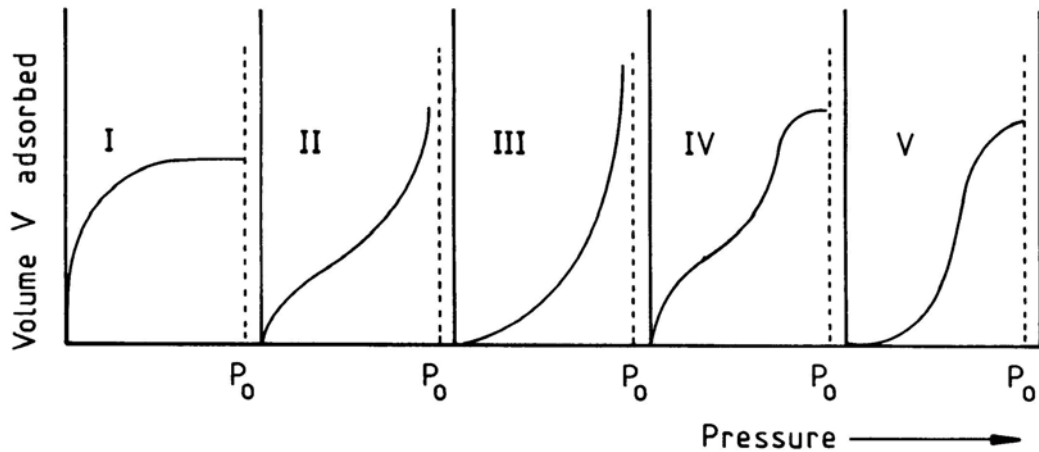


figure 2.15: *The five types of isotherms in the Brunauer classification. Most materials are of type I in this system. The knees in the isotherms refer to monolayer saturation and thus the beginning of multilayer adsorption (adapted from [Thomas and Thomas, 1997]).*

2.4.3.2 Mathematical Description of Adsorption

We will now have a more detailed look at the reversible adsorption-desorption equilibrium with special respect to dynamical considerations [Thomas and Thomas, 1997]. In the following, we will focus on the physical adsorption, but analogous equations can be derived for chemisorption.

Including kinetic gas theory, for the mean Boltzmann statistics velocity $\langle v \rangle$ of a species in the gas-phase, the flux F [molec $\text{cm}^{-2} \text{s}^{-1}$] of molecules striking the surface of an area size A [m^2] to get stuck to the surface after impact at a pressure p [hPa] is given by the Hertz-Knudsen equation to:

$$F = \frac{p}{\sqrt{2 \cdot \pi \cdot m \cdot k \cdot T}} \quad \text{eq. 2.20}$$

where T is the temperature, m the mass [kg] of the molecule and k [$\text{J K}^{-1} \text{Mol}^{-1}$] the Boltzmann constant. Consequently, the number N_a of molecules adsorbed by the surface is the sum of the flux towards the surface and the residence time τ :

$$N_a = F \cdot \tau \quad \text{eq. 2.21}$$

Experimental studies e.g. by Ertl and coworkers [Ertl, 1991] lead to a simple expression for the residence time τ , which includes the activation energy of desorption E_d :

$$\tau = \tau_0 \cdot \exp\left(\frac{-E_d}{R \cdot T}\right) \quad \text{eq. 2.22}$$

It can be shown that this equation is identical to the one presented by [Frenkel, 1948], which was derived from the application of statistical mechanics, by balancing the heat of adsorption with E_d . In this theory, τ is the period of perpendicular vibrations executed by the adsorbed species to the surface.

However, the equations eq. 2.20, eq. 2.21, and eq. 2.22 can be combined, yielding the rate of adsorption r_a simply as the product of the flux on a surface and the sticking coefficient, assuming that the process is non-activated and non-dissociative:

$$r_a = \frac{dN_a}{dt} = F \cdot s = \frac{s \cdot p}{\sqrt{2 \cdot \pi \cdot m \cdot k \cdot T}} \quad \text{eq. 2.23}$$

However, as already mentioned, the sticking coefficient varies with coverage. A simple functional dependence of s upon N_a is given by the Langmuir adsorption isotherms theory [Langmuir, 1918]. The particles striking to the surface at an empty site may either become adsorbed with the probability s_0 or is reflected back into the gas-phase, thus:

$$s = s_0 \cdot (1 - \Theta) \quad \text{eq. 2.24}$$

Sometimes s decreases linearly with coverage, but this is not always the case. This is due to the occurrence of precursor state in secondary adsorption layers. Within this precursor state, a striking molecule is trapped by a species already bond at the surface to a shallow energetic minimum. However, bonding to the surface is lower, thus migration is more likely in the second layer and finally either an empty site can be found for first-layer adsorption or a weak multi-layer adsorption occurs. However, it is obvious that both the findings of empty sites, as well as the multi-layer adsorption are limited and thus s in turn decreases.

We have already mentioned that dissociative chemisorption may occur directly or indirectly via a trapped first-layer precursor state. For direct dissociative chemisorption, negligible activation energy is required. In indirect dissociative chemisorption, a meta-stable chemisorbed transition state often occurs. The energy of this intermediate, which depends also on interatomic distance for the molecule as well as the distance to the surface, is vibrationally or translationally excited. However, an analogous description to that of equation eq. 2.23 may be given for dissociative chemisorption by including the activation energy for chemisorption [Thomas and Thomas, 1997].

It is also possible to derive the rate of adsorption, expressed by equation eq. 2.23 by applying statistical mechanics, especially transition-state theory [Thomas and Thomas, 1997]. We will show this exemplary for a non-dissociative adsorption, but the analogous discussion is valid for a dissociative chemisorption. Here, the adsorption reaction proceeds via an energetically activated transition state, an intermediate in structure between the free gas-phase molecules and the adsorbed state. For a non-dissociative adsorption on a uniform surface, with an equilibrium concentration of activated complexes N^* , N_g [mole.cm⁻³] as number of gas phase molecules and N_s number of surface sites per cm² for adsorption, this yields the equilibrium constant K :

$$K^* = \frac{N^*}{N_g \cdot N_s} = \frac{f^{*'}}{f_g \cdot f_s} \quad \text{eq. 2.25}$$

The f terms are the complete partition functions for the species and surface site given for a degeneracy g_i of a quantum state ε_i by:

$$f_n = \sum_i g_i \cdot \exp\left(\frac{-\varepsilon_i}{kT}\right) \quad \text{eq. 2.26}$$

The activated transitory complex, which has an average velocity $\langle v \rangle$ given by Maxwell-Boltzmann statistics for a 1-dimensional problem, will pass the energetic barrier toward the reaction products along a length of δ :

$$\tau' = \frac{\delta}{\langle v \rangle} = \delta \cdot \sqrt{\frac{2 \cdot \pi \cdot m^*}{k \cdot T}} \quad \text{eq. 2.27}$$

By including the transmission coefficient κ reflecting the probability that the activated complex will surmount the potential barrier to the final adsorbed state, the rate of transmission becomes:

$$r_a = \frac{-dN_a}{dt} = \kappa \cdot \frac{N^*}{\tau'} = \frac{\kappa}{\tau} \cdot \frac{f^{*'} \cdot N_g \cdot N_s}{f_g \cdot f_s} \quad \text{eq. 2.28}$$

Further, we factorize the complete partition function of the activated complex $f^{*'}$ into two terms using the 1-dimensional translation partition function corresponding to motion over a

barrier along a reaction coordinate (as described by quantum-mechanics of a particle in a 1-D box of the length δ):

$$f^{*'} = f^* \cdot f^*_{trans1D} = f^* \cdot \sqrt{2 \cdot \pi \cdot m^* \cdot k \cdot T} \cdot \frac{\delta}{h} \quad \text{eq. 2.29}$$

Finally, we re-define the zero reference energy of the initial state of the system and thus introduce the difference in zero-point energy of reactant and activated complex:

$$r_a = \frac{-dN_a}{dt} = \frac{k \cdot T}{h} \cdot N_g \cdot N_s \cdot \frac{f^*}{f_g \cdot f_s} \cdot \exp\left(\frac{-E_a^0}{R \cdot T}\right) \quad \text{eq. 2.30}$$

2.4.3.3 Description of Kinetic of Desorption

Similar to assumptions performed in chapter 2.4.3.2 and by [Thomas and Thomas, 1997] before, we may write the rate of desorption as given by the Polanyi-Wigner equation:

$$\begin{aligned} r_d &= \frac{-dN_a}{dt} = \nu \cdot N_a^m \cdot \exp\left(\frac{-E_d}{R \cdot T}\right) \\ &= \nu' \cdot N_a \cdot \Theta^m \cdot \exp\left(\frac{-E_d}{R \cdot T}\right) \end{aligned} \quad \text{eq. 2.31}$$

Here, E_d is the activation energy for desorption, ν the pre-exponential factor of the desorption rate coefficient, and N_a the number of binding sites of the admolecules. By using ν' , which differs from ν by a numerical factor and the fractional coverage Θ , we obtain the second part of equation eq. 2.31. However, the kinetic order of the desorption process is of crucial importance, as expressed by m . Zero-order kinetic often indicates desorption from a multi-layer, where the rate of desorption is independent of the coverage. First-order kinetics refers to single surface species, whereas second-order kinetics often results from recombination of adsorbate atoms forming diatomic molecules before desorbed.

Again, arguments similar to those in chapter 2.4.3.2 on the transitory state can be applied. Quantum-mechanical considerations yield:

$$r_d = \frac{-dN_a}{dt} = \frac{k \cdot T}{h} \cdot \frac{f^*}{f_a} N_a \cdot \exp\left(\frac{-E_d^0}{R \cdot T}\right) \quad \text{eq. 2.32}$$

If both the adsorbate and the activated complex are immobile, and further assuming a simple first-order kinetic of desorption, the ratio f^*/f_a is ~ 1 . Thus the pre-exponential factor ν (i.e. excluding N_a) is often observed to be:

$$10^{12} \leq \nu \left(= \frac{k \cdot T}{h} \right) \leq 4 \times 10^{13} \text{ s}^{-1} \quad \text{eq. 2.33}$$

We should finally note at this point that the desorption described by equation eq. 2.31, and eq. 2.32 above is dependent on energetic aspects and the number of molecules adsorbed at the surface, but not on any impact of gas-phase molecules.

2.4.4 Derivation and Applications of Adsorption Isotherms

2.4.4.1 The Langmuir Adsorption-Desorption Isotherms

Various theories and models have been developed to describe the processes of adsorption and desorption [Adamson and Gast, 1997; Thomas and Thomas, 1997]. The easiest approach, however, is equating the rate of adsorption with the rate of desorption. Thus a steady state

equilibrium is established, and we may simply combine the equations of the rate of desorption (eq. 2.31) and the rate of adsorption (eq. 2.23):

$$-\frac{dN_a}{dt} = \nu' \cdot N_a \cdot \Theta^m \cdot \exp\left(\frac{-E_d}{R \cdot T}\right) = \frac{s \cdot p}{\sqrt{2 \cdot \pi \cdot m \cdot k \cdot T}} = +\frac{dN_a}{dt} \quad \text{eq. 2.34}$$

For a non-dissociative adsorption, of 1st order desorption, and a system in which adsorption is non-activated (thus the heat of adsorption becomes equal to the activation energy of desorption: $E_a = E_d$), we obtain:

$$p = \sqrt{2 \cdot \pi \cdot m \cdot k \cdot T} \cdot \frac{\nu'}{s} \cdot N_a \cdot \frac{\Theta}{1 - \Theta} \cdot \exp\left(\frac{\Delta H}{R \cdot T}\right) \quad \text{eq. 2.35}$$

respectively:

$$p = \frac{\Theta}{b \cdot (1 - \Theta)} \quad \text{eq. 2.36}$$

whereas
$$\frac{1}{b} = \sqrt{2 \cdot \pi \cdot m \cdot k \cdot T} \cdot \frac{\nu'}{s} \cdot N_a \cdot \exp\left(\frac{\Delta H}{R \cdot T}\right) \quad \text{eq. 2.37}$$

If the heat of adsorption further remains constant with coverage (this is often valid for low but overall surface coverage), b is a function of the temperature only and we obtain:

$$\Theta = \frac{b \cdot p}{1 + b \cdot p} \quad \text{eq. 2.38}$$

This is well known as the Langmuir isotherm [Langmuir, 1918] for the equilibrium between adsorption and desorption. For dissociative adsorption, when each fragment covers a specific surface site, Θ is replaced by Θ^2 in equation eq. 2.38, and $(1-\Theta)$ by $(1-\Theta)^2$, respectively. For dissociation into n entities, the analogous discussion is valid.

It is of special importance that for the simultaneous adsorption of two gases A and B with comparable adsorption enthalpies (we will show later that this is the case for HONO and H₂O both bond at borosilicate, such as asphalt – see chapter 5.5.1 and [Thompson and Margey, 2003]) the Langmuir equation (eq. 2.38) becomes:

$$\Theta_A = \frac{b_A \cdot p_A}{1 + b_A \cdot p_A + b_B \cdot p_B}, \text{ resp.: } \Theta_B = \frac{b_B \cdot p_B}{1 + b_A \cdot p_A + b_B \cdot p_B} \quad \text{eq. 2.39}$$

We will finally give some general consequences for Langmuir adsorption directly deduced from the equations above: First, non-dissociative adsorption is expected to be favorable at low temperatures, before entropy effects become important. Further, the pressure at a constant temperature influences the equilibrium between molecular and dissociative adsorption. At higher pressures, the molecular adsorption is preferred.

However, it is recognized that Langmuir equations describing isotherms cannot be valid universally. This is mainly due to the decrease of adsorption heat with increasing surface coverage. Lateral interactions between species in the adlayer as well as multi-layer adsorption are neglected. However, semi-quantitative estimates of the relative proportions of dissociated and molecular species can be given.

2.4.4.2 Kinetic of Heterogeneously (Catalyzed) Reactions

We identify the factors b_i corresponding to the fundamental kinetic data of rate constants k_i for adsorption and desorption, respectively:

$$k_{\text{adsorpt.}} = \frac{1}{\sqrt{2 \cdot \pi \cdot m \cdot k \cdot T}} \cdot \exp\left(\frac{-\Delta H}{R \cdot T}\right) \quad \text{eq. 2.40}$$

and

$$k_{desopr.} = \frac{v}{\sqrt{2 \cdot \pi \cdot m \cdot k \cdot T}} \cdot \exp\left(\frac{-\Delta H}{R \cdot T}\right) \quad \text{eq. 2.41}$$

Interpretations on the kinetics of heterogeneously catalyzed reactions will have to include the adsorption-desorption concepts described above. In the following, we will refer to the Langmuir theory of adsorption isotherms and consider a reaction of $A + B \rightarrow C$ taking place at the surface according to either the Langmuir-Hinshelwood (LH) or the Eley-Rideal (ER) mechanism. Thus, we obtain for the surface coverage:

$$\Theta_A = \frac{b_A \cdot p_A}{1 + b_A \cdot p_A + b_B \cdot p_B}, \text{ resp.: } \Theta_B = \frac{b_B \cdot p_B}{1 + b_A \cdot p_A + b_B \cdot p_B} \quad \text{eq. 2.39}$$

Further, we will assume that the product molecule C is only weakly adsorbed (its steady-state concentration is negligible) and thus its surface adsorption site is occupied only by either A or B in a competitive sense. By that, we get the rate law for the LH mechanism to be:

$$r_{LH} = k \cdot \Theta_A \cdot \Theta_B = k \cdot \frac{b_A \cdot p_A \cdot b_B \cdot p_B}{(1 + b_A \cdot p_A + b_B \cdot p_B)^2} \quad \text{eq. 2.42}$$

including the partial pressures p_i of the educts A and B, respectively. Thus, at a constant temperature and a constant p_B , the rate will have a maximum at a certain p_A , when both reactants, A and B, have equal surface concentrations $\Theta_A = \Theta_B$.

By contrast, the ER mechanism for a surface-catalyzed reaction, if B is the striking non-adsorbed gas and A the adsorbed species at the surface yields:

$$r_{ER} = k' \cdot p_B \cdot \Theta_A = k' \cdot \frac{p_B \cdot b_A \cdot p_A}{1 + b_A \cdot p_A} \quad \text{eq. 2.43}$$

and the rate constant will always be of first order kinetic with respect to p_A , but zero in p_B . If the partial pressure of A is high, there is almost complete surface coverage, and the rate becomes equal to $k \times p_B$ and the rate is determined by the collision of B with the adsorbed species. Analogous discussion is valid, if the pressure of A is low, the extent of the surface coverage is important in the determination of the reaction rate.

2.4.4.3 Other Adsorption Isotherms: BET Theory

Several further theoretical descriptions for the adsorption-desorption behavior observed in the various experiments were given. An overview is presented by table 2.7 below, including the isotherm equations as well as their applicability.

By regarding these applicabilities, it becomes obvious, why we have chosen the Langmuir isotherms equation approach to describe our experiments of heterogeneous formation of nitrous acid in the smog chamber (see chapter 5.5.): both chemisorption and physical adsorption can be treated over a relatively wide range of coverage by adsorption and desorption on the macroscopic surfaces asphalt, concrete, tile and polyethylene and Teflon foil.

However, Langmuir theory is limited to monolayers, while multi-layering, as it is often observed for water molecules (resp. relative humidity, see figure 2.16) on these types of surfaces under atmospheric conditions.

Thus, we will here additionally give a brief introduction to Brunauer-Emmett-Teller (BET) theory of adsorption and desorption [Brunauer *et al.*, 1938] here, as it is commonly applied for these cases. The BET theory is based on the assumption that the first layer of adsorbate is taken up with a fixed adsorption heat (H_1), whereas the second and subsequent layers are all characterized by adsorption heats equal to the latent heat of evaporation (H_L). Further a dynamic equilibrium between each layer and the gas-phase is considered, finally yielding the BET equation:

$$\frac{p}{V \cdot (p_0 - p)} = \frac{1}{V_m \cdot c} + \frac{c-1}{V_m \cdot c} \cdot \frac{p}{p_0} \quad \text{eq. 2.44}$$

Here, the volume of gas adsorbed is V , and V_m is the volume equivalent to an adsorbed monolayer, the pressure of the gas is p and p_0 is the saturated vapor pressure of the liquid at a fixed temperature. The constant c is given by:

$$c = \exp\left(\frac{H_1 - H_L}{R \cdot T}\right) \quad \text{eq. 2.45}$$

A plot of $p / V (p_0 - p)$ versus p / p_0 is usually linear in the range of p / p_0 from 0.05 to 0.35, and the slope and intercept of this plot yield both c and the monolayer capacity V_m [Thomas and Thomas, 1997]. When the coefficient c is large ($c \gg 1$), the BET isotherm takes the simple form of:

$$\frac{V}{V_m} = \frac{1}{1 - p/p_0} \quad \text{eq. 2.46}$$

This equation is applicable to an un-reactive gas on a polar surface, for which $c \sim 10^2$ as H_1 is then significantly greater than H_L .

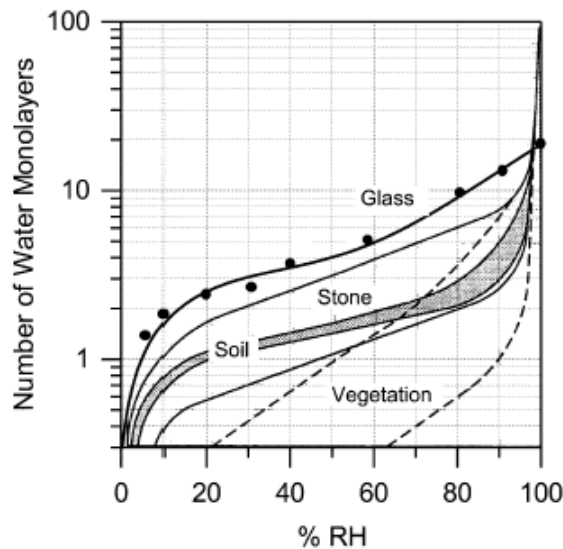


figure 2.16: Number of water-molecule layers taken up by some common materials observed in the Boundary Layer (adapted from [Lammel, 1999]).

To determine the surface area of a porous solid, the volumetric adsorption of an inert gas (such as liquid nitrogen at 77 K, the boiling point of N_2 at 1.05 bar) is widely used, as often one of the adsorption isotherms of type I, II or IV is observed. Then the BET theory is often required for the analysis of this data, plotting the consumed volume $p / V (p_0 - p)$ against p / p_0 . Once the monolayer volume V_m (in $m^3 g^{-1}$) has been ascertained (and by dividing Avogadro's number finally the number of molecules adsorbed in a monolayer by that), the specific surface area S can be calculated by using by:

$$S = \frac{V_m}{22.4 L mol^{-1}} \cdot 6.023 \times 10^{23} \cdot A = 2.69 \times 10^{25} \cdot V_m \quad \text{eq. 2.47}$$

if the area A occupied by each adsorbate molecule is given in m^2 .

Another possibility to determine the surface area size with more respect to the pore size distribution, pore volume, and diameter is the mercury porosimeter. The liquid mercury, which does not wet most surfaces is forced into the capillaries under pressure. Now, the force imparted to Hg by the pressure ($\pi r^2 p$) is equals the capillary tension force of $2\pi r \gamma \cos \alpha$ (γ

being the surface tension and α the contact angle). The slope s of a plot of the volume V of the adsorbed Hg by the solid as a function of the applied pressure p will yield a value for dV / dp at a particular pressure and hence r :

$$\frac{dV}{dr} = \frac{dV}{dp} \cdot \frac{dp}{dt} = -\frac{s \cdot p}{r} \quad \text{eq. 2.48}$$

In this thesis, this method was applied to determine the real surface structure of the asphalt plates used in the smog chamber campaigns (see chapter 5.1.3).

Name	Isotherm equation	Applicability
Langmuir ^(b)	$\frac{V}{V_m} = \theta = \frac{bp}{1 + bp}$	Chemisorption and physical adsorption
Henry ^(c)	$V = k'p$	Chemisorption and physical adsorption at low coverages
Freundlich	$V = kp^{1/n} (n > 1)$	Chemisorption and physical adsorption at low coverages
Temkin	$\frac{V}{V_m} = \theta = A \ln Bp$	Chemisorption
Brunauer–Emmett–Teller (BET)	$\frac{p}{V(p_0 - p)} = \frac{1}{V_m c} + \frac{c - 1}{V_m c} \cdot \frac{p}{p_0}$	Multilayer, physical adsorption
Polanyi ^(d)	$\epsilon = RT \ln(p_0/p)$	Physical adsorption
Dubinin–Radushkevich ^(e)	$\ln x = \ln(W_0 \rho) - D[\ln(p_0/p)]^2$	Multilayer formation in microporous solids
Dubinin–Kaganer–Radushkevich (DKR)	$x = x_m \exp(-B\epsilon^2)$	Physical adsorption up to a monolayer
Virial	$\frac{p}{RT} = x(1 + a_1x + a_2x^2 + \dots)$	Multilayer formation in micropores

^(a) Amounts adsorbed at pressure p are represented either by volume V or mass x . Unless otherwise specified, all other symbols in these equations are constants.

^(b) V_m (and x_m) correspond to monolayer coverage.

^(c) This equation is the limiting form of the Langmuir equation.

^(d) The adsorption potential ϵ is defined by this equation.

^(e) W_0 stands for the total volume of all the micropores in a solid.

table 2.7: A selection of adsorption isotherm as given in [Thomas and Thomas, 1997].

2.5 Basics of Atmospheric Dynamics of the Boundary Layer

Not only laboratory studies in a smog chamber were performed in this thesis, but also field measurements in the real atmosphere. In atmospheric measurements, both chemistry as well as the physical transport processes contribute to the observed trace gas mixing ratios. Thus, we will now give a brief introduction to the dynamics in the troposphere, namely the Planetary Boundary Layer (PBL), and specify the factors used for the parameterization in the model of [Geyer and Stutz, 2003; Stutz et al., 2004a; Stutz et al., 2002; Stutz and Geyer, 2003] applied to our data as presented in chapter 6.2. A more detailed discussion can be found e.g. in [Roedel, 1994; Seinfeld and Pandis, 1998; Stull, 1988].

2.5.1 The Structure of the Planetary Boundary Layer

The PBL typically extends from below 100 to 1000 m of the lowest part of the atmosphere and represents a transition between air masses directly at the Earth's surface and the free troposphere above, which is dominated by the geostrophic wind system. Its height is influenced by several factors and the dynamic processes involve both the transport of momentum as well as that of trace gases. Thus characterization of wind speed and direction also specifies the mixing velocities for trace gases.

Due to friction between that mentioned geostrophic flow and the surface roughness, a logarithmic wind speed profile monotonously decreasing towards the ground occurs in the PBL. The mathematical description of a shear force is based on this friction and thus momentum is exchanged between the two layers moving with different velocities along each other:

$$\tau_{xz} = -(K + \nu) \cdot \rho \cdot \frac{dv_x}{dz} \quad \text{eq. 2.49}$$

Here, the τ_{ij} is the turbulent viscous stress tensor, while K and ν characterize the constants of turbulent and laminar diffusion, respectively. These parameters will be explained in more detail in chapter 2.5.3. ρ labels the density of the air mass and v_x the velocity of the horizontal air stream (a time dependence was neglected therein).

2.5.1.1 The Laminar Surface Layer

Using this equation (eq. 2.49), the PBL is often divided into three sub-layers defined by the dominating transport regime. Within the first 10^{-3} to 10^{-2} m above the surface ("laminar viscous surface layer"), transport is dominated by laminar diffusion of momentum, heat, and trace gases, which is significantly less effective than turbulent diffusion in the boundary layer and the free atmosphere. We can give a measure for that laminar diffusion by taking into account the mean free path length l at a thermal velocity v . The diffusion constant ν for momentum is given by:

$$\nu = \frac{1}{3} \cdot v \cdot l \quad (\nu \approx 1.5 \cdot 10^{-5} \text{ m}^2\text{s}^{-1} \quad \text{for ambient air at } 20^\circ\text{C}) \quad \text{eq. 2.50}$$

and we may link it to the diffusion constant for trace gases by Schmidt's number:

$$Sc = \frac{\nu}{D} \quad (Sc \approx 1 \text{ for all gasses,} \quad \text{eq. 2.51}$$

e.g. 0.85 for CO_2 in ambient air at 20°C)

2.5.1.2 The Prandtl Layer

Above the laminar surface layer, in a range from 10^{-2} to some 10^2 m (“surface layer”) the major components of the viscous stress tensor τ_{ij} feature absolute values of about $0.1 - 0.3 \text{ N m}^{-1}$, corresponding to variations of τ_{ij} by the height z of $d\tau/dz \sim 10^{-3} \text{ N m}^{-1}$. It could be shown (see e.g. [Roedel, 1994]) that the gradient $d\tau/dz$ is at least two orders of magnitude smaller than τ_{ij} , and thus constant turbulent fluxes of momentum, heat, and trace gasses ($\tau = \text{const}$) dominate in the surface layer. This layer characterized by $\tau = \text{constant} \neq 0$ is also often referred to as “Prandtl” layer.

2.5.1.3 The Ekman Layer

In the air masses from some 10^1 to about 10^3 m, the wind velocities increase to the values in the free troposphere. The direction of this wind-vector is influenced by friction, which obviously decreases with distance from the surface, the Coriolis force, and the pressure gradient force. Thus the wind direction turns constantly with increasing height yielding the so-called Ekman spiral (hence, this layer is referred to as the Ekman layer).

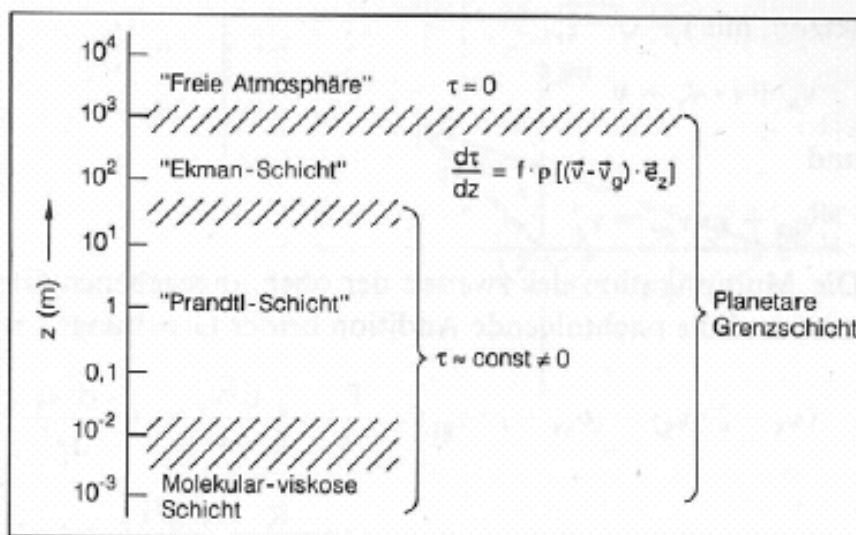


figure 2.17: Dynamic structure of the PBL (adapted from [Roedel, 1994]).

2.5.1.4 The Height of the PBL

As mentioned above, heights of the PBL range from less than 100 m at night over flat surfaces to more than 1000 m by day over a strongly structured surface. This is mainly due to two factors: the stability of the thermal layering and the surface roughness. To explain their trends and impact on the vertical extend of the PBL, we should first explain the three atmospheric layering states. Labile layering is characterized by warmer air situated below colder air, yielding a more effective vertical mixing. Within labile-layered PBL, warmer air climbs adiabatically to higher altitudes, while colder air masses descend adiabatically towards the ground until both air parcels have the same potential energy (including latent and inner heat energy) as the surrounding air. Consequently, the PBL extends to higher altitudes at labile conditions due to more effective vertical mixing. Warmer and therefore less dense air masses above colder and denser air masses are referred to as thermal stable layering. An analogous discussion to the above one is valid, and finally due to the less effective transport,

the height of the PBL is lower. Finally, if an air parcel can be shifted adiabatically to any altitude and always has the same potential energy as the surrounding air mass, the layering is called thermally neutral.

The surface roughness is also known to influence the height of the PBL: rough surfaces (such as tall buildings or trees) cause a more effective vertical mixing and hence extend the height of the PBL, while flat surfaces (such as silent water) cause a thinner PBL. In extremes, the formation of a laminar sub-layer can be inhibited by rough surfaces.

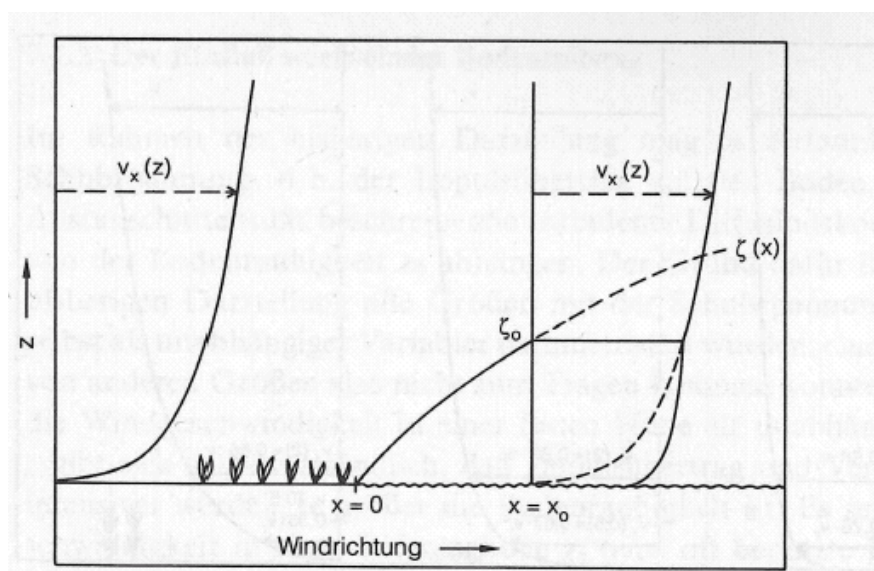


figure 2.18: Variation at $x = 0$ of the logarithmic wind profile $v_x(z)$ due to reduction of surface roughness (adapted from [Roedel, 1994]).

2.5.2 Diurnal Variations of the PBL: Micrometeorological Description

As we will show in more detail in the next chapter, the heat flux and, consequently, the temperature gradient is the forcing parameter in the dynamics of the PBL. Due to the diurnal variation of solar radiation, the heat fluxes from the surface and in the lower atmosphere change, causing the layering in the PBL and its vertical mixing to do so as well. Due to strong turbulences driven by wind shear and convection, the PBL is usually well mixed during daytime.

After sunset, radiative cooling occurs and only wind shear remains as the driving force, and thus turbulence in the PBL decreases. A residual layer is formed containing the air masses of the formerly mixed layer and below, a stable vertical boundary layer of low sporadic turbulence, but also negative buoyancy [Arya, 1988; Businger *et al.*, 1971; Mahrt *et al.*, 1998; Rao and Snodgrass, 1979; Stull, 1988] is established. Trace gases emitted or even formed near the ground surface may accumulate close to the ground and lead to unique vertical profiles for a number of species. Solar radiation increasing after sunrise initiates the development of the well-mixed daytime PBL again.

The PBL is by definition the lowest part of the troposphere, which is further characterized and defined by a negative temperature gradient. Due to the warming of the Earth's surface by solar radiation by day and subsequent heat exchange with the air masses close to the surface, temperatures decrease with increasing height over ground. As a result, this gradient is generally expected to yield an effective mixing, as warmer (i.e. less dense) air is situated below colder (i.e. more dense) air.

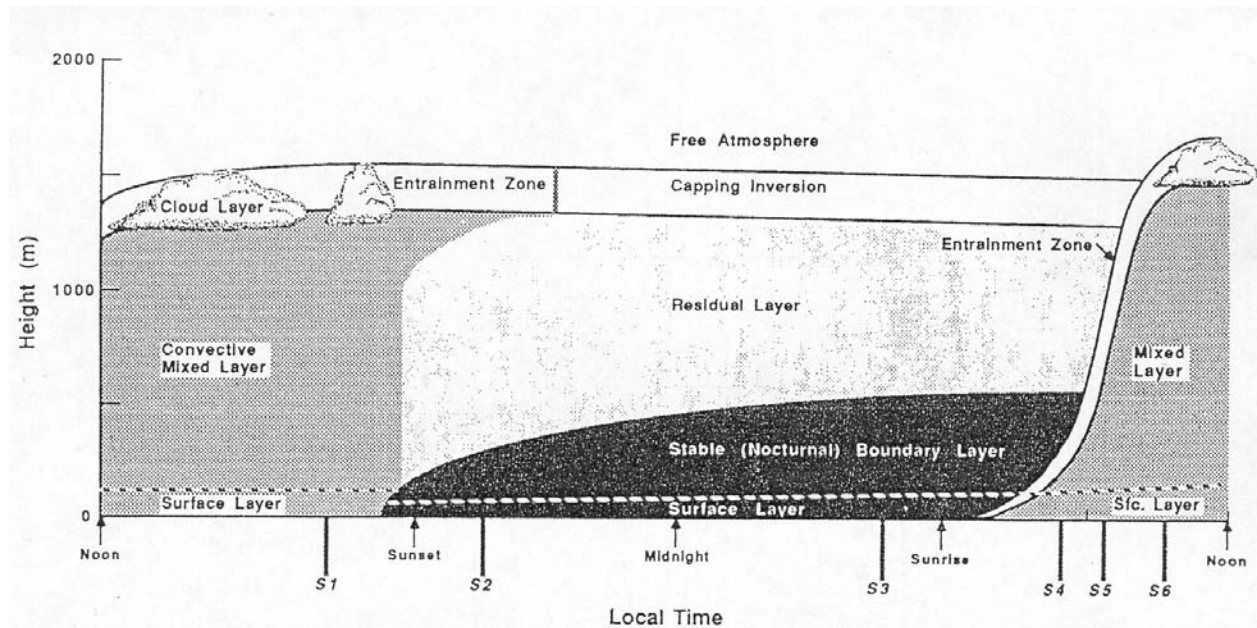


figure 2.19: Typical diurnal variation of the layering of the PBL in high-pressure regions over land (adapted from [Stull, 1988]).

However, the potential energy of the air parcels also has to be considered. An air parcel descending from higher altitudes transforms its potential energy to heat energy while being compressed to the increased pressure of the lower altitude (a process taking place vice versa for the ascending air parcel). To consider this, the potential temperature Θ is introduced, which combines both the potential and the thermal energy of the observed air mass:

$$\Theta = T \cdot \left(\frac{p_0}{p} \right)^{\frac{\chi-1}{\chi}} \quad \text{with} \quad \chi = \frac{c_p}{c_v} \quad \text{eq. 2.52}$$

Here, the actual temperature T , the actual pressure p , the standard pressure p_0 , and the specific heat of air at a constant pressure and volume, c_p and c_v , respectively, have to be combined in this adiabatic equation. Further taking into account the content of water vapor and liquid water in the air mass, one may define the virtual potential temperature [Roedel, 1994; Stull, 1988].

The profile of the potential temperature $\Theta(z,t)$ in the lowest meters may be calculated from the heat flux $H(t)$ according to [Arya, 1988; Haugen, 1973] as:

$$\frac{d\Theta(z,t)}{dz} = -\frac{H(z,t)}{c_p \cdot \rho} \cdot \frac{1}{\kappa \cdot u^*(t) \cdot z} \Phi_H\left(\frac{z}{L^*}, t\right) \quad \text{eq. 2.53}$$

Here, c_p represents the mass heat capacity of air, ρ its density, and $\Phi_H(z/L^*, t)$ a dimensionless correction factor for heat transport suggested by [Businger et al., 1971]. However, the temperature profile may further be explicitly used to calculate temperature dependent rate constants and the profile of water vapor [Geyer and Stutz, 2003].

A layer with a constant potential temperature over its whole range of height is generally well mixed. Increasing potential temperatures with height may avert the formation of a well-mixed layer, especially in the early morning hours, when the air close to the surface is still cooler from the absence of solar radiation during the night, but warmer air lies above. These so-called ground inversions often result in the formation of photochemical smog in polluted urban areas (see chapter 2.2.2).

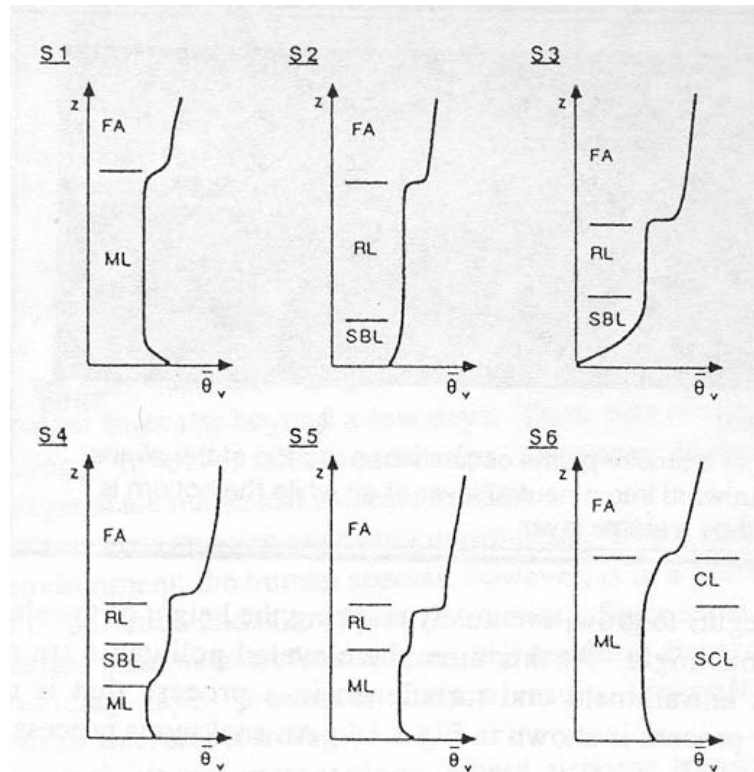


figure 2.20: Profiles of mean virtual temperature showing the PBL evolution during a diurnal cycle at the time markers indicated in figure 2.19 (adapted from [Stull, 1988]). The labels also correspond to the sublayer names introduced in figure 2.19.

However, the ground inversion may also occur in basins or valleys that fall under the influence of an atmospheric subsidence zone (see e.g. [Roedel, 1994; Stull, 1988]), indicating that the layering of the PBL is also influenced by local topography and large-scale atmospheric phenomena such as cyclones. This finally requires the knowledge of the 3D wind field and the heat flux in the PBL (both at different elevations) for an in-depth analysis of transport mechanisms.

2.5.3 Transport Processes in the PBL: The Friction Velocity

In the following, we will name the main parameters, used to quantify these transport processes in the PBL. For thermally neutral stratification, and turbulent mixing surpassing laminar mixing, as both occur in surface and Ekman layers, the wind profile may be calculated based on the stress tensor τ_{ij} by introducing the friction velocity u^* :

$$\tau_{xz} = -\rho \cdot (u^*)^2 \quad \text{eq. 2.54}$$

Using this definition of the friction velocity, the vertical wind profile dv_x / dz in a height z over the ground becomes:

$$\frac{dv_x}{dz} = \frac{1}{\kappa} \cdot \frac{u^*}{z} \quad \text{eq. 2.55}$$

with the Karman-constant $\kappa \sim 0.4$. We have mentioned that the friction velocity only depends on the height z over ground. Thus, combining both equations eq. 2.54, and eq. 2.55, the turbulent diffusion constant $K(z)$ is introduced as a parameter only depending on the height:

$$K(z) = u^* \cdot \kappa \cdot z \quad \text{eq. 2.56}$$

The flux $j_i(z,t)$ of both momentum as well as trace gas transport of a species i , can be described according to Fick's law using the linear flux-gradient relationship (K model):

$$j_i(z,t) = -K(z,t) \cdot \frac{\partial c_i(z,t)}{\partial z} \quad \text{eq. 2.57}$$

Further the equations eq. 2.56, and eq. 2.57, the difference between the concentrations of an atmospheric trace gas in two different heights $z_i > z_j$ is given by:

$$c(z_j) - c(z_i) = \int_{z_i}^{z_j} \frac{dc(z)}{dz} \cdot dz = -j \cdot \int_{z_i}^{z_j} \frac{1}{K(z)} \cdot dz = -\frac{j}{u^* \cdot \kappa} \cdot \int_{z_i}^{z_j} \frac{1}{z} \cdot dz = -\frac{j}{u^* \cdot \kappa} \cdot \ln\left(\frac{z_j}{z_i}\right) \quad \text{eq. 2.58}$$

It is obvious from the treatment of the heights z_j , and z_i that a logarithmic profile will occur. However, a special form of the equation eq. 2.57 is of special interest, yielding the flux of trace gasses between two different layer heights as derived from measured concentration gradients:

$$j = -\frac{c(z_j) - c(z_i)}{\ln\left(\frac{z_j}{z_i}\right)} \cdot u^* \cdot \kappa \quad \text{eq. 2.59}$$

Finally, we will introduce the transfer resistance $R_{i,j}$ as transport time between the heights i and j :

$$R_{i,j} = \frac{c(z_j) - c(z_i)}{j} = -\frac{1}{u^* \cdot \kappa} \cdot \ln\left(\frac{z_j}{z_i}\right) \quad \text{eq. 2.60}$$

However, before any further applications are presented, the calculation of the friction velocity u^* will be discussed. Generally, two different approaches are possible for neutral and non-neutral conditions, differing by the approximations necessary for the calculation of the absolute value of friction velocity.

2.5.3.1 Neutral Layering

For neutral conditions in the surface layer, the assumption of the friction velocity being constant with increasing height over ground is well justified [Roedel, 1994] and equation eq. 2.55 may be integrated:

$$u^* = v_r \cdot \frac{\kappa}{\ln(z_r/z_0)} \quad \text{eq. 2.61}$$

In this approximation, a typical wind speed v_r at a certain reference height h_r is required to be measured. The surface roughness is considered by the factor z_0 as the zero level for advection. The combination with equation eq. 2.54 finally directly yields the turbulent diffusion constant:

$$K(z) = \frac{v_r \cdot \kappa^2}{\ln(z_r/z_0)} \cdot z \quad \text{eq. 2.62}$$

It increases with height over ground due to the larger eddies that are more effective for the mixing of the PBL and also increase with surface roughness. To calculate exemplary typical turbulent diffusion coefficients, for a neutral layering, we will use a wind speed of $v_r = 3 \text{ m s}^{-1}$ at a height of $z_r = 30 \text{ m}$ and a surface roughness parameter $z_0 = 0.5 \text{ m}$. This yields $K(z) = 0.141 \text{ m}^2 \text{ s}^{-1} \cdot z$, a value that is substantially higher than the laminar diffusion constant [Stull, 1988]. It is evident that turbulent mixing under neutral conditions is very effective as trace gasses may be transported from the lower to the upper border of the layers in a timescale of some minutes.

2.5.3.2 Labile and Stable Layering

These circumstance get complicated, however, if the layering deviates from that neutral layering due either to thermal fluctuations or the content of water vapor. As described in detail e.g. by [Roedel, 1994; Seinfeld and Pandis, 1998] measurements of the vertical profiles of the wind speed and heat flux, which has a strong effect on the efficiency of turbulent transport processes, are required to obtain friction velocity for non-neutral layering of the PBL. In general, a more effective mixing of the lower atmosphere and hence larger values for the diffusion coefficients and finally lower trace gas gradients are expected for labile layering of the PBL, while in situations of stable layering, the atmospheric mixing is reduced. This is mainly due to the smaller vertical extension of eddies, but evident for the ground inversion situations in polluted areas.

However, a new measure is required and equation eq. 2.59 needs to be extended for the description of atmospheric trace gas gradients. A common approach is the use of the so-called Monin-Obukhov length L^* as a scale length that is nearly independent from the height z , but only depends on factors characterizing the stability of the stratification (such as the heat flux H) [Businger *et al.*, 1971].

$$L^* = \frac{c_p \cdot \rho \cdot \Theta \cdot u^{*3}}{\kappa \cdot g \cdot H} \quad \text{eq. 2.63}$$

L^* is positive for stable stratification, and negative for labile stratification. According to its definition, L^* becomes infinite for neutral stratification, and is thus useless, as in the case of neutral layering the heat flux H is zero. Taking into account the Monin-Obukhov length, and horizontal uniformity of the observed air mass we can write vertical trace gas gradient (resp. fluxes) corresponding to [Businger *et al.*, 1971] as:

$$\frac{dc}{dz} = \frac{j}{\kappa \cdot u^* \cdot z} \cdot \Phi\left(\frac{z}{L^*}\right) \quad \text{eq. 2.64}$$

whereas $\Phi(z/L^*)$ represents the new stability term as the ratio between the actual wind speed gradient and the wind speed gradient for neutral stratification.

Measuring a 3-D wind field (u, v, w) and the temperature at a single spot (e.g. by using an anemometer), one may directly calculate the friction velocity u^* and the sensible heat flux H :

$$u^* = \frac{1}{n} \cdot \sum_{i=1}^n (v_i - \bar{v}) \cdot (w_i - \bar{w}) = \sqrt{-\overline{vw}} \quad \text{eq. 2.65}$$

and

$$H = -\sqrt{-\overline{wT}} \quad \text{eq. 2.66}$$

Using the Karman-constant $\kappa \sim 0.4$ and $g = 9.81 \text{ m}^2 \text{ s}^{-1}$, this yields the Monin-Obukhov length:

$$L^* = -\frac{T \cdot (u^*)^3}{\kappa \cdot g \cdot H} \quad \text{eq. 2.67}$$

As presented by [Roedel, 1994], the stability function was applied by [Stutz *et al.*, 2002] as:

$$\Phi\left(\frac{z}{L^*}\right) = (1 - 16 \cdot (z - d)/L^*)^{-0.5} \quad \text{for unstable conditions} \left(\frac{z}{L^*} < 0\right)$$

or

$$\Phi\left(\frac{z}{L^*}\right) = (1 + 5 \cdot (z - d)/L^*) \quad \text{for stable conditions} \left(\frac{z}{L^*} > 0\right) \quad \text{eq. 2.68}$$

and the integration of the wind profile (eq. 2.64), including eq. 2.68 for stable layering, yields:

$$v_x(z) = \frac{u^*}{\kappa} \cdot \left(\ln \frac{z}{z_0} + 4.7 \cdot \frac{z-z_0}{L^*} \right) \quad \text{eq. 2.69}$$

By including a shift parameter d of the point of origin necessary for rough ground structures, the turbulent exchange coefficient K was determined as:

$$K(z) = \frac{u^* \cdot \kappa \cdot (z-d)}{\Phi(z/L^*)} \quad \text{eq. 2.70}$$

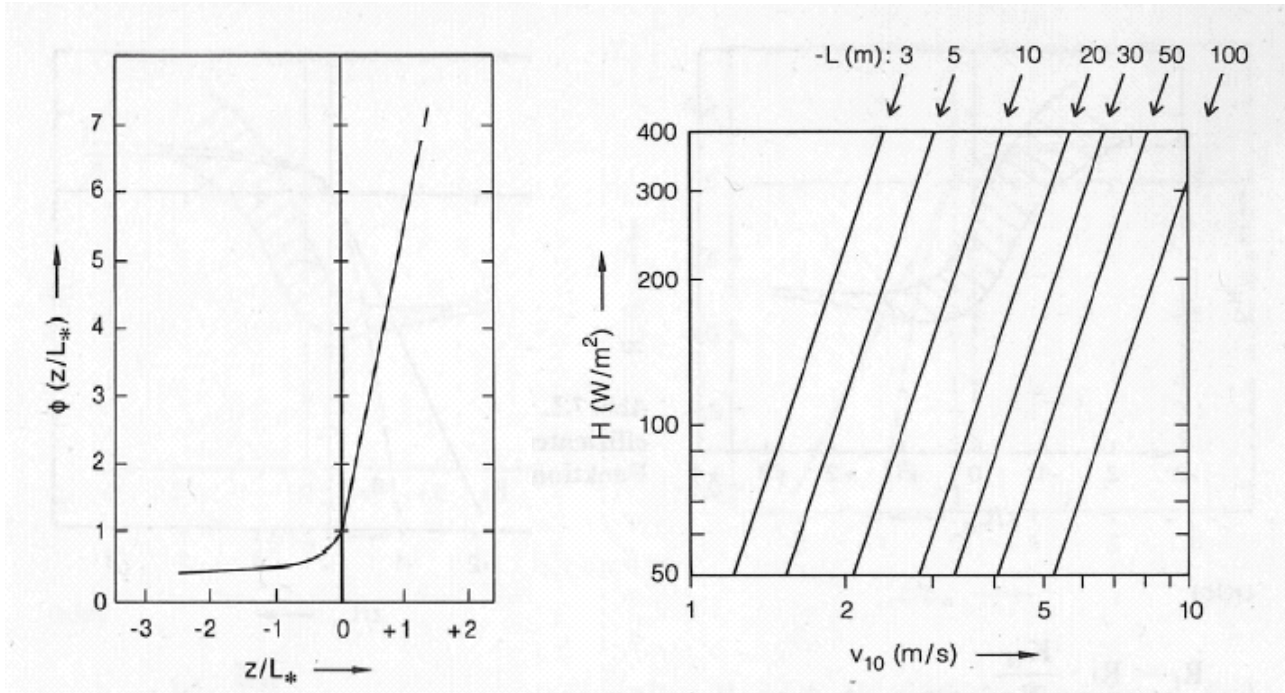


figure 2.21: Left plot: the correction function $\Phi(z/L^*)$ as a function of z/L^* (see [Businger et al., 1971]). Right side: nomogram to determine the Monin-Obukhov length L^* for labile layering as a function of the vertical heat flux H and the horizontal wind velocity $v_{1,0}$ in a reference height of 10 m and a surface roughness of $z_0 = 3$ cm (both adapted from [Roedel, 1994]).

For labile layering, the integration of eq. 2.64 is more complicated but performed in detail by [Paulson, 1970]. Finally, one obtains [Paulson, 1970; Roedel, 1994]:

$$v_x(z) = \frac{u^*}{\kappa} \cdot \left(\ln \frac{z}{z_0} - \Psi \left(\frac{z_0}{L^*} \right) \right) \quad \text{eq. 2.71}$$

with Ψ as another term of correction, given by:

$$\Psi \left(\frac{z_0}{L^*} \right) = 2 \cdot \ln \left(\frac{1 + \Phi^{-1}(z/L^*)}{2} \right) + \ln \left(\frac{1 + \Phi^{-2}(z/L^*)}{2} \right) - 2 \arctg \left(\Phi^{-1}(z/L^*) \right) + \frac{\pi}{2} \quad \text{eq. 2.72}$$

and the vertical diffusion coefficient K as described by equation eq. 2.70.

As we will show, however, in chapter 6.2, the unmodified K models are restricted to inert or slowly reacting gases because the effect of chemistry on the vertical flux of a trace gas is not considered [Brost et al., 1988; Fitzjarrald and Lenschow, 1983; Galmarini et al., 1997; Gao et al., 1991; Hamba, 1987; Hamba, 1993; Lenschow et al., 1982; McDonald-Buller et al., 1999; Schumann, 1989; Thompson and Lenschow, 1984; Vila-Guerau de Arellano, 2003; Vila-Guerau de Arellano et al., 1995]. Thus, a modified K model [Geyer and Stutz, 2003; Stutz et al., 2004a] will be applied to the analysis of our data, which considers the effects of

both the vertical mixing and chemistry (based on the RACM mechanism presented by [Stockwell *et al.*, 1997]) on the vertical flux of a trace gas. Consequently, vertical transport of a gas is no longer only a function of its concentration profile, but also of the concentration profiles of other gases that react or are educts of this gas (cross-diffusion) [Geyer and Stutz, 2003; Stutz *et al.*, 2004a].

2.5.4 Radon as a Tracer for Mixing in and the Height of the PBL

During the Turm 2003 campaign (see chapter 4.3.), measurements were performed at the well-equipped meteorological tower of the IMK, FZ Karlsruhe and temperature profiles as well as wind profiles were available in a height range from ground to 200 m. Additionally, anemometers were mounted at different heights and thus, the PBL could be well characterized based on the equations presented above. During the Milan 2002 measurements, an anemometer was also operated in a height of 2 m and the Monin-Obukhov length was calculated based on the eq. 2.65 to eq. 2.70 as described in detail by [Stutz *et al.*, 2002] and eq. 2.71 for labile layering respectively. Unfortunately, none of these instruments were available for the Rome 2001 field studies and a different approach based on [Febo *et al.*, 2003; Perrino *et al.*, 2001] had to be used.

In general, the time series of all atmospheric trace gasses may be described by the differential equation:

$$\frac{\partial c(z,t)}{\partial t} = \frac{1}{h_{PBL}} [\Phi_P + \Phi_S] - K(z) \cdot \frac{\partial c}{\partial z} + \sum_i P_i - \sum_j L_j - L_S \left[\frac{1}{h_{PBL}}; K(z) \cdot \frac{\partial c}{\partial z} \right] + adv \quad \text{eq. 2.73}$$

whereas:

c = mixing ratio near the ground

h_{PBL} = height of the PBL

Φ_P = primary emission flux

Φ_S = surface emission flux

$K(z)$ = vertical mass exchange due to eddy diffusion and convection

P_i = chemical production rate from the i^{th} pathway

L_j = chemical removal rate from the j^{th} pathway

L_S = removal rate from deposition

adv = advection term forced by horizontal transport

Unfortunately, most of the terms presented by eq. 2.73 are unknown or only poorly characterized in atmospheric field study campaigns. Especially the vertical diffusion coefficient $K(z)$ and the boundary layer height have to be measured to characterize the impact of primary and surface emissions as well as chemical production and the removal of a trace gas in the PBL. Thus, the differential equation eq. 2.73 will generally not be solvable and basic approximations on the atmospheric parameters will have to be assumed for the application of this analysis to measured vertical profiles of trace gases. However, this still requires the analytic solution of the equation eq. 2.73 with respect to an inert tracer gas to obtain the micrometeorological parameters.

Thus we will now present the adaptation of the general atmospheric equation to the Radon activity, as Radon is known to be such a tracer gas, being inert to almost any chemical reaction in the troposphere. It is emitted continuously by the ground, with a typical emission rate of some $80 \text{ Bq m}^{-2} \text{ h}^{-1}$, but varying dependent on the meteorological parameters and the soil type (for a recent detailed overview see e.g. [Levin *et al.*, 2002; Nazaroff, 1992]). [Nazaroff, 1992] further reported 80 – 90 % of the measured emission rates to be in the range of ± 3 times the mean value.

As Radon is an inert trace gas ($P_i = L_j = L_S = 0$) emitted only by the soil ($\Phi_{Rn} = \Phi_S + \Phi_P = \Phi_S$), it is spread out into the atmosphere by turbulent diffusion strongly representing the

present atmospheric dynamic. Its radioactive decay can be considered as the main Radon sink. The radon decay products, being isotopes of heavy metals, become readily attached to aerosol particles and precipitation elements [Jacobi and André, 1963]. Thus, the dependence of the turbulent diffusion constant with altitude and finally atmospheric mixing of other trace gases may be deduced from the measurement of Radon vertical profiles [Jacobi and André, 1963]. Unfortunately, Radon activity data was measured at a single height only and thus profiles are not available. Nether the less, Radon may be used as a tracer for the build-up and break-up of ground inversions. Due to the strongly limited vertical transport in the PBL during nighttime or when e.g. a ground inversion builds up (see the chapters above), Radon activity increases constantly as long as the inversion layer is stable. The Radon activity decreases again, when mixing becomes more efficient, i.e. after sunrise, when the ground inversion breaks up, and the volume of “in-mixing” increases (the inversion height of the PBL rises).

Neglecting advection terms ($adv = 0$), the general equation (eq. 2.73) for Radon for a 1-dimensional vertical transport model approach becomes:

$$\frac{\partial Rn}{\partial t} = \frac{1}{h_{PBL}} [\Phi_{Rn}] - K(z) \cdot \frac{\partial Rn}{\partial z} \quad \text{eq. 2.74}$$

The time series of radon described by equation eq. 2.74 may be used as a combined tracer for atmospheric stability and the height of the PBL even without any knowledge of the vertical diffusion coefficient $K(z)$ as given above in chapter 2.5.3. Since the diurnal profile of radon only depends on terms of atmospheric stability, natural radon-activity usually increases from sunset throughout the night due ongoing stabilization of the atmosphere. The absolute radon values are a function of the ground emission as mentioned above. After sunrise, when the atmosphere is usually characterized by labile layering, radon concentrations rapidly decrease and keep low daytime values throughout the entire daylight period.

In general, advection has to be taken into account, especially near the sea (as no Radon is emitted from oceans), but also in continental air masses because the exhalation of Radon depends on the soil type [Levin *et al.*, 2002]. However, its neglect in 1D models and the discussion of vertical transport is only justified by the fact that variations of the NO_2 and HONO mixing ratio proceed on a much shorter timescale.

3 Measurement Methods

The importance of nitrous acid on the chemistry of the urban atmosphere has been drawn out in detail in chapter 2 already. Measuring HONO as well is of high relevance for the detection and quantification of trace gases related to the formation of tropospheric smog events. However, the measurement of reactive species and species, which strongly interact with surfaces, are a challenge for any analytical technique.

In this chapter, we will only present the most common measurement techniques for atmospheric HONO by briefly explaining their basics. Measurement intercomparisons for HONO were performed during the Milan 2002 campaign (see chapter 4.2) and will be discussed therein. For our trace gas measurements performed in this thesis, Differential Optical Absorption Spectroscopy (DOAS) was used and will therefore be explained afterwards in more detail.

Additional measurements of other trace gases, aerosol particles, radiance data, meteorological parameters, and natural radon-activity were performed in the framework of this thesis. However, the corresponding instruments were either operated by cooperating groups or commercial instruments were used. A very brief description including the specific setup of the instrument will be given in the experimental sections of the specific measurement campaigns (see chapter 4, and 5).

3.1 Overview of Detection Techniques for Nitrous Acid

Since nitrous acid was detected in the atmosphere more than two decades ago [*Perner and Platt, 1979; Platt and Perner, 1980; Platt et al., 1980*], mainly two techniques were used for its measurement: Differential Optical Absorption Spectroscopy (DOAS) [*Platt et al., 1979*] is based on the integrated absorption of UV and visible light along a light path of several kilometers in the atmosphere, and the denuder technique, a wet-chemical sampling technique based on the different diffusion properties of gases compared to particles [*Eathough et al., 1988; Febo et al., 1993; Febo et al., 1990; Ferm and Sjödin, 1985*].

In the last years, several other techniques, which are already known from laboratory studies, were applied to atmospheric trace gas measurements. Recently, a review on different trace gas measurement techniques was presented by [*Parrish and Fehsenfeld, 2000*] or with more respect to HONO by [*Alicke, 2000*]. However, all these different techniques still show controversial results, which is thought to be caused by the cross sensitivities with other nitrogen compounds. In table 3.1, an overview of these different measurement techniques and their possible interferences is given.

3.1.1 Chemical Surface Collection Techniques

In general, wet chemical sampling techniques for HONO, which will be described in this section, show a lower detection limit (in the order of some few ppt) compared to spectroscopic methods, such as DOAS (see table 3.1). The measurement approach (Lagrange approach) is different from that of DOAS (Euler approach): the surface collection techniques

are in-situ instruments and therefore usually have a higher spatial resolution than e.g. the DOAS (see also the discussion in chapter 4.3.3.2). However, to achieve the low detection limits, the in-situ instruments need to sample the ambient air for long times, resulting in a time resolution, which is usually worse than that of spectroscopic methods.

Another disadvantage of these techniques is already included in their basic principle: they collect a specific (reactive) trace gas on a surface by chemical methods. It was shown in chapter 2.3 that the HONO is formed heterogeneously from NO₂. In chapter 5 we will further show that this reaction occurs on all types of surfaces. Thus, the challenge of all chemical sampling techniques is to avoid a generation of HONO in the sampling tubes or units. The interference with NO₂ is therefore a critical point, since in ambient air NO₂ is usually present in some orders of magnitude higher than HONO.

Measurement technique	interference	typical HONO detection limit [ppt]	reference
denuder (wet chemical analysis)	PAN, NO ₂ , SO ₂	1 - 20	[Acker et al., 2001b; Eathough et al., 1988; Febo et al., 1993; Febo et al., 1990; Ferm and Sjödin, 1985]
chemiluminescence	NO ₂ , PAN	~ 100	[Kanda and Taira, 1990; Kanda and Taira, 1992]
DNPH-HPLC (wet chemical analysis)	NO, NO ₂ , PAN, O ₃ , HNO ₃ , HCHO ?	1 - 5	[Zhou et al., 1999]
LOPAP (wet chemical sampling and photometric detection)	?	1 - 5	[Heland et al., 2001; Kleffmann et al., 2002]
ion mass-spectroscopy	?	approx. 500	[Berkowitz et al., 1998; Spicer et al., 1996; Spicer et al., 1993]
UV-Photofragmentation / Laser-Induced Fluorescence	OH	10 - 100	[Rodgers and Davis, 1989]
FT-IR spectroscopy (spectroscopy)	H ₂ O, CO ₂ , CH ₄ ,	2500 - 4000	[Hanst, 1978; Hanst et al., 1982; Tuazon et al., 1978; Tuazon et al., 1980]
DOAS (spectroscopy)	NO ₂	30 - 200	see [Platt, 1994] for an overview and chapter 3.2.1 in this thesis

table 3.1: Overview of the different HONO measurement techniques.

3.1.1.1 The Denuder Technique

The denuder technique is a relatively simple and low-cost in-situ measurement method. Denuders are wet-chemical sampling and analysis methods for the measurements of a various number of atmospheric species: traces gases as well as particles. The principle of the denuder sampling is illustrated in figure 3.1, left side. A laminar flow of air is pulled through a tube. Based on differences in the diffusion properties of gases compared to particles, both are

separated: the particles pass the sampling tube, while the highly diffusive gases strike the walls of the tube several times while passing through.

To detect a particular compound, or group of compounds, from the gas phase, the walls of the denuder sampling tube are coated by a special substance, e.g. by Na_2CO_3 for the measurements of atmospheric HONO (see below). After sampling the reactive gas in the tube as described above, it is recovered and collected in an air stream free of that species. A model of mass concentration depletion by diffusion through air for perfect sink tubes has already been presented by [Gormely and Kennedy, 1949]. Their series solution may be approximated for $C(x) / C(0) < 0.819$:

$$\frac{C(x)}{C(0)} = 0.819^{-11.49 \cdot \frac{x \cdot D}{Q}} \quad \text{eq. 3.1}$$

where $C(x)$ is the average concentration passing the axial distance x , $C(0)$ is the concentration entering the tube, D is the diffusion coefficient in air and Q is the volumetric flow rate. This is valid, if the gas is collected with 100 % efficiency.

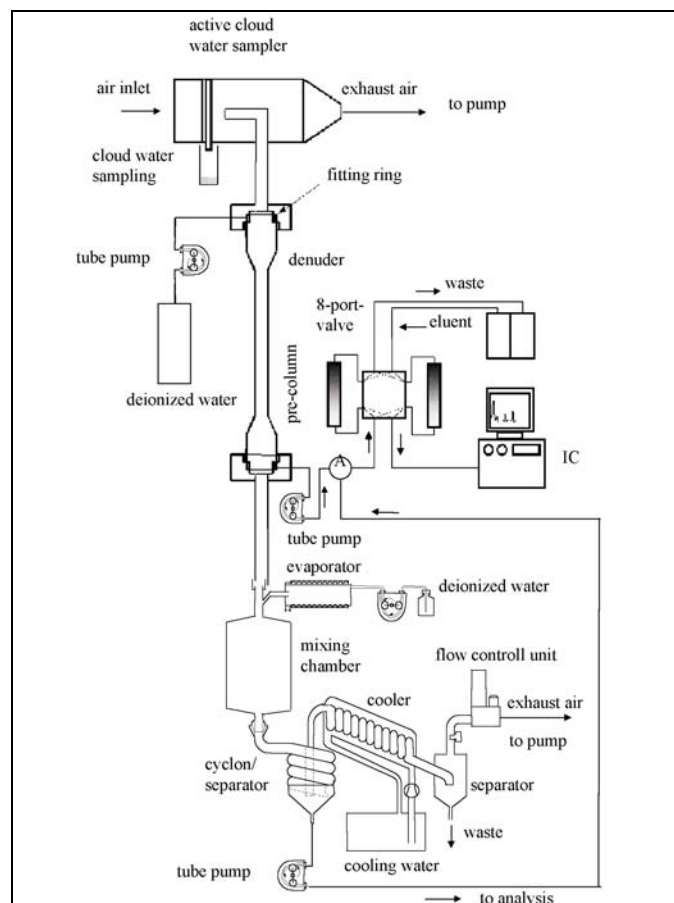


figure 3.1: Left: Schematic of operating principle of denuders. G = gas, P = particles. Right: Schematic diagram of the BTU- Cottbus wet-denuder / steam jet collector / ion chromatography system [Acker et al., 2001b].

A large number of designs of the denuder sampling tube was realized so far: e.g. an incorporating of a number of separate tubes in parallel [Sjodin, 1988] or annular [Harrison and Kitto, 1994] denuders, in which the air flows through the annular space between two concentric tubes (e.g. [Eatough et al., 1993; Koutrakis et al., 1993; Krieger and Hites, 1992]). Another possibility is the diffusion scrubber [Vecera and Dasgupta, 1991]: the coating itself is a stream of water that continuously flows along the walls of the denuder and is collected for

analysis. After sample collection, the denuders are e.g. leached with deionized water and analyzed by ion chromatography. The detection with ion chromatography is the most common way.

First measurements of atmospheric HONO used a two-denuder tube system with a Na_2CO_3 coating [Allegrini *et al.*, 1987; Ferm and Sjödin, 1985; Ferm and Sjoedin, 1983]. In the last decade, HONO detection by denuders was mainly performed by one or two NaCl-coated denuders followed by two Na_2CO_3 plus glycerol-coated denuders [Perrino *et al.*, 1990]. Thereby, the removal of HNO_3 on the NaCl denuders was essentially to distinguish the nitrate yielded on the carbonated denuder by the oxidation of nitrite, and thus due to HONO, from the nitrate due HNO_3 collection. The second Na_2CO_3 -coated denuder (differential technique) allows the small interference of nitrogen oxides to be taken into account [Febo *et al.*, 1990]. During the Rome 2001 campaign (see chapter 4.1 and [Febo *et al.*, 2003; Wiesen, 2003]), a new type of a parallel plate design wet effluent diffusion denuder (WEDD) was operated. The sampling was carried out with deionized water and after pre-concentration the analyte was taken directly to an anion chromatography unit (for more details in this instrument, refer to [Acker *et al.*, 2001b]).

3.1.1.2 Chemiluminescence Detection

HONO can also be detected by the chemiluminescence method [Kanda and Taira, 1990; Kanda and Taira, 1992]. A Na_2CO_3 solution strips gaseous HONO from the atmosphere by means of pulling an air sample and the solution through a glass coil and mixing continuously with ascorbic acid solution, which reduces nitrite to NO. The mixture is lead into a gas-liquid separating coil consisting of microporous PTFE tubing. The NO evolved from the separating coil is swept out by a stream of clean air and detected with a chemiluminescent NO_x monitor. For the chemiluminescence detection of NO, it is converted into NO_2 by the reaction r. 2.9 with ozone. The NO_2 molecules, which are produced by this reaction are electronically excited and show a rapid light emission. The detected light signal is then proportional to the concentration of NO_2 and therefore NO and HONO, respectively. For the measurement of NO_2 the molecules are first transformed to NO by catalytic (e.g. Gold or Molybdenum) or photolytic converters. Further possible converters as well as applications of chemiluminescence to atmospheric measurements were recently reviewed by [Navas *et al.*, 1997].

The technique utilizes a dual flow system and dual channel NO_x monitor to correct positive interferences from NO_2 and peroxyacetylnitrate (PAN). The concentration of HONO is determined by the difference between the two measurements. The sensitivity of the method is a function of the ratio of sampling flow rate to carrier gas flow rate, which permits a highly sensitive measurement.

During the Rome 2001, and the IUP 2002 campaigns, NO, NO_2 , and NO_y were measured by a commercial device from Ecophysics (CLD 770 AL ppt chemiluminescence NO analyzer, PLC 760 photolytic converter and a gold converter operated at 300° C, respectively). The system was calibrated every day using 10 ppm NO in N_2 , which was diluted with synthetic air to approximately 20 ppb. The calibration factors stayed constant during the campaign ($\pm 3\%$). The absolute uncertainty of the NO measurements was ± 20 ppt composed of ± 12 ppt due to photon statistic and ± 15 ppt due to offset variability. Without a converter, NO measurements with the Ecophysics CLD 770 AL ppt were available during the Milan 2002 and the KIP 2003 campaigns, only.

3.1.1.3 The DNPH-HPLC Method

A new method, tested during the Rome 2001 campaign, is based on 2,4-dinitrophenylhydrazone DNPH derivatization and high performance liquid chromatography (HPLC) analysis. The technique is based on aqueous (1 mM phosphate buffer, pH 7.0) scrubbing of HONO using two coil samplers, followed by derivatization (medium containing 300 M DNPH and 8 mM HCl at 45 °C) of the scrubbed nitrite into a highly light-absorbing azo dye. The azide derivative is separated from DNPH reagent and carbonyl derivatives by reverse-phase HPLC and was detected with an UV detector at 309 nm [Zhou *et al.*, 1999].

A denuder was attached to that system during the Rome 2001 campaign (see chapter 4.1), and alternatively switched between the direct sampling line and the line where the denuder was placed. This second line allowed the removal of the signal due to HONO and the detection of the contribution of possible interfering compounds (artifact HONO produced in the sampling line or possible particulate nitrite). The precision of the DNPH-HPLC instrument for HONO determination, as checked by comparing the signals coming from the two independent inlet lines, was estimated to be around 4%.

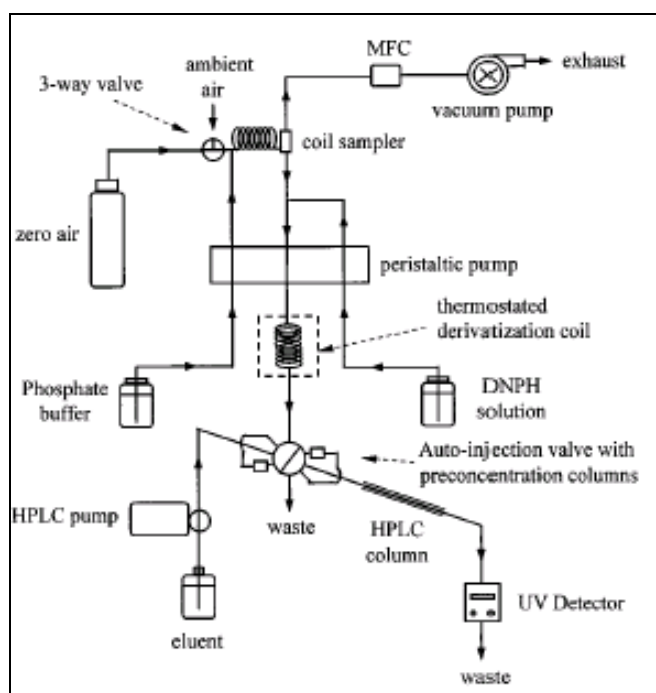


figure 3.2: Schematic diagram of a DNPH-HPLC measurement system for ambient HONO. (taken from [Zhou *et al.*, 1999]).

3.1.1.4 The LOPAP Instrument¹⁴

The LOPAP in-situ instrument (long path absorption photometer) is also based on wet chemical sampling and photometric detection [Heland *et al.*, 2001; Kleffmann *et al.*, 2002]. To overcome problems for the wet chemical sampling of atmospheric HONO, i.e. an interference signal from NO₂, the LOPAP uses a serial two-channel system: in the first stripping coil HONO is taken out and thus in the second, only the interfering species are

¹⁴ The original LOPAP instrument was yet improved and the modified version is called “LOPAP II”. According to [Kleffmann *et al.*, 2002] we will use the term LOPAP to describe the functionality of the LOPAP II instrument as well.

observed. By subtracting both, possible interferences are minimized. The calibration of the channels is performed with a liquid nitrite standard, which is injected into the stripping solution at known amounts or with a pure HONO source. The sampling system consists of a glass stripping coil of 10 cm length with an inner diameter of 2 mm. HONO from the constant sample gas flow is collected continuously into the liquid phase and reacts immediately with the stripping solution (0.06 M sulfanilamide in 1 M HCl) forming a diazonium salt with the nitrite of HONO. By adding 0.8 mM *n*-(1-naphthyl)ethylenediamine-dihydrochloride solution the final azo dye is produced, which now can be detected photometrical (VIS). The absorption cell for the detection consists of a Teflon tube with smaller refraction index than the dye. Now, visible light coupled into the fiber is reflected on the inside walls of the tube yielding a long absorption path-length and is detected by a small grating spectrograph, coupled to the tube with a quartz fiber. For further information, refer to [Heland *et al.*, 2001] or [Kleffmann *et al.*, 2002].

Previous intercomparison campaigns were carried out under various conditions but all in smog chamber measurements, e.g. in CEAM (Valencia /Spain) with a DOAS White system showing a systematical deviation of 15 – 20 % [Heland *et al.*, 2001]. With an absorption length of 1.5 m, the detection limits of 1 – 50 ppt were recorded corresponding to time resolutions of 5 – 1 min and an accuracy of \pm (10 – 15) %. In this thesis, the first field campaign intercomparisons between our DOAS and the LOPAP operated by the BUGH were carried out: during the Milan 2002 campaign, and during the Turm 2003 campaign.

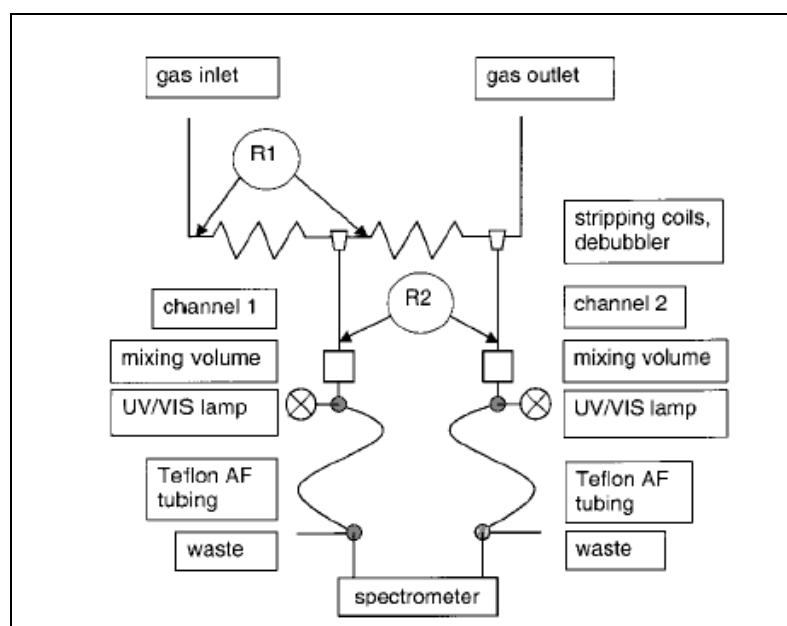


figure 3.3: Schematic view of the LOPAP II instrument by [Heland *et al.*, 2001].

3.1.2 Mass Spectrometry

An analyzing method valid to several problems in physics as well as in chemistry is mass spectrometry. According to the mass-to-charge ratio, constituent atoms, groups of atoms, or molecules are identified. For the detection of atmospheric HONO, the chemical ionization mass spectrometer (CIMS) is used [Zhang *et al.*, 1996]; HONO is ionized by SF₆ and detected as HONO-F ($m/e = 66$), which is produced via a fluoride ion transfer.

3.1.3 Spectroscopic Methods

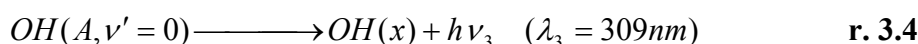
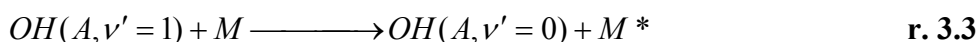
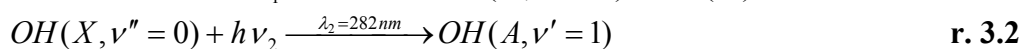
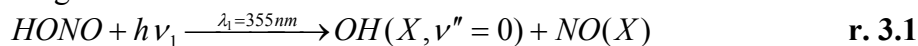
Among the optical measurement techniques for atmospheric nitrous acid, the Differential Optical Absorption Spectroscopy is not only the most common, but also the most proven. However, DOAS was used in this thesis and we will explain it in chapter 3.2. Here, we will only present further optical techniques, which can be reported in literature for the detection of atmospheric HONO.

Generally, spectroscopic methods have several advantages compared to the chemical surface collection techniques [Platt, 1994]: simultaneous measurements of a large variety of different trace gases (e.g. O₃, O₄, OH, CS₂, SO₂, NO, NO₂, NO₃, NH₃, HONO, H₂O, HCHO, halogen oxides especially key species such as ClO, OClO, BrO, and IO, and aromatics) can be performed with one instrument at the same time; measurements are highly sensitive (even to isomers), absolute calibrated and of high precision; measurements are contact-free (preventing reactions on the surface of a sampler resp. without disturbing the trace gases chemical behavior and thus even highly reactive species such as atmospheric radicals can be directly detected); and the time resolution is of a few minutes only.

However, the detection limit of spectroscopic methods is usually higher than that of the chemical surface collection techniques (see table 3.1). Additionally, the spectroscopic methods use the Euler approach and integrate the trace gas concentration along a specific light path. We will show in chapter 3.2 that the length of this light path is linked to the detection limit. However, an enhancement of the light path length hampers the interpretation of the measured trace gas concentrations with respect to spatial information.

3.1.3.1 UV – PF / LIF - Sensor

The ultraviolet photofragmentation laser induced fluorescence (UV-PF / LIF) system was presented by [Rodgers and Davis, 1989] as a measurement technique for atmospheric HONO. We have shown in chapter 2.3.7 that the photolysis of HONO into NO and OH is relatively fast, but high selectively at certain wavelengths. In the UV-PF / LIF measurement technique, the photolysis is simulated by an Nd:YAD laser, but additionally excites the OH molecules from their ground state X²Π into the first electronically excited state A²Σ. Deactivation by collisions occurs in competition with fluorescence. The yielded ground-state OH is detected afterwards by the following schema:



The basics of this technique were also used for the measurement of OH and HO₂ in the atmosphere. A laser beam at a wavelength of 308 nm is generally used for the excitation. HO₂ can be measured by LIF using the conversion to OH by the reaction with NO. However, major problems are artifact formation of OH in the LIF cell, interference with other absorbers, and the still remaining necessity of in field calibration [Hofzumahaus *et al.*, 1998; Hofzumahaus *et al.*, 1997; Holland *et al.*, 1995].

3.1.3.2 IR – Spectroscopy

As will be shown in chapter 3.2, the DOAS method uses absorption structures of trace gases in wavelengths of (near) UV or VIS light. However, self-evidently, the infrared can be used as

well to detect nitrous acid by its absorption structures at a wavelength of 12.6 μm [Chan *et al.*, 1976a] with an FTIR (Fourier Transform Infra Red) spectrometer. The instrumental complexity is high, thus FTIR is still more used in laboratory studies than in the atmospheric measurements. Further, the detection limit of these systems (2 – 4 ppb) is rather high, thus they can be used only in heavily polluted areas.

Usually, a White type setup (see chapter 3.2.3.2 and references therein) is combined with the FTIR for the detection of atmospheric trace gases [Hanst, 1978; Hanst *et al.*, 1982; Tuazon *et al.*, 1978; Tuazon *et al.*, 1980]. During the Milan 2002 campaign (see chapter 4.2), an open FTIR - White system was operated by the Chalmers University of Technology, Gothenburg / Sweden [Galle *et al.*, 1994], for the detection of HCHO.

3.2 Differential Optical Absorption Spectroscopy

3.2.1 An Overview of DOAS Applications

Different techniques have been used for several decades [Dobson and Harrison, 1926]. Nowadays, the most common used and most powerful of all these optical trace gas measurement methods is the Differential Optical Absorption Spectroscopy (DOAS) first applied to atmospheric trace gas measurements by [Platt *et al.*, 1979].

The basic principle of DOAS is rather easy (and will be explained in more detail in the next chapters) [Platt, 1994; Platt *et al.*, 1979]: light (typically in the visible and / or near UV wavelength range) collected by some optics along a specific path through the atmosphere is spectrally analyzed in a spectrograph-detector system based on Lambert-Beers law of light absorption. Except the broadband absorption, narrow-band structures appear in this spectrum and can be identified as the characteristic trace gas absorption structures. Several trace gasses of particular importance for atmospheric chemistry were measured for the first time using this technique (for an overview see [Platt, 1994]). Of special interest for this thesis are the compounds NO_2 , HCHO and O_3 [Platt *et al.*, 1979], nitrous acid [Perner and Platt, 1979; Platt and Perner, 1980; Platt *et al.*, 1980] and the OH radical [Perner *et al.*, 1976].

DOAS applications can generally be divided into two main topics: passive and active DOAS system differing mainly by the light source used. The light source of Passive DOAS systems is either the moon [Wagner *et al.*, 2000], stars [Friedeburg, 2003] or usually the sun. The measurement geometry of Passive DOAS is to collect either direct light from the source to the spectrograph as the absorption pathway or using stray light on its diffuse pathway through the atmosphere. This stray light coming from one or multiple (MAX-DOAS) distinct zenith and azimuth angles is used for several applications: long-term measurements of trace gas concentrations in the upper troposphere or measurements of direct emission plumes (e.g. of a volcano) with instruments located on the ground [Hönninger, 2001], measurements on aircrafts [Leue *et al.*, 2001; Pfeilsticker and Platt, 1994], measurements in the stratosphere with instruments attached to stratospheric balloons [Bösch, 2001; Pfeilsticker *et al.*, 1997; Pfeilsticker and Platt, 1994], but also remote sensing is available, with instruments located on satellites [Goede *et al.*, 2000; Leue *et al.*, 2001; Spichtinger *et al.*, 2001; Wagner *et al.*, 2001; Wagner and Platt, 1998; Wagner *et al.*, 2002a; Wagner *et al.*, 2002b].

For measurements in the lower troposphere, or for kinetic studies (e.g. in smog chambers) an active DOAS system is favorable (see e.g. [Ackermann, 2000; Alicke, 2000; Geyer, 2000; Kah, 1998; Perner and Platt, 1979; Platt, 1994; Platt and Perner, 1980; Platt *et al.*, 1980; Platt *et al.*, 1979; Veitel, 2002]). Thereby, a light beam emitted from an artificial light source is sent through the atmosphere on a well-defined light path. The light is then collected by suitable optics and sent to a spectrograph-detector system, where the spectrum is analyzed to gain information on the structure and amount of absorption by molecules that took place

along the light path. A recent active DOAS development is the DOAS-Tomography by LP-DOAS to resolve the spatial distribution of trace gasses in the atmosphere [Lösch, 2001]. In the following, we will focus on the active DOAS system, which was used in this thesis.

3.2.2 Theoretical Description of DOAS

3.2.2.1 Basic Theory of Absorption Spectroscopy & Lambert-Beers Law

Light passing a medium is reduced in its intensity mainly caused by two effects. Molecules irradiated by electromagnetic radiation absorb at distinct wavelengths directly linked to their electronic, vibrational and rotational states and therefore absorb the radiation energy yielding an excited quantum-mechanical state. Second, scattering processes lower the lights intensity while it is passing a medium. In a gaseous medium (in our case the atmosphere itself), absorption is realized by gas-molecules, but scattering is again due to two processes: Rayleigh scattering on molecules (ε_R) and Mie scattering occurring on aerosol particles larger than the lights wavelength (ε_M). We will not go into their theory in this thesis, but it is important to note that both Rayleigh and Mie scattering strongly depend on two factors: the location l along the observed light path and the wavelength λ . The wavelength dependence is different for both: ε_M , was found to depend on $\approx \lambda^{-1.3}$, while ε_R depends on λ^{-4} [Hulst, 1957].

However, the lowering of intensity with respect to the extinction processes of scattering (ε_R and ε_M) and absorption of a number of trace gases i on the path l of the light with its original intensity $I_0(\lambda)$ is reduced to $I(\lambda)$ as described by Lambert-Beers law of eq. 3.2:

$$I(\lambda, L) = I_0(\lambda) \cdot \exp\left(-\int_0^L \left(\varepsilon_R(\lambda, l) + \varepsilon_M(\lambda, l) + \sum_i \sigma_i(\lambda, p, T) \cdot c_i(l)\right) \cdot dl\right) + N(\lambda) \quad \text{eq. 3.2}$$

The absorption of a trace gas i is characterized by their concentration $c_i(l)$ along the light path l and their absorption cross-section, which only depend on the temperature T , the pressure p , and the wavelength λ . (The pressure und temperature dependence can be omitted for most absorbers in the boundary layer and is no longer labeled.) However, this absorption cross-section is individual to each type and state of molecules (see also figure 3.6), thus the sum of all different trace gases i present in the light path can be measured at the same time. $N(\lambda)$ represents the photon noise (see chapter 3.2.3.6).

This theory of Lambert-Beers law is easy to apply for various chemical and physical studies in the laboratory, where scattering often can be neglected and the initial intensity $I_0(\lambda)$ is measurable, but it is not suitable for atmospheric conditions for mainly four reasons. First, as the absorption of trace gases mainly occurs in the near UV or VIS spectral range, special artificial light sources are needed (see also chapter 3.2.3.3) for an active DOAS system. However, these lamps are not only characterized by Planck's law but also show emission lines with a spectral structure similar to the trace gas absorptions that change both in intensity and spectral shape. Further, the detection and digitalization of a spectrum by any detector defines an instrumental function, which can be dependent on the wavelength as well and might create pseudo spectral features. Stray light (mainly from the sun) scattered on diffuse paths into the DOAS light beam along its way through the atmosphere enhances the intensity detected at the spectrograph. And finally, the broadband absorption in the atmosphere is not only caused by scattering processes, but also by continuum absorption of trace gases. In the next chapter, we will show, how to overcome these problems.

The key to overcome these problems is illustrated in figure 3.4 and figure 3.5: separation of the absorption spectra in different parts representing the broad-band spectral features ($\sigma^B(\lambda)$) due to the light source spectrum and scattering, the narrow-structures of absorption and emission ($\sigma'(\lambda)$), and the noise structure (see below, chapter 3.2.3.6):

$$\sigma(\lambda) = \sigma^B(\lambda) + \sigma'(\lambda) \quad \text{eq. 3.3}$$

σ' is often defined as the differential absorption cross-section varying “rapidly” with the wavelength λ . The broadband structures caused by scattering as well as broadband absorption and the lamp spectrum are separated and characterized by σ^B only. If this procedure is applied to Lambert-Beers law, we finally obtain eq. 3.4 suitable for atmospheric applications:

$$I(\lambda) = I_0(\lambda) \cdot \exp\left(-\int_0^L \left(\varepsilon_R(\lambda, l) + \varepsilon_M(\lambda, l) + \sum_i \sigma_i^B(\lambda) \cdot c_i(l) + \sum_i \sigma'_i(\lambda) \cdot c_i(l)\right) \cdot dl\right) \quad \text{eq. 3.4}$$

Finally, we combine all the broadband extinctions, and assume the instrumental transmission to vary slowly with the wavelength as well and obtain the Lambert-Beers law in its DOAS relevant form:

$$OD = \ln\left(\frac{I(\lambda)}{I'_0(\lambda)}\right) = -\int_0^L \left(\sum_i \sigma'_i(\lambda) \cdot c_i(l)\right) \cdot dl \quad \text{eq. 3.5}$$

where the logarithm of the quotient of $I(\lambda) / I'_0(\lambda)$ is defined as optical density (OD). In practice, $I'_0(\lambda)$ is computed from the measured spectrum $I(\lambda)$ by applying a low-pass filter, which removes all narrow-band structures by triangular smoothing or Savitzky – Golay smoothing, and subsequently dividing the original spectrum by the smoothed spectrum. A different approach for low-pass filtering is a polynomial regression analysis [Geyer, 1997; Stutz and Platt, 1997; Volkamer, 1996]. The differential absorption cross-section σ'_i for all trace gasses that feature characteristic structures in the observed wavelength range have to be computed by the same high pass filter algorithm. Now the only missing variable, apart from the desired trace gas concentration c_i , is the total light path length l . For a LP-DOAS set-up, the light path length can be measured easily and very accurately e.g. by a laser range finder.

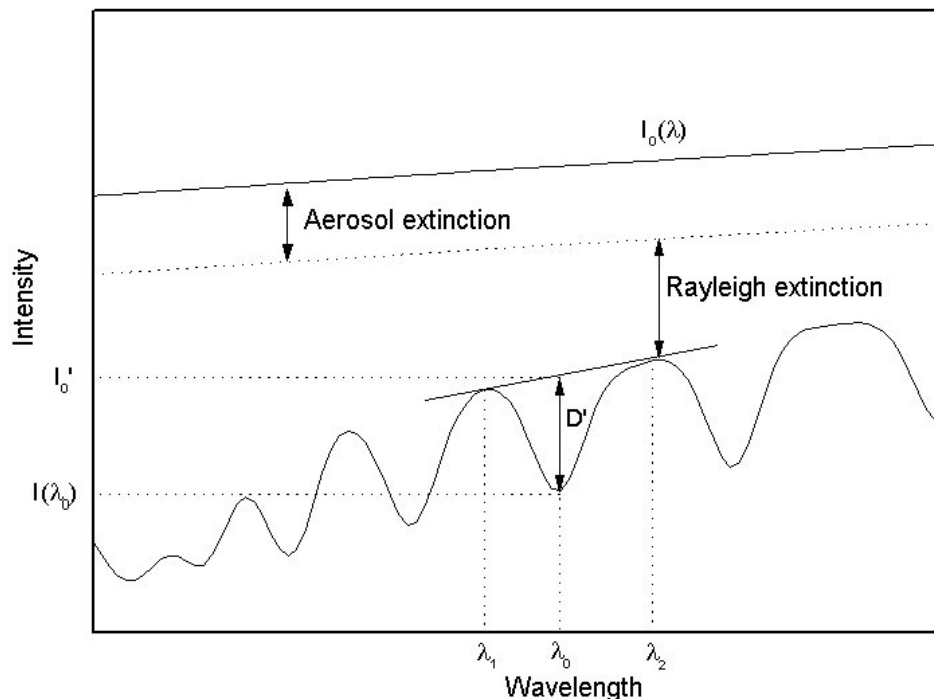


figure 3.4: Separation of extinction of the light intensity $I(\lambda)$ into broadband Rayleigh (at air molecules) and Mie (at aerosols) scattering as well as narrow-band differential absorption by trace gases present at a certain differential optical density D' .

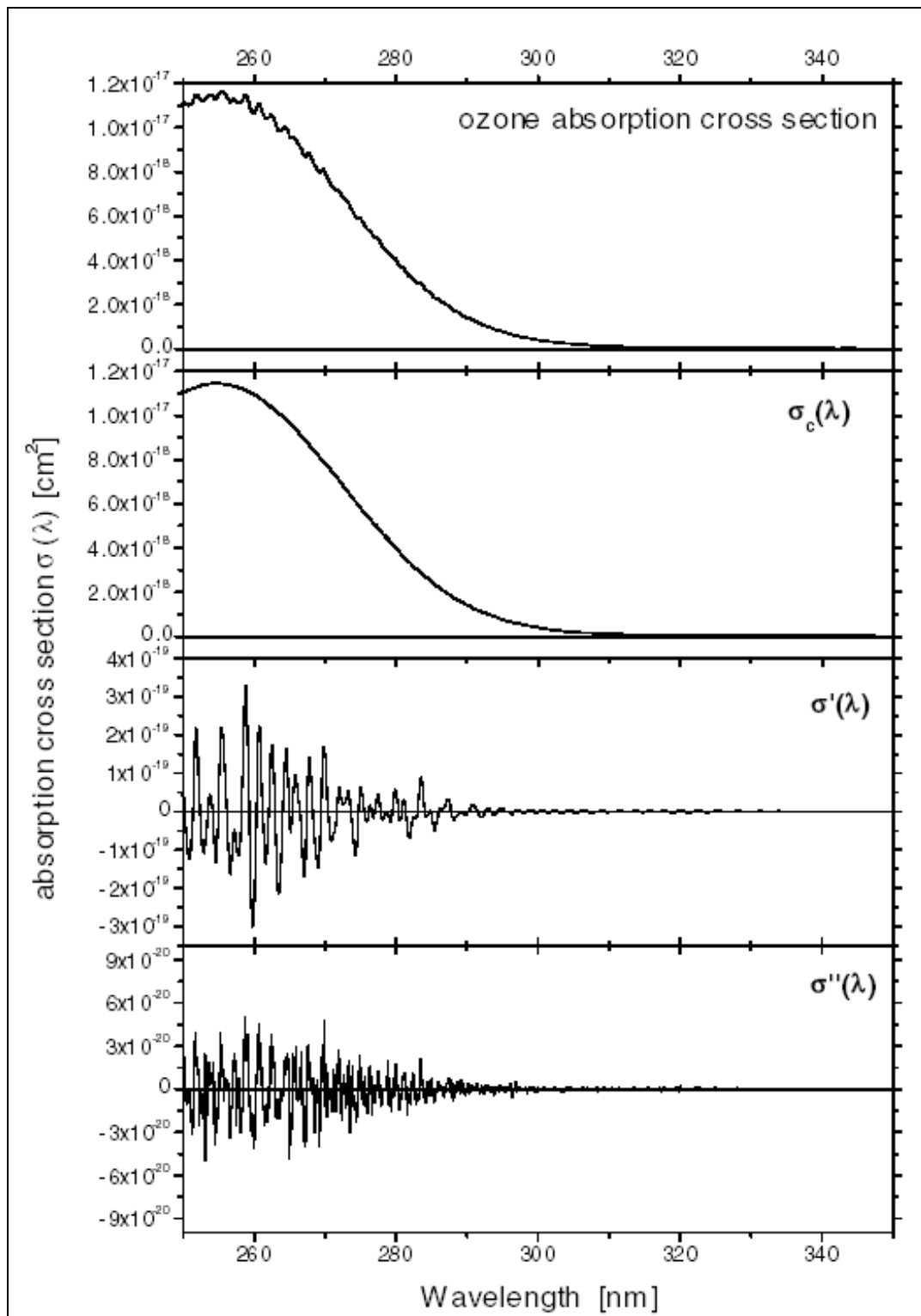


figure 3.5: Separation of the O_3 absorption cross-section according to eq. 3.3 into 'slowly' varying $\sigma_c(\lambda)$, 'rapidly' varying $\sigma'(\lambda)$, and high frequency parts $\sigma''(\lambda)$ by applying a numerical band pass filter to the cross-section.

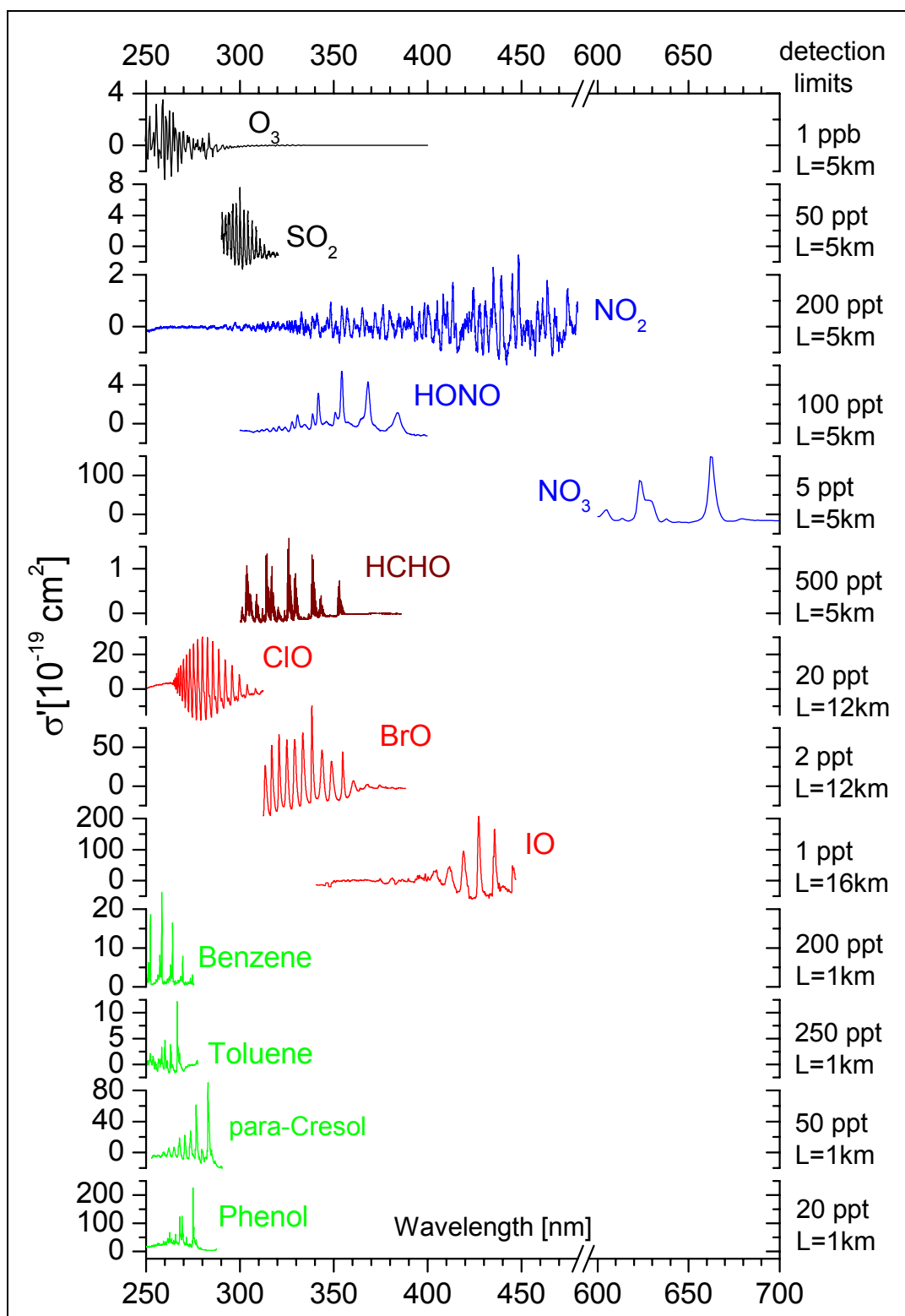


figure 3.6: Differential absorption cross-sections $\sigma'(\lambda)$ of certain atmospheric trace gases, which are measurable by the DOAS technique. On the right, their corresponding detection limit at a certain light path length is calculated, based on the assumption of a minimum detectable optical density of 10^{-3} .

3.2.2.2 DOAS for Atmospheric Measurements: Numerical Description

For detecting atmospheric trace gas concentrations from the measured DOAS spectra, the retrieval process has to account not only for the basic atmospheric spectrum, but also for instrument-specific spectral structures, which were not discussed in the previous chapter 3.2.2.1. We will now re-describe these corrections for the measured atmospheric spectrum (figure 3.7 a), which depend on the setup of the DOAS instrument as well as its optical components. The next chapters directly follow the discussion [Stutz, 1996; Stutz and Platt, 1996].

The figure 3.7 illustrates again the principle of an active DOAS system [Stutz, 1996; Stutz and Platt, 1996]. The light from a suitable broadband source has an initial intensity $I_0(\lambda)$ and is focused by optics to pass through the atmosphere along an absorption light path l . It is collected again by another telescope to be spectrally analyzed by a spectrograph-detector system. Extinction processes generally lower the initial intensity $I_0(\lambda)$ by scattering and absorption according to eq. 3.4.

The spectrograph as well as the detector strongly influences the DOAS measurements by lowering the spectral resolution ($\Delta\lambda / \lambda$) to a value characteristic for that instrument. This is caused by the entrance slit width as well as the fact that the spectra recorded consist of a continuous wavelength interval, but have to be imaged to the discrete numbers of pixels available on the detector.

This is mathematically described by convoluting the initial spectrum of $I(\lambda, l)$ with the so-called instrumental function [Stutz, 1996; Stutz and Platt, 1996]:

$$I^*(\lambda, L) = I(\lambda, L) * H = \int I(\lambda - \lambda', L) \cdot H(\lambda') \cdot d\lambda' \quad \text{eq. 3.6}$$

The wavelength interval $[\lambda, \lambda+1]$ (typically, some tens of nanometers) is integrated mapped to a number i pixels of the detector (which in total consists of $n = 1024$ diodes). The wavelength-to-pixel mapping function of the instrument (or dispersion function) is Γ_I . In the case of a linear dispersion Γ_I , this function is simply $\lambda(i) = \lambda(0) + \gamma_0 \times i$, where the spectral width of a pixel is constant $\Delta\lambda(i) = \lambda(i+1) - \lambda(i) = \gamma_0$ and the intensity detected at a certain pixel (neglecting any instrumental factors) can be written as:

$$I'(j) = \int_{\lambda}^{\lambda+1} I^*(\lambda', L) \cdot d\lambda' \quad \text{eq. 3.7}$$

In reality, the dispersion relation observed is often more complex but can be well approximated by a polynomial function with a degree of q [Stutz, 1996; Stutz and Platt, 1996]:

$$\Gamma_I : \lambda(j) = \sum_{k=0}^q \gamma_k \cdot j^k \quad \text{eq. 3.8}$$

The mapping between the pixel i and the corresponding wavelength $\lambda(i)$ is determined by the vector γ_k . A spectral shift of the spectrum corresponds to a variation of the factor γ_0 , a squeeze (linear stretch) to γ_1 and so on. These changes appear in DOAS measurements mainly temperature drifts in the optical alignment (grating spectrometers usually show a temperature drift of 1 / 10 of a pixel per Kelvin) and variation in air pressure. The latter are observed for example in aircraft measurements, caused by a change in the index of refraction of air, i.e. at the pressure at 2400m height (approx. 750mbar), and the spectrum is typically re-positioned on the detector by roughly 2 / 10 of a pixel compared to ground level [Pfeilsticker and Platt, 1994]. Effect of temperature variations can partly be suppressed by temperature isolation and thermal stabilization, but never the less it must generally be taken into consideration.

The plot b.) of figure 3.7 now presents the convoluted atmospheric spectrum $I^*(\lambda, l)$ projected on the detector after passing the spectrograph. Finally we get the illustration of plot c.) of

figure 3.7, showing the spectrum as it is sent to the computer after being mapped on the PDA and digitized by the electronics.

From eq. 3.5, we see that the spectrum needs to be logarithmed first $J(i) = \ln(I'(i))$:

$$J(i) = \ln(I'(i)) = J_0 - \sum_{j=1}^m a_j(i) \cdot S_j'(i) + B'(i) + R'(i) + A'(i) + N'(i) \quad \text{eq. 3.9}$$

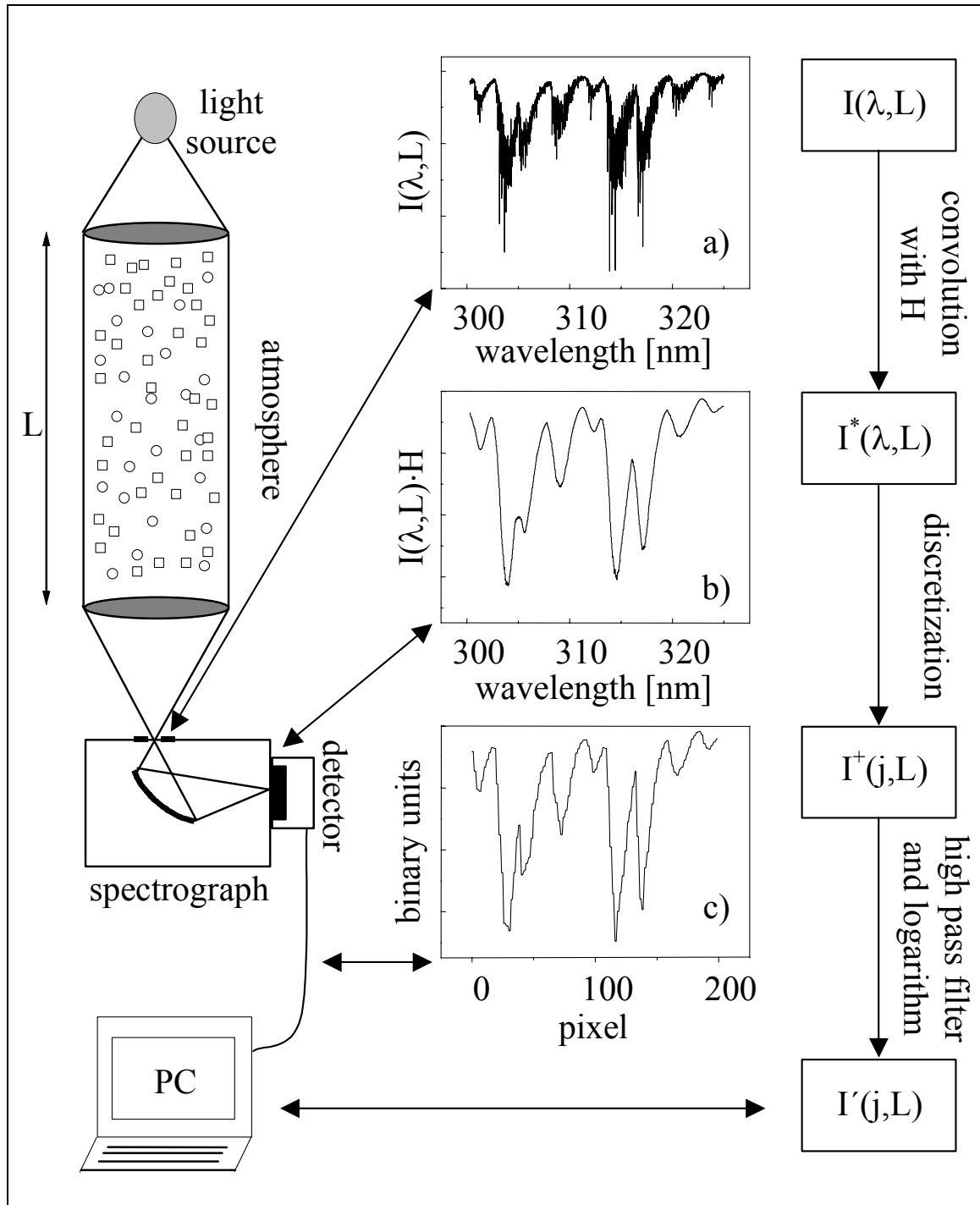


figure 3.7: Schematic view of a DOAS instrument and the analysis procedure of the observed spectrum. The small windows show: (A): an example of the light entering the spectrograph with only one absorber (here: HCHO); (B): the same spectrum convoluted by the spectrograph's instrumental function; (C): the spectrum at the detector, where the wavelength is mapped to discrete pixels (taken from [Stutz and Platt, 1996]).

For the evaluation of the narrow-band absorption structures of absorber i described by its cross-section S , the S_j have to be treated in the same way, resulting in cross-sections $S'_j(\lambda) = \ln(\exp(-\sigma'_j(\lambda)) H)$ of the same resolution as the measured spectra. The scaling factors $a'_j(i)$ (often referred to as the “column density” of the absorber j) are now directly linked to the concentration c_i of a trace gas i . The broad absorption of the trace gases are represented $B'(i)$. Variations in the spectral sensitivity of detector or spectrograph are summarized by $A'(i)$, which is a function of pixel number including variations of their spectral sensitivity. This is due to the fact that all electronics that detect, amplify and digitize the signal also affect the spectrum. The photo diode array (PDA) is not completely homogenous in its specifications, and has different quantum yields, dark current and electronic noise signals of individual diodes. The extinction by Mie- and Rayleigh scattering is represented by $R'(i)$. All noise (impossible to discriminate) is summarized as $N'(i) = \ln(N(\lambda))$ caused by the detector noise as well as by photon statistics [Stutz, 1996; Stutz and Platt, 1996].

The sum of eq. 3.9 represents the fact that several different absorbers are present in an atmospheric air mass. As the strength of the absorption structures varies with wavelength: depending on the wavelength interval observed, only those absorbers with absorption structures sufficiently strong are detectable with DOAS instruments. Thus, the total number m of different absorber is limited and typically $m = 2$ to 10 trace gas absorptions can simultaneously be identified in a single atmospheric DOAS spectrum [Platt, 1994; Stutz, 1996; Stutz and Platt, 1996] by the numerical procedure presented above.

This evaluation procedure needs to retrieve the parameters a'_j (eq. 3.9) and thus the concentration of the trace gases by taking into account all the atmospheric and instrumental effects. Next, the error of the parameters a'_j and therefore of the measured trace gas concentrations must be derived. A linear least-squares method can do so, if no instrumental effects are encountered. Spectral misalignment or change in the dispersion of the reference spectra due to a drift of the spectrograph need to be considered as discussed above. Further spectral structures often appear and can be caused by the instrument itself or by unknown absorbers [Stutz, 1996; Stutz and Platt, 1996].

3.2.2.3 The Analysis Procedure

A simple model, which describes the physics of a measured DOAS spectrum according to equation eq. 3.9, is the basis of any DOAS evaluation procedure [Stutz, 1996; Stutz and Platt, 1996]. It expresses the logarithm of the smoothed discrete intensity $J(i)$ as a function $F(i)$:

$$F(i) = P_r(i) + \sum_{j=1}^m a_j \cdot S'_j(d_{j,0}, d_{j,1}, \dots)(i) \quad \text{eq. 3.10}$$

As can be seen from eq. 3.10, we need the absorption structures of the trace gasses S'_j , (measured in the laboratory or calculated by convolution of high-resolution literature cross-sections with the instrument function H) as input data to the procedure. By adding $P_r(i)$ to eq. 3.10, we summarize all broadband spectral structures given in detail in eq. 3.9. Those are the characteristics of the specific lamp $I_0(i)$, the scattering processes $R'(i)$, the spectral sensitivity $A(i)$ and the broad absorptions by the trace gases $B(i)$:

$$P_r(i) = \sum_{h=0}^r c_h \times (i - i_c)^h \quad \text{eq. 3.11}$$

Here, the parameter $i_c = \text{int}(n / 2)$ is the center pixel of the spectral region, which is used for the evaluation. The polynomial refers to i_c to maximize the influence of the non-linear terms. Applying a linear fit of model function F to the measured intensity $J(i)$, we obtain the scaling factors a_j of eq. 3.10 and the polynomial coefficients c_h of eq. 3.11. They can be used to calculate the concentration c_j of the respective trace gas j :

$$S'_j \cdot a_j = S'_j \cdot \int_0^L c_j(l) \cdot dl \quad \Rightarrow \quad c_j = \frac{a_j}{L} \quad \text{eq. 3.12}$$

Using the wavelength-pixel-mapping function Γ_i , the measured spectra $J(i)$ and the reference spectra $S'_j(i)$ have to be re-aligned. Due to varying environmental conditions, this can be approximated by shifting and stretching / squeezing the reference spectrum in wavelength region yielding $S'_j(i^*)$ used in the linear fit by adopting the wavelength-pixel-mapping Γ_j^* to $S'_j(i)$. As Γ_j is a strictly monotonous function, its inverse can also be described by a polynomial function:

$$\Gamma_j^{-1} : x(\lambda) = \sum_{k=0}^q \beta_k \times \lambda^k \quad \text{eq. 3.13}$$

where the $x(\lambda)$ represent the non-integer pixel number resulting from the inverse transformation. To calculate the reference spectra $S'_j(i^*)$ for the linear fit, the discrete spectra $S_j(i)$ are approximated from the corresponding continuous spectrum $S_j(x)$ using a cubic spline interpolation. Then, the $S'_j(i^*)$ with a wavelength-pixel-mapping Γ_j can be calculated by deriving $S'_j(\lambda)$ with Γ_j^{-1} from $S'_j(x)$, which is approximated by an interpolation on $S_j(i)$, and applying Γ_j :

$$S_j(i) \xrightarrow{\text{interpolation}} S_j(x) \xrightarrow{\Gamma_j^{-1}} S'_j(\lambda) \xrightarrow{\Gamma_j} S'_j(i^*) \quad \text{eq. 3.14}$$

It is possible to refrain from calculating $S'_j(\lambda)$ by combining Γ_j^{-1} and Γ_j to one formula, which links i to x by using a polynomial with parameters δ_k :

$$x(j) = x(\lambda(j)) = \sum_{k=0}^{q_i \times q_j} \delta_k \times j^k \quad \text{eq. 3.15}$$

Modifying slightly the eq. 3.15 can be of an advantage for the analysis procedure, as then the spectral alignment parameters $d_{j,k}$, determining the transformation, are zero if the wavelength-pixel-mappings of J and S_j are equal [Stutz and Platt, 1996]:

$$x = i + f_j(i) \quad \text{with} \quad f_j(i) = \sum_{k=0}^{p_i} d_{i,k} \times (i - i_c)^k \quad \text{eq. 3.16}$$

Using the parameters $d_{j,k}$ according to equations eq. 3.13 and eq. 3.16, and a cubic spline interpolation on $S_j(i)$, we can now calculate the spectrum $S_j(d_{j,0}, d_{j,1}, \dots)(i) = S_j^*(i)$ with the wavelength-pixel-mapping Γ_j .

Performing a non-linear fit of the model F to the spectrum J with fixed parameters a_j and c_h , we get these parameters $d_{j,k}$. A linear shift of $d_{j,0}$ pixels of the spectrum S_j is expressed by $p_j = 0$, while $p_j = 1$ shows an additional linear squeeze or stretch according to parameter $d_{j,1}$ and even higher values of p_j represent a squeeze or stretch of higher order.

Selecting the degree of the squeeze process p_j for every reference spectrum S_j optimizes the fit results and thus best physical description. It is also possible to use one common set of parameters $d_{j,k}$ for two or more reference spectra if the wavelength calibration is identical for these spectra [Stutz and Platt, 1996].

The analysis procedure combines the well-known nonlinear Levenberg- Marquardt method [Levenberg, 1944; Marquardt, 1963], which determines the $d_{j,k}$, and a standard linear least squares fit [Albritton et al., 1976; Bevington, 1969] to derive the a_j and the c_k .

$$\chi^2 = \sum_{i=0}^n (J(i) - F(i))^2 \quad \text{eq. 3.17}$$

Both procedures iteratively minimize χ^2 between F and J . In order to do so, a linear fit from starting values of $d_{j,k}$ is calculated first. Its resulting parameters a_j and c_k are then used as input values for the following nonlinear Levenberg-Marquardt fit. However, only one step of this non-linear iterative method is performed and the resulting parameters $d_{j,k}$ are used for another linear fit next. Afterwards, the results are used as starting parameters of the next

nonlinear fit. Summarily, the DOAS fitting procedure is alternating between both methods of a linear and a nonlinear fit, always using the result of the previous call as input parameters for the next fit-run. The procedure is operated in a loop, repeating until one of the several stopping conditions is fulfilled. Usually, the fit is aborted when the relative changes of χ^2 in the last step are smaller than a given value (usually 10^{-6}) and thus the fit has converged. The fit also stops if a number of repetitions of the iteration determined by the user is exceeded, or if the non-linear method becomes unstable [Stutz and Platt, 1996].

3.2.2.4 Error Estimation

Before applying the method of a least square fit to the DOAS data, which will surely yield best results and the correct errors, we have to verify three assumptions: The errors of the pixel intensity must have a finite variance [Albritton *et al.*, 1976]. Next, the normal least squares fit as discussed in [Albritton *et al.*, 1976; Bevington, 1969] and used in most of the analysis procedures assumes that the intensity errors of the individual pixels are independent. And finally, the systematic error of the pixel intensity is zero [Albritton *et al.*, 1976].

The first assumption can be verified: the error of the $J(i)$ is dominated by photon noise yielding the variations of the intensity, which are Poisson statistically distributed. However, further on, it is well known that for high-count rates, this statistic function can be approximated by a Gaussian distribution. Thus we will use the standard deviation σ of the Gauss distribution as the error of the DOAS intensity.

However, the other two assumptions are not generally fulfilled and a bias can occur in the results. Errors, which are caused by cross-dependencies to the neighboring diodes of the PDA or those caused by endowment errors of the diodes, are well known as PDA-structures [Stutz, 1996] and can be corrected e.g. by applying the multi-channel technique (MCST).

As explained in [Stutz, 1996], we use a correction factor of $3 \cdot \Delta_{\text{Statistics}}$ applied to the pure statistical errors resulted from the fit. This factor was calculated by [Stutz, 1996] in dependence of spectral resolution, the width of the absorption structures observed and the degrees of freedom for the shifting and squeezing / stretching during the non-linear fit. A more detailed description of all error calculations can be found in [Stutz and Platt, 1996].

3.2.2.5 Effects of Residual Structures: X-Absorber and Detection Limit

Another problem with the numerical analysis of DOAS spectra (as described above) is the occurrence of certain and stable structures $R(i) = J(i) - F(i)$ different from suspected pure noise in the residuum of the fit, which cannot be described by statistical method. These structures may indicate an unknown absorber (often referred as X-absorber) or can be caused by the instrument itself and will then occur randomly in most cases.

However, we will try to distinguish between both. To do so, it is important to know that in a pure noise spectrum, the width of any structure should only be one pixel indicating the independence of the diodes intensities. However, in reality it is observed that the errors of the pixel intensities are not independent from one another: in residuals, groups of neighboring pixel intensities appear to change simultaneously in a random way. A way of simulating this would be smoothing a pure noise spectrum, e.g. by a running mean. In a running mean, every pixel intensity is replaced by the average of its neighboring pixel intensities. Therefore the errors of the individual pixel intensities are no longer independent from each other. Smoothed noise spectra look similar to residuals normally found in the analysis of atmospheric spectra. This finding confirms that the single pixel errors are not independent from one another [Stutz and Platt, 1996].

To clarify the second theory, it is important to note that obviously, the numerical analysis of DOAS spectra is not complete. Only those absorbers known are fitted and erased from the measured spectrum yielding the residual structures. However, it is evident that more different trace gases are present in an observed real air mass, which might not be known yet, but still contribute to the obtained residual of the DOAS spectrum. (It was shown above that these X-absorbers only raise the residual, but not influence the trace gas concentration detected for a certain species). A partial correction can be performed by fitting a typical residual or the mean residual of a series of spectra to the measured atmospheric DOAS spectrum as an additional reference.

This is justified, as residual structures due to unknown X-absorbers generally show strong diurnal or seasonal variations and therefore can be separated from other systematic errors [Hönninger, 2001]. However, applying this method has to be done with care, as the systematic errors discussed above, and therefore the detection limits, are decreased.

Finally we should state that residual structures have also a strong effect on the detection limits of trace gas measurements by DOAS technique. Several approaches are used to quantify their influence. First, the minimum detection limits at a certain residual structure can be calculated by comparing both the optical density of the residual and that of the trace gas absorption. Thus, the detection limit only depends on the optical density of the residuum, the differential absorption cross-section of the trace gas and the path-length of absorption through the atmosphere. Another approach was introduced by [Hausmann *et al.*, 1999]: a Monte-Carlo algorithm is used to compute the detection limits with respect to the fitting algorithm and the residuals. Finally, estimations on the total contributions of these effects to the residual structures of a DOAS spectrum were already performed by [Stutz and Platt, 1996]. They suggest multiplying the systematic and statistical 1σ -error of the fit and the resulting detection limits by a factor of 2 to obtain suitable results. We will use their approach in this thesis.

3.2.3 Instrumental Setup of a DOAS System

The most common optical setup of a DOAS system consists of a single very long light path, which is folded only once between the lamp and the detector. These long-path systems average the trace gas concentrations over a large air mass (typically 2 – 16 km). The long path DOAS systems used in this thesis (a scientific active Long-Path DOAS system and a semi-commercial active Long-Path system by Hoffmann Meßtechnik) are both modern versions of the original setup developed by [Platt *et al.*, 1979].

To compare DOAS measurements with in-situ data during the Milan 2002 campaign and perform measurements in a smaller smog chamber, an open White type f / 100 multi-reflection system with a base-length of 15 m (see [Geyer, 1997; Grassi and Guzzi, 2001; Ritz *et al.*, 1992; Trick, 2000; Volkamer, 1996; White, 1942; White, 1976]) was operated.

The principles of these DOAS systems are identical and have already been described in the chapter above. We will now give an overview of the optical components used for each of these systems as well as the instrumental characterizations.

3.2.3.1 The Long Path (LP) DOAS System

A sketch of the setup of a long path DOAS instrument is given in figure 3.8. Basically, the long path telescope consists of two coaxial Newtonian telescopes with transmitting and receiving optic combined in one device. In the optical axis¹⁵ of the telescope, two elliptical plane mirrors are mounted to reflect the light of both outgoing and incoming beams by + / -

¹⁵ Defined as being perpendicular to the centre of the parabolic main mirror.

90°. The main mirror of both instruments, the scientific and the semi-commercial, is parabolic with a diameter 300 mm and 200 mm respectively, and a focal length of 1500 m, 600 mm respectively. Additionally, for the semi-commercial system, the main mirror is movable forwards and backwards along the optical axis by about ± 10 mm. This enables partial correction of the beam divergence generated by the transmitting telescope (see blow and [Rudolf, 1993; Stutz, 1996; Veitel, 2002]).

An active DOAS system uses an artificial light source, which is placed in the focal plane of the main mirror. The arc of the Xe lamps used, however, has a diameter of 0.2 to 0.3 mm, causing a divergent beam and thus the outgoing light beam is not exactly parallel. However, the optical image is not perfect. Since the light source is not a point the light beam slightly diverges along its path through the atmosphere resulting in a loss of light depending on the distance to the retro reflectors. Because of the two plane mirrors in the optical axis of the telescope, only a ring can be sent into the atmosphere leading to a light loss of 50 % compared to a fully enlightened mirror without the shade of the plane mirrors.

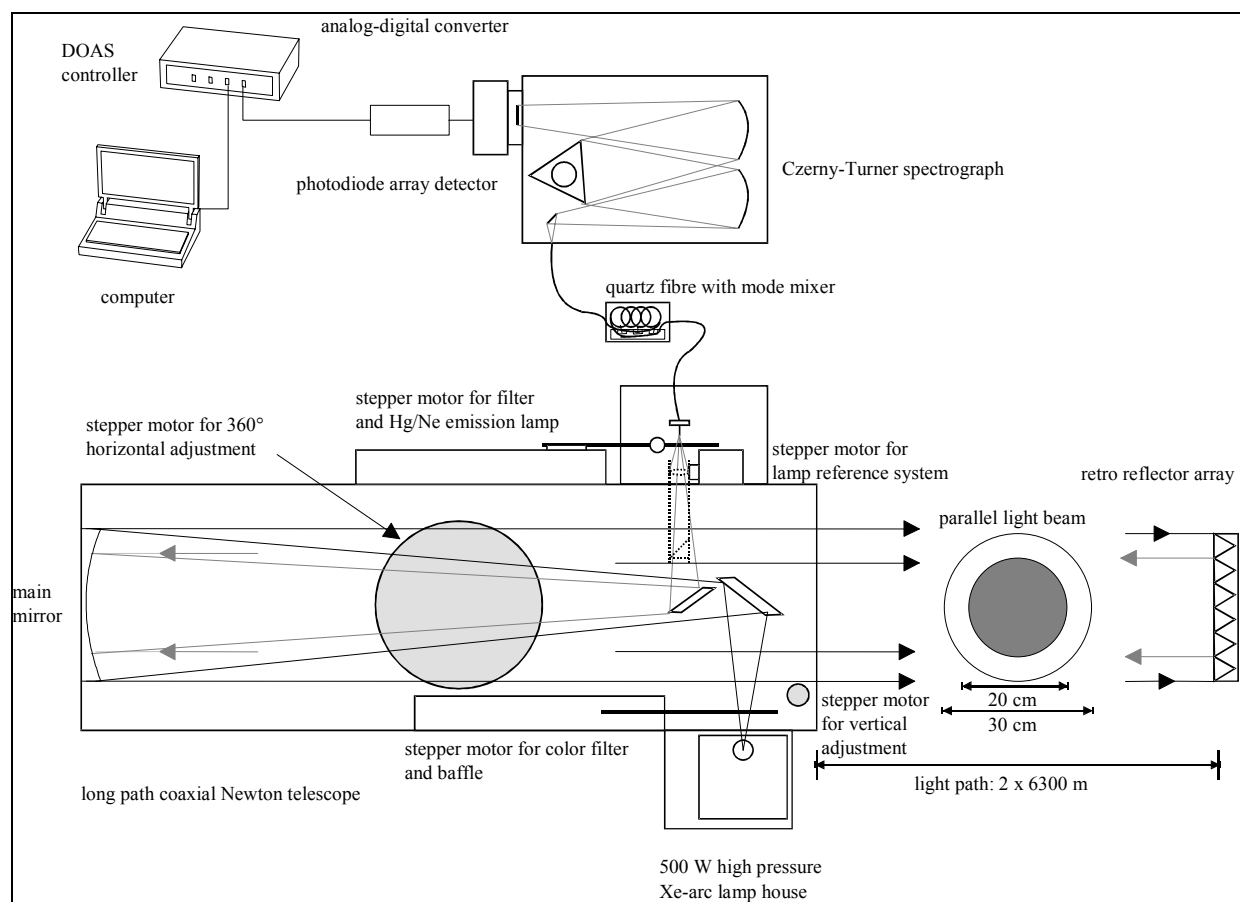


figure 3.8: Sketch of an active DOAS long-path system used for the optical detection of tropospheric trace gases in this thesis.

A retro reflector array is used to reflect the parallel light beam exactly back into the telescope. The specifications of the retro reflectors positioned at a distance of several hundred meters up to several kilometers from the telescope guarantee a maximum deviation of the returned beam from the original below 2". For our measurements on fixed light paths, the reflectors are aligned to meet the optical axis of the beam by hand once. The returning beam is also divergent, which is caused by atmospheric turbulence, but also by interference at the opening of the reflectors and inaccuracies of the reflectors causing deviations in the directions of

received and backscattered light. An exact mathematical description of these processes is not possible, but a resulting Gauss-shaped beam profile enlarged by a factor of two could be measured at the position of the receiving telescope (see also [Stutz, 1996; Veitel, 2002]).

The light is reflected back to the telescope, where it is focused onto a quartz fiber in the second focal plane of the main mirror. The optical layout both of the receiving telescope and of the quartz fiber connecting it to the spectrograph is optimized for the numerical aperture $NA = 0.12$ of the spectrograph to minimize the loss of light intensity.

The telescope has several moving elements: Horizontal and vertical alignment of the telescope is performed by two stepper-motors. Another motor carries a wheel on which optical filters are mounted and which is attached to the telescope hull. The filters are used to remove light at certain wavelengths in order to reduce stray light in the spectrograph and a baffle to record background spectra. For all measurements presented here, the filter wheel was not used.

A mercury lamp is mounted on one motor, which can be positioned in front of the quartz fiber to determine spectral resolution and wavelength calibration several times during the measurements. The fifth motor carries the lamp reference system, which can be moved into the outgoing light beam. The reference system consists of an elliptical plane mirror, which reflects a part of the light of the outgoing light beam onto a quartz lens by which it is focused onto the quartz fiber.

All steppers are connected to the HMT-controller and steered by the measurement software MFC [Gomer *et al.*, 1993].

3.2.3.2 The DOAS White Multi-Reflection System

The multi-reflection cells originally designed by [White, 1942; White, 1976] have proven to be a powerful optical device for absorption spectroscopy, particularly for laboratory studies of photochemical air pollution in smog or environmental chambers (e.g. in CEAM, Valencia / Spain [Becker, 1996; Brockmann *et al.*, 1996]). Up to date, several technical improvements were performed [Geyer, 1997; Grassi and Guzzi, 2001; Ritz *et al.*, 1992; Trick, 2000; Volkamer, 1996; White, 1976], in order to use the White system for measurements in the outdoor atmosphere as well. As the light beam is folded several times on a very small (compared to LP-DOAS) base length of some few meters, both advantages can be used: the DOAS technique as well as the possibility of intercomparison to in-situ measurements.

A basic sketch of the White multi-reflection system used in this thesis is illustrated in figure 3.11. The basic idea is a 1 : 1 image of the lamp passing the White system and finally being spectrally analyzed. Numerical apertures of the light beam have to be adapted to each of the following optical elements using spherical mirrors in well-defined distances.

On a base-length of 15 m (refer to figure 3.11), three spherical concave mirrors of identical radius of curvature are installed: the front mirror A (main mirror, $\varnothing = 250$ mm) facing the two side by side back mirrors B and C (reflecting mirrors, $\varnothing = 150$ mm). The centers of curvature of B and C (c_B and c_C) are on the front surface of A and the center of curvature of A is halfway between B and C. When the back mirror B is lighted up by a source near the front mirror A, a square pattern of pairs of spots on 4 rows appears on the surface of A. The number of pairs on the front mirror is a function of the distance c_B c_C (see figure 3.10). Each spot is the image of the former spot alternatively by B or C. Thus the spot 1 is the image by B of the source, the spot 2 is the image by C of the spot 1, the spot 3 is the image of 2 by B and so on until the last image becomes located outside the front mirror on the exit hole (figure 3.10).

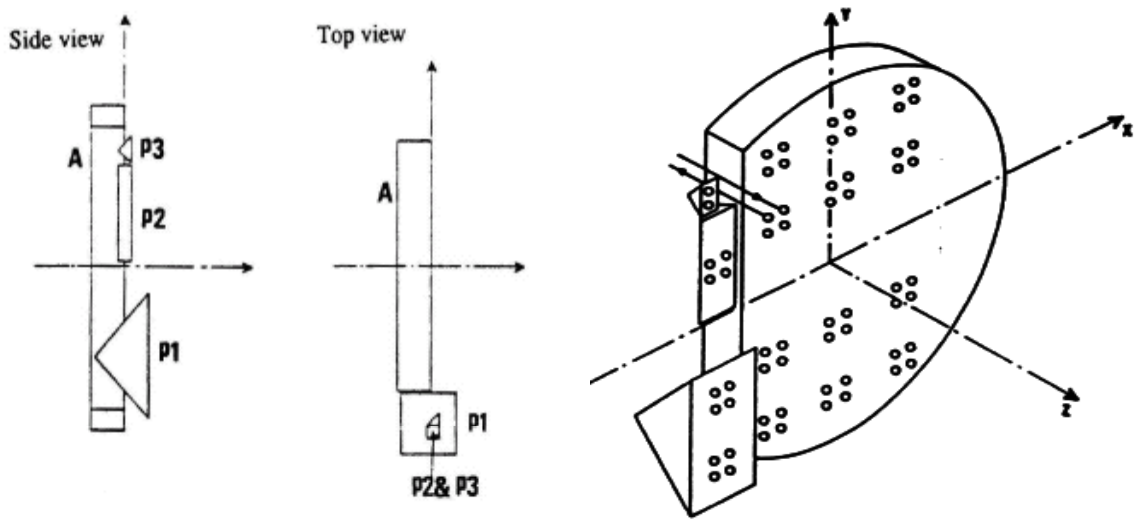


figure 3.9: Schematic diagrams of the prism P1, P2 and P3 assembly with the front mirror of the DOAS White multi-reflection system [Ritz et al., 1992].

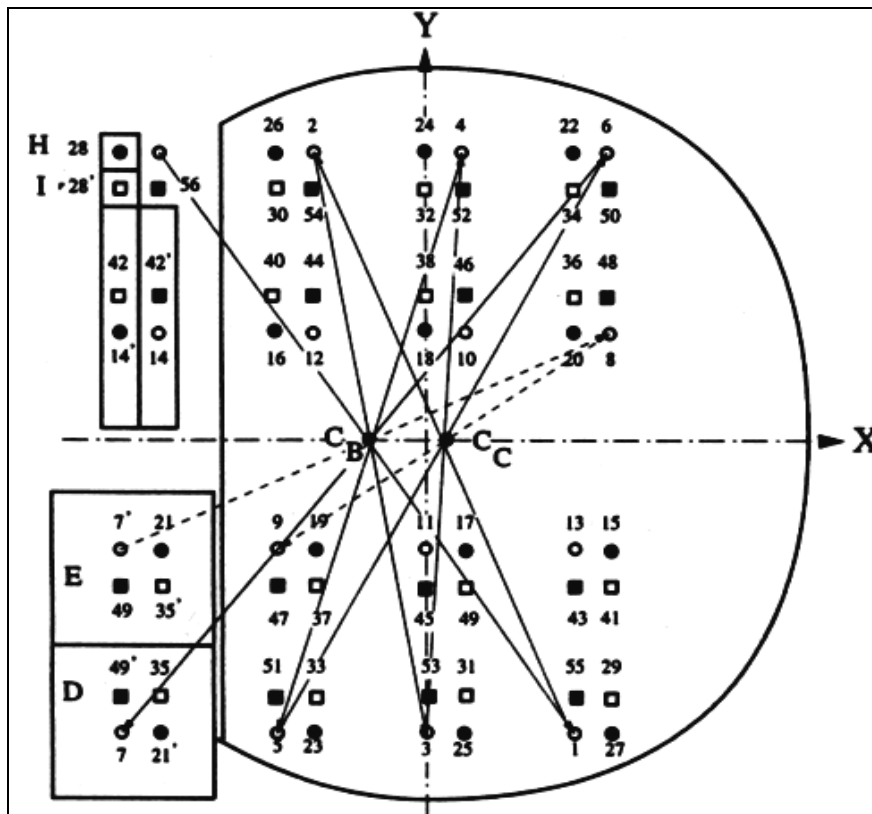


figure 3.10: Example of a pattern of spots on the front mirror of the DOAS White multi-reflection system. The round points are the foci before the reflection on prism 3 and the square points after it [Ritz et al., 1992].

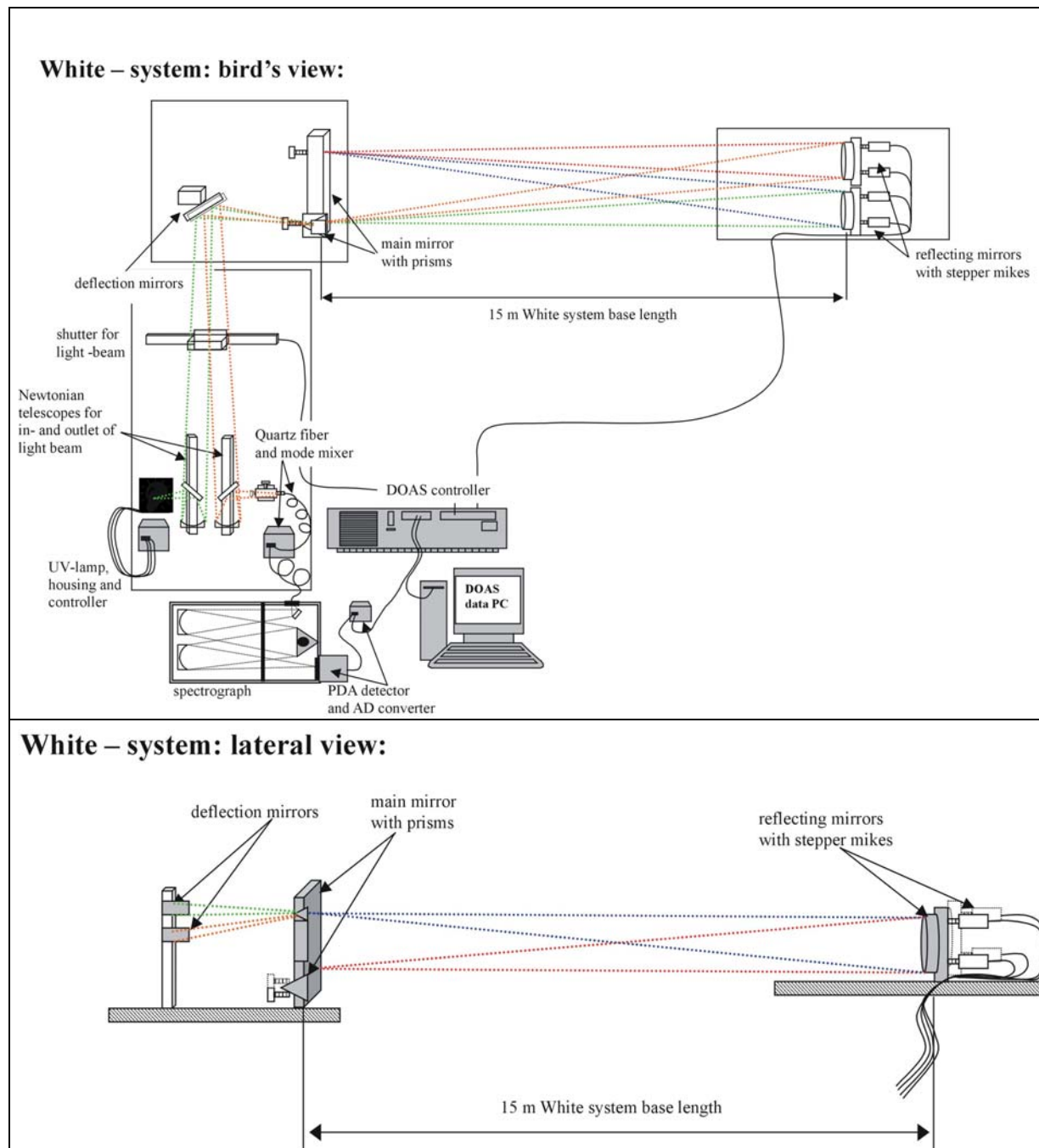


figure 3.11: Schematic view of the DOAS–White multi-reflection system used in this thesis. The upper sketch shows the main components of this system in a lateral view, while in the lower panel (a birds eye view) the measurement electronics and instruments for spectral analysis and data recording can be seen as well.

After a certain number of reflections on A (and by that number of traverses of the light beam in the White system) the three Quartz prisms set up near the front mirror (figure 3.9) are illuminated by the reflected light beam. The original design by [White, 1976] called for mirrors, but for certain reasons of stability of the light beam under atmospheric conditions, [Ritz *et al.*, 1992] attached prisms to the IUP DOAS White system.

The total number of traverses can be varied by moving the stepper-motors of the reflecting mirrors B, C between 16 and 144 for the IUP system, corresponding to light paths of 240 m to 2160 m, respectively.

The light of a Xe-arc lamp is coupled into the White system by a Newtonian type telescope which adapts the divergent light beam to the NA of the White system of $f/100$ and is focused to a pinhole next to the main mirror A (figure 3.11). Depending on the aspired total geometry, this beam is additionally turned by $\pm 90^\circ$ by a plane elliptical mirror (figure 3.11). Finally, the light is coupled out of the multi-reflection system by another Newtonian telescope and transmitted via a Quartz fiber to the spectrograph-detector unit (figure 3.11) which is adapted to its numerical aperture of $NA = 0.12$.

Motors with a filter wheel and a screen (figure 3.11), to optionally block the DOAS light beam for recording background spectra, are attached as well. All steppers and electronics are connected to the HMT-controller and steered by the measurement software MFC [Gomer *et al.*, 1993].

3.2.3.3 The Light Source

The artificial light sources used for all HONO measurements were Xenon high-pressure short arc lamps. A light arc of less than one mm diameter between anode and cathode is produced from a high voltage ignition discharge which plasmasizes the Xenon gas. The spectrum of a Xe arc lamp is the sum of the thermal emission according to Planck's law and single Xe emission lines, which are broadened by pressure and temperature. The distance of the electrodes is generally small, resulting in a short arc length (thus reducing the divergence of the parallel light beam emitted from the telescope). The pressure inside the lamp is very high (up to 100 bar under operating conditions) yielding a high local light intensity. The color temperature of the used Xe lamps of approx. 6000 K is similar to that of the sun. The bulb of a Xe lamp consists of quartz glass, which is extremely resistant to pressure and temperature. The electrode material is tungsten with endowments depending on the lamp type. The cathode has an edged peak to enhance the electron emission. In contrast to that, the anode is made out of massive material to absorb the kinetic energy of the incoming electrons.

Three lamp types are currently in use at the IUP as light sources for active DOAS systems: Osram XBO – 450W, Narva XBO 301 B, and PLI Hanovia HSAX5002. Only the last type, the PLI Hanovia HSAX5002 with an arc size of approx. 0.3×0.3 mm was used in this thesis. It was operated at 500 W (29 A, 17 V) with an approx. lifetime of 200 h. The variability of the emission features of the three different lamp types caused by flaring lamp plasma was studied by [Hermes, 1999]. Xe emission lines are found at several wavelengths including the red spectral region. The emission strength and pressure broadening of the Xe lines was found to change over time and therefore the lamp structures are difficult to remove from a spectrum. It was found that lamp structures are more easily removed from a spectrum in the case of the PLI Hanovia HSAX5002 lamp as its Xe emission bands are broader. Therefore, they can be filtered more easily by high pass filter routines.

3.2.3.4 The Spectrograph

Two different spectrographs were used in this thesis: an ACTON Spectra Pro 500 during the Rome 2001 field campaign, and the KIP 2003 smog chamber campaign and an ACTON Spectra Pro 300i during the IUP 2002 smog chamber campaign, the Milan 2002 field campaign, and the Turm 2003 field campaign. Both devices are based on a setup originally developed by Czerny and Turner in 1930 [Czerny and Turner, 1930]. The quartz fiber, which transmits the light from the telescope to the spectrograph, is positioned in the focal plane (entrance slit) of a convex mirror. The width of the entrance slit was adjusted to 200 μm . The light is paralleled by the spherical mirror and reflected to a plane diffraction grating. A second convex spherical mirror unit then focuses the dispersed light onto the detector.

The focal length of the ACTON Spectra Pro 500 spectrograph is 500 mm, its aperture is 1:6.9. The dispersion of the used 600 grooves / mm grating is 3.08 nm / mm corresponding to 0.077 nm / channel on the used photo diode array (compare to the following chapter). The center of the wavelength region of a spectrum can be changed automatically by a computer controlled stepper motor (tolerance 0.5 steps). In order to minimize thermal disadjustments the whole spectrograph unit is insulated and thermostated to 35 ± 0.2 °C by electrical heating.

For the ACTON Spectra Pro 300i, no entrance slit was used, as the fiber itself forms a pinhole of 200 μm diameters. Instead, the quartz fiber was mounted directly at the spectrograph entrance, in the focal plane of the first convex mirror. The focal length of the spectrograph is 300 mm, its aperture is 1:4 (i.e. NA = 0.12). The dispersion of the grating (1800 grooves / mm) used is 0.54 nm / mm corresponding to 0.038 nm / channel on the photo diode array (see following chapter).

3.2.3.5 The Detector

The detector unit is mounted in the focal plane of the spectrograph. The principal component of the unit is a Hamamatsu (type S3904-1024) photo diode array (PDA) consisting of 1024 Si photo diodes (CMOS) of 25 μm widths and a height of 2.5 mm. The PDA is placed in an evacuated housing filled with 1.2 bar Argon 5.0. A Peltier cascade is used to cool the PDA down to a temperature of -30 °C. The capacity of each diode is 10 pF, the full well depth corresponds to 1.286×10^8 photoelectrons. A detailed discussion of the usage of photo diode arrays as DOAS detectors is given by [Stutz, 1991; Stutz and Platt, 1992].

Every photo diode consists of an n-p semiconductor junction. During operation, an inverse voltage of 2.06 V is applied to the diode inducing a depletion layer, which is almost as large as the whole diode area. At the beginning of the measurement, the PDA is disconnected from the power supply. Subsequently, the incoming light excites a number of electrons proportional to the light intensity into the conducting layer of the semi conductor. These mobile charge carriers reduce the applied inverse voltage. However this is also possible by thermally activated transitions of electrons into the conducting layer. This effect is called dark current and must be considered in the evaluation procedure at low light intensities. In order to reduce dark current, the PDA was cooled down to temperatures between -15 and -25 °C by a Peltier cascade. The dark current decreases exponentially as described by the Stefan Boltzmann law. Dark current depends on temperature, integration time, and on the signal operation of the diode array [Stutz and Platt, 1996].

As soon as the intended integration time is over, the PDA is read out by reconnecting it to the power supply and measuring the current caused by the rechargement of the PDA. The resulting signal of a single scan is amplified electronically by the detection unit. To exclude negative signals under low light conditions (which would reduce the resolution of the digitized values by a factor of two), an offset signal is added to every PDA signal. The offset is proportional to the number of spectra and must be corrected during the evaluation process. The signals are digitized by a 16-bit analog - digital converter (ADC; full saturation corresponds to $2^{16} = 65536$ counts) and then transferred to the computer.

A thin protective silicon oxide layer on the diodes leads to a Fabry - Perot etalon structure in the spectra (cf. [Stutz and Platt, 1996]). This structure is caused by the interference of multi reflected light beams inside this surface layer. Due to the cooling of the detector unit, water vapor could freeze on the PDA and possibly cause an etalon structure. Therefore the detector is evacuated and filled with dry argon as inert gas.

Another effect of PDAs is the so-called memory effect, which means that structures of a former spectrum can be seen in the following spectra. This effect was discussed in detail in [Stutz, 1996; Stutz and Platt, 1996; Stutz and Platt, 1997], however its origin is unclear up to

date. Usually, the memory effect can be significantly reduced by multiple scans with no light on the detector, or just by waiting a short time.

To compute the spectral resolution and the dependence between diode number of the PDA and the wavelengths, emission spectra of an Hg high-pressure lamp are recorded. Fitting a polynomial (of first or second order) to the central wavelengths plotted against the corresponding diode numbers of the line centers yields the dispersion relation which might slightly change with time in shift and squeeze i.e. in the zero and first order constants due to thermal expansion and compression of the spectrograph-detector unit. The width of a single emission line yields the width of the instrument function and therefore the minimal spectral distance between two absorption / emission lines that can be positively distinguished from each other with the instrument. Now, the spectral resolution can be computed using the FWHM of such a line (in nm) as $\Delta\lambda$: the detector – in combination with the grating used – features the spectral resolution ($\Delta\lambda / \lambda$).

3.2.3.6 Characterization of the Detector Unit

For the different campaigns described in chapter 4, only two different detectors were used to determine the mixing ratios of the atmospheric trace gases: number 1 during the Rome 2001, and the KIP 2003 campaign; and number 2 for the second instrument during the Rome 2001, for the Milan 2002, the IUP 2002, and the Turm 2003 campaign. Both are of the same type and produced by Hoffmann Meßtechnik, Rauenberg / Germany. Nevertheless offset, dark current, and the residual noise differ slightly for the two detectors, but remain constant with the time of the campaigns. In the following, the characterization algorithm of the detector regarding the above parameters, including linearity and memory effect, are briefly summarized and the results are given in table 3.2.

	detector 1 (Rome, KIP)	detector 2 (Rome, Milan, IUP, Turm)
offset [counts / scan]	645.9 (628.3 – 663.4)	640.2 (584.2 – 696.1)
dark current [counts / s]	1.32 (0.69 – 1.94) at T = -25 °C	2.79 (1.25 – 4.33) at T = - 25 °C
electronic noise [counts / sqrt(scans)]	2.54	4.23
1 σ -residual noise [arbitrary units]	4.9 x 10 ⁻⁵	4.3·x 10 ⁻⁵

table 3.2: Characterization of the detector units used in this thesis.

The mean offset signal averaged over all 1024 diodes for a whole measurement campaign was measured routinely, at least once in the lifetime of a lamp (corresponding more or less to the time of a campaign). The offset was determined by adding up 10000 scans taken at the minimum integration time available (60 ms) and dark conditions. This spectrum contains the signals of 10000 offsets and a dark current of 600 s (as stated below, the ratio of both signals is larger than 1:10⁴, thus dark current can be neglected in this spectrum).

The dark current was determined by the scanning of one single spectrum with an integration time of 10000 s and dark conditions. Subsequently, the offset signal was corrected for. The resulting dark current spectrum contains only the signal generated by thermal transitions of electrons in the conducting layer. The dark current was found to slightly decrease with

increasing saturation of the PDA; however, this can be neglected in the evaluation procedure (as the resulting error is generally smaller than the errors of the fit.), but it was considered in the calculation of the error of the measurements. The dark current signal exponentially decreases with decreasing temperature of the PDA [Stutz and Platt, 1996]. All ambient measurements were performed at the temperatures given below. Several diodes were shown to possess a dark current signal peak, which probably can be attributed to endowment errors of the diodes, because these peaks do not change with time.

The residual noise of one spectrum consists of two noise signals: the electronic noise and the photon statistic noise. The electronic noise due to the resolution of the digitalization, the noise of the ADC, and of other electronic components, was determined by subtraction of two offset spectra (compare to above) from each other. The root mean square (RMS, corresponds to 1σ noise) of this spectrum was calculated. It is remarkable that the peak-to-peak residual structure was generally found to be 6 - 7 times higher than the RMS of the spectrum. In order to get the electronic noise of one scan, the RMS was divided by the square root of the total number of scans ($2\sqrt{N}$ with N being the number of scans added in one offset spectrum). Another source of noise in a spectrum is the photon noise, which is the square root of the number of photons according to Poisson statistical theory. Considering the well depth of the used diodes (1 count = 1962 photo electrons), the photon noises (1σ) of a spectrum with 10^4 and 10^6 counts are 2.3×10^{-4} and 2.3×10^{-5} , respectively. The photon noise must be added to the electronic noise in order to get the total residual noise.

The residual noise was determined by the division of two spectra (corrected for offset) of the same integration time scanned one directly after the other (the light source was a very stable halogen lamp, which was transmitted into the spectrograph by a optical lens system and the standard quartz fiber, including the mode mixer). In order to remove lamp structures from the resulting spectrum, a high pass filter (1000 times triangular smoothing) was applied. Then the residual structure (peak to peak, 6 - 7 times the RMS) was calculated for this spectrum. As expected from the above theory, the noise decreases with the square root of the number of counts.

Note that the residual noise increases when using a quartz fiber to transmit the light into the spectrograph (even if a mode mixer is included). This can possibly be attributed to the partial illumination of the PDA (200 μm quartz fiber diameter compared to 2.5 mm PDA height) [Stutz and Platt, 1996].

The linearity of the detector is characterized by the dependence of the obtained signal on the integration time. It is important that under constant external conditions a doubling of the integration time of the spectrum should yield a doubling of the signal (number of counts) detected by the PDA. For the PDA types used in this thesis, linearity is well tested (see e.g. [Alicke, 2000; Geyer, 2000; Kah, 1998]), the test yielding them to be linear within 0.3 % of the initial intensity.

Illuminating the PDA with light of high intensity generates a signal, which can be observed in the following spectra although the detector is darkened and the light is removed. This effect is called memory effect and was studied by [Stutz and Platt, 1996]. To remove this effect, an algorithm as described in [Geyer, 2000] was performed: waiting a few seconds after each measurement and recording some dummy spectra (spectra, recorded with shortest integration time) during this time.

A major problem, which occurs when using diode arrays as DOAS detectors, is the high variability of the diode sensitivity from diode to diode. The diode sensitivity depends on the wavelength of the incoming light and can vary up to some percent between the diodes of one

array [Stutz and Platt, 1996]. Since DOAS is intended to observe optical densities down to less than 10^{-3} , it is necessary to remove the diode sensitivity structure from atmospheric spectra.

Different corrections methods to correct these diode-fixed structures are used at the IUP: The simplest way is to use the shortcut system and record a Xe-lamp spectrum after each measurement and to divide the atmospheric spectrum by the associated lamp spectrum. However, it was found that this procedure causes increasing residuals of the fiber since the Xe emission structures are of the same spectral width as the fixed diode structures.

A more common method to eliminate diode sensitivity structures in LP-DOAS spectra is the Multi Channel Scanning Technique (MCST) introduced by [Knoll et al., 1990]. The basic idea of the MCST is the combination of a multi channel detection system (PDA), with the scanning technique generally used to cover a larger spectral region, with a single channel detection system. The procedure is as follows: every spectrum is separated in several (e.g. nine) single spectra with slightly different wavelength calibrations. These single spectra are recorded subsequently one after another. The spectral shift is performed automatically by the spectrograph system. After adding up all single spectra to a sum spectrum, the diode resident sensitivity structure remains at each channel, but the spectral information changes depending on the step width of the MCST. The sum spectra can be compared to the application of a low pass filter to the original spectrum as spectral structures are broadened by the shift. Therefore, the step width must be smaller than any spectral structure (absorption bands), otherwise these structures not only remain in the sum spectra, but would also be duplicated near themselves. Then every single spectrum is divided by the sum spectrum so that diode resident structures are removed from the single spectra. Now the single spectra are re-shifted to the correct wavelength calibration (usually by additional scans of a Hg lamp) and summed up. The MCST was used in this thesis for one DOAS instrument during the Rome 2001 campaign only.

The method of correcting the fixed diode structures mostly used in this thesis was to measure halogen lamp spectra as an additional reference spectrum several times during a campaign. As halogen lamps show a remarkably smooth spectrum lacking any narrow-band structures in the 300 to 400 nm region, all structures that remain after the high-pass filtering algorithm must be caused by variations of the diode sensitivity or by dirt or ice frozen on the PDA surface.

3.2.3.7 The Quartz Fiber Mode Mixer

A quartz fiber was used to transmit the light from the telescope into the spectrograph. During field campaigns the usage of fibers is necessary to ensure a stable illumination of the grating and the PDA. The quartz fiber used was a multi mode step-index fiber with a numerical aperture of 0.12. One problem of the usage of fibers for DOAS is the interference fringes of the light leaving the fiber produced by the total reflections inside the fiber. It was found by [Stutz and Platt, 1997] that the heterogeneous illumination of the grating and the PDA leads to a high residual noise (compare to above). Therefore a quartz fiber mode mixer according to [Stutz and Platt, 1997] was incorporated into the system. Nevertheless, residual noise is generally higher compared to laboratory tests of the PDA without quartz fibers.

3.2.4 Performing HONO Measurements by DOAS

3.2.4.1 The Measurement Algorithm for HONO

The measurement algorithm for the measurement of HONO in the troposphere included recording of spectra from the atmospheric light beam, background spectra, and lamp reference

spectra. All spectra were limited to the spectral range of 300 - 380 nm. The integration time of the measurement spectra was adjusted automatically to the incoming light intensity. Background and lamp reference spectra were generally taken after 10 - 100 measurement spectra. For the Rome 2001 campaign, all LP-DOAS instruments remained on a fixed light path in a single height. During the measurements of vertical trace gas profiles during the Turm 2003 campaign, the procedure described above was performed for the lowest height. Afterwards, the telescope was moved by some steps to miss the reflector and subsequent measurement of an atmospheric stray light spectrum. Then the telescope was moved to the next retroreflector-array at the next heights, the light path was initialized by optimizing the intensity, and atmospheric spectra were measured. After all heights were scanned in this way, a direct lamp spectrum as well as an Hg lamp spectrum was taken using the shortcut system. For measurements performed with the DOAS White system (the smog chamber campaigns and the Milan 2002 campaign), only the longest available light path was used for recording measurement spectra. However, the light path length was changed for recording reference spectra. During a single experiment of several hours only (as occurred during the smog chamber campaigns), manual control is valid. However, due to the aspired long-term and automatic measurement mode of the DOAS system during the Milan 2002 campaign, a new laser adjustment system (CamTrack) was developed [Kern *et al.*, 2002]. As mentioned above, the relative adjustment of the two reflection mirrors (B,C) to the main mirror (A) is essential (see also figure 3.11 and chapter 3.2.3.2). This gets even worse, when the light path length and thus the number of traverses of the light beam are switched (e.g. for taking reference or background spectra). By pointing a commercial laser-pointer at each of the reflecting mirrors (B,C), setting up screens (simple paper sheets on a Plexiglas pane) next to the field mirror on which the laser points can be seen, and monitoring the positions of the laser points, one gets the relative position of the adjustment mirrors (see figure 3.12). By using two commercial web-cams to look at the screens and the CamTrack software, the adjustments can be fully automated.

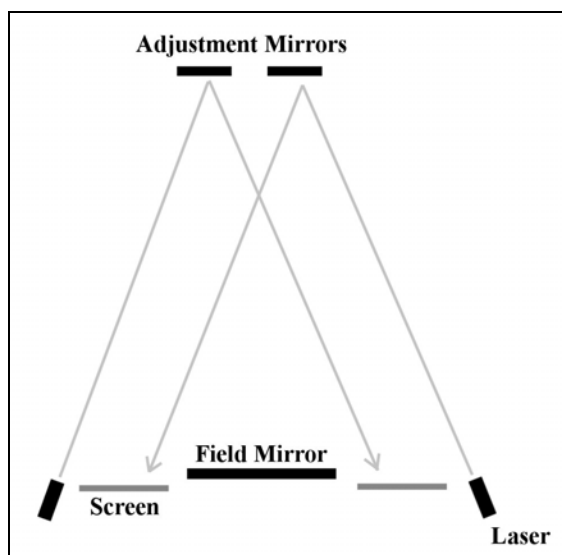


figure 3.12: Schematic arrangement of the laser adjustment system for a White system [Kern *et al.*, 2002].

CamTrack is a digital imaging program that tracks a bright point on a darker background with a very simple tracking algorithm [Kern *et al.*, 2002]: it calculates the center of light intensity. This is the light equivalent of the center of gravity. The algorithm takes each pixel, multiplies the x and y coordinates by its intensity. It sums over all the pixels, then divides by the total

intensity to get the x and y coordinates of the center of intensity. The actual value of the pixel center of highest intensity is compared to a manually set optimum for the corresponding light path number of the White system. In case of disagreement, CamTrack commands the stepper motors to move until the positions of the real and the aspired pixel agree. Two main operation modes can be used: holding a fixed position and moving to a defined position (e.g. for taking reference spectra).

3.2.4.2 Reference Spectra for the DOAS Evaluations

The spectral resolution $\Delta\lambda / \lambda$, and the wavelength-to-pixel mapping function Γ (dispersion relation function) were determined from emission spectra of an Hg high-pressure lamps. A linear correlation was observed by the fitting. The width of the single Hg emission line at 334 nm was used to determine the instrumental resolution (minimal spectral distance between two absorption / emission lines that can be positively distinguished from each other) as the FWHM (in nm) of that line.

An integral part of the spectra evaluation is represented by the trace gas references fitted to the measured spectra. In the wavelength range chosen for the spectral analysis of HONO in this thesis, several trace gases have strong absorption structures: HONO, NO₂, O₃, HCHO, and O₄ (see also table 3.3, and figure 3.6). Among these, the NO₂ structure is dominant, especially due to the high concentrations of this trace gas in heavily polluted urban areas. In table 3.3, an overview of the differential absorption cross-sections used for the DOAS evaluation is given. However, the literature reference spectra of NO₂, HCHO, and SO₂ were only used to scale the corresponding reference cell. Instead of literature references, these cells were fitted to the measured atmospheric spectra: they already include the exact instrumental function of the DOAS system, as well as all scattering effects influencing the atmospheric measurement spectra.

species	rel. error	resolution	reference
NO ₂	± 6 %	0.04 nm	[Schneider et al., 1987]
HONO	± 5 %	> 0.1 nm	[Stutz et al., 2000]
HCHO	± 5 %	0.025 nm	[Meller and Moortgat, 2000]
O ₃	n.a.	0.025 cm ⁻¹	[Bass and Paur, 1984]
O ₄	± 10 %	0.6 nm	[Greenblatt et al., 1990]
SO ₂	± 15 %	2 cm ⁻¹	[Vandaele et al., 1994]

table 3.3: Specifications and references for the trace gas absorption cross-sections used in this thesis.

The absorption cross-section of nitrous acid was showed in figure 3.6. Strong absorption bands can be found at 330.68, 341.68, 354.13, 368.15, and 383.8 nm, respectively. Thus, the range of spectral analysis for HONO was chosen to 300 – 390 nm in this thesis. Several laboratory studies on the cross-section of HONO have been carried out in the past (see e.g. [Alicke, 2000] for a recent review). The relative shapes of the spectrum are in good agreement but there are discrepancies concerning the absolute value. So far, no strong temperature dependence of the cross-section was reported in literature.

The evaluation procedures for data retrieved by LP-DOAS and those from a White multi-reflection system differ significantly. Thus we will now describe the algorithms to determine trace gas concentration of NO₂, HONO, O₃, and HCHO for all DOAS instruments used during the different campaigns. The evaluation was performed with the software MFC [Gomer et al.,

1993], which uses the spectra simulation and analysis model presented in chapters 3.2.2.2 and 3.2.2.3, respectively.

3.2.4.3 Evaluation of LP-DOAS Data

Two different LP-DOAS systems were used in this thesis: the scientific one for the measurements in the city center of Rome during the Rome 2001 campaign, and the semi-commercial in Montelibretti during this campaign as well as for the measurements of vertical profiles during the Turm 2003 campaign. Depending on the spectrograph-detector system used for both instruments, a total spectral range of 309 – 390 nm, and 313 – 376 nm, respectively were available. For analysis, the first few pixels (often afflicted with instrumental errors, see chapter 3.2.3.6) were neglected and the remaining wavelength interval divided into two ranges: 338 – 373 nm, and 313 – 331 nm (340 – 371 nm, and 316 – 333 nm respectively). This division into two wavelength ranges was performed to minimize possible interferences of similar absorption structures at certain wavelengths (e.g. by HONO and HCHO). It was not possible, however, to evaluate the concentrations of HCHO and O₃ with a cutting-edge detection limit. The absorption structures of both absorbers, but especially those of ozone, are too weak in the chosen spectral range to guarantee a satisfying signal-to-noise ratio. Thus in the first interval, spectra were evaluated for NO₂, HONO, O₃, and O₄ (which has some small absorption structures in the region), the second for NO₂, O₃, and HCHO. Generally, background (e.g. atmospheric stray light) and offset spectra were subtracted from the measured atmospheric spectrum first.

Then, these spectra were divided by a reference halogen-lamp spectrum. Using this method to correct for different diode sensitivities was explained in more detail in chapter 3.2.3.6. As halogen lamps have a remarkably smooth spectrum lacking any narrow-band structures in the 300 to 400 nm region, all structures that remain afterwards must be caused by variations of the diode sensitivity or by dirt or ice frozen on the PDA surface, and have additionally to be corrected for. In the spectra evaluation in this work, those peak-structures were either not observed, or only single peaks arose, which could be easily corrected by neglecting the concerning few number of pixels.

To remove further broadband structures, which are caused by scattering processes and broadband absorption, a high pass filter was applied. The spectra were filtered by a triangular smoothing algorithm for all 1024 channels simultaneously, 1000 times. Thus, only the narrow-band absorption structures of trace gases remain, and the logarithm was applied to those filtered spectra. Finally, the spectra were again smoothed by a triangular smoothing algorithm (5 times for the data obtained at the Rome 2001 campaign, but 20 times the spectra from the other measurements). By this additional smoothing, the noise signal is evened and peak residual structures in the spectrum are eliminated. This filter algorithm was applied to all spectra: the corrected atmospheric spectra, the lamp spectra, and all reference spectra.

Then a non-linear least squares fit procedure [Stutz, 1996; Stutz and Platt, 1996; Stutz and Platt, 1997] using the different reference spectra including a polynomial of 7th order were applied. Due to variations of the environmental conditions, linear shift and squeeze were admitted for the NO₂ reference. The HONO reference was linked to the shift and squeeze parameters obtained from that non-linear NO₂ fit to exclude arbitrary shifting and squeezing due to small absorption structures (see [Stutz and Platt, 1996]). For the HCHO and the O₃ reference, a squeeze was permitted. The concentrations of the respective species were calculated from the fitted optical densities of absorption bands in the reference spectra.

If sunlight is scattered in the light path of the LP-DOAS system and collected by the receiving telescope, Fraunhofer structures occur in the spectrum, especially in time periods with changing cloud cover (which cannot be corrected for by division of the atmospheric absorption spectrum by its associated stray light spectrum). To overcome this problem, a

Fraunhofer reference was generated and added to the trace gas reference set. This was performed by adding 10 – 100 stray light spectra measured in broad daylight with the telescope not pointing at the retroreflectors. Applying the high pass filter, logarithm and smoothing leaves only the narrow-band Fraunhofer structures. An additional reference was generated from the residual structures of a prior test evaluation run. This so-called X-absorber is discussed in more detail in chapter 3.2.2.5.

Finally, all the fitted reference spectra were subtracted from the measured spectrum to determine the residual spectrum representing the electronic noise of the instrument. Over the period of observation e.g. during the Rome 2001 campaign, the mean size of the residual structure was $1.5 \cdot 10^{-3}$ (peak to peak) for the LP-DOAS system in Montelibretti and $1.8 \cdot 10^{-3}$ (peak to peak) for the LP-DOAS system in the city center of Rome, and $\sim 10^{-4}$ as $1\text{-}\sigma$ error respectively.

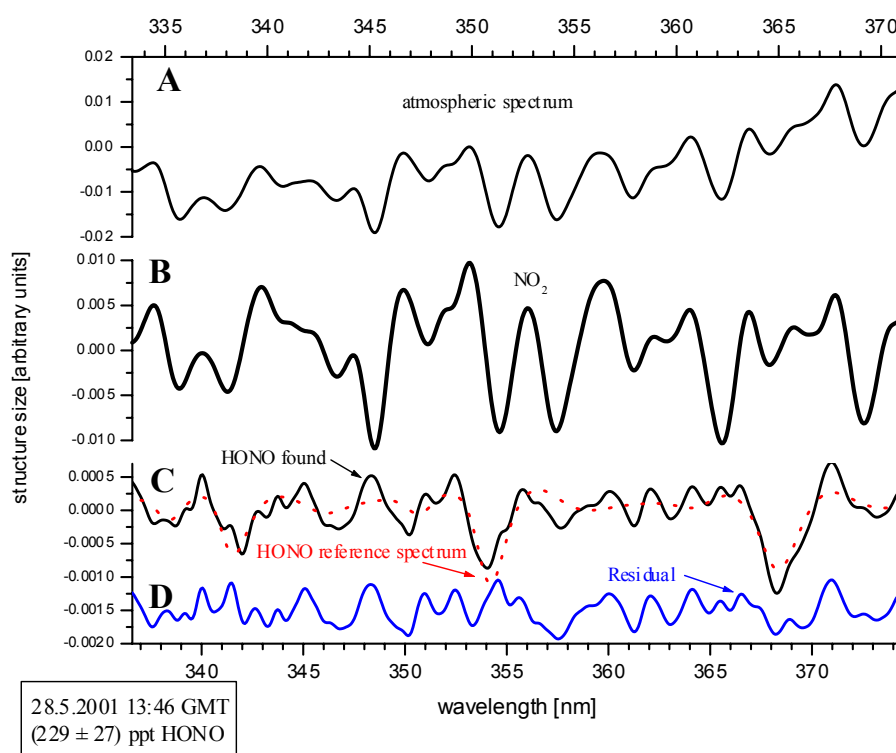


figure 3.13: Example spectra for HONO and NO₂ analysis with the LP-DOAS system in the city of Rome. In (1) line A shows the atmospheric spectra, B is an NO₂ reference spectrum, which is the main absorber. (2) The residual after fitting all trace gases (except of HONO) to the atmospheric spectrum clearly shows the absorption structure of nitrous acid (C, D is a HONO reference spectra. (3) The residual structure of $\approx 10^{-4}$ (1σ) after simultaneous fitting of all trace gases (E).

However, as already stated in chapter 3.2.2.4, this error of the least squares fitting procedure underestimates the true statistical error by a factor of approx. 3 (in some cases up to 6) [Stutz and Platt, 1996] (all errors in this paper refer to the 1σ error). The systematic error of the DOAS system was determined by [Stutz, 1996] as $< 3\%$ (including the errors of the offset ($\sim 0.1\%$), dark current ($\sim 0.15\%$), memory effect ($\sim 0.4\%$) and the error due to stray light in the spectrograph-detector unit ($\sim 2 - 3\%$), the latter being the dominant error source). The uncertainty of the cross-sections (see table 3.3) is $\pm 5\%$ for HONO [Stutz et al., 2000] and $\pm 6\%$ for NO₂ [Schneider et al., 1987]. The systematic error of the DOAS spectrometer was determined by [Stutz, 1996] as $< 3\%$. The total systematic error of the HONO concentration determination by DOAS is therefore $< 7\%$ (NO₂: $< 9\%$).

Further errors concerning the differential absorption cross-section are: inconsistent wavelength calibrations of the cross-sections for the different trace gasses, and in the case of the HONO evaluation, errors can also occur by using NO_2 cross-sections that are contaminated by HONO. Both, as well as the generation of artificial HONO generated by the fitting algorithm, are discussed in detail by [Veitel, 2002]. However, by the use of a NO_2 reference cell instead of the literature absorption cross-section, no evidence for these additional errors could be observed in the evaluation of DOAS data in this thesis.

An example of the HONO LP-DOAS evaluation from the measurements in the city center of Rome in 2001 is provided by figure 3.13. It shows the strong NO_2 absorption structures due to the high mixing ratio of nearly 70 ppb. The residual structure after removing all other trace gas absorption from the spectrum clearly indicates the spectral signature of daytime HONO with a mixing ratio of (229 ± 27) ppb.

3.2.4.4 Evaluation of White-DOAS Data

During the smog chamber campaigns (IUP 2002 and KIP 2003) and during the intercomparison campaign (Milan 2002), a DOAS White multi-reflection system was operated for the measurements of the trace gases. Generally, the filter algorithms and analogous fitting procedure as described in chapter 3.2.4.3 were applied: a combined linear/non-linear least squares algorithm [Stutz and Platt, 1996], fitting trace gas reference spectra and an emission spectrum of the lamp together with a polynomial of 7th order to the atmospheric spectrum.

However, the wavelength interval available for spectral analysis is here mainly determined by the range of high reflectivity of the White systems mirrors with its dielectrical coating (see figure 3.14).

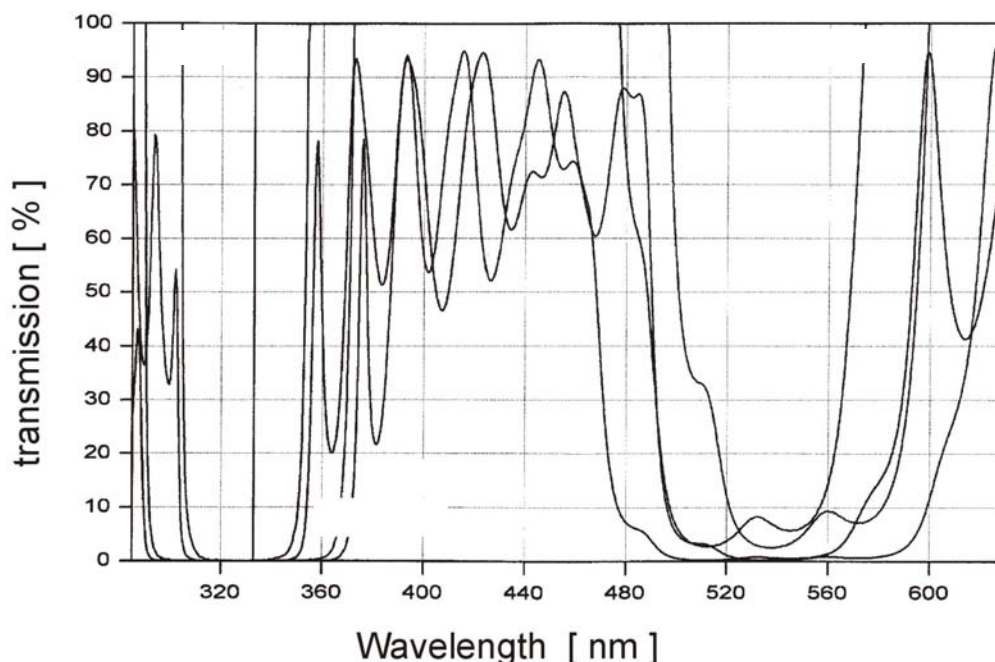


figure 3.14: Transmission (= 1 – Reflectivity) of the dielectric coated mirrors of the DOAS White system, which were optimized ($\lambda_{\text{central}} = 331$ nm) for HCHO measurements. Obviously, only a wavelength interval (“window”) of 311 – 351 nm features DOAS measurements.

Different mirrors were used for the smog chamber campaigns (central wavelength $\lambda_c = 357$ nm) and the Milan 2002 campaign (central wavelength $\lambda_c = 331$ nm), when the detection of atmospheric formaldehyde was the main aim of the measurements. The wavelength range was 333 – 373 nm for the IUP 2002 campaign with the smaller spectrograph (ACTON Spectra Pro 300i), as well as for the KIP 2003 campaign with the larger spectrograph (ACTON Spectra Pro 500), but 295 - 345 nm only for the Milan 2002 campaign.

Thus, the DOAS data obtained from the smog chamber campaigns was not analyzed for HCHO and O₃ as their absorption structures are too weak in this spectral range to guarantee a satisfying signal-to-noise ratio. For the analysis of the dark-chemistry of the NO_x reaction system in the smog chambers, only NO₂, HONO, and an X-absorber were fitted during the evaluation procedure.

During the Milan 2002 campaign, the White system was operated in the outdoor environment, and therefore, O₄ as well as a Fraunhofer scattering again have to be taken into account as references during the fitting process. Therefore, spectra of the scattered sunlight and the stray light from the light beams in the system were additionally recorded by blocking the lamp or one of the prisms, respectively. As the spectral window is more in the UV region, ozone and formaldehyde were analyzed as well. However, no separation of the wavelength interval was performed, due to the absence of the (to HCHO) interfering strong absorption band of HONO at 353 nm in the range of spectral analysis.

Another difference concerning White data was already presented in chapter 3.2.3.2: the short-cut system of the LP-DOAS is implemented by using different light path lengths (corresponding to different number of reflections on the front mirror A (see figure 3.10)). To correct the spectral characteristics of the lamp and the diode-to-diode sensitivity variations, the 144 reflections spectrum can be divided by the 16-path spectrum.

However, this correction was performed differently. During the smog chamber campaigns (see next chapter), an average of several spectra taken on the 144 reflections path during the background measurements at the beginning of each experiment (see next chapter) was used as a reference. Thus, all values are relative, referring to the spectra observed during this period.

During the Milan 2002 campaign, the CamTrack software (see chapter 3.2.4.1) caused various failures in the optical alignment and was therefore de-installed several times. During these periods, no 16-reflection path spectra are available. In these cases, an average of all these light path references was used for the corrections. Additionally, the NO₂ concentration present in this 240 m light path has to be corrected for.

So-called “White system stray light” adds to the errors mentioned above in chapter 3.2.4.3. This is mainly caused by light shortening its well-defined path. A quantification of this effect was performed earlier by [Geyer, 1997; Ritz *et al.*, 1992; Volkamer, 1996]. Using dielectrical-coated mirrors, it can be reduced to < 0.5 %. Finally, thermal de-adjustments of the White systems mirrors and pollutions of these mirrors by rain, dust and soil particles (reducing the transmission efficiency by some factors), also have to be taken into account [Geyer, 1997; Trick, 2000].

4 Field Studies and Results

It was shown in chapter 2.3 that several topics about nitrous acid are not well understood to date. They concern mainly about the exact nighttime formation mechanism of HONO, the (favorable) location of atmospheric production of HONO, as well as the occurrence of daytime values of HONO and their explanation.

For the identification and quantification of HONO daytime values, three field measurement campaigns in Rome, Italy in 2001 (see chapter 4.1), in Milan, Italy in 2002 (see chapter 4.2), and in Karlsruhe, Germany in 2003 (see chapter 4.3) were performed during this thesis. In these chapters, it will be explained, why these locations were chosen, and the experimental setups during these campaigns will be presented: our DOAS systems as well as additional equipment and that of further participating groups.

Before the result of all these different types of measurement campaigns will be analyzed by applying a chemistry and transport model in chapter 6, a brief overview of the obtained data and a qualitative discussion will be presented in this chapter as well.

4.1 The Rome 2001 field campaign: Detection of Daytime HONO

The first field campaign took place in the rural area of Rome, Italy, from 15.05. through 12.06.2001. This campaign was supported by the European Union (contract number EVK2-CT-1999-00025), project name: NITROCAT (NITRous acid and its influence on the Oxidation Capacity of the ATmosphere). Further information can also be found in the final report of this project: [Febo *et al.*, 2003; Wiesen, 2003].

The aim of this field campaign was the detection and quantification of HONO daytime levels. As HONO is linked to atmospheric pollution, three measurement stations were chosen (see figure 4.1): one on top of the CNR headquarter building in the city center of Rome as the photochemical input station, another in the Villa Ada park in the city of Rome as a background station and a third 30 km outside Rome in the Tiber Valley, the main down-wind direction [Febo *et al.*, 2003].

4.1.1 The Area of Rome

Rome (41°54' N, 12°30' E; 46 m a.s.l.) is the capital of Italy, in the region of Lazio, located in the mid of Italy's boot-shaped peninsula, directly at the western coast at the Tyrrhenian Sea (see figure 4.1), a part of the Mediterranean. Its population is 2.7 million inhabitants in the city, 3.8 millions in the region, with an area of 5,352 km². Despite its famous history, presently, Rome is known as a heavy polluted city, though not as polluted as the Milan area in the Po Valley, Italy or the Ruhrgebiet, Germany ([Baltrusch, 1979; Febo *et al.*, 1996; Febo *et al.*, 1987]). Anthropogenic sources of nitrogenous compounds (traffic and industry) are typical for European circumstances [Barnes, 1979; Febo *et al.*, 1996; Febo *et al.*, 1987].



figure 4.1: The city center of Rome and the three measurements sites: the background station in the Roman Villa Ada park (where the in-situ measurements were located), the DOAS light beam in the city center of Rome (CNR Rome), and the DOAS instrument and light beam located outside Rome in Montelibretti.

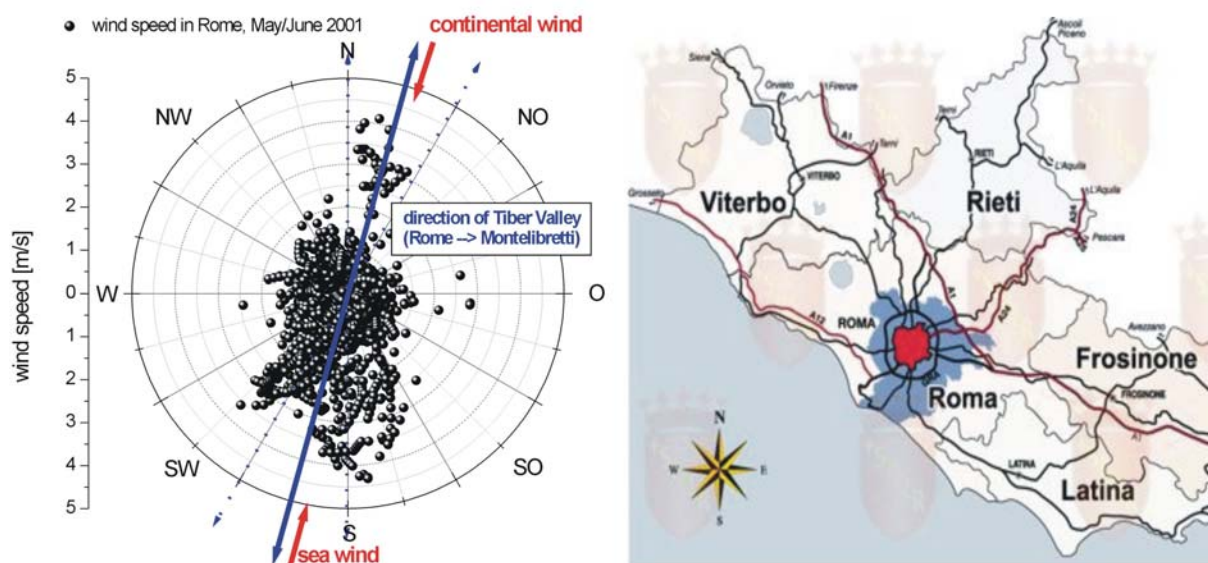


figure 4.2: Mean wind directions and wind speed at 2 m height as measured during the Rome 2001 campaign. As can be seen easily, the meteorology in Rome is mainly dominated by the so-called land-wind–sea-wind–system as described above.

The area of Rome was chosen since its meteorology is easier to model than most other places in Europe. As often found for cities in close proximity to the sea, a well working land-wind–sea-wind–system dominates the meteorology in Rome (see figure 4.2). The principle of this small-scaled circulation (too small to be influence by the Coriolis force) is a thermal stimulation in an area of baroclinic layering: During the day and under conditions of high solar radiation, the land-surface is warmer than the sea-surface. Thus, a wind from the sea pointing inland is observed from early noon until afternoon close to the ground (typically in a height of 1 - 2 km), which is often accompanied by a strong formation of clouds over land with clear-sky conditions over the sea. During the night, the sea is warmer than the land and the circumstances invert: wind blows from the land out to sea. During the early morning hours, a calm is often observed [Roedel, 1994].

4.1.2 Measurements in the City Center of Rome

At the photochemical input station, directly in the city center of Rome, one active long path DOAS telescope was sited on top (13th floor) of the headquarter of the CNR-IIA building (Consiglio Nazionale delle Ricerche, Istituto sull’Inquinamento Atmosferico) on Via Tiburtina, Rome yielding an average altitude of the beam of approx. 50 m above street level [Febo et al., 2003].

4.1.2.1 Instrumental Setup of the LP-DOAS

As illustrated in figure 4.1, one fixed light path of 3690 m (one-way) was realized, pointing from the DOAS telescope to northeastern direction towards Portonaccio. The light beam was then reflected by an array of 69 retroreflectors (Quartz triple prisms). No industrial plants are located near to the light path. The beam did, though, cross several streets and an arterial traffic road (Tangenziale Est), which was closed for traffic during night (10:00–4:00). The vicinity east of this road can be characterized as sub-urban residential area with larger areas of grassland and trees. The area west of the Tangenziale Est belongs to the city center of Rome and both traffic and population densities are high. By the height of the instrument and the area crossed by the light beam, turbulences and transport effects in the building-canyons could unfortunately not be excluded and might play an important role as discussed in the next chapter.

The long path DOAS systems used at this measurement station is a modern version of the original setup developed by [Platt, 1994; Platt et al., 1979], built at the Institut für Umweltphysik, Heidelberg, Germany. The optical path and details on the instruments used are already described in chapter 3.2., so we will only discuss here the specifications for the setup during this particular campaign.

The system used a 500 W Xe high-pressure arc lamp (PLI Hanovia HSAX5002, SN 100307) as light source. The main mirror is a parabolic mirror of 30 cm diameter and a focal length of 150 cm. A standard quartz fiber with a diameter of 200 μm (AS UV..VIS 200/220/245 μm , NA = 0.12) was used to transmit the incoming light, after its reflection at the retro reflectors, from the telescope into the spectrograph. Spectral separation was performed by a Czerny-Turner spectrograph (ACTON Spectra Pro 500) with a focal length of 500 mm and a plane diffraction grating ($f / 6.9$, entrance slit: 200 μm). A grating 600 grooves / nm was used, yielding a measurement’s wavelength interval of 300 to 380 nm, dispersion: 3.08 nm / mm (or 0.077 nm / pixel), spectral resolution: 0.54 nm. The spectrograph was held at a temperature of $(+33 \pm 0.3) ^\circ\text{C}$. Coupled to the spectrograph, a 1024 pixel photodiode array detector (Hoffmann Meßtechnik, photodiode array: Hamamatsu S3904-1024N), of 25 μm center to center spacing and a height of 2.5 mm was mounted in the focal plane of the spectrograph.

The array was cooled by a Peltier element to $(-13 \pm 0.3) ^\circ\text{C}$ to reduce the dark current. Finally, spectra were recorded by a PC using the software MFC [Gomer *et al.*, 1993], which was also used to analyze the spectra.

The measurement algorithm for the different trace gases (NO_2 , HONO, O_3 and HCHO) was recording spectra from the atmospheric light beam on one fixed light path, but also included, background spectra, and lamp reference spectra. The integration time of the measurement spectra was adjusted automatically to the incoming light intensity. Background and lamp reference spectra were generally taken from about 10 measurement spectra. Typically, one HONO measurement was finished every 5 min.

In addition to these measurements in the city center of Rome, the Multi-Channel-Scanning Technique (MCST) [Brauers *et al.*, 1995; Knoll *et al.*, 1990; Stutz and Platt, 1992; Stutz and Platt, 1996] was employed to correct the diode-to-diode variation in the detector sensitivity. As well, spectra measuring scattered solar light and mercury wavelength standards were recorded frequently.

4.1.2.2 Trace Gas Measurements in the City Center of Rome

Data were recorded continuously from 16.05.2001 through 10.06.2001 (except 19.05.2001 only, when reference spectra and the instrumental calibration (see chapter 3.2) were performed). In figure 4.3, an overview of the time series of the trace gases (NO_2 , HONO, O_3 , HCHO) measured by DOAS at the measurement station in the city center of Rome are shown. A strong diurnal variation could be observed for all sunny clear-sky days. The general features of NO_2 show peaks during the early morning and evening hours (as a consequence of the NO peaks). During night NO_2 levels over Rome range between 40 – 60 ppb indicating large sources and a shallow boundary layer during the night. At noon NO_2 is minimal (~ 10 ppb over Rome). During the rainy period around 23.05.2001 and the low emission period during Pentecost (02.–04.06.2001), values remain below 10 ppb even during the night. Between these two events, the maximum values as well as the daytime values increase until the photochemical smog event on 31.05.2001.

Formaldehyde mixing ratios were generally found between 1 ppb during night increasing up to 7 ppb. Similar to NO (see chapter 4.1.3.3), it reached maximum values in the early morning and during evening. These peaks point to a strong contribution of direct emission of HCHO in Rome. The ratio between the peaks of HCHO measured on 29.05. – 30.05.2001 was about 2 (corrected for the HCHO background level of ~ 2.5 ppb). However, the higher ratio for HCHO compared to NO points out the contribution of photochemistry to HCHO formation indicating the high primary VOC reactivity. This can be seen from e.g. 31.05.2001, the day of the strong photochemical smog event.

In the city center of Rome, in the vicinity of the main NO_x emissions, ozone mixing ratios show the expected behavior in the presence of strong sources [Leighton, 1961]. Ozone is only present during the day when it is formed photolytically. During the night, with the high levels of NO, all the ozone reacts to form NO_2 (see figure 4.3)



Due to the lack of ozone formation mechanisms at night and its short lifetime due to reaction r. 2.9 with NO, (for 250 ppb NO the O_3 lifetime is approx. 9 sec) the nighttime ozone levels were very low, often below the detection limit of a few ppb (see table 4.1). The lack of ozone during the night implies that the radical levels at night are also very low since NO_3 is not formed and the production of OH by ozone and alkene reactions is insignificant. During the day, maximum ozone mixing ratios of up to 70 ppb were observed. During the period of Pentecost, low traffic was observed and thus low NO_x emissions. Thus the main sink of

ozone, the titration by NO, is missing and O₃ values remain at some 40 ppb even during the night.

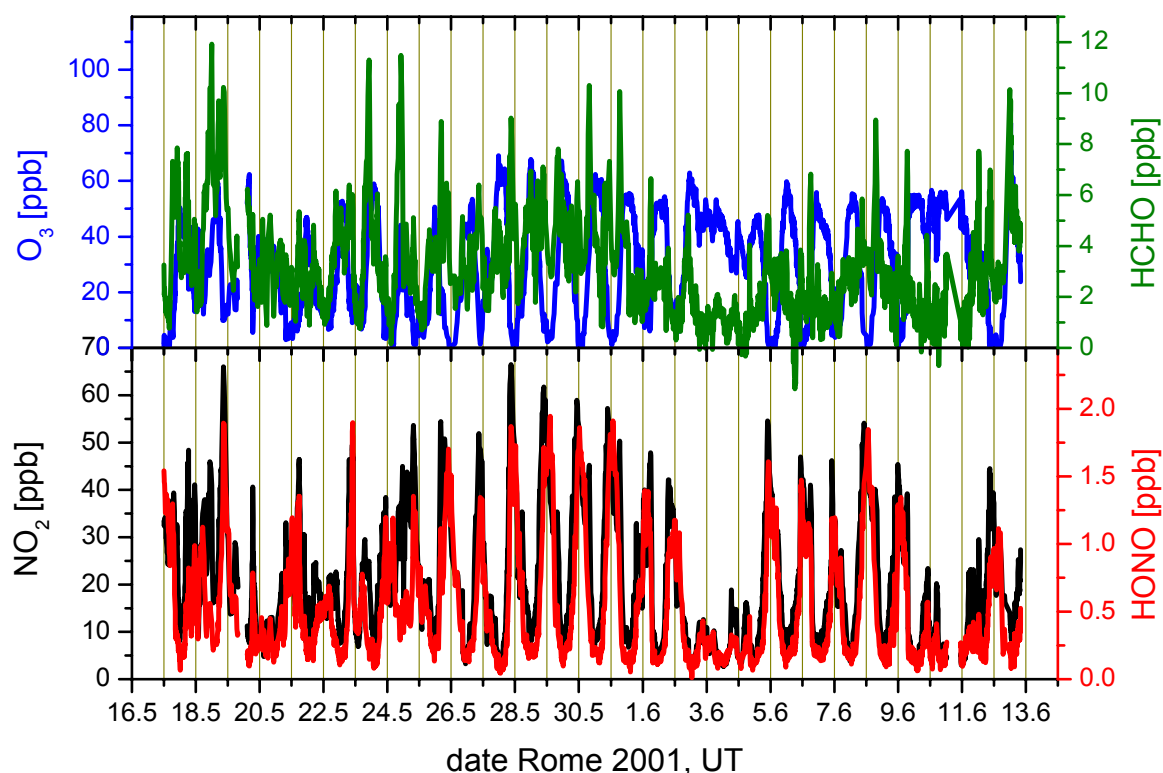


figure 4.3: DOAS data recorded during the whole Rome 2001 campaign by the instrument in the city center of Rome. In the lower graph NO₂ (black line, left scale) and HONO (red line, right scale) are plotted. In the upper, O₃ (blue line, left scale) and HCHO (green line, right scale) can be seen. The errors of the measurements (refer to table 4.1) were omitted for a clearer illustration.

species	instrument	location	average detection limit (ppb)	systematic error
HONO	DOAS	over NE part of city	0.078	±6%
		Montelibretti	0.089	±6%
	WEDD	Villa Ada	0.002	±5%
NO ₂	DOAS	Villa Ada	0.002	±4%
		over NE part of city	0.2	±9%
	chemiluminescence with converter	Montelibretti	0.2	±9%
O ₃	DOAS	Villa Ada	0.05	±5%
		over NE part of city	3.9	±5%
		Montelibretti	3.7	±5%
NO	chemiluminescence	Villa Ada	0.05	±5%
HCHO	DOAS	over NE part of city	0.8	±7%
		Montelibretti	0.5	±7%

table 4.1: Detection limits and systematic errors of traces gases measured at Rome.

Mixing ratios of nitrous acid are more or less linked to the NO_2 trend and show a typical strong diurnal cycle. HONO values over Rome increase during the night with increasing atmospheric stabilization and increasing NO_2 levels and reached 2 ppb in the middle of the night (e.g. on 30.05.2001). Two sources of HONO are present in Rome, direct emission and heterogeneous formation in the presence of NO_2 . After sunrise (approx. 3:30 UT), after the initial onset of photolytic reactions, and a destabilization of the nighttime boundary layer, the HONO levels decreased over three hours (as suspected by basic knowledge and explained in chapter 2.3.2) and stabilized at ~ 200 ppt during the day. Except during weekends, when pollution levels were low, daytime HONO levels did always exceed this 100 - 200 ppt.

For most time of the Rome field campaign in 2001, HONO daytime levels were measured clearly above the detection limit in the city (see figure 3.13). For an average day (see next chapter) unexpected high daytime values of 190 ppt HONO (up to 600 ppt during rainy and cloudy days around 23.05.2001) were observed.

On May, 31, a day of particular high photochemical smog, it could be shown that HONO is the key species initializing further photochemical processes in the urban atmosphere at sunrise. While photochemical smog in Rome forms early in the morning, ozone is around zero at this time. However, HONO, which is accumulated during the night, is still high, when its photolysis starts at 5:00. This provides an initializing push of OH-radicals. A more detailed quantitative description and model test will be shown in chapter 6.

4.1.2.3 Radiance Data

In the city center of Rome, a spectroradiometer was operated to measure the actinic flux (actinic flux spectroradiometer, Bentham, typ DTM300), from which photolysis frequencies were calculated. This commercial instrument consists of a spectrograph with a double monochromator with 2400 g / mm gratings. It was characterized in detail by [Friedeburg, 2003]. During the Rome 2001 campaign, the temperature of the photo multiplier was set to -10°C , the high voltage to 7.45 kV and the fiber bundle with the 2-Pi-head was sited on the roof of the CNR headquarter.

Measurements were performed in the range of 280 to 425 nm, suitable for $J(\text{NO}_2)$, $J(\text{HONO})$, $J(\text{O}^1\text{D})$, and $J(\text{HCHO})$. The step-width was set to 1 nm yielding a temporal resolution of approx. 5 min. Moved by a filter wheel in the DM, only one type of a filter was used additionally during the measurement by the spectral radiometer: an UG 5 UV pass filter (to keep out VIS when looking at UV) was introduced at 260 nm and removed at 420 nm. (The filter wheel also contains a black disk for dark current recording after each solar spectrum).

The figure 4.4 shows the recorded photolysis frequencies [s^{-1}] for NO_2 , and HONO. The frequencies for $J(\text{O}^1\text{D})$ and the radical part of the $J(\text{HCHO})$ were multiplied by a factor of 100 for this illustration. On the right hand side of this plot, the corresponding lifetime of the trace gases are plotted (see figure 4.4).

Generally, sun irradiation was high. Of course, the photolysis frequencies are zero (within the errors of the instrumental offset) during the night, increasing during daytime with solar radiation and depending on the cloud coverage. Thus lower values are observed on the rainy days (23.05.2001), than on sunny days (31.05.2001). Photolysis frequencies for NO_2 , HONO, O^1D and HCHO peaked at noon on 30.05.2001 at $1 \times 10^{-2} \text{ s}^{-1}$, $2 \times 10^{-3} \text{ s}^{-1}$, $7 \times 10^{-5} \text{ s}^{-1}$, and $1 \times 10^{-4} \text{ s}^{-1}$, respectively.

The photolysis frequency of NO_2 was additionally measured by 4- π -steradian filter-radiometer (Meteorology Consult, 4 π -sr- $J(\text{NO}_2)$ Radiometer Nr. 631 / 632). It is a plug-in-only instrument, described in more detail elsewhere [Hofzumahaus *et al.*, 1999; Muller *et al.*, 1995]. Results agree well with those measured by the spectral radiometer. Additional information on solar radiance can be obtained since this instrument has an upward and down looking sensor. Thus backscattering and albedo effects can be taken into account.

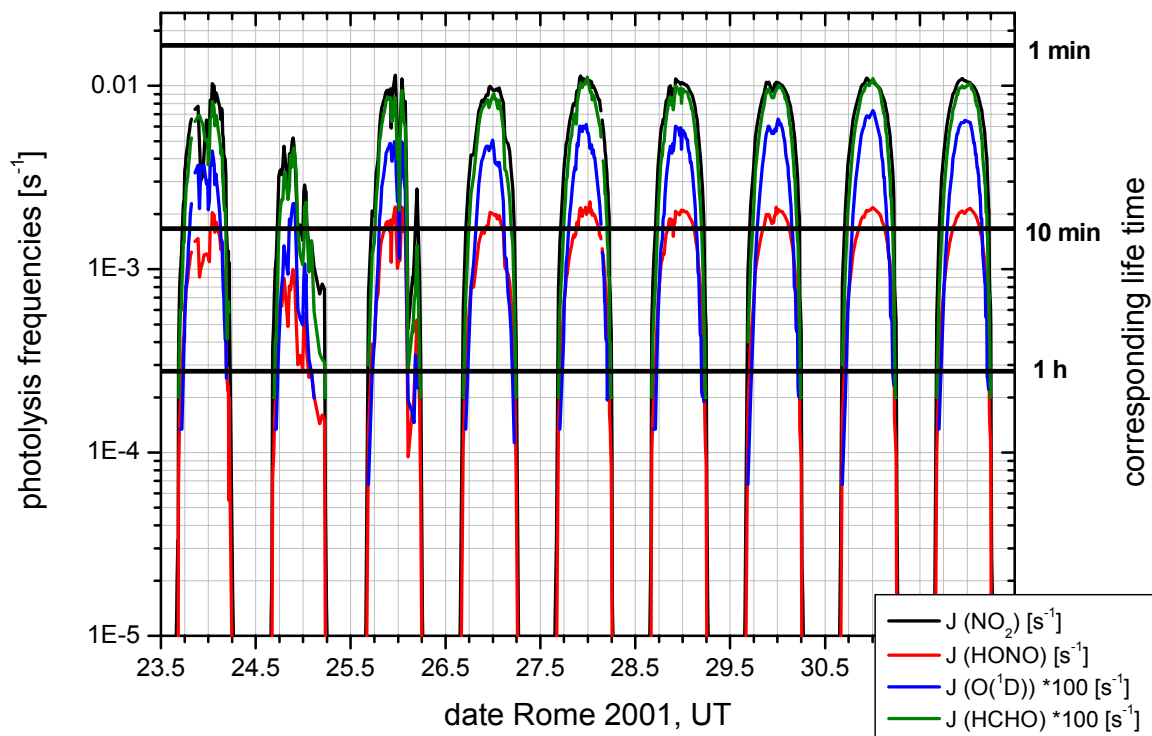


figure 4.4: *Photolysis frequencies as measured during the Rome 2001 campaign. The values for $J(O(^1D))$ and $J(HCHO)$ are multiplied by a factor of 100 for a better illustration.*

4.1.2.4 Aerosol Particles

A commercial optical particle counter (OPC, Pallas, PCS 2000) was operated at the CNR headquarters in Rome. The air-flow rate through the measurement volume ($220 \mu\text{m} \times 220 \mu\text{m} \times 203 \mu\text{m}$) was set to $V = 5 \text{ l / min}$ ($\sim 83.3 \text{ cm}^3 \text{ s}^{-1}$), yielding a particle velocity of $v = 8.9 \text{ m / s}$ at a tube diameter of 3.45 mm . The measurement interval and therefore the time resolution was 5 min . Particle size range measurements between 154 nm and $10 \mu\text{m}$ diameters, in 10 size classes, were recorded. The inlet tube (2 m length) was sited near the DOAS telescope on top of the CNR-IIA building. For an intercomparison to other aerosol measurement instruments refer to [Alicke, 2000].

Results of these measurements for the time of the Rome 2001 campaign are shown in figure 4.5. The values are standardized to the time of measurement, the airflow and the particle velocity. Generally, the sum of particles in the range of $0.2\text{--}10 \mu\text{m} / \text{cm}^3$ shows a more or less distinct diurnal cycle: low values in the morning (after the sea-wind has cleaned out the air inside the city of Rome), increasing by some hundred with pollution during daytime until the late afternoon, and dropping again when the wind changes its direction (due to the land-wind–sea-wind–system). In more detail, a trend can be observed, as values decrease from 450 on the 17.05.2001 (sunny weather conditions at the beginning of the campaign) to below 100 on the 23.05.2001, during a rainy and cloudy period. At the end of May, values increase again to values of 500. This time was shown to be a period of high photochemical activity with a photochemical smog event on 31.05.2001. After this event, the sum of particles drops again below 100 on the weekend of Pentecost, when no traffic and thus no pollution occurred. When the workdays start again, the particle sum also increases again to ~ 300 . While the particle sum increases and decreases with these different periods of weather conditions and emission rates, no diurnal variation can be observed for the particle surface area. The particles surface (determined as spherical-symmetrical with the mean diameter for each size-class as

radius) remains more or less constant at values of approx. $100 \mu\text{m}^2 / \text{cm}^3$ over the whole time of the period of the campaign. This indicates small sized particles being the main component of the aerosols in Rome, as can also be seen from figure 4.6 of the particle distribution in the 10 size classes.

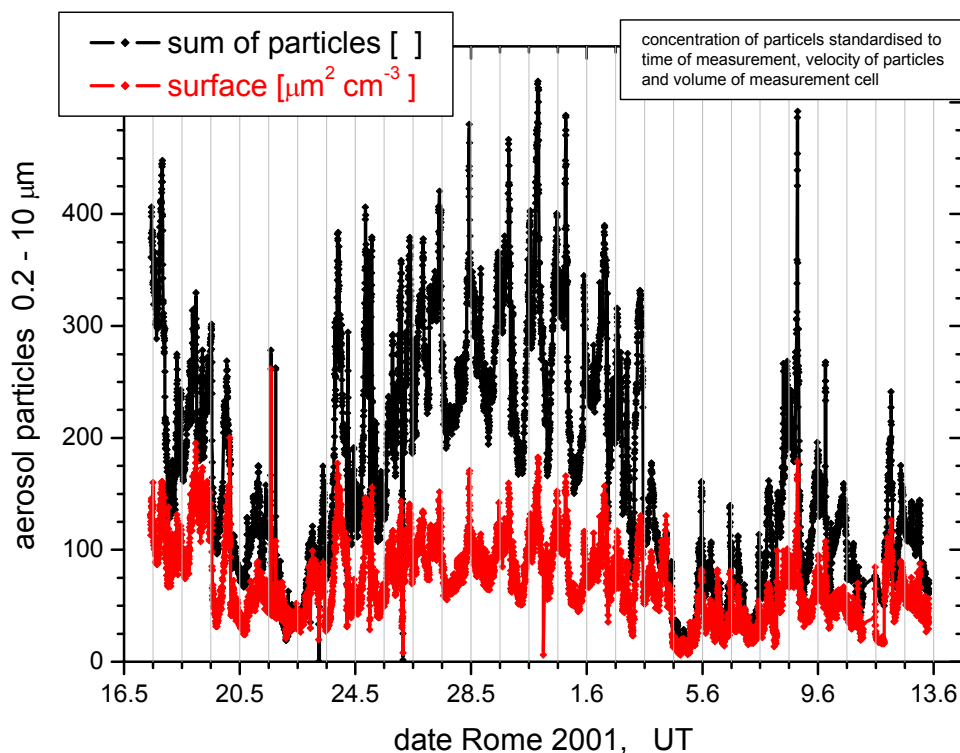


figure 4.5: *Sum of particles and their surface as measured during the Rome 2001 campaign. The surface was calculated as a spherical one.*

An intercomparison campaign of different aerosol measurement techniques and instruments involving our optical particle counter system by Pallas as well was performed by [Alicke, 2000] during the LOOP / PIPAPO field campaign in Bresso, Milan, Italy (see chapter 4.2) in May and June 1998. It suggests multiplying the aerosol volume data obtained from our Pallas instrument by factor of 4.5 and those for the surface size area by a factor of 11. The Pallas system seemed to underestimate the true aerosol surface information due to the fact that only a small fraction of the total amount of particles size clusters was even measured [Alicke, 2000]. The reason for the discrepancies between this and other aerosol measurement instruments is still not known, but might either be due to a loss in the sampling line, or a simple malfunction in the Pallas system, which was originally designed for laboratory measurements only [Alicke, 2000].

For HONO formation assumed to proceed heterogeneously on the aerosols, the surface area size of these particles should be relevant. While an increase in the HONO mixing ratios in the atmosphere was observed during the campaign, the aerosol surface remains constant. This indicates aerosols being of minor importance for the atmospheric formation of HONO compared to the ground surface. Thus we will neglect the aerosols in the following discussion of HONO values and formation. These considerations will also be confirmed by the model results (see chapter 6) using the Rome 2001 trace gas data.

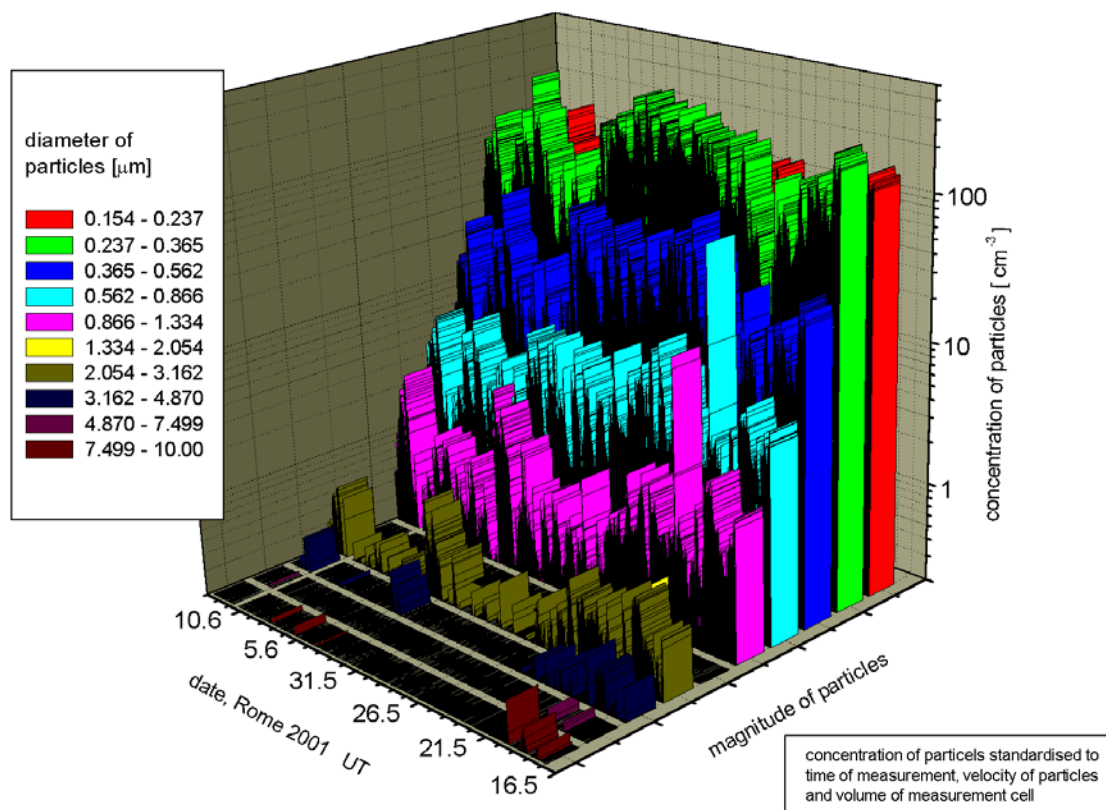


figure 4.6: Distribution of particles as measured during the Rome 2001 campaign. The magnitude of particles is separated into 10 classes.

4.1.3 The Villa Ada Background Measurement Station

The Villa Ada area, a large park, is located at the northern end of the city center of Rome (figure 4.1). The park is situated west of Via Salaria, which had high traffic density throughout the day. In the center of this park, a measurement station of the Consiglio Nazionale delle Ricerche, Istituto sull'Inquinamento Atmosferico Roma, Italy (CNR) took continuous measurements. During the Rome 2001 campaign this site was defined as a background urban station sited inside the urban area of Rome, where the groups of the CNR and the Brandenburgische Technische Universität Cottbus, Germany (BTU) were measuring. All samples were taken at 3 m altitude above grass [Febo *et al.*, 2003].

4.1.3.1 The HONO Measurements at Villa Ada

A dual channel DNPH derivatization / High Performance Liquid Chromatography technique (DNPH-HPLC) instrument was run by the CNR at the Villa Ada station to determine the HONO concentrations. The precision of the DNPH-HPLC instrument for HONO determination can be checked by comparing the signals coming from the two independent inlet lines. The overall precision during the field campaign was estimated to be around 4 % (see chapter 3.1.1.3 and [Febo *et al.*, 2003]).

During the first two weeks of the Rome 2001 campaign, the group from the BTU was also measuring HONO at Villa Ada station by a wet effluent diffusion denuder (WEDD) described in detail by [Acker *et al.*, 2001b]. The wet denuder system was extended by a jet steam to detect the nitrite and nitrate (and sulfate and chloride) concentrations in the atmospheric

aerosol phase also with a high time resolution. Via a low and a high pressure 8–port valve the solutions containing the scavenged acids and aerosol compounds are alternatively collected in flow through cells and pumped through pre-concentration columns before ion chromatographic detection. The airflow through the denuder / jet steam is 10 l / min using a 30 min sampling time. Concentrations of $0.010 \mu\text{g m}^{-3}$ of $\text{HNO}_2 / \text{NO}_2^-$ and $\text{HNO}_3 / \text{NO}_3^-$ can be reliably measured. This equipment was used to determine the distribution of reactive components between gas phase (nitrous and nitric acid) and particle phase (nitrite, nitrate) at the measurement site Villa Ada [Acker *et al.*, 2001b].

4.1.3.2 Intercomparison of HONO Measurement Techniques

The comparison of HONO data obtained by BTU and CNR groups at the Villa Ada station is reported in figure 4.7. Analysis shows that the temporal structures of the two data sets are in good agreement [Febo *et al.*, 2003]. The correlation analysis of 30-minute data in figure 4.7, can be judged to be very satisfactory.

From a quantitative point of view, a difference of about 20 % between the two data sets can be observed and the value of the intercept of about 45 ppt, is satisfactory. The comparison between the data yielded by different groups has been also carried out for O_x measurements (sum of ozone and nitrogen dioxide) and for NO_x . The results of the comparison, over 10–minute average measurements, show good agreement and a high quality level of the two data sets as reported in detail by [Febo *et al.*, 2003].

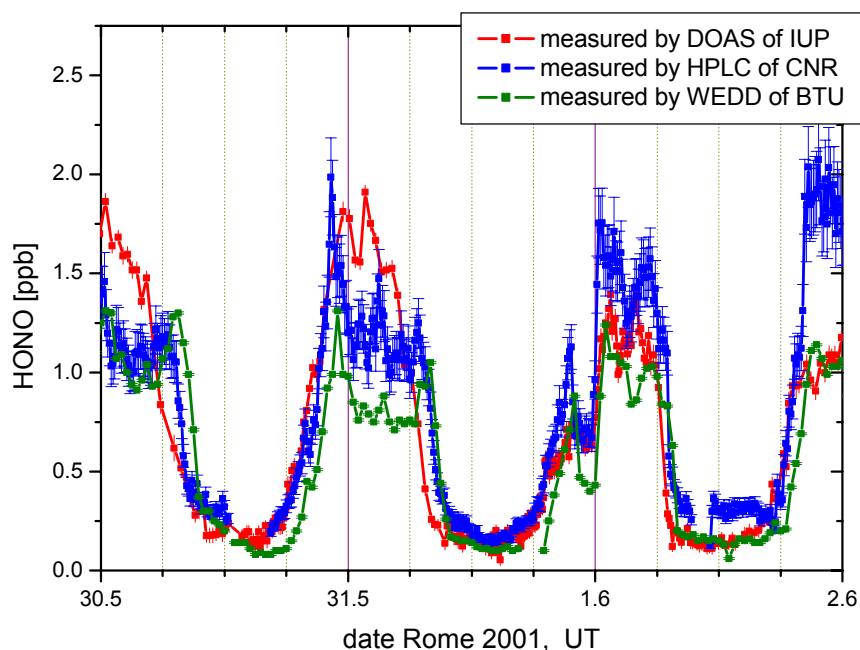


figure 4.7: Comparison of the results of HONO measurements carried out at the CNR building by DOAS (operated by IUP) and at the Villa Ada station (DNPH-HPLC by CNR and WEDD by BTU).

As far as HONO measurements carried out at different locations are concerned, a comparison between the results of the 30 - minute determinations obtained at the CNR building by DOAS measurements and at Villa Ada by WEDD and DNPH-HPLC shows that the agreement between the temporal trends is good, as well as the order of magnitude of the maximum values, in spite of the different location of the measurement points (figure 4.7).

By the reasons of good agreement between the CNR and BTU data as discussed above, we will use a arithmetic mean of both datasets for further analysis. It will be referred to as Villa Ada data only.

4.1.3.3 Additional Trace Gases measured at Villa Ada

At the Villa Ada station several additional measurements were performed. They included ozone, nitrogen oxides and carbon monoxide, measured by commercial continuous analyzers, PAN, measured by semi-continuous analyzers, and, for some weeks, benzene, measured by a GC-FID analyzer, all operated by the CNR [Febo *et al.*, 2003]. Quality assurance is not available for these data, so we will focus on those data reported by the BTU and use the CNR values of CO and PAN as indicators for emission and photochemistry respectively only (see chapter 4.1.6, and 4.1.7).

Additional measurement by the BTU at the Villa Ada station included NO₂, NO, O₃, SO₂, by continuous analyzers, and the sum and chemical constitution of aerosols by the WEDD: HNO₂ / HNO₃ (WEDD); O₃ (Dasibi 1108); SO₂ (TE 43RS); NO and NO₂, (Ecophysics CLD 770 ppt chemiluminescence NO analyzer and PLC 760 photolytic converter); NO and NO_y, (Ecophysics CLD 770 ppt NO chemiluminescence analyzer and gold converter). The gold converter was operated at 300° C outside the van, but near the gas inlet in order to catch all NO_y compounds without losses. Immediately before the campaign in Rome the analyzers and the calibration unit had been checked and intercalibrated against transfer standards at the IMK-IFU calibration centre, (Germany). All the BTU analyzers for gas phase measurements at Villa Ada site were operated in an air-conditioned environment. Samples were also taken in 3 m altitude above grass [Febo *et al.*, 2003].

The constantly low levels of SO₂ indicated the absence of industrial sulfur emissions. Two strong peaks of NO with mixing ratios up to 80 ppb arose in the early morning hours and during evening, when the vertical stability of the PBL was high. These NO maxima are coincident with the time of the rush-hour in Rome. The NO peak developed in the early morning hours was generally higher than the evening peak. The ratio between morning and evening peak of NO was for example 1.5 on 29.–30.05.2001. During day and in the middle of the night NO levels were low (at noon often < 1 ppb) at Villa Ada. NO_x as the sum of NO and NO₂ is dominated by NO₂ throughout the day, except during the rush hours in the morning and the evening, when NO drastically boosted the NO_x values.

The diurnal variation of particulate nitrite, nitrate and nitric acid at Villa Ada, which was measured by the BTU group, showed that the partition between nitric acid and particulate nitrate formed by the oxidative chain was in favor of nitrate. This is typical for urban areas with high NH₃ concentrations available for aerosol nitrate formation from nitric acid in the first hours of the morning [Febo *et al.*, 2003]. The source of this ammonia was identified by [Febo *et al.*, 2003] as the results of emission from catalytic converters, which lead the atmospheric concentration of ammonia in Villa Ada to reach levels of 7-8 µg / m³. Later on, the dilution of the lower atmosphere causes a fast decrease of the concentration level of aerosol nitrate.

4.1.3.4 Natural Radioactivity Measurements and Meteorology

Natural radioactivity measurements were carried out by means of a Stability Monitor with an integration time of 1 h instead of the traditional 2 h determinations. We have stated in chapter 2.5.4 that the temporal gradient of radioactivity is a function of the change of the vertical mixing strength. The time series of chemically stable products emitted near the ground should, in principal, be similar to that of natural radioactivity. Natural radioactivity was

generally a magnitude higher during night than during afternoon. Therefore primary pollutants could enrich over night and build a base for the start of the photochemistry during the morning hours [Febo *et al.*, 2003].

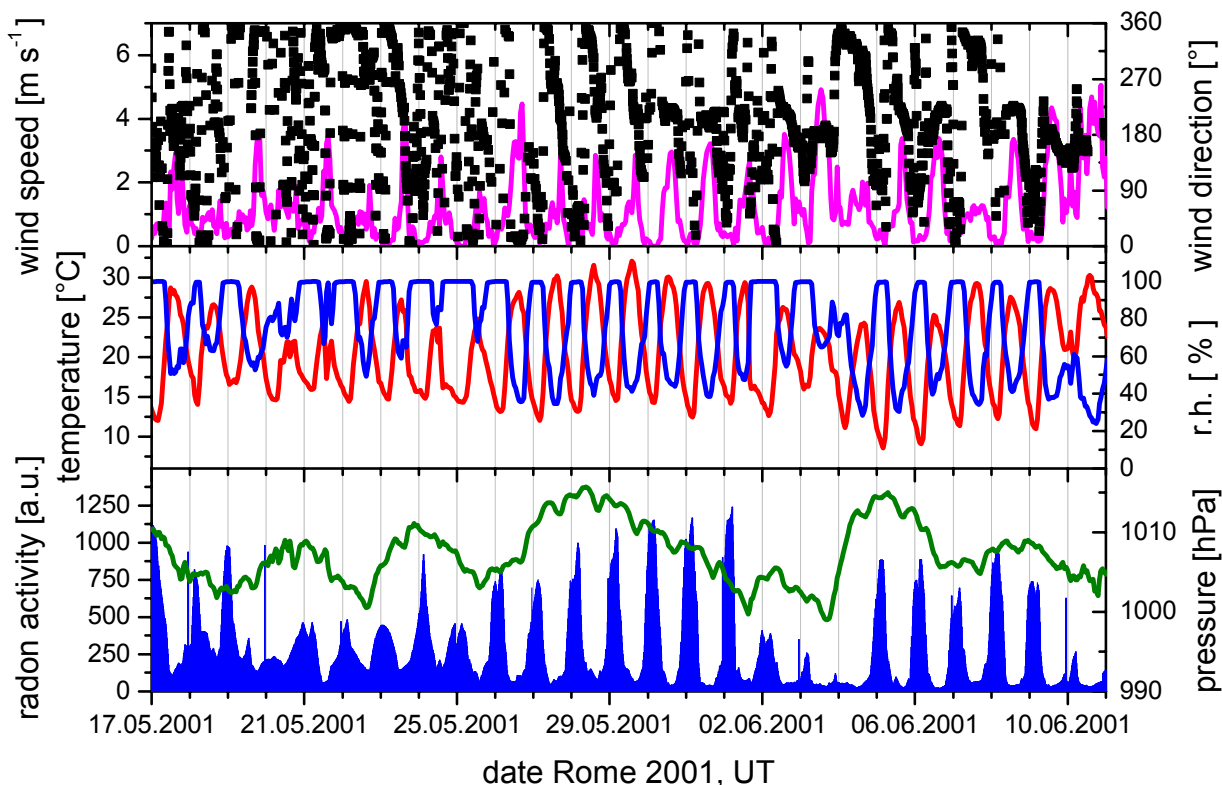


figure 4.8: Meteorological Data recorded during the Rome 2001 campaign: wind speed (upper panel, magenta line, left scale) and the wind direction (upper panel, black squares, right scale), the temperature (mid panel, red line, left scale) and the relative humidity (mid panel, blue line, right scale). In the lowest panel, the pressure (green line, right scale) is illustrated as well as the natural radon activity (blue bars, left scale) in arbitrary units.

Meteorological parameters were measured by the Air Quality Network of the Municipality of Rome, Italy. Temperatures varied between 15 °C at night and ~30 °C in the afternoon. A strong variation in relative humidity was observed. While water vapor was generally saturated during night (R.H. = 100%), relative humidity decreased to ~40% in the afternoon. During the afternoon, wind speeds did not exceed ~2.5 m s⁻¹ (from easterly directions). The wind speed was generally below 1 m s⁻¹ during night (from NW directions). The reduced horizontal advection leads to enhanced levels of primary pollutants such as NO_x and VOCs. Nocturnal atmospheric stabilities were high while strong convective vertical mixing occurred during daytime [Febo *et al.*, 2003].

4.1.4 The Measurements in Montelibretti

As explained in the description of the land-wind-sea-wind-system in chapter 4.1.1, the winds in Rome are generally from the northeaster. Thus 30 km outside Rome in northeastern direction (42°06' N, 12°38'E) in the area of the CNR Montelibretti, an additional measurement station was set up to measure the air masses coming from Rome with a delay of approx. ~ 2 – 2.5 hours. During that time, photochemical reactions should proceed and the instruments in Montelibretti should observe the smog products in the plume [Febo *et al.*, 2003].

4.1.4.1 Setup of the LP-DOAS System

A semi-commercial active LP-DOAS system measured the trace gases NO₂, O₃, (thus Ox as indicator for photochemical smog) HONO, and HCHO. Again, we will now only briefly discuss the specifications of the instrument used at this measurement station and refer to chapter 3.2 and literature therein for a more detailed description of the DOAS system.

A 500 W Xe high-pressure arc lamp (PLI Hanovia HSAX5002, SN 100305) was used as the light source. The telescope was a smaller one with a parabolic main mirror of diameter of 200 mm and a focal length of 600 mm.

Two different kinds of a quartz fibers transmitted the reflected light into the spectrograph: from 16.05.2001 to 04.06.2001 a complex system of a mono fiber (600 μm, NA 0.22) coupled to a fiber bundle consisting of 19 fibers (100 μm, NA 0.12) was used, while from 04.06.2001 to 14.06.2001, this bundle was exchanged by a standard 200 μm mono-fiber (AS UV-VIS 200/220/245 μm, NA = 0.12, length 3 m). As discussed by [Veitel, 2002], the dataset provided the opportunity to compare the results of the trace gas evaluation of approximately 1500 and 3000 spectra recorded at a wide variety of atmospheric conditions using the 600 μm fiber assembly and the 200 μm standard fiber, respectively. Apart from a significant loss of light transmission and therefore time resolution when using the fiber assembly, no consistent effect of the fiber type on the residuals or measurement errors of the trace gas evaluation could be found. However, most mean values for residuals and detection limits do not differ significantly from each other when the respective errors are considered.

This DOAS system used a Czerny-Turner spectrograph (ACTON Spectra Pro 300i). The focal length of the spectrograph is 300 mm, its aperture is 1:4 (i.e. NA = 0.12). The dispersion of the grating (1800 grooves / mm) used is 0.54 nm / mm in a spectral interval from 330 to 370 nm corresponding to 0.038 nm / channel on the photo diode array. The spectrograph is isolated and its temperature stabilized by electrical heating at 35°C to minimize optical errors due to temperature changes. As the fiber itself forms a pinhole of 200 μm diameters, no entrance slit was used for the measurements. Instead, the quartz fiber was mounted fixed directly at the spectrograph entrance, in the focal plane of the first convex mirror. The standard type of a detector (Hoffmann Meßtechnik, Rauenberg) was used: a 1024 diode array (Hamamatsu S3904-1024N), cooled by a Peltier element to (-13 ± 0.3) °C. Typically, a HONO measurement was recorded every 10 min by the software MFC [Gomer *et al.*, 1993].

A light path of 5.4 km towards northwestern direction (see figure 4.1) across the Tiber valley was set up measuring the plume of Rome in a height of approx. 20 m. Most of the distance covered by the light beam was farmland and meadows, but the 72 Quartz triple prism retroreflectors had to be mounted on the roof of a hotel closed to the high-frequented A1 highway between Florence and Naples. Resulting direct emission from traffic will be discussed in the next chapters.

4.1.4.2 Trace Gas Measurements in Montelibretti

An overview of the time series of the trace gases NO₂, HONO, O₃, HCHO measured by DOAS outside Rome in Montelibretti during the whole Rome 2001 campaign is shown in figure 4.9. Between 01. – 02.06.2001, no data are available and so even during some hours in the morning of each day, caused by problems of the DOAS system with scattering light (see chapter 3.2).

Again, a strong diurnal variation of nitrogen dioxide mixing ratios could be observed for all sunny and clear-sky days. During the rainy period around 23.05.2001 and during Pentecost, values remain below some few ppb even during the night. Maximum values of ~ 50 ppb on

31.05.2001 are smaller than in the city of Rome. Daytime values sometime drop down to zero indicating emissions along the Montelibretti DOAS light path being weaker.

In absence of further strong NO_x sources, ozone levels recorded a Montelibretti represent the air mass coming from Rome subject to 4 additional hours of photooxidation. Thus ozone values increase to higher levels of maximum 125 ppb on 31.05.2001 and often remain at values around 0 during the night.

HCHO mixing ratios again undergo a diurnal cycle. Generally, in absence of direct emission sources, background values are smaller than in Rome, ranging between 0 ppb in the night of the 04.06.2001 up to daytime levels of 6 ppb on 09.06.2001. We will discuss the peak structure in chapter 4.1.5.

Nitrous acid behaves different from that in the city centre of Rome. As already mentioned above, direct emission as a source of HONO is much weaker, thus values often drop below the detection limit of approx. 78 ppt and average during daytime at some 65 ppt.

Thus, a statistical evaluation of the measured data was applied to compensate for the errors of the individual data points for daytime HONO mixing ratios and to obtain a mean value typical for the defined time period of meteorological situations. In this frequency analysis, the total number of all HONO daytime data observed under conditions of clear-sky only and high solar radiation between 10:00 and 16:00 UT in Montelibretti during the whole Rome 2001 campaign were plotted against the interval mean. A Gaussian distribution function was fitted to the resulting curve, to obtain the distribution mean and the standard deviation.

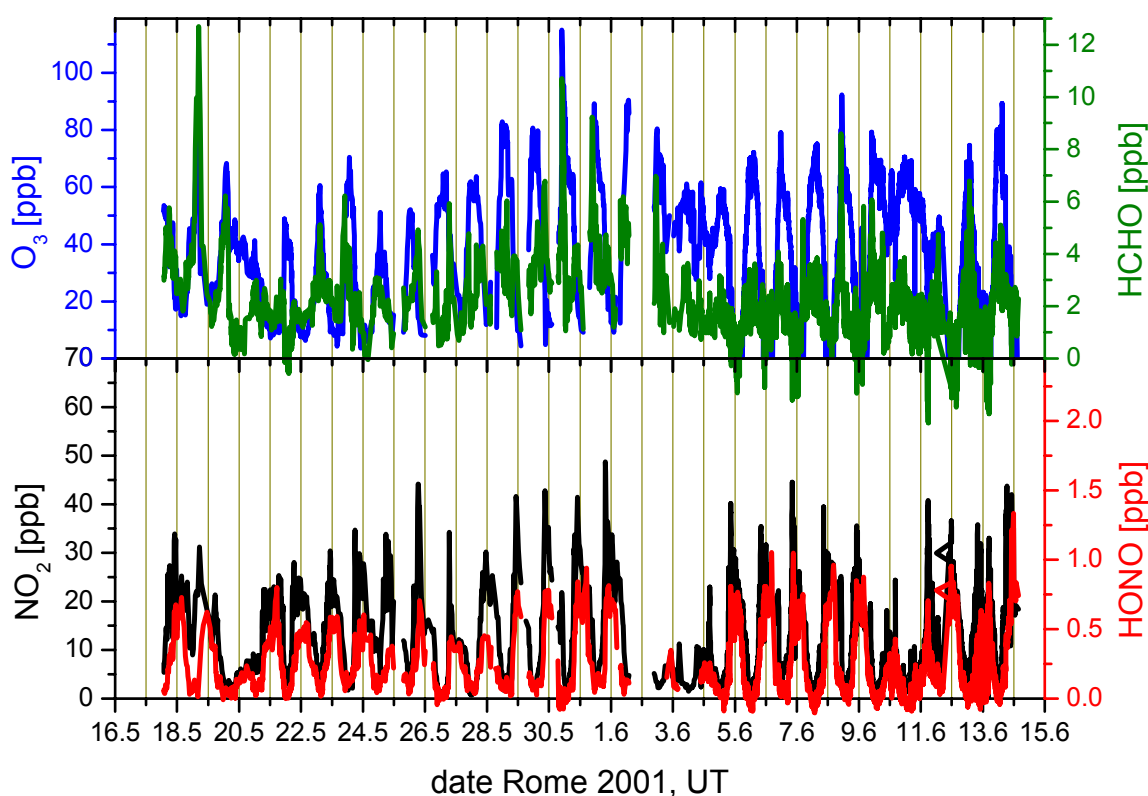


figure 4.9: DOAS data recorded during the whole Rome 2001 campaign by the instrument in Montelibretti. In the lower graph NO_2 (black line, left scale) and HONO (red line, right scale) are plotted. In the upper, O_3 (blue line, left scale) and HCHO (green line, right scale) can be seen. The errors of the measurements (refer to table 4.1) were omitted for a clearer illustration.

The confidence interval as criteria for the significance of data obtained from the evaluation by a Gauss distribution was applied (see e.g. [Taylor, 1990]):

$$\Delta U = \mu \pm \frac{Z \cdot \sigma}{\sqrt{n}} = \mu \pm \varepsilon \quad \left(\text{with } \varepsilon = \frac{Z \cdot \sigma}{\sqrt{n}} \right) \quad \text{eq. 4.1}$$

Here, μ represents the distribution mean, Z is the probability factor depending on the desired level of confidence ([Taylor, 1990] defines $Z = 3$ for a confidence level of 99.74 %) and n is the number of values of the distribution. If σ exceeds ΔU , a value differs significantly from zero. To decide whether the distribution mean value differs significantly from zero, the confidence interval of eq. 4.1 should not include 0. Thus (see figure 4.10), we have strong evidence for HONO daytime values of 65 ppt in Montelibretti during the Rome 2001 campaign, below the detection limit but different from 0.

However, even nighttime values of HONO in Montelibretti are below those measured in Rome. Again this indicates the absence of sources of NO_x in this area. However, as can be seen from figure 4.2 and the explanation given in chapter 4.1.1, the land-wind–sea-wind system tends toward very low wind speeds during the night. Thus fewer pollutants are transported from Rome towards Montelibretti during the night resulting in lower maximum HONO nighttime mixing ratios (of e.g. 1.0 ppb on 31.05.2001) than observed in the city center of Rome.

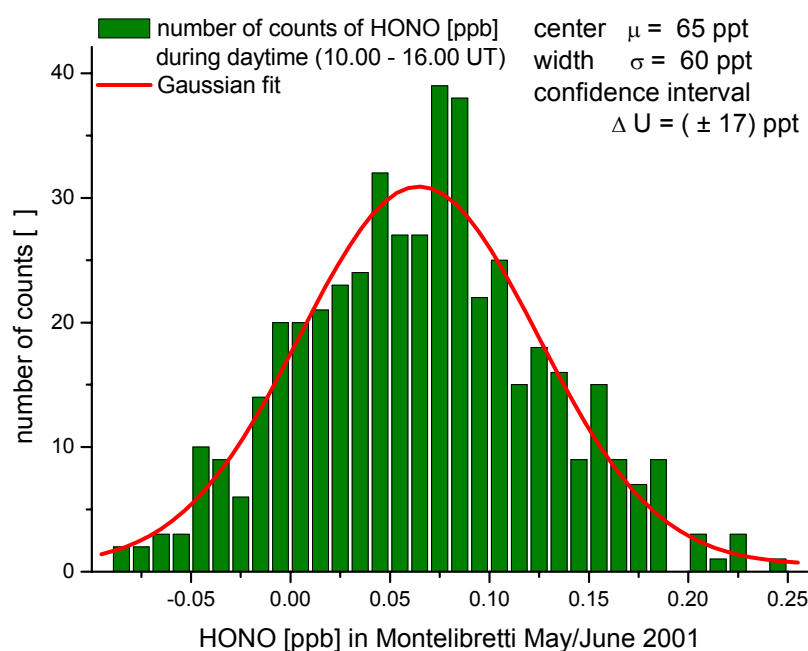


figure 4.10: Results of the sensitivity test for significance of daytime values of HONO in Montelibretti.

4.1.4.3 Additional Measurements in Montelibretti

At the measurement station in Montelibretti, none additional equipment was operated by the IUP Heidelberg. However, measurements of ozone and nitrogen oxides were carried out by the CNR during the whole study. Natural radioactivity was measured by means of a Stability Monitor with an integration time of 2 hours. Meteorological parameters were determined at the Montelibretti station by the CNR group [Febo et al., 2003].

4.1.5 Intercomparison between Rome and Montelibretti Trace Gas Data

Another interesting topic is the spatial and temporal difference between the trace gas peaks in Rome and Montelibretti as can be seen from figure 4.11. As already mentioned, Montelibretti is approximately 30 km in northeastern direction of Rome down the Tiber valley (see figure 4.1). With a typical wind speed of 3 m s^{-1} (see figure 4.2), the air mass observed in the city center of Rome is expected to be in Montelibretti with a time delay of $\sim 2 - 2.5$ hours. This can be found for all trace gases measured from figure 4.11. As no further strong sources of NO_x are located between Rome and Montelibretti, respectively in the DOAS light path, the polluted air with its ongoing photochemistry is observed in Montelibretti.

The peaks in the formaldehyde mixing ratios as already observed in the dataset from the city center of Rome appear with a time delay of approximately $\sim 2 - 2.5$ hours as expected by a wind speed of some few m s^{-1} . The intensity of these peak events is sometimes stronger than that in Rome, indicating the proceeding photochemistry in the polluted air mass transported from the urban area of Rome downwind area of the Tiber valley towards Montelibretti. Events of this type are typical of the Rome area, particularly during the late spring and the early summer, when the breeze is particularly significant (see the direction and intensity of wind in figure 4.2).

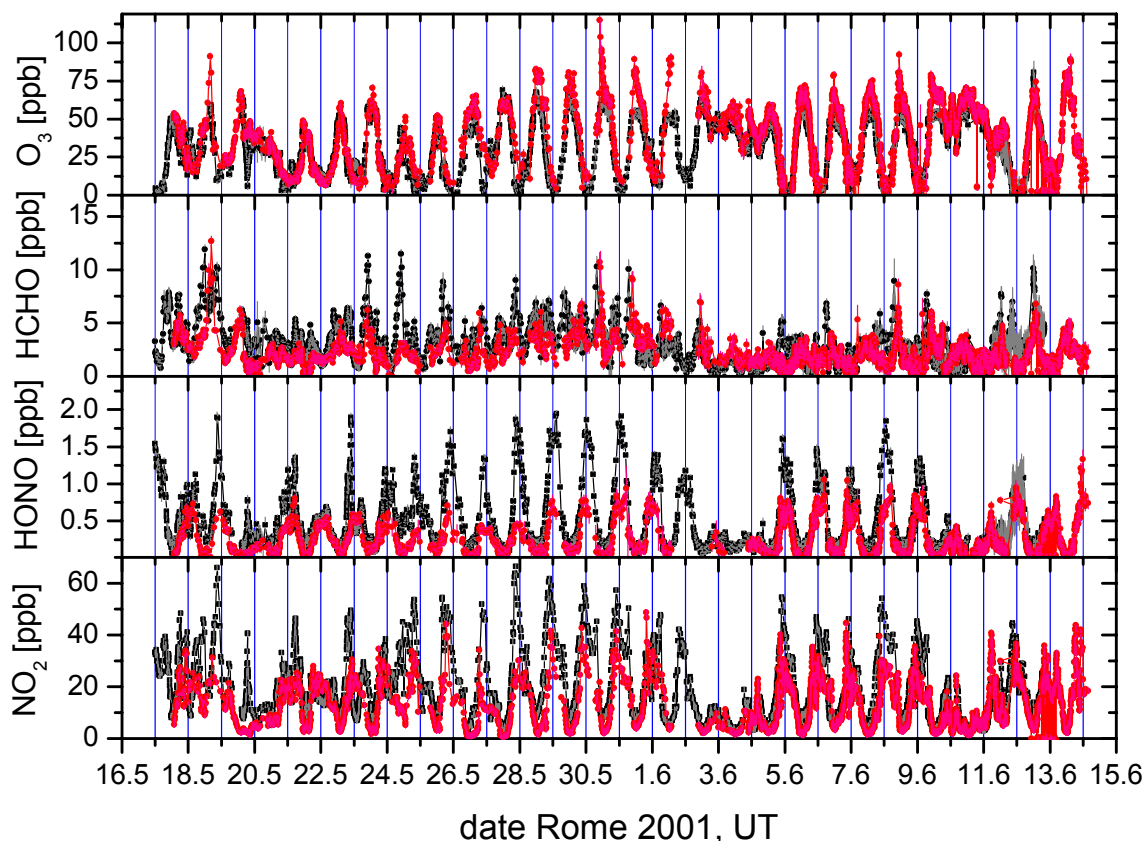


figure 4.11: All DOAS data reported during the field campaign in May / June 2001 in Rome. One instrument measured in the city of Rome (black line) the second in Montelibretti (red line) in the plume of Rome.

4.1.6 Photochemical Smog Events

To identify periods of high photochemical activity and, especially, photochemical smog events, where HONO is suspected to play a key role as a source of OH radicals, the temporal

trend of pollutant trace gases, especially PAN and HCHO, which are known to be mainly products of the photooxidation processes in the troposphere were analyzed. In smog situations, high amounts of OH radicals, especially from HONO photolysis in the early morning hours (see chapter 2.3), can trigger the reaction chain leading to PAN, nitric acid, aerosol nitrate and, most of all HCHO, which, on its turn, can add a relevant contribution to the OH budget, causing the formation of high ozone levels (see also chapter 2.2).

Additionally, the O_x concentration (as sum of NO_2 and O_3) was compared with the ozone background value, as O_x is independent of both the titration process of O_3 with NO, and the photolysis of NO_2 (see chapter 2.2). The background values¹⁶ of ozone in the PBL were determined from days characterized by high mixing of the atmosphere, which show a low and constant value of natural radioactivity also during the night. The typical background value of ozone for this period of the year at the latitude of Rome was found to be ~ 60 ppb. Thereby, the contribution of NO_2 was neglected, as it is present in lower mixing ratios (typically some ppb during daytime), it is mainly emitted close to the ground and shows remarkable short lifetime due to photolysis.

This value of 60 ppb constitutes the threshold for the identification of photochemical smog events during the Rome 2001 campaign. The most intense photochemical episode was therefore between 27.-31.05.2001. However, this certain limit is also valid to identify the strong photochemical activity on the 24.05.2001.

4.1.6.1 The Smog Event on 31.05.2001

During the entire period of 27.05.-31.05.2001, O_x , as well as the photooxidation products (PAN and HCHO) show a similar time series with the highest concentration levels on 30., and 31.05.2001. The aerosol nitrate and HNO_3 , which are both final oxidation products of NO_2 , show the high photochemical activity as well (see [Febo et al., 2003]).

On 31.05.2001, the strongest photochemical smog event of the Rome 2001 campaign occurred [Febo et al., 2003]. The meteorological conditions, however, were characterized by a high-pressure period, very weak horizontal wind, and high intensity of solar radiation. As can be seen from the natural radioactivity in figure 4.8, a diurnal inversion layer was established at low altitude, distinguishing this smog episode from a typical summer day in Rome [Febo et al., 2003; Perrino et al., 2001].

From figure 4.12, it can be seen that at 7:30, the mixing ratio of PAN had already reached its maximum daily value of about 4 ppb in the urban area of Rome and the entire smog event was already developed by 9:30. The maximum value of the time derivative of O_x concentration in the urban area of Rome occurred between 6.00 and 7.00 in the morning (see figure 4.12) corresponding to the maximum smog production rate. The start of the photochemical process was therefore deduced by [Febo et al., 2003] to occur at about 5:00.

The urban plume of the city of Rome reached the area of Montelibretti at $\sim 9:30$, about 30 km downwind. O_x and O_3 values had increased in less than half an hour during this horizontal transport. The time derivative of this increase was ~ 140 ppb h^{-1} with maximum values of 130 ppb for O_x and 115 ppb for ozone. The increase in the concentration of HCHO in Montelibretti is in temporal coincidence with the concentration increase of ozone (figure 4.12). The maximum HCHO value in Montelibretti reached at 9:30 was ~ 12 ppb, which is about the same value observed in Rome at 6:30. This again indicates HCHO being of secondary origin on 31.05.2001.

During the early morning hours, when the event on 31.05.2001 started, HONO photolysis is the most significant source of OH radicals, because its photolysis occurs already at lower wavelengths [Stockwell and Calvert, 1978; Stutz et al., 2000]. As high values of HONO of ~ 1

¹⁶ In this case, O_3 and O_x become indistinguishable values

ppb until 7:00 were observed on 31.05.2001, it seems likely that nitrous acid was the key oxidizing species in the generation of this early-morning photo-smog in Rome, starting immediately after sunrise. The OH radical originating from further sources (see chapter 2.2.3), such as HCHO and O₃ photolysis, contributes as well to the chain of photooxidation [Alicke *et al.*, 2003; Alicke *et al.*, 2002; Stutz *et al.*, 2002; Stutz and Geyer, 2003], but was of secondary origin only and triggered by HONO. HONO was therefore the initial source of OH radicals during the photo-smog event on 31.05.2001 in Rome.

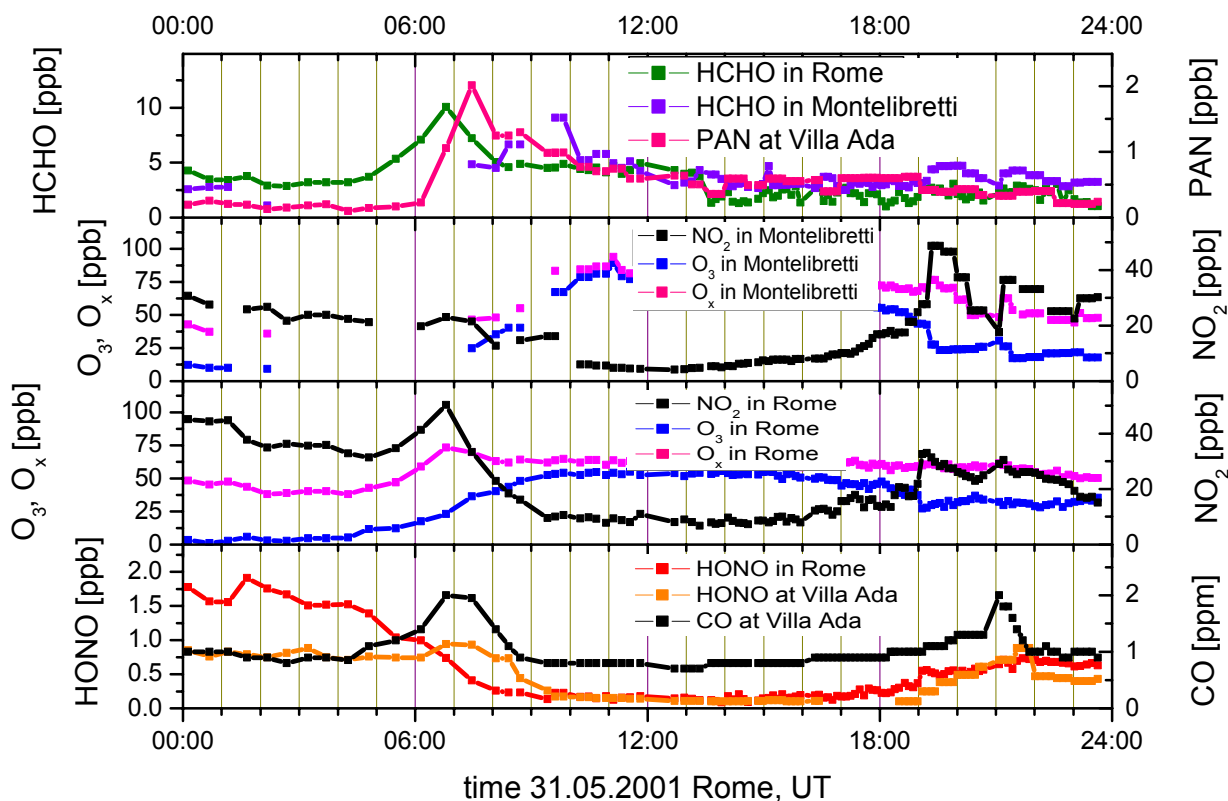


figure 4.12: Time series on 31.05.2001 of HONO in the city center of Rome and in Villa Ada (lowest panel, left scale), O_x and O₃ (middle plot, left scale) in the city center of Rome and in Montelibretti, as well as NO₂ (middle plot, right scale), and the photooxidation products HCHO in Rome and Montelibretti (upper panel, left scale) and PAN in Villa Ada (upper panel, right scale).

The high levels of HONO were not only caused by the heterogeneous hydrolysis of NO₂, which showed moderate concentrations on this day, but transport effects and primary emission contributed as well. This is indicated by a HONO decrease after 7:00 showing a similar temporal pattern as CO, which is a primary emittant from combustion processes of road traffic only. However, this first and more qualitative calculation neglects vertical transport and, especially, interactions between transport and chemistry. The vertical transport can significantly influence the concentrations of trace gases, especially in the early morning hours when stable nighttime conditions rapidly change to strong vertical mixing during the day.

4.1.6.2 Pollution Event on 24.05.2001

On 24.05.2001, which was a cloudy day, with some drizzle episodes, and, as a consequence, reduced photolysis frequencies (figure 4.4), the HONO mixing ratio level was higher than 500

ppt during the entire day (figure 4.13). The mixing ratios of PAN and HCHO simultaneously reached maximum levels of 3 and 12 ppb, respectively, on 24.05.2001 (see figure 4.13). As especially PAN is an oxidation product only, this day can be an episode of strong oxidation activity as well.

The yield of OH radicals by ozone photolysis is suspected to be negligible during this episode [Alicke *et al.*, 2003; Alicke *et al.*, 2002; Stutz *et al.*, 2002; Stutz and Geyer, 2003], but the HONO photolysis requires light at longer wavelengths only [Stockwell and Calvert, 1978; Stutz *et al.*, 2000]. This type of photochemical activity being mainly due to HONO photolysis is generally more typical of the wintertime period [Aumont *et al.*, 2003].

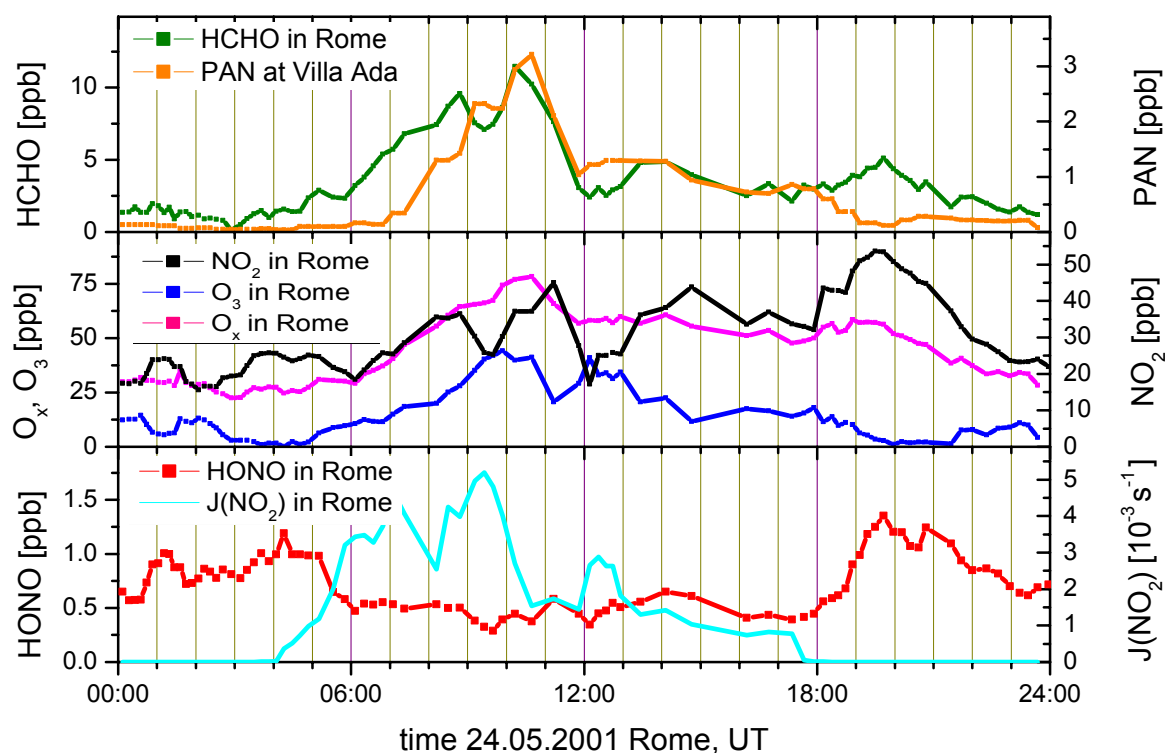


figure 4.13: Time series on 24.05.2001 of HONO (lowest panel, left scale), O_x and O_3 (middle plot, left scale), NO_2 (middle plot, right scale), and its photolysis (lowest panel, right scale), as well as the photooxidation products HCHO (upper panel, left scale) and PAN (upper panel, right scale).

4.1.7 Qualitative Correlations of HONO and Radon Data

Before we analyze the HONO time series by applying a complex model based on the $K(z)$ theory in chapter 6.2, a qualitative description of the influence of the PBL stability will be given here. This approach is based on the general differential equation eq. 2.73 (see chapter 2.5.4) that describes the temporal behavior of the concentration of a trace gas at the ground including the key variables, such as its sources and sinks, and the parameters describing the dynamic properties of the atmosphere.

For nitrous acid, some of the parameters of the equation eq. 2.73 can be directly identified. Daytime HONO removal pathways are mainly the photolysis ($L_{\text{photolysis}}$) and dry deposition (L_s) on surfaces, while homogeneous loss processes, i.e. the self-reaction and that with nitric acid, were reported to be negligible (see chapter 2.3.7). Primary HONO emission (Φ_P) is mainly due to combustion processes from road traffic, which is well quantified by [Ackermann, 2000; Kessler and Platt, 1984; Kurtenbach *et al.*, 2001; Pitts *et al.*, 1984a;

Winer and Biermann, 1994], and thus, the HONO emission is strictly linked to that of NO_x ($= [\text{NO}] + [\text{NO}_2]$). Volumetric HONO formation on particle surface (P_{particls}) is suspected to be of minor importance for the atmospheric concentrations observed. The heterogeneous HONO production at the ground is of higher relevance and dependent on various parameters such as the surface type, its roughness and the relative humidity, but in general not directly linked to the atmospheric concentration of NO_2 . This circumstance is due to the fact that HONO adsorption-desorption phenomena on the surface may cause a temporal shift between the heterogeneous production of HONO at the surface and its release into the atmosphere. This is of particular interest in urban areas with high interior surfaces (e.g. buildings). Finally, we can write equation eq. 2.73 for HONO, valid for qualitative discussions of its sources and sinks that contribute to the observed HONO mixing ratios, as follows:

$$\frac{\partial[\text{HONO}](z,t)}{\partial t} = \frac{1}{h_{\text{PBL}}} [\Phi_p + \Phi_s] - K(z) \cdot \frac{\partial[\text{HONO}]}{\partial z} + P_{\text{particles}} - L_{\text{photolysis}} - L_s \left[\frac{1}{h_{\text{PBL}}}; K(z) \cdot \frac{\partial[\text{HONO}]}{\partial z} \right] + adv \quad \text{eq. 4.2}$$

The contribution of the advection processes to the local variations of a trace gas concentration can be deduced from the horizontal wind speed and direction. From e.g. 02.06.-04.06.2001 and on both 10., and 11.06.2001, the wind speed was high and advection dominated eq. 4.2 and therefore the temporal pattern of trace gases.

However, the quantitative characterization of the vertical transport of trace gases, particularly in the lower part of the boundary layer, is more complex, but qualitatively accessible from the temporal trends of the natural radioactivity, as deduced in detail in chapter 2.5.4. This is of particular importance during high-pressure conditions in a transition phase between labile layering of the atmosphere and its strong stabilization (during the first few hours after sunset), when vertical transport due to turbulence is strongly reduced, or, on the other hand, if a strong mechanical or convective mixing occurs, when the atmospheric stability breaks. The $K(z)$ values of these periods become extreme and thus are either negligible or dominate eq. 4.2 and therefore the concentration and time derivative of a trace gas (changing algebraic sign between the two situations described above). Especially from 28.05.-31.05.2001 and from 04.06.-07.06.2001 the atmosphere was characterized by these high-pressure conditions, and both, the concentration level and temporal pattern of any trace gas, is well describable by that of natural radioactivity. In the following, we will give this qualitative discussion of source apportionment study on some selected periods.

4.1.7.1 HONO-Time-Derivative by Vertical Mixing of the PBL

During high-pressure conditions, when the nocturnal atmospheric stability is high, ozone concentrations near the ground are generally removed by titration with NO in the polluted air masses after sunset. As NO is primarily emitted from traffic combustion processes near the ground, higher ozone levels are typically observed at higher altitudes.

In the morning, when the height of the well-mixed PBL increases, O_3 levels rise again. This is mainly caused by the stronger vertical mixing, which “in-mixes” ozone from higher altitudes and “out-spreads” NO from the lower layers. Photochemical activity even enhances local ozone production.

Nitrous acid as a product of the polluted urban air near ground, is consequently expected to mirror the ozone variations as can be seen in figure 4.14 (a transition phase between a high-pressure period and an advection period). The time derivatives of HONO concentration can be described as a function of these dynamic forces of the atmosphere indicated by the natural radioactivity based on equation eq. 4.2.

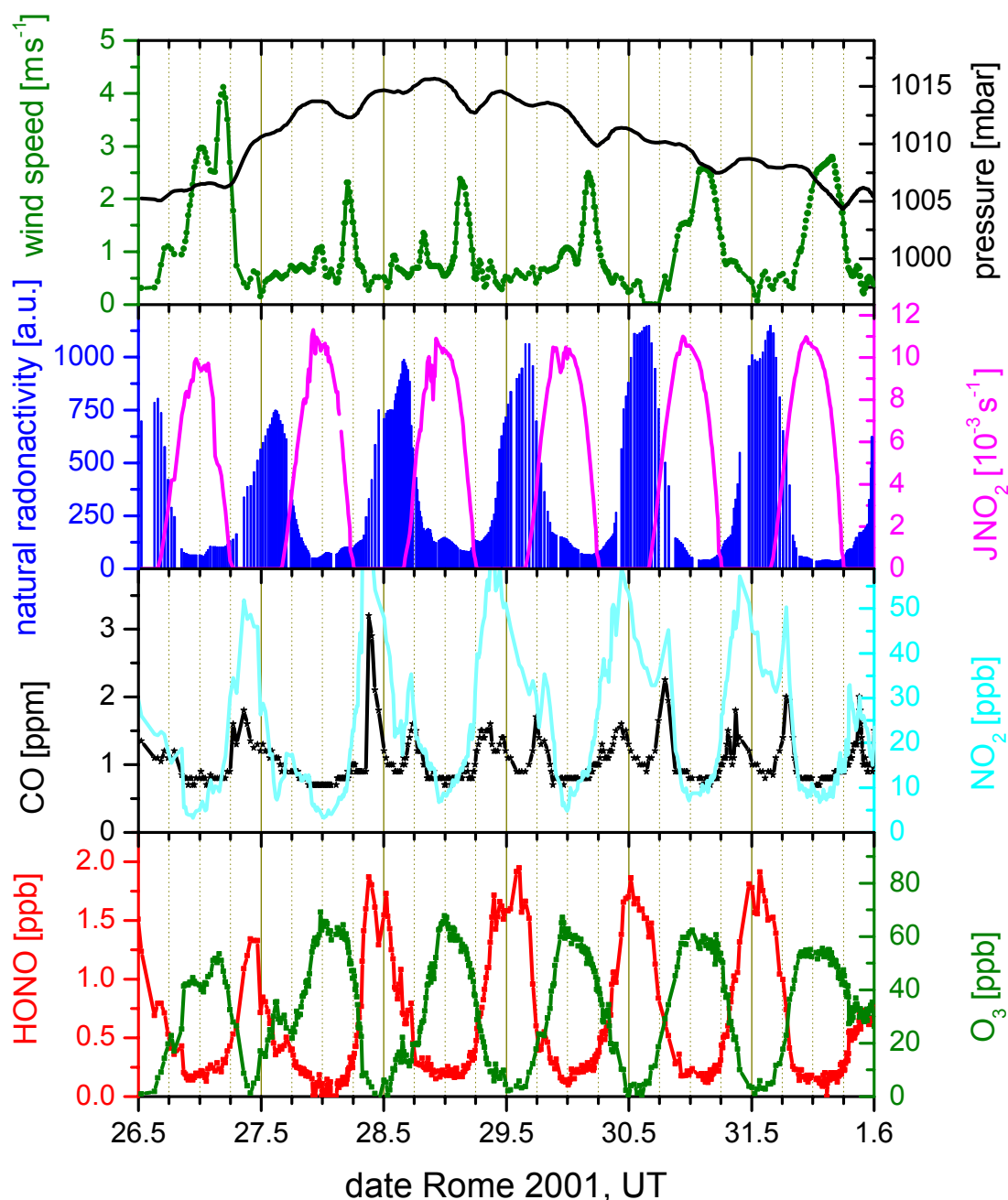


figure 4.14: *Mirrored variations of HONO and ozone (lowest plot, left and right scale respectively) for a high-pressure period. The influencing meteorological parameters are illustrated in the upper plot (wind speed – left scale and air pressure – right scale), and as well the natural radioactivity (left scale).*

For example on the night of 31.05.-01.06.2001 (see figure 4.14) ozone suddenly increases from a few ppb to ~ 40 ppb after a short initial stabilization of the atmosphere, while HONO immediately reacts by decreasing more than 0.5 ppb. Afterwards the atmosphere continues to stabilize (positive derivative of natural radioactivity in figure 4.14) after midnight, and ozone sharply decreases again due to NO titration down to some ppb typical for nighttime stability conditions. At the same time, HONO mixing ratio increases by about 1.2 ppb in half an hour, which cannot be explained by any chemical production. A more or less constant value of HONO of ~ 1.7 ppb is observed through the next 3 hours of the night, until the mixing of the

atmosphere breaks the inversion layer (negative derivative of natural radioactivity in figure 4.14) in the morning hours, and an increase of ozone coming from the upper layers is observed.

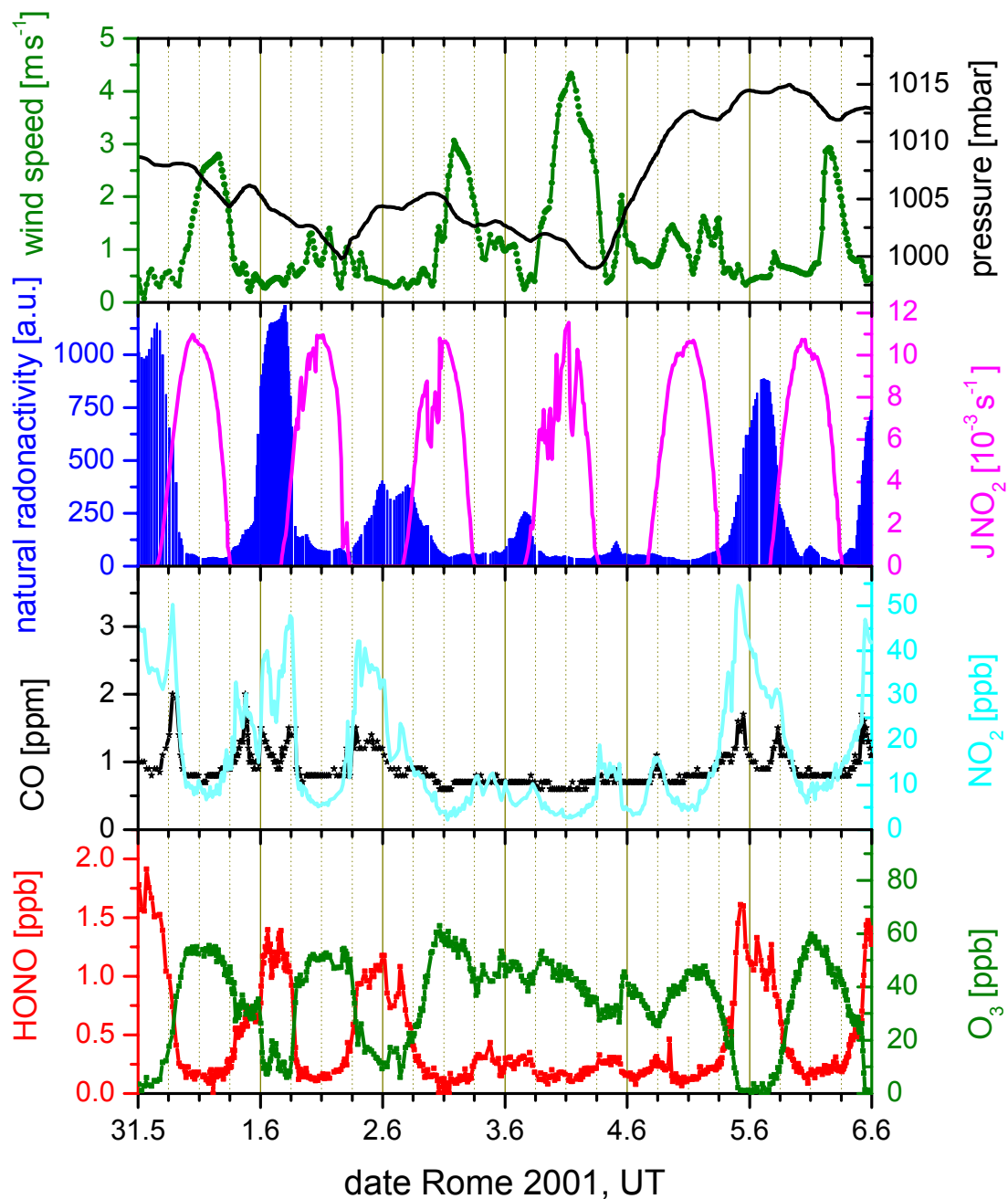


figure 4.15: Mirrored variations of HONO and ozone (lowest plot, left and right scale respectively) for a low-pressure period. The influencing meteorological parameters are illustrated in the upper plot (wind speed – left scale and air pressure – right scale), and as well the natural radioactivity (left scale).

A case study for a low-pressure period in the Rome area with higher advection but very weak day-night modulation of the natural radioactivity is illustrated by figure 4.15. In particular, on the night of 02.-03.06.2001, no atmospheric stabilization occurred (see temporal pattern of the natural radon-activity in figure 4.15), and the ozone values remain at their high levels of ~ 40 ppb even close to the ground (figure 4.15).

From a qualitative point of view, one can state that the mixing of ozone downwards from higher altitudes dominates with respect to removal process of titration by NO near the ground. However, both cannot be separated here and a model is needed for the quantification of the different processes. The HONO time derivatives mirror those of ozone even in the finest structures; and mixing ratios remain at relatively low values < 0.4 ppb in the late night, moderately increasing only during the early morning (figure 4.15). However, the fluctuations of both trace gases, HONO and O₃, seem to be directly linked to the time derivative of the natural radioactivity, and thus to fluctuations in the mixing properties of the boundary layer.

More evidence for the link of HONO variations due to atmospheric vertical transport can be obtained from the slight stabilization of the atmosphere, which occurred immediately after sunrise at 4:00 on 12.06.2001, followed by a sudden increase of the HONO concentration, in spite of the already active photolysis processes. In the following night, when a very quick stabilization (positive derivative of natural radioactivity) of the atmosphere is observed between midnight and 2:00, a sharp decrease of ozone values mainly due to NO titration was mirrored by a sharp increase of 1.4 ppb h⁻¹ of HONO up to 2 ppb. At this time of the night, the direct emission flux of HONO from car exhausts is known to be negligible in the area of Rome. These high levels of HONO remained for 3 more hours until the mixing of the atmosphere broke the inversion layer (negative derivative of natural radioactivity and increase of ozone coming from the upper layers).

The importance of primary emission of HONO can be discussed for the period of 26.-28.05.2001 (see figure 4.14) by comparing its trend with that of CO mixing ratios, as CO is known as a primary pollutant only. In the night of 25.-26.05.2001, HONO reached its maximum mixing ratio of ~ 1.7 ppb at $\sim 3:00$, with an increase of about 1 ppb in less than one hour (figure 4.14). As traffic intensity is negligible at that time, CO did not show any significant variation. During 26.-27.05.2001, a similar HONO maximum was reached at $\sim 23:00$ and CO level showed a simultaneous moderate increase due to the traffic emission (figure 4.14). Contrastingly, during the night of 27.-28.05.2001, HONO mixing ratio rose quicker to ~ 2 ppb, while CO mixing ratio reached a maximum value of more than 4 ppm, with an increase of > 3 ppm h⁻¹ (figure 4.14). During this night, a second peak can be obtained from the radon data and its fast increase indicates a second period of strong atmospheric stabilization until sunrise (figure 4.14).

The difference in the behavior of CO concentration during these three episodes indicates CO concentration only depending on the temporal coincidence between atmospheric stabilization and intensity of the traffic emission. Despite, frequent HONO increases during the late night, when the traffic emission is negligible, shows that the direct emission from exhaust is likely not the main source of nitrous acid.

4.1.7.2 Influence of Atmospheric Stability on Daytime HONO Values

Daytime HONO concentrations in the urban area of Rome were generally high, also when the solar radiation intensity was typical of a high-pressure sunny day (e.g. 29.-31.05.2001 in figure 4.14). HONO typically kept values of ~ 2.0 ppb until 5:00 followed by a sharp decrease, reaching the mixing ratio value of 0.2 ppb, which was then kept until noon (see figure 4.14) and the ozone level reach the value of 60 - 70 ppb.

A first hint for the strong influence of the height of the PBL on these HONO concentrations can be deduced from the time derivative of the natural radioactivity. Radon values decreased from > 1000 counts per minute rapidly down to 200 counts per minute in a first slow increase of the atmospheric mixing between 4:00 to 6:00 (see figure 4.14). Afterwards, it decreased only slightly to values of ~ 100 counts per minute (see figure 4.14) indicating the almost constant height of the well-mixed PBL during the next 2 hours, before it decreased strongly again for more than one hour, between 9:00 and 10:00. [Febo *et al.*, 2003; Perrino *et al.*,

2001] estimated this to be consistent with the development of a new inversion layer between 5:00 and 10:00, which increased from a height of 50-100 meters in the first hours of the morning to 300-400 meters, and then kept the same height until noon.

This re-stabilization of the atmosphere occurring in the late morning is one of the peculiar features of smog episodes. The ratio between maximum nighttime concentration levels of HONO and its concentration during the first morning hours is typically about 5 during these smog episodes [*Febo et al.*, 2003; *Perrino et al.*, 2001]. This value is of the same order of magnitude than the night-to-day ratio of a compound emitted only at the ground such as radon.

4.2 The Format 2002 campaign: Intercomparison of Trace Gas Measurements

For this study, a second campaign in Italy was conducted between 19.07.2001 and 20.08.2002 in Milan, Italy. This campaign was supported by the European Union (contract number EVK2-CT-2001-00120), project name: FORMAT (formaldehyde as a tracer of oxidation in the troposphere).

The proper aim as outlined by the projects founder was the comparison of different measurement techniques for HCHO, validation with satellite measurements of GOME during that time, the detection of the unusually high formaldehyde levels in the Po Valley and the quantification of the HCHO inhomogeneities in the atmosphere.

In addition to these aims, and in cooperation with the group from Bergische Universität und Gesamthochschule Wuppertal, Germany (BUGH), we performed measurements of HONO mixing ratios by two measurement techniques: LOPAP II and DOAS in the same air mass. In combination with several other trace gas measurements and meteorological parameters, we ensured the unusual high daytime values found during the Rome 2001 campaign.

4.2.1 The Measurement Location

Milan is the capital of the industrially developed region of Lombardy (23.859 km², 8.910.000 inhabitants) in the northern part of Italy known as Po Valley (see figure 4.16). The Cities population is 1.4 Million inhabitants with a city area of 200 km². A few kilometers north of Milan, the Alps form a basin with respect to horizontal wind-jets and thus, traces gases are trapped and can accumulate.

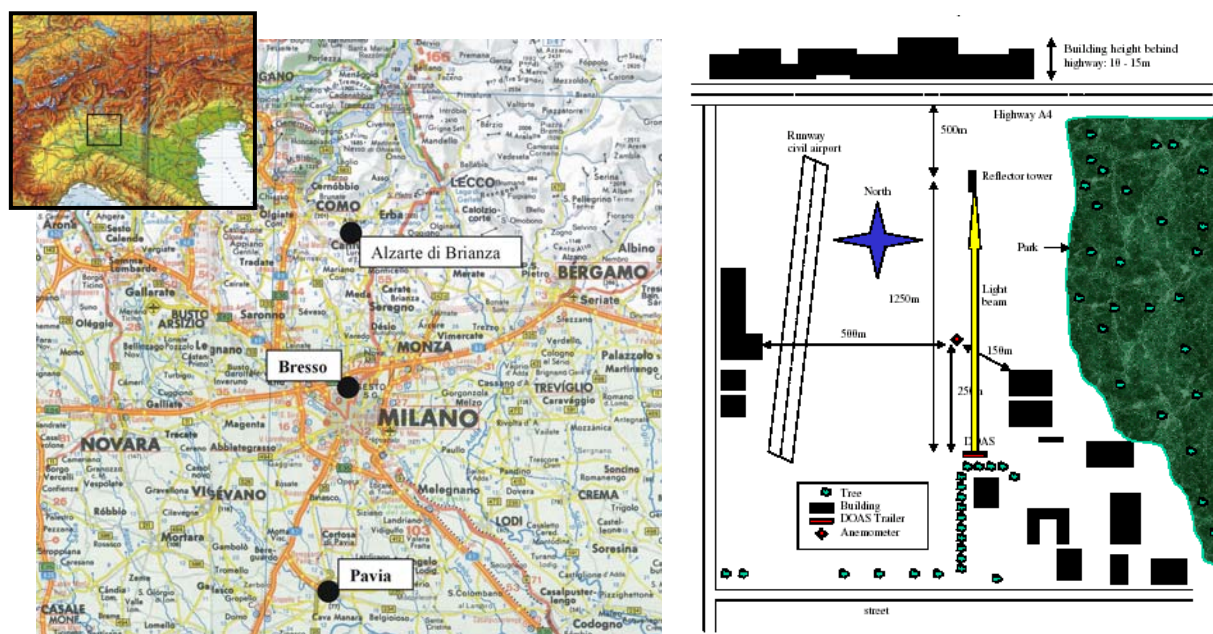


figure 4.16: Left: The area of Milan and the measurement station in its district Bresso at the northern end of Milan. Right: Sketch of the Red Cross Military Air Base in Bresso, Milan, where the DOAS–White system measurements took place (adapted from [Alicke, 2000]).

The measurements were carried out at an airport at Bresso (45°32' N, 9°12' E; 103 m a.s.l.), a district of the usually heavily polluted area of Milan at a distance of 8 km north of the city center (see figure 4.16)¹⁷. The urban area in which the airport is located is a mixture of residential buildings and small businesses. The airport of Bresso is further surrounded by surface streets and a highway at the northern end of the airfield (see figure 4.16), which showed particularly high traffic density early in the morning and in the late afternoon. The main local source for pollutants was, therefore, most likely traffic from the highway A4 connecting Novarra and Bergamo. The complete system was set up in a trailer on the Red Cross Military base in Bresso. This military base was no longer in operation, but a small civil airport for sport airplanes was located directly next to the military base. It was only in use for take-offs and landings during the day, and primarily on the weekend. The trailer was sited on a forecourt of a hangar buildings (~ 8 m high) at the northern end of the military runway (see figure 4.16). The southeastern end of the measurement site is marked by low (~4 m high) buildings and sparse trees (~ 8 m high). The trees are located about 250 m to the east of the runway. To the northern end of the measurement site a ~250 m long flat area was followed by a slight slope toward a highway which ran ~ 500 m north, perpendicular to the light path. A park area with trees was located to the east (see figure 4.16).

4.2.2 DOAS Measurements at Bresso

4.2.2.1 Setup of the DOAS White-Multi-Reflection System

A DOAS system, which integrates over smaller air masses than a LP-DOAS system, is needed for an intercomparison of DOAS measurements and in-situ monitor techniques. The multi-reflection White system (see [Geyer, 1997; Grassi and Guzzi, 2001; Ritz *et al.*, 1992; Trick, 2000; Volkamer, 1996; White, 1942; White, 1976] and chapter 3.2) was operated for the DOAS trace gas measurements. Due to its setup, it is less sensitive to the horizontal wind system transports and thus data are directly comparable to in-situ measurements. Consequently, the White system is less sensitive to fluctuations of the trace gas concentrations and less influenced by local sources.

The basics of the White system were described in chapter 3.2.3.2, thus we will again now only name the individual modifications and the setup operated during the Milan 2002 campaign. The three spherical concave mirrors: the front mirror A facing the two side by side back mirrors B and C had a dielectrically coating (Laser Optics, Garbsen, Germany) optimized to HCHO measurements. Formaldehyde has strong structures in the differential absorption cross-section at 321 nm, thus a wavelength window of highest reflectivity of 321 ± 20 nm was chosen including NO₂, HONO, and O₃ absorption structures as well. A light path of 2160 m, corresponding to the maximum number of traverses of the light beam in the White system of 288 with a base-length of 15 m, was set for the measurements. Only for the recording of reference spectra (see chapter 3.2), the light was shortened to 16 reflections, corresponding to 216 m total light path length. The stability of the optical alignment was controlled by the self-developed laser-web-cam-adjustment system (see chapter 3.2.4.1). The two Newtonian telescopes to couple the light beam of the Xe-arc lamp (PLI Hanovia HSAX5002, SN 182276) into the White system and to couple it out for adaptation to the spectrograph-detector-system as well as all the electronics and all the other components of the DOAS system were located inside the air-conditioned measurement container, while the

¹⁷ During the FORMAT 2002 campaign two additional measurement stations were operated: at Pavia in the south of Milan (as background station under conditions of southern wind directions) and in Alzate di Brianza (to detect and quantify the product of the proceeding photochemistry in the polluted urban air mass transported from the city of Milan). However, those will not be discussed in this thesis.

White system itself with the three mirrors measured the air outside in a distance of 3 m to the container.

Again, two different kinds of quartz fibers were used transmitting the reflected light into the spectrograph: from 24.07.2002 to 02.08.2002, the standard 200 μm mono-fiber (AS UV..VIS 200/220/245 μm , NA = 0.12, length 3 m) and from 07.08.2002 to 20.08.2002, the complex system of a mono fiber (600 μm , NA 0.22) coupled to a fiber bundle consisting of 19 fibers (100 μm , NA 0.12). As already shown in chapter 4.1.4.1, no consistent effect of the fiber type on the residuals or measurement errors of the trace gas evaluation could be found. The DOAS system used a Czerny-Turner spectrograph (ACTON Spectra Pro 300i). The focal length of the spectrograph is 300 mm, its aperture is 1:4 (i.e. NA = 0.12). The dispersion of the grating (1800 grooves / mm) used is 0.54 nm / mm in a spectral interval from 300 to 360 nm, which was mainly defined by reflection and transmission structures of the dielectrical coating of the mirrors of the DOAS White system. The spectrograph is isolated and its temperature stabilized to 35°C. The detector (Hoffmann Meßtechnik, Rauenberg) consisted of a 1024 diode array (Hamamatsu S3904-1024N), cooled by a Peltier element to (-13 ± 0.3) °C. Typically, a measurement spectrum was recorded every 2 min by the software MFC. The ground between the mirrors of the DOAS White system was flat and the vegetation consisted of uncut grass with a height of approximately 0.5– 0.7 m.

4.2.2.2 Measurement of Trace Gases in Bresso

Between 24.07.2002 and 20.08.2002 trace measurements of NO_2 , HONO, O_3 , and HCHO were performed. Results are illustrated in figure 4.17. Especially during the period of the first days, scattering light caused problems in the laser-web-cam-adjustment system and thus data are not available at each day between 23:00 and 7:00 (the errors of the measured mixing ratios are approx. a factor of 3 higher for the DOAS data than during the rest of the Milan 2002 campaign). This also leads to the noisy structure of the DOAS data in the period of 24. - 27.07.2002, which is also neglected for analysis. Between, 02. - 07.08.2002, electronic failures resulted in a gap of the DOAS data. Averaged detection limits for the DOAS trace gas data of the whole time of the Milan 2002 campaign are summarized in table 4.2.

As can be seen from figure 4.17, the anti-correlated diurnal variations of ozone and nitrogen dioxide were observed, as suspected by Leighton theory. NO_2 values increased from daytime levels of 3.7 ppb e.g. on 29.07.2002 during the night to 53.7 ppb. On the same day, ozone reaches a maximum daytime level of 94.3 ppb in the late afternoon but is totally destroyed by the NO titration during the night. The overall maximum O_3 mixing ratio was found to be 120.7 ppb in the second part of the campaign on 17.08.2002, when an additional strong peak in the O_x ($= [\text{NO}_2] + [\text{O}_3]$) of 158.9 ppb gave evidence for a photochemical smog event.

The expected high mixing ratios of HCHO for Bresso, the city station, declined from about 10 ppb to 5 - 6 ppb or less during the rest of the campaign most probably due to the holiday season with significantly reduced traffic in Milan. A pronounced and reproducible diurnal variability was weakly defined. Background values of 2 ppb were observed during most time of the campaign.

HONO was observed to be strictly correlated to its precursor NO_2 . Nighttime values of 2.9 ppb were recorded, rapidly decreasing after sunrise (3:30 UT) by photolysis and atmospheric dynamics. Daytime values of HONO average over the whole campaign at levels of (0.34 ± 0.24) .

On 30.07.2002, the measurements of atmospheric trace gas mixing ratios were interrupted and an experiment was performed. A heavy truck was parked closed to the measurement instruments and its Diesel engine kept running. As expected, concentrations of all trace gases with primary emissions as a source increased rapidly. NO reached at 12:41 UT, maximum

values of (791.3 ± 39.6) ppb, NO_2 (130.3 ± 1.1) ppb, (5.37 ± 0.43) ppb HONO, and HCHO to (29.6 ± 1.2) ppb. This corresponded to ratios by direct emission of $\text{HONO} : \text{NO}_x = (0.6 \pm 0.1)$ %, $\text{HONO} : \text{NO}_2 = (4.1 \pm 0.6)$ %, and $\text{NO}_2 : \text{NO} = (16.5 \pm 0.9)$ %. These values are in good agreement with other data reported elsewhere in literature [Ackermann, 2000; Kessler and Platt, 1984; Kurtenbach et al., 2001]. Later that day, ozone, as a product of photochemical oxidation of these primary emittants, reached (101.7 ± 7.1) ppb.

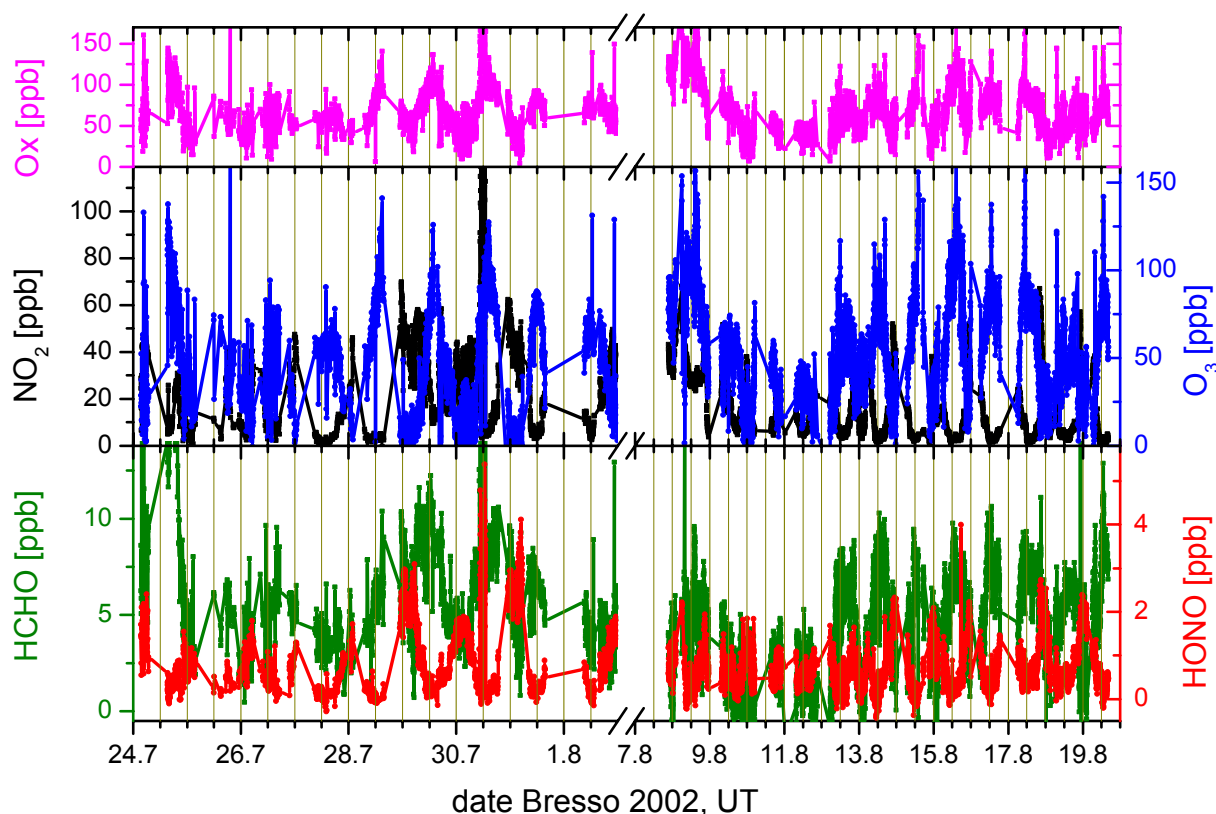


figure 4.17: DOAS trace gas data recorded during the Milan 2002 campaign. Lower graph: HCHO (green line, left scale), HONO (red line, right scale). Middle graph: NO_2 (black line, left scale), O_3 (blue line, right scale). Upper graph illustrates the Ox, the sum of NO_2 and O_3 . The errors of the measurements (refer to table 4.2) were omitted for a clearer illustration.

species	instrument	average detection limit (ppb)	Systematic error
HONO	DOAS	0.18	$\pm 6\%$
NO_2	DOAS	0.16	$\pm 9\%$
O_3	DOAS	4.8	$\pm 5\%$
HCHO	DOAS	0.86	$\pm 7\%$
NO	chemiluminescence	0.2	$\pm 5\%$
O_3	UV absorption	1	$\pm 5\%$

table 4.2: Average detection limits of trace gases during the Milan 2002 campaign.

Between 10. - 11.08.2002, a heavy rain period occurred. Consequently, all trace gas mixing ratios remain at very low levels of 10 ppb NO_2 during the night, 25 ppb daytime ozone, and thus 0.6 ppb HONO, 2.0 ppb HCHO respectively.

4.2.3 Additional Equipment at Bresso

4.2.3.1 In-situ Trace Gas Measurements

During this campaign, NO was measured by a commercial chemiluminescence device from Eco Physics (CLD 770 AL ppt). This method is based on the rapid light emission of NO₂ molecules, which are electronically excited by the reaction r. 2.9 of NO with ozone. The detected light signal is then proportional to the concentration of NO. Refer to the recent review on the application of chemiluminescence to atmospheric measurements by [Navas *et al.*, 1997] for more information. The system was calibrated, unfortunately, only before the campaign using 10 ppm NO in N₂, which was diluted with synthetic air to approximately 5 ppb. However, the calibration factor stayed constant compared to the re-calibration after the campaign. The absolute uncertainty of the NO measurements was ± 20 ppt composed of ± 12 ppt due to photon statistics and ± 15 ppt due to offset variability. Unfortunately, only manual data logging was available, thus, nighttime data are missing. NO mixing ratios of below 1 ppb were usually observed during the night. Values increased with the rush hour in the morning to approx. 60 - 80 ppb. On 31.07.2002, the experiment with a heavy truck parked directly close to the measurement instruments and the motor kept running was performed. Thus emissions of this Diesel truck were determined and inferences of the instruments tested. NO reached maximum values of (791.3 ± 39.6) ppb during that time.

Ozone was measured with a commercial short path UV-absorption instrument (Horiba, APOA 360) with a time resolution of 1 min and a detection limit of 1 ppb. Values undergo the expected diurnal variation: low levels below a few ppb during the night, as the titration with NO destroys the ozone, which is not reproduced in the absence of photolysis. Depending on photochemical activity, daytime values reach a maximum of 90 ppb.

The intercomparison of the data from the ozone in-situ monitor with those by the DOAS-White system showed very good agreement within the errors with a correlation coefficient of $R^2 = 95\%$, And a similar slope of (0.88 ± 0.02) , and intercept of (0.07 ± 0.05) , which is not significantly different than zero.

It is important to mention that the DOAS data have large errors, but a reduction would have been only accessible by measuring in a wavelength region farer in the UV with stronger absorption bands. However, as the main focus in this thesis was on nitrous acid, an additional ozone measurement would have reduced the DOAS time resolution, and thus O₃ was only determined in the HONO wavelength region.

4.2.3.2 Radiance Data

Radiance data were recorded during the Milan 2002 campaign again with an actinic flux spectroradiometer, Bentham DTM300. Its basic principles, characterization, and the setting used during this campaign were described above in chapter 4.1.2.3. The wavelength interval of 280 to 425 nm with a step-width of 1 nm yielding a temporal resolution of approx. 5 min was used to calculate $J(\text{NO}_2)$, $J(\text{HONO})$, $J(\text{O}^1\text{D})$, and $J(\text{HCHO})$. Photolysis frequencies for NO₂, HONO, O¹D and HCHO are zero during the night and peaked at noon on 30.07.2002 at $1.5 \times 10^{-2} \text{ s}^{-1}$, $2.5 \times 10^{-3} \text{ s}^{-1}$, $3 \times 10^{-5} \text{ s}^{-1}$, and $1 \times 10^{-4} \text{ s}^{-1}$, respectively, corresponding to life-times of 1 min, 10 min, 1 h, and 6 h respectively.

4.2.3.3 Aerosol Particles

The commercial optical particle counter (OPC) by Pallas (PCS 2000) was used for measurements of particles in the range of 154 nm and 10 μm diameters. The main parameters of this instrument and its settings during the campaign are described in detail in chapter 4.1.2.3. The inlet tube (2 m length) was mounted on top of the DOAS measurement container. The sum of particles (standardized to time of measurement, velocity of particles and volume of the measurement cell) again showed a diurnal cycle dominated by variations of the emissions. Values below 100 particles were observed during the low emission period on 07.08.2002 and a maximum of 600 particles is reached on 17.08.2002. The total surface area of these particles (calculated as spherical shape) was linked to that trend, but very low at maximum 150 μm^2 . Thereby, aerosols were again neglected for any relevance for possible location for the formation of atmospheric HONO.

4.2.3.4 Meteorological Data at Bresso

The vertical exchange coefficient was determined in Milan with an ultrasonic anemometer (type FMTU4-USA-1 standard, SN 2001-005008701, Metek, Elmshorn, Germany) that measured the 3-D wind field and the temperature with a 21 Hz frequency at 2.5 meters above the ground. The data were processed over 30 minute periods, which started exactly on the hour or half-hour. Coordinate rotation transforms, which result in zero vertical and transverse mean wind speeds are applied before the fluxes are computed [Stutz *et al.*, 2004a; Stutz *et al.*, 2002]. This ultrasonic anemometer was placed approx. 150 m away from the DOAS measurement container.

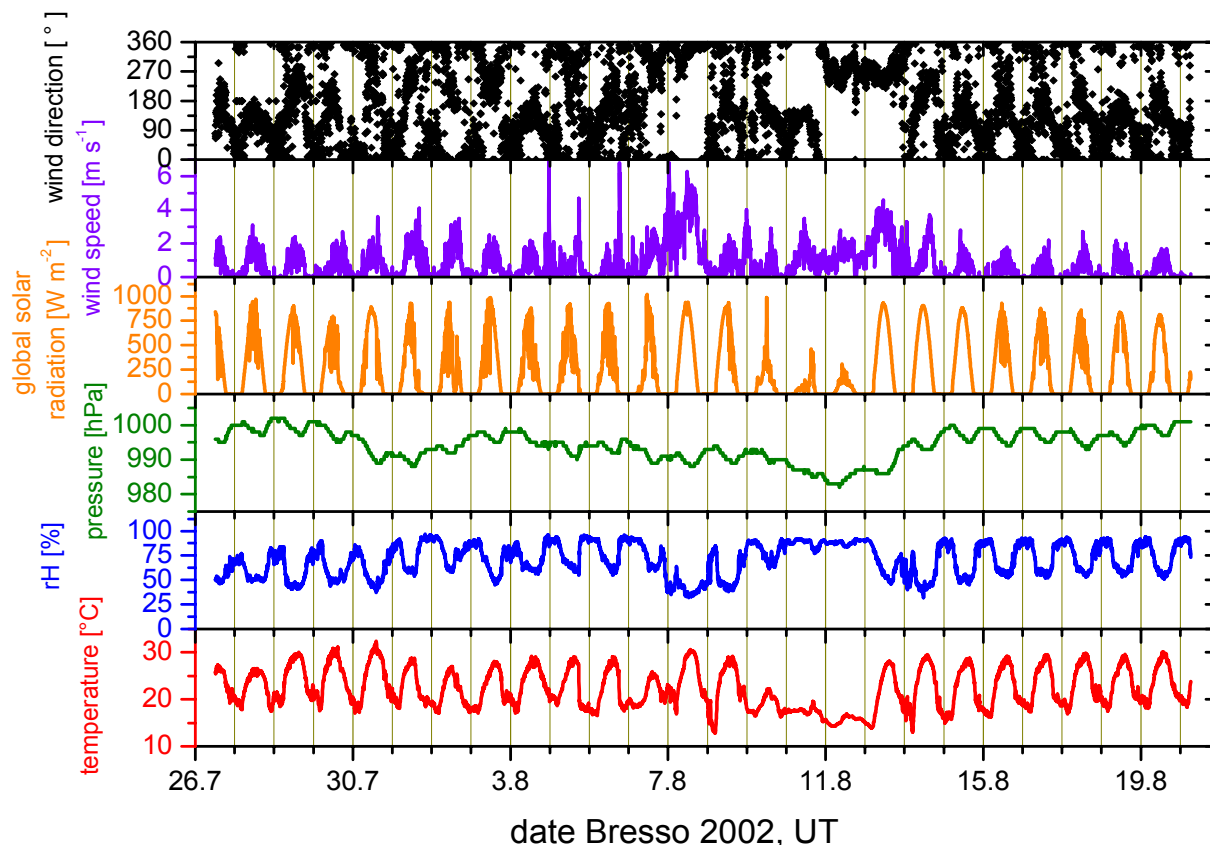


figure 4.18: Meteorological parameters recorded during the period of the Format campaign in July / August 2002.

Additionally, a commercial mobile weather station (Hoffmann Meßtechnik, Rauenberg, Germany) was operated in Bresso: Kipp & Zonen global radiance sensor (type CM11, SN CM11903077 – HMT 10182), THIES combined wind sensor (arch, vane, 3 half shells, SN 4.3155.21.908), psychrometer (SN 12696), wetting sensor (SN 13235), all recorded by the HMT data logger AME 70 (SN 024203), where also the pressure-sensor (Silicon element) and the temperature sensor (Pt – 1000) were included. A 2 m high tower was located approx. 30 m away from the DOAS container. The time resolution of these data was 5 min.

Except for the heavy rain period on 10. - 12.08.2002, all parameters show the expected diurnal variations (see figure 4.18). Temperatures reach 31 °C during the day, dropping down during the night to values of 13 °C. Relative humidity is anticorrelated, in a range from daytime values of 27 % on days with highest temperatures to usual 100 % during the nighttime. The wind speed was weak at 0 - a few m s^{-1} . Higher values were only observed before the rainy period on 07.08.2002. The wind was predominantly from northeast and southwest. On rare occasion, wind directions from Milan (south = 180°) were observed and wind directions showed sudden changes. Additionally, natural radon activity was measured routinely by the University of Milan, Italy and access to these data was offered.

4.2.4 Intercomparison of HONO Measurements

In addition to the DOAS measurements of nitrous acid, the BUGH Wuppertal operated the LOPAP II (long path absorption photometer) sampling system (see chapter 3.1.1.4 and [Heland *et al.*, 2001; Kleffmann *et al.*, 2002]), which is an in-situ measurement technique, based on a wet chemical sampling system and the photometrical detection of an azo dye produced in an acid solution out of the nitrite of the HONO. During the Milan 2002 campaign the instrument had a time resolution of 5 min and a detection limit of 2 ppt. The HONO mixing ratios determined by LOPAP (blue symbols) and by DOAS (red symbols) are illustrated in figure 4.19.

A previous intercomparison campaign was carried out in a smog chamber (CEAM) in Valencia, Spain with a DOAS White system showing a systematic deviation of 15 – 20 (c.f. [Heland *et al.*, 2001; Kleffmann *et al.*, 2002]). However, intercomparisons of this in-situ measurement technique and the spatial integration DOAS have not been performed outside in the real atmosphere.

The error of the HONO mixing ratios measured by DOAS is in the range of 200 ppt (see table 4.2). Values below the detection limit have to be handled with care and analysis on this kind of data is not valid. We therefore focus on the mixing ratios of HONO above the DOAS detection limit.

For an intercomparison of the DOAS data and those recorded by the LOPAP, we linearly interpolated the values to a common time-scale. A 10 min interval was chosen and values in this interval were error-weighted averaged. The error is thus calculated as a Gaussian propagation of the statistical error, the systematic errors (the residual noise structure of the DOAS respectively), and the detection limits. The linear regression yields (in figure 4.20) a correlation fit coefficient of 87 % with a slope of close to 1 within its errors (0.99 ± 0.02) and an intercept of (-13 ± 7) ppt, which is indistinguishable from zero.

For the correlation carried out in figure 4.20, both, daytime and nighttime values of nitrous acid were taken into account. The squares in figure 4.20 in the left-side region of lower values of HONO refer mainly to the daytime levels. It can be seen from figure 4.20 that the overall-values linear regression is valid for both daytime and nighttime HONO mixing ratios. Contrastingly to previous findings (e.g. by [Alicke, 2000]) the HONO measurements agree well for the different techniques and instruments. However, we have to mention that only a short 2 weeks measurement overlap was available from the Milan 2002 field campaign, which was further depleted by malfunctions of the DOAS White system during the first week.

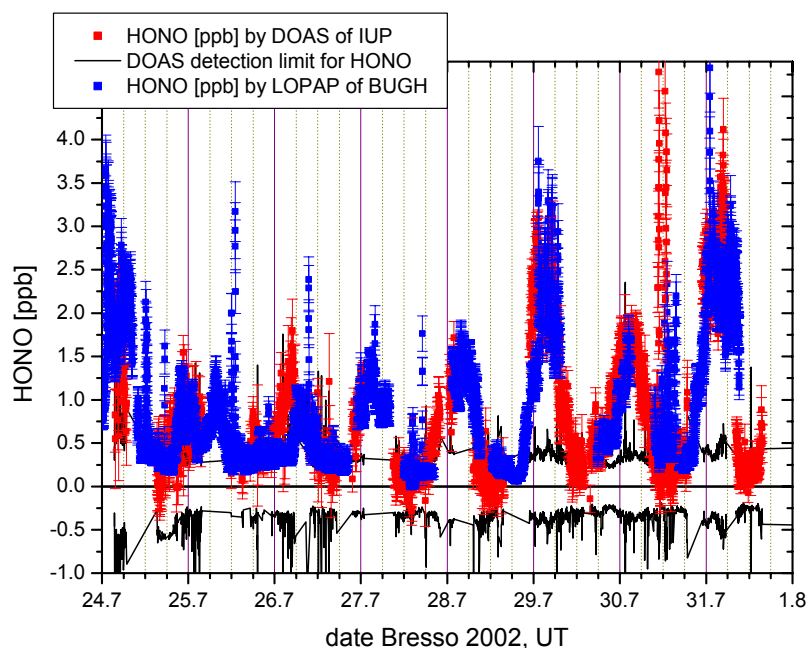


figure 4.19: Time series of HONO measured during the Milan 2002 campaign by the different HONO measurement techniques: DOAS data (red squares), DOAS detection limit (black line) and LOPAP (blue squares).

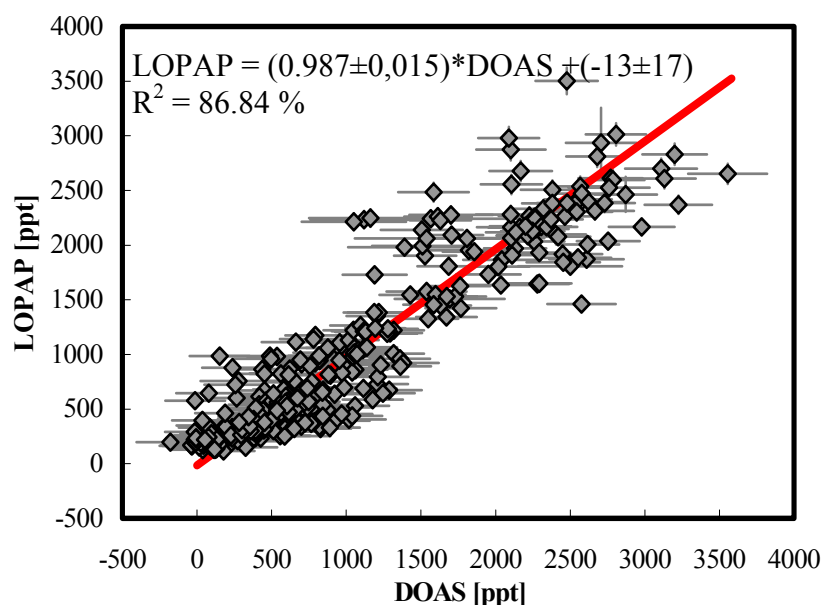


figure 4.20: Correlation between HONO measured by DOAS and LOPAP.

Additionally, we should note that the period, when the intercomparison between the two instruments for the atmospheric HONO detection is valid, was characterized by a monotonous meteorological situation of a cloudy and drizzly high-pressure period, a typical diurnal pattern of the temperature between 17 °C at night and 33 °C during the day, and very low wind speeds ($< 1.5 \text{ m s}^{-1}$) only in the afternoon (see figure 4.18). The directions of these low breezes often changed to a northern direction (see figure 4.18) during the afternoon. Due to the holiday season in Italy, traffic in Milan was significantly reduced. Thus, neither the plume from the polluted city of Milan nor direct emissions were detected at this time of the Milan 2002 campaign.

4.3 The Turm 2003 campaign: Vertical Profiles of HONO

One of the main topics of research activity on nitrous acid is the question of the primary location of the atmospheric HONO formation [Finlayson-Pitts *et al.*, 2003; Stutz *et al.*, 2002]. To distinguish between the two possibilities suspected (a ground-near source and formation on aerosols) the DOAS measurements of vertical trace gas profile are a powerful tool [Stutz *et al.*, 2002; Veitel, 2002]. Meteorological parameters are inalienable for an analysis of these profiles. Thus vertical profiles of trace gases and meteorology were measured during this thesis at the Research Center Karlsruhe, Germany between 03.–16.06.2003, where a 200 m high meteorological tower with continuously working meteorological instrumentation is available. Groups of the Bergische Universität und Gesamthochschule Wuppertal, Germany (BUGH) and the Forschungszentrum Karlsruhe GmbH, Germany (FZK) were participating during this campaign as well. We will now describe the measurement location in more detail, the DOAS instrumentation and retrieval of vertical profiles as well as the equipment of the other groups.

4.3.1 The Area of the FZ Karlsruhe and the Meteorological Tower

4.3.1.1 The location of the Forschungszentrum Karlsruhe

The Forschungszentrum Karlsruhe (FZK) is located (48°55' N, 8°22'E; 110 m a.s.l.) in a semi-rural region in the upper Rhine valley, Germany. It is 15 km north of the city of Karlsruhe (see figure 4.21), surrounded by a forest on the western side, a highway and the Rhine River on the eastern side. The comprising forest is mixed forest, typically for southern Germany. Only very small cities (thus causing only low direct emissions of NO_x) are directly enclosed, though bigger cities (e.g. Karlsruhe in the south and Bruchsal in the north) and a high-frequented interstate highway more in the west might influence the measurements. An oil-refinery is sited on the northern end of Karlsruhe, which, evidently, emits high amounts of atmospheric pollutants and thus high NO_x levels might originate from this source. Air mass trajectories calculated by the FZK will be presented in the next chapter and help to exclude situations influenced by this direct NO_x source.

The area of the research center itself can be seen in more detail from the air photograph and schematic birds-eye view of figure 4.23. Several buildings are close to the IMK headquarter, where the DOAS telescope was sited at a height of 20.5 m pointing towards the meteorological tower. The building density is obviously much less than in a city and several are storehouses or big experimental halls with one or two floors only. Some rise to near 40 m. Additionally, the FZK has its own industrial power plant located in the north-eastern area of the FZK being a strong local source of NO_x and other pollutants. Its plume might also cause interferences in the measurements at the meteorological tower. Using wind speed and wind direction data measured at the tower, we will discard also these situations in the next chapter of the data analysis.

4.3.1.2 The Meteorological Tower

The meteorological tower itself is sited in a forest clearing at the north-western end of the FZK, close to the street in front of the research center. On average, the trees rise to

approximately 25 m, defining a new surface roughness and z_0 (see chapter 2.5). The tower consists of a steel-scaffold in a cubic form of 3 x 3 m, narrowing to 1.5 x 1.5 m from 100 m to the top of 200 m. The frame is unbent by thick steel cables to stabilize the tower and minimize horizontal movements supported from of (strong) horizontal wind. Platforms are mounted in 10, 20, 30, 40, 50, and 100 m. Inside the frame, a lift is operated, driven by an old commercial VW-Gulf I automobile motor. Emissions of NO_x and other pollutants from burning the high impure gas in this motor as well as other disturbances of the measurements caused by this lift will also be discussed in the next chapter.

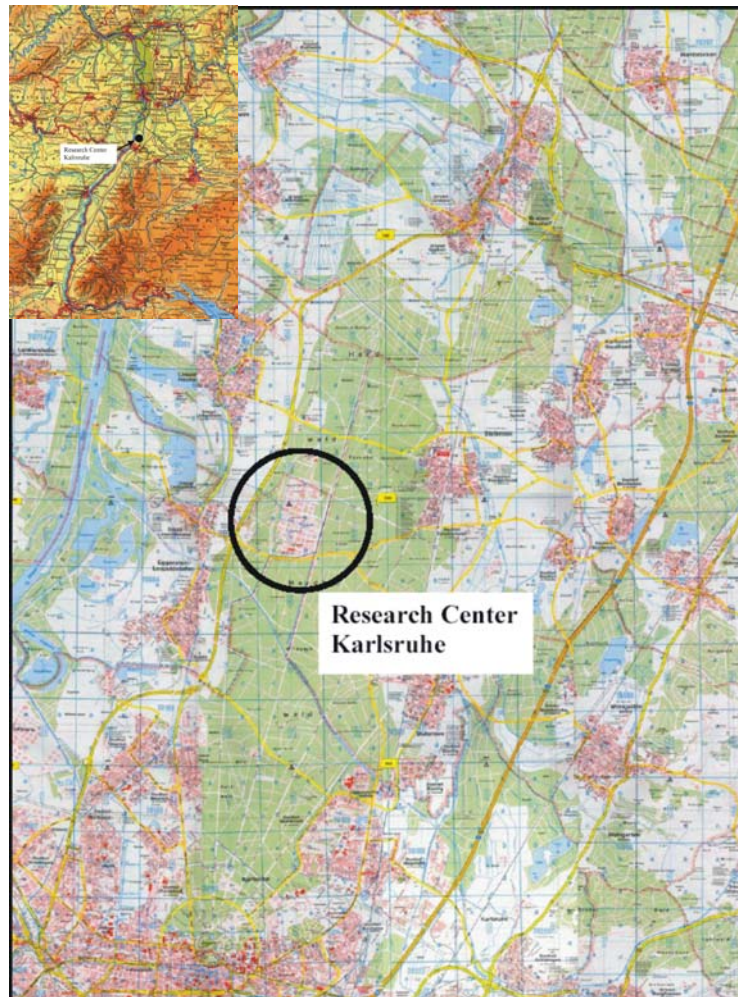


figure 4.21: *Map of the area of the Research Center Karlsruhe. The research center is located in a forest closed to a highway, approximately 15 km north of Karlsruhe city.*

The meteorological instrumentation of the tower and the density of measurements stations is of a very high quality (see also figure 4.22): the wind speed is measured in western and eastern direction at 20, 30, 40, 60, 80, 100, 130, 160 and 200 m, the wind direction in western direction at 40, 60, 80, 100, 160, 200 m, and additionally an anemometer is mounted at 40, 100 and 200 m, the temperature on the eastern side at 30, 60, 100, 130, 160, 200 m, the humidity by capacitive sensor at 30, 100, 200 m.

Additional meteorological measurement equipment is located directly on the ground, where short-wave and long-wave global radiance, pressure, and precipitations are measured. On an additional tower of 10 m height, the instruments for measuring the temperature, humidity, and wind speed and an anemometer are mounted (see right side of figure 4.22).

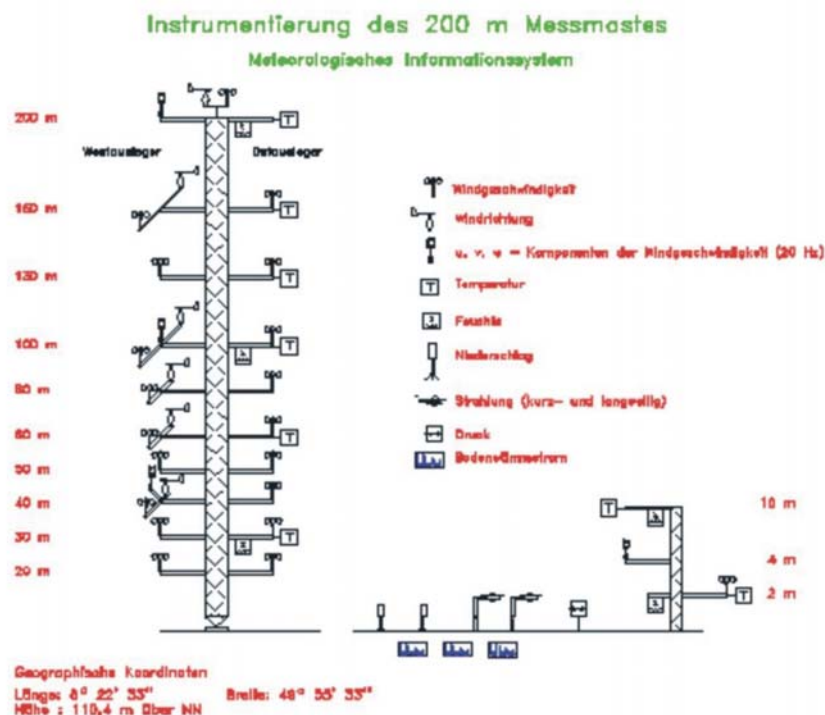


figure 4.22: *Technical sketch of the Meteorological Tower of the Research Center Karlsruhe.*

Temperatures at 2 m height vary between 30.8 °C during daytime on 10.06.2003 and decrease to 14.1 °C during the night (e.g. on 10.06.2003). The relative humidity measured in 2 m height follows this trend inversely with maximum values of 100 % during all nights except 08.06.2003 and 42.4 % in the afternoon of the 09.06.2003. The horizontal wind at 100 m height is roughly constant and weak at 0.6–4.8 m s⁻¹ from 05.06.2003 and increases during the afternoon of the 08.06.2003 to a maximum value of 8.5 m s⁻¹. The wind direction does not show any regular diurnal trend. Caused by a power failure, no meteorological data are available after 10.06.2003, 14:00.

4.3.2 The Active Long Path DOAS System

As was already described in chapter 4.1.4, the semi-commercial active LP-DOAS system was used to measure the trace gases NO₂, O₃, HONO, and HCHO. Again, we will only briefly discuss the specifications of the instrument used at this measurement station (refer to chapter 3.2 and literature therein for a more detailed description of the DOAS system).

A 500 W Xe high-pressure arc lamp (PLI Hanovia SX5002 SN 201580) was used as light source. The parabolic main mirror of diameter of 200 mm and a focal length of 600 mm in the telescope. Light coupling to the spectrograph was performed by a standard 200 μm monofiber (AS UV..VIS 200/220/245 μm, NA = 0.12, length 3 m). The spectrograph itself was again a Czerny-Turner spectrograph (ACTON Spectra Pro 300i: 200 μm entrance slit, focal length 300 mm, aperture 1 : 4 (i.e. NA = 0.12), dispersion of the grating (1800 grooves / mm) used 0.54 nm / mm, spectral interval from 330 to 370 nm corresponding to 0.038 nm / channel on the photo diode array). The spectrograph is isolated and its temperature stabilized by electrical heating at 33°C. The standard type of a detector (Hoffmann Meßtechnik, Rauenberg) was used: a 1024 diode array (Hamamatsu S3904-1024N), cooled by a Peltier element to (-13 ± 0.3) °C.

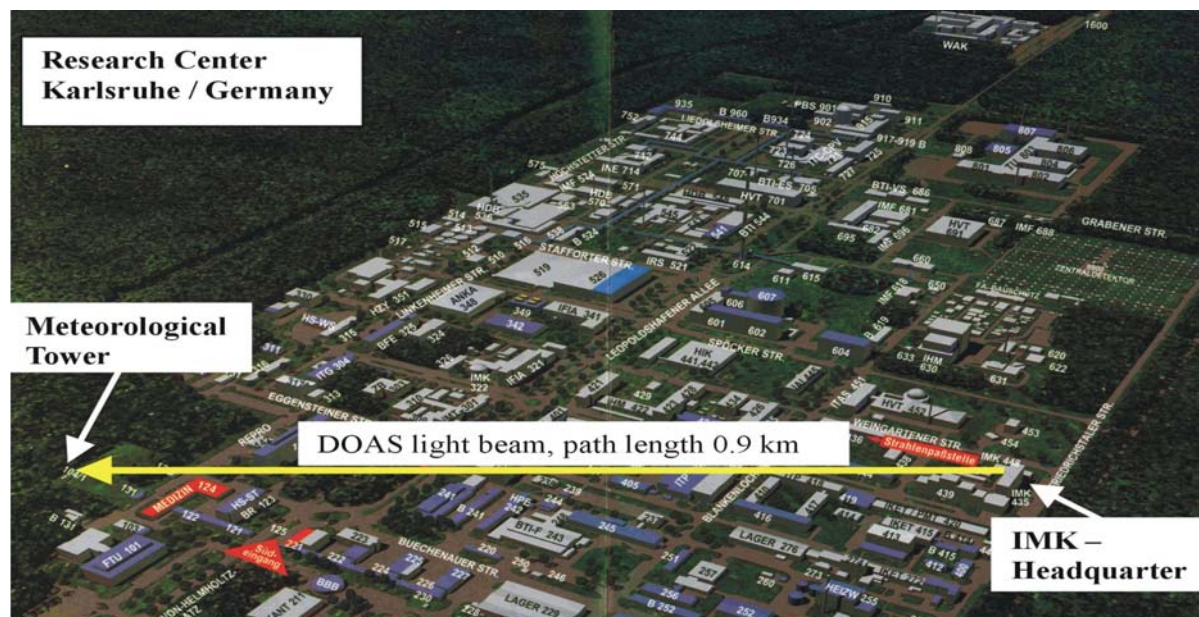


figure 4.23: Air photograph and schematic birds-eye view of the Forschungszentrum Karlsruhe. The IMK headquarter, where the DOAS telescope was located and the Meteorological Tower, were the retroreflectors were mounted mark the end-points of the DOAS light path(yellow line).

For the measurements at the FZK, the HMT-DOAS instrument was set up in a laboratory on the 6th floor of the main building of the Institut für Meteorologie und Klimaforschung (IMK, Institute for Meteorology and Climatology). For the needed visibility, only a light path length of 0.9 km (one-way) could be realized. The beam pointed from the headquarters of the IMK towards the meteorological tower. In a height of 40 (LP1), 100 (LP2), and 200 m (LP3) retroreflector-arrays of 16 retroreflectors at each height were mounted. The purpose of the highest light-paths was to measure, at least partially, above the boundary layer, especially during the nights.

As discussed in chapter 3.2, DOAS detection limits vary with the length of the light path, the differential cross-section of the trace gas, and the systematic and statistical 1σ - error of the fit [Stutz and Platt, 1996], and were defined in this thesis by multiplying this random 1σ - error by a factor of 2 yielding results as summarized in table 4.3.

light path name	reflector height [m]	light path length [m]	detection limit [ppb]			
			NO ₂	HONO	O ₃	HCHO
LP 1	40	887.0	0.42	0.31	5.9	1.2
LP 2	100	890.4	0.43	0.34	5.8	1.2
LP 3	200	904.7	0.44	0.41	5.4	1.2

table 4.3: Characteristics of the three light paths. The reflector locations are listed as height above ground. The light path lengths are given as twice the distances to the reflector, which is the actual absorption path in the atmosphere. The detection limits (defined as the 1σ -error multiplied by a factor of 2) are the mean values for the whole campaign.

Due to the limitation of the maximum light path lengths within the perimeter of the FZK to ~ 1800 meters, daytime measurements of NO₂ are generally of a “lower-risk” than those of HONO as daytime mixing ratios range typically between 10 and 40 ppb in the PBL. The differential cross-section allows detection limits well below 1 ppb for such light path lengths. However, the DOAS data were evaluated for the HONO mixing ratios as well, but have to be handled with care due to the high detection limit (see table 4.3).

The results of the DOAS trace gas measurements for NO₂, HONO, O₃, and HCHO on the different light paths so far include information of the heights below. Further corrections and calculations are needed to obtain information for a specific height interval.

4.3.3 Retrieval of trace gas profiles from LP-DOAS data

4.3.3.1 Deconvolution of Temporal and Spatial Information

The data evaluation from raw DOAS spectra is described in chapter 3.2. However, LP-DOAS measurements yield only the mean concentrations integrated over the different light paths including all information from the heights below (integrated vertical column). Thus, spatial distributions of the trace gases need to be calculated from LP-DOAS trace gas measurements using reflectors mounted on the different heights h_i of 40, 100, and 200 m as follows (described in more detail in [Alicke *et al.*, 1999; Stutz *et al.*, 2004a; Stutz *et al.*, 2002; Veitel, 2002; Veitel *et al.*, 2002]).

Sequential measurements were performed for each height: starting at the lowest height of 40 m (background and scattering light additionally directly afterwards (see chapter 3.2), then repeating this procedure at 100 m, and finally at 200 m. Thus, a temporal spacing exists between the measurements of the three light paths, which inhibit the direct calculation of vertical profiles and the evaluation and distinction of chemical and physical processes in the PBL. All data need to be linearly interpolated to a common time-scale. The errors caused by this interpolation are dominated by the individual measurements, which were used to compute the error for the interpolated concentrations by Gaussian error propagation. We define the start of the first measurement at LP height 1 until the end of the last spectrum taken at LP height 3 as one time-interval of a vertical gradient. The arithmetic mean of this interval is the center time of a vertical profile.

Next, the boundary layer is divided into parallel horizontal layers with upper and lower limits defined by the reflector heights yielding height intervals of 0–40 m, 40–100 m, and 100–200 m minus the height of the DOAS telescope $H = 20.5$ m. Assuming the vertical concentration gradient is constant or linearly decreasing or increasing in each layer, the mean concentrations c_i in the layers can be calculated from the mean concentrations \bar{c}_i measured over the light paths. The concentration in the lowermost layer is measured directly:

$$c_1 = \bar{c}_1 \quad \text{eq. 4.3}$$

For the following light paths, the measured concentrations are assumed to be composed of the mean concentrations in the layers passed en route to / from the respective reflector. The concentrations are summarized and weighted by the height of the respective layer and the concentrations in the layers can be calculated using only the measured mean concentration and the reflector heights of the current and the previous light path:

$$c_i = \frac{(h_i - H) \cdot \bar{c}_i - (h_{i-1} - H) \cdot \bar{c}_{i-1}}{h_i - h_{i-1}} \quad \text{eq. 4.4}$$

with $i = 2$ for the height interval of 40–100 m and $i = 3$ for the interval of 100–200 m. The errors of the mean concentrations c_i can be calculated neglecting the errors of the reflector

heights. These can be measured with high precision of approx. 0.1 m, based on the Gaussian propagation of the errors of the individual path-averaged concentrations by:

$$\Delta c_i = \sqrt{\left(\frac{\Delta \bar{c}_i \cdot (h_i - H)}{h_i - h_{i-1}}\right)^2 + \left(\frac{\Delta \bar{c}_{i-1} \cdot (h_{i-1} - H)}{h_i - h_{i-1}}\right)^2} \quad \text{eq. 4.5}$$

Applying this calculation procedure to the DOAS data, we get the spatial distribution of the trace gases NO₂, HONO, and O₃ as presented in figure 4.25. Measurements were performed for all three heights continuously from 03.–16.06.2003, except the night of the 15.06.2003, when reference spectra were taken and instrumental characterization was performed.

4.3.3.2 Error Estimation and Limitations of the DOAS Vertical Profiles

Some additional comments are necessary for the interpretation of DOAS vertical profiles and for the error estimation of these data. We have already mentioned, in chapter 3.2 that DOAS-measurements of trace gas concentrations always represent an average value over a large air mass in time and space. Thus LP-DOAS is highly sensitive to the horizontal transport and vertical and horizontal inhomogeneities of the air mass [Stutz *et al.*, 2004a; Stutz *et al.*, 2002]. However, point measurements also yield an average over time and space only, as the horizontal wind system transports an usually inhomogeneous air mass past the sampling inlet of the measurement device during its sampling time. For our set-up of the LP-DOAS system with a distance between telescope and reflector of approx. 2 km and a weak tropospheric wind speed of 1 m s⁻¹, the horizontal averaging time for the observed air mass is about 30 minutes along the light path. As the integration times for the DOAS system was in the range of 1 min, this value adds up to the averaging time [Stutz *et al.*, 2004a; Stutz *et al.*, 2002].

Very often, DOAS light paths are not only separated in the vertical, but also to some extent in the horizontal. Therefore one has to ensure that the concentrations c_i , do indeed yield information about the vertical distribution of trace gases in the respective height intervals, and are not influenced by horizontal inhomogeneities [Stutz *et al.*, 2004a; Stutz *et al.*, 2002]. The degree of the horizontal trace gas homogeneity can easily be determined by a simple comparison between light path characteristics. With our setup during the Turm 2003 campaign, geometric considerations reveal that the three light paths overlap by 100% in their horizontal coverage, but by only 40 % for LP 1–LP 2 and 50 % for LP 2–LP 3 in the vertical coverage. Thus, horizontal inhomogeneities in trace gas concentrations should not lead to differences in the observations, and vertical gradients can be observed.

Another method to study the horizontal mixing of an air mass is the comparison of the temporal behavior of trace gas concentrations from the DOAS and the in-situ measurements [Stutz *et al.*, 2004a; Stutz *et al.*, 2002]. Concentration changes due to the advection of air masses that are well mixed on scales larger than the length of the DOAS light paths lead to similar concentrations in the DOAS and the in-situ observations. In contrast, plumes that are smaller than the extent of the DOAS light paths lead to a stronger response in the in-situ data. During periods, when the in-situ instruments remained at 10 m height (see chapter 4.3.4), different from the DOAS light paths, this test is not valid. However, during movements of the towers lift to obtain vertical profiles by the in-situ instruments (this was performed during the days and in the night of the 11.06.2003), we could detect these plumes. In the next chapter, we will show that a number of small scale plumes passed over the FZK area and the meteorological tower causing a sudden increase in the concentration of the in-situ instruments and in only one of DOAS light path, but not in the others.

After performing the tests described above, we identified periods when a comparison between the DOAS data on different light paths indicates that the air mass was horizontally well mixed. In addition, the temporal behavior of DOAS and in-situ measurements showed a very

good agreement, strengthening this conclusion. The DOAS data during these periods thus clearly allow the derivation of vertical trace gas profiles. In the following chapters of our data analysis, we will thus focus on the period of 05.–11.06.2003, when the data of the different instruments and groups have their best overlap and a complete dataset is available. Within this period, various meteorological situations and different emission scenarios are included.

Finally, we should state that this averaging over both temporal and spatial variations of the concentration is an advantage in situations when strong local variations distort the overall picture of the atmospheric processes. This is particularly important as a time resolution of some minutes is sufficient to describe most processes taking place in the atmosphere from the measurements (see e.g. [Stutz *et al.*, 2004a]). DOAS data measured on different light paths, and the comparison with in-situ data as described above, offer a powerful tool to investigate the spatial distribution of trace gases. For example, this method allows the determination of how representative in-situ measurements are for a larger area, and thus helps in the extrapolation of point data to larger scales, such as those used in air pollution models.

4.3.3.3 Calculation of Vertical Gradients

The concentrations c_i of a trace gas, e.g. NO_2 and HONO, already corrected for the contribution of the lower light-path(s) $i-1$ as discussed in detail in chapter 4.3.3.1, usually decrease or increase with the altitude z above the ground. Linking these mixing ratios with that in the layer below, one obtains the absolute concentration gradient:

$$\frac{dc}{dz} = \frac{c_i - c_{i-1}}{z_i - z_{i-1}} \quad \text{eq. 4.6}$$

which is a measure for the variations of concentrations by the altitude due to mixing and transport of the PBL, but also chemistry occurring in the ascending or descending air masses. Normalized by the trace gas concentration in the lowermost layer, the relative gradient is defined by:

$$\left(\frac{dc}{dz}\right)_{rel} = \frac{dc}{dz} \cdot \frac{1}{c_1} = \frac{1}{dz} \cdot \left(\frac{c_i}{c_1} - 1\right) \quad \text{eq. 4.7}$$

During our measurements, the height intervals were constant for the whole period of the campaign and thus the factor $1 / dz$ can be omitted. However, the sign of a trace gas gradient indicates its flux is pointing upwards, if it is positive or downwards, i.e. the mixing ratio decreases with height over ground, for a negative sign respectively. A higher absolute value of a trace gas gradient ($\text{abs}(dc_i / dz)$), which depends on the difference between the trace gas concentrations between the two respective layers, yields a steeper profile of the corresponding trace gas.

Generally, one may calculate vertical fluxes and deposition velocities from the gradients of a trace gas for a detailed analysis, further requiring the meteorological data for the friction velocity u^* and eddy diffusion constant K as described in chapter 2.5. However, during our measurements of vertical profiles of HONO and NO_2 during the Turm 2003 campaign, only a minimum height of 40 m for the light beam could be realized. Additionally, this light path crossed several surface types (asphalt roads, but also the forest closer to the meteorological tower), and not a single representative monotype surface. Thus, it seems at least rather questionable to calculate deposition velocities on the ground from our data. We will therefore use those presented by [Alicke, 2000; Stutz *et al.*, 2002], who studied in detail the dry deposition of NO_2 and HONO on a grass surface for the polluted nighttime atmosphere at near neutral or slightly stable or unstable conditions.

4.3.4 Additional Equipment and cooperating groups

Except the meteorological data obtained in a continuous mode operated by the FZK at the tower, additional equipment was used during the Turm 2003 campaign.

4.3.4.1 Ozone Measurements

Ozone was also measured by a commercial short path UV-absorption instrument (Horiba, APOA 360) with a time resolution of 1 min and a detection limit of 1 ppb at the IMK headquarter closed to the DOAS telescope. Data received from this in-situ monitor and the DOAS are, with respect to the different air masses observed, in good agreement at a linear correlation of $R^2 = 83.9\%$, with a slope of (1.14 ± 0.03) and an intercept of (9.2 ± 0.16) .

4.3.4.2 The Radiance Data

At 100 m, the photolysis frequency of NO_2 was measured by the IUP with a $4\text{-}\pi$ -steradian filter-radiometer (Meteorology Consult, $4\pi \text{ sr } \tilde{J}(\text{NO}_2)$ Radiometer Nr. 631 / 632). This instrument was mounted on a lateral extension bar fixed to the towers frame to exclude shadow effects of the tower. HONO photolysis frequencies were calculated based on [Hofzumahaus *et al.*, 1999].

4.3.4.3 Natural Radon Activity and Atmospheric Dynamic

At heights of 30 m and 100m at the meteorological tower and at a height of 2 m on the meadow closed to the tower, natural radioactivity in the atmosphere was measured by the IUP as an indicator of the atmospheric stability [Allegrini *et al.*, 1994; Cuntz, 1997; Doerr *et al.*, 1983; Genthon and Armengaud, 1995; Jacobi and André, 1963; Levin *et al.*, 2002; Liu *et al.*, 1984; Perrino *et al.*, 2001]. Therefore, the progeny of ^{222}Ra attached to the aerosol is collected on a filter and subsequently analyzed online by α -spectroscopy. The measurement technique and the Rn-monitor developed and used at the IUP is discussed in detail by [Cuntz, 1997; Levin *et al.*, 2002]. The absolute values of the radon activity and its diurnal cycle are dominated by the radon flux from the ground and the atmospheric dynamics.

As expected (see figure 4.24 and chapter 2.5.4), radon activity reaches its minimum of 1 Bq m^{-3} during the night and increases with atmospheric stabilization during the night to values of 12 Bq m^{-3} in the late morning of the 07.06.2003. This indicates an atmospheric dynamic as expected from basic theory presented in chapter 2.5.

In the nights of the 06.06., and 09.06., and partially on 11.06.2003, radon activity remains at its low afternoon level, indicating the absence of atmospheric stabilization during these periods.

As radon has a well-defined and constant ground-based source of approx. $(70 \pm 5) \text{ Bq m}^{-2} \text{ h}^{-1}$ [Levin, 2003], a decrease of radon with the altitude corresponding to the decreasing aerosol profiles is expected. From this decrease, eddy diffusion constants, K_z , can be calculated (see chapter 2.5.4). However, the absolute radon activity values are higher (or even equal) in 100 m than in 30 m. This phenomenon was also observed by [Levin, 2003] at other sites during the summer 2003, and is believed to be caused by advection, but requires further investigation [Levin, 2003].

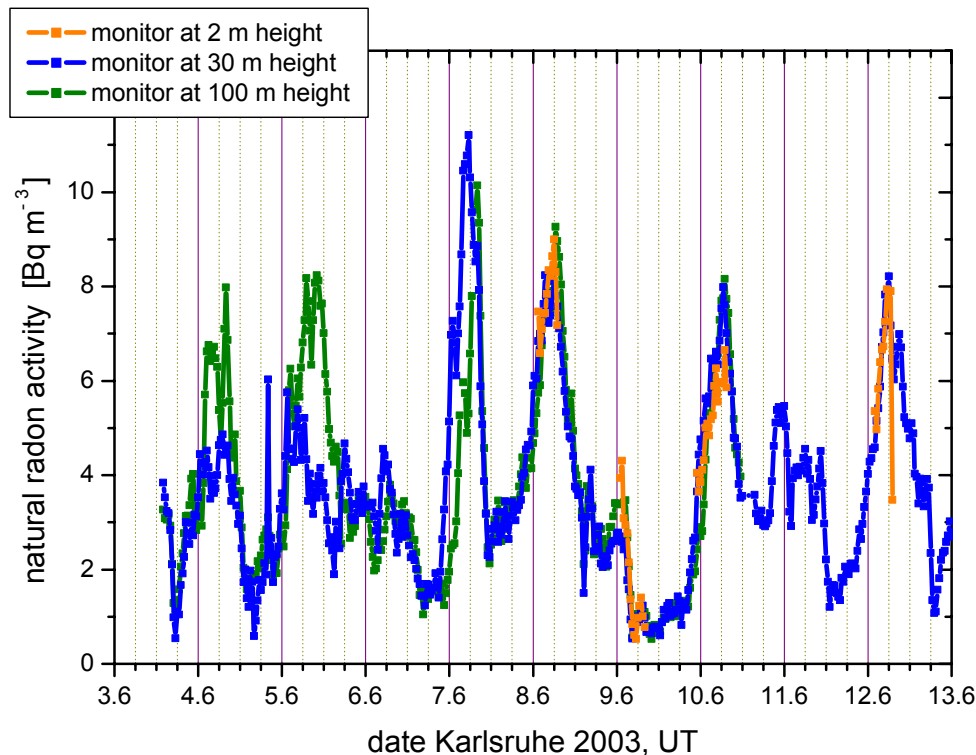


figure 4.24: Natural radon activity measured by the IUP during the Turm 2003 campaign.

4.3.4.4 In-situ Instruments of cooperating groups at the Tower

As already performed during a previous campaign [Kleffmann *et al.*, 2003; Vogel *et al.*, 2003] at the meteorological tower of the FZK, the BUGH Wuppertal operated a LOPAP II sampling system (see [Heland *et al.*, 2001; Kleffmann *et al.*, 2002] and chapter 3.1.1.4 of this thesis). During the campaign the instrument had a time resolution of 3.5 min and a detection limit of 3 ppt.

NO and NO₂ were measured with a commercial NO_x monitor (Unisearch Luminox LMA-4), which was calibrated with certified NO and NO₂ gas mixtures. In the instrument NO₂ is directly measured while NO is detected after conversion to NO₂ by a CrO₃ converter. The detection limits for NO₂ and NO were 50 and 100 ppt, respectively. The particle size distribution was determined with a scanning mobility particle sizer (SMPS: TSI Inc. DMA model 3071A, CNC model 3022A). The surface area density of the particles was determined from the size distribution under the assumption of a spherical shape of the particles. Particles in the diameter range 12–750nm were measured by the instrument, which represent the dominant fraction of the urban aerosol surface [Seinfeld and Pandis, 1998].

All these instruments were mounted in a closed box on the roof of the lift of the meteorological tower. The sampling unit of the LOPAP II instrument and the inlets of the stainless and PFA tubes for the SMPS and the NO_x-monitor, respectively, were installed on the top of this box (for more information on these instruments and their setup for the measurements of vertical profiles at the meteorological tower of the FZ Karlsruhe refer also to [Kleffmann *et al.*, 2003; Vogel *et al.*, 2003]).

During the night the instruments remained at the lowest possible height of 10 m at the tower, which is still in the forest. By the reason of this totally different measurement location, an intercomparison to the DOAS trace gas data is not valid. It was intended as a fourth measurement height supplementing the DOAS profiles. For the gradient measurements the lift was moved in an altitude range of 10–190 m with stops at 10, 40, 100, 130 and 190 m. The

mixing ratios of the different compounds were continuously measured for typically 15 min at each altitude. To minimize influences of the lift motor, the engine was operated for only 3 min during the ascent and descent between different altitudes.

4.3.5 Time Series of Traces Gases

In chapter 4.3.6, we will give a qualitative analysis of vertical profiles of the trace gases HONO, NO₂, and O₃ with special respect to influencing parameters. However, one has to ensure that the chosen period for this 24-hour analysis is either representative or at least suitable. Thus, we will now give an overview of the time series of the trace gases obtained during the Turm 2003 campaign.

4.3.5.1 Temporal Trends of O₃ and HCHO

Generally, in all layer heights, ozone was found to undergo a strong diurnal variation (see figure 4.25), as expected from the Leighton relationship and already discussed in more detail in chapters 4.1.2.2, and 2. Low values of (6.5 ± 4.9) ppb during the night (e.g. on 07.06.2003) around the detection limit of the DOAS instrument were observed when the reaction $r. 2.9$ of NO destroyed O₃ yielding NO₂. Nighttime mixing ratios were similar in all boxes at its different altitudes, except on 07.06.2003 (see figure 4.25 and the discussion below). Thus, no gradients in the ozone levels were observed for the different altitudes. During the night of 11.06.2003, coincident with a weak atmospheric stabilization (see figure 4.24), ozone mixing ratios remain rather constant at (33.9 ± 3.2) ppb (see figure 4.25), but again similar in all height-boxes. After sunrise and the onset of photooxidation of NO_x in the troposphere, ozone values increase during the day up to (132.2 ± 3.5) ppb on 12.06.2003 (see figure 4.25). No daytime gradients between the different layer heights above the error range could be observed for O₃, except on 12.06., and 13.06.2003 (see below).

For the majority of the campaign, formaldehyde concentrations do not show any significance with respect to its error: neither vertical gradients, nor a clear diurnal variation. Values range between (0.2 ± 0.2) ppb up to (7.4 ± 0.6) ppb during day as well as during the nights in all heights (see figure 4.25). Only at noon of 12.06.2003 a peak maximum mixing ratio of (11.1 ± 0.9) ppb was observed. In combination with the high ozone levels of (132.2 ± 3.5) ppb measured during that time (see above and figure 4.25), a period of high photochemical activity, or a smog event might be identified. Unfortunately, no meteorological data are available for that time, thus no horizontal advection of polluted air masses could be excluded.

4.3.5.2 Time Series of HONO, and NO₂ in Different Altitudes

Very often, NO₂ mixing ratios were very low at (0.5 ± 0.2) ppb during daytime on 09.06.2003 and even below (8.7 ± 0.2) ppb in the same night (see figure 4.25). Only a weak diurnal trend but no gradient between the different heights could be observed during that time. On 05.06., 07.06., and 12.06.2003, values reach higher nighttime levels of up to (45.4 ± 0.2) ppb, but daytime mixing ratios again drop down to some (0.5 ± 0.2) ppb around the detection limit (see figure 4.25). During this period, a stronger diurnal cycle and a clear gradient with higher mixing ratios in the lower box could be found and will be discussed in more detail in chapter 4.3.6.

In general, the diurnal variation of NO₂ is likely dominated by three effects. First, an anti-correlation of NO₂ levels to the solar radiation is already expected from the Leighton relationship and a photostationary steady state between NO, NO₂ and O₃ is established (see

chapter 2.2.1). Second, direct emissions cause additional morning and evening peaks during the rush hours. Finally, atmospheric dynamics can cause higher concentrations of NO_2 closer to the ground under conditions of high stability of the PBL due to weaker vertical transport. We will discuss the different influencing parameters qualitatively in chapter 4.3.6, but from a quantitative point of view, only a complex model treating both chemistry and transport as well as their interlink will be able to distinguish between the different processes contributing. Nitrous acid showed the suspected diurnal variation, explained in chapter 2.3.2: values increasing with the nighttime stabilization of the atmosphere, and rapidly decreasing with sunrise to low levels of some ppt during daytime due to its rapid photolysis and dilution by the stronger vertical mixing.

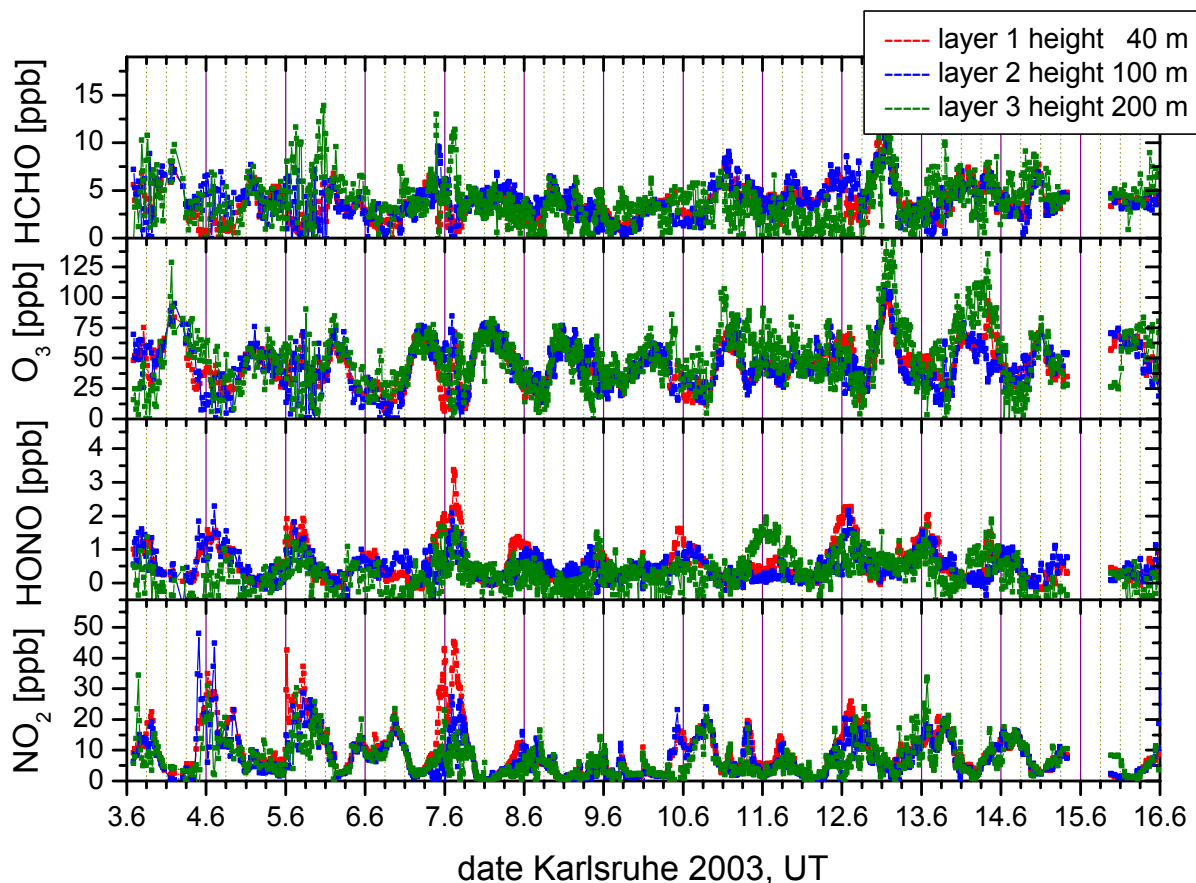


figure 4.25: Measured DOAS concentration–time series of NO_2 (lowest graph), HONO, O_3 , and O_x (upper plot) during the Turm campaign in June 2003. The data are correction for spatial height information from the light paths below: red line for the height interval of 0–40 m, blue line for that of 40–100 m, and green lines for the values measured in the upper interval of 100–200 m. The errors of the measurements were omitted for a clearer illustration. The errors and detection limits on the different light paths are listed in table 4.3.

Nighttime mixing ratios of HONO often reach (1.9 ± 0.3) ppb only in the lowest layer on 05.06.2003, but (1.3 ± 0.4) ppb in the middle and (1.0 ± 0.8) ppb in the highest layer (see figure 4.25). Accordingly, a gradient pointing downwards could be observed for most of the nights of the Turm 2003 campaign. The strongest gradients were recorded on 05.06., and 07.06.2003 (see figure 4.25), and a clear link to the trend of the higher NO_2 concentrations during these nights on the lower light paths. During the night of 11.06.2003, (0.4 ± 0.1) ppb HONO was found in the lowest, (0.3 ± 0.1) ppb in the middle layer, but contrastingly highest

levels of (1.5 ± 0.5) ppb in the upper box (see figure 4.25). Unfortunately, no meteorological data are available for that period of the Turm 2003 campaign, so advection cannot be excluded.

4.3.5.3 The Altitude Dependent HONO-to-NO₂ ratio

The HONO to NO₂ ratio (c.f. the slope in figure 4.26) during the Turm 2003 field campaign has mostly been around (5 ± 1.5) % in the lowest box and generally increased through the night up to ~ 10 % shortly before sunrise whereon it decreases again with a rate mainly depending on solar radiation after dusk. The ratio showed some distinctive peaks up to 40 %, which cannot be quantified in the absence of meteorological data.

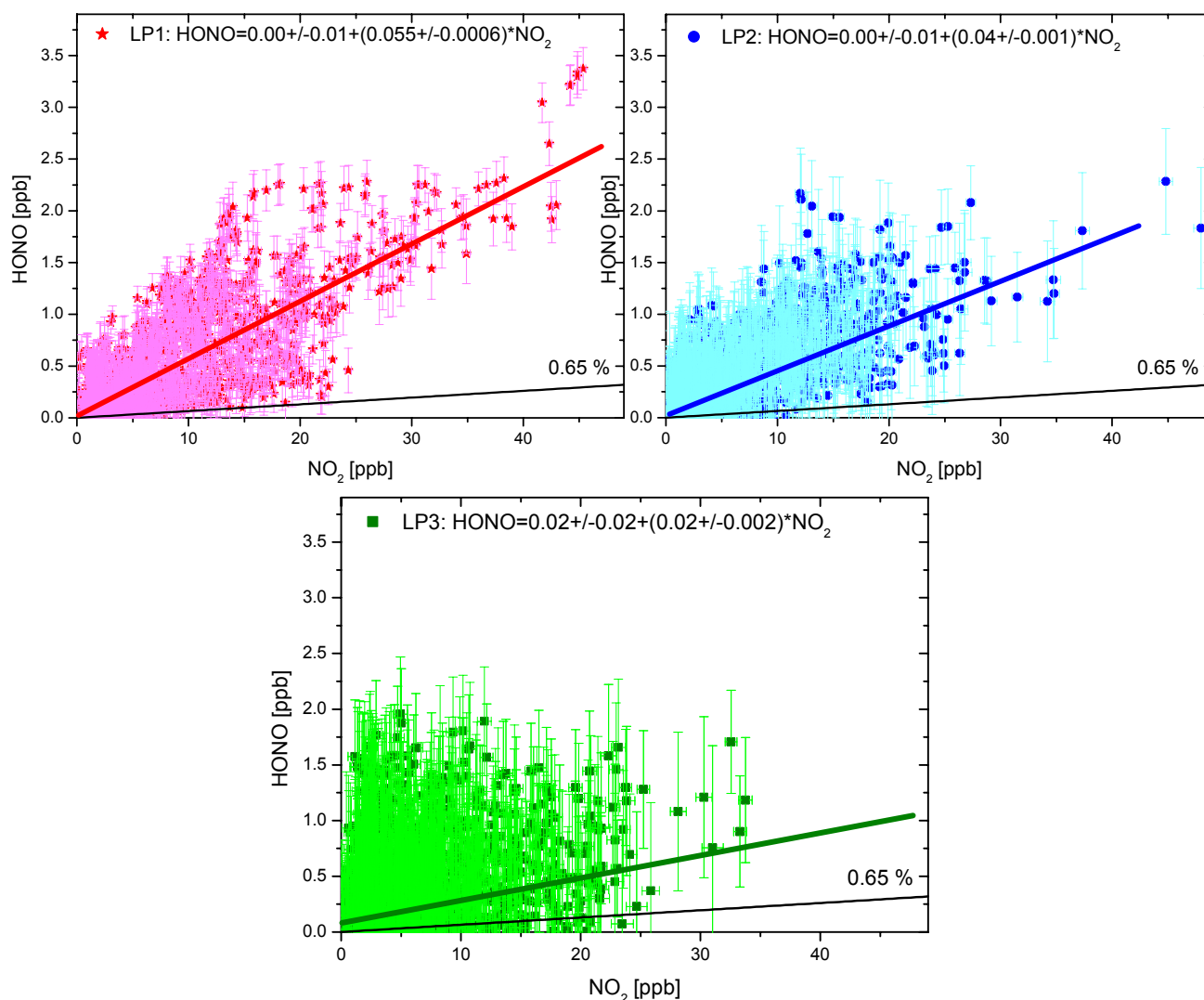


figure 4.26: Linear regression to the dependence of nitrous acid on nitrogen dioxide each measured during night and day of the Turm 2003 campaign on the different light path height intervals of up to 40 m (LP1, red stars, and line respectively), up to 100 m (LP2, blue dots, and line respectively) and up to 200 m (LP3, green squares, and line respectively). Additionally, the HONO-to-NO₂ ratio for direct emission from on-road fuel combustion is illustrated (black line).

Neglecting further chemical formation or destruction during the time of vertical transport upwards, HONO mixing ratios of ~ 2 ppb can be calculated from the NO_2 mixing ratio of ~ 20 ppb at a HONO-to- NO_2 ratio of $\sim 10\%$, only consistent with the observations in specific nights (see figure 4.25) that will be discussed in detail later (see chapter 4.3.6). The errors of the ratio often prohibit an evaluation of the variation of the HONO-to- NO_2 ratio with altitude above ground.

The HONO data as a function of NO_2 , show a monotonous decrease from the lower to the upper layer (see figure 4.26). Apart from distinctive variations, the dependence of HONO on NO_2 can be approximated by a linear fit, which has satisfactorily fit correlation coefficients of $\sim 81\%$ for LP1 and $\sim 73\%$ for LP2. This indicates that HONO formation is indeed of first order in NO_2 . However, for LP3 the poorly fit correlation coefficient of $R^2 \sim 20\%$ is already identifiable from figure 4.26. It is also obvious that the errors of both trace gases NO_2 and HONO are remarkable higher than for the lower light paths. Additionally, advection of polluted air masses (this will be discussed in chapter 4.3.6) cannot be excluded for LP3 and can lead to a new HONO-to- NO_2 ratio different from that in the height intervals below.

The consequent decrease of the HONO-to- NO_2 ratio by height suggests that the ground has a strong influence on the formation of nitrous acid. However, this can also indicate that HONO is formed near the ground and only small amounts are transported upwards due to a weak vertical mixing of the boundary layer during the night (assuming the upper light path still in the boundary layer).

If both trace gases HONO and NO_2 were formed exclusively near or at the ground, they should decrease similarly with altitude and no gradient in the HONO-to- NO_2 ratio would be observed. Since the vertical transport processes are identical for both species, only different sources and sink pathways (including chemical reactions and surface exchange processes) would yield a gradient in the ratio of both compounds. The removal of NO_2 from the gas phase onto surfaces and the subsequent heterogeneous formation of HONO causes such an increase in the HONO-to- NO_2 ratio. As this ratio is observed to decrease with altitude above ground, this serves as evidence for HONO formation being favorable at ground compared to that on airborne particles, such as aerosols.

In close proximity to direct emission sources of NO_x , additional amounts of nighttime NO_2 may primarily originate in the reaction r. 2.9 of ozone with NO from on-road traffic with fuel combustion. However, as mentioned above, the ozone levels were generally very low during the night and traffic was reduced at that time as well. Further, the sum of daytime $\text{O}_3 + \text{NO}_2$ was found to be similar to the observed nighttime amount of nitrogen dioxide, thus additional nighttime sources of NO_2 were excluded.

The analogous discussion with respect to HONO is more complicated but direct emissions by cars are well quantified [Ackermann, 2000; Kessler and Platt, 1984; Kurtenbach et al., 2001; Pitts et al., 1984a; Winer and Biermann, 1994]. The slope of the black line in figure 4.26 illustrates an emission ratio of 0.65% as indicated by [Ackermann, 2000; Kurtenbach et al., 2001], but the HONO-to- NO_2 ratio was always higher than expected from direct emission solely. Thus, either additional (heterogeneous) reactions yielding HONO or additional sinks for NO_2 are required to explain the observed ratio of both trace gases. However, the higher HONO concentrations at the lower light path (see figure 4.25) can also be highly correlated with the mixing layer height, and during the night with a small closed system the formation is much more efficient compared to the open atmosphere of the upper light path. In the next chapters, the natural radon-activity (see figure 4.24) will be used as a measure for a qualitative discussion of the influence of the vertical transport effects of the atmosphere on the formation of HONO.

4.3.6 Nighttime Vertical Gradients of the Trace Gases

To gain information of the favorable surface for the HONO formation, i.e. to distinguish between a ground-near source of nitrous acid or a production on airborne particles, such as aerosols, we will, in the following, focus on 07.06.2003 as an exemplary day. On 07.06.2003, the atmospheric dynamics show the expected diurnal variation with a clear stabilization during the night and a labilization after sunrise (see figure 4.24). Further, we have chosen the 07.06.2003 for the following analysis, because the vertical gradients of the trace gases (see figure 4.25) show a clear gradient above the detection limit of the DOAS instrument (see table 4.3). However, the discussion below is valid for most days of the Turm 2003 campaign with comparable meteorological situations (see chapter 4.3.5). The time series of HONO, NO₂, NO, and, O₃, natural radon-activity, solar radiation, wind speed and wind direction, which characterize the transport phenomenon in the PBL, from the period around 07.06.2003 are illustrated in detail by figure 4.27.

4.3.6.1 NO₂ Gradients

After sunset (~ 19:00), NO₂ concentrations increase in all height intervals (see figure 4.27). In the box closest to the ground, NO₂ values increase in the late afternoon from its low noon-time level of a few ppb, slowly to ~ 10 ppb due to the reduction of photolysis, the absence of OH radicals, and, to production from the destruction of O₃ by NO (reaction r. 2.9).

Additionally, the vertical transport is reduced and thus dilution of NO₂ into higher air masses is suppressed. With ongoing atmospheric stabilization, maximum mixing ratios of ~ 45 ppb are reached at midnight. Nearly 50 ppb (see figure 4.27) until sunrise were found in the box close to the ground and therefore closer to the sources of NO_x by fuel-combustion processes.

As vertical mixing is suppressed, NO₂ is continuously deposited on the ground and subsequently chemical transformed (e.g. yielding HONO), lower mixing ratios of ~ 10 ppb were found in the middle box. Consequently, a negative gradient of the NO₂ of ~ 0.7 ppb m⁻¹ is observed between these two boxes with the higher concentrations in the lower layer (see figure 4.27). The fine substructure can also be caused by changes in the vertical transport and advection as will be discussed in detail in chapter 4.3.7.

The mixing ratios of NO₂ of ~ 25 ppb in the height interval up to 200 m is even higher than that in the middle box, which was only ~ 10 ppb, resulting in a positive gradient of 0.1 - 0.2 ppb m⁻¹ (see figure 4.27). There are different possible explanations from a qualitative point of view. First, advection of air masses containing large amounts of NO₂, which have essentially longer lifetimes in this altitude due to the absence of surfaces for heterogeneous interactions. This may be confirmed by the fact that no enhanced HONO concentrations were found at this altitude at that time (see below). Second, the structure of dynamics of the PBL. Its stabilization starts from the ground proceeding towards higher altitudes during the night. Thus, the higher air masses may act as a reservoir for pollutant as long as it is above the nocturnal boundary layer. Within this open atmosphere reservoir, mixing is much less effective and thus chemical transformations as well. Finally, the reaction r. 2.4 of NO₂ with the most important nighttime radical NO₃ represents an effective volumetric sink in the presence of O₃. NO₃ concentrations are influenced by reactions with VOCs, which in the forest of the FZK are mainly of biogenic origin. A maximum concentration of the nitrate radical may therefore have occurred at the middle box, but unfortunately could not be measured.

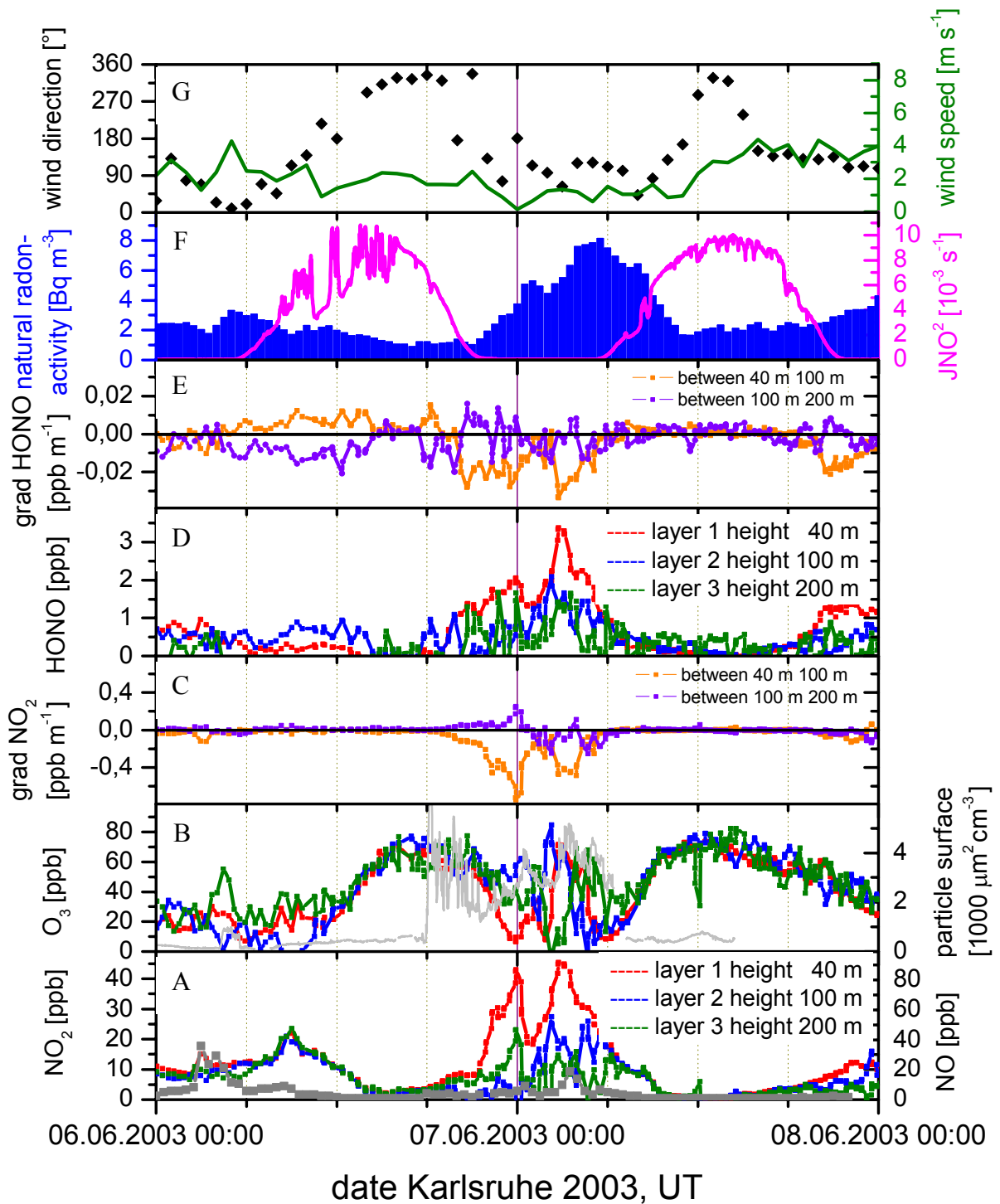


figure 4.27: Temporal trend of NO_2 (graph A), O_3 (graph B), and HONO (graph D) in the three different height intervals: red symbols for layer up to 40 m, blue symbols for layer between 40 - 100 m, and green symbols for layer between 100 - 200 m. Additionally, the NO concentration (grey symbols in graph A), and the particle surface (grey line in graph B), both measured at 10 m height were added. The corresponding meteorological parameters (natural radon-activity and solar radiation (graph F), wind speed and wind direction (graph G), which mainly influence the vertical transport in the PBL, are given. In the plots C and E, the absolute gradient of NO_2 and that of HONO between the boxes of upper height 40 m and 100 m (orange symbols) as well as that between 100 m and 200 m (violet symbols) is illustrated. All corresponding errors were omitted for a clearer illustration.

4.3.6.2 HONO Gradients

The main volumetric sink of HONO, i.e. its fast photolysis¹⁸, is no also longer present after sunset. Homogeneous reactions destroying HONO were reported to be negligible and heterogeneous reactions are questionable in the absence of suitable surfaces in the higher boxes. Thus, the mixing ratio levels of HONO increase from late afternoon values of ~ 100 ppt on 06.06.2003 to maximum mixing ratios of ~ 2.2 ppb around midnight on 07.06.2003 (see figure 4.27). This increase of the mixing ratio of HONO is highest in the lowest height interval (0.5 ppb h^{-1}), minimum in the second (0.2 ppb h^{-1}) and in the third (box-height up to 200 m) as fast as in the lowest box. This minimum in the second box is most likely caused by advection as indicated in figure 4.28.

Consequently, a gradient of the HONO is observed between the different height interval boxes (see figure 4.27). This concentration gradient of $\sim -0.02 \text{ ppb m}^{-1}$ is rather weak compared to field observations over grass surface by [Alicke, 2000; Stutz *et al.*, 2002]. However, the sign of the HONO gradient is negative indicating a net flux of HONO upwards from the ground surface, which also seems to be the favorable surface for the heterogeneous production of nitrous acid during the night.

This finding is confirmed by the time series of the aerosols surface as well (see figure 4.27). After sunset, the surface of these airborne particles increases by a factor of ~ 3 , reaching an average value of $\sim 2700 \mu\text{m}^2 \text{ cm}^{-3}$ before midnight on 07.06.2003. However, such an increase of the aerosols should also enhance the volumetric production of nitrous acid. Consequently, the more HONO in higher altitudes and a lower gradient between the different boxes heights would be expected, but was not observed. The gradient in the HONO mixing ratios between the upper height intervals, however, shows either a very weak positive sign or is equal to zero (see figure 4.27), which cannot be distinguished within its errors. However, weak positive gradients of nitrous acid of $\sim 0.5 \text{ ppb m}^{-1}$ were also reported by [Alicke, 2000; Stutz *et al.*, 2002] under conditions of suppressed vertical mixing of the PBL during the night and high NO pollution.

4.3.6.3 The HONO-to-NO₂ Ratio

Contrastingly to [Alicke, 2000; Stutz *et al.*, 2002], a built up of a maximum amount of HONO corresponding to a steady state, i.e. constant values of HONO except due to temporal changes of NO₂ during the night, was never observed during the Turm 2003 campaign. At the end of each night, the HONO-to-NO₂ ratio in the lower layer clearly exceeded the steady state ratio of 5.5 % postulated by [Stutz *et al.*, 2002] for the compensation point between HONO exhalation from the surfaces and HONO deposition on the surfaces. Despite [Stutz *et al.*, 2002] reported higher ratios being observed due to increased NO_x emissions, this is also still not sufficient to our data. However, a mixture of different natural and artificial surface types was present below the light paths during the Turm 2003 campaign, instead of the complex and biologically active grass meadow in Milan, Italy during the experiments of [Alicke, 2000; Stutz *et al.*, 2002]. We should finally mention that the measurement heights are totally different between our studies and those of [Alicke, 2000; Stutz *et al.*, 2002]. While during the Turm 2003 campaign, trace gas mixing ratios were observed in a range of 40 – 200 m, it is well known ([Alicke, 2000; Stutz *et al.*, 2002]) that concentrations show largest variations in the lowest few meters above ground.

¹⁸ The HONO photolysis frequency was estimated for the Turm 2003 campaign from that of NO₂ by the empirically relationship suggested by [Kraus and Hofzumahaus, 1998] as: $J(\text{HONO}) = 0.189 \times (J(\text{NO}_2)) + 8.433 \times 10^{-2} \times (J(\text{NO}_2))^2$

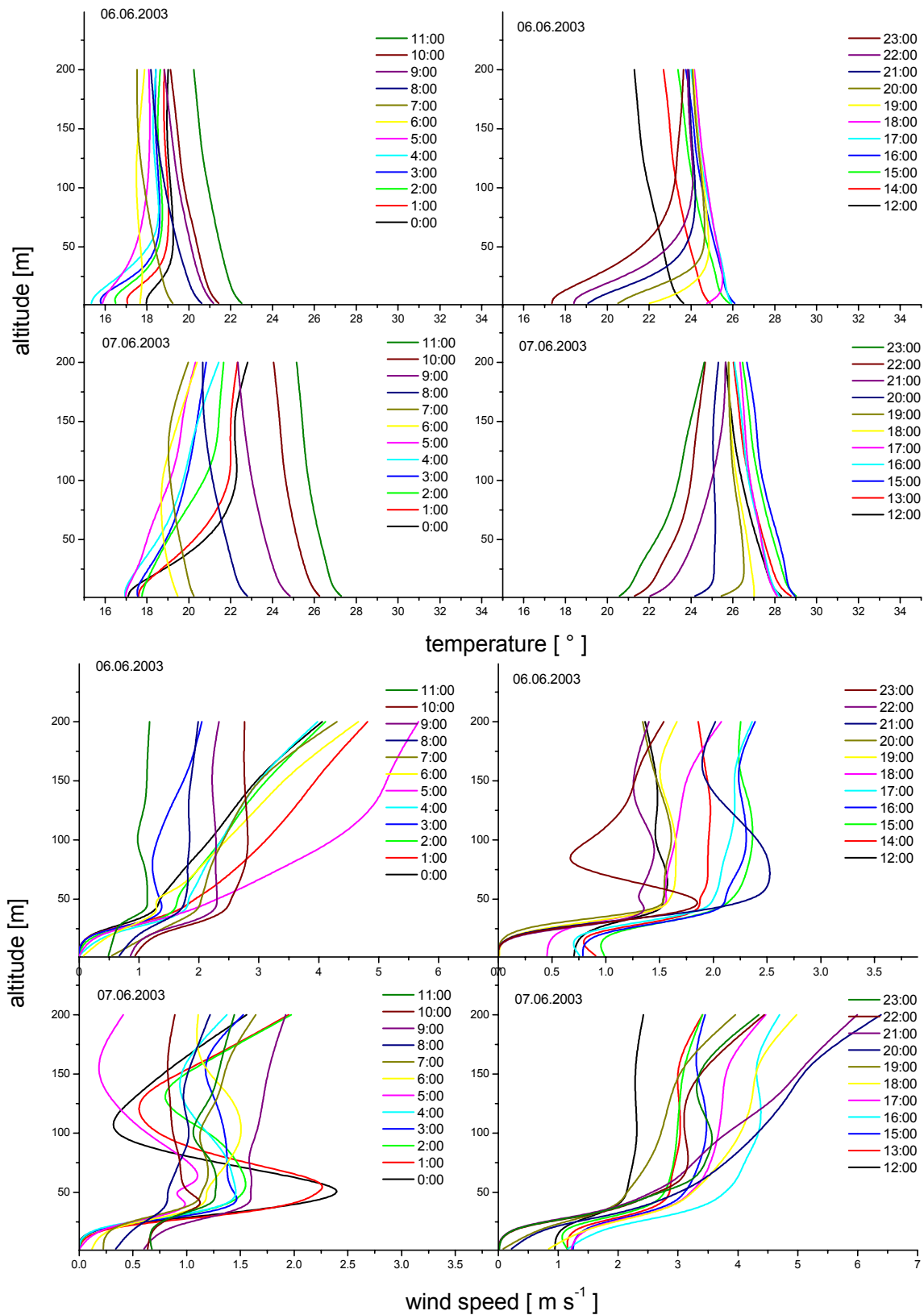


figure 4.28: Vertical Profiles of the temperature (upper plots) and the vertical profiles of the horizontal wind speed (lower plot) measured at different altitudes at the meteorological tower during the Turm 2003 campaign. The different colors refer to different times of the day, thus the temporal trend is visible as well. The upper plots correspond to the time until noon of 06.06.2003 (left side), and the right side to the afternoon until midnight. For the 07.06.2003, the lower plots illustrated these periods.

4.3.6.4 O₃ and NO Gradients

During most time of the night of the 07.06.2003, no gradient in the ozone concentration was observed (see figure 4.27), except a short time before midnight when the stabilization of the atmosphere started. At this time, lower mixing ratios of O₃ were found near the ground while O₃ remained at high levels of ~ 50 ppb at higher altitudes > 100 m (see figure 4.27).

Dry deposition of ozone onto the ground (in the order of 0.1 – 0.8 cm s⁻¹ [Alicke, 2000; Lovett, 1994]) is too slow to exclusively explain the difference in the O₃ mixing ratios observed at the different heights. The loss of ~ 20 ppb ozone before midnight on 07.06.2003 (see figure 4.27) can be explained by the reaction with NO from sources near the ground according to reaction r. 2.9 [Taylor et al., 1999]. This also explains the anti-correlated higher NO₂ concentration at the lower light path (see figure 4.27), which occurs if the upper light path was at least partially above the boundary layer height.

After a period of high advection around midnight of 07.06.2003, ozone increased immediately to ~ 60 ppb in all boxes at the three different heights (see figure 4.27). Since a strong NO₂ gradient is established until sunrise, the concentrations of both trace gases O₃, and NO₂ are not satisfied by reaction r. 2.9 only.

The lowest DOAS light path was in a height of 40 m (a few meters above the forests line in the rural area of the FZ Karlsruhe). Thus, the influence of primary biogenically emitted organic compounds, and especially reactions of ozone with VOC, which may occur in a certain height interval only, cannot be generally excluded. Unfortunately, organic compounds could not be measured during the Turm 2003 campaign.

NO was measured at a constant altitude of 10 m during the night. Thus, no gradients may be derived from NO nighttime measurements. The height of 10 m at the meteorological tower was the lowest available, but still beyond the average height of the trees of the surrounding forest. Thus influences on its mixing ratio by organic compounds, which are primarily of biogenic origin in this clearing, may again not be excluded. By that location of the NO measurement inlet both, the NO from combustion processes of the power plant of the FZK, which might have been subsequent horizontally transported into the DOAS light-beam at higher altitudes, and that nitrogen oxide from on-road primary emission nearby the FZK may have been essentially underestimated. Thus, in this thesis we will use the NO data only as indicators for the time of special events, such as the rush hour. Additionally, malfunctions of the NO in-situ monitor caused several gaps in the time series of NO during the nights.

4.3.7 Influence of Vertical Transport in the PBL on Gradients

It is obvious from figure 4.27 that the dynamics of the PBL also influence this increase of HONO, as indicated by the time derivatives of the natural radon-activity. On 07.06.2003, an initial stabilization of the atmosphere started directly after sunset and radon values increased from ~ 1.5 Bq m⁻³ to a first maximum of ~ 5 Bq m⁻³ short after midnight (see figure 4.27). This more stable layering of the PBL corresponds to the initial increase of HONO mixing ratios from ~ 100 ppt to ~ 2.2 ppb until midnight.

After this initial stabilization of the PBL, a short break is observed and radon values drop again to ~ 4.5 Bq m⁻³ in the next 1.5 hours (see figure 4.27). The corresponding stronger vertical transport directly impacts on the concentrations of the trace gases HONO and NO₂. Both show a sudden decrease of ~ 0.5 ppb for HONO and even more than ~ 25 ppb for NO₂ (see figure 4.27). Due to the enhanced vertical transport, the mixing ratios of HONO and NO₂ in each height interval become again similar and the gradients of the trace gases approximate to zero. This situation is usually only observed during conditions of high vertical mixing at day. However, from the vertical profiles of the meteorological parameters, i.e. the temperature

and the wind speed at different altitudes of the meteorological tower (see figure 4.28), a distinctive period of strong advection can be observed in a height interval of ~ 40-60 m short time after midnight. Thus, the trace gas concentrations as well as radon can be diluted by horizontal transport. At this point, we cannot distinguish.

After this event of 1.5 hours the atmospheric stability increases again, and radon maximum levels of ~ 8.5 Bq m⁻³ are reached through the rest of the night of 07.06.2003 until sunrise. Within that second period of the night of 07.06.2003, the maximum values of HONO of ~ 3.5 ppb and NO₂ of ~ 45 ppb are observed, highest concentrations of both trace gases in the lowest height interval, but ~ 50 % lower levels above (see figure 4.27). Due to the stronger stabilization (time derivative of radon ~ 1.5 Bq m⁻³ h⁻¹) the gradients of both NO₂ and HONO reach maxima as well (0.5 ppb m⁻¹, and 0.035 ppb m⁻¹, respectively). The flux of both gases is pointing downwards between the lowest two boxes and is almost equal in the height intervals of 100 m to 200 m.

The fact that short-time periods of atmospheric stability (indicated by a short increase of the time derivative of natural radon-activity) are correlated with an increase of HONO gives strong evidence for HONO production predominantly on or near the ground. These correlations would not occur if the major part of the HONO is formed by a volumetric source because any stronger atmospheric stability obviously influences trace gases primary emitted or formed at or near the ground surface as well as airborne particles, such as aerosols. The rate of this HONO formation is independent from atmospheric stability but the transport into higher altitudes is more effective at less stable layering in the PBL. Thus, the occurrence of vertical gradients of HONO depends strongly on the vertical mixing in the PBL.

However, the influence of atmospheric dynamics cannot be separated from chemical production or removal, thus a model is required and will be applied in chapter 6.2 of this thesis.

4.3.8 Temporal Trends of Vertical Gradients

Another point of view is of the qualitative description, especially with respect to the temporal generation of the vertical gradients, which can be obtained from figure 4.29 and figure 4.30 respectively, where the measured concentration in each box is plotted against its altitude (the different colors refer to different times of day).

From the night of 06. to 07.06.2003, generally higher values of NO₂ of ~ 40 ppb were observed in the lowest box and decreasing gradually with the height above ground (figure 4.30; 0:00 – 6:00) down to values of ~ 10 ppb at 200 m. As NO₂ is the main precursor of HONO, this trend is observed in the HONO as well (see figure 4.29; 0:00 – 6:00). Most of the nitrous acid is located near the ground (up to ~ 3 ppb) decreasing with height to ~ 2 ppb at 100 m, and only ~ 1 ppb in the highest box. This again indicates the nighttime HONO formation being favorable from heterogeneous hydrolysis of NO₂ at or near the ground surface.

After sunrise, photolysis starts and vertical mixing gets stronger. Thus, the measured NO₂ levels decrease to ~ 15 ppb in the highest box, by ~ 25 ppb in the lowest box, while the concentrations of NO₂ in the middle box were observed at that time to decrease most slowly (figure 4.30; 6:00 – 12:00). The behavior of nitrous acid at this time yields different profiles as can be seen from figure 4.29; 6:00 – 12:00. Again, a weak gradient is observed between concentrations in the lowest box and at a height of 100 m (figure 4.29; 6:00 – 12:00). The mixing ratios decrease after sunrise from ~ 1 ppb to < 200 ppt, which is close to the detection limit of the DOAS instrument. Before noon on 07.06.2003, highest mixing ratios of ~ 0.6 ppb seem to be present in the highest box (200 m).

A satisfying explanation for this phenomenon cannot be given to date. It may be due to advection of air masses in a certain height only. The horizontal wind can significantly differ

by speed (see figure 4.28) or by its directions between the different altitudes. Thus different air masses may have been observed by the different light beams of the DOAS instrument: one of cleaner air closer to the ground, and another with more pollutants (e.g. from the exhaust of the power plants of the FZK) in higher altitudes. This explanation is supported by the time series of natural radon-activity, which shows higher values in 30 m altitude than in 100 m on 07.06.2003 (see figure 4.24).

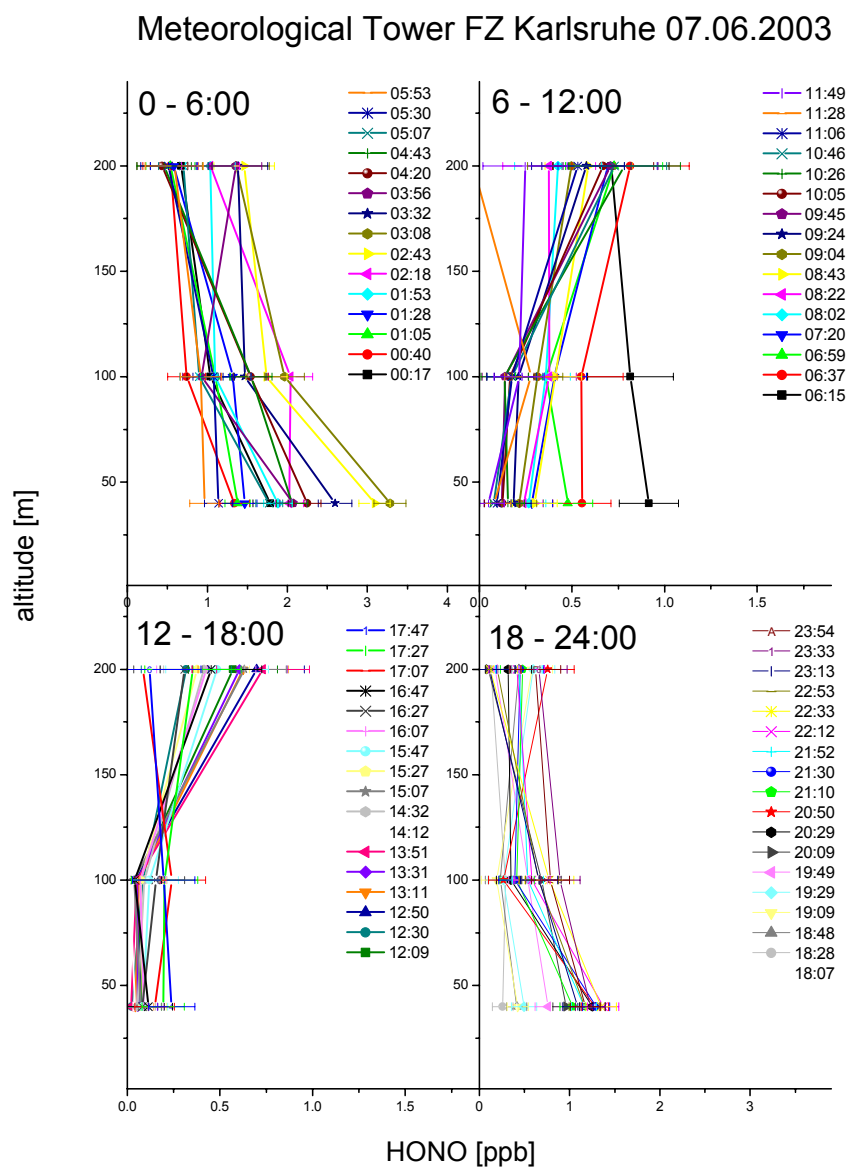


figure 4.29: Vertical profiles of HONO during different periods of the day: nighttime accumulation until sunrise, morning until noon variations, afternoon levels, and beginning of the next night and atmospheric stabilization. Only three measurement heights were available, thus the gradients become highly sensitive to fluctuations in the DOAS data.

Chemical production or removal processes may also contribute to the enhanced concentrations of HONO and NO₂ in the altitude around 100 m. A volumetric daytime source of NO₂ is for example the gas-phase reaction of NO and alkylperoxy and hydroperoxy radicals. Traffic emissions during the rush-hour may present a significant source of NO at this time, while especially the photochemical oxidation of biogenic VOCs (isoprene) can yield large amounts of RO₂ and HO₂. However, we cannot quantify this by our data.

A reduced HONO deposition in higher altitudes may occur due to the less surfaces (the ground surface or walls of buildings) present for heterogeneous interactions. However, this should also reduce the heterogeneous production of HONO.

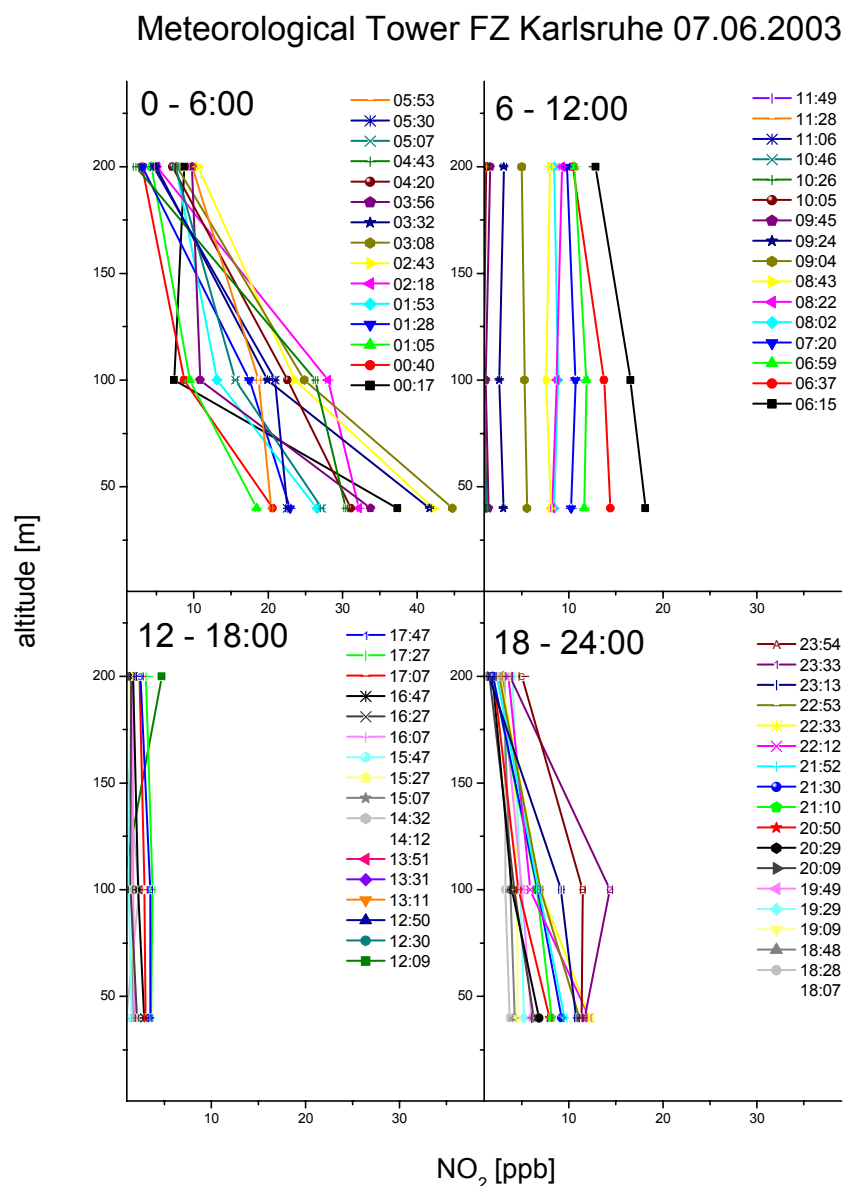


figure 4.30: Vertical profiles of NO₂ during different periods of the day: nighttime gradients until sunrise, morning until noon variations, afternoon levels, and beginning of the next night and atmospheric stabilization. Only three measurement heights were available, thus the gradients become highly sensitive to fluctuations in the DOAS data.

When a labile layering is completely established in the entire PBL, the concentrations in the different boxes become equal. Consequently, no gradient of NO₂ is observed at noon (figure 4.30; 6:00 – 12:00). This situation becomes more evident throughout the day (figure 4.30; 12:00 – 18:00) until sunset, when low mixing ratios in the range of < 5 ppb were recorded. During this period of day, the HONO gradients become insignificant within the errors of the DOAS system and thus a gradient indistinguishable from zero is observed figure 4.29; 12:00 – 6:00) between the two lower boxes. The daytime values of HONO range between ~ 50 ppt and 150 ppt on 07.06.2003 (see figure 4.29; 12:00 – 18:00), which are both below the DOAS

detection limit. Again, highest values seem to be present in an altitude of 200 m, but cannot be fully explained (see above).

At the beginning of the next night and re-stabilization of the PBL, a gradient of nitrogen dioxide is established. Again NO_2 levels of 15 ppb were found in the middle box, while 10 ppb and 5 ppb were measured in the lowest and upper box respectively (figure 4.30; 18:00 – 24:00). HONO as well re-built its gradients as discussed for the night before. Highest mixing ratios in the lowermost layer (~ 1.3 ppb) decreased gradually with the height above ground to values of ~ 0.8 ppb and ~ 0.6 ppb in the box up to 100 m and up to 200m respectively (figure 4.29; 18:00 – 24:00). However, the profile shows a stronger gradient between the two lower boxes, than that observed between the middle and the highest box (figure 4.29; 18:00 – 24:00).

4.3.9 Daytime Gradients of the Trace Gases

After sunrise ($\sim 5:00$) on 07.06.2003, a rapid decrease of HONO due to its photolysis and atmospheric labialization is observed. During four hours, the HONO mixing ratios drop from the accumulated maximum nighttime value to ~ 100 ppt in all height intervals (see figure 4.27). These low levels are maintained throughout the entire day until sunset on 07.06.2003. In figure 4.27 the HONO mixing ratios in the highest box seem to be somewhat higher, but this cannot be clarified due to the larger errors of the data from that light path. The gradients of HONO are therefore zero within its errors during daytime on 07.06.2003 (see figure 4.27). NO_2 mixing ratios decrease as well during that time from initial ~ 15 ppb in the higher boxes and ~ 45 ppb in the lowest box respectively, to typical minimum daytime levels of some few ppb at noon (see figure 4.27). This daytime value of NO_2 is observed in all height intervals and consequently, a gradient of NO_2 indistinguishable from zero is observed through the entire day between all boxes in the different altitudes (see figure 4.27).

The interpretation of the NO_2 gradient is difficult due to the fact that NO_2 undergoes a variety of reactions in the daytime atmosphere, represented by the large change in its mixing ratio from sunrise until noon as discussed above. In particular, the simultaneous measurements of NO and O_3 are required to interpret NO_2 gradients close to NO_x sources, which in our case are not only close to or at the ground. Further, detailed information on reactive atmospheric compounds, such as OH and peroxy radicals formed from VOCs would be needed, even to derive the photochemical state which is described by the extended Leighton ratio. Thus, only the model (see chapter 6.2) will be able to distinguish between the different contributing chemical sources and sinks, and the vertical transport on the other hand.

The ozone concentration was, however, found to be equal in all three heights of the boxes, thus no gradient is observed throughout the day (see figure 4.27). The time series mirrors that of NO_2 as expected from the Leighton relationship, and daytime maximum values of ~ 80 ppb are observed after noon and nighttime minimum levels again becoming zero due to the total oxidative destruction by the titration reaction r. 2.9 with NO (see figure 4.27). Only directly after sunrise, during the start of the rush hour and thus higher emissions of NO by on-road traffic, a gradient in the ozone levels at the different heights can be observed. At this time, the lower concentrations of O_3 in the boxes closer to ground are mainly caused by the reaction r. 2.9, destroying ozone in the presence of NO, which dominates the vertical transport effects at this time of day.

5 The Smog Chamber Studies: Heterogeneous HONO Formation

The atmospheric formation of nitrous acid is believed to proceed heterogeneously as a 1st order process in NO₂. The exact mechanism of this formation has to follow the stoichiometry of reaction r. 2.33:



is still unknown. Several laboratory studies have been performed on aerosols of various types: cloud droplets [Harrison and Collins, 1998; Lammel and Perner, 1988; Li, 1994; Notholt *et al.*, 1992], soot [Ammann *et al.*, 1998; Kalberer *et al.*, 1999], sulfuric acid droplets [Kleffmann *et al.*, 1998; Longfellow *et al.*, 1998], and different carbonaceous surfaces [Kalberer *et al.*, 1999; Kleffmann *et al.*, 1998]. The determined HONO formation rates lead, even under assumption of favorable conditions to a HONO formation rate, which is about a factor of two up to four orders of magnitude lower than observed in the atmosphere [Kleffmann *et al.*, 1998; Platt, 1986].

Laboratory studies of the kinetics of the HONO formation on macroscopic surfaces, which seem more likely were thus far only performed on Teflon and quartz glass (e.g. [Pitts *et al.*, 1984c; Svensson *et al.*, 1987]). The values for the HONO formation rate coefficient cannot explain the atmospheric HONO concentrations. It is therefore evident to measure HONO formation on real (urban) surfaces. These surfaces, for example high-frequented asphalt roads, are more complex, are exposed to the weather, consist of several pores and cracks and they contain several inclusions (e.g. silica stones), abrasions (e.g. from car tires) and they do not consist of a pure chemical substance.

Thus special laboratory studies about the formation of nitrous acid by reaction r. 2.33 on different types of surfaces were performed in this thesis. Aim of these experiments was to investigate PE, Teflon, real urban surfaces, such as asphalt, concrete, roof-tiles, flagstone-tiles, and grass for their formation potential of HONO as well as to determine the effective NO₂ uptake coefficients. For these experiments an isolated and well controllable smog chamber was set up. After background characterizations and humidification of the smog chamber, nitrogen dioxide was added to the system and the formation of nitrous acid was observed by a White-type DOAS multi-reflection system. Two campaigns were carried out: one at the Institut für Umweltphysik, Heidelberg, Germany (IUP) in April 2002, and another at the Kirchhoff Institut für Physik, Heidelberg, Germany (KIP) in April 2003. During both campaigns, the same smog chamber was used. The measurement techniques used during both of these campaigns and the smog chamber itself will be described in chapter 5.1. The exact procedure and the results of the experiments will be addressed to in chapter 5.2. In chapter 5.3 the basic and so far “usual” calculations analyzing smog chamber experiments of heterogeneous HONO formation were applied, but could not explain the observed behavior of HONO during the entire time of the experiments (see chapter 5.4.1, and 5.4.2). A model was employed to explain both, the heterogeneous HONO formation by NO₂ addition as well as the variations of HONO with external parameters, such as R.H. This model will be described in chapter 5.5. Finally, atmospheric implications and limitations of this approach will be show in chapter 5.6.

5.1 Experimental Setups

5.1.1 The Smog Chamber

The reaction chamber consists of two aluminum boxes placed at a distance of 15 m (the base length of the DOAS White system) and a PE tube stretched between them (see figure 5.1). The aluminum boxes had a size of 450 mm x 550 mm x 550 mm, and 650 mm x 550 mm x 310 mm, respectively yielding a volume of 0.14 m³, and 0.11 m³, respectively. The smog chamber is explained in more detail in [Volkamer, 1996].

During the KIP 2003 campaign, the whole inner surface of each box was covered by PE foil used for the tube of the smog chamber (exclusively the main mirror and prisms of the DOAS White system, respectively the two back reflection mirrors located in these boxes). Thus the number of different surface types was reduced. This was particularly important because the metal surfaces are suspected to catalyze nitrogen oxides chemistry.

A water–manometer was attached by a $\varnothing = 50$ mm flange at the backside of each box in the longitudinal axis of the smog chamber (see figure 5.1). The manometers consisted of a Perspex tube of $\varnothing = 50$ mm, bent 90° and ended in a tumbler, which is filled with m.q. water (Merck Chemikalien, Darmstadt, Germany). The difference pressure between inside the reaction chamber and the atmospheric pressure could be determined as the difference of the water-level in- and outside the tube¹⁹. The determination limit was approx. 0.1 mbar. An over-pressure was needed to hold up the PE tube itself.

At each of the faced sides of the boxes, a 150 mm wide conic flange of 2 mm thick aluminum material was attached. The flange at the box with the White main mirror is spherical that at the box with the reflecting White mirrors elliptical to minimize the openings and thus reduce leakage. A tube of 15 m length with a diameter of 445 mm was connected to both boxes (see figure 5.1).

During the IUP 2002 campaign the tube was Teflon (Hostaflon; Folitec, Bremen, Germany) of a thickness of 0.12 mm, during the KIP 2003 campaign a commercial transparent PE foil (Folitec, Bremen, Germany).

Both boxes had three KF - flanges (two at $\varnothing = 16$ mm, and one at $\varnothing = 25$ mm) to connect in-situ–measurement instruments, and the gas and humidification tubes, respectively. Additionally, the front box, which included the main mirror of the DOAS White system, had a Quartz window ($\varnothing = 150$ mm, material Suprasil II (Fleige-Optik, Holm-Wedel, Germany) for the inlet and outlet of the DOAS light beam.

The setup resulted in a total surface area of the reaction chamber of $S_{\text{total}} = 23.4$ m², including the boxes ($S = 1.6$ m², and $S = 1.5$ m², resp.) as well as that of the PE tube ($S_{\text{foil}} = 20.3$ m²) itself. The total volume of this reaction chamber was therefore 2.53 m³ yielding a surface to volume ratio of $S / V = 9.33$ m⁻¹. By these calculations, neither an arising of the surface by the mirror holders and the mirrors themselves are taken into account, nor the different surface types of these instruments [Trick *et al.*, 2003].

During the KIP 2003 experiments, the whole tube of the smog chamber was covered by a black felt drapery to exclude photolysis by impinging sunlight. During the IUP 2002 campaign, experiments were performed in the dark basement of the IUP building with indoor illumination by Halogen lamps only.

¹⁹ 1 mm water-level corresponds to 0.098 hPa

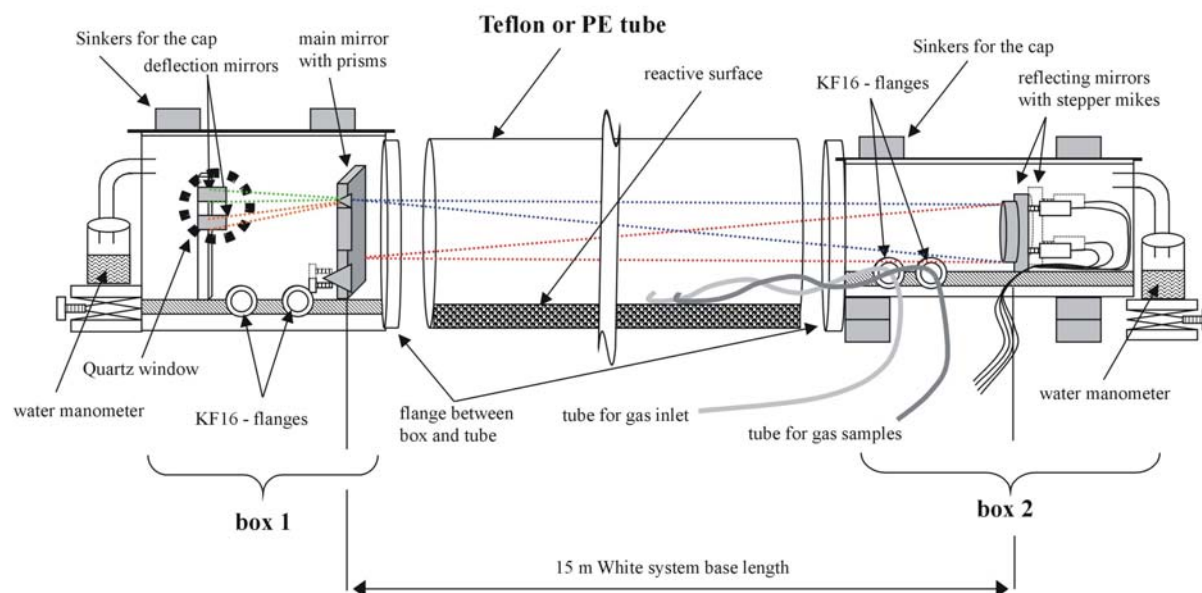
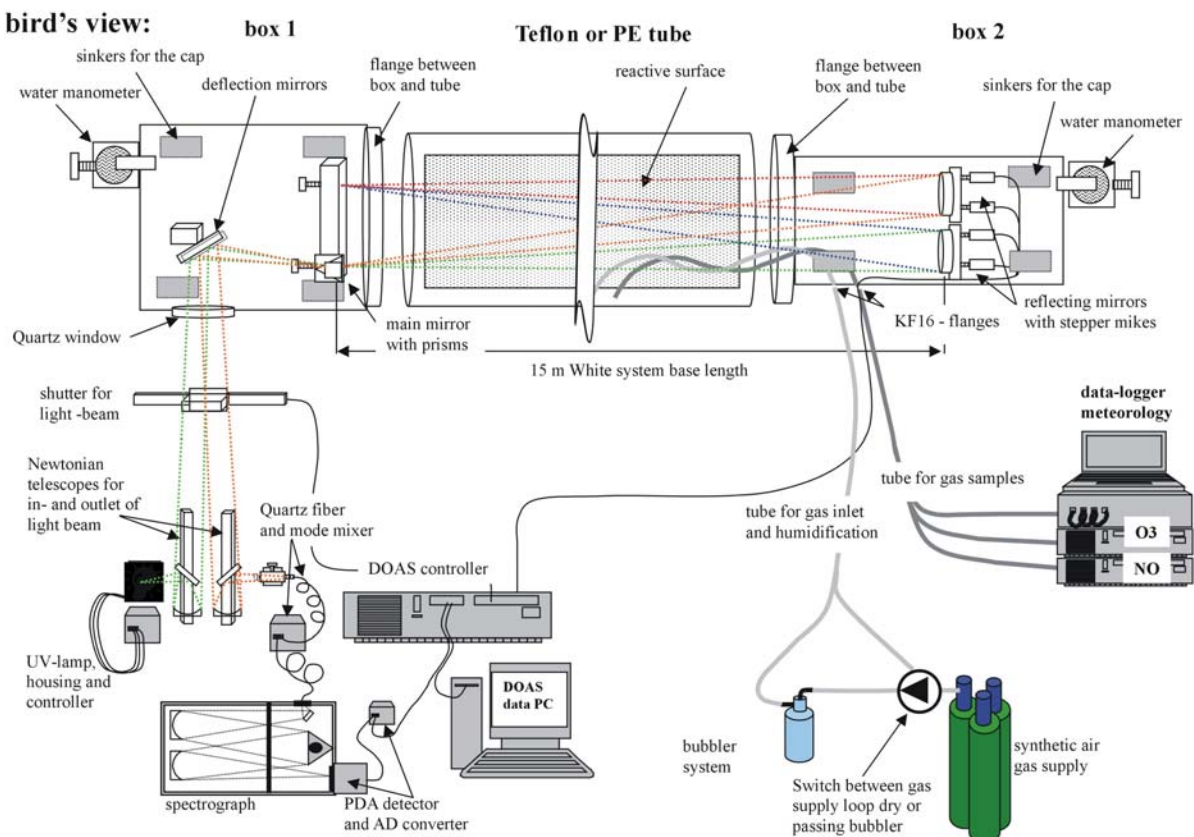
lateral view:**bird's view:**

figure 5.1: Sketch of the smog chamber and its main components appended as well as the DOAS –White system.

5.1.1.1 Characteristics of the Gas Supply

A commercial mixture of dry synthetic air (Messer–Griessheim, Ludwigshafen, Germany) of a purity of 5.0 with humidity below 1 %. was used for the generation of the artificial

atmosphere inside the smog chamber. Contaminations of the 79.5 Vol.% N₂ / 20.5 Vol.% O₂ atmosphere are given by the manufacturer (see table 5.1). The gas was connected to the smog chamber by a pressure-regulator of brass (Typ FMD 500-18; Druva Heidelberg, Germany) and $\varnothing = 8$ mm Teflon tubes (Rala, Ludwigshafen, Germany).

component	impurities
N ₂	79.5 Vol.%
O ₂	20.5 Vol.%
H ₂ S	2000 ppbV
HCs (total)	50 ppbV
CO ₂	100 ppbV
CO	100 ppbV
NO _x	10 ppbV
SO ₂	5 ppbV

table 5.1: Impurities of the synthetic air 5.0 used during the smog chamber campaigns as given by the manufacturer Messer Griessheim.

5.1.1.2 The Leakage of the Smog Chamber

During the experiments, leakage was balanced by continuous addition of synthetic air through external mass flow controllers (type 1259C-05000S-SPCAL with a maximum flow gas mass rate of 5 L min⁻¹; MKS, München, Germany). During the IUP 2002 campaign an additional mass flow controller (type F201C-FA-22V SN 962050B with a maximum flow rate of 15 L min⁻¹; Bronkhorst Ruurlo, The Netherlands via Iberfluid Instruments, Barcelona, Spain) was needed due to the higher consumption of gas due to the additional in-situ instruments (WEDD and LOPAP II, see chapter 5.1.4.2).

As shown by previous characterizations of [Volkamer, 1996] the smog chambers leakage could be reduced depending on the over-pressure inside the smog chamber, which was mostly set to 5 mbar at the water-manometers during both campaigns. In total it was 5 l / min up to 20 l / min corresponding to a leakage loss frequency of $0.67\text{--}1.67 \cdot 10^{-4} \text{ s}^{-1}$. This loss by leakage was always a first order exponential decay. As will be shown in chapter 5.3 and table 5.3., these values are almost two orders of magnitude below those observed of the reactive trace gases, but must be corrected for.

Calculating the net loss frequencies of any trace gases in the smog chamber, the loss by leakage needs to be corrected. For every trace gas *i*, the observed total loss frequency f_{observed} is the sum of the loss frequencies of this gas by leakage f_{leak} and by homogeneous and heterogeneous chemistry f_i :

$$f_{\text{observed}} = f_i + f_{\text{leak}}. \quad \text{eq. 5.1}$$

Thus, this leakage loss frequency is simply subtracted from the observed total loss frequency of any trace gas before any further calculations were performed.

5.1.1.3 Mixing and Homogeneity of the Smog Chamber

The air mass inside the smog chamber was mixed by two tube-fans (type RUG 105 RE; RUG, Mannheim, Germany) with a flow rate of 396 m³ h⁻¹. The mixing of the injected NO₂ and water was enhanced by using specially prepared Teflon tubes. These tubes were 16 m long and crossed the entire smog chamber. Several holes were drilled in the tubes with distances between the holes decreasing to the end of the tubes. The flow inside these tubes follows

Hagen-Poiseuille's law, and the flow throughout the holes is constant over the length of the tubes.

5.1.1.4 Humidification of the Smog Chamber

The synthetic air replenishing leakage, was sent through a bubbler system to humidify the air. The bubbler consisted of a laboratory's water bottle filled with water of highest purity available (m.q. water; Merck, Darmstadt, Germany). Flowing through a frit the dry synthetic air saturates, and the H₂O partial pressure, which depends on temperature, is reached. The bubbler was placed in a water bath at a well-defined temperature, yielding a specific saturation of the dry synthetic air. Therefore the terminal R.H. value in the smog chamber was settable. To vary this saturation point, the temperature of the water bath was. A different set of $\varnothing = 8$ mm Teflon tubes (Rala, Ludwigshafen, Germany) was used for the transport of the wet air into the smog chamber to exclude possible reactions of trace gases in the injections tubes. Further, the time of humidification was varied in a range from 1 up to 3.5 hours to achieve the terminal R.H. levels of 10 up to 80 % in the smog chamber.

5.1.2 Generation of the Injected NO₂

For the IUP 2002 campaign, a commercial bottle of pure NO₂ (purity 1.8; ≥ 98.8 Vol.% NO₂, KF1 with 0.96 bar at 20°C; Messer Griessheim, Ludwigshafen, Germany) was used. To clean the NO₂ further, it was distilled through freezing to -189°C and re-heating to -30°C. Thus most impurities were removed, especially H₂O, which would form HONO in the glass containers. Then the NO₂ was injected to the smog chamber via a syringe into the flow of dry synthetic air.

During the KIP 2003 experiments, gaseous NO₂ was produced by mixing NO of the highest available purity from a testing-gas of 9.94 ppm NO in N₂ (Messer Griessheim, Ludwigshafen, Germany) and O₂ (cleanness 5.0). In the dark, NO₂ is formed in this gas mixture. This NO₂ was flushed from the glass flask into the smog chamber by the flow of dry synthetic air.

5.1.3 The Investigated Surfaces

During the experiments different kinds of real urban surfaces were investigated for their formation potential of nitrous acid. Additionally the PE foil and Teflon, of which the smog chamber consisted, were studied.

During the IUP 2002 campaign, asphalt plates (of approx. 300 x 200 mm) and a thickness of ~30–70 mm (see figure 5.2) were inserted in the reaction chamber. This real urban surface was taken from a street in front of the Institut für Umweltphysik Heidelberg, Germany, which was ripped open one week before the start of the campaign.

The chemical consistence of the asphalt street at the location of measurements (e.g. the ratio of asphalt to concrete) is not known, but is coarse grained and contains many silica particles (see figure 5.2).

Other types of real urban surfaces were also investigated: commercial concrete (Bauhaus Heidelberg, Germany), roof-tiles, flagstone-tiles (Näher Baustoffe, Heidelberg, Germany) and grass, which was taken from a meadow in front of the Kirchhoff Institut für Physik Heidelberg, Germany a few minutes before the experiment. The surfaces analyzed and their surface areas are listed in table 5.2.



figure 5.2: Picture of the asphalt plates and comparison of their size as used for the analysis in the smog chamber (left side) and closer picture illustrating the substructures of the asphalt used (right side).

date	surface type	surface area [m ²]	
		walls of the smog chamber	additional „reactive“ surface
campaign in basement at IUP in 2002:			
12.04.02	Teflon	$S_{\text{Teflon}} = 23.4$	---
13.04.02	Teflon	$S_{\text{Teflon}} = 23.4$	---
15.04.02	Teflon + PE + asphalt	$S_{\text{Teflon}} - (S_{\text{PE}} - S_{\text{asphalt}}) - S_{\text{asphalt}}$	$S_{\text{asphalt}} = 4.2 = 0.3 \times 14.0$
16.04.02	Teflon + PE + asphalt	$S_{\text{Teflon}} - (S_{\text{PE}} - S_{\text{asphalt}}) - S_{\text{asphalt}}$	$S_{\text{asphalt}} = 4.2 = 0.3 \times 14.0$
17.04.02	Teflon + PE + asphalt	$S_{\text{Teflon}} - (S_{\text{PE}} - S_{\text{asphalt}}) - S_{\text{asphalt}}$	$S_{\text{asphalt}} = 4.2 = 0.3 \times 14.0$
18.04.02	Teflon + PE + asphalt	$S_{\text{Teflon}} - (S_{\text{PE}} - S_{\text{asphalt}}) - S_{\text{asphalt}}$	$S_{\text{asphalt}} = 4.2 = 0.3 \times 14.0$
19.04.02	Teflon + PE + asphalt	$S_{\text{Teflon}} - (S_{\text{PE}} - S_{\text{asphalt}}) - S_{\text{asphalt}}$	$S_{\text{asphalt}} = 4.2 = 0.3 \times 14.0$
21.04.02	Teflon + PE + asphalt	$S_{\text{Teflon}} - (S_{\text{PE}} - S_{\text{asphalt}}) - S_{\text{asphalt}}$	$S_{\text{asphalt}} = 4.2 = 0.3 \times 14.0$
22.04.02	Teflon + PE	$S_{\text{Teflon}} - S_{\text{PE}}$	$S_{\text{PE}} = 4.4 = 0.3 \times 14.5$
23.04.02	Teflon + PE	$S_{\text{Teflon}} - S_{\text{PE}}$	$S_{\text{PE}} = 4.4 = 0.3 \times 14.5$
campaign at Experimental Hall at KIP in 2003			
12.04.03	PE only	$S_{\text{PE}} = 23.4$	---
13.04.03	PE only	$S_{\text{PE}} = 23.4$	---
14.04.03	PE only	$S_{\text{PE}} = 23.4$	---
15.04.03	PE only	$S_{\text{PE}} = 23.4$	---
16.04.03	PE + asphalt	$S_{\text{PE}} - S_{\text{asphalt}}$	$S_{\text{asphalt}} = 3.4 = 0.25 \times 13.5$
17.04.03	PE + asphalt	$S_{\text{PE}} - S_{\text{asphalt}}$	$S_{\text{asphalt}} = 3.4 = 0.25 \times 13.5$
18.04.03	PE + asphalt	$S_{\text{PE}} - S_{\text{asphalt}}$	$S_{\text{asphalt}} = 3.4 = 0.25 \times 13.5$
19.04.03	PE + asphalt	$S_{\text{PE}} - S_{\text{asphalt}}$	$S_{\text{asphalt}} = 3.4 = 0.25 \times 13.5$
20.04.03	PE + concrete	$S_{\text{PE}} - S_{\text{concrete}}$	$S_{\text{concrete}} = 3.4 = 0.25 \times 13.5$
21.04.03	PE + asphalt	$S_{\text{PE}} - S_{\text{asphalt}}$	$S_{\text{asphalt}} = 3.4 = 0.25 \times 13.5$
22.04.03	PE + roof-tiles	$S_{\text{PE}} - S_{\text{roof-tiles}}$	$S_{\text{asphalt}} = 3.0 = 0.25 \cdot x2.0$
23.04.03	PE + tiles (flagstone)	$S_{\text{PE}} - S_{\text{flagstone-tiles}}$	$S_{\text{flagstone-tiles}} = 3.0 = 0.21 \times 14.0$
24.04.03	PE + grass	$S_{\text{PE}} - S_{\text{grass}}$	$S_{\text{grass}} = 2.8 = 0.20 \times 14.0$
25.04.03	PE only	$S_{\text{PE}} = 23.4$	---
26.04.03	PE only	$S_{\text{PE}} = 23.4$	---
27.04.03	PE only	$S_{\text{PE}} = 23.4$	---
28.04.03	PE only	$S_{\text{PE}} = 23.4$	---

table 5.2: Dates of experiments performed during the smog chamber campaigns IUP 2002 and KIP 2003 with the surfaces types and its sizes analyzed.

If more than one type of surfaces is present in the smog chamber, all surfaces contribute to the heterogeneous reactions [Trick *et al.*, 2003]. Therefore measured loss frequencies e.g. of NO₂

and formation frequencies of HONO consist of different parts arising from the reaction on the different surfaces. To correct for the effects of the smog chamber walls, experiments were carried out, when no additional surfaces were inside the chamber (see chapter 5.2.1). From the loss of trace gases during these experiments the loss frequency on the walls of the smog chamber can be derived. The correction for leakage according to eq. 5.1 must be applied first to all observed loss frequencies.

We define the leakage-corrected total loss frequency $f_{i,\text{total}}$ of a trace gas i on a certain surface area S_j [m^2], which consist of one surface type j only, as $g_{i,j}$ [$\text{m}^2 \text{s}^{-1}$]. By geometrical considerations we get:

$$\begin{aligned} f_{i,\text{tot.surf}} \cdot (S_{\text{react.surf}} + S_{\text{walls}}) &= g_{i,\text{react.surf}} \cdot S_{\text{react.surf}} + g_{i,\text{walls}} \cdot S_{\text{walls}} \\ \Rightarrow g_{i,\text{react.surf}} &= \frac{f_{i,\text{tot.surf}} \cdot (S_{\text{react.surf}} + S_{\text{walls}}) - g_{i,\text{walls}} \cdot S_{\text{walls}}}{S_{\text{react.surf}}} \end{aligned} \quad \text{eq. 5.2}$$

This term of correction of eq. 5.2 is based on the assumption of a plane surface in the smog chamber (esp. a plane asphalt surface) and was applied to all observations. The real surface area including sub-structures of the asphalt was not considered. Results of BET surface analysis [Finlayson-Pitts, 2004] show that these substructures of urban surfaces such as the asphalt used in this thesis yield an arising from the geometrical to the real surface area size of a factor of 150.

5.1.4 The Measurement Techniques

5.1.4.1 The DOAS White System inside the Smog Chamber

The trace gases HONO and NO_2 (and additional O_3 and HCHO) were measured by Differential Optical Absorption Spectroscopy (DOAS) (see [Platt, 1994; Platt et al., 1979] and chapter 3.2). A White multi-reflection system [Geyer, 1997; Grassi and Guzzi, 2001; Ritz et al., 1992; Trick, 2000; Volkamer, 1996; White, 1942; White, 1976] was used and adapted to the geometry of the smog chamber.

The light of the high-pressure Xe-arc lamp (PLI Hanovia SX5002 SN 1999-80) was coupled into the White system by a Newtonian type telescope with the same aperture as the White system of $f : 100$. Between the three mirrors (A, B, C) the number of traverses was set to 288 during the experiments, corresponding to a light path 2160 m for a base-length of 15 m of the White system. The length of the light path was only changed to record lamp reference spectra. The three spherical concave mirrors: the front mirror A facing the two side by side back mirrors B and C had a dielectrically coating (Laser Optics, Garbsen, Germany) optimized for HONO measurements with the highest reflectivity between 357 ± 20 nm. Absorption of NO_2 , HCHO, and O_3 could be measured as well.

The spectrograph - detector system was coupled to the White system by another Newtonian telescope connected via a standard 200 μm Quartz-fiber (AS UV..VIS 200/220/245 μm , NA = 0.12, length 3 m). The spectrograph for the KIP 2003 campaign was a Czerny-Tuner (ACTON Spectra Pro 500) type with a focal length of 0.5 m, $f = 6.9$. entrance slit: 200 μm , thermostated to $(+ 33 \pm 0.5)^\circ\text{C}$. Using a 600 grooves / mm grating, a spectral resolution of 0.54 nm was achieved. For the experiments during the IUP 2002 campaign, a Czerny-Turner spectrograph (ACTON Spectra Pro 300i) with a focal length of 300 mm, aperture 1:4 (i.e. NA = 0.12), dispersion of the grating (1800 grooves / mm) 0.54 nm / mm (corresponding to 0.038 nm / channel on the photo diode array) was used. The spectrograph was isolated and its temperature stabilized by electrical heating at 35°C to minimize optical errors due to temperature changes. As the fiber itself forms a pinhole of 200 μm diameters, it was used as the spectrographs entrance slit. Both spectrographs had the standard IUP – DOAS detector

(Hoffmann Meßtechnik, Rauenberg, Germany) consisting of a 1024 photodiode array detector (Hamamatsu S3904-1024). The arrays were cooled to $(-13 \pm 0.5)^\circ\text{C}$ to reduce dark current. The time resolution for HONO and NO_2 was about 30 seconds. The software MFC was used. Data evaluation was performed as described in detail in chapter 3.2.4. However, all DOAS spectra were evaluated relatively to a lamp reference spectrum. This reference spectrum was recorded during the background measurements (see chapter 5.2), which took place at the start of each experiment.

The mirrors of the DOAS White system were placed in the aluminum boxes. Therefore the DOAS integrated the trace gas concentrations of NO_2 , HONO, O_3 , and HCHO in the entire smog chamber. The DOAS measurement light beam was investigated for photolysis, but no significance could be observed (see figure 5.7).

5.1.4.2 Additional Measurements during the IUP 2002 campaign

In April 2002, during the extension of the NITROCAT project a cooperation with the groups of the Brandenburgische Technische Universität Cottbus, Germany (BTU) and the Bergische Universität und Gesamthochschule Wuppertal, Germany (BUGH) was performed, combining field studies and laboratory work and further additional measurement techniques were available.

At the box 2 (refer to figure 5.1), where the White reflecting mirrors were located, the LOPAP II instrument (see chapter 3.1.1.4, and [Heland *et al.*, 2001; Kleffmann *et al.*, 2002]) was operated by the BUGH, and measured HONO with a time resolution of 1 min and a detection limit of 5 ppt.

At this box, the temperature and the dew point were measured by a mirror-sensor system (sensor type S 3000 80D; Michell Instruments, Friedrichsdorf, Germany) with an error of 0.2°C . Additionally, the ozone concentration was measured by a commercial short path UV-absorption instrument (Horiba APOA 360; Horiba Europe GmbH Oberursel, Germany) with a time resolution of 1 minute and a detection limit of 1 ppb, and the NO concentrations by a gas-phase chemiluminescence system (Ecophysics CLD 770 AL ppt; Ecophysics GmbH München, Germany) at time resolution of 1 min, with a detection limit of 50 ppt were measured.

At the other box, box 1 (also refer to figure 5.1), the WEDD (see chapter 3.1.1.1 and [Acker *et al.*, 2001b]) with a time resolution of 10 min and a detection limit of 2 ppt was sited. Additional measurements included NO and NO_2 , (Ecophysics CLD 770 ppt chemiluminescence NO analyzer and PLC 760 photolytic converter; Ecophysics GmbH München, Germany); NO and NO_y , (Ecophysics CLD 770 ppt NO chemiluminescence analyzer and gold converter; Ecophysics GmbH München, Germany) as well as temperature and relative humidity, all measured by the BTU.

As both in-situ instruments have a lower detection limit for HONO than the DOAS system, they characterized the background level of HONO, NO_2 and NO in the chamber (typically as low as some 10 ppt up to a few 100 ppt) before the inlet of additional NO_2 as well as the mixing in the reaction system.

5.1.4.3 Measurement Equipment during the KIP 2003 campaign

During the KIP 2003 campaign, the ozone concentrations in the smog chamber were additionally measured by a commercial short path UV-absorption instrument (Horiba APOA 360; Horiba Europe GmbH Oberursel, Germany) with a time resolution of 1 minute and a detection limit of 1 ppb. However, as suspected no significant ozone levels (remaining zero in

the range of the detection limit during the whole time of the KIP 2003 campaign) were observed for the NO_x chemistry system inside the smog chamber.

NO was detected by a gas-phase chemiluminescence system (Ecophysics CLD 770 AL ppt; Ecophysics GmbH München, Germany). The measurement frequency of this system was variable, set to 1 min, with a detection limit of 50 ppt.

The inlets to both monitors were located in the middle of the smog chamber and therefore in the middle of the DOAS light beam. They are therefore suspected to measure the same air mass as the DOAS White system.

Temperature and relative humidity (both psychrometer, SN 12696) and an additional R.H. (thin-film sensor) inside the smog chamber were measured by components of a commercial meteorological weather measurement station (Hoffmann Meßtechnik, Rauenberg, Germany) and recorded by the HMT data logger AME 70 (SN 024203), where also the pressure-sensor (Silicon element) and an additional temperature sensor (Pt – 1000) were located outside the smog chamber. The sensors were also located in the middle of the smog chamber.

5.2 Results of the Experiments

The following experimental procedure was applied during all experiments. In particular, each experiment consisted of 7 steps:

(step 1.):

The smog chamber was rinsed three times with the dry synthetic air (purity 5.0; Messer-Griessheim, Ludwigshafen, Germany) before each experiment started. The starting values of NO decreased by a factor of ~ 5 – 10 during this procedure. Unfortunately, no DOAS trace gas measurements are available for that period of the experiments, as the collapsed tube blocks the light beam.

(step 2.):

The smog chamber was filled with the dry synthetic air through the special-prepared Teflon tube (see chapter 5.1.1.1). The final filling was stopped at an over-pressure defined by the water-manometers (usually, it was set to 1-5 mbar). As explained in chapter 5.1.1.1, the over-pressure defines the leakage rate of the smog chamber, thus its was set to a low value. Using the external mass-flow-controllers (see also chapter 5.1.1.1) to balance the leakage loss of air from inside the smog chamber, the smog chamber was retained at this state. Flow rates of 5 l/min up to 20 l/min corresponding to a leakage loss frequency of $0.67\text{--}1.67 \cdot 10^{-4} \text{ s}^{-1}$ were adjusted. The temperature in the reaction chamber was constant at ~ 297 K.

(step 3.):

The background values were measured for approx. 1-2 hours. Starting values (see figure 5.3) of NO₂ were found to be almost constant at values in the range of 0.1 up to 1.5 ppb at the different days of experiments. HONO was found to decrease by 0.3 ppb (sometimes even 1.0 ppb) down to values of 0.1-0.8 ppb. No ozone or formaldehyde were observed inside the smog chamber, while NO was found in the range of 1.0 up to 9.0 ppb on several days. R.H. starting values varied between 6.5 and 13.7 %.

(step 4.):

The chamber was humidified for up to 4 hours. The terminal R.H. was varied by the temperature of the water bath between 20 % and 80 %. The humidification was found to be well described by a polynomial increase of 2nd order.

During this humidification, an increase of HONO from background values of approx. 0.1-0.8 ppb up to maximum mixing ratios of 9.5 ppb was generally observed (see figure 5.3). The R.H. and HONO are clearly correlated. Each variation in the humidification of the smog chamber, even short-time interruptions or irregularities, were immediately reflected in the HONO mixing ratios (see e.g. figure 5.10, when a change of the synthetic air bottle caused an

interruption in the R.H. increase of some minutes). No time-delay was observed between the HONO and the R.H. increase. We will discuss these observations and give physical explanations in chapters 5.4.2 and 5.5. An increase of HONO could also be observed after addition of NO_2 , if the smog chamber was humidified again at this time (see figure 5.3). No changes of the NO_2 mixing ratios were found at this period of the experiment. NO_2 remained constant at its background values of ~ 0.5 ppb.

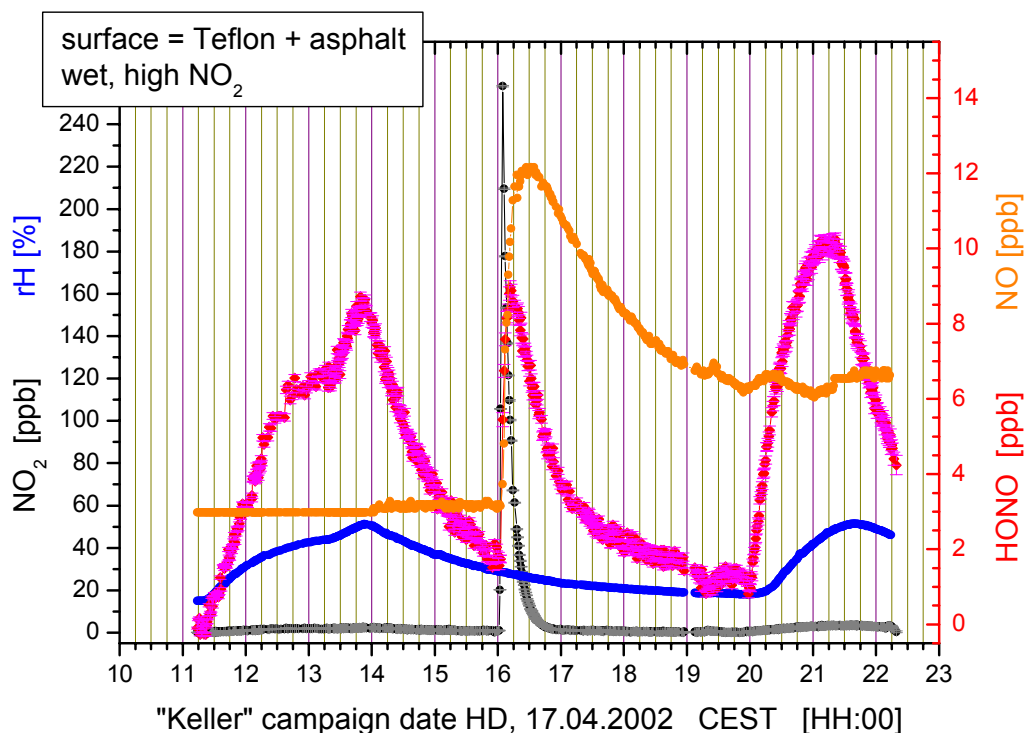


figure 5.3: Temporal trends of the trace gases HONO (red symbols; right scale), NO_2 (black and grey symbols; left scale), and NO (orange symbols; right scale), as well as R.H. (blue line; left scale) during the experiment on Teflon + PE + asphalt surfaces in the smog chamber on 17.04.2002 during the IUP 2002 campaign.

The NO mixing ratios were observed different. NO either remained constant (figure 5.3) at its starting value of $\sim 3 - 6$ ppb or decreases to ~ 1 ppb (see e.g. figure 5.5, figure 5.10) until the addition of NO_2 into the smog chamber. This can be caused by impurities of dry synthetic air (see table 5.1). The bubbler may act as a filter for NO_x , thus NO levels decrease, when the smog chamber was humidified and increased again, when the bubbler was disconnected again. However, chemical production of NO is another possible explanation for its increase from 6.5 ppb to 19.3 ppb during some experiments. This production is believed to be caused by secondary reactions of HONO and will be discussed in detail in chapter 5.5.3.4. (step 5.):

After the bubbler was disconnected again, R.H. decreased with leakage loss frequency as can be seen from figure 5.3, and figure 5.4. The decay of R.H. could be well quantified to be a 1st order exponential decay, as can be seen from figure 5.4. Fitting results were sometimes better than 99 %. Those values were compared to those, calculated from the leakage set at the mass flow controllers [L / min] yielding the corresponding leakage loss frequencies of the smog chambers volume of 2.503 m³. Within the errors both values are in good agreement. Thus, the loss of water from the smog chamber is by leakage only, and an uptake of H_2O onto the surfaces is negligible.

HONO directly followed the trend of R.H. and decreases from 9.5 ppb to 3.7 ppb during these next two hours.

During this period of the experiment, photolysis tests were performed, when the DOAS light beam was blocked. These tests are illustrated by the thin lines in figure 5.5 connecting the DOAS measurements. No evidence on a faster HONO decay caused by the DOAS light beam could be observed (see figure 5.5).

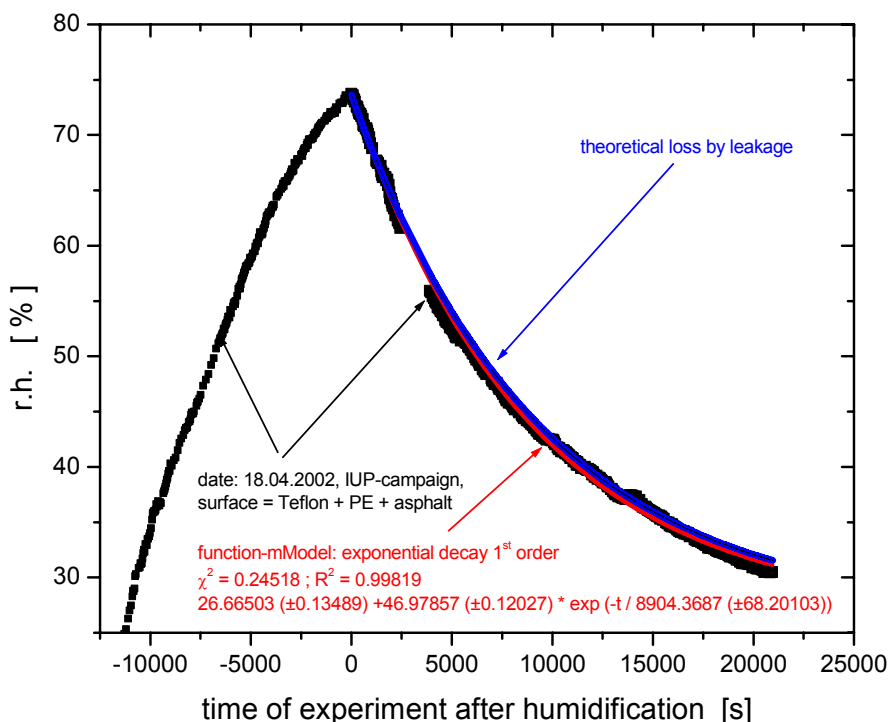


figure 5.4: Humidification of the smog chamber and decay of R.H. in the smog chamber, exemplary for the experiment on 19.04. of the KIP 2003 campaign (see also figure 5.10). The decay was observed to be a 1st order exponential process in good agrees with the theoretical loss by leakage.

(step 6.):

In the next step, an equivalent to 80-360 ppb of NO₂ was added to the system, which is reflected by the fast decrease of NO₂. The addition was observed to be completed within 5 min. NO₂ was generally found to decrease following a first order exponential with time constants in the range of 20 min, corresponding to net loss frequencies (corrected for leakage) of $1.3 \cdot 10^{-4} \text{ s}^{-1}$.

After addition of NO₂, HONO increased from 3.7 ppb up to 7.3 ppb. Since the maximum level of HONO is reached several minutes after the NO₂ addition was finished, this increase of HONO is not caused by impurities of the NO₂, but by chemical production. The concentration time profiles of NO₂ and HONO indicate a consecutive process converting NO₂ partly into HONO, which further decomposes into other products. The physical processes observed during steps 4 and 5 are still ongoing and falsify the pure kinetics. Thus, no analytical solutions based on steady state assumptions can be drawn and a model is necessary to interpret the observations.

NO mixing ratios increases at the same time from 16.7 ppb to 110 ppb, but reached its maximum later than the HONO mixing ratio. Generally, higher NO values were achieved on the PE foil than on Teflon.

(step 7.):

After reaching the maximum HONO mixing ratio of 7.2 ppb, a first order loss process of HONO is observed (see figure 5.3) until the end of the experiment. The HONO loss is slower than that for NO₂, but faster than leakage alone.

Secondary reactions of HONO yielding NO are most likely responsible that the decrease of NO is the slowest of all trace gases observed in the smog chamber.

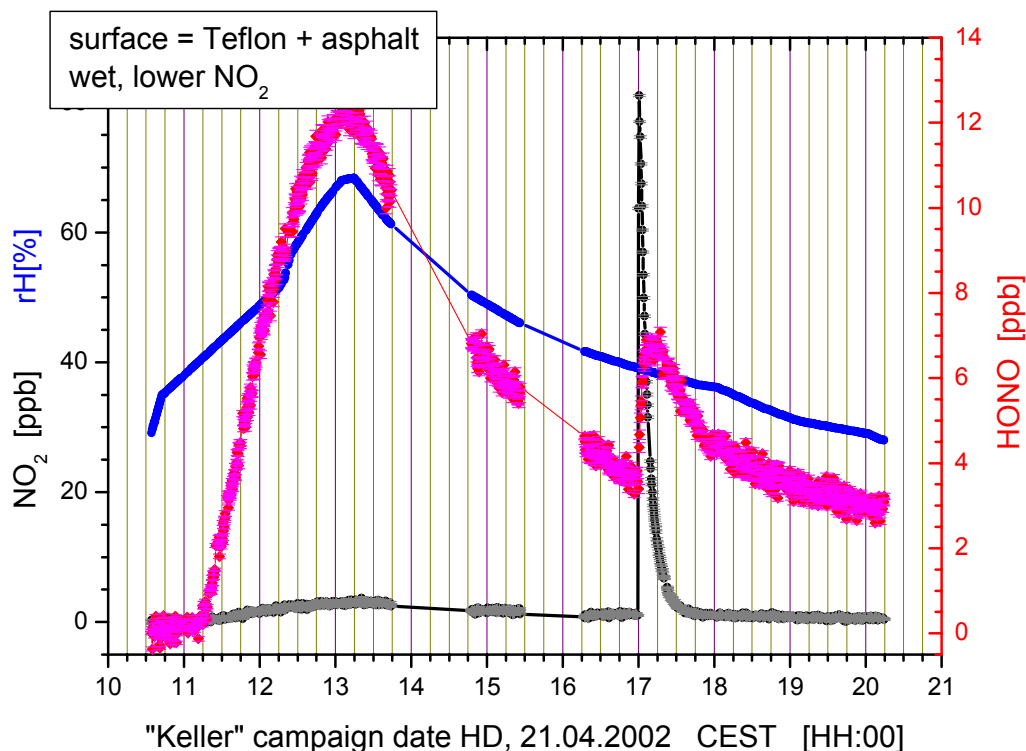


figure 5.5: Temporal trends of the trace gases HONO (red symbols; right scale), NO₂ (black symbols; left scale), and R.H. (blue line; left scale) during the experiment on Teflon + PE + asphalt surfaces in the smog chamber on 21.04.2002 during the IUP 2002 campaign. Gaps in the time series relate to the tests of photolysis by the DOAS light beam.

5.2.1 Experiments on Teflon and PE Surface

Experiments on Teflon and PE foil (figure 5.6, figure 5.7), of which the walls of the smog chamber consisted, were performed by the procedure described above. As explained in chapter 5.1.3 and eq. 5.2, these experiments were needed to correct for the contribution of the smog chambers walls to the heterogeneous HONO formation.

During these experiments, the whole inner surfaces of the smog chamber including the boxes were covered by the Polyethylene or Teflon foil (total surface area $S = 23.4 \text{ m}^2$). Since during the IUP 2002 campaign the asphalt plates were insert into the smog chamber on a slide of PE foil, additional measurements with the surfaces Teflon + PE were performed for this campaign. Thereby, the same PE slide of a size of 4.4 m^2 was insert into the Teflon tubes smog chamber.

Generally, the background values of all trace gases, measured during the first two hours of each experiment were lower for experiments on Teflon or PE, than for the other surfaces (figure 5.6, figure 5.7). This is most likely due to the consistence and “history” of these urban surfaces (see chapter 5.1.3). The yield of HONO in the gas phase during the humidification of the smog chamber and the amount formed by reaction r. 2.33 was as well lower compared to the experiments on urban surfaces. Of crucial importance is that all, the NO₂ loss frequencies and that of HONO and NO (figure 5.6, figure 5.7) observed during the experiments on Teflon and PE foil are lower than those observed during experiments on additional urban surfaces (see table 5.2). This will be quantified in chapter 5.3.

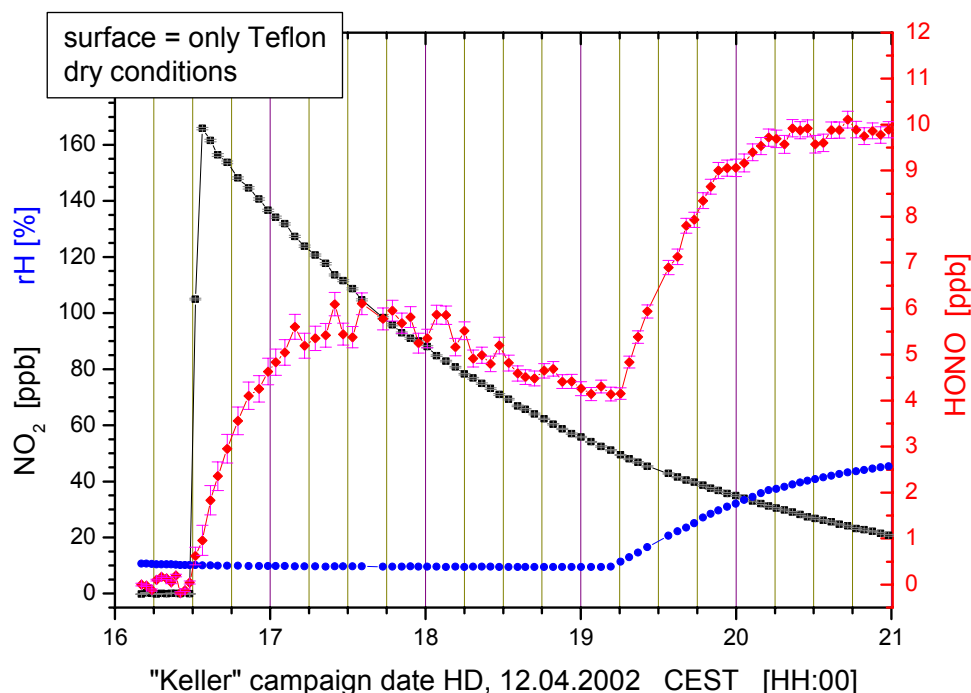


figure 5.6: Temporal trends of the trace gases HONO (red symbols; right scale), NO₂ (black and grey symbols; left scale), and R.H. (blue line; left scale) during the experiment on Teflon surface only in the smog chamber on 12.04.2002 during the IUP 2002 campaign.

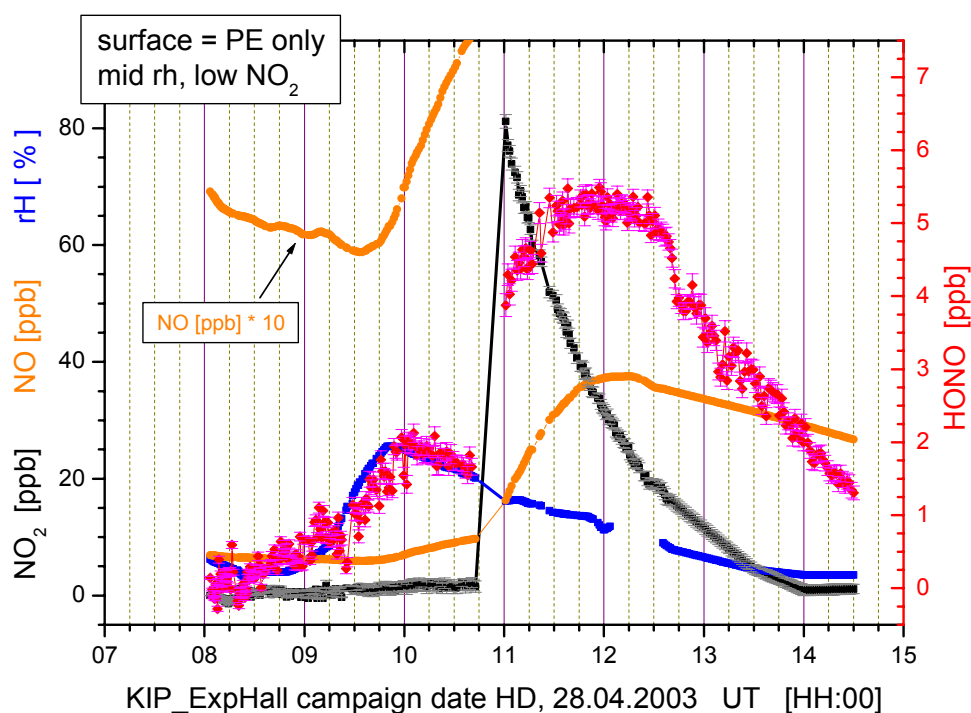


figure 5.7: Temporal trends of the trace gases HONO (red symbols; right scale), NO₂ (black symbols; left scale), and NO (orange symbols; left scale – additionally a second line, multiplied by a factor of 10 is illustrated), as well as R.H. (blue line; left scale) during the experiment on PE surface only in the smog chamber on 28.04.2003 during the KIP 2003 campaign.

The experiments with Teflon and PE foil as exclusive surfaces inside the smog chamber were performed under dry ($R.H. < 10\%$), and wet conditions ($R.H.$ up to 70%) two times during each campaign: before the experiments with different urban surfaces started and repeated afterwards to elucidate any changes in the background environment. No changes were found in these comparisons.

5.2.2 Experiments on Real Urban Surfaces

The experiments on the other surfaces (see table 5.2) were also performed by the procedure described above. To insert these different surfaces into the smog chamber, they were placed on a slide of PE foil ($0.3\text{ m} \times 14.5\text{ m} = 4.4\text{ m}^2$). This slide was pulled through the smog chamber foil tube a few hours before the experiments started. For the IUP 2002, when the smog chamber was built of a Teflon tube, this PE slide represents an additional surface type and had to be corrected for as well.

The background values of HONO and NO observed above these surfaces are higher than for the laboratory surfaces PE or Teflon. Additionally, the asphalt is by some few percent more humid (figure 5.5, figure 5.8, figure 5.9, and figure 5.10). Both effects could only partially reduced by rinsing the smog chamber.

Several experiments on asphalt were performed varying the most important influencing parameters: the initially injected amount of NO_2 and the $R.H.$ NO_2 was injected in a range from low values of 50 ppb up to highest values of approx. 350 ppb . Due to limitations from the experimental setup of our smog chamber, $R.H.$ could only be varied in a range from 10% to 80% (figure 5.5, figure 5.8, figure 5.9, and figure 5.10).

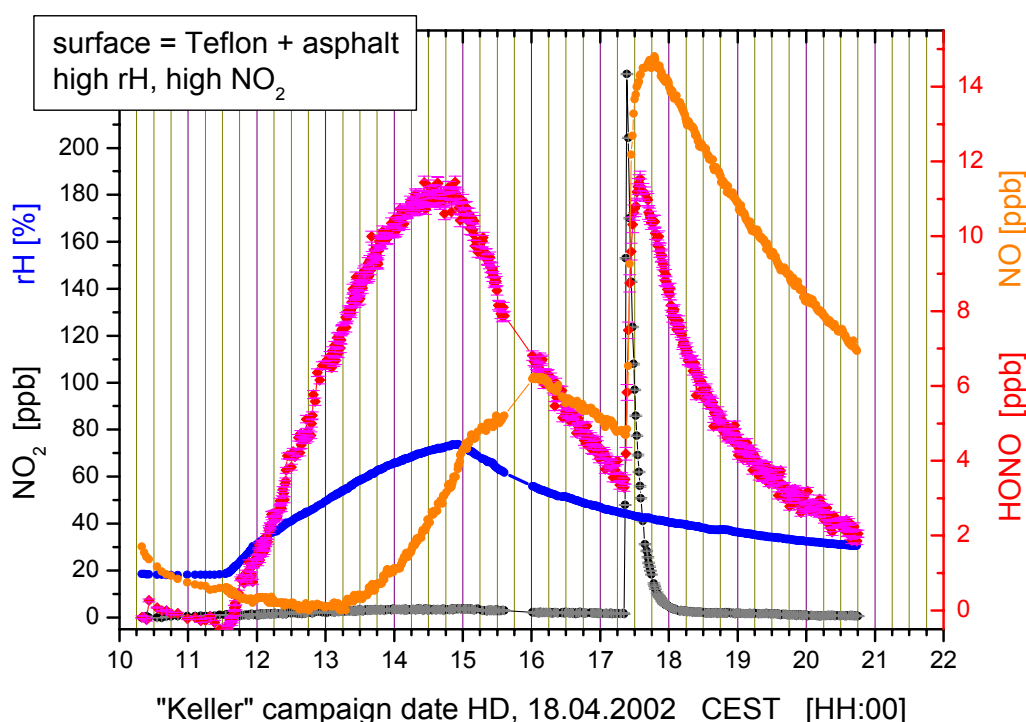


figure 5.8: Temporal trends of the trace gases HONO (red symbols; right scale), NO_2 (black and grey symbols; left scale), and NO (orange symbols; right scale), as well as $R.H.$ (blue line; left scale) during the experiment on Teflon + PE + asphalt surfaces in the smog chamber on 18.04.2002 during the IUP 2002 campaign.

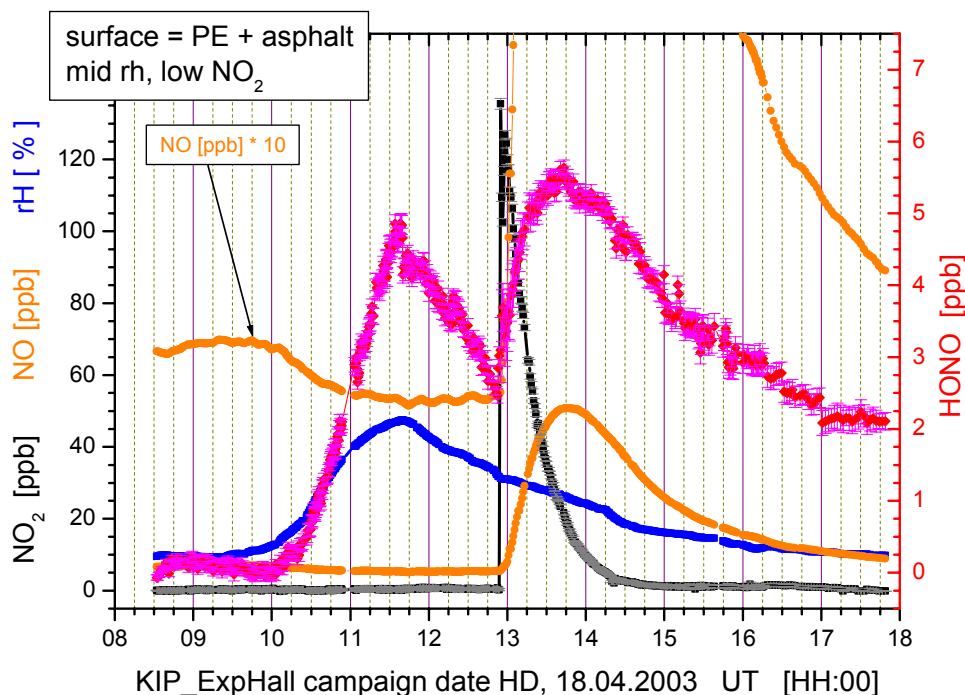


figure 5.9: Temporal trends of the trace gases HONO (red symbols; right scale), NO_2 (black symbols; left scale), and NO (orange symbols; left scale – additionally a second line, multiplied by a factor of 10 is illustrated), as well as R.H. (blue line; left scale) during the experiment on PE + asphalt surfaces in the smog chamber on 18.04.2003 during the KIP 2003 campaign.

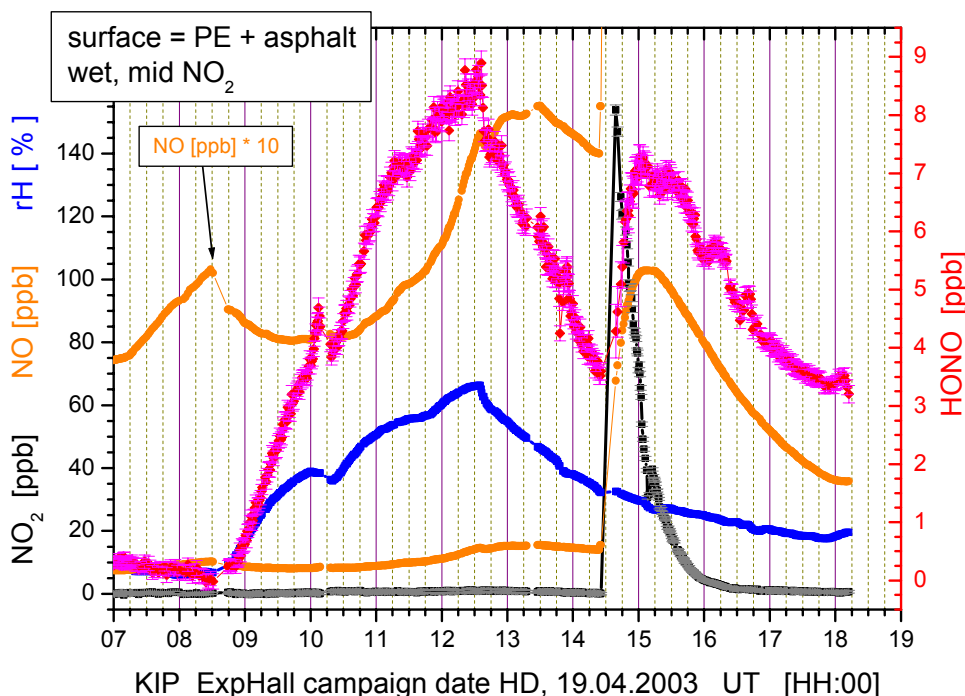


figure 5.10: Temporal trends of the trace gases HONO (red symbols; right scale), NO_2 (black symbols; left scale), and NO (orange symbols; left scale – additionally a second line, multiplied by a factor of 10 is illustrated), as well as R.H. (blue line; left scale) during the experiment on PE + asphalt surfaces in the smog chamber on 19.04.2003 during the KIP 2003 campaign.

HONO values up to 14 ppb were observed in the smog chamber, when it was humidified. The amounts of nitrous acid formed from NO_2 by reaction r. 2.33 reach up to 13 ppb, which is higher than on the laboratory surfaces PE or Teflon. NO mixing ratios up to 110 ppb were observed in the smog chamber, when the asphalt plates were insert.

The decays of the trace gases NO , NO_2 , but also HONO (figure 5.5, figure 5.8, figure 5.9, and figure 5.10) are faster on the urban surfaces than on Teflon or PE foil (figure 5.6 and figure 5.7). This will be quantified in chapters 5.3 and 5.5.

The same experimental procedure was applied, when concrete, roof-tiles and flagstone-tiles were investigated. The yield of HONO and the decay of NO_2 slightly differ from those on asphalt. This is quantified in table 5.3.

5.2.3 Experiment of HONO Formation on Grass

The experiment on the grass meadow is outstanding (see figure 5.11). The grass was dogged out a short time before this experiment started. The roots and the ground-soil were left at it, thus the grass was alive. It is well known that living materials, such as plants, are mostly a very complex system and both can appear: uptake of a specific trace gases as well as out-gassing at the same time [Delmas *et al.*, 1995; Ganzeveld *et al.*, 2002; Gao *et al.*, 1993; Klepper, 1979; Lenzian and Kahlert, 1988; Wild *et al.*, 1997]. The ratio of both is dependent on various numbers of environmental as well as biological parameters, which could not be characterized in this thesis.

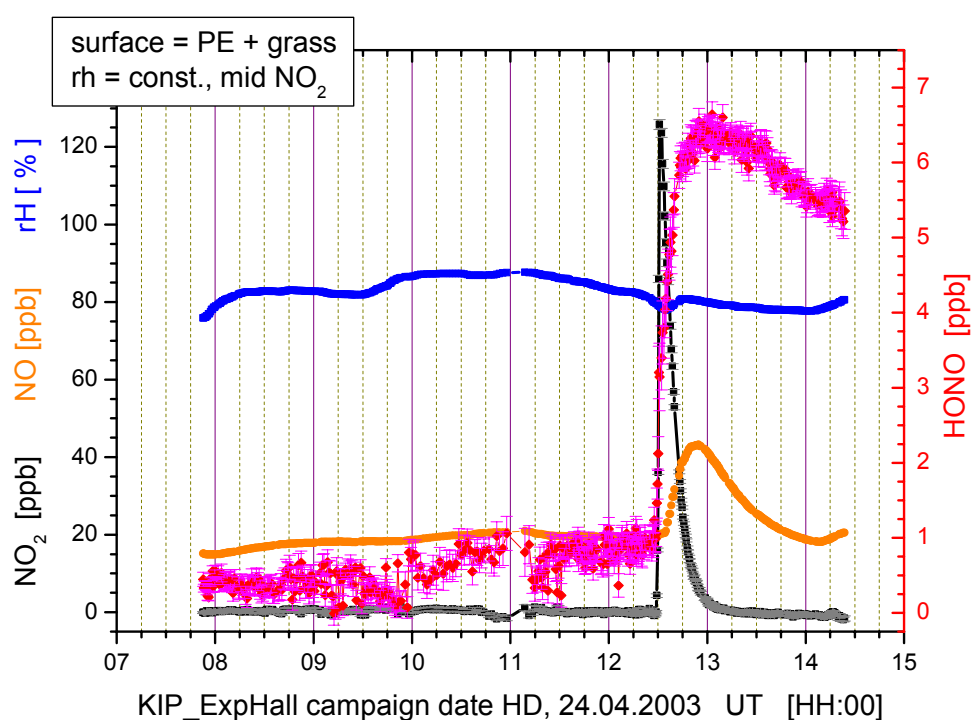


figure 5.11: Temporal trends of the trace gases HONO (red symbols; right scale), NO_2 (black symbols; left scale), and NO (orange symbols; left), as well as R.H. (blue line; left scale) during the experiment on PE + grass in the smog chamber on 24.04.2003 during the KIP 2003 campaign.

However, all background values were found at high levels at the start of this experiment: HONO \sim 1 ppb, NO_2 \sim 1 ppb, and NO at even \sim 15 ppb. It was not possible to reduce these starting values by rinsing the smog chamber.

The relative humidity of this biological system started at ~ 80 % and remained constant throughout the entire experiment. No additional humidification was performed, and variations of the R.H. are most likely due to the living grass.

The fastest NO₂ decay was observed for this experiment (see table 5.3), while the HONO decay was the slowest. The maximum NO value during this experiment was ~ 40 ppb, and showed a shaper peak structure than during the other experiments.

These effects are suspected to be caused in the biological processes ongoing during this experiment. This cannot be quantified by our studies. All results from these experiments should be handled with care and any comparison to other surface types drawn later (see e.g. table 5.3), should be understood as a raw hint only. Further investigations of interactions of NO_x species with plants should be performed.

5.3 Analysis of NO₂ Decays

In this chapter, the temporal trend of the NO₂ observed during the experiments in the smog chamber will be quantified. We will apply the basic analytical evaluations (see e.g. [England and Corcoran, 1974; Finlayson-Pitts et al., 2003; Harrison and Collins, 1998; Jenkin et al., 1988; Kleffmann et al., 1998; Pitts et al., 1984c; Sakamaki et al., 1983; Svensson et al., 1987; Wiesen et al., 1995]) and show their limitations, which lead to the model in chapter 5.5.

5.3.1 Calculation of the NO₂ Uptake Coefficients

It was mentioned that HONO is believed to be formed by heterogeneous reactions of NO₂ (reaction r. 2.33). Thus parameters concerning this precursor trace gas are of major interest for the HONO formation potential on different surfaces. The rate-limiting step of the reaction mechanism, which determines the loss of NO₂, is assumed to be the adsorption of gaseous NO₂ into the liquid bulk [Finlayson-Pitts and Pitts, 2000; Finlayson-Pitts et al., 2003; Kleffmann et al., 1998; Wiesen et al., 1995].

The observed decays of NO₂, which was injected at initial amounts between 80 and 350 ppb, are illustrated by figure 5.12. It can be seen that NO₂ is initially lost by a first order exponential decay (rectilinear in the logarithm scaled plot):

$$[NO_2](t) = [NO_2](t = 0) \cdot e^{-f_{NO_2} \cdot t} \quad \text{eq. 5.3}$$

The life times of NO₂ range between 15 minutes on e.g. asphalt to > 100 min on the PE or Teflon foil.

At the end of the initial HONO formation, the NO₂ loss is no longer a strictly exponential decay. This is most likely due to secondary reactions and a steady state, which established at that time (see figure 5.12). Thus, we will only use the initial loss of NO₂ for the analysis of NO₂ uptake coefficients.

Although the loss by leakage is between 3 - 40 times smaller than the observed NO₂ decays (see table 5.3), the correction for leakage was applied according to eq. 5.1. The correction for the different surface types possibly contributing to the heterogeneous formation of HONO (according to in eq. 5.2 in chapter 5.1.3) leads the deposition frequencies g_{NO₂} per surface area.

In order to study the heterogeneous interaction of a gas, for example NO₂, with a liquid bulk on a surface the so-called uptake of a trace gas expressed in terms of an uptake coefficient γ_{NO₂} is of particular interest [Fuchs and Sutugin, 1971].

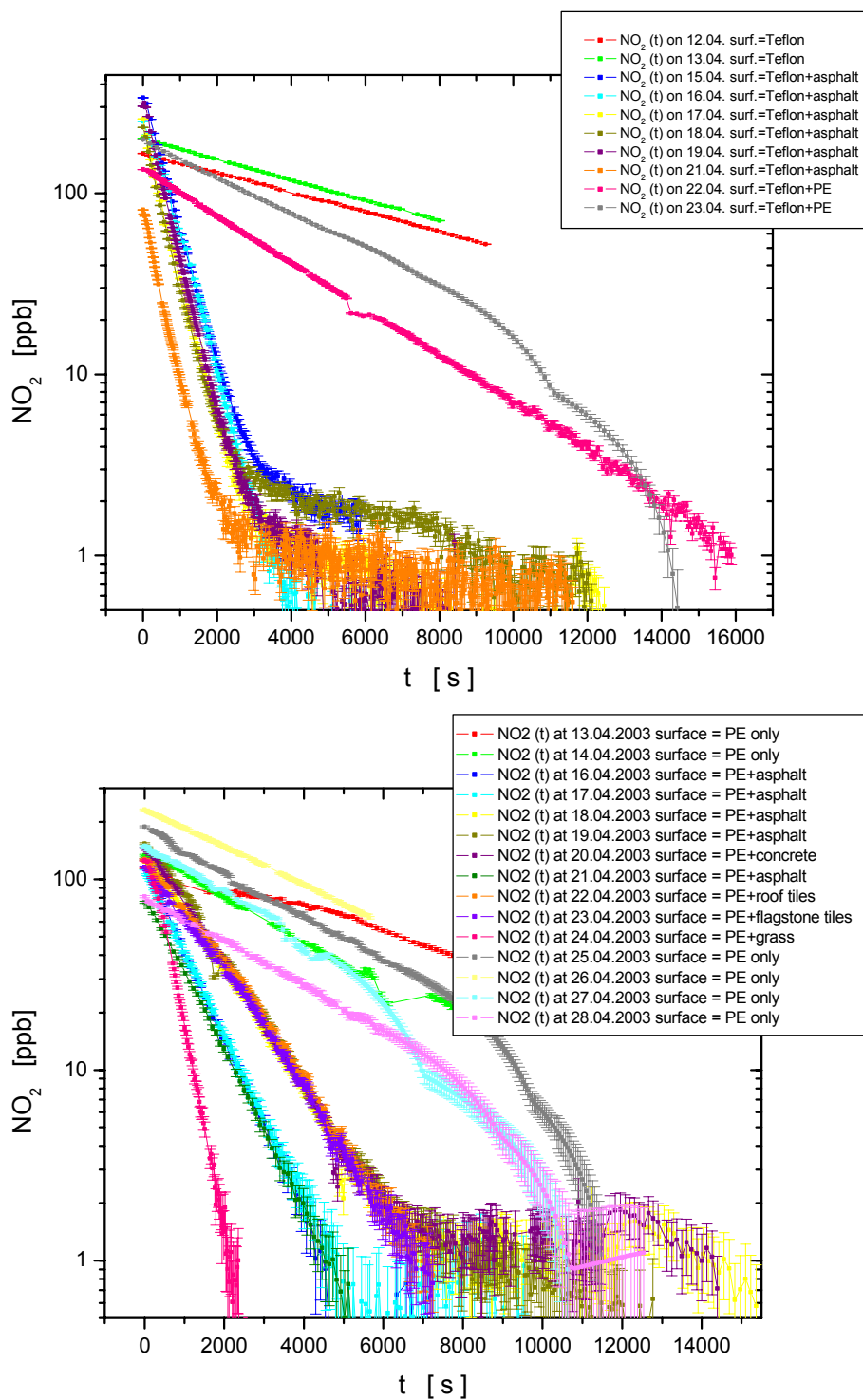


figure 5.12: NO_2 decay in the smog chamber for the experiments during the IUP 2002 campaign (upper plot) and the KIP 2003 campaign (lower plot). Different colors refer to the different experiments on the various surfaces. The strongest slope was observed for grass as reactive surface, weaker for asphalt, concrete and the different kinds of tiles, but lowest slopes were observed for the decay of NO_2 on the PE foil or Teflon.

date	surface type	temp. [°C]	$\langle v \rangle$ [m s ⁻¹]	[NO ₂] ⁰ _{max} [ppb]	d / dt NO ₂ [10 ⁻³ s ⁻¹]	f _{leak} [10 ⁻⁴ s ⁻¹]	f _{NO₂,depos} [10 ⁻³ s ⁻¹]	g _{j,NO₂} [10 ⁻⁵ m ² s ⁻¹]	γ _{NO₂} [10 ⁻⁶]
12.4.2002	Teflon	24.9 ± 2.5	370.4 ± 1.6	171.1 ± 0.3	0.12 ± 0.1	1.0 ± 0.1	0.02 ± 0.01	0.10 ± 0.39	0.03 ± 0.11
13.4.2002	Teflon wet	25.1 ± 2.5	370.5 ± 1.6	193.3 ± 1.2	0.13 ± 0.1	1.0 ± 0.1	0.03 ± 0.01	0.13 ± 0.39	0.03 ± 0.11
15.4.2002	Asphalt	24.9 ± 2.5	370.4 ± 1.5	351.2 ± 1.6	1.71 ± 0.2	1.3 ± 0.1	1.57 ± 0.03	34.62 ± 0.69	9.36 ± 0.19
16.4.2002	Asphalt	25.0 ± 2.5	370.4 ± 1.6	260.3 ± 1.7	1.47 ± 0.2	1.3 ± 0.1	1.34 ± 0.02	28.86 ± 0.59	7.80 ± 0.16
17.4.2002	Asphalt	24.9 ± 2.5	370.4 ± 1.5	247.8 ± 1.4	2.05 ± 0.7	1.3 ± 0.1	1.92 ± 0.08	42.98 ± 1.81	11.61 ± 0.49
18.4.2002	Asphalt	25.0 ± 2.5	370.4 ± 1.6	230.7 ± 1.1	2.06 ± 0.3	1.3 ± 0.1	1.93 ± 0.03	43.26 ± 0.75	11.69 ± 0.21
19.4.2002	Asphalt	24.8 ± 2.5	370.3 ± 1.5	327.5 ± 1.2	2.01 ± 0.2	1.3 ± 0.1	1.87 ± 0.03	41.99 ± 0.70	11.35 ± 0.19
21.4.2002	Asphalt	24.5 ± 2.5	370.1 ± 1.5	82.7 ± 0.4	2.20 ± 0.3	1.0 ± 0.1	2.10 ± 0.03	47.42 ± 0.75	12.82 ± 0.21
22.4.2002	Teflon + PE	24.5 ± 2.5	370.1 ± 1.5	137.0 ± 0.2	0.30 ± 0.1	1.3 ± 0.1	0.17 ± 0.01	3.44 ± 0.44	0.93 ± 0.12
23.4.2002	Teflon + PE	24.5 ± 2.5	370.1 ± 1.5	197.4 ± 12.5	0.24 ± 0.1	1.0 ± 0.1	0.14 ± 0.01	2.78 ± 0.39	0.75 ± 0.10
12.4.2003	PE only	18.3 ± 1.8	366.2 ± 1.1	n.a.	n.a.	1.3 ± 0.1	n.a.	n.a.	n.a.
13.4.2003	PE only	19.2 ± 1.9	366.8 ± 1.2	n.a.	n.a.	1.3 ± 0.1	n.a.	n.a.	n.a.
14.4.2003	PE only	19.6 ± 2.0	367.0 ± 1.2	133.3 ± 1.2	0.23 ± 0.8	1.7 ± 0.2	0.06 ± 0.08	0.28 ± 0.35	0.08 ± 0.09
15.4.2003	PE only	21.0 ± 2.1	367.9 ± 1.3	n.a.	n.a.	1.3 ± 0.1	n.a.	n.a.	n.a.
16.4.2003	PE + asphalt	21.4 ± 2.1	368.2 ± 1.3	126.0 ± 0.5	1.10 ± 0.2	1.3 ± 0.1	0.96 ± 0.02	49.30 ± 1.03	13.40 ± 0.28
17.4.2003	PE + asphalt	21.0 ± 2.1	368.0 ± 1.3	112.1 ± 0.3	1.00 ± 0.1	1.0 ± 0.1	0.90 ± 0.01	45.51 ± 0.83	12.38 ± 0.23
18.4.2003	PE + asphalt	21.6 ± 2.2	368.3 ± 1.3	130.7 ± 0.3	0.68 ± 0.1	1.0 ± 0.1	0.59 ± 0.01	26.68 ± 0.81	7.25 ± 0.22
19.4.2003	PE + asphalt	20.8 ± 2.1	367.8 ± 1.3	162.5 ± 1.2	0.71 ± 0.1	1.3 ± 0.1	0.58 ± 0.01	26.44 ± 0.86	7.19 ± 0.23
20.4.2003	PE + concrete	21.7 ± 2.2	368.4 ± 1.4	150.3 ± 0.4	0.71 ± 0.1	1.0 ± 0.1	0.61 ± 0.01	27.93 ± 0.82	7.59 ± 0.22
21.4.2003	PE + asphalt	20.8 ± 2.1	367.8 ± 1.3	79.3 ± 0.4	0.90 ± 0.1	1.0 ± 0.1	0.80 ± 0.01	39.32 ± 0.84	10.70 ± 0.23
22.4.2003	PE + roof-tiles	20.4 ± 2.0	367.6 ± 1.3	127.7 ± 0.5	0.63 ± 0.1	1.7 ± 0.2	0.47 ± 0.02	11.05 ± 0.93	3.01 ± 0.25
23.4.2003	PE + flagst.-tiles	20.8 ± 2.1	367.8 ± 1.3	116.1 ± 0.4	0.64 ± 0.1	1.7 ± 0.2	0.47 ± 0.02	11.08 ± 0.93	3.01 ± 0.25
24.4.2003	PE + grass	21.2 ± 2.1	368.1 ± 1.3	144.9 ± 1.3	1.98 ± 0.3	1.7 ± 0.2	1.81 ± 0.04	72.78 ± 1.49	19.79 ± 0.41
25.4.2003	PE only	22.1 ± 2.2	368.6 ± 1.4	187.3 ± 0.9	0.28 ± 0.1	1.7 ± 0.2	0.11 ± 0.02	0.53 ± 0.07	0.14 ± 0.02
26.4.2003	PE only	22.1 ± 2.2	368.6 ± 1.4	243.7 ± 1.1	0.23 ± 0.1	0.7 ± 0.1	0.16 ± 0.01	0.76 ± 0.05	0.21 ± 0.01
27.4.2003	PE only	21.6 ± 2.2	368.3 ± 1.3	154.5 ± 1.0	0.32 ± 0.1	0.7 ± 0.1	0.25 ± 0.01	1.17 ± 0.03	0.32 ± 0.01
28.4.2003	PE only	22.1 ± 2.2	368.6 ± 1.4	81.4 ± 0.5	0.28 ± 0.1	0.7 ± 0.1	0.21 ± 0.01	0.98 ± 0.03	0.03 ± 0.11

table 5.3: Overview on all experiments performed in the smog chamber campaigns of the IUP 2002 and KIP 2003. To the corresponding date of experiments, its surface type(s), the mean temperature, the maximum amount of NO₂ injected, the loss frequency by leakage, the total NO₂ loss frequency, the NO₂ loss frequency corrected for leakage and that corrected for effects of different surface types as well as the resulting reactive uptake coefficient.

This uptake coefficient can easily be calculated from the deposition frequencies per surface area ($g_{NO_2,depos.}$) on each surface (for asphalt as an example):

$$\gamma_{NO_2,asphalt} = \frac{4}{\langle v_{NO_2} \rangle} \cdot \frac{V_{tent}}{S_{asphalt}} \cdot \frac{d[NO_2]}{[NO_2] dt} = \frac{4}{\langle v_{NO_2} \rangle} \cdot V_{tent} \cdot g_{NO_2,depos.asphalt} \quad \text{eq. 5.4}$$

and $V_{chamber} = 2.502 \text{ m}^3$ is the volume of the smog chamber, the area size of the reactive surface area $S_{react.surf} = \text{m}^2$ and $\langle v_{NO_2} \rangle$ is the mean velocity of the NO_2 molecules calculated by a Maxwell-Boltzmann – statistic. The amount of NO_2 added to the system, the total NO_2 loss frequency, the leakage loss frequencies at each day of an experiment, the NO_2 loss frequency corrected for leakage and that corrected for effects of different surface types as well as the resulting reactive uptake coefficient are summarized in table 5.3.

For the KIP 2003 campaign, the averaging NO_2 deposition frequency per surface area on PE foil was $(7.1 \pm 1.1) \times 10^{-6} \text{ s}^{-1} \text{ m}^{-2}$ corresponding to an uptake coefficient of $(1.9 \pm 0.3) \times 10^{-7}$. Higher values were obtained for roof-tiles and flagstone-tiles with an average NO_2 deposition frequencies per surface area of $(1.1 \pm 0.1) \times 10^{-4} \text{ s}^{-1} \text{ m}^{-2}$ corresponding to an uptake coefficient of $(3.0 \pm 0.3) \times 10^{-6}$. One order of magnitude higher values were observed for asphalt and concrete surfaces with a NO_2 deposition frequency per surface area of $(3.6 \pm 0.1) \times 10^{-4} \text{ s}^{-1} \text{ m}^{-2}$ corresponding to an uptake coefficient of $(1.0 \pm 0.2) \times 10^{-5}$ and approx. double these values for grass.

During the IUP 2002 campaign only three different types of surfaces were investigated for their uptake of NO_2 . Teflon was observed to yield a loss frequency of NO_2 per surface area of $(1.2 \pm 0.4) \times 10^{-6} \text{ s}^{-1} \text{ m}^{-2}$, corresponding to an uptake coefficient of $(3.1 \pm 1.1) \times 10^{-7}$, the PE foil to be $(3.1 \pm 0.1) \times 10^{-5} \text{ s}^{-1} \text{ m}^{-2}$, corresponding to $(8.4 \pm 1.1) \times 10^{-7}$, and highest values of $(4.0 \pm 0.1) \times 10^{-4} \text{ s}^{-1} \text{ m}^{-2}$, $(1.1 \pm 0.2) \times 10^{-7}$ respectively for asphalt as reactive surface insert into the smog chamber. The differences of the NO_2 uptake coefficient on asphalt between the IUP 2002 and KIP 2003 are not understood thus far.

5.3.2 Dependence of the NO_2 Uptake Coefficients on R.H.

Further parameters (besides the surface type) were suspected to influence the frequency of NO_2 loss in the smog chamber. Unfortunately, the set up of the smog chamber did not allow variations of the temperature, which would influence the rate constants and equilibrium constants as mentioned in chapter 2.

However, the influence of relative humidity on the uptake of NO_2 was investigated in this thesis as well. Therefore, the initial decay of NO_2 per NO_2 (this corresponds nearly to the uptake coefficient of NO_2), is plotted versus the relative humidity [%] in the figure 5.13. Due to experimental limitations, the maximum of the relative humidity inside the smog chamber could only be varied in a range from $\sim 0\%$ to 80% in this thesis. It can be seen from figure 5.13 that the NO_2 uptake is not dependent on R.H.

The experiments on 12.04. and 13.04.2003 during the KIP2003 campaign were stopped too early, and the NO_2 decay had not completely established. Thus, it was not possible to evaluate these data for their HONO formation potential and they were therefore not taken into account for the calculations of the NO_2 uptake coefficients.

One has to mention that the range of R.H. variations (only from 15 up to 45 % when NO_2 was added to the system) in this thesis is small. The maximum R.H. is limited by the setup of our smog chamber and by leakage. Thus, our results cannot be generally extended to atmospheric conditions and further investigations are needed (see chapter 5.6.3).

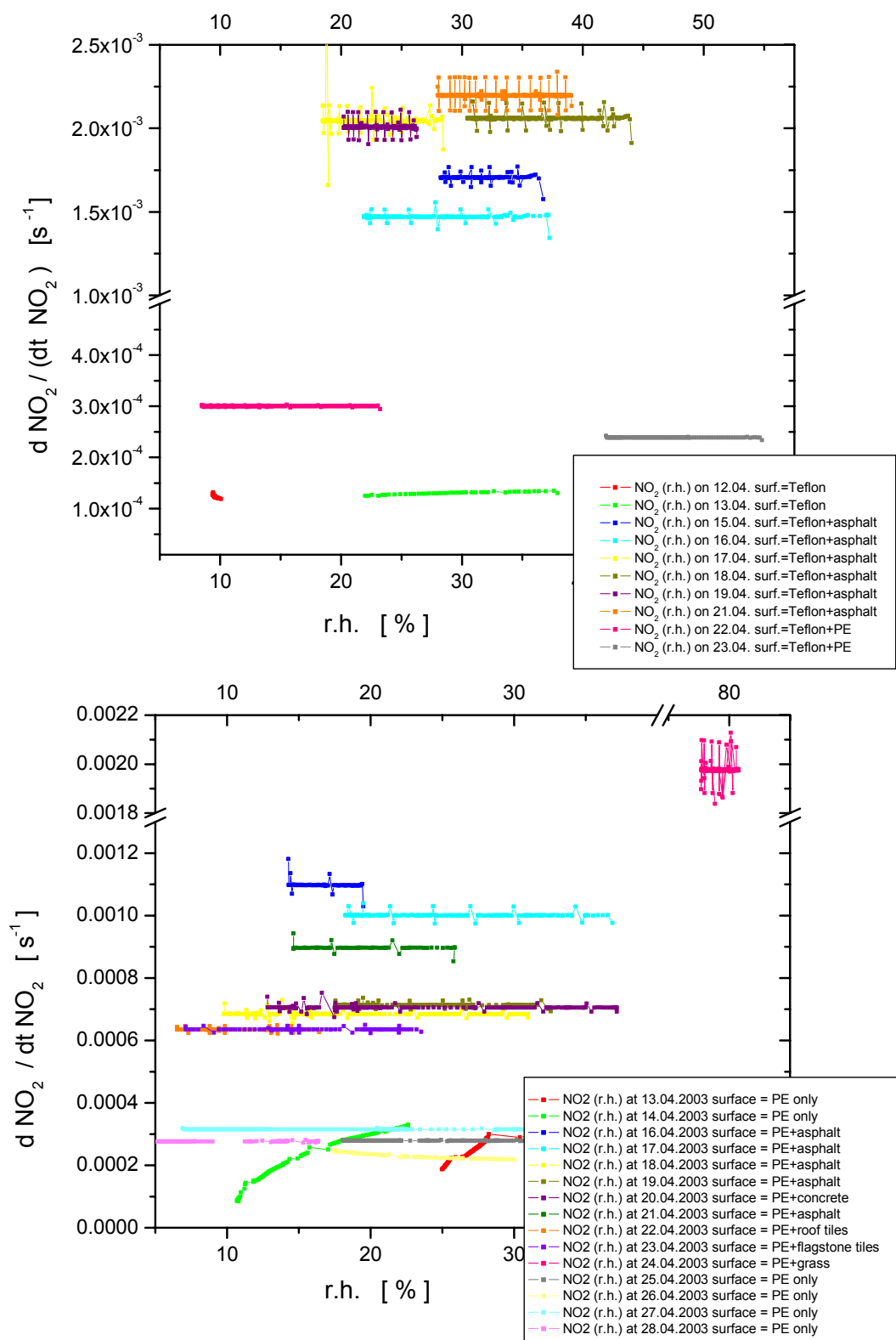


figure 5.13: Dependence of the relative NO_2 decay, which corresponds directly to the uptake coefficients, in the smog chamber observed during the experiments of the IUP 2002 (upper plot) and the KIP 2003 campaign (lower plot).

5.4 Analysis of HONO in the Smog Chamber

The temporal trends of the HONO in the smog chamber can be subdivided in three periods:

- (I): slowly decreasing or even constant value at a constant R.H. during the background measurements at the start of each experiment. However, this period is characterized by establishing the initial steady only and will thus not further analyzed.
- (II): increase and decrease of HONO both clearly correlated to R.H.
- (III): additional formation of HONO after NO₂ addition.

During period (III), HONO increased again, which is caused by chemical production, but the physical processes of the period (II) are still ongoing. This averts pure analytic solutions or equations based on steady state assumptions on the kinetics. Thus, it demands on a model to handle all these processes simultaneously (see chapter 5.5).

In the following, we will show the thus far applied analysis of the HONO time series during these three periods and study the influence of both NO₂ (chapter 5.4.1) and R.H. (chapter 5.4.2) IT will also be shown that this analysis procedure is limited to a qualitative point of view for our smog chamber studies.

5.4.1 Dependence of HONO Yield on NO₂

During period I, and II, the concentrations of NO₂ remained constant at values close to zero. Thus, it is expected that reaction r. 2.33 and therefore NO₂ as the precursor of HONO has no influence on the HONO trends at these periods of the experiment.

Obviously, NO₂ has to be considered for the period III, when the HONO mixing ratios observed in the smog chamber originate from chemical production as well. According to [Finlayson-Pitts *et al.*, 2003; Jenkin *et al.*, 1988; Lammel and Cape, 1996; Pitts *et al.*, 1984c; Platt, 1986; Sakamaki *et al.*, 1983; Svensson *et al.*, 1987], we analyze the HONO formation at this time assuming a 1st order kinetic with respect to NO₂ for reaction r. 2.33. This leads to the overall rate-law of:

$$\text{rate} = + \frac{d[\text{HONO}]}{dt} = - \frac{1}{2} \frac{d[\text{NO}_2]}{dt} = k \cdot [\text{H}_2\text{O}]^a \cdot [\text{NO}_2]^b \quad \text{eq. 5.5}$$

The reaction orders of the reaction r. 2.33 with respect to water and nitrogen dioxide are then represented by the constants a and b, respectively. If the reaction is 1st order with respect to NO₂, a plot of the HONO formation versus the initial NO₂ concentration should be linear. The constant b can be obtained from the slope of the appropriate log-log plot. A summary of observations of the reaction orders from previous studies was recently performed by [Finlayson-Pitts *et al.*, 2003].

However, to analyze the dependence of HONO formation on NO₂ based on eq. 5.5, a constant R.H. is required, when the added initial amount of NO₂ is varied. During the experiments of this thesis, the R.H. continuously decreased by the rate of leakage, when NO₂ was injected at various amounts into the smog chamber (see chapter 5.2). Thus, not only chemical production of HONO but also the variations of HONO due to Langmuir theory occurred simultaneously during this period III. Consequently, any analysis based on equation eq. 5.5 is falsified by this fundamental physical principle of adsorption and desorption of HONO. Thus, only a first and qualitative dependence of the HONO formation on the NO₂ concentration can be derived in this thesis. Therefore, the initial amount of NO₂ injected and the subsequent observed maximum yield of the concentration of HONO in the smog chamber are compared in table 5.4.

The different experiments with their different surface types as well as different R.H. and variations of the NO₂ injected are listed in table 5.4.

date	surface type	$f_{\text{leak.}}$ [10^{-4} s^{-1}]	at R.H. [%]	$[\text{NO}_2]_{\text{max}}^0$ [ppb]	$[\text{HONO}]_{\text{max}}$ [ppb]	$[\text{NO}]_{\text{max}}$ [ppb]
12.4.2002	Teflon	1.0 ± 0.1	9.6	171.1 ± 0.3	10.1 ± 0.2	n.a.
13.4.2002	Teflon wet	1.0 ± 0.1	34.4	193.3 ± 1.2	7.3 ± 0.3	7.0
15.4.2002	Asphalt	1.3 ± 0.1	35.1	351.2 ± 1.6	n.a.	27.7
16.4.2002	Asphalt	1.3 ± 0.1	34.9	260.3 ± 1.7	5.0 ± 0.1	14.4
17.4.2002	Asphalt	1.3 ± 0.1	27.8	247.8 ± 1.4	8.6 ± 0.1	12.2
18.4.2002	Asphalt	1.3 ± 0.1	42.8	230.7 ± 1.1	11.1 ± 0.2	14.8
19.4.2002	Asphalt	1.3 ± 0.1	25.7	327.5 ± 1.2	3.1 ± 0.1	n.a.
21.4.2002	Asphalt	1.0 ± 0.1	38.6	82.7 ± 0.4	12.2 ± 0.2	n.a.
22.4.2002	Teflon + PE	1.3 ± 0.1	18.6	137.0 ± 0.2	2.2 ± 0.1	n.a.
23.4.2002	Teflon + PE	1.0 ± 0.1	50.4	197.4 ± 12.5	5.2 ± 0.1	n.a.
12.4.2003	PE only	1.3 ± 0.1	n.a.	n.a.	n.a.	n.a.
13.4.2003	PE only	1.3 ± 0.1	n.a.	n.a.	n.a.	n.a.
14.4.2003	PE only	1.7 ± 0.2	15.1	133.3 ± 1.2	2.5 ± 0.1	90.4
15.4.2003	PE only	1.3 ± 0.1	n.a.	n.a.	n.a.	n.a.
16.4.2003	PE + asphalt	1.3 ± 0.1	18.2	126.0 ± 0.5	3.0 ± 0.1	35.0
17.4.2003	PE + asphalt	1.0 ± 0.1	31.5	112.1 ± 0.3	5.5 ± 0.2	102.8
18.4.2003	PE + asphalt	1.0 ± 0.1	26.4	130.7 ± 0.3	5.6 ± 0.1	102.8
19.4.2003	PE + asphalt	1.3 ± 0.1	29.4	162.5 ± 1.2	7.3 ± 0.2	50.7
20.4.2003	PE + concrete	1.0 ± 0.1	31.2	150.3 ± 0.4	8.7 ± 0.4	102.7
21.4.2003	PE + asphalt	1.0 ± 0.1	25.7	79.3 ± 0.4	6.3 ± 0.2	45.8
22.4.2003	PE + roof-tiles	1.7 ± 0.2	12.7	127.7 ± 0.5	5.8 ± 0.1	13.3
23.4.2003	PE + flagst.-tiles	1.7 ± 0.2	20.0	116.1 ± 0.4	4.8 ± 0.1	64.3
24.4.2003	PE + grass	1.7 ± 0.2	80.4	144.9 ± 1.3	6.6 ± 0.2	21.9
25.4.2003	PE only	1.7 ± 0.2	28.0	187.3 ± 0.9	5.3 ± 0.2	43.2
26.4.2003	PE only	0.7 ± 0.1	26.0	243.7 ± 1.1	6.0 ± 0.3	92.8
27.4.2003	PE only	0.7 ± 0.1	22.5	154.5 ± 1.0	8.6 ± 0.3	102.8
28.4.2003	PE only	0.7 ± 0.1	11.4	81.4 ± 0.5	5.4 ± 0.1	73.1

table 5.4: Maximum values of HONO [ppb] and NO [ppb] achieved after injection of a certain amount of NO_2 [ppb] listed. This injection was performed at the R.H. listed as well.

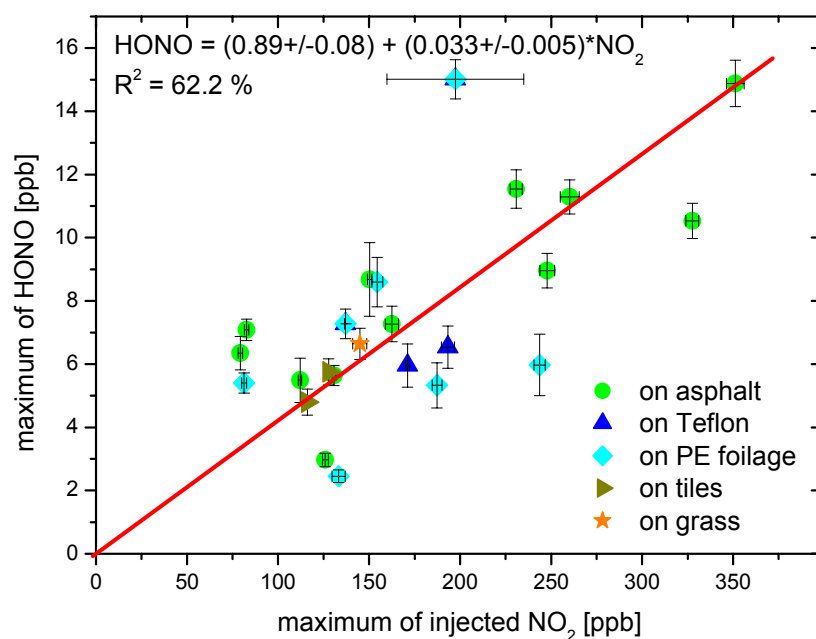


figure 5.14: Maximum HONO mixing ratios achieved in all smog chamber experiments after the injection of the maximum amount of NO_2 on all different kind of surfaces and at different R.H.

The maximum concentration of HONO formed after the injection of pure NO₂ is additionally plotted in figure 5.14 versus the maximum concentration of NO₂ added. In this figure 5.14, the various surface types are highlighted by different colors. For this illustration, the different R.H. existing at the injection of NO₂ were not taken into account. A good linear correlation of the maximum amount of HONO formed and the maximum concentration of NO₂ injected initially could be observed (see figure 5.14). The slope of this linear regression was (0.033 ± 0.005) supporting 1st order kinetics for the formation of HONO from NO₂. This is in good agreement with previous studies [England and Corcoran, 1974; Febo and Perrino, 1991; Finlayson-Pitts et al., 2003; Harrison and Collins, 1998; Jenkin et al., 1988; Kleffmann et al., 1998; Pitts et al., 1984c; Pitts et al., 1985; Sakamaki et al., 1983; Svensson et al., 1987; Wiesen et al., 1995]. However, it should be mentioned again that this is a brief qualitative overview only. The quantification of the HONO dependence on NO₂ can only be obtained from the model presented in chapter 5.5 and at a constant R.H.

5.4.2 Dependence of HONO on Relative Humidity

The relative humidity was varied during the entire time of the individual experiments in contrast to previous laboratory studies investigating the heterogeneous HONO formation at a constant R.H. In our studies, the R.H. increased during a period of humidification of the smog chamber and decreased by the rate of leakage afterwards, and especially continued decreasing when NO₂ was added to the system. Thus, the dependence of HONO formation on the R.H. cannot be studied by the basic analysis of eq. 5.5 so far performed.

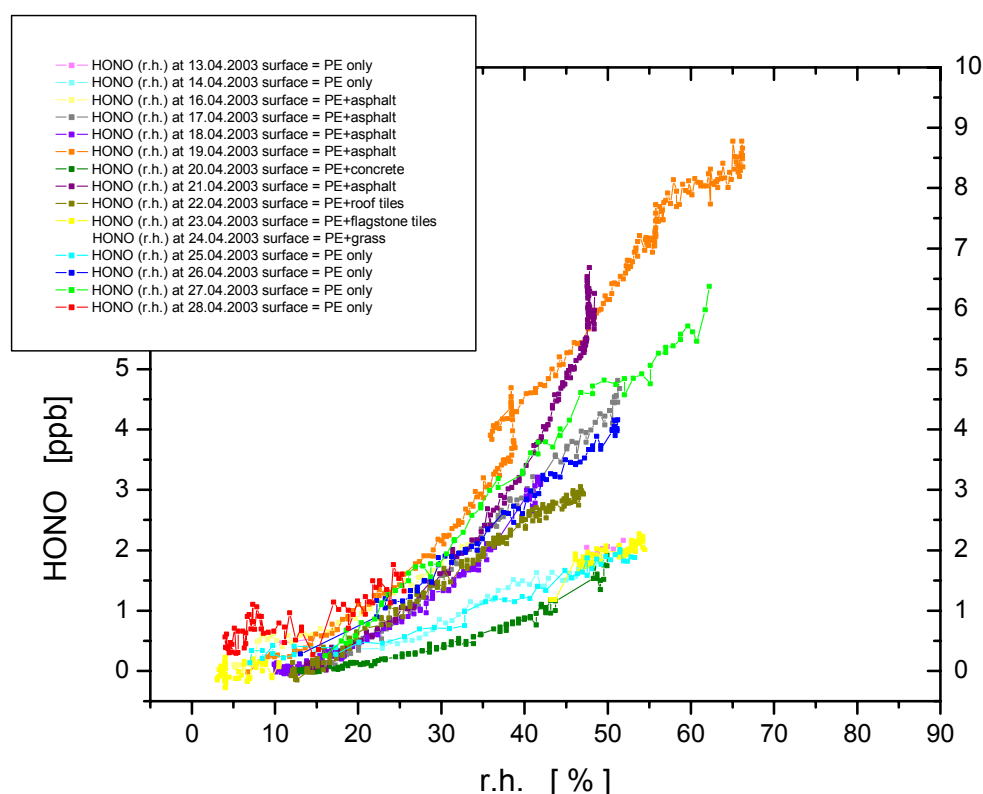


figure 5.15: Increase of the HONO concentration in the smog chambers during the humidification. Upper panel: during the IUP 2002 campaign, lower: during the KIP 2003 experiments. The errors of the measurements were omitted for a clearer illustration.

The first two periods of each experiment, i.e. the measurements of the constant background conditions and the increase of HONO in the gas phase during humidification and dehumidification of the smog chamber are illustrated by figure 5.15 for the KIP 2003 campaign. A linear correlation between the increase of HONO and R.H. can be seen from figure 5.16). The slope of this linear correlation between HONO and R.H. is similar for all different types of surfaces (see figure 5.15) and becomes equal within the errors.

Even sudden interruptions of the humidification of the smog chamber at $\sim 10:00$ (see figure 5.10) immediately appeared in the HONO mixing ratio. The absence of any time delay between the variation of R.H. and the corresponding change of HONO concentration is too fast to be caused by any chemical reaction. Thus, a physical equilibrium seems most likely. We will show in chapter 5.5 that the Langmuir adsorption-desorption isotherm theory (see also chapter 2.4) is valid to describe these observations.

Of crucial importance is further the fact that the HONO inside the smog chamber decrease by the rate of leakage, as the R.H. did so as well (see chapter 5.2). The slope of a plot of the decreasing mixing ratio of HONO versus the R.H. in the smog chamber is in essentially agree with that for the increasing HONO concentration, when R.H. increased as well (see figure 5.16). Especially, the absolute values of the HONO mixing ratios drop to those prior observed, when the smog chamber was humidified (see figure 5.16). Thus, no hysteresis, which is often observed for heterogeneous catalysis, especially when including chemisorption (see e.g. [Adamson and Gast, 1997; Thomas and Thomas, 1997]), occurred in our experiments.

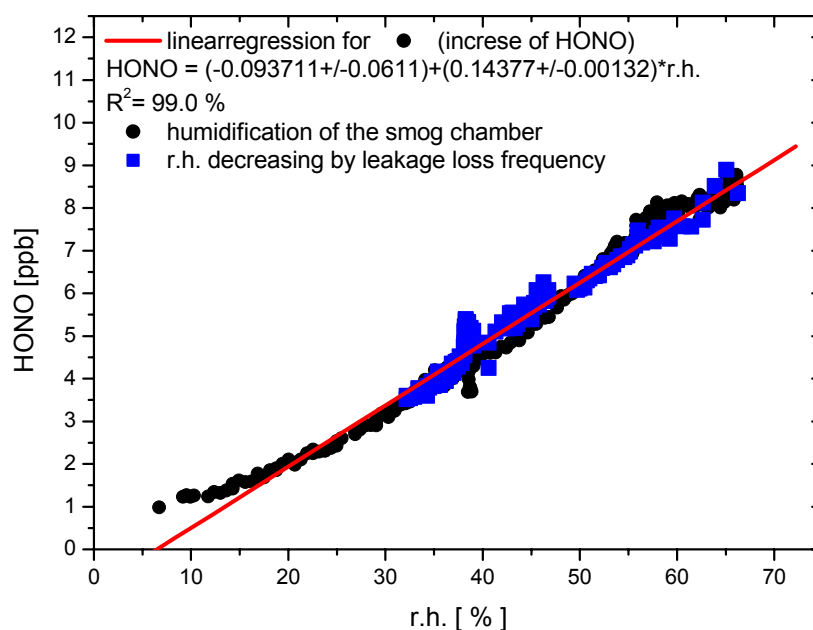


figure 5.16: Correlation of the HONO increase during the humidification of the smog chamber, and decrease with R.H. by leakage loss frequency. Both exemplary for the 19.04. of the KIP 2003 campaign with surfaces PE + asphalt plates.

From these facts, we conclude the HONO molecules are adsorbed at the surface by a weak physical bonding and have a possibility to be released into the gas-phase. At least one of these processes must be dependent on R.H. to explain the correlation between HONO and R.H.

To quantify this effect, table 5.5 summarizes the yield of HONO by humidifying the smog chamber. It can be seen that the mixing ratio of HONO in the gas phase depends on the terminal R.H. in the smog chamber and the surface type. However, the absolute values of HONO derived from changes of the R.H. depend on the background values. Since the surface

type itself is involved in the process yielding HONO in the gas phase during period II, this indicates the surface adsorbed form of HONO to do so as well. The bonding structure and the total amount of this HONO adsorbed at the surface may contribute to the mechanism releasing HONO into the gas phase. Both inhibit an analytical solution of the dependence of HONO release on R.H., because they were not measured in this thesis. This again calls for a model description of the HONO time series.

date	surface type	R.H. max. [%]	[HONO] _{max} [ppb]	[NO] _{max} [ppb]
12.4.2002	Teflon	45.3	10.1 ± 0.2	n.a.
13.4.2002	Teflon wet	58.4	13.3 ± 0.3	4.6
16.4.2002	Asphalt	41.0	5.0 ± 0.1	5.9
17.4.2002	Asphalt	51.2	8.6 ± 0.1	3.3
18.4.2002	Asphalt	73.7	11.1 ± 0.2	6.2
19.4.2002	Asphalt	37.5	3.1 ± 0.1	n.a.
21.4.2002	Asphalt	68.4	12.2 ± 0.2	n.a.
22.4.2002	Teflon + PE	39.2	2.2 ± 0.2	n.a.
23.4.2002	Teflon + PE	63.7	5.2 ± 0.1	n.a.
13.4.2003	PE only	51.9	4.4 ± 0.1	29.1
14.4.2003	PE only	49.0	4.3 ± 0.1	9.7
16.4.2003	PE + asphalt	34.2	5.1 ± 0.1	4.9
17.4.2003	PE + asphalt	51.4	6.5 ± 0.2	29.3
18.4.2003	PE + asphalt	47.4	4.4 ± 0.1	5.5
19.4.2003	PE + asphalt	66.3	8.9 ± 0.2	15.5
20.4.2003	PE + concrete	56.9	5.0 ± 0.1	4.9
21.4.2003	PE + asphalt	48.4	6.3 ± 0.2	9.5
22.4.2003	PE + roof-tiles	47.1	3.1 ± 0.1	2.2
23.4.2003	PE + flagst.-tiles	54.5	2.3 ± 0.1	1.8
25.4.2003	PE only	67.8	6.3 ± 0.2	1.7
26.4.2003	PE only	51.2	4.9 ± 0.2	8.1
27.4.2003	PE only	49.7	5.1 ± 0.2	10.5
28.4.2003	PE only	25.5	3.5 ± 0.1	9.7

table 5.5: Maximum values of HONO [ppb] and NO [ppb] achieved during the humidification of the smog chamber up to the value aspired (listed as well).

The table 5.5 shows also that significant amount of NO are sometimes formed during the end of period II. Generally, more NO is formed, if both the maximum HONO mixing ratio in the smog chamber and the maximum R.H. are high (see table 5.5). There are no comparable observations reported in literature thus far. However, no clear correlation between NO observed in the gas phase and the levels of HONO and / or R.H. could be derived from our data. It seems that NO formation in the smog chamber starts, if both HONO and R.H. levels are above a certain threshold, which depends on both parameters. Recent measurements by [Finlayson-Pitts, 2003; Finlayson-Pitts, 2004] show that the formation of NO from secondary reactions of HONO as well as its yield (compared to other products) is dependent on R.H. It is therefore assumed that the secondary reactions of HONO, which form NO, become only significant above this threshold. Its value cannot be quantified at this point and will be analyzed by the model (see chapter 5.5).

Another possible explanation for the increase of NO concentrations is a contamination of the dry synthetic air by certain amounts of NO_x (see table 5.1). The bubbler system used for the humidification is separated from the gas supply of the smog chamber, when an aspired R.H. is reached. During its time of operation, it may act as a sufficient filter for NO_x, thus reducing the impurities of NO_x in the synthetic air. After disconnecting, this filter is no longer present, thus NO concentrations increase inside the smog chamber due to their flush from the exterior gases. Since the solubility of gaseous NO is low [Finlayson-Pitts and Pitts, 2000], a filtering

of NO can only be caused by a heterogeneous reaction with the surfaces of the frit. However, this remains unclear, and by our data, we cannot exclude one of these possibilities above, thus both approaches were considered in the model (see chapter 5.5).

At this point, an additional remark about the origin of HONO in the smog chamber is very important. Since the synthetic air is contaminated by NO_x (=NO + NO₂), these NO_x may be converted into HONO and HNO₃ on surfaces in the bubbler according to r. 2.33 and r. 2.32, respectively. However, this conversion has an efficiency, which can be derived from field measurements of [Stutz *et al.*, 2002] to be in the order ~ 30 %. A previous study by [Trick, 2000] also showed that significant amounts of NO and NO₂ are accompanied by r. 2.33, when HONO was generated in a glass gadget and emitted into the gas phase by flushing synthetic air upon. Consequently, if HONO is flushed into the smog chamber, NO and NO₂ would also be added into the chamber during the steps 4 and 5. Both NO and NO₂ were not found to increase during period II of humidification of the smog chamber. Furthermore, NO was found to decrease sometimes, when the bubbler was connected to the flush of synthetic air. Therefore, the majority of HONO, which was observed in the order of some up to ten ppb in the smog chamber at that time, cannot origin from an artificial production in the flush of synthetic through the bubbler.

5.5 Analysis of NO_x Chemistry in the Smog Chamber: Modeling Studies

From the analysis above it became obvious that the uptake coefficients of HONO cannot be derived from a simple analysis of its decay as performed for NO₂ in chapter 5.3.1. In particular, the assumption that the surface can act as an infinite sink for NO_x is not justified in a smog chamber. In this chapter, we will quantify the equilibrium of adsorption and desorption of HONO using the Langmuir isotherm theory and present and validate a model to determine the constants of adsorption and desorption of HONO in this smog chamber.

5.5.1 Modifications of Langmuir Theory for HONO

The dependence of the HONO concentrations in the smog chamber on R.H. point to a fast - and therefore most likely physical - equilibrium between HONO and H₂O. Since no gas-phase reactions are known to be sufficiently fast to describe this correlation (see chapter 2.3), heterogeneous chemistry with the surfaces of the smog chamber seems more likely. As shown later, the dependence of HONO on R.H. can be described by Langmuir adsorption and desorption isotherms, which state the dependence of two species, if they compete for the same surface sites to be adsorbed at. We have described the Langmuir theory in detail in chapter 2.4. Here we will focus on its modifications with respect to the NO_x-chemistry system inside the smog chamber.

In chapter 2.4 we have presented the desorption of a species to be a statistical process depending proportional on the amount of HONO molecules adsorbed at a surfaces inside the smog chamber ([HONOs]) and sufficiently characterized by a rate constant k_{des} including the probability of desorption. Considering the total number of all sites (N) available on the surface for adsorption and the fraction of surface coverage by HONO Θ_{HONO} according to equation eq. 2.18, the rate of HONO desorption (see equation eq. 2.41) can be expressed as:

$$\frac{d[HONO]}{dt} = k_{des} \cdot \Theta_{HONO} \cdot N = k_{des} \cdot [HONO]_s \quad \text{eq. 5.6}$$

It is important to note that HONO desorption is a statistical process and comparable to the (natural) radioactive decay. The rate constant k_{des} can further depend on temperature and

pressure, but is independent from the concentrations of other species, such as water, and therefore R.H.

According to the uptake coefficient γ , which is the probability for a trace gas to be adsorbed by the frequency of adsorption k_{ads} , we define an out-gassing probability Θ_{HONO} for HONO. The latter is a non-dimensional parameter, which can be derived from the desorption frequency k_{des} by division through the surface to volume ratio of the smog chamber, the mean velocity of the NO_2 molecules calculated by a Maxwell-Boltzmann – statistic, and a factor 4 analogous to eq. 5.4 for γ_{NO_2} . Thus, Θ_{HONO} differs from k_{des} only by a factor, which is constant during a specific experiment or model run.

Adsorption of HONO from the gas-phase can only occur onto surface sites, which are unoccupied and provide the bonding enthalpy and geometry needed for adsorption. If the total number of surface sites available is N and a certain fraction Θ_{HONO} is already occupied by HONO molecules, adsorption can occur at $N(1 - \Theta_{HONO})$ sites on the surface.

Ab-initio calculations by [Thompson and Margey, 2003] first showed that the bonding enthalpy of both HONO and H_2O are similar in particular on SiH_3OH and $Si(OH)_4$. The latter molecules are typical for the urban surfaces asphalt and concrete, which were investigated in our studies. Thus, HONO and H_2O are competing for the same surface sites to be adsorbed in the smog chamber. In this case, the adsorption isotherms of HONO onto the surfaces of the smog chamber can be expressed according to eq. 2.40:

$$\frac{d[HONO]_{(g)}}{dt} = k_{ads} \cdot (1 - \Theta_{HONO} - \Theta_{H_2O}) \cdot [HONO]_{(g)} \quad \text{eq. 5.7}$$

The fraction of surface coverage can be derived from a steady state assumption of the rate of desorption (eq. 5.6), and the rate of adsorption (eq. 5.7). Exemplary, Θ_{HONO} is given by:

$$\Theta_{HONO} = \frac{\frac{k_{ads}}{k_{des}} \Big|_{HONO} \cdot [HONO]_{(g)}}{1 + \frac{k_{ads}}{k_{des}} \Big|_{HONO} \cdot [HONO]_{(g)} + \frac{k_{ads}}{k_{des}} \Big|_{H_2O} \cdot [H_2O]_{(g)}} \quad \text{eq. 5.8}$$

Here, the concentration of water in the gas phase was calculated according to [Murray, 1966] at the measured temperature [K] and R.H. [%] using the Boltzmann constant $k_B = 1.38 \cdot 10^{-23} \text{ J K}^{-1} \text{ mol}^{-1}$, the molecular weight of H_2O of $M_{H_2O} = 18.02 \text{ g mol}^{-1}$ as:

$$[H_2O]_{(g)} = \frac{6.1078 \cdot \exp\left(\frac{M_{H_2O} \cdot (T - 273.16)}{T - 35.86}\right) \cdot \text{R.H.}[\%]}{k_B \cdot T \cdot 10000} \cdot \frac{100}{100} \quad \text{eq. 5.9}$$

While HONO mixing ratios in the smog chamber were measured in the order of some ppb, R.H. was in the range of 5 - 60 %, which yields a $[H_2O]$ several orders of magnitude higher. Thus, nearly all surface sites are occupied by H_2O ($N \times \Theta_{H_2O}$), and those sites occupied by HONO ($N \times \Theta_{HONO}$) can be neglected in eq. 5.7. Consequently, the uptake of a HONO molecule onto the surface requires the desorption of an H_2O molecule and eq. 5.7 becomes:

$$\frac{d[HONO]_{(g)}}{dt} = k_{ads} \cdot (1 - \Theta_{H_2O}) \cdot [HONO]_{(g)} \quad \text{eq. 5.10}$$

where:

$$\Theta_{H_2O} = \frac{\frac{k_{ads}}{k_{des}} \Big|_{H_2O} \cdot [H_2O]_{(g)}}{1 + \frac{k_{ads}}{k_{des}} \Big|_{H_2O} \cdot [H_2O]_{(g)}} \quad \text{eq. 5.11}$$

From eq. 5.10, and eq. 5.11 it becomes obvious that the HONO uptake frequency is now linear depending on relative humidity. Thus, the observed linear correlation of the HONO

concentrations on R.H. in the smog chamber is caused by the R.H. dependence of the HONO uptake. The Langmuir steady state is present at the beginning of each experiment, when the R.H. is more or less constant during the period of background measurements. When R.H. is varied in the experiments, the HONO concentrations change as expected from eq. 5.10, and eq. 5.11.

5.5.2 Description of the Model

Besides the physical-chemical theory of Langmuir adsorption-desorption isotherms for HONO, its chemistry in the smog chamber is driven by only a few more chemical reactions (see figure 5.17). These reactions and Langmuir theory are considered in the box model of Heterogeneous Chemistry and Surface Interactions (HeCSI). The source code of the HeCSI model in its so far final applied version 4.05 can be found in appendix A, a schematic illustration is summarized in figure 5.17.

3D view:

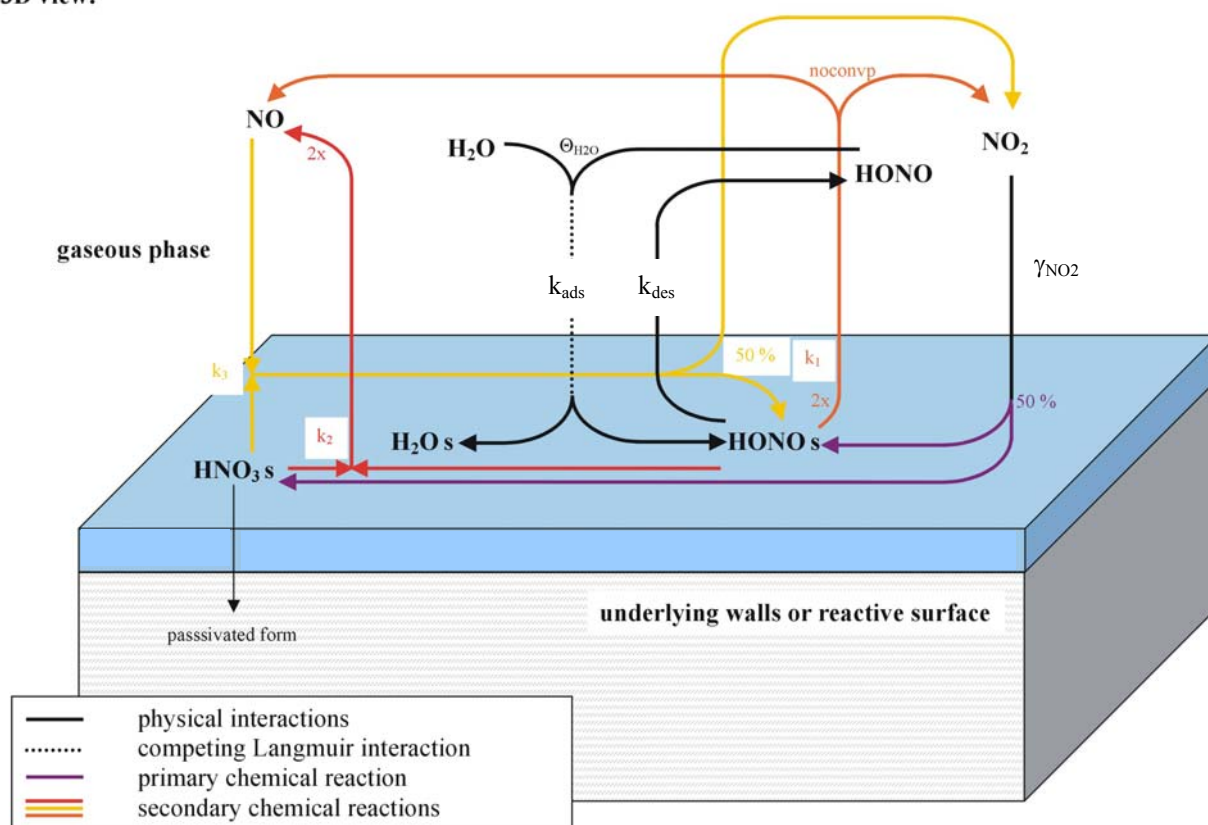


figure 5.17: Schematic illustration of the “HeCSI” model drawn out in this thesis to describe the whole temporary trends of the trace gases during the smog chamber experiments.

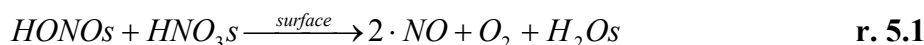
HONO molecules are desorbed (black arrow in figure 5.17) from their surface bond state HONO_s by the out-gassing frequency k_{des} according to equation eq. 5.6. For the uptake of HONO (dashed arrows in figure 5.17), HONO competes with H₂O molecules for the same surface sites to be adsorbed. The frequency k_{ads} of this uptake is according to eq. 5.10 dependent on the factor Θ_{H_2O} , which is expressed by eq. 5.11. In the following, we will use the total number of molecules for the surface adsorbed species in the smog chamber.

Another source of the surface adsorbed HONOs is the chemical production via reaction r. 2.33, which involves NO_2 . NO_2 is adsorbed at the surface by the uptake frequency uno_2 (black line in figure 5.17), but instantaneously converted (violet arrows in figure 5.17) into nitrous and nitric acid, which primary remain at the surface as HONOs and HNO_3s , respectively. Both species are yielded at 50 %. On a longer time-scale, HNO_3s can be converted into a “passivated” form, which migrates from the thin water layer, where the chemistry proceeds into underlying surface structures (see figure 5.17).

Three more chemical reactions are included in the HeCSI model, which will be discussed in more detail in the following chapters. A secondary reaction of two molecules of surface adsorbed nitrous acid (HONOs) yields NO , NO_2 and H_2O at a rate constant k_1 (see orange arrows in figure 5.17):



Another reaction of HONOs includes the “fresh” surface adsorbed HNO_3s (see red arrows in figure 5.17) producing NO at a rate constant of k_2 , which is immediately released into the gas-phase:



Finally, the NO can be removed from the gas-phase (see yellow arrows in figure 5.17) by a rate constant of k_3 :



This reaction r. 2.37 recycles NO_2 in the gas-phase and HONOs adsorbed on the surface. In chapter 5.5.3 it will be shown that this chemistry and Langmuir physics above is sufficient to describe the mechanism of the NO_x chemistry inside the smog chamber.

The initialization of HeCSI requires some parameters, such as temperature, the surface area size, the volume of the smog chamber, and the surface to volume ratio, which remained constant during all experiments. Their values are listed in table 5.2, and table 5.3 for the experiments on the various surface types. In the following, we will discuss in more detail the procedure of applying the HeCSI model exemplary for the 19.04.2003 during the KIP campaign (see figure 5.10). However, the discussion is valid for all experiments performed on the various surfaces. Their different results will be compared in chapter 5.5.5.

The model considers further the loss of trace gases by leakage using a frequency of leakage of $1.3 \times 10^{-4} \text{ s}^{-1}$ on 19.04.2003 (see table 5.2). The leakage frequency was determined by a mass-flow controller (see figure 5.1) and constant during an entire experiment.

The R.H. inside the smog chamber changed only due to external engagement. It is not influenced by chemical reactions or physical interactions. This approximation was already justified in chapter 5.4.2, as the gas-phase water concentration is ~ 4 order of magnitude higher than that of the trace gases and therefore can be treated as infinite reservoir. The time series of R.H. was therefore approximated in HeCSI by a 2nd order polynomial increase and a 1st order exponential decay. During the experiment on 19.04.2003, R.H. increased from an initially constant value of $\sim 5\%$ to a maximum of $\sim 70\%$ in ~ 3.5 h and decreased again to $\sim 20\%$ due to the leakage (see figure 5.18). However, short-time fluctuations of the measured time series of R.H. are smoothed out in the model (see figure 5.18).

Considering the definition of $\Theta_{\text{H}_2\text{O}}$ according to equation eq. 5.11, the time series of $\Theta_{\text{H}_2\text{O}}$ can be derived from the R.H. time series (see figure 5.18). The surface coverage H_2O (cyan line, left scale) is constant during the background measurements at $\sim 80\%$. Due to the humidification of the smog chamber it increased to $\sim 93\%$, when the R.H. is $\sim 70\%$. A slight decrease due to the dehumidification by the rate if leakage occurred throughout the rest of the experiment (see figure 5.18).

A final initialization parameter is the injection of NO_2 at a certain time of the experiment. It was realized as an instantaneously injection. Since the real injection of NO_2 took approx. 1 - 5

min (see figure 5.19), the instant injection in the model leads to small time shifts of the modeled and measured time series (see figure 5.21, and figure 5.22).

HeCSI is written in facsimile[®] [Curtis and Sweetenham, 1987] and simulates the time series of NO, NO₂, and HONO based on the heterogeneous chemistry and the Langmuir theory. Therefore, the differential equations of the chemical reactions as well as those of the physical parameters changing the framework for these chemical reactions are solved simultaneously for the trace gas and the species adsorbed at the walls of the smog chamber.

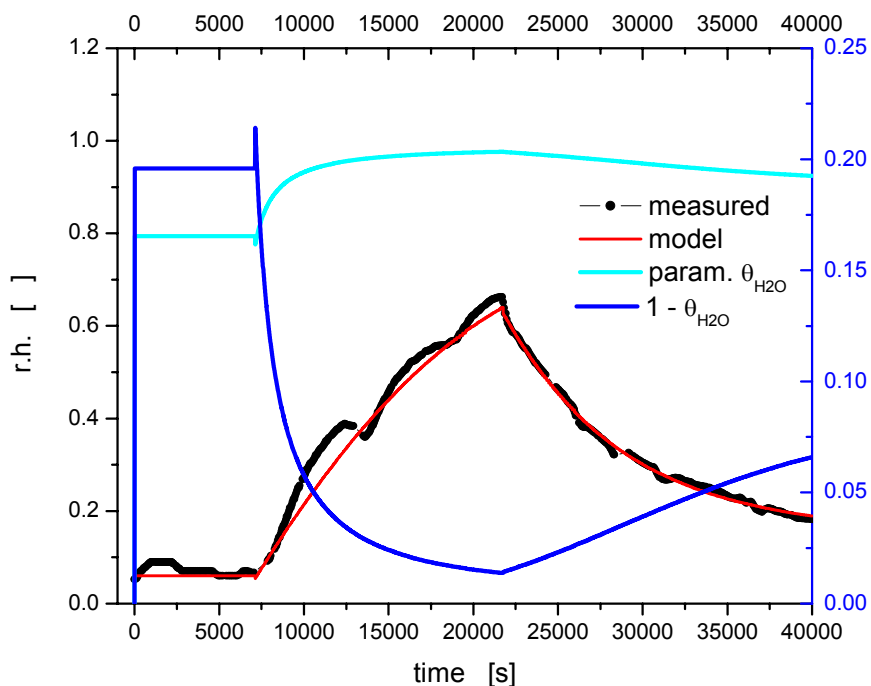


figure 5.18: The relative humidity (R.H.) as exemplary measured (black symbols, left scale) during the experiment on 19.04.2003 is set as a parameter in the HeCSI model and thus well reproduced (red line, right scale).

5.5.3 The Mechanism of the NO_x Chemistry in the Smog Chamber

5.5.3.1 Modeled NO₂ Chemistry

The concentration time series of NO₂ is generally modeled quite well as can be seen from figure 5.19. The starting mixing ratio of NO₂ at $t = 0$ was ~ 0.1 ppb on 19.04.2003 (see figure 5.19).

Since NO₂ is immediately converted into HONOs and HNO₃s on the surface, there exists no surface adsorbed form of NO₂, and thus, NO₂ cannot be desorbed from the surface. However, a chemical production of NO₂ according to the heterogeneous reactions r. 2.54, or r. 2.37 cannot be excluded during this period and needs to be included in the model. The observation that the NO₂ concentrations remain at their initial equilibrium value for ~ 8 h, even during the humidification and dehumidification of the smog chamber is anyway well found by the model (see figure 5.19).

At $t = 29000$ s ~ 160 ppb NO₂ were modeled to be instantaneously injected. After this addition of NO₂, a constant loss of NO₂ from the gas phase is observed, which can be described by the first order exponential decay of eq. 5.3. The uptake of NO₂ is $\sim 10^{-6}$ in the model. Since this is an uptake onto all surfaces inside the smog chamber, it has to be corrected for the loss by leakage and the loss on the different types of surfaces in the smog chamber as described by

eq. 5.1, and eq. 5.2 respectively. The surface-specific uptake coefficients of NO_2 derived from the model and those from table 5.3 are in good agreement in the range of their errors (see also table 5.3).

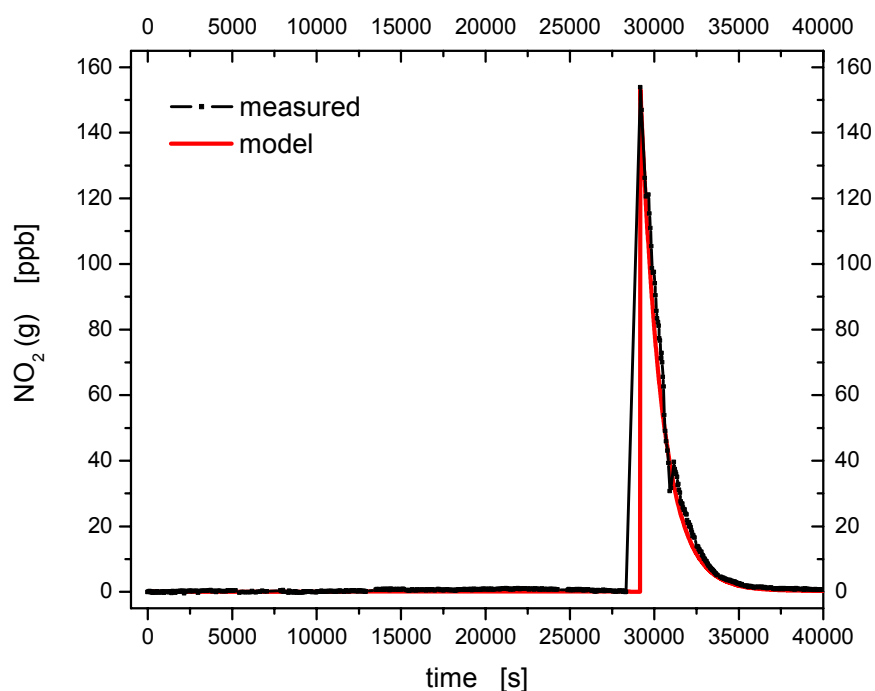


figure 5.19: The time series of NO_2 measured (black symbols, right scale) inside the smog chamber on 19.04.2003 is well reproduced by the HeCSI model (red line, left scale).

In the HeCSI model, the NO_2 adsorbed on the surfaces is instantaneously converted to nitrous acid, which primarily remains adsorbed at the surface as (HONOs). A stoichiometric yield of HONO of 50 % was assumed according to reaction r. 2.33, while the remaining 50 % are adsorbed on the surface as HNO_3 :



According to [Ammann *et al.*, 1998; Becker *et al.*, 1995; Calvert *et al.*, 1994; Goodman *et al.*, 1999; Jenkin *et al.*, 1988; Junkermann and Ibusuki, 1992; Kalberer *et al.*, 1999; Kleffmann *et al.*, 1998; Lammel and Perner, 1988; Longfellow *et al.*, 1998; Sakamaki *et al.*, 1983; Svensson *et al.*, 1987], we assume only the reaction r. 2.33 to produce significant amounts of HONO in the smog chamber. Thereby, the rate of NO_2 uptake is the step limiting the total production rate of HONOs. The influence of further chemical reactions included in the model, i.e. secondary reactions of HONO regenerating NO_2 , is discussed in chapter 5.5.3.4.

The production rate of HONOs by reaction r. 2.33 is independent from R.H., because one HONO molecule can be adsorbed at the surface site previously occupied by the H_2O molecule, which was consumed by the reaction of NO_2 and H_2O (reaction r. 2.33).

5.5.3.2 Chemistry of Surface Adsorbed Species

While the starting parameters of the trace gases HONO, NO_2 , and NO for the model were directly measured, it is not possible to measure HONOs and HNO_3 s. Thus, reasonable estimates of HONOs and HNO_3 s at the time $t = 0$ were used. Since during the first two periods of the experiments, when only R.H. was varied, no reactive chemicals were added to the system, all HONO appearing in the gas-phase must have been released from the surface

adsorbed state. This yields a first approximation of $\sim 10^{18}$ molecules for HONOs. We will discuss variations of this starting parameter in chapter 5.5.4 below.

As NO production was not observed during the first periods of the experiment, the rate of NO production according to reactions r. 2.54, or r. 2.37 must become negligible. Therefore, HNO_3s was set to a low value of $\sim 10^{16}$ molecules. Because HNO_3 has a higher affinity to surfaces, one would expect HNO_3s to be higher than 10^{18} molecules. However, we distinguish between “fresh” and “passivated” surface forms of HNO_3s , and only “fresh” HNO_3s reacts according to reactions r. 2.54, or r. 2.37. These terms are discussed in more detail in chapter 5.5.3.4.

At a constant R.H. of $\sim 5\%$ during the background measurements, the HONO adsorbed at the surface (HONOs) remains constant at its initial value of 4.5×10^{18} molecules (see figure 5.20) according to the Langmuir equilibrium of adsorption and desorption. Humidifying the smog chamber disturbs this equilibrium concentration. Due to the increased $[\text{H}_2\text{O}]$ less HONO is taken up onto the surfaces (see chapter 5.5.1). The HONO, which is now present in the gas-phase, can be lost by leakage. Due to both, HONOs decreases linearly (according to the linear increase of R.H. and the 1st order exponential function for leakage loss) to $\sim 2 \times 10^{18}$ molecules at $t = 22000$ s (see figure 5.20). When the R.H. is reduced by leakage, the rate of HONO uptake is increasing again, when the smog chamber is dehumidified. In this state of the experiments, HONOs is also influenced by secondary reactions (see chapter 5.5.3.4).

After the addition of NO_2 into the smog chamber at $t = 29000$ s, NO_2 is taken up onto the surfaces and converted into HONOs according to reaction r. 2.33. This “fresh” produced HONOs can be released as HONO into the gas-phase by a rate defined by the out-gassing frequency of eq. 5.6. Significant amounts of HONOs also primary remain on the surfaces. Thus, the concentration of HONOs increases to $\sim 6 \times 10^{18}$ molecules about 5000 s after the NO_2 injection. HONOs slightly decreases afterwards due to several effects. First, gas-phase HONO is lost by leakage. According to the Langmuir equilibrium, this amount will be replaced by HONO desorbed from the surfaces. On the other hand, HONOs undergoes secondary reactions, yielding NO (see chapter 5.5.3.4).

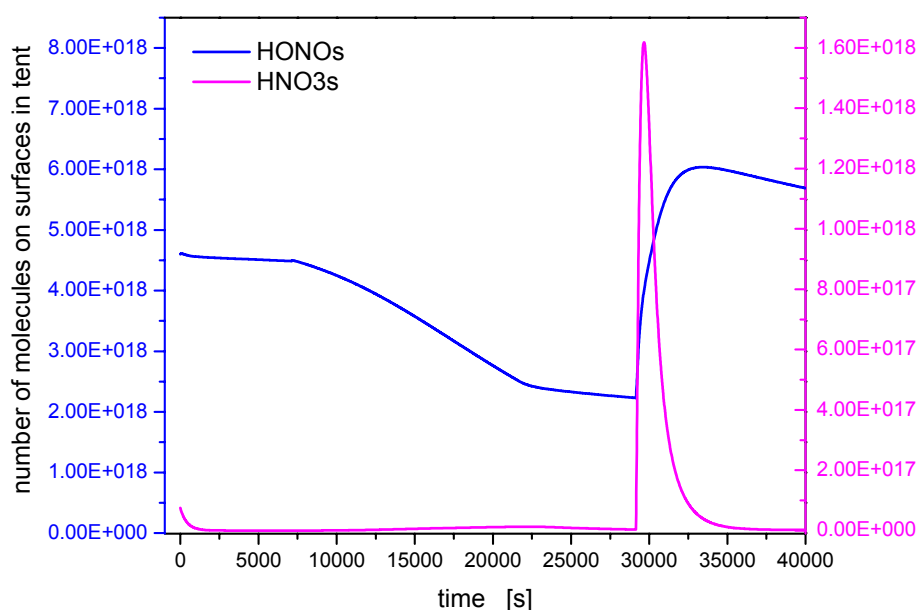


figure 5.20: Modeled time series of the surface adsorbed species HONOs (blue line) and HNO_3s (magenta line) for the experiment on 19.04.2003.

It is interesting to note that the nitric acid (HNO_3), which is present on the different surfaces of the smog chamber, can be converted into a passivated bonding form and removed from the thin water film on the surface, where the heterogeneous reactions occur, into the underlying surface structures. Unfortunately, the bonding structure of HNO_3 could not be measured in our studies and thus we cannot confirm this hypothesis. However, experiments of [Finlayson-Pitts, 2003; Finlayson-Pitts, 2004; Finlayson-Pitts *et al.*, 2003] give strong evidence that the co-adsorbed water molecules of strongly influence the reactivity surface adsorbed HNO_3 .

5.5.3.3 Modeled Time Series of HONO

The time series of the gas-phase HONO concentration in the smog chamber is the logical consequence of the chemical reactions and physical interactions mentioned above and can be generally well reproduced by the HeCSI model.

HONO is constant at a mixing ratio of ~ 1 ppb during the background measurements. Due to the disturbance of the Langmuir equilibrium by humidifying the smog chamber HONO increases up to ~ 10 ppb in the next 4 h. While the out-gassing of HONO, i.e. the release of primary surface adsorbed HONOs into the gas-phase according to eq. 5.6, has a constant frequency, the uptake of gaseous HONO onto the surfaces of the smog chamber is R.H. dependent as described by eq. 5.10. Thus, the uptake of HONO becomes less effective and the HONOs is gassed out into the gas-phase. When the R.H. decreases again, the uptake of HONO onto the surfaces becomes again effective, thus the mixing ratio of HONO decreases in the next 2 h to ~ 5 ppb. After adding NO_2 to the NO_x system at $t = 29000$ s, the chemical production according to reaction r. 2.33 has to be considered as well. HONOs is enhanced by the production from NO_2 , and out-gassed to re-establish the Langmuir equilibrium. Thus, a peak of HONO of ~ 8 ppb is observed.

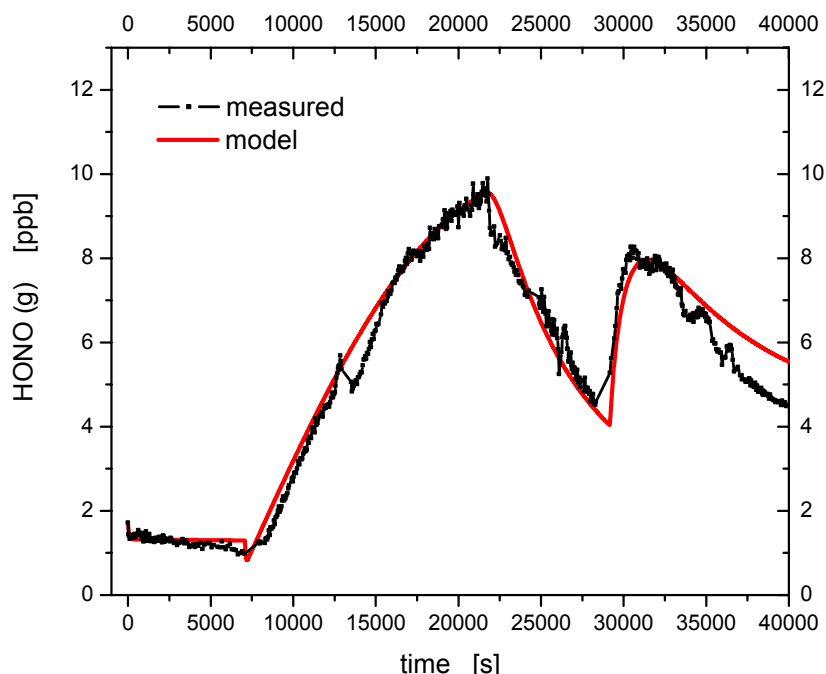


figure 5.21: HONO mixing ratios measured (black symbol, right scale) and modeled (red line, left scale) exemplary for the 19.04.2003.

5.5.3.4 Secondary Reactions yielding NO

The NO mixing ratios during the background measurements vary for the different experiments in the range of few ppb (6.5 ppb on 19.04.2003 as can be seen from figure 5.22), but significantly differ from zero. It was already mentioned in chapter 5.4.2 that NO can be flushed into the smog chamber as the synthetic air is contaminated by NO_x listed as upper limits in table 5.1. Thus an additional flux of NO was implemented in the HeCSI model and occurs at a rate equal to that of leakage. However, this is not sufficient to exclusively explain the later observed NO mixing ratios of ~ 15 - 100 ppb in the smog chamber.

It is obvious from the figures in chapter 5.2 that gas-phase NO is produced at different amounts during the periods of R.H. variations and after NO₂ addition to the system. Thus, minimum two paths of NO production in the smog chamber are needed to explain the observed time series NO. These NO sources are both secondary chemical reactions of the surface-adsorbed HONO (HONOs).



The reaction r. 2.54 is the inverse of the reaction r. 2.32, which forms HONO by the heterogeneous disproportionation on NO and NO₂.

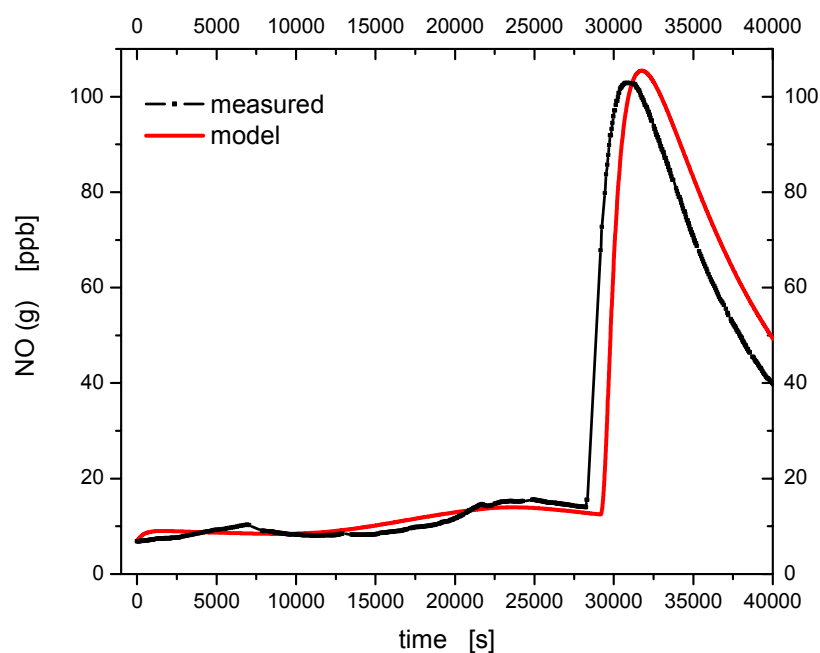
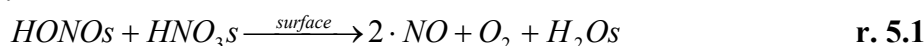


figure 5.22: NO mixing ratios measured (black symbol, right scale) and modeled (red line, left scale) exemplary for the 19.04.2003.

While only a slight increase of NO₂ was observed in the smog chamber, we assume the yield of NO compared to that of NO₂ according to reaction r. 2.33 is R.H. dependent as indicated by experiments of [Finlayson-Pitts, 2003; Finlayson-Pitts, 2004]. The higher R.H. favors the more NO production. It should be mentioned here that the production of NO₂ can be masked by its subsequent fast uptake onto the surfaces. However, the rate constant of the HONO self-reaction r. 2.54 derived by several groups [Mertes and Wahner, 1995; Svensson et al., 1987; TenBrink and Spoelstra, 1998] is too slow to explain our observations and not dependent on R.H. The HeCSI model therefore uses the rate constant for reaction r. 2.54 in a range from 1.1 and $2.5 \times 10^{-20} \text{ cm}^2 \text{ molec}^{-1} \text{ s}^{-1} \times \text{R.H.}$ It was adapted in the individual model runs to achieve best agreement with the observed gas-phase concentrations of HONO and NO. As the reaction proceeds on the surface and not in the gas-phase, its unit is $\text{cm}^2 \text{ molec}^{-1} \text{ s}^{-1}$ and

further needs to be multiplied by the R.H. to obtain this dependence as well. In reaction r. 2.54, HONO_s is consumed and forms NO. Thus, HONO_s is not strictly increasing as expected from Langmuir theory, but remains rather constant (see figure 5.20), when the R.H. is decreasing and HONO uptake is more effective.

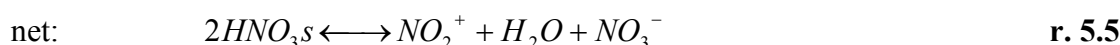
A second and strong increase of the NO concentration is observed after the addition of NO₂ (see figure 5.22) and its peak levels are approx. one order of magnitude higher than in the period before. The increase of HONO_s due to the addition of NO₂ is in the order of a factor 2 (see figure 5.20), thus reaction r. 2.54 above cannot exclusively explain this second NO peak as well. Additionally, its R.H. dependent rate constant is still in the same order of magnitude because of the only slightly differing R.H. Consequently, an additional and strong chemical production of NO yielding ~ 100 ppb (see figure 5.22) after adding NO₂ is present in the smog chamber:



Reaction r. 5.1 may be first thought to yield two molecules of NO₂ and thus to be the inverse of the heterogeneous hydrolysis of NO₂ forming HONO and HNO₃ according to reaction r. 2.33. The production of two molecules of NO₂ by reaction r. 5.1 should be detectable by the DOAS instrument. However, NO₂ in the gas-phase was not observed to increase significantly by any of these reactions neither while humidifying the smog chamber nor after an injection of a certain amount of NO₂, when it only decreased by a clear exponential first order decay according to eq. 5.3, and analyzed in detail in chapter 5.3. As suggested by [Finlayson-Pitts *et al.*, 2003], reaction r. 5.1 may proceed heterogeneously on a thin surface film via the NO₂⁺:



[Finlayson-Pitts *et al.*, 2003] combined this with the reactions involved in the formation of NO₂⁺ on the surface:



and finally obtain reaction r. 5.1 as the net reaction scheme for NO production on the surface. However, we have not measured surface adsorbed species and therefore cannot justify this mechanism. We will therefore refer to reaction r. 5.1 as the needed additional strong chemical source of NO. The mechanism of NO production remains unclear.

However, “fresh” and therefore reactive HNO_{3s} was shown in figure 5.20 to increase after addition of NO₂, making reaction r. 5.1 sufficient to explain the second increase of NO. In the different model runs, its rate constant was varied between 10⁻¹⁷ and 10⁻¹⁸ cm² molec⁻¹ s⁻¹ x R.H. during the KIP 2003 measurements, when the walls of the smog chamber consisted of PE foil, and 5 x 10⁻¹⁶ and 5 x 10⁻¹⁷ cm² molec⁻¹ s⁻¹ x R.H. on the Teflon walls during the IUP 2002 campaign.

In the presence of small amounts of reactive (“fresh”) HNO_{3s} before addition of NO₂ into the smog chamber (see figure 5.22), the reaction r. 5.1 becomes negligible and the production of NO occurs only via the heterogeneous reaction r. 2.54. Thus, the first slight increase of NO to ~ 15 ppb (see figure 5.22) at t = 250000 s (after disconnecting the bubbler for humidification) is caused by the reaction r. 2.54. On the other hand, the second increase of NO, which is observed after addition of NO₂, is due to the additional HNO_{3s} and thus, mainly caused by the inverse of reaction r. 2.54.

NO concentrations in the gas-phase are observed to decrease faster in the smog chamber than exclusively by the rate of leakage. Thus, a third reaction is needed to reduce the gas-phase concentrations of NO, which is produced by the secondary reactions r. 2.54, and r. 5.1 of HONO. Therefore, the “fresh” and surface adsorbed HNO₃ can also react with NO, which

impacts upon it from the gas-phase according to the Langmuir-Hinshelwood mechanism presented in chapter 2.4.2:



The reaction r. 2.37 was mentioned in chapter 2.3.5.3 as the renoxification, where HNO_3 is converted back to photochemically active NO_x in the atmosphere after the impact of gaseous NO onto surface adsorbed HNO_3 [Saliba *et al.*, 2000]. The lower limit for the reaction probability was reported by [Mochida and Finlayson-Pitts, 2000; Rivera-Figueroa *et al.*, 2003; Saliba *et al.*, 2000; Saliba *et al.*, 2001] to be $\gamma_{NO} = (6 \pm 2) \times 10^{-9}$, but generally larger under conditions of higher R.H.

HNO_3s is adsorbed on surface sites energetically different from those of HONOs and H_2Os . Since one molecule of HONOs is formed by reaction r. 2.37, an unoccupied surface site, where HONOs can be bond, is required. Thus, reaction r. 2.37, i.e. its rate constant, must be dependent on R.H. as well.

In our modeling studies, the rate constant for reaction r. 2.37 was varied between 1 and $5 \times 10^{-18} \text{ cm}^2 \text{ molec}^{-1} \text{ s}^{-1} \times \text{R.H.}$ to achieve best simulation results for the gas-phase concentrations of NO and HONO.

Obviously, the topics this chapter 5.5.3.4 concerning the NO production from secondary reactions of HONO and their subsequent detection in the gas-phase, but also the bonding structures and therefore reactivity of HNO_3s , i.e. also the definition of a “fresh” produced molecules, need further investigations. The HeCSI model may over-simplify the NO_x chemistry with respect to their secondary and subsequent reactions. However, it describes very sufficiently the HONO and NO_2 concentration time series in the smog chamber under conditions of changing R.H. using only the simple physical approach of Langmuir adsorption-desorption isotherms.

5.5.4 Sensitivity Studies of the HeCSI Model

From a first point of view, the HeCSI model seems to be under-determined. However, since the model is restricted to fulfill the conditions of the Langmuir theory and the chemical reactions simultaneously at all times during the experiments, only some sets of parameters become valid. This is of particular importance for the intrinsic results of the model, i.e. the out-gassing frequency of HONO and its R.H. dependent uptake. Both variables are linked in the model, thus only their ratio can be derived distinctively. However, the out-gassing of HONO is according to eq. 5.6 further dependent on the amount of surface adsorbed HONOs and needs to fit the initial increase of HONO in the gas-phase at the beginning of the humidification period. Simple tests of the number of HONO molecules initially adsorbed at the surface will show however that this parameter can be determined in the range of a factor of 2.

In the absence of chemical reactions yielding HONO, minimum the total amount of ~ 9.5 ppb HONO on 19.04.2002, which was detected in the gas-phase after humidifying the smog chamber (see figure 5.10 and figure 5.21), must have been present at the surfaces of the smog chamber before the experiment started. Considering the total volume of the smog chamber of $\sim 2.5 \text{ m}^3$ (see table 5.2), this corresponds to $\sim 6.5 \times 10^{17}$ molecules of HONO adsorbed on the surfaces.

An upper limit can be derived from the fact that after addition of NO_2 and subsequent conversion of NO_2 into HONOs, significant amounts (~ 8 ppb) of HONO are released back into the gas-phase (see figure 5.10 and figure 5.21). If the number of surface-adsorbed HONO is above a certain threshold, the NO_x chemistry of r. 5.1, r. 2.54, and r. 2.37 inside the smog chamber would be insensitive to this additional push of HONOs. Consequently, the concentration-time-series of HONO in the gas-phase would be characterized by a constant

decrease by the rate of leakage after reaching the first maximum due to the humidification of the smog chamber.

Therefore, several test runs of the HeCSI model were performed, varying the initial amount of HONOs in the range from 8×10^{17} to 6×10^{20} molecules. If the number of HONO molecules adsorbed at the surface is in the order of $\sim 1 \times 10^{18}$, the first peak of HONO, which occurred during varying R.H. only, cannot be reproduced by the HeCSI model (see figure 5.23). This is due to the fact that the out-gassing frequency of HONO, which defines the release of HONO into the gas-phase during the period after NO_2 addition as well, is too low.

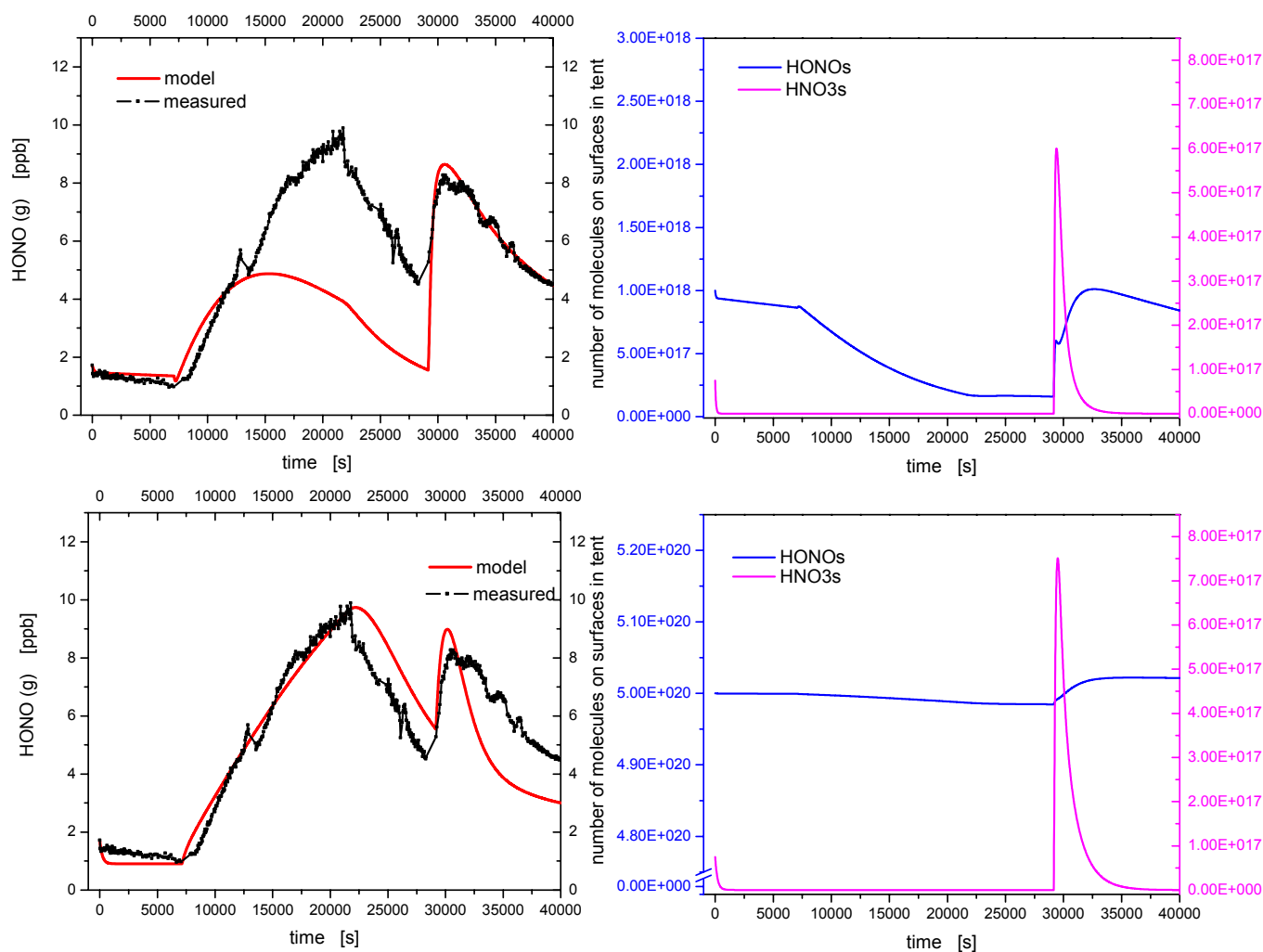


figure 5.23: False reproduction of the HONO time series in the smog chamber due to variations of the surface adsorbed HONOs. Upper plots: $\text{HONOs} (t = 0) = 1 \times 10^{18}$ molecules; Lower plots: $\text{HONOs} (t = 0) = 6 \times 10^{20}$ molecules.

Enhancing this rate yields an over-estimation of the HONO production from NO_2 during this third period of the experiment. If the number of surface-adsorbed HONOs is initially above $\sim 2 \times 10^{19}$ molecules, the HONO time series is reproduced false as well (see figure 5.23). Then, the second peak of HONO, which is caused by chemical production from NO_2 , is too sharp (see figure 5.23) and the HONO is rapidly re-adsorbed onto the surfaces. Thus, we predict $\sim 4 (\pm 3) \times 10^{18}$ molecules of HONO initially adsorbed at the walls of the smog chamber as a reasonable best guess value.

From these considerations above, we estimate the maximum error of the parameters derived from the HeCSI model, namely for those parameters, which depend on HONOs, i.e. mainly

the out-gassing frequency, to be in the order of a factor of 2. This error has to be kept in mind for the discussion of the HeCSI results presented by the table 5.6.

5.5.5 Model Results for the different Surface Types

In table 5.6, the type(s) of surface(s) present inside the smog chamber, the used rate of leakage, and the NO₂ uptake coefficient calculated by the HeCSI model (and in good agree with those presented in table 5.3) are finally summarized for the individual dates of the experimental runs. Some parameters derived from the model simulations need further discussions, i.e. the initial amount of HONO and HNO₃ adsorbed on the surfaces (HONOs and HNO₃s, respectively), the out-probability (α_{HONO}) of HONO (and the corresponding desorption frequency k_{des} according to eq. 5.6), and the uptake coefficient of HONO, which were calculated from the adsorption frequency of eq. 5.10, assuming an artificial R.H. of 0 %. The absolute amount of the species initially adsorbed on the surfaces present in the smog chamber was estimated in chapter 5.5.4 above. The values of HONOs and HNO₃s, respectively, differ relatively between the various types of surfaces by a factor of 100 (see table 5.6). This becomes clear, if we take into account the larger surface size of the real urban surfaces such as asphalt, which were found to be 150 times their geometrical area [Finlayson-Pitts, 2004]. The artificial laboratory surfaces, such as Teflon or the PE foil are suspected to be more flat. Thus, they provide less surface sites for the adsorption of trace gases, in particular HONO and H₂O. If initially 2×10^{13} molec cm⁻² of HONO were adsorbed on the PE foil plus asphalt plates on 19.04.2003 during the KIP campaign (see table 5.6), it seems reasonable that less than one tenth of that amount is bond on the PE foil on e.g. 28.04.2003. While a clear distinction between Teflon and PE foil on the one hand side and asphalt and concrete on the other hand is obvious from table 5.6, the surfaces of roof-tiles and flagstone-tiles, both seem to be more clogged as well. A BET type surface analysis is required to overcome this problem. The amount of HONO and HNO₃ initially adsorbed on the grass surface is however found by the model to be of the same order as for Teflon or PE foil. A reason for these results from the model cannot be given so far. We believe this to be caused by the biological processes involving the NO_x species, which proceed in the living plants as indicated by [Delmas *et al.*, 1995; Ganzeveld *et al.*, 2002; Gao *et al.*, 1993; Klepper, 1979; Lenzian and Kahlert, 1988; Wild *et al.*, 1997]. The formation and destruction of HONO on these biological surfaces obviously needs further investigation.

The out-gassing probability of HONO is extremely dependent on the type of the surface and its physical and chemical constitution. Thus, absolute values (modeled to be in the range of 10^{-7} to 10^{-5} , see table 5.6) are specific for our smog chamber, but cannot be generalized to atmospheric conditions or other smog chambers. The relative values of α_{HONO} mirror the trend of the HONOs for the various surface types(see table 5.6). This becomes reasonable, as the amount of HONO desorbed, is the product of its rate of desorption and the amount of HONO adsorbed on the surfaces and has to match the measured concentration of HONO in the gas-phase (see e.g. figure 5.10, or figure 5.21). Since the slope of the HONO increase by humidification is similar for all experiments, especially similar for the different types of surfaces present inside the smog chamber (see figure 5.15 in chapter 5.4.2), the less HONOs requires the higher α_{HONO} . On the other hand, the lower out-gassing probability from asphalt may indicate the stronger bonding of HONO on it. The bonds on the artificial surfaces Teflon and the PE foil are therefore weaker, consequently, the out-gassing probability for HONO is higher (see table 5.6). However, we cannot further quantify this topic and a more detailed analysis of the bonding structure of HONO on these surfaces is needed.

date	surface type	f_{leak} [10^{-4} s^{-1}]	γ_{NO_2} [10^{-6}]	$k_{\text{des, HONO}}$ [10^{-4} s^{-1}]	O_{HONO} [10^{-7}]	$k_{\text{ads, HONO}}$ [10^{-2} s^{-1}]	γ_{HONO} [10^{-3}]	HONOs [$10^{12} \text{ molec cm}^{-2}$]	HNO_3s [$10^9 \text{ molec cm}^{-2}$]
12.4.2002	Teflon	1.00	0.04	86.4	100.0	0.9	1.0	0.5	0.3
13.4.2002	Teflon wet	1.00	0.04	129.6	150.0	1.3	1.5	0.5	0.3
15.4.2002	asphalt	1.33	9.90	3.5	4.0	12.5	14.5	29.3	32.1
16.4.2002	asphalt	1.33	9.00	3.5	4.0	10.8	12.5	30.0	32.1
17.4.2002	asphalt	1.33	13.20	3.5	4.0	13.4	15.5	30.0	32.1
18.4.2002	asphalt	1.33	13.00	3.5	4.0	13.0	15.0	29.0	32.1
19.4.2002	asphalt	1.33	12.50	6.9	8.0	13.4	15.5	20.0	32.1
21.4.2002	asphalt	1.00	12.90	3.5	4.0	14.2	16.5	30.0	32.1
22.4.2002	Teflon + PE	1.33	0.95	69.1	80.0	1.7	2.0	2.0	3.2
23.4.2002	Teflon + PE	1.00	0.82	51.1	60.0	1.1	1.3	1.5	3.2
12.4.2003	PE only	1.33							
13.4.2003	PE only	1.67	0.09	59.8	70.0	1.7	2.0	2.0	3.2
14.4.2003	PE only	1.33	0.15	32.2	40.0	1.7	2.0	2.0	3.2
15.4.2003	PE only	1.00							
16.4.2003	PE + asphalt	1.00	11.60	3.2	3.7	9.0	10.5	29.3	32.1
17.4.2003	PE + asphalt	1.33	11.50	3.5	4.1	8.5	9.9	20.3	32.1
18.4.2003	PE + asphalt	1.00	11.10	3.0	3.5	7.7	9.0	26.3	32.1
19.4.2003	PE + asphalt	1.00	11.10	3.3	3.8	7.7	9.0	29.3	32.1
20.4.2003	PE + concrete	1.67	11.10	3.0	3.5	6.9	8.0	29.3	32.1
21.4.2003	PE + asphalt	1.67	10.40	3.4	3.9	9.1	10.9	28.3	32.1
22.4.2003	PE + roof-tiles	1.67	3.11	8.2	9.5	6.4	7.5	11.5	3.2
23.4.2003	PE + flagst.-tiles	1.67	3.11	2.1	2.5	6.9	8.0	10.3	3.2
24.4.2003	PE + grass	0.67	20.50	60.1	70.0	38.6	45.0	1.9	3.2
25.4.2003	PE only	0.67	0.20	34.4	40.0	1.7	2.0	2.5	3.2
26.4.2003	PE only	0.67	0.19	51.6	60.0	2.6	3.0	2.5	3.2
27.4.2003	PE only	1.00	0.25	51.6	60.0	1.7	2.0	2.0	3.2
28.4.2003	PE only	1.00	0.30	34.4	40.0	1.7	2.0	2.5	3.2

table 5.6: HeCSI model results for all analyzed experiments of the IUP 2002 and KIP 2003 smog chamber campaigns: the corresponding date of experiments, its surface type(s), leakage loss frequency, the NO_2 uptake coefficients, the out-gassing frequency for HONO, its uptake coefficient and the initial amounts of the surface adsorbed species HONOs and HNO_3s .

Due to the R.H. dependence according to the Langmuir theory of adsorption-desorption isotherms (see eq. 5.10), the HONO uptake coefficients presented in table 5.6 are not comparable to values reported in literature. For a qualitative discussion, we have listed the γ_{HONO} at an artificial R.H. of 0 %, which is obviously unrealistic, as no HONO formation would occur under absolutely dry conditions (see r. 2.33).

As already observed for the NO_2 uptake coefficients, the HONO uptake is more than one order of magnitude higher onto all real urban surfaces, such as asphalt or concrete, but also the roof-tiles or flagstone tiles (see table 5.6). We believe this again to be caused by their higher real surface compared to their plane geometrical area, but also due to the more complex structure of these surface types. Highest γ_{HONO} values were modeled for the adsorption on grass (see table 5.6), but again cannot be separated from further chemical transformations of the NO_x species in the biological system.

5.6 Atmospheric Relevance

5.6.1 Discussion of NO_2 Uptakes & Comparison to Literature

For a comparison of our values, the rate constants of the HONO formation from the heterogeneous NO_2 hydrolysis derived by other studies at different surface to volume ratios of their chamber and at different relative humidity were normalized to a S/V of 1 m^{-1} . The R.H. was taken into account for that calculation as given in the corresponding references (see also table 5.7). Finally, our uptake coefficients were converted into values of k^* using equation eq. 5.12, the Boltzmann velocity of NO_2 and the surface to volume ratio of 9.33 m^{-1} of our smog chamber.

$$k^* = \frac{1}{8} \cdot \langle v_{\text{NO}_2} \rangle \frac{S}{V} \cdot \gamma_{\text{NO}_2} \quad \text{eq. 5.12}$$

reference	$k^* [10^{-6} \text{ s}^{-1}]$	surface	remarks
[Svensson <i>et al.</i> , 1987]	~ 1.5	on Teflon	at R.H. = 54 %
[Pitts <i>et al.</i> , 1984c]	~ 1.3	on glass	at R.H. = 50 %
[Sakamaki <i>et al.</i> , 1983]	~ 1.3	on quartz	at R.H. = 47 %
[Finlayson-Pitts <i>et al.</i> , 2003]	~ 1.4	on borosilicate	at R.H. = 50 %
[Kleffmann <i>et al.</i> , 1998]	~ 50	on aqueous surfaces	
[Ackermann, 2000]	(50 ± 30)	on wainscoting	
[Kurtenbach <i>et al.</i> , 2001]		of a traffic tunnel	
this study	(1.4 ± 0.3) ²⁰	on Teflon	see chapter 5.3
this study	(15.7 ± 6.6) ²⁰	on PE foil	see chapter 5.3
this study	(470.6 ± 73.4) ²⁰	on asphalt	see chapter 5.3
this study	(326.0 ± 96.5)	on concrete	see chapter 5.3
this study	(129.0 ± 100.2)	on roof-tiles	see chapter 5.3
this study	(129.3 ± 108.2)	on flagstone-tiles	see chapter 5.3
this study	(849.4 ± 178.3)	on grass	see chapter 5.3

table 5.7: Comparison of HONO formation frequencies by heterogeneous hydrolysis of NO_2 determined in this study with some previous reported.

Generally, the values for the artificial and so-called “laboratory” surfaces are in good agreement to others reported in literature (see table 5.7). However, the uptake of NO_2 onto the

²⁰ The error is the 1- σ standard deviation of the weighted average value.

real urban surfaces asphalt and concrete seems to be a least two orders of magnitude higher (see table 5.7).

An accompanied study by [Finlayson-Pitts, 2003; Finlayson-Pitts, 2004] analyzed the BET surface by mercury porosimetry (see chapter 2.4.4.3) of the asphalt plates, we have used during our experiments in the smog chamber. This surface size was found to be ~ 150 time its geometrical. Thus, the higher NO_2 uptake coefficients of NO_2 onto asphalt can be due to the amplification of the real surface size.

We may re-define heterogeneous catalytic activity (see chapter 2.4.1) to be the enhancement of a chemical reaction after chemisorption of a gas onto a surface and subsequent providing of a new path for the chemical reaction, which requires these chemical bonding(s) between the gas and the adsorbent. Under these circumstances, a catalytic enhancement of the heterogeneous HONO formation after uptake of gaseous NO_2 seems at least rather questionable. However, we cannot exclude a catalytic effect, as we have not measured the surface adsorbed species. Further investigations are needed to study the mechanistic sequences and the bonding structure of NO_2 or HONO (see chapter 5.5.5) on these surfaces.

5.6.2 Influence of Enhanced NO_2 Uptakes on HONO Formation

Finally, the HONO formation efficiencies, which were determined in this study for real urban surfaces, such as asphalt, need to be compared to the measured NO_2 -to-HONO rates in the atmosphere.

Thereby the surface to volume ratio of the atmosphere is a critical parameter. For the atmosphere, this implicates that the height of the planetary boundary layer and the total surface size in a city (ground surface and vertical walls of buildings) must be taken into account. The height of the nighttime planetary boundary layer, however, varies a lot, depending on parameters like the temperature and geographical situation. For the following rough estimation, it is assumed to be 100 m yielding a surface to volume - ratio of 10^{-2} m^{-1} for a plane surface. Further, the k^* for asphalt (see table 5.7) divided by the surface-to-volume ratio of the smog chamber ($S / V = 9.33 \text{ m}^{-1}$) was used. A water concentration needs not be considered, since we have shown in chapter 5.3.2 that the NO_2 uptake coefficients are independent from R.H. These assumptions can be combined to calculate the HONO production rate per NO_2 in the NBL:

$$\frac{d[\text{HONO}]}{dt} = 5 \cdot 10^{-5} \text{ m s}^{-1} \cdot 10^{-2} \text{ m}^{-1} \approx 0.2 \% / h \quad \text{eq. 5.13}$$

While atmospheric measurements give a typical HONO formation ratio with respect to NO_2 of about $1 \% \text{ h}^{-1}$ (see e.g. [Alicke, 2000; Alicke et al., 2003; Alicke et al., 2002; Harrison et al., 1996; Lammel, 1999; Lammel and Cape, 1996; Perner and Platt, 1979; Platt and Perner, 1980; Platt et al., 1980; Stutz et al., 2004b; Stutz et al., 2002; Stutz and Geyer, 2003; Veitel, 2002; Winer and Biermann, 1994]), the HONO nighttime production cannot be explained by these assumptions. First be mentioned that further sources for HONO in the troposphere exist, e.g. direct emission from automobile exhaust, as recently quantified by [Ackermann, 2000; Kurtenbach et al., 2001]. Second, the assumption of a plane surface is certainly only a lower limit. While this first calculation was performed for a flat terrain, without houses, the urban surface area is much larger. In model studies, the geometric surface of the ground is therefore often multiplied by a factor scaled by the increased surface area associated with the porosity of the soil and buildings in urban areas. Assuming 50 % of the city is covered by buildings of a height of 40 m, this factor becomes 5 and therefore $S_{\text{real}} = 5 \cdot S_{\text{plane}}$. Then the calculated NO_2 -to-HONO conversion on ground surfaces is of the order of atmospheric observations.

However, the influence of an arising of the surface on atmospheric HONO mixing ratios and especially that of vertical walls of buildings (part of the canopy) will be discussed in more detail in the next chapter.

5.6.3 Importance R.H. Independence of NO₂ Uptake Coefficients

The fact that the uptake coefficients of NO₂ are not dependent on R.H., as shown in chapter 5.3.2 can be combined with the results of a recent field study by [Stutz *et al.*, 2004b]. They measured the concentrations of NO₂, HONO and R.H. at different locations under various atmospheric conditions. According to their previous findings [Stutz *et al.*, 2002], a pseudo steady state was assumed between the heterogeneous conversion of NO₂ towards HONO and the loss of HONO on the surface, characterized by the ratio of the reactive uptake coefficients for each process. It was could be shown by [Stutz *et al.*, 2004b] that the reaction probability for the HONO-NO₂ conversion is more dependent on R.H. than the loss of HONO:

$$\frac{d \gamma_{NO_2 \rightarrow HONO}}{d R.H.} > \frac{d \gamma_{HONO}}{d R.H.} \quad \text{eq. 5.14}$$

However, the analysis of the NO₂ uptake coefficients in chapter 5.3.2 of this study show:

$$\frac{d \gamma_{NO_2 \rightarrow HONO}}{d R.H.} = 0 \quad \text{eq. 5.15}$$

Combining equations eq. 5.14, and eq. 5.15, we directly obtain that:

$$\frac{d \gamma_{HONO}}{d R.H.} < 0 \quad \text{eq. 5.16}$$

This anti-proportionality of HONO concentrations and R.H. as expressed by eq. 5.16 is of crucial importance for atmospheric observations. A forthcoming publication [Finlayson-Pitts, 2004; Stutz, 2004] and the following chapter 5.6.4 of this thesis will illustrate this relation in more detail.

5.6.4 Influence of a Constant R.H. on HONO Formation

To show a first consequence of the mechanism in the HeCSI model, it was run at a constant R.H. throughout the entire simulated time. Thereby, exemplary the starting parameters of the 19.04.2003 as described above were used. A conversion of NO₂ towards HONO and secondary reactions of HONO yielding NO were included. An additional loss from the gas-phase by leakage was neglected and the R.H. was set to a constant value for an entire model run. Simulations before and after addition of 200 ppb NO₂ were performed with an R.H. from 0 % up to 100 % and are illustrated by figure 5.24 below.

Under dry conditions (R.H.= 0 %), the HONO uptake rate is at its maximum (see eq. 5.10) and HONO mixing ratios in the gas-phase remain close to zero (see figure 5.24). The HONOs adsorbed on the surface remains at its initial value of $\sim 5 \times 10^{18}$ molec. All HONO, which was desorbed statistically is immediately re-adsorbed, as no H₂O molecules are present to occupy the surface sites of HONO on the surface, before HONO can be bond at these sites. The production of NO from secondary reactions of HONO is consequently rather zero as well (see figure 5.24). After addition of NO₂ to this system, only a few ppb HONO are released into the gas-phase, but the major part remains adsorbed on the surface as HONOs. The production of NO from secondary reactions of HONO is consequently again at its lower limit (see figure 5.24). A new level of HONOs of $\sim 10^{19}$ molec is reached, which is not reduced by time. The uptake of NO₂ onto surfaces was found in chapter 5.3.2 to be independent from R.H. The

slightly differing exponential decays of NO_2 in figure 5.24 are caused by its production from the secondary reactions of HONO and NO (r. 2.54, and r. 2.37).

The situation changes continuously by increasing the constant level of R.H. and finally significantly differing at an R.H. of constantly 100 %. Most surface sites are occupied by H_2O molecules, thus the uptake of HONO onto the surface is inhibited. Consequently, huge amounts (~ 22 ppb) of HONO are observed in the gas-phase (see figure 5.24). Due to the secondary reactions of HONO, its mixing ratio decreases to ~ 15 ppb and HONO is continuously converted into NO, which increases by ~ 80 ppb. The amount of HONOs adsorbed at the surface decreases by a factor of 4 from its initial value (see figure 5.24). This is due to the fact that there is only a small probability for a HONO molecule to be taken up onto the surfaces, when it was desorbed. The huge amounts of H_2O present sufficiently block the HONO surface sites on the surface. After addition of NO_2 to this system, ~ 45 ppb HONO are formed (see figure 5.24), but rapidly react towards its secondary product NO (~ 350 ppb). In the absence of further sinks of NO, its mixing ratios continue to increase (see figure 5.24). The peak of HONOs, which originates from the uptake of NO_2 onto the surface is desorbed by a rate equal to that for dry conditions, but its re-adsorption is inhibited. Consequently, HONOs decreases by a factor of 2 during the next 10 h.

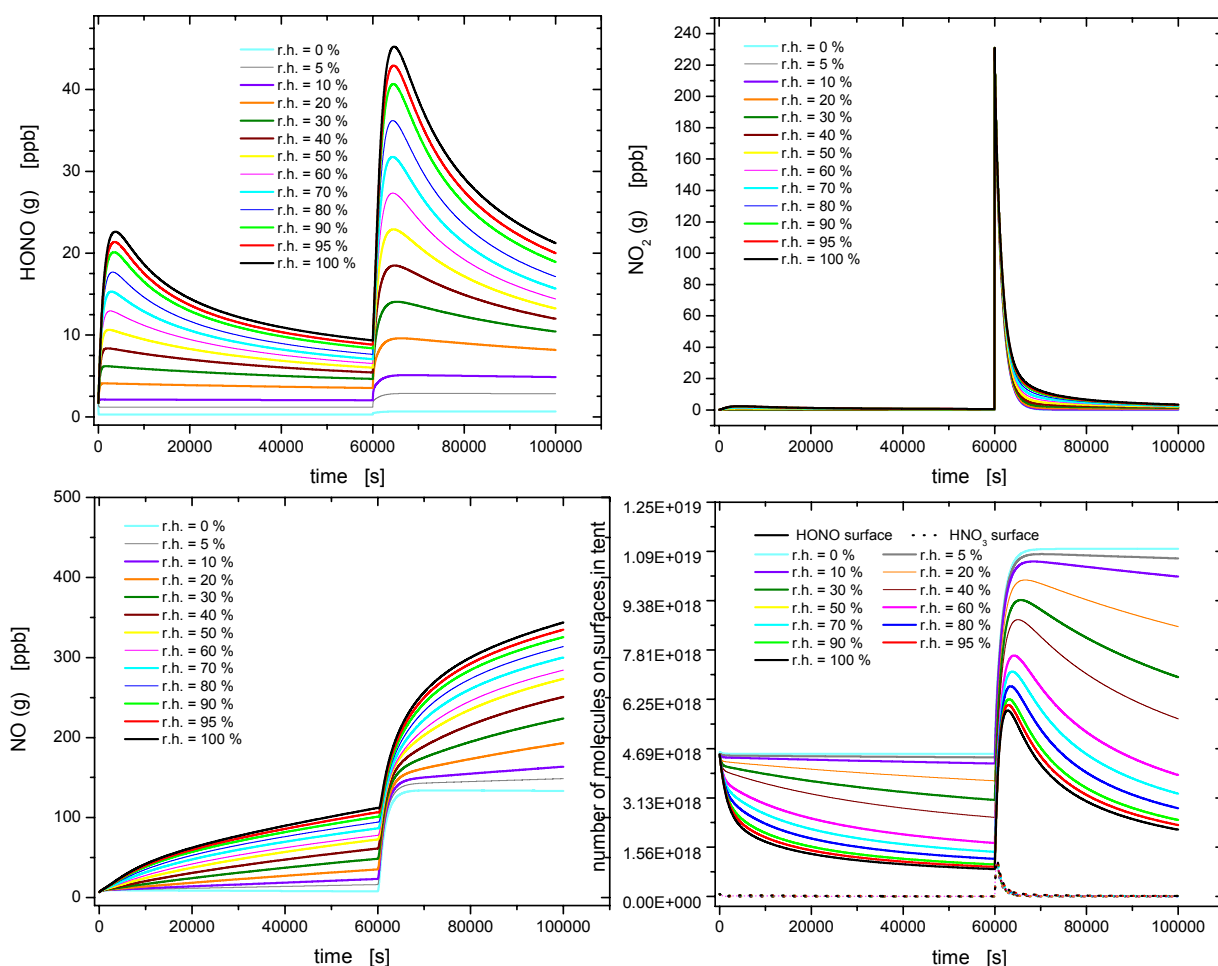


figure 5.24: Yield of HONO (upper left), NO_2 (upper right), NO (lower left) and the surface adsorbed species HONOs and HNO_3 s respectively (lower right). All were obtained from the HeCSI model for different R.H. (different colored lines), which was constant through an individual model run.

This discussion is of special importance for atmospheric conditions, because the R.H. is changing from high nighttime values (often $\sim 100\%$) to daytime conditions, when in summer often an R.H. of $\sim 35\%$ is observed (see chapter 4). Thus, during the night one expects the higher amounts of HONOs released into the gas-phase and a more effective uptake of HONO onto the different surfaces at daytime.

5.6.5 Limitations of the HeCSI Mechanism

The steady state between HONO and H_2O (and therefore R.H.) was shown to establish very fast, and even short-time interruptions in the humidification of the smog chamber were found to immediately influence the HONO concentrations (see e.g. figure 5.10). Both species are described by the Langmuir equilibrium throughout the entire time of the experiments. As HONO is mainly produced by the heterogeneous hydrolysis of NO_2 according to r. 2.33, this steady state includes the concentrations of NO_2 as the precursor of HONO as well. Only the injection of a peak amount of ~ 150 ppb NO_2 into the smog chamber interrupted this physical equilibrium during the third period of the experiments, but it was re-established rapidly. The fast adjustment of this steady state was found for all different surface types investigated in this thesis. Thus, it seems likely that it is also rapidly established on and directly above urban surfaces in the real atmosphere.

However, a sudden injection of NO_2 is at least unlikely for conditions in the real atmosphere. Thus, R.H., HONO, and NO_2 should always be in the steady state described by the Langmuir theory and only long-term shifts as discussed in chapter 5.6.4 above can occur.

On the other hand, the higher amounts of HONOs released into the gas-phase during the night, when R.H. is often close to 100% , can be masked by the reduced vertical mixing at that time. Field measurements by [Stutz *et al.*, 2002] show that a steady state between HONO and NO_2 of $\sim 5\%$ is established in the lowest few meters of the nocturnal boundary layer. The exact value of the HONO-to- NO_2 ratio is thereby dominated by the vertical transport into and out of this layer of the lowest meter of the NBL. Due to the stronger mixing, both processes are enhanced at daytime: the mixing of NO_2 into the laminar layer, but also the out-spreading of HONO. During day, the uptake of HONO onto the ground surfaces is more effective due to the lower R.H., but competes with the stronger dilution of HONO into higher altitudes due to the enhanced vertical mixing. At higher altitudes, additionally less surface area is present for a heterogeneous uptake of HONO.

Some uncertainties of the HeCSI mechanism also limit thus far its application for modeling of real atmosphere conditions. First, this concerns the possible temperature dependence of the out-gassing frequency, which could not be determined in the smog chamber used in this thesis. The higher temperatures at day can possibly enhance the release of HONOs into the gas-phase. However, these circumstances remain speculative.

It can be seen from figure 5.18 that the differences between the values of $\Theta_{\text{H}_2\text{O}}$ by increasing or decreasing R.H. become smaller at the higher the R.H. While at an R.H. of $\sim 5\%$ an $\Theta_{\text{H}_2\text{O}}$ of $\sim 80\%$ is modeled, $\Theta_{\text{H}_2\text{O}}$ is $\sim 96\%$ at R.H. = 60% and slightly differs by 6% by dehumidification of the smog chamber to R.H. = 40% . This situation becomes even worse at the higher R.H., but is in general not described by a linear dependence. At an R.H. of > 50 , the $\Theta_{\text{H}_2\text{O}}$ vary within a factor 2, which is in the order of the error of the model. Thus, we cannot distinguish between a stronger uptake of HONO onto the surfaces due to the lower R.H. or the due to the higher physical constants.

It should be mentioned that Langmuir theory is limited to “medium” surface coverage. At a higher R.H., multi-layering becomes more likely and the BET isotherms (see chapter 2.4.4.3) should be applied. Due to this multi-layering, new surface sites of H_2O and thus for HONO as well may be generated. Thus, the less effective HONO uptake at higher R.H. could partly be

compensated by the more surface sites available for its uptake. However, this could also not be investigated in the smog chamber used in this study and therefore needs further investigations.

The basic assumption of a monolayering of an adsorbent according to the Langmuir theory becomes false at higher R.H. and multi-layering has to be taken into account. However, the application of BET theory seems difficult for real urban surfaces by several reasons. The chemical consistence and the sub-structure of the real urban surfaces are very complex and several surface-specific parameters are needed for the BET theory. Thus far, the HeCSI model was designed to explain the NO_x reaction system inside our smog chamber as simply as possible. Less assumptions and less parameters (besides the trace gas concentrations) are needed to apply Langmuir theory compared to the more complex BET theory, but still gives an accurate and satisfactorily parameterization of the NO_x system in the smog chamber. Thus, Langmuir adsorption-desorption isotherms were chosen in this thesis to explain the observation of a correlation between HONO and R.H.

6 Modeling Studies: Analysis of Atmospheric Daytime HONO

The influence of heterogeneous conversion of NO_2 (reaction r. 2.33) was considered unimportant during the day to date because NO_2 levels are generally lower and HONO is more diluted by convective mixing [Alicke *et al.*, 2003; Alicke *et al.*, 2002; Harrison *et al.*, 1996]. HONO was expected to primarily follow the OH-NO-HONO steady state (reactions r. 2.24 and r. 2.26). Considering the observed NO levels at noon (< 1 ppb), HONO mixing ratios of 200 ppt (see chapter 4) would correspond to extremely high OH mixing ratios of ~ 5 ppt in this conventional view. We will show here that the NO_2 conversion rate and atmospheric stability play crucial roles for the diurnal cycle of HONO and its source rate in urban areas, even during the day.

In chapter 6.1, three diurnal stages of HONO will be defined according to the HONO-to- NO_2 ratio variation. The HONO formation mechanisms and rates are discussed for each diurnal stage separately (chapters 6.1.1, 6.1.2, and 6.1.3). The limitations of this discussion will be shown and require a complex chemistry and transport model. These modeling studies on the daytime chemistry of nitrous acid are discussed in chapter 6.2. This especially includes a description of the model (chapter 6.2.1), the extensions performed in this thesis (in chapter 6.2.1.3), but also sensitivity studies (chapter 6.2.2). The results of the model are presented in detail for an exemplary day (chapter 6.2.3), and compared for the three field campaigns of this thesis in chapter 6.2.4. Conclusions are drawn regarding the consequences of the approach of this model for the contribution of HONO to the photochemistry (HO_x source) in urban areas (chapter 6.2.5).

6.1 The Diurnal Variation of HONO Chemistry in Urban Areas

A period from the Rome 2001 field campaign with smog conditions (high levels of O_3 and NO_2 , high pressure system over Italy, clear skies) from 28.05. to 01.06.2001 was chosen as an example to study the diurnal cycle of HONO and its influence on photochemistry in an urban area. This period was a high-pressure period with low wind speeds ($v < 3.0 \text{ m s}^{-1}$), strong differences in temperature for day / night and a maximum temperature of $\sim 27 \text{ }^\circ\text{C}$ at noon, with only clear-sky, sunny days and therefore high solar irradiation at noon ($J(\text{NO}_2)_{\text{max}} > 1 \times 10^{-3} \text{ s}^{-1}$).

Since heterogeneous conversion of NO_2 to HONO is the main source of HONO in the boundary layer, especially at night, HONO-to- NO_2 ratios are independent of the NO_2 level and thus the level of pollution in first approximation. In addition, transport processes generally influence this ratio less than the individual concentrations (see chapter 6.1.1 for restrictions). We therefore decided to use the HONO-to- NO_2 ratio as an indicator for the different stages of the diurnal cycle of HONO in the urban environment of Rome.

The HONO-to-NO₂ ratio from 28.05. to 01.06.2001 over Rome is shown in figure 6.1. Additionally, the time series of the HONO photolysis frequency and natural radioactivity are given in figure 6.1.

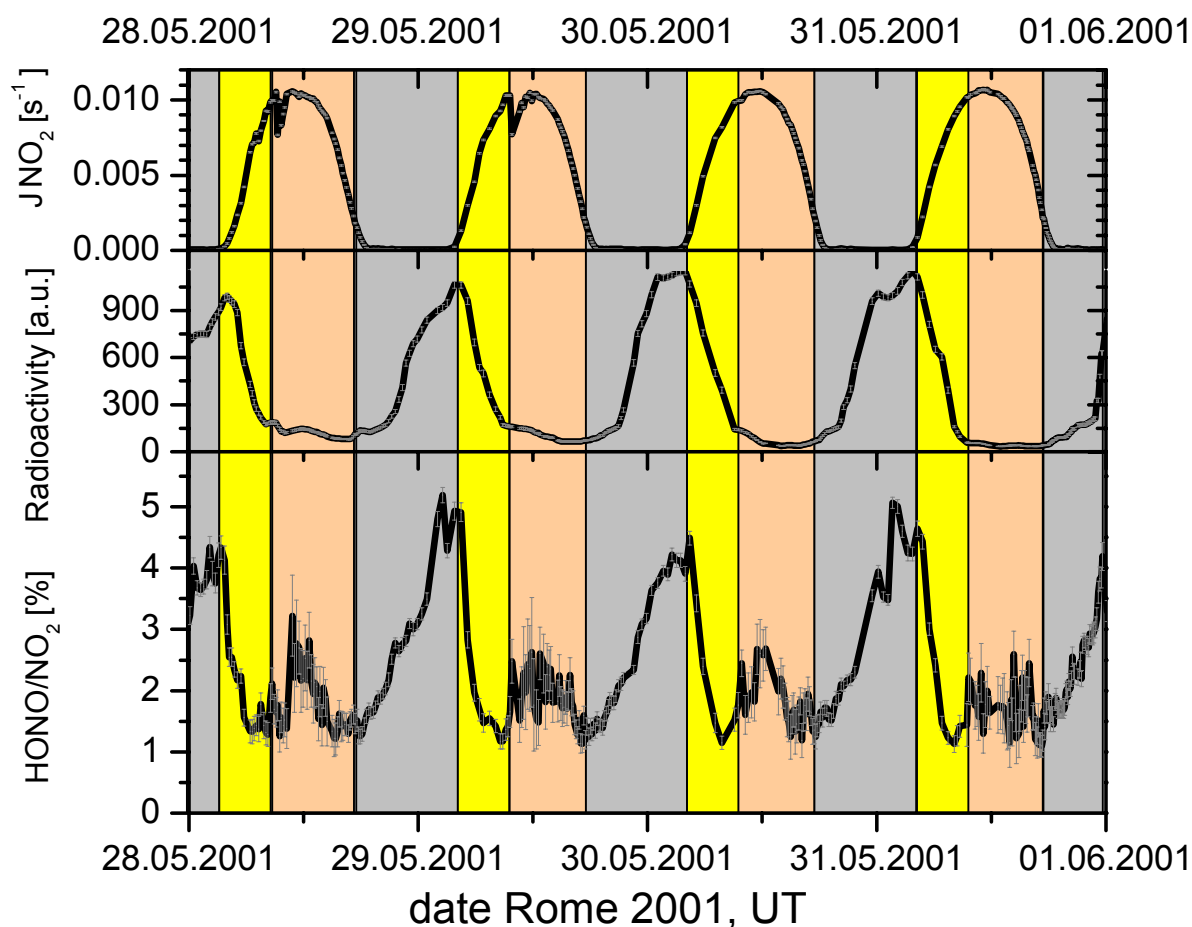


figure 6.1: Time series of the HONO-to-NO₂ ratio observed over Rome. The diurnal pattern uncovers three different stages for HONO: Nocturnal accumulation (shaded gray), early morning photolysis (shaded yellow), and daytime OH-NO-HONO steady state (shaded red). The correlation of the HONO-to-NO₂ ratio to radioactivity and the anti-correlation to photolytic flux is apparent.

A clear diurnal pattern of the HONO-to-NO₂ ratio is apparent: With the beginning of the night, the ratio increases during several hours from ~1 % to 4 – 5 % in the middle of the night. During the last hours of the night, the ratio remains at this high level. Over the three hours following sunrise, the HONO-to-NO₂ ratio declines back to ~1 %. During midday, the ratio increases again to a maximum value of ~2 %, which is reached around noon. The HONO-to-NO₂ ratio decreases again to ~1 % at the beginning of the night.

This diurnal pattern suggests defining three diurnal stages of HONO formation over Rome:

- HONO accumulation during nighttime during the night (shaded grey in figure 6.1)
- HONO photolysis and dilution during morning hours (shaded yellow in figure 6.1)
- OH-NO-HONO steady state during noon and afternoon (shaded red in figure 6.1)

The contributions and mechanisms of HONO formation and destruction are discussed and quantified separately for each diurnal stage in the following chapters.

6.1.1 HONO Accumulation in the Nocturnal Boundary Layer (Stage 1)

As can be seen from figure 6.3, the concentration levels of both HONO and NO_2 rose at the beginning of the night due to the absence of photolysis, which is the main sink of HONO and NO_2 during day, and due to the intensifying of vertical stability (as can be seen from figure 6.2). While the HONO mixing ratio continued to grow or remain at a constant level after midnight, the NO_2 decreased again as soon as O_3 levels were below ~ 10 ppb (figure 6.3). This observed NO_2 trend is caused by the reaction r. 2.9 of NO with O_3 , which cannot balance the NO_2 loss anymore. The NO_2 loss is caused by dry deposition on the ground, the reactions yielding $\text{NO}_3 / \text{N}_2\text{O}_5$ at O_3 levels below ~ 10 ppb [Geyer and Stutz, 2003; Stutz et al., 2004a], reduced direct emission from traffic, and especially vertical transport. However, the ratio of HONO-to- NO_2 increased over night as a consequence from 1 % to 4 – 5 % and remained at this level during the last hours (figure 6.1).

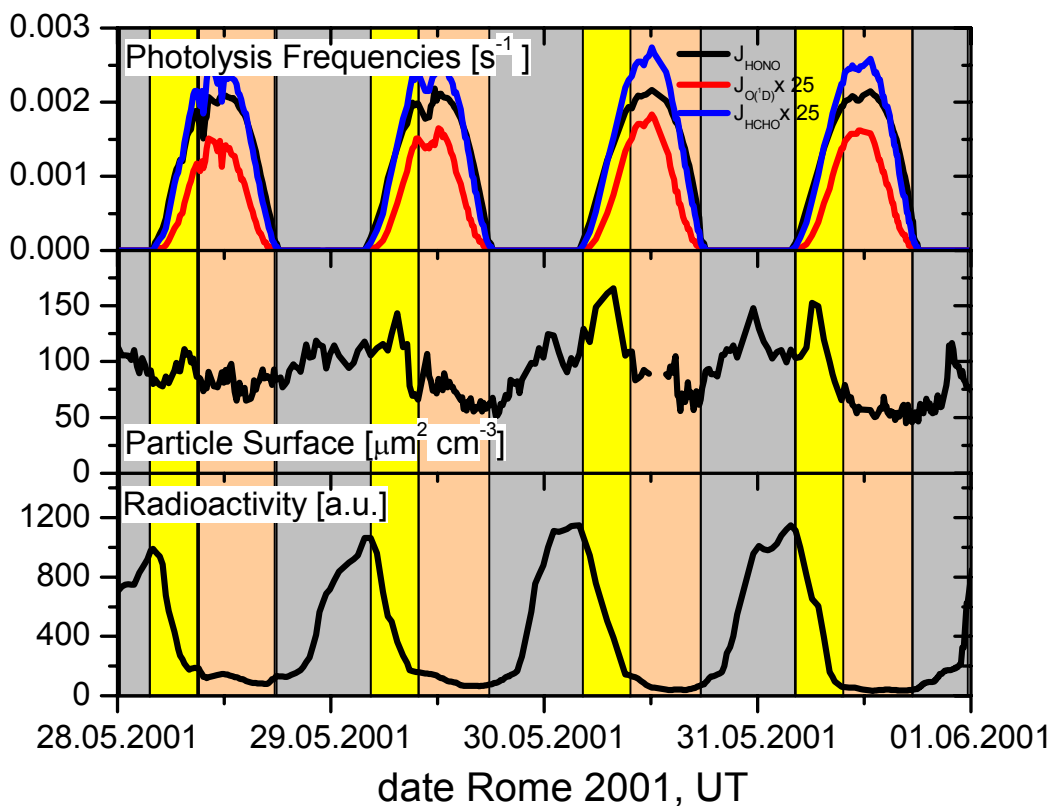


figure 6.2: Time series of photolysis frequencies, particle surface area, and natural radioactivity from 28.05.–01.06.2001 of the Rome 2001 field campaign.

The continuous increase of the HONO mixing ratio of the measurement height of 50 m altitude is due to ongoing production during the night. A distinction between a formation of atmospheric nitrous acid primarily near the ground or on airborne particles in the whole air volume of the nocturnal boundary layer (NBL) can be achieved from the correlation of the HONO-to- NO_2 ratio with the time derivative of natural radioactivity (see chapter 4.1). In times of strong vertical stability, gases emitted or formed near the ground are suspected to be “trapped” at lower altitudes, where their levels increase as long as they are produced (also see chapter 2.5). To identify these periods of stable layering, we use the time derivative of the natural radioactivity measured by the Radon concentration illustrated in figure 6.1, which was already discussed in chapter 2.5.4. From figure 6.1 it can already be seen that the HONO, NO_2 , and consequently the HONO-to- NO_2 ratios are positively correlated with the

radioactivity levels in the lowest air masses of the PBL. This strongly indicates that HONO is formed primarily near or at the ground.

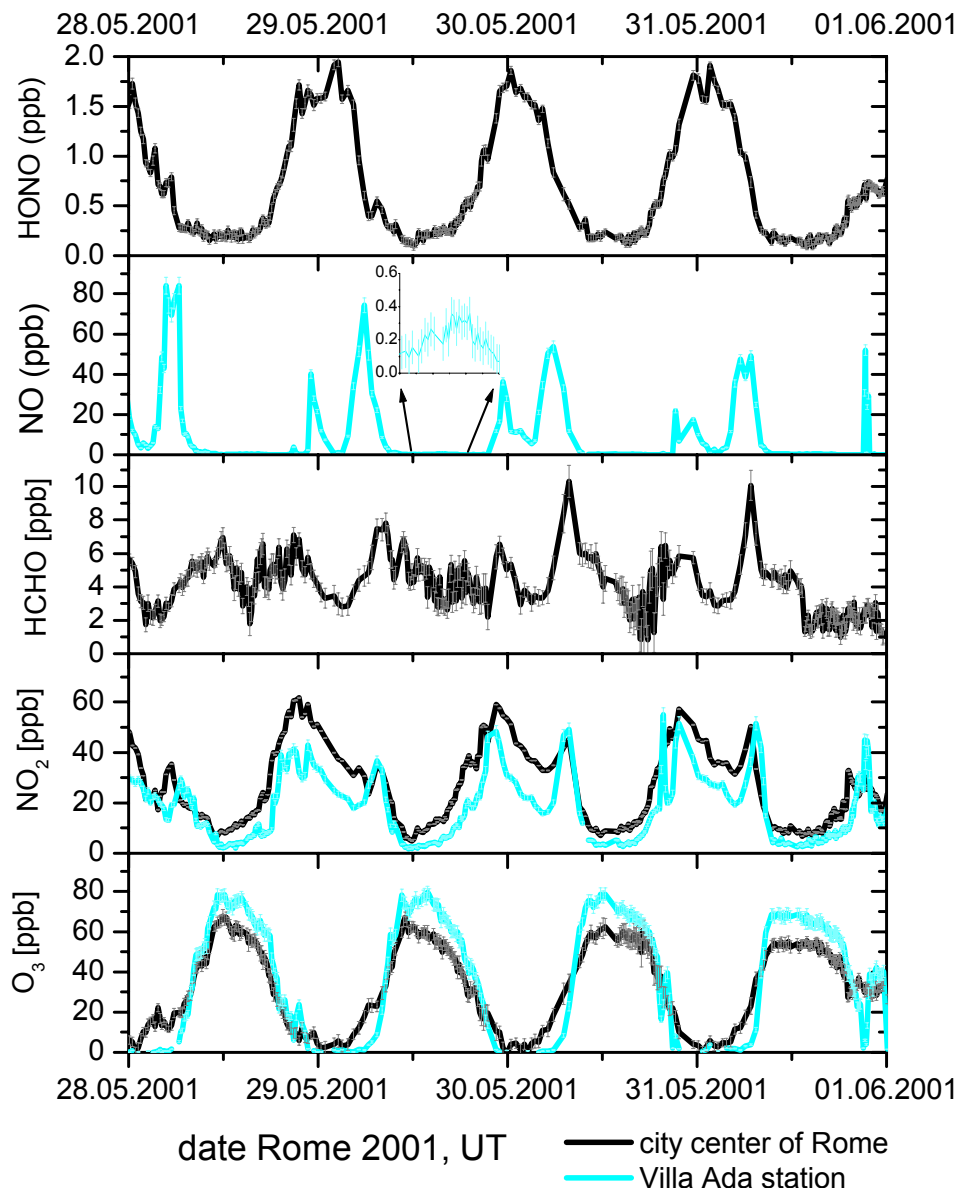


figure 6.3: Time series of the mixing ratios of HONO, HCHO, NO₂, and O₃ measured over Rome (black lines). In-situ data of NO, NO₂, and O₃ observed at Villa Ada is included as cyan lines.

However, the heterogeneous formation of HONO on airborne particles, such as aerosols, seems unlikely for a number of reasons. First, HONO levels are not clearly correlated to the particle surface area, as can be seen from figure 6.1 and figure 6.2. On the evening of 29.05.2001, for example, the surface area was about half of the area of the day before but the rate of increase of the HONO-to-NO₂ ratio is practically identical. Second, the aerosol surface area is not expected to show a sufficiently strong negative vertical gradient shortly after sunset. Consequently, we suspect aerosols being of minor importance for the heterogeneous formation of nitrous acid during the night in Rome.

Direct emission was presented in chapter 2.3.3 as possible source for atmospheric HONO. However, it was observed that the road traffic in Rome was very low during the later part of the night, while HONO levels were still increasing. Further, high HONO-to-NO₂ ratios of up

to 5 % were measured during night in Rome in 2001, while emission ratio of only 0.8 % were reported by [Ackermann, 2000; Kessler and Platt, 1984; Kurtenbach *et al.*, 2001; Pitts *et al.*, 1984a; Winer and Biermann, 1994]. As the lifetimes of both HONO and NO₂ are of the order of several hours during the night (see chapter 2.1.2, and 2.3.7), direct emission of HONO was concluded to be of minor importance as a HONO source.

By the considerations presented above, we finally conclude that the heterogeneous formation of HONO from NO₂ on surfaces on the ground is the dominant source for HONO in Rome during the night. Therefore, our observations will be analyzed based on a steady state approach of HONO and NO₂ recently suggested by [Stutz *et al.*, 2002] and illustrated by figure 6.4 A. In this approach, three different processes are involved in the formation of the steady state of HONO in the atmosphere:

- Deposition of NO₂ onto the ground, where the deposition flux of NO₂ can be described by the product of its deposition velocity and concentration:

$$D_{NO_2} = v_{dep}(NO_2) \cdot [NO_2] \quad \text{eq. 6.1}$$

- Deposition of HONO onto the ground analogous to that of NO₂:

$$D_{HONO} = v_{dep}(HONO) \cdot [HONO] \quad \text{eq. 6.2}$$

- A heterogeneous conversion of NO₂ into HONO with a conversion factor χ (number of HONO molecules formed per NO₂ molecules deposited on the surface), which further depends on the surface type:

$$P_{HONO} = \chi \cdot D_{NO_2} \quad \text{eq. 6.3}$$

If a steady state for HONO (eq. 6.2 equals eq. 6.3, i.e. $P_{HONO} = D_{HONO}$ and consequently $d[HONO] / dt = 0$) is established, the HONO-to-NO₂ ratio at the compensation point for HONO may be calculated [Stutz *et al.*, 2002]:

$$\left. \frac{[HONO]}{[NO_2]} \right|_{comp. point} = \chi \frac{v(NO_2)}{v(HONO)} \quad \text{eq. 6.4}$$

At this compensation point, the net flux of HONO from the ground becomes zero and NO₂ conversion on the ground is no longer a net source for HONO. Observations by [Stutz *et al.*, 2002] in Milan, Italy during many nights determined a fast development of that steady state ratio between HONO and NO₂ of 3 ± 1 % some meters above grassland, which is of the order of the ratio measured at the end of the nights in Rome (figure 6.1).

To analyze the HONO trends through the entire night, this steady state approach needs to be extended by including vertical transport of NO₂ from higher altitudes towards the ground and of HONO out of the steady state layer (figure 6.4). By this new approach, the net pseudo HONO production on the ground is now defined by the transport rate of NO₂ onto the ground and of HONO upwards. Consequently, the HONO formation rate in the NBL becomes a function of atmospheric stability: At stronger stabilities vertical transport is more suppressed and less HONO is formed in the NBL.

The ground surface can even represent a sink for HONO during the night. Due to a strongly reduced vertical mixing, NO₂ may be transported downwards to the ground in smaller amounts than required for the steady state according to eq. 6.4. When this steady state between HONO and NO₂ is established in the NBL, the HONO-NO₂ system reacts by a deposition of HONO onto the ground surface.

The dependence of the HONO formation on atmospheric stability is also indicated by the slope of the HONO-to-NO₂ ratio versus natural radioactivity indicated by figure 6.1: While the ratio is proportional to radioactivity at levels < 200 and > 600 , it remains more or less constant at radioactivity levels of $200 - 600$. This interval corresponds to the period of the night with the highest temporal gradient of radioactivity indicating highest vertical stability, and consequently, the lowest HONO formation rate.

Although the steady state ratio of HONO, and thus that of the HONO-to- NO_2 , can rapidly be established in a layer directly above the ground, the suppressed vertical mixing of NO_2 and HONO can lead to a delayed build-up at higher altitudes (figure 6.4 B). Our observations, for example, suggest that the steady state at 50 m altitude was reached after ~ 7 h in Rome. As a consequence, the increase of HONO at higher altitudes is not determined by the NO_2 -to-HONO conversion rate at the ground, but solely by the vertical mixing strength, if the dry deposition of HONO is its dominant sink. Following this approach, the temporal gradient of HONO at higher altitudes during night cannot be used to estimate the NO_2 conversion into HONO during daytime (cf. [Alicke *et al.*, 2003]).

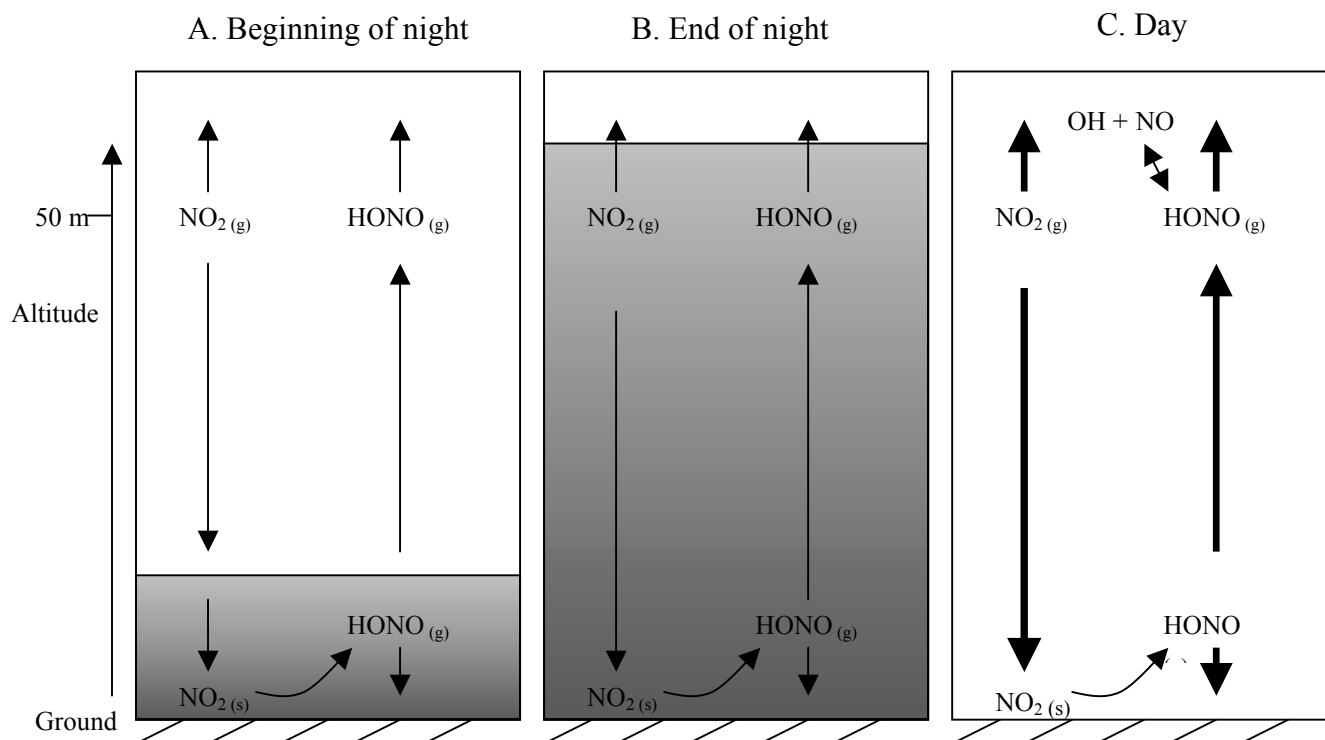


figure 6.4: Illustration of the processes involved in the steady state formation of HONO at the beginning and end of the night and during day. HONO and NO_2 establish a steady state in the mixed layer (gray shaded areas).

6.1.2 HONO Photolysis and Dilution after Sunrise (Stage 2)

During roughly 3 - 5 hours after sunrise, the HONO mixing ratio rapidly decreases from ~ 1.7 ppb to levels of ~ 190 ppt due to intensifying convective mixing and photolysis (see figure 6.3, and figure 6.5 A, respectively). As the NO_2 levels remain more or less constant (figure 6.3) during this time, the HONO-to- NO_2 ratio consequently decreases from $\sim 4\%$ to $\sim 1\%$ (figure 6.1).

During the first $\sim 2 - 3$ hours in the morning (referred to as first part of stage 2) the gradient of HONO is high and thus a steady state approach for HONO is not longer valid. However, the decrease of the HONO concentration after sunrise (see figure 6.5 A) yields a nearly linear change of HONO with time as illustrated in figure 6.5 B for three exemplary days of the Rome 2001 campaign.

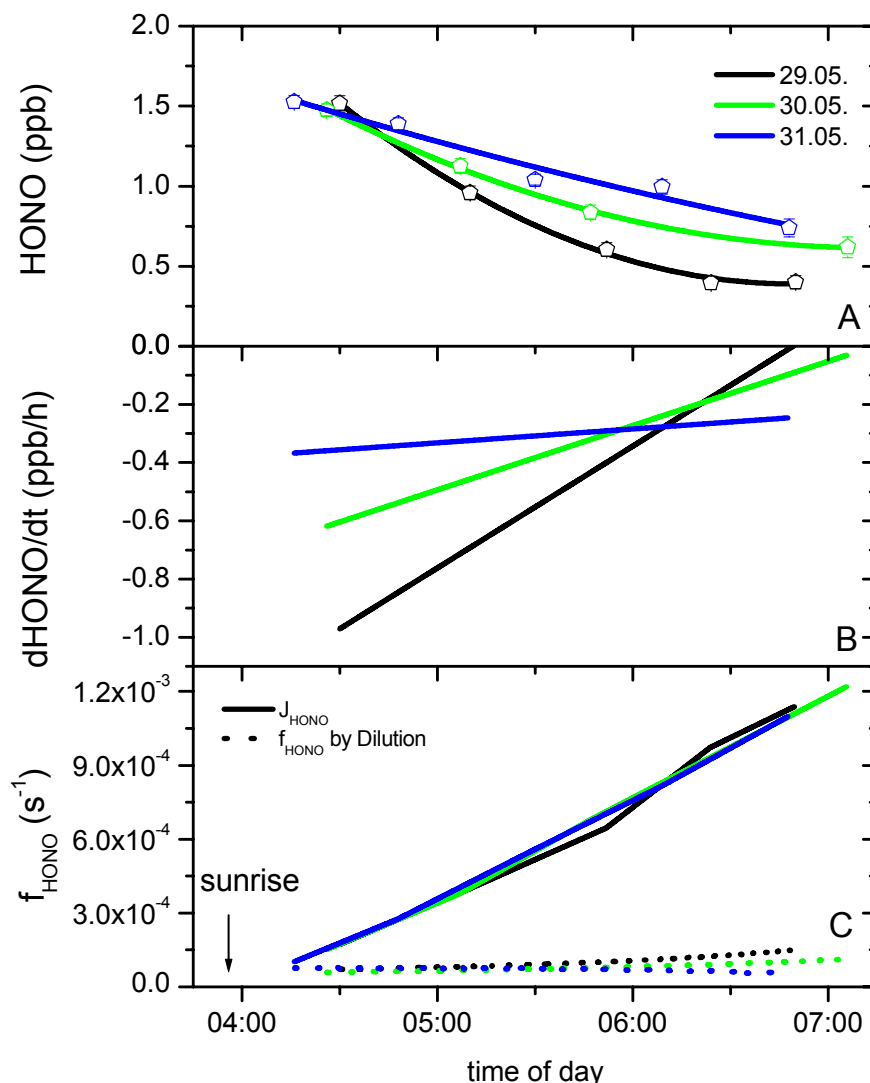


figure 6.5: A and B.: Temporal change of the HONO concentration after sunrise (stage 2) exemplary for the 29.05., 30.05., and 31. 05.2001. C.: The calculated HONO loss frequencies due to photolysis (J_{HONO}) and due to convective dilution ($f_{\text{HONO-Dilution}}$).

This can be expressed by further including the photolysis frequency J_{HONO} , the total source rate of HONO P_{HONO} , and a dilution frequency of HONO $f_{\text{HONO-Dilution}}$:

$$\frac{d[\text{HONO}]}{dt}(t) = -(f_{\text{HONO-Dilution}}(t) + J_{\text{HONO}}(t)) \cdot [\text{HONO}](t) + P_{\text{HONO}}(t) \quad \text{eq. 6.5}$$

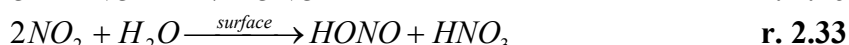
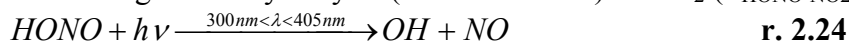
The temporal gradient some minutes after sunrise in stage 2, i.e. the slope of $d[\text{HONO}] / dt$, varied from -1 ppb h^{-1} on 29.05. to -0.4 ppb h^{-1} on 31.05.2001.

The new parameter, the dilution frequency of HONO ($f_{\text{HONO-Dilution}}$), which is dependent on atmospheric stability and thus vertical transport, can be derived from the variation of natural radioactivity (figure 6.2). While on 29.05. and 30.05. $f_{\text{HONO-Dilution}}$ increased from $(6 - 7) \times 10^5 \text{ s}^{-1}$ shortly after sunrise to $(11 - 15) \times 10^5 \text{ s}^{-1}$ three hours later, the dilution frequency remained constant at $\sim 7 \times 10^5 \text{ s}^{-1}$ on 31.05.2001 (figure 6.5 C). As the photolysis frequency increased from $\sim 10^{-4} \text{ s}^{-1}$ some minutes after sunrise to more than 10^{-3} s^{-1} three hours later (figure 6.5 C), it was therefore the dominant sink process during stage 2 in Rome.

In eq. 6.5, the HONO concentration, and the photolysis frequency are directly measured parameters, and the dilution is derived from the measured values of natural radioactivity and their variation. Thus, the total HONO source rate P_{HONO} during the morning hours can be

determined. Generally, P_{HONO} was found to increase during the first three hours of the day, but the rate of increase of P_{HONO} reduces over time. The initial HONO source rate was around 0.5 ppb h^{-1} directly after sunrise and reached maximum values of 1.5 ppb h^{-1} on 29.05.2001, up to $\sim 3 \text{ ppb h}^{-1}$ on 31.05.2001 after 3 hours.

We have mentioned in chapter 2.3 that mainly three types of HONO sources contribute to the total HONO production rate observed during daytime: direct emission from (road) traffic ($P_{\text{HONO-traffic}}$), the homogeneous recombination ($P_{\text{HONO-OH+NO}}$) of OH radicals and NO (reaction r. 2.26), and the heterogeneous hydrolysis (reaction r. 2.33) of NO_2 ($P_{\text{HONO-NO}_2}$):



Their HONO production rates can be combined:

$$P_{\text{HONO}} = P_{\text{HONO-traffic}} + P_{\text{HONO-OH+NO}} + P_{\text{HONO-NO}_2} \quad \text{eq. 6.6}$$

The quantification of direct emission as HONO source is complicated due to the high chemical lifetime of NO_x (several hours). The HONO, which was emitted some hours ago, might be derived from multiplying the measured NO_x levels by the HONO-to- NO_x emission ratio. The HONO emission rate during the morning rush hour was estimated by comparing the increase of NO_x in 50 m altitude during this time of day. The missing measured values of NO in 50 m altitude were derived from comparison of the $\text{NO-O}_3\text{-NO}_2$ photostationary states at Villa Ada and over Rome (see also [Geyer *et al.*, 2001b]):

$$\left. \frac{[\text{NO}_2]}{[\text{NO}][\text{O}_3]} \right|_{\text{DOAS}} = \left. \frac{[\text{NO}_2]}{[\text{NO}][\text{O}_3]} \right|_{\text{VillaAda}} \quad \text{eq. 6.7}$$

In equation eq. 6.7 the concentration of peroxy radicals was implicitly assumed to be identical at both locations. The subsequent values of NO in 50 m altitude calculated by equation eq. 6.7 are shown in figure 6.6. From the comparison with figure 6.3, it can be seen that the peaks in the NO mixing ratios of maximum 15 – 25 ppb are generally lower at this altitude than near the ground. During the first hours after sunrise, when vertical stability is still high and traffic has already increased, NO_x increases by 7 – 13 ppb h^{-1} . Taking into account the HONO-to- NO_x emission ratio by traffic of 0.8 % determined by [Ackermann, 2000; Kessler and Platt, 1984; Kurtenbach *et al.*, 2001; Pitts *et al.*, 1984a; Winer and Biermann, 1994], this NO_x increase would correspond to a HONO source rate of $P_{\text{HONO-traffic}} < 0.1 \text{ ppb h}^{-1}$ in 50 m altitude. This is a factor of 5 below the initial HONO increase during stage 2 (see above), and even 30 times smaller than the HONO production 3 hours after sunrise. Thus, we again conclude direct emission of HONO by traffic being of minor significance as a source of the observed atmospheric nitrous acid in Rome.

For the quantification of the amount of HONO produced by reaction r. 2.26, the recombination of OH radicals with NO ($P_{\text{HONO-OH+NO}}$), the concentrations of OH in 50 m altitude is required, but not measured. It was calculated from the measured OH production rates by photolysis of HONO (reaction r. 2.24), O_3 , and HCHO (see also chapter 2.2.3) and the reaction frequency of OH with NO_2 (r. 2.2). Since other sinks of OH are neglected here, the true OH levels are expected to be lower, and thus represent an upper limit only. These upper limits for the OH levels are below $3 \times 10^6 \text{ cm}^{-3}$ during the first three hours of daytime during 28.05. to 01.06.2001 but increase up to $3 \times 10^7 \text{ cm}^{-3}$ at noon as illustrated by figure 6.6 B.

The corresponding upper limit of the production rate of HONO by reaction r. 2.26 ($P_{\text{HONO-OH+NO}}$) increased from $\sim 0.2 \text{ ppb h}^{-1}$ 30 minutes after sunrise up to 1.4 ppb h^{-1} at 07:00, because of the high NO levels during the morning rush hour. On 31.05.2001, about 25 % of the total P_{HONO} one hour after sunrise can be explained by reaction r. 2.26. After three hours, about half the total nitrous acid produced is caused by $P_{\text{HONO-OH+NO}}$. Thus it was concluded that the

high values and the steady increase of P_{HONO} are partly based on HONO formation from reaction r. 2.26.

In the absence of further production pathways for HONO, the HONO formation rate by heterogeneous conversion of NO_2 at the ground surface during daytime is calculated from equation eq. 6.6 as the difference of the total P_{HONO} and the time series of $P_{\text{HONO-OH+NO}}$. Consequently, $P_{\text{HONO-NO}_2}$ increases from $0.2 - 0.5 \text{ ppb h}^{-1}$ about 30 minutes after sunrise to 1.0 ppb h^{-1} on 29.05.2001 and 1.5 ppb h^{-1} on 30.05., and 31.05.2001, respectively.

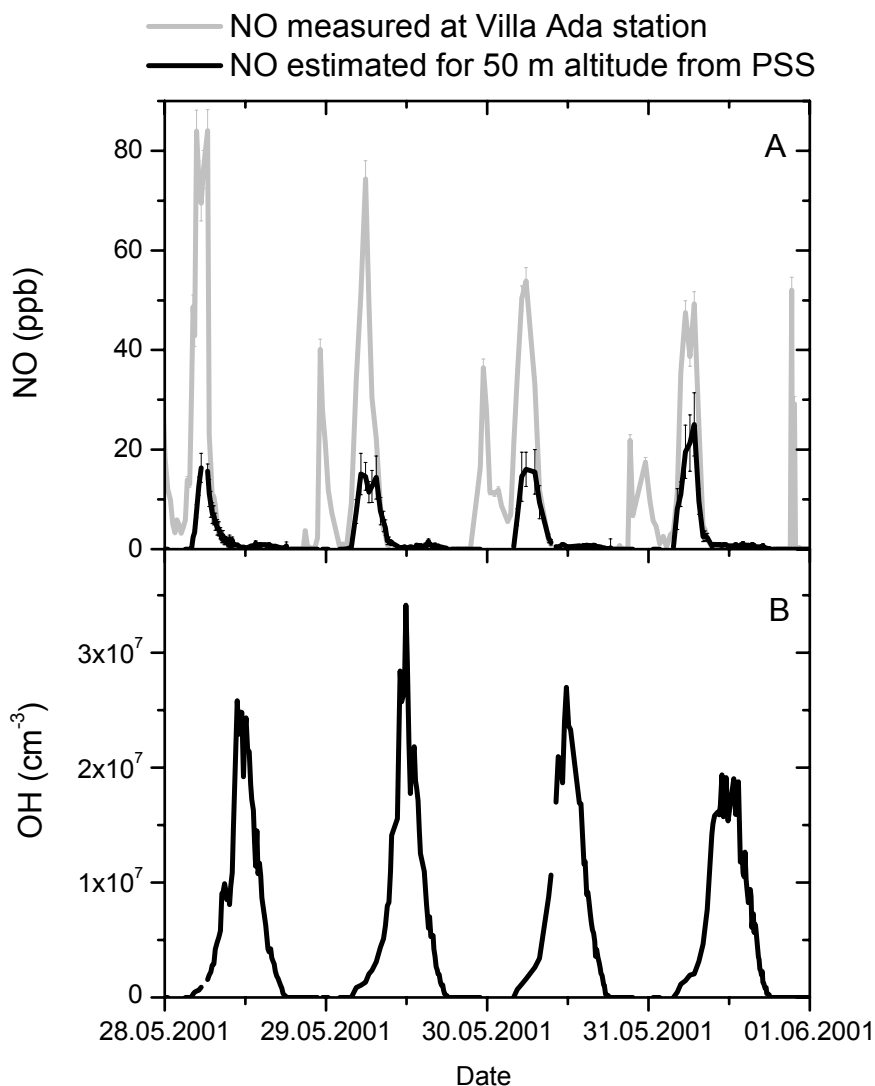


figure 6.6: *A. NO concentration in 50 m altitude calculated from equation eq. 6.7. B. Upper limit of the OH concentration derived from the OH production rate by photolysis of HONO, O_3 , and HCHO and the reaction of with NO_2 as only OH sink. Note that all calculations are restricted to daytime.*

Since the aerosol surface area does not change significantly between night and day, aerosols seem not to offer a significant surface for heterogeneous NO_2 conversion to HONO and are therefore again suspected to be of minor importance as a HONO source.

Thus, the increase of $P_{\text{HONO-NO}_2}$ by a factor of 3 or more during the first 3 hours of stage 2 can only be caused by an increasing efficiency of the $\text{NO}_2 \rightarrow \text{HONO}$ conversion on the ground, although the NO_2 concentrations close to the ground are generally lower at this time due to an arising vertical mixing (cf. chapter 6.1.1).

6.1.3 The OH-NO-HONO Steady State during Daytime (Stage 3)

About 5 hours after sunrise, the HONO pool, which was accumulated during night, is completely removed and more or less constant mixing ratios of HONO of ~ 190 ppt were observed (figure 6.3). As the NO_2 levels at this time are ~ 10 ppb (figure 6.3), the HONO-to- NO_2 ratio is around 2 % at noon and in the afternoon (figure 6.1). In the evening the ratio decreases back to 1 % because of rising NO_2 levels. However, during this period of the day, the importance of HONO photolysis as its sink increases, and HONO deposition is no longer the dominant HONO sink. Consequently, the approach described in chapter 6.1.1 above is no longer valid, but HONO levels are controlled by the gas-phase formation of nitrous acid (reaction r. 2.26), the NO_2 conversion on the ground (reaction r. 2.33), and photolysis (reaction r. 2.24). A different steady state approximation for HONO is applicable, restricted to the time between 09:00 (5h after sunrise) and 17:00 (1.5 h before sunset):

$$J_{\text{HONO}}(t) \cdot [\text{HONO}](t) = P_{\text{HONO-OH+NO}}(t) + P_{\text{HONO-NO}_2}(t) \quad \text{eq. 6.8}$$

The diurnal variation of the three components from eq. 6.8 contributing to the total HONO production is illustrated in figure 6.7. The grey shaded boxes refer to stage 1 (see chapter 6.1.1), and stage 2 (chapter 6.1.2), respectively, when atmospheric dynamics in the PBL allow the application of steady state approximations and thus eq. 6.8. The HONO loss rate by photolysis ($J_{\text{HONO}} \times [\text{HONO}]$) was discussed to peak in the early morning hours after sunrise (at the end of stage 2, see chapter 6.1.2). Afterwards, it remains relatively constant at ~ 1.5 ppb h^{-1} throughout the entire day (stage 3), but finally decreases rapidly a few hours before sunset. Due to the lower NO concentrations at noon and in the afternoon (see figure 6.3), the levels of $P_{\text{HONO-OH+NO}}$ are a factor ~ 3 lower than in stage 2. Further due to the anti-correlation of OH and NO during day, the HONO formation by reaction r. 2.26 is relatively constant at ~ 0.3 ppb h^{-1} through the day, but slightly drops down and becomes negligible some hours before sunset.

The diurnal variations of the production rate $P_{\text{HONO-NO}_2}$ of HONO in 50 m altitude by NO_2 conversion on the ground can be calculated from equation eq. 6.8 using the measured values of $J(\text{HONO})$; $[\text{HONO}]$, and $[\text{NO}_2]$. Due to lower NO_2 levels and a stronger atmospheric mixing, $P_{\text{HONO-NO}_2}$ is slightly lower during stage 3 than before, but rather constant at ~ 1 ppb h^{-1} (similar to $P_{\text{HONO-OH+NO}}$). The constant level of $P_{\text{HONO-NO}_2}$ is evident in the scope of relatively constant NO_2 and radioactivity levels during the day (figure 6.3, and figure 6.2). The decrease of $P_{\text{HONO-NO}_2}$ between stage 2 and 3 is most likely based on the lower NO_2 levels during stage 3. Since equation eq. 6.8 is not valid in the last hour before sunset, no conclusions can be drawn regarding the change of $P_{\text{HONO-NO}_2}$ during the late afternoon.

It is interesting to note that HONO production by heterogeneous NO_2 conversion is the major HONO source throughout the day (compare to figure 6.7). Even at noon, $P_{\text{HONO-NO}_2}$ is about two times higher than $P_{\text{HONO-OH+NO}}$. This result is in conflict with the common view, which proposes that heterogeneous HONO production is negligible during day (e.g., [Alicke *et al.*, 2003; Alicke *et al.*, 2002; Harrison *et al.*, 1996]). This conclusion was based on comparison of nighttime production rates with daytime conditions considering the lower NO_2 levels and stronger dilution by atmospheric mixing. In this approach, however, the efficiency of HONO production on the ground is strongly suppressed during the night. Therefore, $P_{\text{HONO-NO}_2}$ at 50 m altitude is actually higher during the day than during the night despite the lower NO_2 levels and stronger dilution.

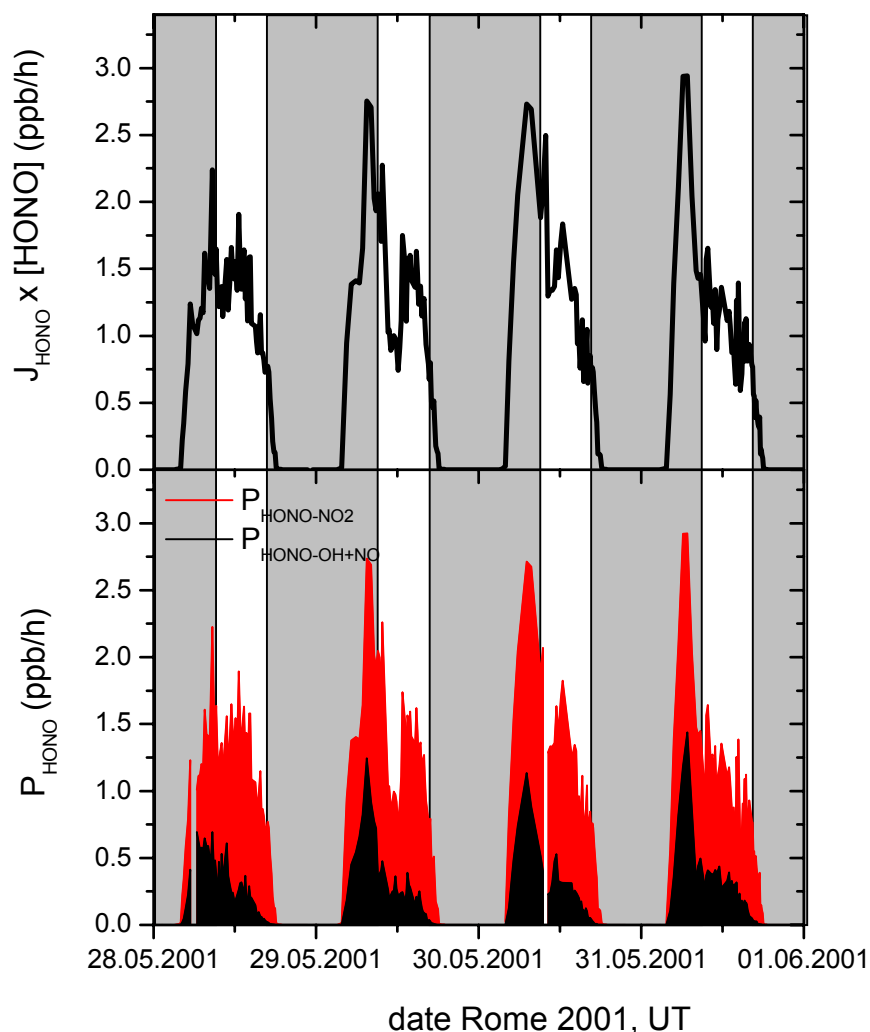


figure 6.7: HONO loss rate ($J_{\text{HONO}} \times [\text{HONO}]$) and production rates ($P_{\text{HONO-OH+NO}}$ and $P_{\text{HONO-NO}_2}$) as a cumulative plot during stage 3 in Rome. The steady state approximation is not valid in the grey shaded areas.

Besides these uncertainties of the temporal trend of HONO, which are caused by the unknown chemical composition of the observed air masses, vertical transport is not quantified by equation eq. 6.5. In the discussion above it was thus far only included by qualitative considerations to separate the diurnal stages of the HONO-to-NO₂ ratio. Thus, any further analysis of the atmospheric daytime HONO concentrations is inhibited.

6.2 Modeling Daytime HONO and Vertical Transport

From the chapters in 6.1, we have seen that there is a strong need to link both the chemical reactions yielding HONO during the night and day as well as the influence of vertical transport (see chapter 6.1) in order to explain the observed HONO daytime. This cannot be achieved by analytical analysis anymore, thus a model including not only the daytime and nighttime chemical reactions as well as transport mechanisms of the PBL, but also their interlink is required. In this PhD thesis we have therefore chosen to use a one-dimensional model designed by [Geyer and Stutz, 2003; Stutz et al., 2004a] and described therein in detail. However, as we have performed some modifications and extensions to urban troposphere daytime chemistry and transport, we will give a brief introduction in chapter 6.2.1 before we present the modeling results in chapter 6.2.2 and finally discuss their influence on daytime HONO chemistry and OH production in chapter 6.2.3.

6.2.1 Description of the RCAT 8.1.2 Model

The RCAT 8.1.2 model is a combination of the highly resolved one-dimensional Nocturnal Chemistry And Transport model (NCAT) [Geyer and Stutz, 2003; Stutz et al., 2004a] with its altitude dependent calculation of vertical trace gas fluxes and the established gas-phase Regional Atmospheric Chemistry Mechanism (RACM) [Stockwell et al., 1997], which is described in more detail in appendix B. It also includes variable biogenic and anthropogenic emissions, dry deposition, surface chemistry on aerosols, and the calculation of photolysis frequencies (all according to the RACM mechanism).

In the framework of this thesis, the influence of the urban canopy, i.e. the ground surface and walls of buildings, on the daytime vertical transport were implemented, except for liquid phase chemistry, which was not considered thus far. In our studies the model was run on a vertical grid subdividing the lowest 1000 m of the (nocturnal) boundary layer into 20 layers with logarithmic spacing below 1 m. The following upper box heights were used: 10^{-4} , 10^{-3} , 10^{-2} , 0.1, 1, 5, 7, 10, 20, 35, 50, 65, 80, 100, 125, 150, 175, 200, 250, 1000 m. The variations of trace gas concentrations were calculated for 12 hours from midnight to noon, specifically including sunrise. Realistic values were assumed for the variation of the traffic emission rates and meteorological parameters during this time. The model was operated in a diagnostic mode to simulate the measured data as well as possible.

6.2.1.1 Calculations of Vertical Transport

The vertical transport in the RCAT 8.1.2 is based on a system of 1D transport kinetics equations, which express the change of the concentration $c_i(z, t)$ of a trace gas i at an altitude z at the time t according to the general atmospheric equation eq. 2.73, presented in chapter 2.5.4 and described in detail by [Geyer and Stutz, 2003]. In this equation, the rate of change of a trace gas concentration is caused by the vertical flux $j_i(z,t)$, the total chemical production rate $P_i(z,t)$, the total chemical loss rate $L_i(z,t)$, and the emission rate $E_i(z,t)$ of a compound i . The equation system is solved with the program facsimile, a Gear-type solver [Curtis and Sweetenham, 1987].

In a first step, the eddy diffusivity constant $K(z,t)$ and the turbulent time scale τ (see below), which the whole model is based on, are calculated as hourly means for the further use in the RCAT 8.1.2. Therefore, the profile of the potential temperature $\Theta(z,t)$ in the lowest 50 meters is calculated from the heat flux $H(t)$ according to [Arya, 1988; Haugen, 1973] as already

presented in equation eq. 2.53 in chapter 2.5.2. Above 50 m, the potential temperature is set to its value at 50 m altitude. The temperature profile is explicitly used to calculate temperature dependent rate constants and the profile of $[H_2O]$. Subsequently, the friction velocity u^* and the vertical profile of the eddy diffusivity $K(z,t)$ are computed (c.f. [Reichardt, 1951]) from the vertical profile of the friction velocity, $u^*(z,t)$ and the horizontal wind speed at a reference altitude of 50 m using Monin-Obukhov similarity theory. Dimensionless empirical stability correction factors $\Phi(z/L^*, t)$ given by [Businger et al., 1971] are applied. At altitudes below 1 m the laminar diffusivity effects are added to $K_{inert}(z,t)$. Stable and neutral layering of the PBL have already been included in the NCAT model and were described in chapter 2.5.3, see also [Geyer and Stutz, 2003].

For the calculation of $u^*(z,t)$, three vertical regimes are distinguished [Geyer and Stutz, 2003]. In the Prandtl layer above the height h of urban canopy, or an altitude of 70 m, a constant friction velocity is assumed, which depends on the horizontal wind speed v_r at a reference altitude of 50 m, the surface roughness z_0 , and the displacement height z_d caused by the urban canopy [Pielke, 2002]. While a logarithmic wind profile is assumed above the displacement height, the wind speed decreases with z^{-1} towards the ground. Above the height of the Prandtl layer of ~ 50 m $K_{inert}(z,t)$ is set to its value in 50 m altitude [Geyer and Stutz, 2003]. Inside the urban canopy, $u^*(z,t)$ is calculated according to an equation adapted from [Belcher et al., 2003; Inoue, 1963] for shallow canopies, where the mixing length is similar to the urban canopy height. The friction velocity exponentially decreases inside the urban canopy from $u^*(h,t)$ at the top of the urban canopy to $1/e \cdot u^*(h,t)$ at the ground. Note that this approach is restricted to shallow canopies, for example in urban areas. For deep canopies some adjustments of $u^*(z,t)$ are required.

We have also mentioned in chapter 2.5 that the vertical flux, $j_i(z,t)$, of an inert or slowly reacting trace gas is only dependent on the vertical concentration gradient of a gas i , and on the altitude dependent eddy diffusivity $K_{inert}(z,t)$. In the framework of a local closure, it can easily be calculated by a linear flux-gradient relationship (K model):

$$j_i(z,t) = -K_{inert}(z,t) \cdot \frac{\partial c_i(z,t)}{\partial z} \quad \text{eq. 6.9}$$

However, the situation becomes more difficult for reactive trace gases (e.g., NO, NO₂, NO₃, O₃, RO₂, HO₂)²¹ by considering effects of chemistry on the vertical flux of a trace gas as pointed out by several studies [Brost et al., 1988; Fitzjarrald and Lenschow, 1983; Galmarini et al., 1997; Gao et al., 1991; Hamba, 1987; Hamba, 1993; Lenschow et al., 1982; McDonald-Buller et al., 1999; Schumann, 1989; Thompson and Lenschow, 1984; Vila-Guerau de Arellano, 2003; Vila-Guerau de Arellano et al., 1995] which give restrictions to this unmodified K model above. The transport of an air parcel, which travels between two grid points, takes a finite time, during which the compound can undergo various reactions. In the presence of sinks, pure K-theory would lead to an overestimation of the vertical fluxes. If the compound has net sources, pure K-theory underestimates real fluxes. Thus [Geyer and Stutz, 2003] included a modified K model in NCAT, which considers the effects of both vertical mixing and chemistry on the vertical flux of a trace gas. The vertical net flux of a reactive species i was therefore approximated by [Geyer and Stutz, 2003] to:

$$j_i(z,t) = \overline{w'(z,t) \cdot z'} \cdot \frac{\partial c_i(z,t)}{\partial z} + \overline{w'(z,t) \cdot z'} \cdot \frac{\partial (P_{ij}(z,t) - L_{ij}(z,t))}{\partial z} \cdot \tau_{i,eff}(z,t) \quad \text{eq. 6.10}$$

where $w'(z,t)$ is the fluctuation of the vertical component of the wind speed, z' the turbulent mixing length, and $\tau_{i,eff}(z,t)$ an effective time scale for the transport. Using the parameterization $K_{inert}(z,t) = \overline{w' \cdot z'}$, the flux of a reactive species can be expressed by:

²¹ However, corrections are negligible for OH (transport is negligible) and long-lived species (such as alkanes and alkenes)

$$j_i(z,t) = -K_{inert}(z,t) \cdot \left(\frac{\partial c_i(z,t)}{\partial z} + \frac{\partial (P_i(z,t) - L_i(z,t))}{\partial z} \cdot \tau_{i\text{eff}}(z,t) \right) \quad \text{eq. 6.11}$$

Equation eq. 6.11 is similar to the modified K model discussed in [Hamba, 1993; Hamba, 1994; Verver, 1994]). The effective time $\tau_{i\text{eff}}$ was approximated by [Hamba, 1987] using the Two Scale Direct Interaction Approximation (TSDIA) theory [Yoshizawa, 1982].

$$\tau_{i\text{eff}}(z,t) = \frac{1}{\tau_{i\text{turbulent}}^{-1}(z,t) + \sum_l |j_{il}| + \sum_{l,m} |k_{ilm}(c_l + c_m)|} = \frac{z}{\kappa \cdot u^*} \quad \text{eq. 6.12}$$

In equation eq. 6.12, j_{il} represents the reaction rate constant of an unimolecular reaction, k_{ilm} the rate constant of a bimolecular reaction involving the gas i . The turbulence time scale $\tau_{i\text{turbulent}}$ is in the order of 100 s in the NBL [Fitzjarrald and Lenschow, 1983; Lenschow, 1981]. By introducing the modified K model (equation eq. 6.11), vertical transport of a gas is no longer only a function of its concentration profile, but also of the concentration profiles of other gases that react or are educts of this gas (cross-diffusion). Equation eq. 6.11 is particularly useful if turbulent transport and chemistry occur on comparative timescales. If the chemical timescale of a gas is very short, its vertical flux is solely determined by chemistry and the vertical transport of reacting species and precursors. At the other extreme, vertical transport of a gas is hardly influenced by chemistry if its chemical timescale is very long, and equation eq. 6.9 can be used to calculate $j_i(z,t)$. Generally, the higher the atmospheric stability, the larger the effect of K-correction on the transport of a trace gas.

6.2.1.2 Chemical Mechanisms

As mentioned above, the chemical reactions and mechanisms included in the RCAT 8.1.2 were adopted from the RACM mechanism presented in appendix B. All direct anthropogenic emissions in the urban scenarios are linked to that of NO from traffic in the height-interval between 0.1 – 1 m quantified by [Kurtenbach *et al.*, 2002; Kurtenbach *et al.*, 2001] as: [alkanes] / [NO] = 0.18, [alkenes] / [NO] = 0.44, [aromatics] / [NO] = 0.13, [carbonyls] / [NO] = 0.06, [CO] / [NO] = 6, [NO₂] / [NO] = 0.058, and [HONO] / [NO] = 0.008. Emission of NO from soil, e.g. from some types of bacteria, is considered as a constant flux from the surface of 10^{10} molec cm⁻² s⁻¹. Further, biogenic emissions of monoterpenes (classed by α -pinens and limunol at an emission ratio of 2) and those of isoprene are included in the model between 1 – 10 m altitudes as well. They exponentially increase with temperature and active solar radiation [Fuentes *et al.*, 2000; Guenther *et al.*, 1993].

In total, 77 model species and 237 reactions are considered in the RACM mechanism. The hundreds of VOCs in the real atmosphere are lumped into 23 model classes (4 alkanes, 4 alkenes, 3 biogenic, 3 aromatics, and 9 carbonyls). Even at night, 24 different types of organic peroxy radicals and HO_x radicals are formed via higher peroxy radicals from the oxidation of VOCs initiated by NO₃, O₃, and OH or directly via ozonolysis [Paulson and Orlando, 1996]. Nocturnal gas phase HONO chemistry is restricted to its production by the reaction of OH and NO (r. 2.26), and HONO loss by the reaction with OH (r. 2.53). Additionally, [Geyer and Stutz, 2003] included the gas-phase reaction r. 2.5 of N₂O₅ with water vapor (first and second order in H₂O) [Wahner *et al.*, 1998a]. Updated rate constants are taken from [Sander *et al.*, 2003].

A vertical profile of the aerosol surface to air volume ratio is used by the model of [Geyer and Stutz, 2003] to calculate uptake rates on aerosols for O₃ ($\gamma = 5 \times 10^{-5}$) [Longfellow *et al.*, 2000], NO₂ ($\gamma = 10^{-5}$) [this study], HONO ($\gamma = 10^{-4}$) [this study], N₂O₅ ($\gamma = 0.044$) [Jacob, 2000], HO₂ ($\gamma = 0.1$), NO₃ ($\gamma = 0.0013$) [Rudich *et al.*, 1996], HNO₄ ($\gamma = 0.01$), and HNO₃ ($\gamma = 0.2$) according to the mass-transfer equation given by [Fuchs and Sutugin, 1971], assuming a particle diameter of 150 nm. In particular, the uptake of two molecules of NO₂ from the

laminar layer onto an aerosol yields one molecule of HONO released from the surface back into the gas-phase.

The same uptake coefficients γ as for the uptake onto the airborne particles were used to calculate the dry deposition fluxes of a species in the lowest box onto typical tropospheric surfaces. Therefore, the number of collisions with the ground surface is calculated from kinetic gas theory and multiplied by the appropriate γ , assuming a flat ground (cf. [Geyer and Stutz, 2003]).

However, depending on the type of aerosol and the material of the ground surfaces, the real uptake probability can differ from these values. For HONO, its heterogeneous formation from NO_2 conversion is considered using a conversion factor of 50 % as well as its re-adsorption from the laminar layer onto the surface [Geyer and Stutz, 2003; Stutz et al., 2002]. The transport of NO_2 to the surfaces and HONO from the surfaces is limited by a laminar layer of a thickness of $11 D / u^*$.

6.2.1.3 Extension of the Model to Daytime Urban Scenarios

In this thesis, the NCAT model was extended to daytime conditions. For this purpose, labile layering of the daytime PBL was added according to equations eq. 2.71, and eq. 2.72 [Paulson, 1970]. A detailed discussion of the calculation of diffusion coefficients for labile conditions was shown in chapter 2.5.3.2 of this thesis and can also be found in [Arya, 1988; Haugen, 1973; Roedel, 1994; Stull, 1988].

Photolysis frequencies of the compounds were included according to the MOCCA²² model of [Sander, 2001] (see appendix B., table 2a). They are calculated for an exactly 12 h day and 12 h night interval for an ozone column of 300 Dobson units. The actinic flux is computed by a sine function (-1 to +1), which becomes positive for the next 12 hours after the set time of sunrise [Sander, 2001]. While stray light is considered before sunrise and some minutes after sunset, a factor is calculated to set night values to zero. Finally, the results are multiplied by a cloud coverage factor, which was defined to match the measured values [Geyer, 2004].

The gases additionally interact with walls of building parameterized by the uptake coefficient mentioned above (see chapter 6.2.1.2). These interactions of trace gases with buildings have to be taken into account for certain boxes for several reasons [Geyer, 2004]. First, they provide reactive surfaces for heterogeneous chemistry. This was empirically indicated by [Etymesian et al., 1998], who observed higher deposition rates in higher altitudes, which was thought to be due to the higher wind speed. The effect of surface structures smaller than 1 mm on the uptake and the out-gassing of gases, described by a microstructure factor MSfactor ($1 < \text{MSfactor} < \infty$), may be significantly [Geyer, 2004].

Therefore, a quasi-laminar layer directly above the surface of the urban canopy is defined at a thickness of x_l , depending on a factor of the horizontal drag coefficient caused by the urban canopy. In this thesis, we set this factor to a value of $4 \times 10^{-3} \text{ m}^2 \text{ s}^{-1}$. Only molecules in this layer interact with the surface, and their uptake onto a surface is calculated from the number of collisions of the molecules with the surface and its uptake coefficient. For this purpose we assume an instantaneous mixing of gases in the laminar layer (concentration c_l). The fluxes between the air directly above the surface and the open atmosphere (assumed to be in a distance of 5 m for a street canyon) are calculated by a transport resistance approach similar to established dry deposition models [Wesely and Hicks, 2000]. The transfer resistance $R(x_t)$ is the sum of the laminar and turbulent resistances between a urban canopy surface and the atmosphere, and can be calculated from micrometeorology. Similar to the ground, building surfaces cause a horizontal wind shear, which can be associated with a friction velocity u_{sb} . Due to the wind shear being a function of the horizontal wind speed, the friction velocity u_{sb}

²² MOCCA = Model Of Chemistry Considering Aerosols

(assumed to be constant in horizontal directions) becomes a function of the horizontal wind speed, and depends on altitude and u^* by a logarithmic wind profile.

An effective volume factor $V_{\text{effrat}} = V_{\text{with buildings}} / V_{\text{without buildings}}$ ($0 < V_{\text{effrat}} < 1$) was used to correctly calculate the concentration change by emission as well as the concentration change in the box above the buildings by vertical fluxes with the lower box. The surface to air-volume ratio SV_{rat} ($0 < SV_{\text{rat}} < \infty$) was used to convert fluxes from buildings into concentration changes in the box. Only surface structures > 1 mm were considered [Geyer, 2004]. The reduction of the air volume by buildings has two consequences: The emission by traffic is mixed into a smaller volume and thus the effective emission rate in the box, where the emission occurs, increases in the presence of buildings by a factor $1 / V_{\text{effrat}}$. However, a surface emission flux (e.g., NO from soil) does not need to be corrected (see [Geyer and Stutz, 2003]). Second, the effect of a vertical flux on the concentration in a box usually changes in the presence of buildings except in boxes where V_{effrat} increases and in the first box above the buildings (because the flux enters the box through a smaller area compared to the case without buildings) [Geyer, 2004]²³.

6.2.2 Setup of Parameters & Model Sensitivity Studies

Before analyzing the vertical profiles of any trace gas obtained from the RCAT 8.1.2 model in chapter 6.2.3 or discussing its atmospheric implications in chapter 6.2.3.3 with special respect to urban troposphere daytime HONO mixing ratios, we obviously need to perform sensitivity studies of the RCAT 8.1.2 mechanism. The challenge of any modeling study is to reproduce the time series of the trace gases observed during the measurements. This will be presented in the following chapter 6.2.2.2. Additionally, we will show the sensitivity of the chosen mechanism in chapter 6.2.2.3 by varying some initial values that could not be measured directly during the corresponding campaign. These tests were performed for all days of the corresponding field campaigns analyzed by the RCAT 8.1.2 model, but we will only discuss the 29.05.2001 of the Rome 2001 campaign here as an example.

6.2.2.1 Model Parameters for Scenarios

Parameters, such as the height of the urban canopy, the surface roughness, the displacement height, the (reduced) surface to air-volume ratio, and the effective volume factor (see table 6.1), are obviously characteristic for a specific measurement site. Thus they are fixed for a whole set of model runs performed on the corresponding measurement campaign and neither show diurnal nor seasonal variations. For the Rome 2001 campaign, these values were derived in detail from official municipal geographical information datasets.

The fluxes of NO from the soil were not changed for the different runs of the model for a certain campaign. The biogenic emissions of α -pinene and isoprene are caused by vegetation, which also did not change during the corresponding measurement campaigns. The NO_x emission rates from on-road traffic was varied for each hour of the day in the range given in table 6.1 below to match the measured values. If the NO measurements was performed at a different location (during the Rome 2001 campaign) or at a different height (Turm 2003 campaign), the NO data observed during these field studies were used as an indicator to estimate the begin of the diurnal rush-hour(s) and relative strength in relation to the NO₂ levels observed.

Even though no strong diurnal cycle of the aerosol surface size was observed at any of the field campaigns in our studies, it is expected to vary at least from low nighttime to somewhat

²³ The change of the $K(z)$ profile is however not considered in the present version of the RCAT 8.1.2 model.

higher daytime values. Unfortunately, this could not be realized in the RCAT 8.1.2 model so far. On the other hand, only little information is available concerning the vertical profile of aerosols. Thus, the arithmetic mean throughout the entire day of a model analysis was used for all altitudes instead. In table 6.1 the range of the aerosols surface size for the different days analyzed by the RCAT 8.1.2 model is given.

	Rome 2001	Milan 2002	Turm 2003
surface roughness z_0 [m]	1	1	1
displacement height z_d [m]	12	12	12
height of buildings h_c [m]	20	20	20
S / V_{rat} [m^{-1}]	0.5	0.4	0.2
V_{effrat} []	0.6	0.7	0.8
relative humidity ⁴ [%]	85 - 95 %	78 - 92 %	88 - 97 %
aerosol surface ²⁴ [$\mu\text{m}^2 \text{cm}^{-3}$]	150 - 900	650 - 1250	800 - 2500
emission rate ²⁵ of α -pinene [$\text{molec cm}^{-3} \text{s}^{-1}$]	1×10^6	3×10^6	2×10^6
emission rate ²⁶ of isoprene [$\text{molec cm}^{-3} \text{s}^{-1}$]	1×10^6	2×10^6	3×10^6
NO flux from soil [$\text{molec cm}^{-2} \text{s}^{-1}$]	1×10^{10}	1×10^{10}	2×10^{10}
NO _x emission rate from cars for each hour [$\text{molec cm}^{-3} \text{s}^{-1}$]	$(1 - 50) \times 10^9$	$(1 - 25) \times 10^9$	$(0.5 - 30) \times 10^9$

table 6.1: Specific parameters set to fixed values in the RCAT 8.1.2 model runs for the simulations of the different field measurement campaigns of this thesis.

Diurnal variations of the relative humidity were thus far only considered as variation of the (absolute) water vapor concentration due to the temperature (see figure 6.10). The starting value of the R.H. corresponding to the different days analyzed by the RCAT 8.1.2 model are given in table 6.1 above. However, the R.H. variations have more evident consequences with respect to the uptake of trace gases, in particular that of nitrous acid. It was shown in chapter 5.5. of this thesis that the HONO uptake onto a surface may only be described physically correctly by Langmuir isotherm-adsorptions theory and thus is strongly dependent on the gas-phase water concentration (and therefore the R.H.). Unfortunately, the R.H. dependence of the HONO uptake for an R.H. > 70 % could not be analyzed in the smog chamber studies performed in this thesis. Further investigations of the HONO-R.H. equilibrium are required to include this dependence to the RCAT mechanism. Therefore and by the reasons mentioned in chapter 5.6, we neglect the changes of the uptake of HONO onto the surfaces with R.H. in the first order approximations of the model presented here as analysis of real atmospheric scenarios. A constant values of $\gamma_{\text{HONO}} \sim 10^{-4}$ (see also chapter 6.2.1.2), which was determined for ~ 40 % R.H. and an uptake of HONO onto asphalt, was used in the present version of the RCAT 8.1.2 model.

²⁴ This parameter was set to a fixed value for the entire model run. Variations are caused by the different starting conditions of the days analyzed.

²⁵ at $T = 290$ K

²⁶ at $T = 290$ K and overhead sun

6.2.2.2 Reproduction of the Time Series of Trace Gases

The vertical grid of 20 layers, the corresponding box heights, the site-specific parameters (such as the height of the urban canopy, buildings, the surface roughness, the displacement height, the (reduced) surface to air-volume ratio), and the effective volume factor are listed in table 6.1, as well as the surface emission fluxes and the range of the NO emission by traffic. The model was run for 12 hours from 0:30 until approximately noon (12:30). On 29.05.2001 of the Rome 2001 field measurements, sunrise was at 4:26²⁷, as can be seen from the photolysis frequencies. In the absence of temperature and horizontal wind measurements at the station in the city center of Rome, those observed at the Villa Ada station were used to estimate them.

As we have mentioned above and in the chapters 2.5, 4.1.7, and 4.3, the vertical transport processes are expected to have a strong influence on the observed trace gases in the PBL. These dynamical effects may be directly observed from the natural radon-activity, as radon is an inert trace gas in the troposphere, which is not involved in any further chemical reactions. Therefore the vertical profile of radon is only dependent on the emission flux from the ground surface and the altitude dependent eddy diffusivity, which is the measure for the actual transport processes in the PBL used in the RCAT 8.1.2. Consequently, the time series of the radon data needs to match the measured ones first. The emission flux of Radon from the ground surface is quantified by [Levin *et al.*, 2002] to be $\sim 85 \text{ Bq m}^{-3} \text{ h}^{-1}$ for the area of Rome in May and June. From figure 6.8 we see that the measured natural radon-activity (shown at the same time resolution as that of the DOAS instrument) and that modeled by the K_z module of the RCAT 8.1.2 model generally agree well.

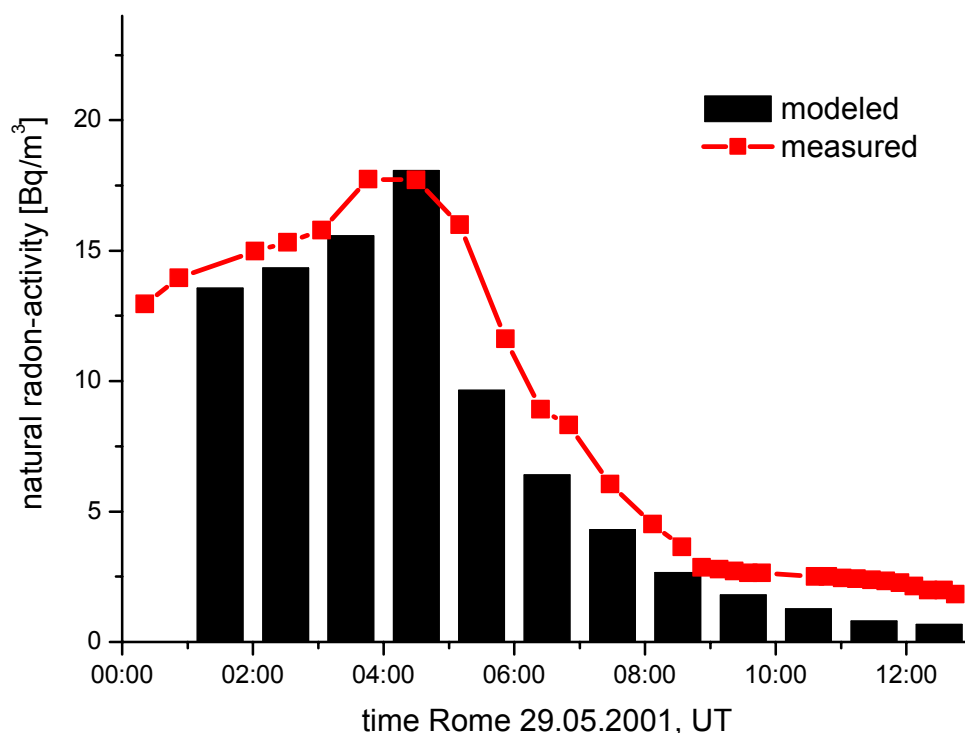


figure 6.8: The atmospheric stability indicated by the natural radon-activity as measured (red dots and line) and modeled (black bars) for the 29.05.2001 of the Rome campaign.

²⁷ Again, all time values refer to universal time (UT).

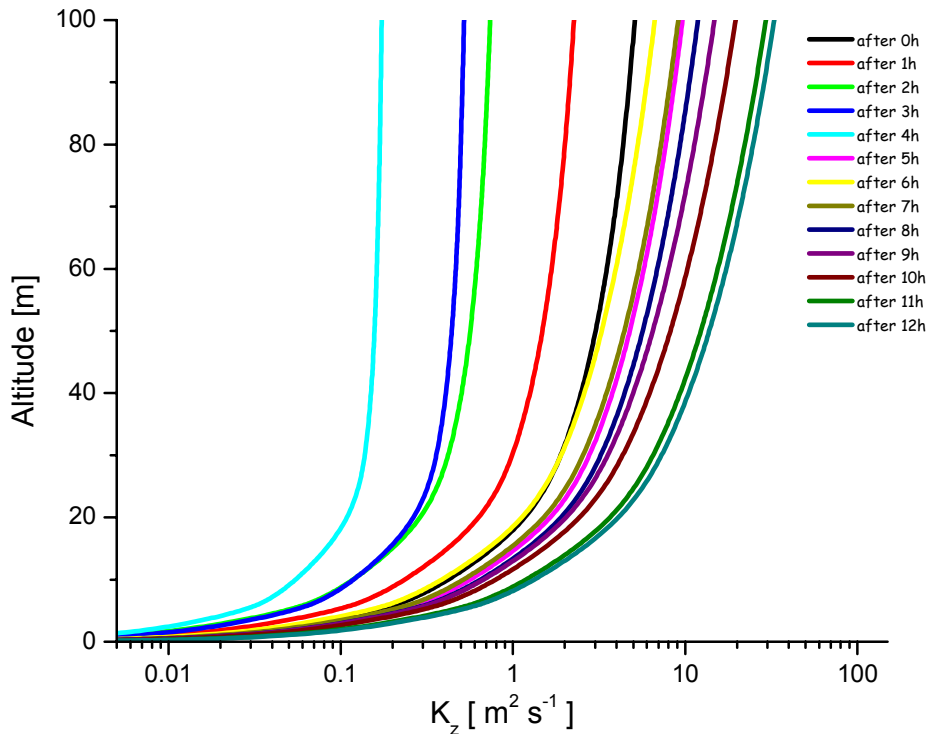


figure 6.9: The increase by altitude above ground of the eddy diffusivity modeled. The different colors refer to the times on 29.05.2001 from midnight until noon.

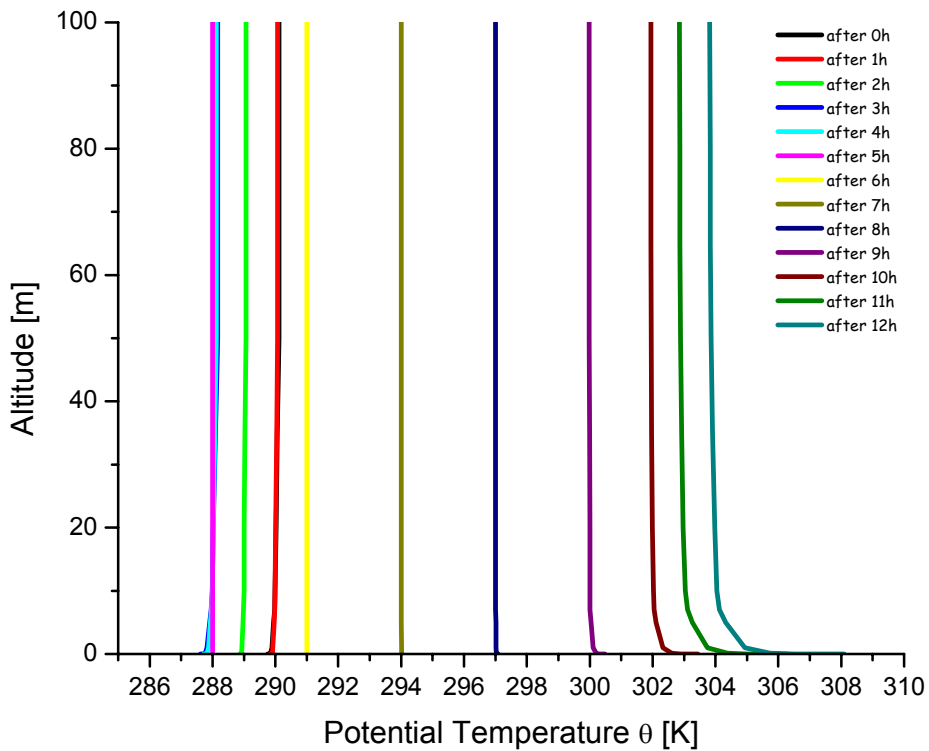


figure 6.10: The vertical profiles for the lowest 100 m of the PBL of the potential temperature obtained from the K_z -module of the RCAT 8.1.2 model for a given diurnal variation of the absolute temperature on 29.05.2001 in Rome at an altitude of 50m. The different colors refer to the times from midnight until noon.

This is of crucial importance, as the height of the Prandtl layer as well as the Monin-Obukhov length were best-guess values only. With increasing atmospheric stability throughout the night until sunrise, the Monin-Obukhov length increased from + 1000 m at midnight to + 50 m at 4:30, while the nighttime Prandtl layer was at a constant height of 50 m. After sunrise, the height of the Prandtl layer increased to 100 m at noon, while the Monin-Obukhov length ranged from -7500 m to - 500 m, indicating a labile layering of the atmosphere during the day.

The eddy diffusivities K_z that were calculated from the K_z module of the RCAT 8.1.2 model are illustrated by figure 6.9. Generally, during the increase of atmospheric stabilization (see figure 6.8) from midnight until sunrise, a decrease of K_z is calculated by the model down to a minimum of $\sim 0.1 \text{ m}^2 \text{ s}^{-1}$ at 100 m at noon on 29.05.2001 (see figure 6.9). These low transport coefficients indicate that there was no effective vertical transport in the urban area of Rome at night on 29.05.2001. According to the diurnal variation of the logarithmic shape of the wind profile, they increase with altitude to maximum values of $\sim 20 \text{ m}^2 \text{ s}^{-1}$ at 100 m at noon on 29.05.2001 (see figure 6.9). This again indicates the strong vertical transport during daytime.

The figure 6.10 shows the modeled vertical profiles of the potential temperature Θ . The modeled diurnal variation of the absolute temperature in 50 m altitude was measured as well. The potential temperature remained constant in the entire PBL from the 5th through the 8th hour of the model run(see figure 6.10), and only very weak gradients in the lowest 10 m can be observed before and after that. During the day, negative gradients are modeled with the higher potential temperatures closer to the ground. This can be explained by the heat capacity of the ground surface, and also explains the nighttime conditions, where a positive gradient in Θ was found (see figure 6.10). However, in combination with the very low vertical exchange coefficients in figure 6.9, an inversion layer at ~ 20 m height could be identified.

species	initial concentration [molec cm ⁻³]
CH4	5×10^{13}
ETH	1×10^{10}
HC3	1×10^{11}
HC5	2×10^{11}
HC8	4×10^{10}
ETE	1×10^{10}
OLT	6×10^{10}
OLI	2×10^{10}
DIEN	1×10^{10}
ISO	1×10^9
API	1×10^9
LIM	0.5×10^9
TOL	3×10^{11}
XYL	8×10^{10}
CSL	1×10^9
ALD	2.5×10^{10}
KET	1×10^9
TPAN	0.5×10^{10}

table 6.2: Initial concentrations of some classes of VOCs to start the RCAT 8.1.2 model. For explanations of the species abbreviations see appendix B.

The photolysis frequencies measured and those calculated by the RCAT 8.1.2 mechanism for the 29.05.2001 are illustrated by figure 6.11. A cloud-coverage factor of up to 36 % was used to match the measurement observations. Fluctuations, which occurred on a very short time-scale only, are obviously not reproducible by the model (see figure 6.11).

The aerosol surface area density was set to a fixed value of $900 \mu\text{m}^2 \text{ cm}^{-3}$. The use of the arithmetic mean of the aerosols surface size as a constant value in the RCAT 8.1.2 model is

justified, as only variations of a factor of 2 around that value occurred throughout the day of 29.05.2001 as can be seen from figure 6.13. As no direct measurements of VOCs were available for the Rome 2001 campaign, its values were estimated based on [Geyer, 2004; Geyer *et al.*, 2003b; Rivett *et al.*, 2003] as summarized in table 6.2 in the classes given by the RACM mechanism.

The starting values of the species (NO, NO₂, O₃, SO₂, CO, HCHO, PAN, and HONO) either observed at midnight of 29.05.2001 at the DOAS measurement site in the city center of Rome or at the Villa Ada station (see chapter 4.1) were directly used to initiate the corresponding RACAT 8.1.2 model run.

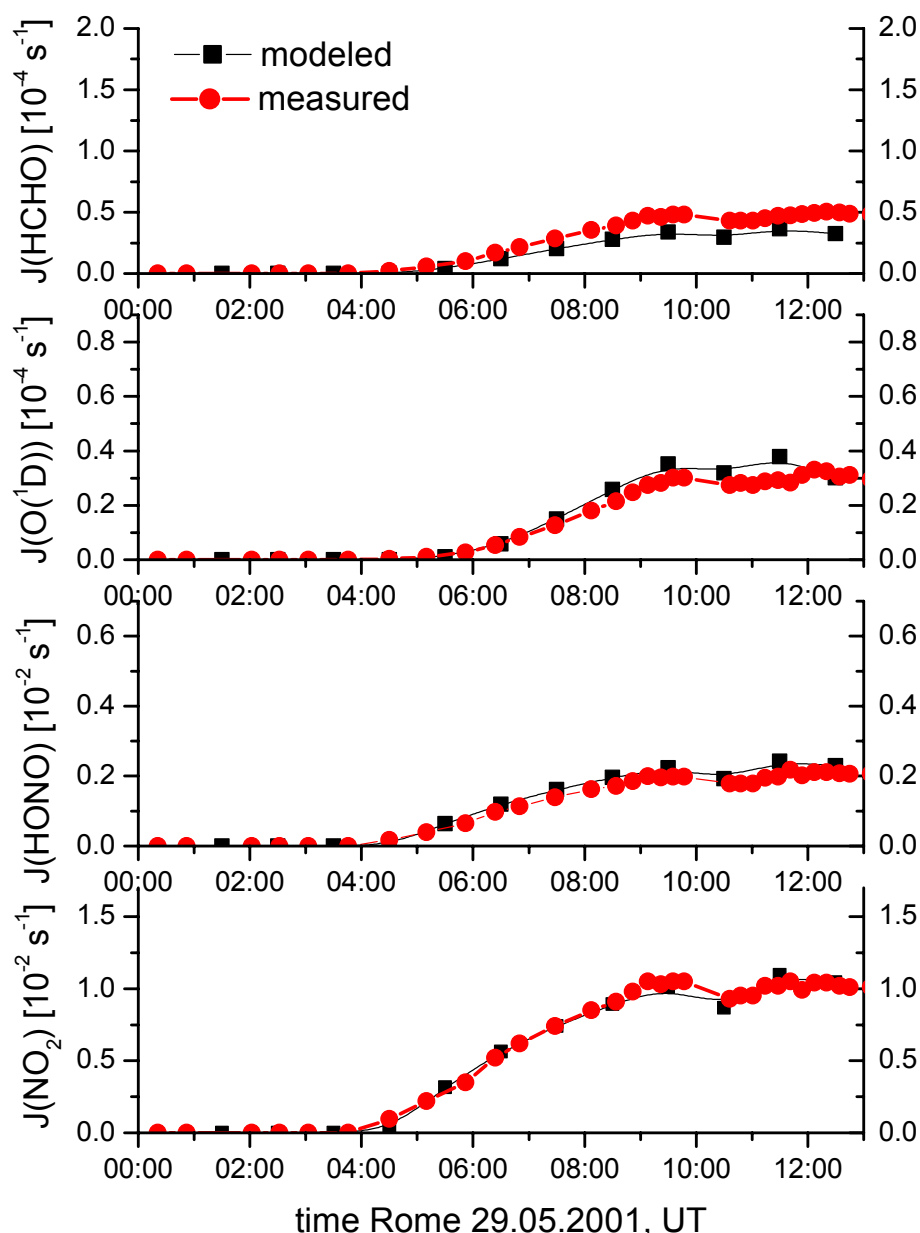


figure 6.11: Measured (red dots and line) and modeled (black squares and line) photolysis frequencies for NO₂ (lowest panel), HONO, O₃ as $J(\text{O}(^1\text{D}))$ and HCHO via the radicals channel (see chapter 2.2.3).

From figure 6.12 and figure 6.13 we see that the time series of all trace gases is well reproduced by the RACAT 8.1.2 model, except those fluctuations occurring on a short time-scale only (e.g. HONO at 2:00 and 4:00, or NO₂ at 6:00 in figure 6.12). Especially the decay

of the nighttime pool of ~ 2 ppb of HONO in the morning hours to its low daytime values (~ 150 ppt on 29.05.2001) are well captured by the model (see figure 6.12). The double-peak structure to maximum levels of ~ 2.2 ppb at 2:00 and 4:00 in the night of the 29.05.2001 is not found by the model, however. It is believed to be caused by short time-scale dynamics of the nocturnal PBL, which is not implemented in the RCAT 8.1.2.

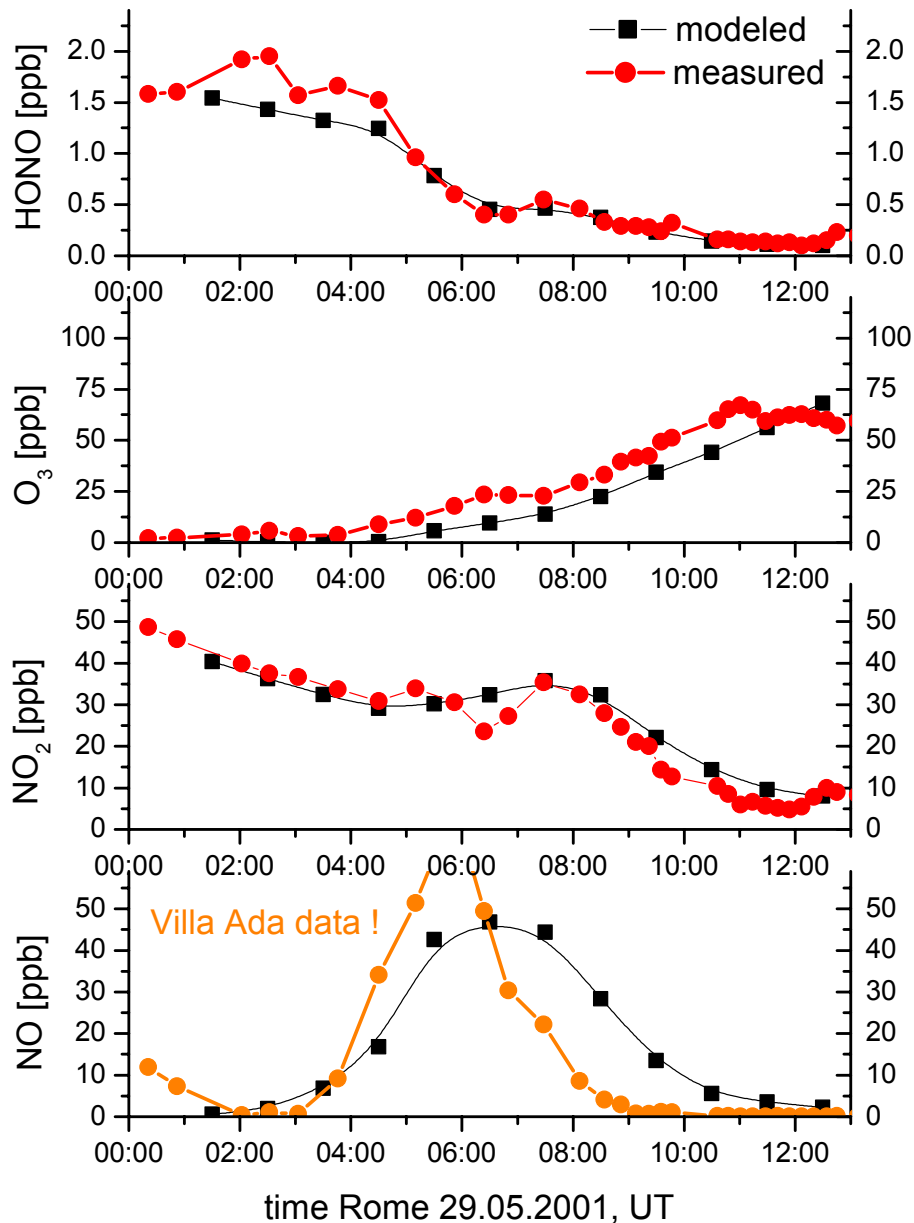


figure 6.12: The most important trace gases NO , NO_2 , and O_3 with respect to HONO chemistry as measured (red dots and line) and modeled (black squares and line). NO was not measured along the DOAS light-path. Thus, those data obtained at the Villa Ada station were plotted (orange dots and line) in the lowest panel.

Further, the NO_2 decay of ~ 45 ppb from midnight on with a plateau of ~ 30 ppb during the morning rush-hour is well modeled, while on the other hand, the increase of ozone throughout the day shows a time delay of ~ 30 min and the values do not remain constant at ~ 60 ppb after 11:00 (see figure 6.12). The NO emission ratio from cars was varied to match the measured NO values at the Villa Ada station, but also to finally obtain the NO_2 mixing ratios detected at the DOAS measurement station in the city center in Rome. Therefore, we started

at low nighttime values of $1 - 3 \times 10^9 \text{ molec cm}^{-3} \text{ s}^{-1}$ NO emission from on-road combustion processes due to the reduced traffic in Rome at that time. During the morning rush-hour, a strong peak of $50 \times 10^9 \text{ molec cm}^{-3} \text{ s}^{-1}$ NO was prescribed at 5:00, decreasing to $10 \times 10^9 \text{ molec cm}^{-3} \text{ s}^{-1}$ NO afterwards. At noon, the traffic in Rome increased again due to noon-siesta and is represented by emission rates of $15 \times 10^9 \text{ molec cm}^{-3} \text{ s}^{-1}$ NO.

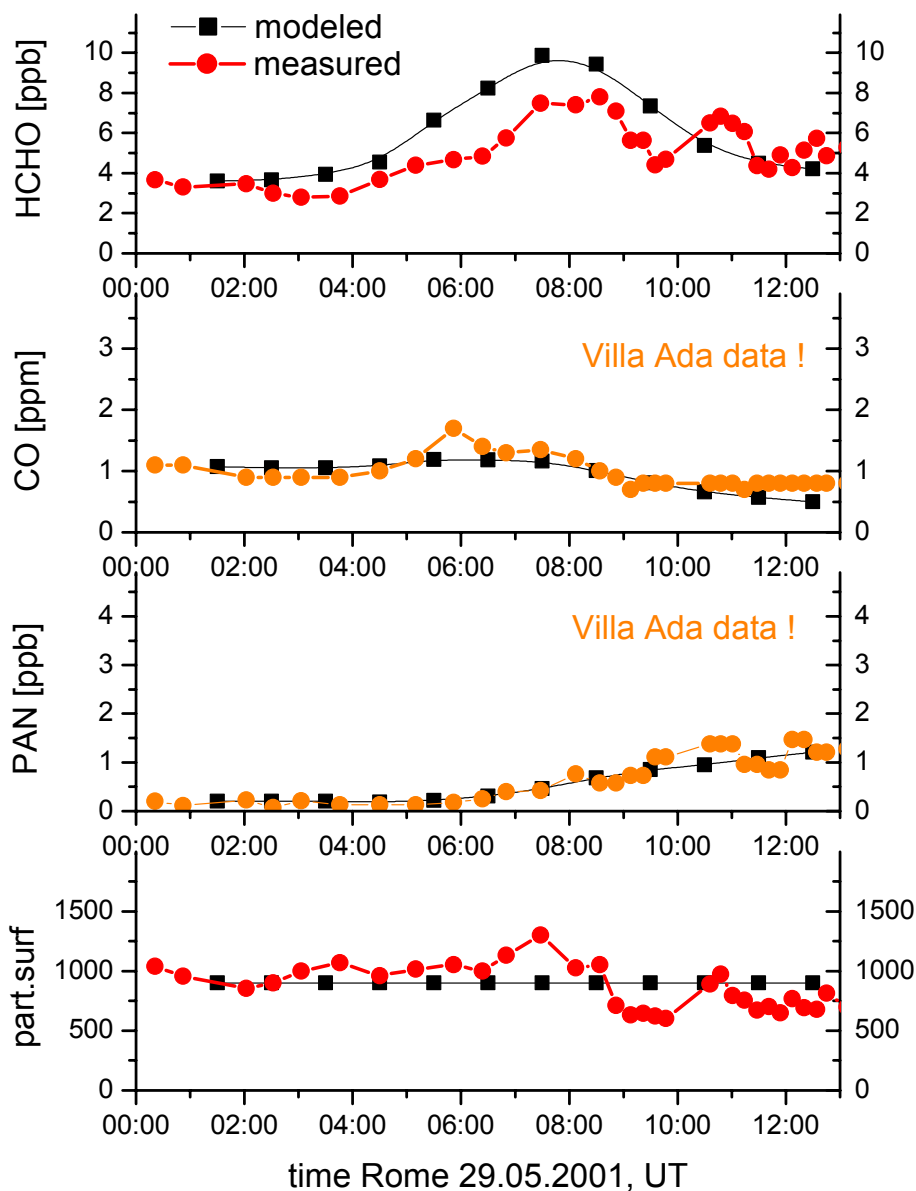


figure 6.13: Further trace gases (HCHO, CO, PAN) that were measured during the Rome 2001 field campaign (red dots and line) versus the results of the RACT 8.1.2 model (black squares and line). Additionally, the aerosol surface size as the fixed parameter in the model (black squares and line) is illustrated in the lowest panel. The measured values (red dots and line) vary around this arithmetic mean. PAN and CO were not measured along the DOAS light-path. Thus, the data obtained at the Villa Ada station were plotted (orange dots and line) versus the modeled ones.

Both NO and CO may not be compared directly to the measurements, as those took place at a different location and altitude. However, the general temporal trend and especially the morning rush hour is identified to have similar and reasonable values of ~ 50 ppb, and 1 ppm

respectively in the modeled data as well (see figure 6.12, and figure 6.13, respectively). For the PAN, an analogous discussion is valid, while the absolute mixing ratios of ~ 1 ppb at noon are well reproduced (see figure 6.13). This indicates the homogeneity of the photooxidative PAN production throughout the day in the urban air of Rome. However, the maximum amount of HCHO of ~ 8 ppb at 8:00 is overestimated and ~ 10 ppb were modeled. An explanation cannot be given so far, but the deviation may be due to the large inhomogeneities of the urban air with respect to formaldehyde, as the DOAS light-beam integrated over a length of ~ 7.4 km.

6.2.2.3 Influence of Starting Parameters

Some sensitivity studies on the days of the different campaigns analyzed by the RCAT 8.1.2 model were performed with respect to all starting parameters. The aerosols surface size, the VOCs summarized in table 6.2, the NO emission rates from cars, but also the atmospheric stability were varied. More detailed sensitivity studies on further trace gases, which are not directly involved in HONO chemistry, and for a large number of atmospheric conditions, emission scenarios, and different surface canopy structures can be found in [Geyer and Stutz, 2003; Stutz *et al.*, 2004a].

The aerosol surface size was multiplied by a factor of 10 and $1/10$ respectively, in order to study their contribution as an additional surface for heterogeneous chemistry, i.e. especially the production of HONO from the hydrolysis of NO_2 at the uptake coefficients mentioned in chapter 6.2.1.2. However, only negligible influence was observed in the HONO production and its loss onto surfaces as well as for the time series of further trace gases. This is another strong indicator for the minor contribution of aerosols to the heterogeneous production of atmospheric nitrous acid.

The initial VOC concentrations were varied within a factor of 2 and a dependence corresponding to that expected from the known urban troposphere chemistry presented in chapter 2 was observed. At lower VOC levels, less ozone was produced until noon, while the case with increased VOCs overestimated its production. We therefore accepted the best-guess parameters of table 6.2 as suitable to describe the scenario, which occurred on 29.05.2001 in the heavily polluted urban air of Rome.

The NO_x emission rates from on-road traffic were varied within a range of 2 as well. Again, the expected (see chapter 2.1.2) reaction of the chemistry-transport system of the RCAT 8.1.2 was found. The lower NO_x emitted during the rush hour inhibits the high amounts of NO_2 measured from that time on until noon. In the presence of stronger direct emission sources of NO_x , the NO_2 mixing ratios are overestimated and the ozone levels cannot reach their measured maximum value due to the titration of O_3 with NO according to r. 2.9.

Finally, tests on the influence of the atmospheric stability terms were performed on the RCAT 8.1.2 model. For only labile layering conditions of the PBL, the high nighttime concentrations of none of the trace gases could be achieved by simulations in RCAT 8.1.2. This is not unexpected, as e.g. the high mixing ratios of HONO of ~ 2 ppb at midnight on 29.05.2001 are well known to correlate to a reduced vertical mixing in the nocturnal PBL [Alicke, 2000; Geyer and Stutz, 2003; Stutz *et al.*, 2004a; Stutz *et al.*, 2002; Stutz and Geyer, 2003; Veitel, 2002]. On the other hand, only stable layering of the PBL, even throughout the day, overestimates the NO and NO_2 , as both are mixed into a smaller air-volume due to reduced vertical transport dynamics. However, the vertical mixing of the PBL was determined by the measurements of the natural radon-activity, and was therefore only adjusted in the RCAT 8.1.2 model runs to match those values.

6.2.3 Results of the Model

6.2.3.1 The Vertical Profiles of NO, O₃ and VOCs

In figure 6.14 and figure 6.17, the temporal trends of the vertical profiles of some trace gases as obtained from the RCAT 8.1.2 model are illustrated for the 12-hour period of model run initiated at midnight of the exemplary day 29.05.2001. However, the modeled data represents idealized chemistry as well as vertical transport, and thus may not always accurately reproduce the measured observations. On the other hand, the qualitative model results offer valuable insight with respect to the interpretations of the observations.

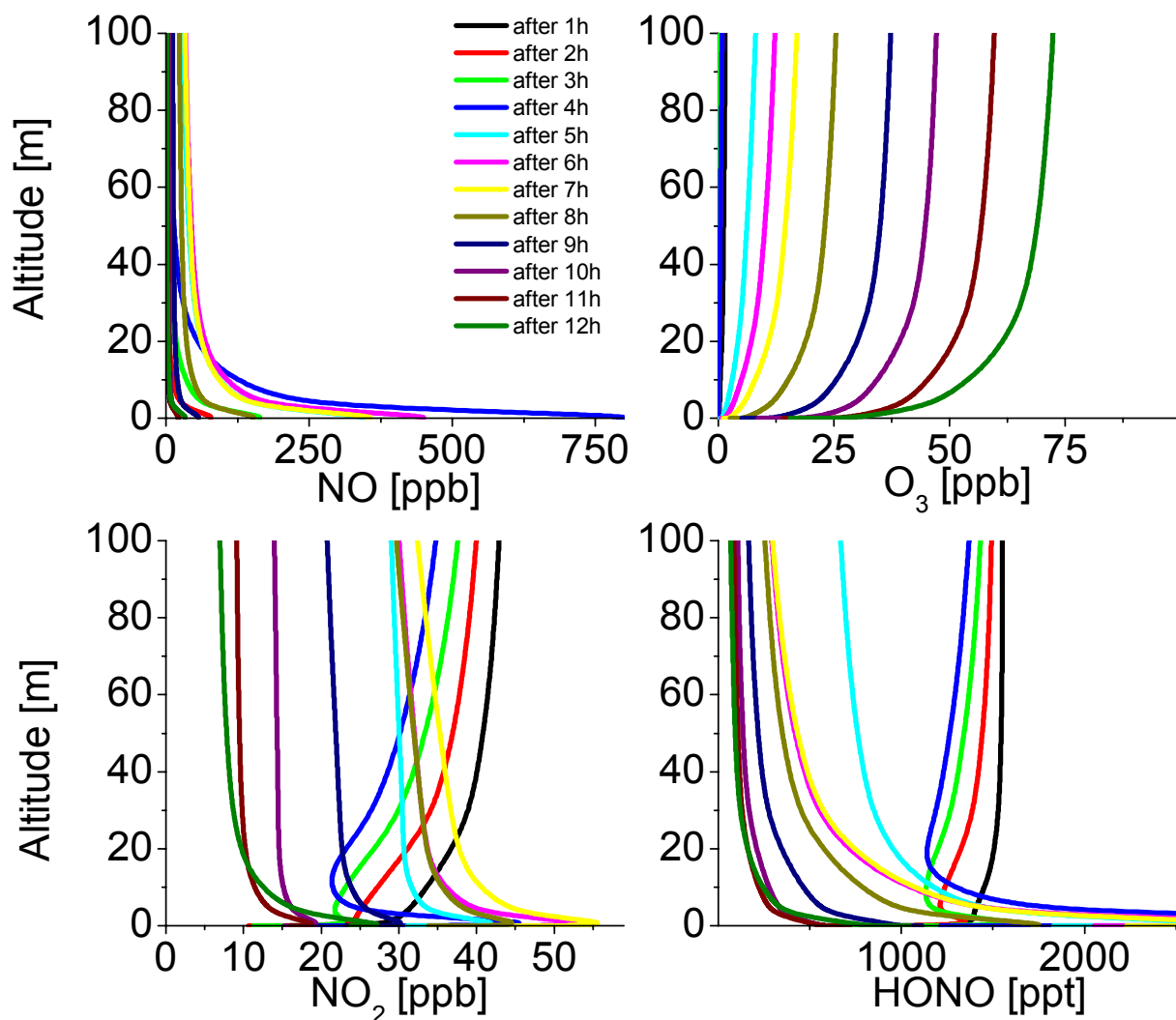


figure 6.14: Temporal development in 12 hours of vertical profiles of NO, O₃, NO₂, and HONO.

From figure 6.14 we see that NO has its highest values close to the ground during the whole modeling period, with mixing ratios of up to ~ 90 ppb between 0.1 – 1 m during the night (see figure 6.14), as expected for a surface emitted species. Due to its fast simultaneous titration by ozone and a variety of further reactions destroying NO, as well as its slow transport upwards, a strong vertical profile with a net upward flux of NO (negative gradient) is modeled. NO

mixing ratios drop below the ppb limit at higher altitudes (~ 70 m), as can be seen in figure 6.14. While the chemical reactions, especially throughout the day, and the reduced emission during the night usually keep the NO levels below ~ 10 ppb above 10 m, the morning rush hour is clearly visible, and causes NO mixing ratios of ~ 700 ppb (see figure 6.14). It is important to note that the NO mixing ratio of 700 ppb is emitted by traffic and only occurs in this box of 0.1 – 1 m altitude. It therefore directly represents the mixing ratio at the exhaust tube of the cars. The trend of distinctive negative gradients and peak due to the morning-rush hour is modeled in the CO concentration as well. At the top of the PBL, the influence of the primary NO emissions is negligible, and a chemical pseudo steady state of NO is obtained.

As expected from reaction r. 2.9, O₃ concentrations show the opposite vertical distribution of NO (see figure 6.14). During the night, the ozone-mixing ratio is low ($\sim 0 - 5$ ppb) at all altitudes (see figure 6.14), because it was destroyed by the titration with NO after sunset and dry deposition occurred as well. The loss of O₃ near the ground is replenished by the downward transport of O₃, which acts as the dominant sink for O₃ in the upper NBL and the residual layer throughout the night. During the day, a positive gradient is modeled fairly constantly in altitudes above ~ 30 m (the urban canopy height was 20 m), with the exception of the lowest meters (see figure 6.14). Ozone levels are approx. 25 ppb at 20 m and ~ 35 ppb at 90 m after 9 hours. However, both the total amount of O₃ and the positive gradient in the lowest meters increase until noon (see figure 6.14).

Vertical profiles were modeled for all other trace gases, but will only partly be presented here. While the peroxy radicals RO₂ and HO₂ generally showed a weak positive gradient in the NBL, a distinctive layer of elevated OH levels ($\sim 7 \times 10^5$ molec cm⁻³) was found close to the ground in the NBL, as already reported for various scenarios by [Geyer and Stutz, 2003]. During the day, the concentrations of both increase up to 1.3×10^7 molec cm⁻³ OH radicals and up to ~ 8 ppt RO₂, and even ~ 11 ppt HO₂ were modeled at noon of 29.05.2001 in the heavily polluted urban air of Rome. Both show a distinctive positive gradient in the lowest 30 m of the PBL, which is just above the urban canopy height, but constant values for the higher altitudes during the day (see table 6.1).

The levels of RO₂ and HO₂ radicals are essentially low compared to $\sim 50 - 100$ ppt observed by [Cantrell et al., 1996; Hofzumahaus et al., 1998; Holland et al., 2003; Mihelcic et al., 2003; Ren et al., 2003] or obtained from modeling studies by [Geyer and Stutz, 2003; Stutz and Geyer, 2003] using the NCAT mechanism. This can either indicate a fast photochemistry ongoing in the urban air of Rome, or it can be caused by the high NO concentrations, which were modeled. In the absence of direct measurements of RO_x, and NO along the DOAS light-beam, we cannot distinguish and further sensitivity studies of the RCAT model with respect to the RO_x chemistry are needed [Geyer, 2004; Stutz, 2004].

The various VOCs, the alkanes, alkenes, aromatics, the biogenic, and even the carbonyls all showed a similar behavior during night and day. Negative gradients are modeled for all species in the NBL, becoming more distinctive in the early morning hours. Generally, the absolute values at all altitudes increase from midnight throughout the night until the morning rush hour and drop down to their lowest levels at noon. This is caused by two competing effects: the direct emissions linked to those of NO, but also the subsequent reaction including NO during daytime. However, a slightly different trend is observed for the biogenic VOCs, showing a maximum in the altitude of $\sim 1 - 7$ m and a weak positive gradient below towards the ground surface. A sensitivity study of the VOCs profiles depending on various parameters, such as their emission rates, but also the atmospheric stability, may be found in [Geyer and Stutz, 2003] and forthcoming publications.

6.2.3.2 Vertical Distribution, Sources and Sinks of NO₂

From figure 6.15, we see that close to surfaces, i.e. the ground surface or the walls of buildings, NO₂ loss by dry deposition (and possible subsequent heterogeneous conversion into e.g. HONO) is larger than the formation of NO₂ by other processes (i.e. mainly the titration of O₃ by NO after sunset predominantly below ~ 5m). Consequently, a positive gradient of NO₂ is observed above 5 – 20 m altitude. As the buildings height was set to 20 m (see table 6.1) for the scenario of the 29.05.2001 in Rome, this positive gradient of NO₂ can be found for the nighttime model results of NO₂ vertical profiles to be strongest below ~ 30m (see figure 6.14, and figure 6.15). NO₂ sources, such as the reactions of NO₃ with VOCs, and reactions of NO with NO₃, RO₂, and HO₂, as well as HO₂NO₂ and N₂O₅ chemistry, contribute only insignificantly to the positive NO₂ gradient, and the NO₂ removal by these reactions is highest in the upper part of the boundary layer, because of the lower NO₃ and N₂O₅ levels in the lower NBL (see figure 6.15 and for more details [Geyer and Stutz, 2003]).

The vertical transport of NO₂ from the NO rich ground layer into higher altitudes is the main sink below ~20 m, and the main source for NO₂ above this altitude (see figure 6.15), but partly compensated by the reaction r. 2.4 with NO₃. Due to the reduced traffic during the night in Rome (and therefore less emissions of NO_x) and in the absence of further NO₂ sources, the average concentration of NO₂ slowly decreases during the night (see figure 6.14). It is interesting that the dry deposition rate of NO₂ is only weakly dependent on atmospheric stability because the effects of reduced NO₂ levels near the ground and faster transport towards the surface compensate for each other. However, NO₂ deposition is a strong function of the NO emission rate, and levels at a reference height (for example 50 m) are different from the ground surface values.

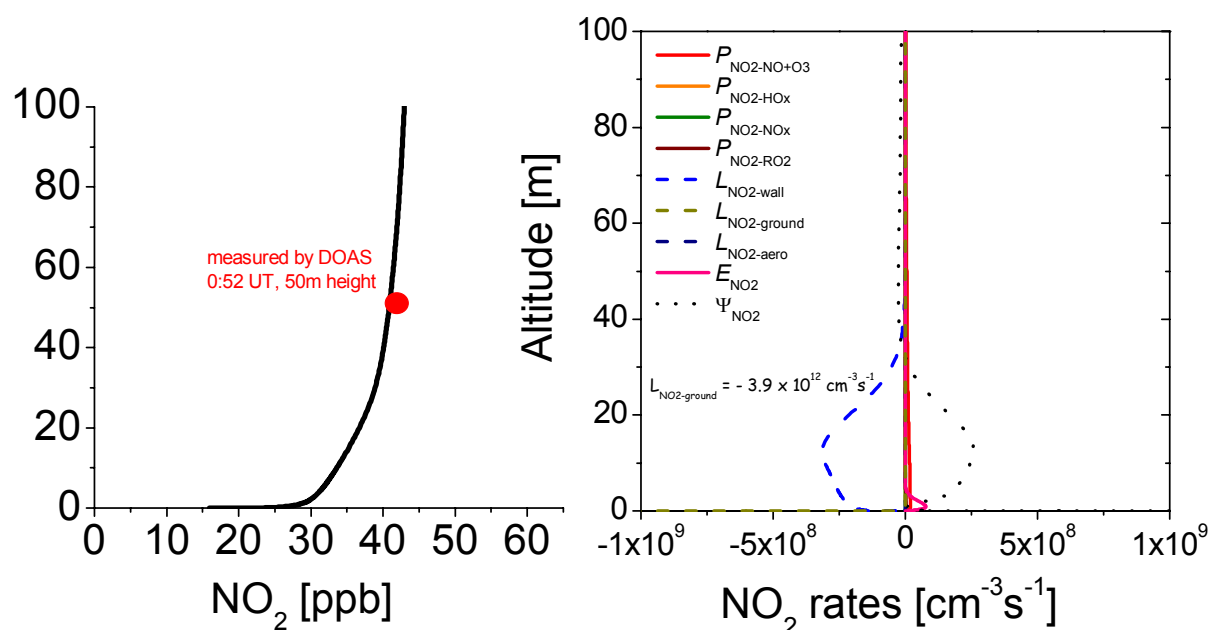


figure 6.15: Vertical profile of NO₂ (black line, left plot) modeled for 1 hour after midnight and the concentration measured (red dot) at the corresponding time by the DOAS instrument at 50 m altitude. On the right side, the vertical distribution of chemical rates and the rate of change by vertical transport and emission of NO are illustrated for 1 hour after the model start.

During the day, NO₂ shows a negative gradient above 1 m, with a maximum of 25 ppb at 0.5 – 5 m altitude and ~ 10 ppb above 50 m after 12 hours (see figure 6.14, and figure 6.16).

During this period, direct emission rates (E_{NO_2}) from traffic near the ground are stronger (see figure 6.16), but the higher amounts of O_3 present also force the NO_2 formation according to reaction r. 2.9 from NO ($P_{\text{NO}_2\text{-NO}+\text{O}_3}$), which outbalance the loss by dry deposition (see figure 6.16). This loss by dry deposition is found to be responsible for $\sim 30\%$ of the total NO_2 loss during the day by the RCAT 8.1.2 model. The loss on aerosols ($L_{\text{NO}_2\text{aerosol}}$) is negligible, while the dry deposition on the ground surface ($L_{\text{NO}_2\text{ground}}$) is the most effective sink, but only for the lowest box, which has direct contact to the ground surface. Thus, dry deposition of NO_2 on the walls of buildings ($L_{\text{NO}_2\text{wall}}$) is the dominant loss process by deposition integrated over the first 100 m of the PBL (see figure 6.16). As already discussed for the NBL, the vertical transport of NO_2 (Ψ_{NO_2}) from the NO rich ground layer into higher altitudes is the main total sink below ~ 20 m (see figure 6.16), while the main source for NO_2 above this altitude is different from nighttime conditions. Due to daytime photolytic oxidation processes in the urban atmosphere, more NO_2 is converted into ozone throughout the day further involving VOCs. The production of NO_2 from reactions involving HO_x and RO_x contributes as the main source of NO_2 integrated over the lower 100 m of the daytime PBL (see figure 6.16). However, the loss of NO_2 by the reaction r. 2.2 with OH becomes more significant as well throughout the day with elevated OH levels (see figure 6.16). The local maximum of the NO_2 loss rate at ~ 1 m altitude is caused by the reaction of NO_2 with OH radicals. Measurements at 3 and 10 m will, in most cases, overestimate the relative contribution of this NO_2 loss path in the PBL.

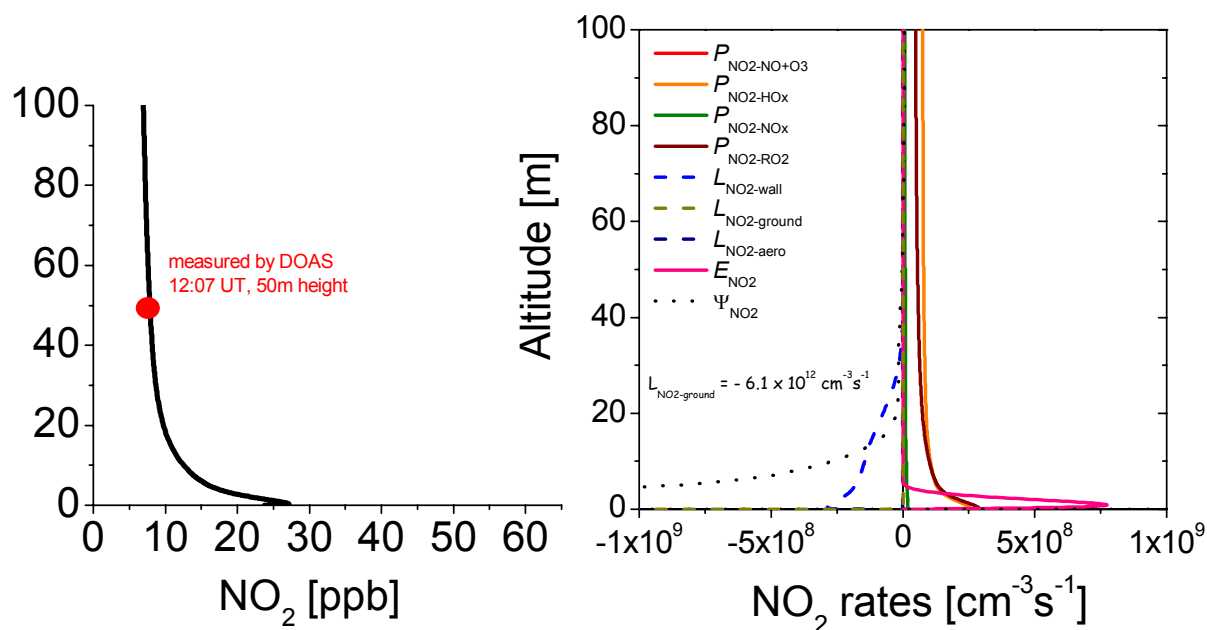


figure 6.16: Vertical profile of NO_2 (black line, left plot) modeled for 12 hours after midnight and the mixing ratio measured (red dot) at the corresponding time by the DOAS instrument at 50 m altitude. On the right side, the vertical distribution of chemical rates and the rate of change by vertical transport and emission of NO_2 , is illustrated for 12 hours after the model start.

6.2.3.3 Vertical Distribution, Sources and Sinks of HONO

The vertical profiles of nitrous acid for the subsequent 12 hours after initialization of the RCAT 8.1.2 model are illustrated in figure 6.14. As expected from its precursor NO_2 , HONO shows similarly shaped vertical and temporal profiles. From midnight on, and in the period of further nighttime atmospheric stabilization, a weak positive gradient is modeled above ~ 20 m,

reaching nighttime maximum mixing ratios of ~ 1.5 ppb on 29.05.2001 (see figure 6.14). Below this height, which is the upper limit of the urban canopy (see table 6.1) and therefore in presence of huge surfaces for its heterogeneous formation, a distinctive negative gradient of HONO is found by RCAT 8.1.2. In the lowest layer, nighttime HONO values reach a maximum of ~ 3 ppb directly above the surface (see figure 6.14).

Due to photolysis, but also due to labilization and therefore a stronger vertical transport in the atmosphere after sunrise, a negative gradient is observed throughout the whole PBL. Daytime values decrease steadily (see figure 6.14) and reach ~ 100 ppt in 100 m altitude at noon. When the morning rush-hour has finished, even the HONO mixing ratios in the lower boxes (below 20 m) decrease to noontime levels of ~ 800 ppt directly above the ground surface (see figure 6.14).

The HONO-to-NO₂ ratio is shown in figure 6.17. At night, it is $\sim 4\%$ at 100 m altitude. Since a steady state between HONO and NO₂ is not established, it slightly increases throughout the night to $\sim 4.5\%$. The vertical gradient of the HONO-to-NO₂ ratios at this time is slightly negative above 20 m, but clearly negative below, reaching maximum nighttime values shortly before sunrise of $\sim 10\%$. Due to the depletion of the HONO pool, which was accumulated during the night, the HONO-to-NO₂ ratio decreases to daytime values of $\sim 4\%$ close to the ground and $\sim 1\%$ in 100 m respectively. However, the shape of the negative gradient is kept clearly negative, especially below 20 m during the entire period of the model run.

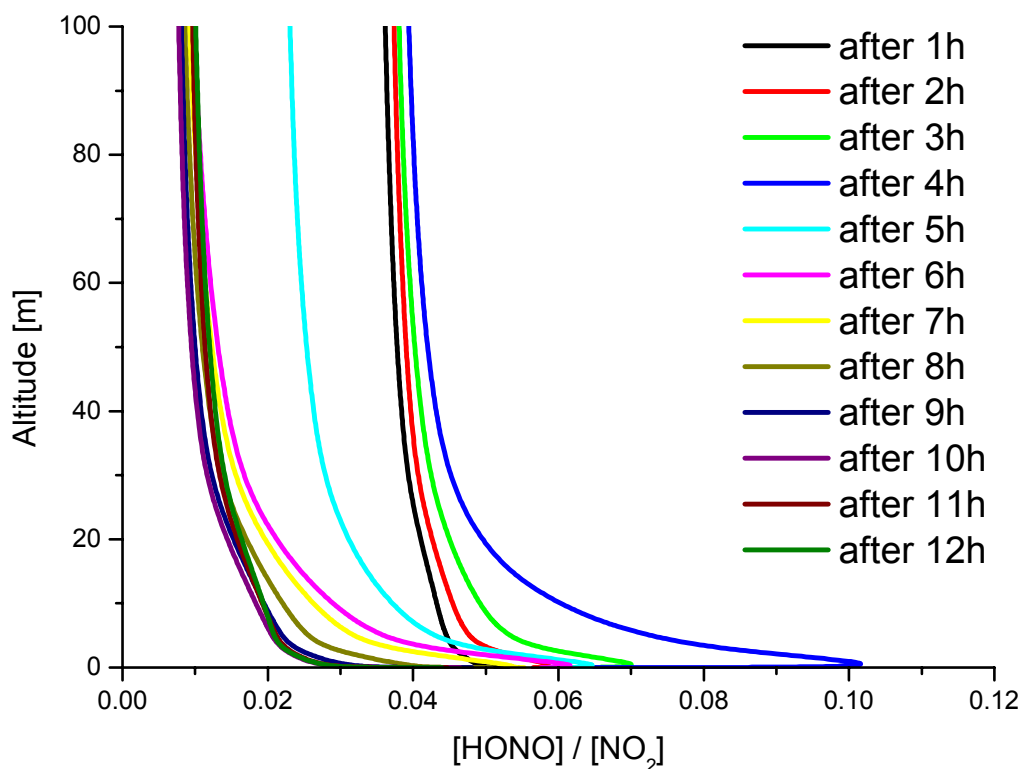
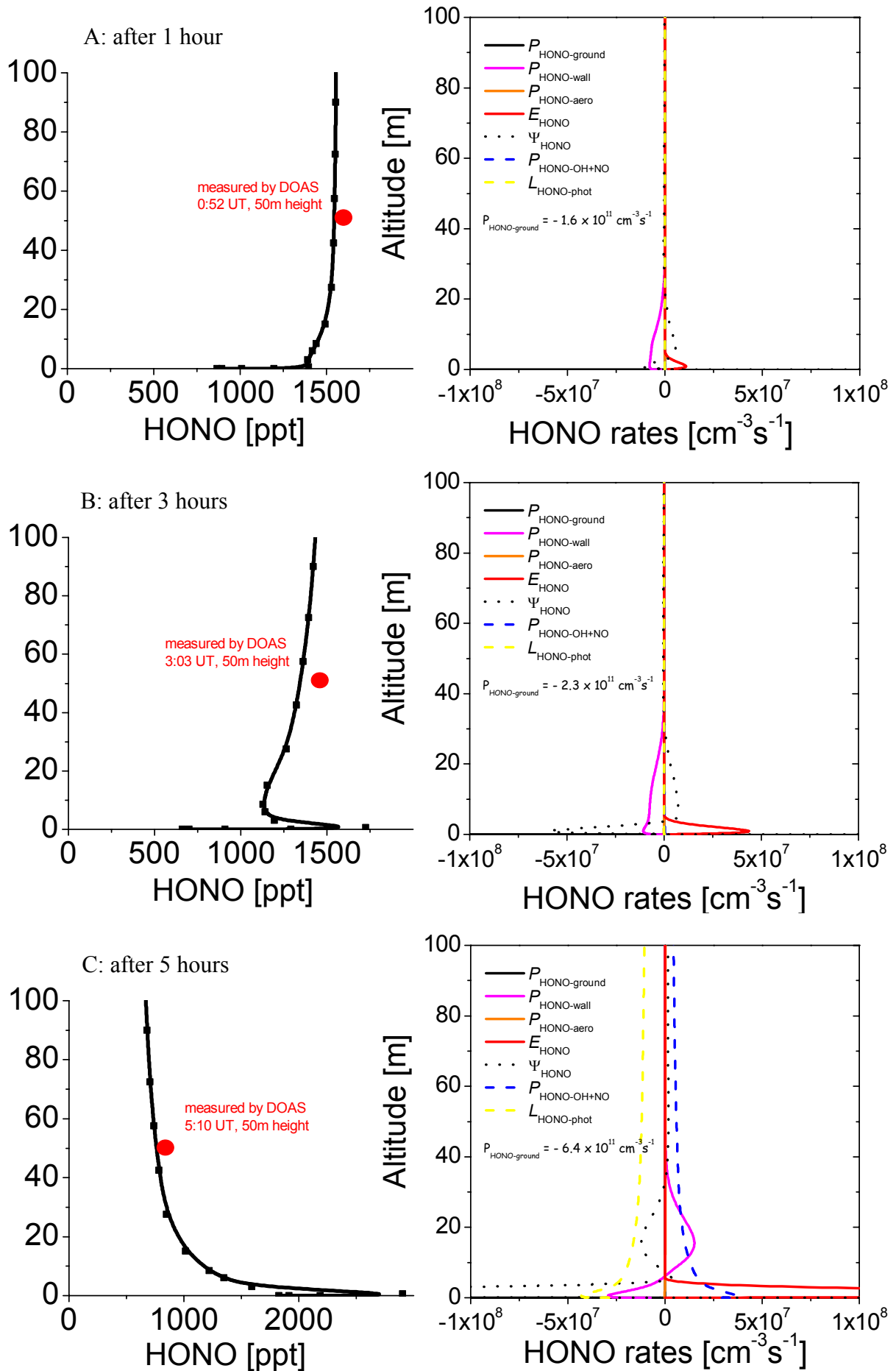


figure 6.17: Modeled temporal development of the vertical profile of the HONO-to-NO₂ ratio.

Of particular interest for the analysis of the vertical profiles of HONO is the contribution, the temporal changes, the vertical structure of the different source mechanisms, and the individual removal processes. This is illustrated in figure 6.18 in the plots A to E for 1, 3, 5, 9, and 12 hours after initiation of the model run.



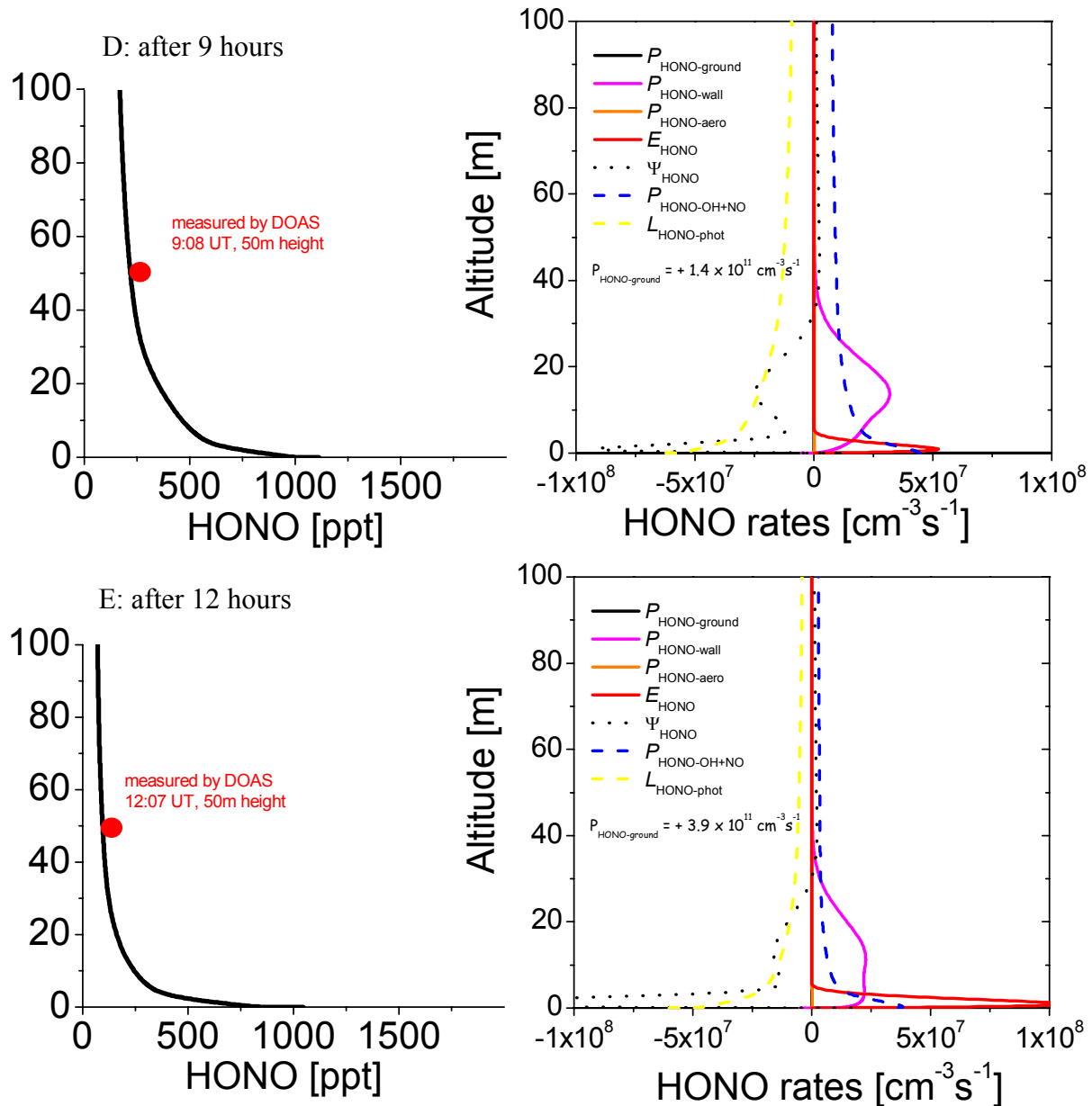


figure 6.18: On the left hand side of the plots a to E, the vertical profile of HONO (black line, left plot) modeled for 1 to 12 hours after midnight and the mixing ratio measured (red dot) at the corresponding time by the DOAS instrument at 50 m altitude are shown. On the right side, the vertical distributions of chemical rates and the net rate of change by vertical transport and emission of HONO are illustrated. The plot A refers to 1 hour after the model start and the subsequent plots to later times until plot E represents the period 12 hours after the start of the model. For the abbreviations, refer to the text below.

The main sources and sinks of atmospheric HONO are shown in figure 6.18 A – E as net production or net loss rates: the heterogeneous conversion on the ground surface ($P_{\text{HONO-ground}}$), on walls ($P_{\text{HONO-walls}}$) of buildings, and on aerosols ($P_{\text{HONO-aerosols}}$). Further, direct emission of HONO (E_{HONO}) and its vertical transport (Ψ_{HONO}) were considered for the calculations. During the day, the homogeneous production of HONO from the recombination of the NO and OH radicals ($P_{\text{HONO-OH+NO}}$) and the loss by photolysis of HONO ($L_{\text{HONO-phot}}$) obviously have to be taken into account. A positive sign of these terms indicates a net production of HONO, while a negative values corresponds to a removal. In general, these terms may change their

contributions (being a source or a sink) from nighttime to daytime conditions and with altitude above ground. However, before finally discussing the individual contribution of these processes to the daytime HONO values observed at all the different campaigns (chapter 6.2.3.4), we will have a more detailed exemplary look at the 29.05.2001 in Rome.

Obviously, the photolysis of HONO as well as the homogeneous production only contribute during daytime. The photolysis is always a sink, which is $\sim 5 \times 10^7 \text{ molec cm}^{-3} \text{ s}^{-1}$ close to the ground (see figure 6.18 D), decreasing with altitude to $\sim 1 \times 10^7 \text{ molec cm}^{-3} \text{ s}^{-1}$ at 100 m (see figure 6.18 D). This shape is mirrored by the competing recombination of the NO and OH radicals, but distinctively smaller values are modeled. Close to the ground HONO may be formed 9 hours after the start of the model at a rate of $\sim 4 \times 10^7 \text{ molec cm}^{-3} \text{ s}^{-1}$ (see figure 6.18 D), while only $0.7 \times 10^7 \text{ molec cm}^{-3} \text{ s}^{-1}$ HONO are formed at 100 m homogeneously (see figure 6.18 D). Under conditions of strong vertical mixing (thus less steep gradients of NO) and heavier pollution, both processes may balance each other.

It also becomes obvious from figure 6.18 that aerosols only play a minor role for the HONO production and they are only an insignificant sink by dry deposition of HONO. Their production rates remain close to zero during the night (figure 6.18 A, and B), in the morning (figure 6.18 C) and around noon (figure 6.18 D, and E).

The absolute values of the contribution of the ground surface are by far the highest during all times of day. However, as only the lowest layer is in direct contact with this surface, its influence on HONO concentrations at higher altitudes depends on the vertical transport. During the night of 29.05.2001 in Rome, HONO is deposited on the ground surface from the lowest box at a rate between $1.6 \times 10^{11} \text{ molec cm}^{-3} \text{ s}^{-1}$ and $6.4 \times 10^{11} \text{ molec cm}^{-3} \text{ s}^{-1}$ between 1 and 5 hours after midnight (figure 6.18 A and C). This is believed to be due to the enhanced NO levels in the layers closer to ground favoring secondary reactions for longer retention periods. Therein, NO is destroyed as discussed in detail for the analysis of the laboratory studies in the smog chambers (see chapter 5.5.3.4). Due to the stronger vertical mixing, the situation changes under daytime conditions and between $1.4 \times 10^{11} \text{ molec cm}^{-3} \text{ s}^{-1}$ (figure 6.18 D) up to $3.9 \times 10^{11} \text{ molec cm}^{-3} \text{ s}^{-1}$ (figure 6.18 E) of HONO are produced at the ground.

A similar discussion is valid for the contribution of walls of buildings. Layer above the ground up to the upper limit (see table 6.1) of the canopy for the corresponding (urban) scenario contribute to this term. Thus the vertical walls represent a sink for HONO during the night at a rate of $\sim 1 \times 10^7 \text{ molec cm}^{-3} \text{ s}^{-1}$ (figure 6.18 A, and B), and change to a source during the day of $\sim 2.5 \times 10^7 \text{ molec cm}^{-3} \text{ s}^{-1}$ (figure 6.18 D, and E). Due to the strong dependence on the vertical transport of the type of contribution of walls of buildings to either production or removal of HONO, the changes appear rapidly.

It is not surprising that direct emission of HONO represents a source of HONO in the lowest $\sim 5 \text{ m}$ of the PBL during all times modeled by the RCAT 8.1.2. As HONO emission is directly linked to that of NO from cars, at night only $\sim 1 \times 10^7 \text{ molec cm}^{-3}$ HONO originate from this source each second due to the reduced traffic (see figure 6.18 A). However, during the morning rush hour (5 hours after the start of the model) HONO may be formed at a rate of up to $\sim 2.5 \times 10^8 \text{ molec cm}^{-3} \text{ s}^{-1}$ (see figure 6.18 C).

The contribution of the vertical transport changes with altitude. In the NO rich layer below $\sim 3 \text{ m}$, Ψ_{HONO} always acts as a removal mechanism for HONO, and increases throughout the day from $\sim 1 \times 10^8 \text{ molec cm}^{-3} \text{ s}^{-1}$ directly at the ground at midnight (see figure 6.18 A) up to $\sim 2 \times 10^8 \text{ molec cm}^{-3} \text{ s}^{-1}$ at noon (see figure 6.18 E). This values increases with altitude, showing a minimum at $\sim 5 \text{ m}$ during all times of day. Between $\sim 5 \text{ m}$ and $\sim 30 \text{ m}$, which is close to the upper height of the Roman urban canopy, the upward transport of HONO represents its main source in the nocturnal boundary layer of $\sim 1 \times 10^7 \text{ molec cm}^{-3} \text{ s}^{-1}$ (see figure 6.18 B). During the day, vertical mixing in the PBL is generally stronger and NO levels are higher due to increased on-road traffic. Consequently, a second layer of enhanced NO concentrations can establish themselves in the street canyons, turning the vertical transport of

HONO to a sink, which is subsequently observed at $\sim 2 \times 10^7$ molec $\text{cm}^{-3} \text{s}^{-1}$ in figure 6.18 D. Above ~ 35 m, Ψ_{HONO} is always a source of HONO, reaching maximum levels of $\sim 0.2 \times 10^7$ molec $\text{cm}^{-3} \text{s}^{-1}$ at noon on 29.05.2001 in Rome (see figure 6.18).

6.2.3.4 Contribution of the Different Sources and Sinks to Daytime HONO Values

To draw conclusions about the origin of the observed elevated daytime values of HONO, we will now have a look at all days of the different field study campaigns modeled with RCAT 8.1.2. The quality assurances, i.e. the reproduction of the measured time series of the corresponding trace gases and the interference tests of the influence of the emitted species VOCs and NO_x from on-road traffic were performed analogous to those described in detail for the 29.05.2001 in Rome. The values summarized by table 6.3, table 6.4, and table 6.5 represent the different sources and sinks of atmospheric HONO multiplied by the midpoint height of the corresponding box where they appear and divided by the lowest 100 m of the PBL. Therefore, they are rates of HONO formation and removal respectively, integrated and weighted by their height information (vertically averaged).

This treatment has crucial consequences for the production of HONO on the ground surface. Only the lowest box of 1×10^{-4} m altitude has contact to the ground, thus values become insignificantly small. However, this indicates that the transport of HONO upwards (in the case of production) or towards the ground (in the case of deposition) limits its influence with respect to a distinctive height interval of the PBL. In table 6.6, the relative contribution of the corresponding mechanism divided by the absolute value of all rates of sources and sinks is given.

For the Rome 2001 campaign, the 29.05.2001, 30.05.2001, when a photochemical smog event occurred (see chapter 4.1.6), and the 04.06.2001, which is characterized by the absence of atmospheric nighttime stabilization, were modeled. The results are summarized by table 6.3 for the situation in the NBL (1 and 3 hours after the start of the model), at sunrise and the morning rush hour (5 hours after the model start), until noon (9 and 12 hours respectively). Generally, the discussion presented in the chapters above for the 29.05.2001 is valid for the next day as well (see table 6.3). During the night, the majority of the vertically integrated concentration of HONO is lost on the walls of buildings (~ 90 %) and to the ground surface (~ 10 %) (see table 6.3, and table 6.6). On the other hand, the aerosols contribute to ~ 15 %, the direct emission to ~ 20 % and the vertical transport to ~ 65 % to the HONO formation in the total column of 100 m of the NBL (see table 6.3, and table 6.6). Due to the stronger daytime vertical transport, especially to and out of the laminar layer at the ground surface and walls of buildings, both contribute in large amounts (~ 4 %, and ~ 45 % respectively) to the production of HONO in a 100 m high column (see table 6.3, and table 6.6).

At daytime, the influence of aerosols is negligible (< 1 %), but ~ 40 % of HONO originates from the homogeneous recombination of NO and OH radicals in the gas-phase. While photolysis is the main sink of atmospheric HONO (at ~ 60 %), vertical transport mixes the HONO out of the analyzed volume at comparable amounts (~ 40 %) (see table 6.3, and table 6.6). In addition to the absolute values or relative contribution of the different sources and removal processes, the exact time of change of the sign of e.g. P_{HONOwall} differs (see table 6.3). This indicates the strong dependence on the strength of atmospheric stability and therefore the vertical transport Ψ_{HONO} in the PBL. Due to stronger vertical mixing in the NBL on 04.06.2001, when only labile layering occurred, the contribution of the different terms was not found to change from night to day by the RCAT 8.1.2 model (see table 6.3). HONO formation proceeds even during the night on vertical walls of buildings P_{HONOwall} , and that on the ground surface $P_{\text{HONOground}}$, while the vertical transport always represents a sink (see table 6.3). Under these conditions, no influence of aerosols ($P_{\text{HONOaerosols}}$) (see table 6.3, and table 6.6) was found by the model. While the vertical transport represents the only sink of HONO

in the NBL, the stronger influence of direct emissions of HONO (~ 20 % at day) are due to the stronger mixing as well (see table 6.3, and table 6.6). The aerosols only represent a significant location for HONO formation or removal respectively, under conditions of very stable layering of the PBL. Only under these conditions, the transport towards and upwards the ground surface is suppressed and therefore volumetric sources of HONO contribute to larger amounts considering the entire height column of 100 m.

The model results for the Milan 2002 campaign are listed in table 6.4. Three days were modeled, which all refer to the first period of this measurement campaign, characterized by clear atmospheric stabilization during the night and a labilization at day. During these days, the wind was predominantly from southern directions, thus the plume of the heavily polluted area of Milan was detected by the instruments (see chapter 4.2). Generally, the contribution of the different sources and removal processes for atmospheric HONO does not differ from those for the Rome 2001 scenarios in (see table 6.3, table 6.4, and table 6.6). Due to the reduced traffic, the direct emissions contributed only ~ 3 % during the night and ~ 10 % during the day to the HONO production in the lowest 100 m of the PBL (see table 6.4, and table 6.6). The vertical transport was modeled to be most effective production in a 100 m high column during the night (~ 95 %), and during the day it was a more effective sink (~ 45 %) than during the Rome 2001 campaign (see table 6.4, and table 6.6).

For the Turm 2003 campaign, three days were analyzed with the RCAT 8.1.2 model: the 06.06.2003, when no atmospheric stabilization occurred in the NBL and no vertical gradients of the trace gases could be found, the 07.06.2003, with a strong nighttime stabilization of the atmosphere and subsequent strong vertical gradients of HONO and NO₂, and the 10.06.2003, when an atmospheric nighttime stabilization was observed, but no vertical gradients of the trace gases could be measured (see chapter 4.3.5). The vertical gradients of the corresponding trace gases were generally reproduced by the model within the errors of the DOAS instrument, which were significantly higher than e.g. during the Rome 2001 campaign due to the shorter DOAS light beam. However, the model results of the Turm 2003 campaign (see table 6.5, and table 6.6) differ significantly from the Rome 2001 or Milan 2002 data. In contrast to the other scenarios, the measurement site was rural and thus less influence of direct emissions of ~ 5 % during the day was found (see table 6.5, and table 6.6). Due to the lower urban canopy height and its smaller density, the vertical walls of buildings only contribute ~ 10 % to the daytime HONO production (see table 6.5, and table 6.6). Their lower contribution to the nighttime loss of HONO (~ 60 %) is partly compensated by the increased removal of HONO at the ground surface (~ 20 %), while aerosols contribute in similar amounts during the night as a sink for HONO (see table 6.5, and table 6.6).

hour	$P_{\text{HONOground}}$	P_{HONOwall}	$P_{\text{HONOaerosols}}$	E_{HONO}	Ψ_{HONO}	$P_{\text{HONO-NO+OH}}$	L_{HONOphot}	net
	[ppb h ⁻¹]	[ppb h ⁻¹]	[ppb h ⁻¹]	[ppb h ⁻¹]	[ppb h ⁻¹]	[ppb h ⁻¹]	[ppb h ⁻¹]	[ppb h ⁻¹]
Rome, 29.05.2001								
1	-0.020	-0.130	0.010	0.020	0.040	0.000	0.000	-0.08
3	-0.030	-0.210	0.010	0.080	0.060	0.010	0.000	-0.08
5	-0.090	0.270	0.020	0.520	-0.770	1.060	-1.960	-0.95
9	0.020	0.900	0.030	0.100	-0.620	1.520	-2.150	-0.02
12	0.060	0.700	0.010	0.210	-0.660	0.630	-1.060	-0.11
Rome, 30.05.2001								
1	-0.020	-0.160	0.020	0.020	0.080	0.000	0.000	-0.06
3	-0.030	-0.220	0.010	0.090	0.080	0.010	0.000	-0.06
5	-0.140	-0.200	0.020	0.520	-0.290	1.440	-2.410	-1.06
9	0.040	1.170	0.030	0.050	-0.780	1.140	-1.750	-0.01
12	0.070	0.750	0.010	0.210	-0.750	0.570	-0.980	-0.12
Rome, 31.05.2001								
1	0.000	0.050	0.000	0.020	-0.080	0.000	0.000	-0.01
3	0.000	0.180	0.000	0.110	-0.300	0.000	0.000	-0.01
5	-0.050	0.550	0.000	0.470	-0.930	0.350	-0.730	-0.34
9	0.020	0.400	0.000	0.260	-0.660	0.630	-0.830	-0.18
12	0.020	0.490	0.000	0.310	-0.670	0.790	-1.120	-0.18

table 6.3: Quantification of the averaged (up to 100 m) HONO production and loss [ppb h⁻¹] from the RCAT 8.1.2 model results for the Rome 2001 campaign.

hour	$P_{\text{HONOground}}$	P_{HONOwall}	$P_{\text{HONOaerosols}}$	E_{HONO}	Ψ_{HONO}	$P_{\text{HONO-NO+OH}}$	L_{HONOphot}	net
	[ppb h ⁻¹]	[ppb h ⁻¹]	[ppb h ⁻¹]	[ppb h ⁻¹]	[ppb h ⁻¹]	[ppb h ⁻¹]	[ppb h ⁻¹]	[ppb h ⁻¹]
Milan, 29.07.2002								
1	-0.070	-0.990	-0.030	0.020	0.810	0.000	0.000	-0.26
3	-0.070	-0.400	-0.020	0.210	0.070	0.010	0.000	-0.20
5	-0.050	-0.140	0.020	0.160	-0.110	1.440	-2.610	-1.29
9	0.010	0.630	0.040	0.160	-0.370	1.460	-2.060	-0.13
12	0.090	0.420	0.010	0.210	-0.710	0.510	-0.640	-0.11
Milan, 30.07.2002								
1	-0.030	-0.280	0.000	0.010	0.190	0.000	0.000	-0.11
3	-0.060	-0.280	0.000	0.210	0.050	0.010	0.000	-0.07
5	-0.050	-0.140	0.010	0.160	-0.040	1.230	-1.790	-0.62
9	0.030	0.560	0.010	0.080	-0.360	1.100	-1.530	-0.11
12	0.020	0.150	0.000	0.060	-0.130	0.260	-0.380	-0.02
Milan 31.07.2002								
1	-0.030	-0.410	-0.010	0.020	0.230	0.000	0.000	-0.20
3	-0.070	-0.320	-0.010	0.210	0.040	0.020	0.000	-0.13
5	-0.050	-0.120	0.030	0.160	-0.130	1.460	-2.640	-1.29
9	0.030	0.700	0.020	0.020	-0.460	1.030	-1.410	-0.07
12	0.060	0.240	0.000	0.080	-0.360	0.310	-0.390	-0.06

table 6.4: Quantification of the averaged (up to 100 m) HONO production and loss [ppb h⁻¹] from the RCAT 8.1.2 model results for the Milan 2002 campaign.

hour	$P_{\text{HONOground}}$	P_{HONOwall}	$P_{\text{HONOaerosols}}$	E_{HONO}	Ψ_{HONO}	$P_{\text{HONO-NO+OH}}$	L_{HONOphot}	net
	[ppb h ⁻¹]	[ppb h ⁻¹]	[ppb h ⁻¹]	[ppb h ⁻¹]	[ppb h ⁻¹]	[ppb h ⁻¹]	[ppb h ⁻¹]	[ppb h ⁻¹]
Turm 06.06.2003								
1	-0.010	-0.040	-0.010	0.010	0.030	0.000	0.000	-0.02
3	-0.010	-0.020	-0.010	0.020	0.010	0.000	0.000	-0.01
5	0.000	0.030	0.010	0.090	-0.070	0.130	-0.470	-0.28
9	0.020	0.120	0.050	0.050	-0.120	1.020	-1.270	-0.13
12	0.030	0.110	0.050	0.050	-0.060	0.750	-1.010	-0.08
Turm 07.06.2003								
1	-0.060	-0.080	-0.040	0.160	0.080	0.010	0.000	0.07
3	-0.020	-0.060	0.010	0.020	0.000	0.010	0.000	-0.04
5	-0.010	-0.010	0.090	0.010	0.000	1.090	-2.190	-1.02
9	0.000	0.030	0.030	0.010	-0.020	1.630	-1.710	-0.03
12	0.010	0.010	0.010	0.020	-0.030	0.350	-0.370	0.00
Turm 10.06.2003								
1	-0.040	-0.140	-0.020	0.010	0.130	0.000	0.000	-0.06
3	-0.010	-0.040	-0.010	0.040	0.010	0.000	0.000	-0.01
5	-0.060	-0.030	0.010	0.310	0.000	0.480	-0.970	-0.26
9	0.020	0.080	0.020	0.030	-0.060	0.700	-0.830	-0.04
12	0.020	0.030	0.000	0.050	-0.040	0.230	-0.280	0.01

table 6.5: Quantification of the averaged (up to 100 m) HONO production and loss [ppb h⁻¹] from the RCAT 8.1.2 model results for the Turm 2003 campaign.

hour	$P_{\text{HONOground}}$ [%]	P_{HONOwall} [%]	$P_{\text{HONOaerosols}}$ [%]	E_{HONO} [%]	Ψ_{HONO} [%]	$P_{\text{HONO-NO+OH}}$ [%]	L_{HONOphot} [%]
Rome, 29.05.2001							
midnight	-13.3	-86.7	14.3	28.6	57.1	0	0
noon	3.7	43.5	0.6	13.0	-38.4	39.1	-61.6
Rome, 30.05.2001							
midnight	-11.1	-88.9	16.7	16.7	66.7	0	0
noon	4.3	46.6	0.6	13.0	-43.4	35.4	-56.6
Rome, 31.05.2001							
midnight	0	71.4	0	28.6	-100	0	0
noon	1.2	30.4	0	19.3	-37.4	49.1	-62.6
Milan, 29.07.2002							
midnight	-6.4	-90.8	-2.8	2.4	97.6	0	0
noon	6.8	31.6	0.8	15.8	-52.6	38.3	-47.4
Milan, 29.07.2002							
midnight	-9.7	-90.3	0	5.0	95.0	0	0
noon	4.1	30.6	0	12.2	-25.5	53.1	-74.5
Milan, 29.07.2002							
midnight	-6.7	-91.1	-2.2	8.0	92.0	0	0
noon	8.7	34.8	0	11.6	-48.0	44.9	-52.0
Turm, 06.06.2003							
midnight	-16,7	-66,6	-16,7	25,0	75,0	0	0
noon	3,0	11,1	5,1	5,1	-5,6	75,8	-94,4
Turm, 07.06.2003							
midnight	-33,3	-44,4	-22,2	66,7	33,3	0	0
noon	2,5	2,5	2,5	5,0	-7,5	87,5	-92,5
Turm, 10.06.2003							
midnight	-20,0	-70,0	-10,0	7,1	92,9	0	0
noon	6,1	9,1	0	15,2	-12,5	69,7	-87,5

table 6.6: Relative contribution [%] of the different sources and sink mechanisms to the total HONO production and loss respectively. The RCAT 8.1.2 model results for the different campaigns were averaged up to 100 m altitude.

6.2.4 Comparison to previous Models in Literature

Our model results and especially the detailed differentiation into the various rates contributing to HONO production and removal processes at different altitudes and times of day are only partly comparable to those reported in literature. However, some final remarks will show the enormous consequences of the treatment of trace gases, the vertical mixing, and the urban canopy as done in the RCAT 8.1.2 model.

Box models including HONO chemistry (e.g. [Harrison *et al.*, 1996]) neglect the influence of vertical transport. It was shown in chapter 4.3.9 that this approach oversimplifies the atmospheric reality. Many 1-D models that include both chemical reactions and vertical do not consider the inter-dependence of transport and chemistry. However, in a recent publication by [Geyer and Stutz, 2003; Stutz *et al.*, 2004a] it was shown that a “chemistry correction” of the eddy diffusivity is necessary to model the correct vertical profile of NO²⁸. The modified effective eddy diffusivity of NO around 20 m results in a suppression of the mixing of NO from the ground to higher altitudes, thus forming a sharper borderline between the chemistry in the NO filled ground layer and at higher altitudes. Therefore, the modeling studies of this thesis were based on the NCAT model of [Geyer and Stutz, 2003; Stutz *et al.*, 2004a], which includes the corrections of eddy diffusivities for chemistry.

Our findings are largely in agreement with a recent study by [Vogel *et al.*, 2003], which already gave strong evidence for a larger amount of daytime HONO produced by the homogeneous recombination of the NO and OH radicals considering the new reaction rate constant, which is two times higher than the old one. The importance of direct emissions as a source of HONO was shown as well as the importance of the heterogeneous formation from NO₂ hydrolysis at the ground surface [Vogel *et al.*, 2003].

However, the urban canopy structure, i.e. mainly the verticals walls of buildings, was not taken into account by [Vogel *et al.*, 2003] to explain the measurements by [Kleffmann *et al.*, 2003]. In contrast to their studies, our model indicates these walls being responsible for up to ~ 45 % of the daytime HONO production in the urban scenarios of Rome and Milan. Including these walls, an additional photochemical source of HONO [Kleffmann *et al.*, 2003; Vogel *et al.*, 2003] was not required in our model to reproduce the measured data of nitrous acid. The explicit implication of the walls as an additional urban surface is not identical to a simple multiplication of the surface to volume ratio by a certain factor. This is due to the fact that the walls arise also into higher boxes of the model. A laminar layer is present above the walls and treated similar to that on the ground: a high spatial resolution and transfer resistances for the transport of the trace gases into the layers. Thus, any interaction of trace gases with these walls is determined by the transport, which depends on the wind speed. Since a logarithmic wind speed profile is assumed in the model, the transport of trace gases towards and apart from the surfaces is faster in higher altitudes.

6.2.5 Contribution of HONO to the Daytime OH Budget

It was shown in chapter 2.2.3 that the hydroxyl radical (OH) is the most important oxidizing species in the daytime atmosphere [Crutzen and Zimmermann, 1991]. The mechanisms producing OH radicals are therefore amongst the most important processes influencing the oxidation capacity and ozone formation in the atmosphere. The high HONO daytime levels of ~ 200 ppt can have significant consequences for the OH budget in urban areas.

²⁸ In the case of O₃ and NO₂, the eddy diffusivities are only weakly changed by chemistry because for both gases the gradient of the total reaction rate is small compared to its concentration gradient.

To quantify the different OH production and removal processes, they are illustrated in figure 6.19 for 29.05.2001 of the Rome campaign as an example. The contribution of HONO photolysis to the total daytime HO_x formation is calculated by the RCAT 8.1.2 model according to r. 2.24.

Another source of HO_x is the photolysis of O₃ (r. 2.17) at wavelengths below 319 nm with subsequent reaction of the O(¹D) radical with water vapor. Since not all O(¹D) radicals react with water according to reaction r. 2.18, we derived the branching ratio from meteorological data, which includes in particular the absolute water concentration (see for example [Alicke, 2000; Alicke et al., 2003; Alicke et al., 2002; Finlayson-Pitts and Pitts, 2000] and chapter 2.2.3 of this thesis).

The production rate of HO_x by photolysis of HCHO (P_{OH-HCHO} in figure 6.19) was determined from the photolysis frequency towards H + CHO (r. 2.20) and the concentrations of HCHO. It was assumed that the HO₂ produced by reaction (r. 2.20) followed by (r. 2.22) and (r. 2.23) is immediately converted into OH by reaction (r. 2.11). The rate-limiting step is the photolysis of HCHO [J(HCHO_{rad})], with a lifetime of about 10 hours at noon. Note that two HO_x molecules are formed in the subsequent reactions r. 2.22, and r. 2.23, and in the reaction (r. 2.18) of O(¹D) with water.

The reactions of ozone with alkenes (P_{OH-O₃+VOC} in figure 6.19) were presented as another possible source for HO_x radicals in the troposphere [Paulson and Orlando, 1996]. It was calculated from the reaction of ozone with several olefins²⁹ using the corresponding rate constants, which are listed in appendix B.

Further sources of OH radicals were summarized as P_{OH-other} in figure 6.19. Those are the photolysis of HNO₃, HNO₄, H₂O₂, methyl hydrogen peroxide, higher organic peroxides, peroxyacetic acid, and higher analogs, as well as the reactions of ozone with aromatic-HO adducted from TOL, XYL, CSL (see appendix B.), or the reactions of HO₂ with O₃ and HO₂ with NO₃. All are suspected to be of minor importance for the daytime production of OH radicals [Alicke, 2000; Alicke et al., 2003; Alicke et al., 2002]. This is also confirmed by our results (see figure 6.19 and table 6.7) and therefore not considered in the following discussion. The loss of the OH radicals via oxidation of VOCs is dominant in the morning (~ 50 %) and only slightly decreases to ~ 40 % at noon (see figure 6.19 and table 6.7). Another ~ 25 % of OH is lost by reaction r. 2.2 with NO₂. Further sinks of OH, i.e. reactions with O₃, HO₂, H₂O₂, HONO, HNO₃, HNO₄, and CO, become more important throughout the day and their sum reaches ~ 25 % at noon.

It is important to note that the OH radicals produced by r. 2.24 can also react with NO in the gas phase (r. 2.26) and recycle HONO. Thus, a net production rate of OH radicals from HONO photolysis can be calculated by:

$$P_{HO_x}(HONO) = J_{r.2.24} \cdot [HONO] - k_{r.2.26} \cdot [OH] \cdot [NO] \quad \text{eq. 6.13}$$

The rate constant of reaction r. 2.26 and the photolysis frequency of reaction r. 2.24 as used in the RACM mechanism [Stockwell et al., 1997] and the photolysis module [Sander, 2001], respectively, are listed in see appendix B. In fact, a comparison of the net OH production rates of the different sources would be more evident. However, the OH radicals from ozone photolysis (r. 2.17) for example, can undergo a variety of reactions with several VOCs (see chapter 2.2.2) to recycle O₃. The problem can become arbitrarily complex depending on the number of VOCs considered. In the absence of direct measurements of VOCs we will thus discuss the gross OH production rates in this thesis. More details about the contribution of HONO to the daytime OH radical budget and the comparison to other sources can be found in [Alicke, 2000; Alicke et al., 2003; Alicke et al., 2002].

The variations of the HO_x sources are shown in figure 6.19 for 5, 9, and 12 hours after the start of the model, which was midnight of 29.05.2001, and thus represent the HO_x source at

²⁹ Those are ETE, OLT, OLI, DIEN, ISO, API, LIM, MACR, DCB, and TPAN as specified in appendix B.

the corresponding time of day. Generally, the production rate of OH radicals by all source mechanisms increases from $6.1 \times 10^7 \text{ molec cm}^{-3} \text{ s}^{-1}$ after sunrise to $1.4 \times 10^8 \text{ molec cm}^{-3} \text{ s}^{-1}$ at noon and decreases with altitude (see figure 6.19). This is obvious, as the corresponding trace gases decrease with altitude as well (see figure 6.12 and figure 6.13, respectively). The gradient of $P_{\text{OH-HONO}}$, i.e. the OH production by photolysis of HONO, is steepest (see figure 6.19) and $P_{\text{OH-HONO}}$ decreases from $\sim 3.3 \times 10^8 \text{ molec cm}^{-3} \text{ s}^{-1}$ directly at ground level to $\sim 0.2 \times 10^7 \text{ molec cm}^{-3} \text{ s}^{-1}$ in 100 m. This becomes reasonable by taking into account that HONO is primarily formed at or near the ground via reaction r. 2.33 (see chapter 6.2.3.4) and HONO concentrations rapidly decrease with altitude due to photolysis. This leads to a short HONO lifetime of ~ 10 min at noon (see chapter 2.3.7). Instead, ozone photolysis becomes a stronger source of OH radicals with altitude (see figure 6.19). Again, this is caused by the gradient of the trace gas, which is positive during the day in the case of O_3 (see figure 6.12).

Besides the altitude dependence of the HO_x sources, their changing of strength throughout the day is of interest. In the following, we will discuss the P_{OH} as vertically (up to 100 m of the PBL) averaged values, as already done for the HONO production rates in chapter 6.2.3.4.

The reaction of HO_2 with NO (r. 2.11) is dominant at all times of 29.05.2001. It increases from sunrise by a factor 3 to reach its maximum of $\sim 1.2 \times 10^8 \text{ molec cm}^{-3} \text{ s}^{-1}$ at noon. $P_{\text{OH-HO}_2+\text{NO}}$ therefore contributes $\sim 80\%$ to the total OH production (see figure 6.19 and table 6.7). The HO_2 radicals, which originated from photolysis of HCHO (see above), were subtracted to calculate the OH production by (r. 2.11), as it is listed in table 6.7. However, the OH radicals from reaction r. 2.11 are of secondary origin, as the HO_2 radicals need to be formed via other reaction pathways first. The high NO concentrations can even enhance the importance of r. 2.11 as an OH source, but NO was not measured during the Rome 2001 along the DOAS light-beam. In the following, we will focus on the primary direct OH or HO_2 sources, which are illustrated by the zoomed plots on the right side of figure 6.19.

From figure 6.19 and table 6.7, it can be seen that the production by ozone photolysis, which requires light at wavelengths below 320 nm, is negligible at 5:00, which is ~ 30 min after sunrise. Throughout the day, its contribution increases to $\sim 30\%$ at noon of 29.05.2001 (see figure 6.19 and table 6.7). Photolysis of HCHO is an earlier source for HO_x since it only requires light below 370 nm. The production rate directly after sunrise is slightly below $1.5 \times 10^6 \text{ molec cm}^{-3} \text{ s}^{-1}$ and increases up to $7.1 \times 10^6 \text{ molec cm}^{-3} \text{ s}^{-1}$ at noon (see figure 6.19 and table 6.7). However, it has to be mentioned that during day, HCHO is as well a product of the photooxidation processes in the PBL (see chapter 2.2) and thus, of secondary origin. Quantifying only primary sources of OH radicals at day, one has to subtract the contribution of this part of HCHO, which is formed via reactions including HO_x radicals at day. Thus far, this was not considered for the OH production rates calculated in this thesis.

Directly after sunrise, the HONO pool accumulated during night leads to HO_x production rates of $1.4 \times 10^7 \text{ molec cm}^{-3} \text{ s}^{-1}$. Due to the declining HONO concentrations, the HO_x production rates by HONO photolysis decrease to $7.4 \times 10^6 \text{ molec cm}^{-3} \text{ s}^{-1}$ at noon (see figure 6.19 and table 6.7). Since O_3 and most VOCs show a contrary diurnal variation (See chapter 6.2.3.1), the VOC ozonolysis produces OH radicals at a rate of $\sim 1.7 \times 10^6 \text{ molec cm}^{-3} \text{ s}^{-1}$ after sunrise as well as at noon.

The relative contribution of HONO photolysis to primary HO_x formation can be seen in table 6.7 vertically averaged for the lowest 100 m of the PBL. Directly after sunrise, it is the dominant primary source ($\sim 80\%$). Its contribution decreases over the morning to $\sim 30\%$ at noon. At this time of day, O_3 photolysis ($\sim 30\%$) and HCHO photolysis ($\sim 30\%$) all contribute similar amounts (see table 6.7). Therefore, HONO photolysis acts not only as starter of photochemistry in the early morning hours, but also plays a significant role as precursor of photo-oxidants throughout the entire day.

It is interesting to compare our results to data recently published by [Alicke, 2000; Alicke *et al.*, 2003] for Berlin. They also observed enhanced production rates of HO_x by photolysis of

the nocturnal HONO pool of $\sim 10^7$ molec cm^{-3} s^{-1} , which is in the same order of magnitude as our results (see table 6.7). However, the calculated diurnal variation of the $P_{\text{OH-HONO}}$ differs significantly. [Alicke, 2000; Alicke *et al.*, 2003] found HONO photolysis to peak in the early morning hours and to decrease to $\sim 10^5$ molec cm^{-3} s^{-1} at noon, two orders of magnitude lower than our results.

	P(OH) [10^6 molec cm^{-3} s^{-1}]	relative contribution [%]	relative contribution to primary OH sources [%]
at 5:00 (sunrise)			
sources:			
HO ₂ +NO reaction	44.4	72.5	
HONO photolysis	13.6	22.3	81.1
HCHO photolysis	1.4	2.3	8.4
O ₃ photolysis	0.0	0.0	0.1
VOCs ozonolysis	1.8	2.9	10.4
others	0.0	0.0	0.1
loss:			
OH+NO ₂ reaction	-10.6	18.0	
OH+VOCs reactions	-32.2	54.6	
others	-16.1	27.4	
sum sources	61.2		
total sum	2.3		
at 9:00			
sources:			
HO ₂ +NO reaction	117.7	77.8	
HONO photolysis	15.0	9.9	44.4
HCHO photolysis	12.6	8.3	37.3
O ₃ photolysis	4.5	3.0	13.4
VOCs ozonolysis	1.5	1.0	4.4
others	0.2	0.1	0.6
loss:			
OH+NO ₂ reaction	-37.2	26.7	
OH+VOCs reactions	-61.5	44.1	
others	-40.7	29.2	
sum sources	151.3		
total sum	-11.9		
at 12:00 (noon)			
sources:			
HO ₂ +NO reaction	117.7	83.1	
HONO photolysis	7.4	5.2	30.8
HCHO photolysis	7.1	5.0	29.5
O ₃ photolysis	6.7	4.8	28.2
VOCs ozonolysis	1.7	1.2	7.2
others	1.0	0.7	4.3
loss:			
OH+NO ₂ reaction	-31.2	24.2	
OH+VOCs reactions	-50.5	39.2	
others	-47.1	36.6	
sum sources	141.6		
total sum	12.8		

table 6.7: The different production rates of OH radicals and their contribution to the total daytime production of OH in the lowest 100 m of the PBL.

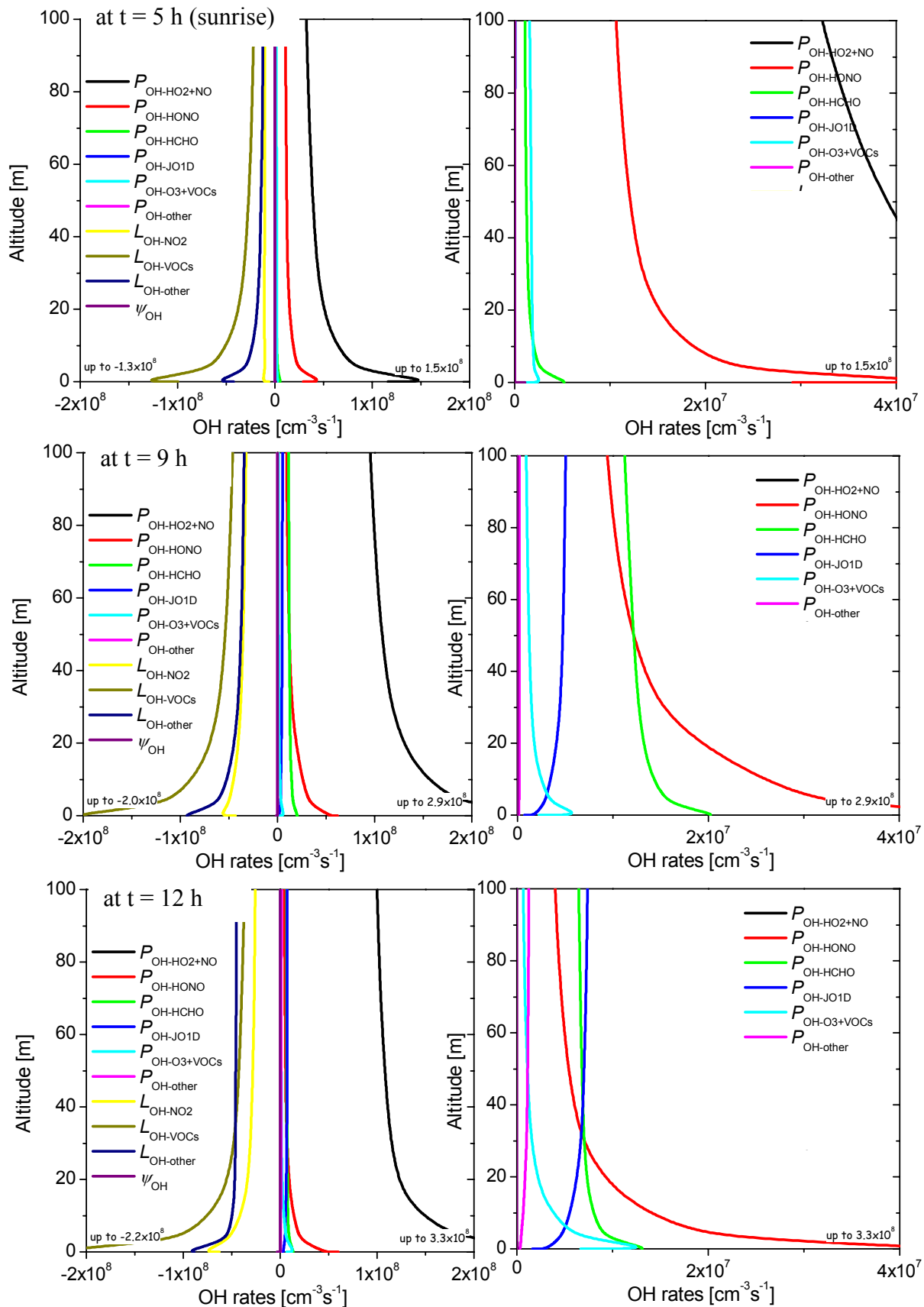


figure 6.19: Left plots: The reactions rates of OH radical production in the lowest 100 m of the PBL and removal modeled by the RCAT for the 29.05.2001 of the Rome campaign. Right plots (zoomed): The primary OH production by photolysis of O_3 , HCHO, and HONO and by the ozonolysis of VOCs.

A possible explanation is that the measurement site of [Alicke, 2000; Alicke *et al.*, 2003] was characterized by less pollution. Thus, [Alicke, 2000; Alicke *et al.*, 2003] did not directly observe daytime HONO concentrations above the detection limit of their DOAS instrument, but the daytime HONO levels in Berlin were derived from the OH-NO-HONO steady state. Further HONO sources such as HONO formation by NO₂ conversion on the walls of buildings, and the vertical transport into higher altitudes are not considered by [Alicke, 2000; Alicke *et al.*, 2003]. As discussed in chapter 6.2.3.4, both can cause higher HONO production rates in 50 m altitude than the rates by reaction r. 2.26 of OH and NO. Therefore, the calculated HONO mixing ratios of ~1 ppt at noon are more than two orders of magnitudes lower than the measured HONO levels in Rome.

The high daytime values of HONO of ~ 200 ppt, which were measured during the field campaigns in this thesis, are therefore of essential importance for the OH radical budget in the daytime PBL. Thus, HONO photolysis is not only responsible for an additional OH peak in the early morning hours, but contributes as a significant OH source throughout the entire day, and cannot be neglected in modeling studies.

7 Conclusions and Outlook

The goal of this thesis was to detect and verify daytime concentrations of nitrous acid, and to investigate its formation pathways. To pursue the first goal, HONO was measured in the urban Planetary Boundary Layer by Differential Optical Absorption Spectroscopy (DOAS) during three field campaigns in Europe. Furthermore, a quantification of the contribution of different HONO sources was performed by applying a chemistry-and-transport model (RCAT 8.1.2). The formation and loss processes of HONO were investigated in smog chamber studies, in particular with respect to potential enhancement of the heterogeneous NO_2 hydrolysis on real urban surfaces.

While nitrous acid (HONO) has been studied for more than 20 years in the polluted Nocturnal Boundary Layer with nighttime mixing ratios of up to 10 ppb, HONO daytime levels were for long times thought to be in the order of ~ 50 ppt and below, due to the rapid photolysis of HONO. Recently, more and more field measurements using multiple detection techniques have shown elevated daytime mixing ratios of HONO of ~ 200 ppt in polluted urban as well as in rural areas. Thus far, these elevated daytime levels could not be explained by the current state of knowledge. Since HONO photolysis in the early morning is known as a direct source of OH radicals, which drive the tropospheric ozone formation, the high daytime levels of HONO can lead to an additional and large contribution of OH radicals to tropospheric daytime chemistry.

Despite the atmospheric importance and two decades study of HONO, its sources and formation mechanisms remain poorly understood. Direct emission of HONO by traffic related combustion processes and homogeneous reactions in the gas phase have been quantified, but cannot explain the high HONO-to- NO_2 -ratios often observed in the boundary layer. Today, it is generally accepted that atmospheric HONO is formed by the heterogeneous disproportionation of NO_2 with water. However, large uncertainties about the nature of the surfaces and the chemical conversion mechanism remain. While several studies indicate that the ground is a more important surface than the aerosol, investigations of the HONO formation on macroscopic surfaces (such as the ground or the building walls) were thus far only performed on laboratory and artificial surfaces (e.g. on Teflon or glass surfaces). These laboratory results may not easily be generalized to atmospheric scenarios that include real urban surfaces. This is mainly due to the fact that real surfaces are more complex, and have an effective surface area, which was thus far not well quantified. Variations of rate constants due to changing meteorological parameters in the atmosphere have also not been considered thus far.

7.1 Conclusions from the Field and Modeling Studies: Daytime HONO Levels, Explanation and Consequences

In this thesis, the diurnal variations of HONO, NO_2 , O_3 , HCHO (using DOAS techniques) and supporting parameters (including nitrogen monoxide mixing ratios, aerosol properties, meteorological parameters, solar fluxes, and atmospheric stability) were measured during three field campaigns: in the urban area of Rome, Italy, in May and June of 2001, in the urban area of Milan, Italy, in July and August 2002, and at the rural site of the Forschungszentrum

Karlsruhe, Germany, the latter including measurements of vertical profiles of the trace gases towards the 200 m high meteorological tower as well.

High daytime values of HONO, clearly above the detection limit of the DOAS systems of ~ 70 ppt were observed during these field studies. For quality assurance of our observations, an intercomparison of different HONO measurement techniques was performed by using a White-type DOAS multi-reflection system, which observed the same air masses as the in-situ monitors. The diurnal pattern of HONO was found identical by the different techniques: HONO showed a rapid increase after sunset to nighttime mixing ratios of up to 2 ppb, decreasing after sunrise to mixing ratios of ~ 200 ppt at noon. From a quantitative point of view, a very good agreement of the different instruments was obtained, with a slope of (0.99 ± 0.01) and an intercept indistinguishable from zero. Therefore, we can confirm the high daytime values of HONO, which were recently reported in literature [Kleffmann *et al.*, 2003; Neftel *et al.*, 1996; Ren *et al.*, 2003; Staffelbach *et al.*, 1997a; Zhou *et al.*, 2002a].

The measurements of clear negative vertical gradients of HONO and its precursor NO_2 at night confirm previous findings by other groups of a formation of nitrous acid primarily on or near the ground surface during the night [Alicke, 2000; Harrison *et al.*, 1996; Kleffmann *et al.*, 2003; Stutz *et al.*, 2002; Veitel, 2002]. Aerosols were found to be of minor importance in this thesis. However, at daytime, a distinct profile could not be derived from our data. This may be due to the enhanced vertical mixing of the atmosphere, which was also shown in this thesis to strongly influence the observed concentrations of nitrous acid. Natural radon-activity was used as a qualitative measure to characterize the vertical dynamics of the PBL according to [Febo *et al.*, 2003; Perrino *et al.*, 2001]. Changes in the time derivatives of radon were found to be directly correlated with a change of HONO and NO_2 mixing ratios. While HONO and NO_2 accumulate very effectively in a stable PBL featuring ineffective vertical mixing, they are mixed when labile conditions occurred in the PBL.

Three diurnal stages of HONO were defined in this thesis, which were derived from the diurnal patterns of HONO and the HONO-to- NO_2 ratio. At night, a pool of HONO can accumulate because of missing photolysis and reduced vertical dilution (stage 1: “nocturnal HONO accumulation”). During this period, the HONO production by heterogeneous conversion of NO_2 on surfaces competes with the deposition of HONO on these surfaces. Finally, a steady state in a layer directly above them is established during night, as shown by [Stutz *et al.*, 2002]. Within the 3 – 5 hours following sunrise the HONO pool accumulated in stage 1 is depleted by increasing photolysis and simultaneous convective mixing (stage 2: “photolysis and dilution of the HONO pool”). Finally, during midday, HONO, OH, and NO are in steady state (stage 3: “the OH-NO-HONO steady state”). Besides the reaction of OH and NO, most HONO is formed by a heterogeneous NO_2 conversion.

For a quantitative description of the HONO time series, a recently developed chemistry-and-transport model (RCAT 8.1.2 by [Geyer and Stutz, 2003; Stutz *et al.*, 2004a]) was applied to study the individual contribution of the vertical transport effects, chemical production or removal processes, and an interlink of both by chemistry dependent eddy diffusivities. In the framework of this thesis, the model was extended to daytime urban scenarios including calculation of photolysis frequencies, and labile layering of the PBL. An urban canopy, i.e. mainly vertical walls of buildings, was also implemented in the model. Thus far, the latter was not considered in modeling studies. The time series and vertical profiles of the trace gases were generally well modeled for nighttime conditions. In this thesis, we could also reproduce daytime levels of HONO, which has not been achieved in literature thus far [Vogel *et al.*, 2003].

The sources and sinks of HONO obtained from the model were discussed for different times of day, and the high vertical resolution of the model allowed a highly selective altitude dependent analysis. It was found that aerosols are of minor importance for atmospheric HONO levels under most circumstances. Further, direct emission ($\sim 25\%$) of HONO near the ground and its subsequent upward transport ($\sim 65\%$) represent the strongest HONO source in

the lowest 100 m of the NBL during night. At this time of day, HONO is lost by deposition on the ground surface (~ 10 %) and the walls of buildings (~ 80 %). The ground surface was likewise identified by [Stutz *et al.*, 2002] as a possible sink for HONO in the NBL.

During the day, photolysis (~ 60 %) and vertical transport due to the more effective vertical mixing are the main HONO removal processes in the lowest 100 m of the PBL. The recombination of the NO and OH radicals is a strong source of HONO, but contributes only ~ 40%, in contrast to previous findings reported in literature. While ~ 5 % of the observed HONO daytime concentrations are formed by heterogeneous hydrolysis of NO₂ on ground surfaces, the majority (~ 45 %) is formed on walls of buildings.

This urban canopy structure was not taken into account by previous modeling studies. The implication of vertical walls as an additional urban surface was not a simple multiplication of the surface to volume ratio [Aumont *et al.*, 2003; Moussiopoulos *et al.*, 2000; Vogel *et al.*, 2003]. Including the walls of buildings, an additional photolytic source of HONO is not needed to explain the observed daytime levels of nitrous acid. These high HONO values can be explained using the current state of knowledge of HONO chemistry in the PBL, by strong direct emissions and subsequent upward transport, as well as the special implication of walls of buildings.

The importance of HONO as a source of OH radicals was compared to ozone and formaldehyde photolysis and VOC ozonolysis. According to a recently published study [Alicke, 2000; Alicke *et al.*, 2003], HONO is the dominant OH source (~ 80 %) in the early morning hours. Thus, HONO is most likely the initiator of photooxidation and subsequent development of photochemical smog events. In addition, due to high daytime levels of HONO of ~ 200 ppt, up to 30 % of the noontime OH radical production stems from HONO photolysis. Its contribution to the OH radical production during the entire day needs to be considered in modeling studies.

7.2 Conclusions from Laboratory Studies: Interactions of HONO with Real Urban Surfaces

The processes of HONO formation were furthermore investigated in a smog chamber and analyzed as heterogeneous hydrolysis of NO₂ on various real urban surfaces (Teflon, PE foil, asphalt, concrete, roof-tiles, flagstone-tiles, and grass). A White-type DOAS multi-reflection system was used for the measurement of HONO and NO₂. NO, O₃, temperature, pressure, and relative humidity inside the smog chamber were measured as well.

The kinetics of HONO formation after addition of an equivalent to 80-350 ppb NO₂ was studied by the observed NO₂ decays. The yield of HONO was found to be in the order of ~ 2 - 14 ppb, in a good linear correlation to the amount of NO₂ injected. Uptake coefficients of NO₂ onto these surfaces were calculated as $\gamma_{\text{NO}_2} \sim 10^{-8}$ on Teflon, $\sim 10^{-7}$ on PE foil, $\sim 10^{-5}$ on asphalt plates and concrete, $\sim 3 \times 10^{-6}$ on roof-tiles and flagstone-tiles, and $\sim 2 \times 10^{-5}$ on grass. The uptake coefficients onto the laboratory surfaces (Teflon PE foil) derived in this thesis are in good agreement with those reported in literature [Finlayson-Pitts *et al.*, 2003; Pitts *et al.*, 1984c; Sakamaki *et al.*, 1983; Svensson *et al.*, 1987]. However, the uptake coefficients of NO₂ onto real urban surfaces were found to be two orders of magnitudes higher than reported in a recent study in a traffic tunnel [Ackermann, 2000; Kurtenbach *et al.*, 2001]. An accompanying study by [Finlayson-Pitts, 2003; Finlayson-Pitts, 2004] showed that the BET surface size of our asphalt plates is ~ 150 times higher than its geometrical size. Thus, the faster production of HONO on these real urban surfaces seems to be caused by the higher surface size of these real urban surface types, and catalytic enhancement of the heterogeneous hydrolysis of NO₂ may not occur.

The uptake of NO₂ was found to be independent of R.H. in the range of ~ 0 to 80 % R.H. In combination with a recent field study by [Stutz *et al.*, 2004b], which investigated the dependence of HONO formation on R.H., we obtained an inverse proportionality of HONO concentrations and R.H., and is of crucial importance for the atmosphere, which will be shown in detail in forthcoming publications [Finlayson-Pitts, 2004; Stutz, 2004].

The relative humidity was varied during the entire time of the individual experiments, in contrast to all previous laboratory studies, which investigated the heterogeneous HONO formation at a constant R.H. In our experiments, the R.H. increased during an initial period of humidification of the smog chamber, and decreased by leakage afterwards. The gas phase concentration of HONO was observed to directly follow the trend of R.H. The derived linear correlation between HONO and R.H. indicated an adsorption-desorption equilibrium, which is established very rapidly. The rapid adjustment of this steady state was found for all surface types investigated in this thesis.

A plausible explanation is that HONO and H₂O compete for the same surface sites to be adsorbed. This was confirmed by a recently reported ab-initio calculation of the adsorption enthalpies of HONO and H₂O, which are both comparable. Consequently, the uptake of HONO onto all surfaces inside the smog chamber becomes dependent on R.H., but the desorption of HONO is independent from R.H. The observed linear correlation of HONO with R.H. was described by Langmuir theory of adsorption-desorption isotherms. This theory was implemented in a model (HeCSI), which was employed to handle chemical reactions and the physical processes of adsorption-desorption of HONO simultaneously. Besides the production of HONO from the heterogeneous hydrolysis of NO₂, only three more chemical reactions were considered, which involve NO formation in the smog chamber by secondary reactions of HONO.

The HeCSI model, which was developed in this thesis, describes the observed HONO, NO₂, and NO concentration-time series in the smog chamber well. The model is based on a simplified chemistry and a fast Langmuir adsorption-desorption equilibrium between HONO and H₂O. Since HONO is mainly produced by the heterogeneous hydrolysis of NO₂, this steady state includes the concentrations of NO₂ as the precursor of HONO as well. This was observed for all different surface types, and thus it seems likely that this steady state is also rapidly established above urban surfaces in the real atmosphere. Based on this new model approach, HONO uptake coefficients, the amount of HONO adsorbed on the surfaces of the smog chamber, and the desorption frequency could be determined. The desorption frequency of HONO was found to be in the order of ~ 10⁻⁷ to 10⁻⁶ s⁻¹, and the uptake frequency of HONO of ~ 10⁻⁴ to 10⁻⁵ s⁻¹ at an “artificial R.H.” of 0 %.

Thus far, the HONO uptake onto real urban surfaces and its R.H. dependence was not investigated in previous laboratory studies, and comparisons are therefore limited. The rate of formation of HONO was derived from the uptake of NO₂ onto the surfaces, and interactions of HONO with the surfaces were neglected in literature. Any analysis of HONO formation, which takes into account chemical reactions only, is therefore incomplete.

The HeCSI model is not contradictorily to thus far reported mechanisms of the heterogeneous HONO formation. It combines the basic chemistry included in a recently presented integrated mechanism [Finlayson-Pitts *et al.*, 2003] and the Langmuir theory to describe the dependence of the HONO uptake on R.H. Previous findings about the HONO formation, such as its heterogeneous reaction pathway, its first order kinetic with respect to NO₂, and its independence from NO concentrations, are included in this model approach.

7.3 Final Conclusions, Summary and Outlook

The results of the field campaigns, the modeling studies, and the laboratory experiments, are directly linked. All indicate that a re-consideration of the heterogeneous interactions of HONO with real urban surfaces is necessary. This concerns the treatment of an urban canopy structure in modeling studies, which was identified as the most important surface for the atmospheric HONO production at day, the effective surface area of real urban surfaces, which can be orders of magnitude higher than their geometrical one, and the dependence of HONO uptake on R.H., which is described by the Langmuir theory of adsorption-desorption isotherms. The latter causes a rapidly established steady state between HONO, NO₂, and R.H. directly above the urban surfaces, and underlies all heterogeneous chemical reactions of the HONO related chemistry.

In particular, four major topics about the formation and the importance of atmospheric HONO at day and at night were satisfyingly answered in this thesis:

- The nighttime formation of HONO was quantitatively explained. It was found to be caused by higher NO₂ uptake coefficients onto real urban surfaces compared to e.g. on Teflon. However, these urban surfaces types are characterized by a larger “real” surface area and the chemical mechanism of the HONO formation does not differ from previous findings.
- In contrast to previous laboratory work about the heterogeneous HONO formation is the fact that the HONO uptake coefficients were found to be dependent on R.H., which was well described by a Langmuir adsorption-desorption equilibrium. This new description has several consequences for the atmospheric HONO production. However, the NO₂ uptake coefficients were found to be independent from R.H.
- For the first time, elevated daytime mixing ratios of HONO of ~ 200 ppt were measured under sunny clear-sky conditions clearly above the detection limit of the DOAS system and found in good agreement with in-situ instruments. Daytime vertical gradients of HONO were not observed.
- The elevated daytime levels of HONO were explained from the current state of knowledge of tropospheric chemistry and no additional photochemical source was needed in the model description. At day, high HONO levels are caused by strong emissions near the ground and a strong vertical transport, as well as a formation on walls of buildings. The latter differ from a formation on the ground surface or on aerosols by the more effective transport of trace species towards and apart from their surface.

However, some assumptions, which were implemented in the present version of the RCAT 8.1.2 model in this thesis, need to be verified by direct measurements in future work. Because the quality of modeling studies strongly depends on its input parameters, the vertical profiles of trace gases and aerosols should be measured simultaneously in a very high spatial and temporal resolution. Thus, light-path integrating (with their high time resolution) and in-situ techniques (with their low detection limit) should be combined, including direct measurements of free radicals, such as HO_x and RO_x. In particular, measurements of vertical profiles of trace gases, aerosols and meteorology directly in urban areas are needed to prove the importance of the urban canopy.

In comparison with other models, our model is favored by the simultaneous accurate description of chemical mechanisms, the strong influence of the vertical transport on trace gas profiles, their interaction, the high vertical resolution, and the conditioning of the urban canopy. However, since advection is thus far not included in the 1D chemistry-transport model of this thesis, the RCAT should also be extended to a 3D simulation in future work.

Although the HeCSI model developed in this thesis was shown to correctly describe the heterogeneous NO_x chemistry under all circumstances in the smog chamber, several

experimental limitations inhibited the investigation of all details concerning the proposed mechanism. Experiments at a constant R.H. are necessary to compare our mechanistic sequences with previous laboratory results. Furthermore, an investigation into the temperature dependence of the constants derived in this thesis should be performed.

Since Langmuir theory is limited to “medium” surface coverage, multi-layering becomes more likely and the BET isotherms should be applied at the higher R.H. In this thesis we could not achieve a terminal R.H. above $\sim 80\%$. Experiments should also be performed at high R.H. (close to the saturation point) to prove our mechanism, which thus far only considers monolayering. However, the application of BET theory requires the knowledge of several further parameters which need to be measured, and is limited to physisorption only.

In addition, the detection and quantification of the reaction intermediates during HONO formation from NO_2 , and especially the surface-adsorbed species, is therefore essential to justify the application of Langmuir theory of adsorption-desorption isotherms. The knowledge of the exact chemical bonding and structure of these species on the surfaces is the key for any further detailed mathematical description. This also concerns the experimental proof of the comparable bounding enthalpies of HONO and H_2O and therefore the competition of both species for the same surface-sites to be adsorbed. This was not attempted in our studies.

Finally, it has to be mentioned that the mechanisms of NO production could not be satisfyingly explained in this thesis. The characterization of the surface-adsorbed species could clarify not only the mechanism of the secondary reactions of HONO, which yield NO (and N_2O), but also the theory of the “passivated” form of surface-adsorbed nitric acid.

Literature

- Acker, K., S. Mertes, D. Möller, W. Wiedrecht, R. Auel, and D. Kalass, Case study of cloud physical and chemical processes in low clouds at Mt. Brocken, *Atmospheric Research*, 64, 41 - 45, 2002.
- Acker, K., D. Möller, W. Wiedrecht, R. Auel, D. Kalass, and W. Tschewenka, Nitrous and nitric acid measurements inside and outside of clouds at Mt. Brocken, *Water, Air, and Soil Pollution*, 130, 331 - 336, 2001a.
- Acker, K., W. Wiedrecht, and R. Auel, Coupling of wet denuder and ion chromatography technique for sensitive measurements of nitrous and nitric acid in Melpitz, *J. Aerosol. Sci.*, 32, 523 - 542, 2001b.
- Ackermann, R., Auswirkungen von Kraftfahrzeugemissionen in der urbanen Atmosphäre, PhD thesis, University of Heidelberg, Heidelberg, 2000.
- Adamson, A.W., and A.P. Gast, *Physical Chemistry of Surfaces*, John Wiley & Sons Inc. Interscience Publications, New York Chichester Weinheim Brisbane Singapore Toronto, 1997.
- Ahmed, M., C.J. Apps, C. Buewnel, I. Hillier, C. Hughes, N. Watt, and J.C. Whitehead, Absorption of N_xO_y -based molecules on large water clusters: an experimental and theoretical approach, *J. Phys. Chem., A* (101), 1254 - 1259, 1997.
- Akimoto, H., H. Takagi, and F. Sakamaki, Photoenhancement of the Nitrous Acid Formation in the Surface Reaction of Nitrogen Dioxide and Water Vapor, *J. Phys. Chem. A*, 19, 539 - 551, 1987.
- Albritton, D.L., A.L. Schmeltekopf, and R.N. Zare, *An introduction to Least-Squares fitting of Spectroscopic data*, 1-68 pp., London, 1976.
- Alicke, B., The role of nitrous acid in the boundary layer, PhD thesis, University of Heidelberg, Heidelberg, 2000.
- Alicke, B., A. Geyer, A. Hofzumahaus, F. Holland, S. Konrad, H.-W. Pätz, J. Schäfer, J. Stutz, A. Volz-Thomas, and U. Platt, OH formation by HONO photolysis during the BERLIOZ experiment, *J. Geophys. Res.*, 108 (D4), 8247, doi:10.1029/2001JD000579, 2003.
- Alicke, B., K. Hebestreit, M. Mössner, U. Platt, and J. Stutz, Measurements of the vertical gradient of nitrous acid during the LOOP/PIPAPPO experiment in Milano, in *European Geophysical Society, Spring Meeting*, edited by A.K. Richter, pp. 515, European Geophysical Society, Germany, Den Haag, 1999.
- Alicke, B., U. Platt, and J. Stutz, Impact of nitrous acid photolysis on the total hydroxyl radical budget during the Limitation of Oxidant Production/Pianura Padana Produzione di Ozono study in Milan, *J. Geophys. Res.*, 107 (D22), doi:10.1029/2000JD000075, 2002.
- Allegrini, I., A. Febo, A. Pasini, and S. Schiarini, Monitoring of the nocturnal mixed layer by means of particulate radon progeny measurement, *J. Geophys. Res.*, 99 (D9), 18,765-18,778, 1994.
- Allegrini, I., F.d. Santis, V.d. Palo, A. Febo, C. Perrino, and M. Possanzini, Annular Denuder Method for Sampling Reactive Gases and Aerosols in the atmosphere, *Environ. Sci. Technol.*, 67, 1-16, 1987.
- Ammann, M., M. Kalberer, D.T. Jost, L. Tobler, E. Rossler, D. Piguet, H.W. Gaggeler, and U. Baltensperger, Heterogeneous production of nitrous acid on soot in polluted air masses, *Nature*, 395 (6698), 157-160, 1998.
- Andres-Hernandez, M.D., J. Notholt, J. Hjorth, and O. Schrems, A DOAS Study On the Origin of Nitrous Acid At Urban and Non-Urban Sites, *Atmospheric Environment*, 30 (2), 175-180, 1996.
- Appel, B.R., A.M. Winer, Y. Tokiwa, and H.W. Biermann, Comparison of Atmospheric Nitrous Acid Measurements By Annular Denuder and Differential Optical Absorption Systems, *Atmospheric Environment Part a-General Topics*, 24 (3), 611-616, 1990.
- Arya, S.P., *Introduction to Micrometeorology*, Academic Press, Inc., San Diego, 1988.
- Atkinson, R., Atmospheric chemistry of VOCs and NO_x , *Atmos. Environ.*, 34 (12 - 14), 2063 - 2101, 2000.
- Atkinson, R., and S.M. Aschmann, OH Radical Production From the Gas-Phase Reactions of O_3 With a Series of Alkenes Under Atmospheric Conditions, *Environ. Sci. Technol.*, 27 (7), 1357-1363, 1993.
- Atkinson, R., S.M. Aschmann, J. Arey, and B. Shorees, Formation of OH Radicals in the Gas Phase Reactions of O_3 with a Series of Terpenes, *J. Geophys. Res.*, 97, 6065-6073, 1992.
- Atkinson, R., A.M. Winer, and J.N.P. Jr., Estimation of night-time N_2O_5 concentrations from ambient NO_2 and NO_3 radical concentrations and the role of N_2O_5 in night-time chemistry, *Atmos. Environ.*, 20, 331-339, 1986.
- Aumont, B., F. Chervier, and S. Laval, The contribution of HONO sources to the NO_x / HO_x / O_3 chemistry in the polluted boundary, *Atmos. Environ.*, 37, 487 - 498, 2003.
- Aumont, B., S. Madronich, M. Ammann, M. Kalberer, U. Baltensperger, D. Hauglustaine, and F. Brocheton, On the NO_2 soot reaction in the atmosphere, *Journal of Geophysical Research*, 104 (D1), 1729-36, 1999.

- Baltrusch, M., Flugzeugmessungen von Schwefeldioxid und Sulfat in der Abgasfahne des Ruhrgebietes, *Z. Staub. Reinhalt. Luft*, 39, 252-256, 1979.
- Baria, A., V. Ferraro, L.R. Wilson, D. Luttinger, and L. Husaina, Measurements of gaseous HONO, HNO₃, SO₂, HCl, NH₃, particulate sulfate and PM_{2.5} in New York, NY, *Atmos. Environ.*, 37, 2825 - 2835, 2003.
- Barnes, R.A., The long range transport of air pollution: A review of European experience, *J. Air Poll. Control Assoc.*, 29, 1219-1235, 1979.
- Barney, W.S., and B.J. Finlayson-Pitts, Enhancement of N₂O₄ on porous glass at room temperature: A key intermediate in the heterogeneous hydrolysis of NO₂?, *J. Phys. Chem. A*, 104 (2), 171 - 175, 2000.
- Bartram, M.E., and B.E. Koel, *J. Vac. Sci. Tech.*, A6, 786, 1988.
- Bass, A.M., and R.J. Paur, The Ultraviolet Cross-Section of Ozone: I. The Measurements / Atmospheric Ozone, in *Quadrennial Ozone Symposium 1984*, edited by C. Czerefos, and A. Ghazi, pp. 606-616, Reidel, D., D. Reidel Publishing Company, Dordrecht/Boston/Lancaster, 1984.
- Becker, K.H., The European Photoreaktor EUPHORE, 1996.
- Becker, K.H., J. Kleffmann, R. Kurtenbach, and P. Wiesen, Line Strength Measurements of Trans-HONO Near 1255 Cm⁻¹ By Tunable Diode Laser Spectrometry, *Geophysical Research Letters*, 22 (18), 2485-2488, 1995.
- Beckett, W.S., M.B. Russi, A.D. Haber, R.M. Rivkin, J.R. Sullivan, Z. Tameroglu, V. Mohsenin, and B.P. Leaderer, Effect of Nitrous Acid On Lung Function in Asthmatics - a Chamber Study, *Environmental Health Perspectives*, 103 (4), 372-375, 1995.
- Beierle, S., U. Platt, M. Wenig, and T. Wagner, Weekly cycle of NO₂ by GOME measurements: A signature of anthropogenic sources, *Atmos. Chem. Phys. Discuss.*, 3, 3451-3467, 2003.
- Belcher, S.E., N. Jerram, and J.C.R. Hunt, Adjustment of a turbulent boundary layer to a canopy of roughness elements, *J. Fluid Mech*, 488, 369 - 398, 2003.
- Berges, M.G.M., R.M. Hoffman, D. Scharffe, and P.J. Crutzen, Nitrous oxide emissions from motor vehicles in tunnels and their global extrapolation, *JGR*, 98, 18527 - 18531, 1993.
- Berkowitz, C.M., J.D. Fast, S.R. Springston, R.J. Larsen, C.W. Spicer, P.V. Doskey, J.M. Hubbe, and R. Plastringe, Formation Mechanisms and Chemical Characteristics of Elevated Photochemical Layers over the Northeast United States, *Journal of Geophysical Research-Atmospheres*, 103 (D9), 10631-10647, 1998.
- Bevington, P.R., *Data reduction and error analysis for the physical sciences.*, New York, 1969.
- BMBF, Photosmog, Bundesministerium für Bildung, Wissenschaft, Forschung und Technologie - Referat Öffentlichkeitsarbeit, Bonn, 1996.
- Bösch, H., Stratospheric profiles of iodine oxide, PhD thesis, Universität Heidelberg, Heidelberg, 2001.
- Brauer, M., P.B. Ryan, H.H. Suh, P. Koutrakis, J.D. Spengler, N.P. Leslie, and I.H. Billick, Measurements of Nitrous Acid Inside 2 Research Houses, *Environmental Science & Technology*, 24 (10), 1521-1527, 1990.
- Brauers, T., U. Aschmutat, U. Brandenburger, H.P. Dorn, M. Hausmann, M. Healing, A. Hofzumahaus, F. Holland, C. Plass-Dilmer, and D.H. Ehhalt, Intercomparison of tropospheric OH radical measurements by multiple folded long- path laser absorption and laser induced fluorescence, *Geophys. Res. Lett*, 23, 2545-2548, 1996.
- Brauers, T., M. Hausmann, U. Brandenburger, and H.-P. Dorn, Improvement of Differential Optical Absorption Spectroscopy with a multichannel scanning technique, *Appl. Opt.*, 34, 4472-4479, 1995.
- Brockmann, K.J., V. Krieche, T. Etzkorn, R. Volkamer, and K. Wirtz, The European photoreactor EUPHORE: A technical description, in *EUROTRAC symposium 1996, Transport and transformation of pollutants in the troposphere, volume 2: Emission, deposition, laboratory work and instrumentation*, edited by P.M. Borell, P. Borell, K. Kelly, and W. Seiler, 1996.
- Bröske, R., J. Kleffmann, and P. Wiesen, Heterogeneous conversion of NO₂ on secondary organic aerosol surfaces: A possible source of nitrous acid (HONO) in the atmosphere?, *Atmos. Chem. Phys. Discuss.*, 3, 597 - 613, 2003.
- Brost, R.A., P.L. Haagenson, and Y.-H. Kuo, The effect of diffusion on tracer puffs simulated by a regional scale Eulerian model, *J. Geophys. Res.*, 93 (D3), 2389-2404, 1988.
- Brunauer, S., P.H. Emmett, and E. Teller, *J. Am. Chem. Soc.*, 60, 309, 1938.
- Businger, J.A., J.C. Wyngaard, Y. Izumi, and E.F. Bradley, Flux profile relationships in the atmospheric surface layer, *J. Atmos. Sci.*, 28, 181-189, 1971.
- Calvert, J.G., and W.R. Stockwell, Deviations from the O₃ - NO - NO₂ photostationary state in tropospheric chemistry, *Can. J. Chem.*, 61, 983-992, 1983.
- Calvert, J.G., G. Yarwood, and A.M. Dunker, An Evaluation of the Mechanism of Nitrous Acid Formation in the Urban Atmosphere, *Research On Chemical Intermediates*, 20 (3-5), 463-502, 1994.

- Cantrell, C.A., R.E. Shetter, T.M. Gilpin, J.G. Calvert, F.L. Eisele, and D.J. Tanner, Peroxy radical concentrations measured and calculated from trace gas measurements in the Mauna Loa Observatory Photochemistry Experiment 2, *J. Geophys. Res.*, *101* (D9), 14,653-14,664, 1996.
- Carroll, M.A., and A.M. Thompson, NO_x in the non-urban troposphere, in *Progress and Problems in Atmospheric Chemistry*, edited by J.R. Baker, pp. Chapter 7, World Scientific, Singapore, 1995.
- Chan, W.H., R.J. Nordstrom, J.G. Calvert, and J.H. Shaw, An IRFTS spectroscopic study of the kinetics and the mechanism of the reactions in the gaseous system, HONO, NO, NO₂, H₂O, *Chem. Phys. Lett.*, *37*, 441-446, 1976a.
- Chan, W.H., R.J. Nordstrom, J.G. Calvert, and J.H. Shaw, Kinetic study of HONO formation and decay reactions in gaseous mixtures of HONO, NO, NO₂, H₂O, and N₂, *Environ. Sci. Technol.*, *10*, 674-682, 1976b.
- Cheung, J.L., Q.Q. Li, J. Boniface, Q. Shi, P. Davidovits, D.R. Worsnop, J.T. Jayne, and C.E. Kolb, Heterogeneous interactions of NO₂ with aqueous surface, *J. Phys. Chem. A*, *104*, 2655 - 2662, 2000.
- Chou, A., Z. Li, and F.-M. Tao, Density Functional Studies of the Formation of Nitrous Acid from the Reaction of Nitrogen Dioxide and Water Vapor, *J. Phys. Chem. A*, *103*, 7848 - 7855, 1999.
- Cox, R.A., The photolysis of gaseous nitrous acid, *J. Photochem.*, *3*, 175-188, 1974.
- Crutzen, P.J., The influence of nitrogen oxides on the atmospheric ozone content, *Quart. J. Roy. Met. Soc.*, *96*, 320-325, 1970.
- Crutzen, P.J., and P.H. Zimmermann, The changing photochemistry of the troposphere, *Tellus*, *43 AB*, 136 - 151, 1991.
- Cuntz, M., Der Heidelberger 222Radon-Monitor: Kalibrierung, Optimierung, Anwendung, Diploma thesis, Universität Heidelberg, Heidelberg, 1997.
- Curtis, A.R., and W.P. Sweetenham, FACSIMILE release H user's manual, London, 1987.
- Czerny, M., and A. Turner, *Z. Phys.*, *61*, 792, 1930.
- Delmas, R., J.P. Lacaux, J.C. Menaut, L. Abbadie, X. Leroux, G. Helas, and J. Lobert, Nitrogen compound emission from biomass burning in tropical African savanna FOS/DECAFE 1991 experiment (Lamto, Ivory Coast), *J. Atmos. Chem.*, *22*, 175-193, 1995.
- DeMore, W.B., S.P. Sander, R.R. Friedl, A.R. Ravishankara, D.M. Golden, C.E. Kolb, M.J. Kurylo, R.E. Hurie, V.L. Orkim, M.J. Molina, G.K. Moortgart, and F.-P. B.J., Chemical kinetics and photochemical data for use in atmospheric studies, Jet Propulsion Laboratory, NASA National Aeronautics and Space Administration, Pasadena, California, 2003.
- DeMore, W.B., S.P. Sander, D.M. Golden, R.F. Hampson, M.J. Kurylo, C.J. Howard, A.R. Ravishankara, C.E. Kolb, and M.J. Molina, *Chemical kinetics and photochemical data for use in stratospheric modeling*, Pasadena / CA, 1997.
- Dentener, F.J., and P.J. Crutzen, Reaction of N₂O₅ on tropospheric aerosols: impact on the global distributions of NO_x, O₃ and OH, *J. Geophys. Res.*, *98*, 7149-7163, 1993.
- Dibb, J.E., M. Arsenault, M.C. Peterson, and R.E. Honrath, Fast Nitrogen Oxide Photochemistry in Summit, Greenland Snow, *Atmos. Environ.*, *36*, 2501 - 2511, 2002.
- Dobson, G.M.B., and D.N. Harrison, Measurements of the amount of ozone in the earth's atmosphere and its relation to other geophysical conditions, Part 1, *Proc. R. Soc. London*, *110*, 660 - 693, 1926.
- Doerr, H., B. Kromer, I. Levin, K.O. Muennich, and H.J. Volpp, CO₂ and Radon-222 as tracers for atmospheric transport, *J. Geophys. Res.*, *88*, 1309-1313, 1983.
- Eathough, N.L., S.M. Gregor, E.A. Lewis, D.J. Eathough, A.A. Huang, and E.C. Ellis, Comparison of six denuder methods and a filter pack for the collection of ambient HNO₃(g), HNO₂(g) and SO₂(g) in the 1985 NSMC study, *Atmos. Environ.*, *22*, 1601-1618, 1988.
- Eatough, D.J., A. Wadsworth, D.A. Eatough, J.W. Crawford, L.D. Hansen, and E.A. Lewis, A Multiple-System, Multi-Channel Diffusion Denuder Sampler for the Determination of Fine-Particulate Organic Material in the Atmosphere, *Atmos. Environ.*, *27*, 1213-1219, 1993.
- Ehhalt, D.H., H.-P. Dorn, and A. Hofzumahaus, *The measurement of OH radicals in the troposphere*, 157-173 pp., J. G. Calvert, London, 1994.
- Ehhalt, D.H., F. Rohrer, A. Wahner, M.J. Prather, and D.R. Blake, On the use of hydrocarbons for the determination of tropospheric OH concentrations, *J. Geophys. Res.*, *103* (D15), 18981-97, 1998.
- Eisele, F.L., G.H. Mount, D. Tanner, A. Jefferson, R. Shetter, J.W. Harder, and E.J. Williams, Understanding the production and interconversion of the hydroxyl radical during the tropospheric OH photochemistry experiment, *J. Geophys. Res.*, *102*, 6457-6465, 1997.
- England, C., and W.H. Corcoran, Kinetics and mechanisms of the gas-phase reaction of water vapor and nitrogen dioxide, *Ind. Eng. Chem., Fundam.*, *13*, 373-384, 1974.
- EPA, National air pollutant emission trends 1900-2001, U.S. Environmental Protection Agency, 2002.
- Ertl, G., *Science*, *254*, 1750, 1991.
- Farman, J.C., B.G. Gardiner, and J.D. Shanklin, Large losses of total ozone in Antarctica reveal seasonal ClO_x/NO_x interaction, *Nature*, *315*, 207-210, 1985.

- Febo, A., and C. Perrino, Prediction and Experimental Evidence For High Air Concentration of Nitrous Acid in Indoor Environments, *Atmospheric Environment Part a-General Topics*, 25 (5-6), 1055-1061, 1991.
- Febo, A., and C. Perrino, Measurement of High Concentration of Nitrous Acid Inside Automobiles, *Atmospheric Environment*, 29 (3), 345-351, 1995.
- Febo, A., C. Perrino, and I. Allegrini, Measurement of Nitrous Acid in Milan, Italy, by DOAS and Diffusion Denuders, *Atmos. Environ.*, 30 (21), 3599 - 3609, 1996.
- Febo, A., C. Perrino, and M. Cortiello, A Denuder Technique For the Measurement of Nitrous Acid in Urban Atmospheres, *Atmospheric Environment Part a-General Topics*, 27 (11), 1721-1728, 1993.
- Febo, A., C. Perrino, M. Giusto, S. Trick, A. Geyer, H. Veitel, U. Platt, K. Acker, W. Wieprecht, and D. Möller, WP2: Field Measurements, in *NITROCAT: NITRous acid and its influence on the Oxidation Capacity of the ATmosphere*, pp. 23 - 68, European Union, 2003.
- Febo, A., F.D. Santis, and C. Perrino, *Measurement of Atmospheric Nitrous and Nitric Acid by Means of Annular Denuders*, 121-125 pp., 1987.
- Febo, A., F.D. Santis, C. Perrino, and M. Giusto, Evaluation of laboratory and field performance of denuder tubes: a theoretical approach, *Atmos. Environ.*, 19, 1517-1530, 1990.
- Ferm, M., and A. Sjödin, A sodium carbonate coated denuder for determination of nitrous acid in the atmosphere, *Atmos. Environ.*, 19, 979-983, 1985.
- Ferm, M., and A. Sjoedin, *A simple method for determination of gaseous nitrous acid in the atmosphere*, Swed. Environ. Res. Inst., 1983.
- Fine, D.H., N-Nitroso compounds in the environment, *Adv. Environ. Sci. Technol.*, 10, 39 -123, 1980.
- Finlayson-Pitts, B.J., personal communication, , 2003.
- Finlayson-Pitts, B.J., personal communication, , 2004.
- Finlayson-Pitts, B.J., and J.N. Pitts, *Chemistry of the upper and lower atmosphere: theory, experiments and applications*, Academic Press, San Diego, CA; London, 2000.
- Finlayson-Pitts, B.J., L.M. Wingen, A.L. Sumner, D. Syomin, and K.A. Ramazan, The heterogeneous hydrolysis of NO₂ in laboratory systems and in outdoor and indoor atmospheres: An integrated mechanism, *Physical Chemistry Chemical Physics*, 5 (2), 223-242, 2003.
- Fitzjarrald, D.R., and D. Lenschow, Mean concentration and flux profiles for chemically reactive species in the atmospheric surface layer, *Atmos. Environ.*, 17 (12), 2505-2512, 1983.
- Flatoy, F., and O. Hov, NO_x from lightning and the calculated chemical composition of the free troposphere, *Journal of Geophysical Research*, 102 (D17), 21373-81, 1997.
- Frenkel, Y.L., *Kinetic Theory of Liquids*, Clarendon Press, Oxford, 1948.
- Fried, A., S. McKeen, S. Sewell, J. Harder, B. Henry, P. Goldan, W. Kuster, E. Williams, K. Baumann, R. Shetter, and C. Cantrell, Photochemistry of formaldehyde during the 1993 Tropospheric OH Photochemistry Experiment, *Journal of Geophysical Research-Atmospheres*, 102 (D5), 6283-6296, 1997.
- Friedeburg, C., Derivation of Trace Gas Information combining Differential Optical Absorption Spectroscopy with Radiative Transfer Modelling, PhD thesis, University of Heidelberg, Heidelberg, 2003.
- Fuchs, N.A., and A.G. Sutugin, *Highly dispersed aerosols*, Ann Arbor Science, Ann Arbor, MI, 1971.
- Fuentes, J.D., M. Lerdau, R. Atkinson, D. Baldocchi, J.W. Bottenheim, P. Ciccioli, B. Lamb, C. Geron, L. Gu, A. Guenther, T.D. Sharkey, and W.R. Stockwell, Biogenic Hydrocarbons in the atmospheric boundary layer: A review, *Bulletin of the American Meteorological Society*, 81 (7), 1537 - 1575, 2000.
- Galle, B., L. Klemetsson, and D.W.T. Griffith, Application of a Fourier transform IR system for measurements of N₂O fluxes using micrometeorological methods, an ultralarge chamber system, and conventional field chambers, *J. Geophys. Res.*, 99 (D8), 16,575-16,584, 1994.
- Galmarini, S., P.G. Duynkerke, and J. Vilà-Guerau de Arellano, Evolution of nitrogen oxide chemistry in the nocturnal boundary layer, *J. Appl. Meteo.*, 36 (7), 943 - 957, 1997.
- Ganzeveld, L.N., J. Lelieveld, F.J. Dentener, M.C. Krol, and G.J. Roelofs, Atmosphere-biosphere trace gas exchanges simulated with a single-column model, *Journal of Geophysical Research-Atmospheres*, 107 (D16), 4297, 2002.
- Gao, W., M.L. Wesely, and P.V. Doskey, Numerical Modeling of the Turbulent Diffusion and Chemistry of Nox, O₃, Isoprene, and Other Reactive Trace Gases in and above a Forest Canopy, *Journal of Geophysical Research-Atmospheres*, 98 (D10), 18339-18353, 1993.
- Gao, W., M.L. Wesely, and I.Y. Lee, A numerical study of the effects of air chemistry on fluxes of NO, NO₂, and O₃ near the surface, *J. Geophys. Res.*, 96, 18,761-18,770, 1991.
- Genthon, C., and A. Armengaud, Radon 222 as a comparative tracer of transport and mixing in two general circulation models of the atmosphere, *J. Geophys. Res.*, 100 (D2), 2849-2866, 1995.
- Gerecke, A., A. Thielmann, L. Gutzwiller, and M.J. Rossi, The chemical kinetics of HONO formation resulting from heterogeneous interaction of NO₂ with flame soot, *Geophys. Res. Lett.*, 25, 2453-2456, 1998.

- Geyer, A., Konzentrationsbestimmung des Nitratradikals und atmosphärischer Kohlenwasserstoffe mittels eines DOAS-Vielfachreflexionssystems in Heidelberg, Diploma thesis, University of Heidelberg, Heidelberg, 1997.
- Geyer, A., The importance of the nitrate radical in the planetary boundary layer, PhD thesis, University of Heidelberg, Heidelberg, 2000.
- Geyer, A., personal communication, 2004.
- Geyer, A., R. Ackermann, R. Dubois, B. Lohrmann, T. Müller, and U. Platt, Long-term observation of nitrate radicals in the continental boundary layer near Berlin, *Atmos. Environ.*, *35* (21), 3619 - 3631, 2001a.
- Geyer, A., B. Alicke, R. Ackermann, M. Martinez, H. Harder, B. Brune, E. Williams, T. Jobson, S.R. Hall, R. Shetter, and J. Stutz, Direct observations of daytime NO₃: Implications for urban boundary layer chemistry, *J. Geophys. Res.*, doi:10.1029/2002JD002967, 2003a.
- Geyer, A., B. Alicke, S. Konrad, T. Schmitz, J. Stutz, and U. Platt, Chemistry and oxidation capacity of the nitrate radical in the continental boundary layer near Berlin, *J. Geophys. Res.*, *106* (D8), 8013 - 8025, 2001b.
- Geyer, A., K. Bächmann, A. Hofzumahaus, F. Holland, S. Konrad, T. Klüpfel, H.W. Pätz, D. Perner, D. Mihelcic, H.J. Schäfer, A. Volz-Thomas, and U. Platt, Nighttime formation of peroxy and hydroxyl radicals during BERLIOZ - Observations and modeling studies, *J. Geophys. Res.*, *108* (D4), doi:10.1029/2001JD000656, 2003b.
- Geyer, A., and J. Stutz, Interaction of chemistry and vertical mixing: New insight in the development of the vertical profiles of NO₃, N₂O₅, and the NO-O₃-NO₂ system in the nocturnal boundary layer, *submitted to J. Geophys. Res.*, 2003.
- Goede, A.P.H., C.P. Tanzi, I. Aben, J.P. Burrows, M. Weber, D. Perner, P.S. Monks, D. Llewellyn-Jones, G.K. Corlett, D.W. Arlander, U. Platt, T. Wagner, K. Pfeilsticker, P. Taalas, H. Kelder, and A. Piters, GODIVA, a European project for ozone and trace gas measurements from GOME, in *Advances in Remote Sensing of the Atmosphere from Space and from the Ground*, pp. 951-954, 2000.
- Gomer, T., T. Brauers, F. Heintz, J. Stutz, and U. Platt, MFC User Manual V 1.98, Institut für Umweltphysik der Universität Heidelberg., Heidelberg, 1993.
- Goodman, A.L., G.M. Underwood, and V.H. Grassian, Heterogeneous reaction of NO₂: Characterization of gas-phase and adsorbed products from the reaction, 2 NO₂ (g)+H₂O(a)-> HONO(g)+NO₃(a) on hydrated silica particles, *Journal of Physical Chemistry a*, *103* (36), 7217-7223, 1999.
- Gormely, P.G., and M. Kennedy, Diffusion from a stream flowing through a cylindrical tube, *Proc. Roy. Irish Acad., Sec. A* (52), 163 - 169, 1949.
- Grassi, L., and R. Guzzi, Theoretical and practical consideration on the construction of a zero geometrical loss multi-pass cell based on the use of monolithic multiple-face retro-reflectors, *Appl. Opt.*, *40* (33), 6062-6071, 2001.
- Grassian, V.H., Heterogeneous uptake and reaction of nitrogen oxides and volatile organic compounds on the surface of atmospheric particles including oxides, carbonates, soot and mineral dust: implications for the chemical balance of the troposphere, *International Reviews in Physical Chemistry*, *20* (3), 467-548, 2001.
- Greenblatt, G.D., J.J. Orlando, J.B. Burkholder, and A.R. Ravishankara, Absorption measurements of oxygen between 330 and 1140nm, *J. Geophys. Res.*, *95*, 18577-18582, 1990.
- Guenther, A.B., P.R. Zimmerman, P.C. Harley, R.K. Monson, and R. Fall, Isoprene and Monoterpene Emission Rate Variability - Model Evaluations and Sensitivity Analyses, *J. Geophys. Res.*, *98*, 12609-12617, 1993.
- Gutzwiller, L., F. Arens, U. Baltensperger, H. Gaggeler, and M. Ammann, Significance of Semivolatile Diesel Exhaust Organics for Secondary HONO Formation, *Environ. Sci. Technol.*, *36*, 677 - 682, 2002.
- Hamba, F., Statistical analysis of chemically reacting passive scalars in turbulent flows, *J. Phys. Soc. Jpn.*, *56*, 79-96, 1987.
- Hamba, F., A modified K model for chemically reactive species in the planetary boundary layer, *J. Geophys. Res.*, *98* (D3), 5173-5182, 1993.
- Hamba, F., Reply to comment on: A modified K model for chemically reactive species in the planetary boundary layer, *J. Geophys. Res.*, *98* (D3), 5173-5182, 1994.
- Hammeed, S., and J. Dignon, Global emissions of nitrogen and sulfur oxides in fossil fuel combustion, *J. Air Waste Manage. Assoc.*, *42*, 159 - 163, 1992.
- Hanst, P.L., Air pollution measurement by fourier transform spectroscopy, *Appl. Opt.*, *17*, 1360-1366, 1978.
- Hanst, P.L., N.W. Wong, and J. Bragin, A long-path infra-red study of Los Angeles smog, *Atmos. Environ.*, *16*, 969-981, 1982.
- Harris, G.W., W.P.L. Carter, A.M. Winer, J.N. Pitts, U. Platt, and D. Perner, Observations of nitrous acid in the Los Angeles atmosphere and implications for the predictions of ozone-precursor relationships, *Environ. Sci. Technol.*, *16*, 414-419, 1982.

- Harrison, R.M., and G.M. Collins, Measurements of reaction coefficients of NO₂ and HONO on aerosol particles, *Journal of Atmospheric Chemistry*, 30 (3), 397-406, 1998.
- Harrison, R.M., and A.M.N. Kitto, Evidence for a Surface Source of Atmospheric Nitrous Acid, *Atmos. Environ.*, 28 (6), 1089-1094, 1994.
- Harrison, R.M., J.D. Peak, and G.M. Collins, Tropospheric Cycle of Nitrous Acid, *Journal of Geophysical Research-Atmospheres*, 101 (D9), 14429-14439, 1996.
- Haugen, D.A., *Workshop on Micrometeorology*, A. Haugen, Eprata, 1973.
- Hausmann, M., U. Brandenburger, T. Brauers, and H.-P. Dorn, Simple Monte Carlo methods to estimate the spectra evaluation error in DOAS, *Applied optics*, 38 (3), 462-475, 1999.
- Heland, J., J. Kleffmann, R. Kurtenbach, and P. Wiesen, A new instrument to measure gaseous nitrous acid (HONO) in the atmosphere, *Environ. Sci. Technol.*, 35 (15), 3207-3212, 2001.
- Hermes, T., *Lichtquellen und Optik für die Differentielle Optische Absorptionsspektroskopie*, Diploma thesis, University of Heidelberg, Heidelberg, 1999.
- Hofzumahaus, A., U. Aschmutat, U. Brandenburger, T. Brauers, H.P. Dorn, M. Hausmann, M. Hessling, F. Holland, C. Plass-Dulmer, and D.H. Ehhalt, Intercomparison of tropospheric OH measurements by different laser techniques during the POPCORN campaign 1994, *Journal of Atmospheric Chemistry*, 31 (1-2), 227-246, 1998.
- Hofzumahaus, A., T. Brauers, U. Aschmutat, U. Brandenburger, H.P. Dorn, M. Hausmann, M. Hessling, F. Holland, C. Plass-Dülmer, M. Sedlacek, M. Weber, and D.H. Ehhalt, The measurement of tropospheric OH radicals by laser-induced fluorescence spectroscopy during the POPCORN field campaign and Intercomparison of tropospheric OH radical measurements by multiple folded long-path laser absorption and laser induced fluorescence - Reply, *Geophysical Research Letters*, 24 (23), 3039-3040, 1997.
- Hofzumahaus, A., A. Kraus, and M. Muller, Solar actinic flux spectroradiometry: a technique for measuring photolysis frequencies in the atmosphere, *Appl. Optics*, 38 (21), 4443-4460, 1999.
- Holland, F., U. Aschmutat, M. Hessling, A. Hofzumahaus, and D.H. Ehhalt, Highly time resolved measurements of OH during POPCORN using laser-induced fluorescence spectroscopy, *J. Atmos. Chem.*, 31 (1-2), 205-225, 1998.
- Holland, F., M. Hessling, and A. Hofzumahaus, In-Situ Measurement of Tropospheric OH Radicals by Laser-Induced Fluorescence - a Description of the KFA Instrument, *J. Atmos. Sciences*, 52, 3393-3401, 1995.
- Holland, F., A. Hofzumahaus, and J. Schäfer, Measurements of OH and HO₂ Radical concentrations during BERLIOZ by Laser Induced Fluorescence Spectroscopy, *J. Geophys. Res.*, 108 (D4), 8246, doi:10.1029/2001JD001393, 2001.
- Holland, F., A. Hofzumahaus, J. Schäfer, A. Kraus, and H.-W. Pätz, Measurements of OH and HO₂ radical concentrations and photolysis frequencies during BERLIOZ, *J. Geophys. Res.*, 108 (D4), 8246, doi:10.1029/2001JD001393, 2003.
- Hönninger, G., MAXDOAS: First application for boundary layer bromine oxide studies and comparison with LP-DOAS, PhD thesis, Universität Heidelberg, Heidelberg, 2001.
- Honrath, R.E., Y. Lu, M.C. Peterson, J.E. Dibb, M.A. Arsenault, N.J. Cullen, and K. Steffen, Vertical fluxes of NO_x; HONO, and HNO₃ above the snowpack at Summit, Greenland, *Atmos. Environ.*, 36, 2629 - 2640, 2002.
- Hoshino, M., T. Ogata, H. Akimoto, G. Inoue, F. Sakamaki, and M. Okuda, Gas Phase Reactions of N₂O₅ with Propylene, *Chemistry Letters, Chem. Soc. of Japan*, 1367-1370, 1978.
- Howard, C.J., Kinetics of the Reaction of HO₂ with NO₂, *J. Chem. Phys.*, 67, 5258-5263, 1977.
- Hulst, H.C.v.d., *Light scattering by small particles*, Wiley, New York, 1957.
- Inoue, E., On the turbulent structure of airflow within crop canopies, *J. Met. Soc. Japan*, 49, 121 - 124, 1963.
- Jacob, D.J., Heterogeneous chemistry and tropospheric ozone, *Atmos. Environ.*, 34 (12-14), 2131-2159, 2000.
- Jacobi, W., and K. André, The vertical distribution of radon 222, radon 220 and their decay products in the Atmosphere, *J. Geophys. Res.*, 63 (13), 3799-3814, 1963.
- Jenkin, M.I., R.A. Cox, and D.J. Williams, Laboratory studies of the kinetics of formation of nitrous acid from the thermal reaction of nitrogen dioxide and water vapour, *Atmos. Environ.*, 22, 487-498, 1988.
- Johnston, H.S., Reduction of stratospheric ozone by nitrogen oxide catalyst from supersonic transport exhaust, *Science*, 173, 517-522, 1971.
- Junkermann, W., and T. Ibusuki, FTIR Spectroscopic Measurements of Surface Bond Products of Nitrogen Oxides On Aerosol Surfaces - Implications For Heterogeneous HNO₂ Production, *Atmospheric Environment Part a-General Topics*, 26 (17), 3099-3103, 1992.
- Kah, O., *Spektroskopische Langzeitmessung von NO₂, SO₂, O₃, HCHO und HONO in Heidelberg*, Diploma thesis, Universität Heidelberg, Heidelberg, 1998.
- Kaiser, E.W., and C.H. Wu, A kinetic study of the gas phase formation and decomposition reactions of nitrous acid, *J. Phys. Chem.*, 81, 1701-1706, 1977a.

- Kaiser, E.W., and C.H. Wu, Measurement of the rate constant of the reaction of nitrous acid with nitric acid, *J. Phys. Chem.*, *81*, 187-190, 1977b.
- Kalberer, M., M. Ammann, F. Arens, H.W. Gaggeler, and U. Baltensperger, Heterogeneous formation of nitrous acid (HONO) on soot aerosol particles, *Journal of Geophysical Research-Atmospheres*, *104* (D11), 13825-13832, 1999.
- Kanda, Y., and M. Taira, Chemiluminescent Method For Continuous Monitoring of Nitrous Acid in Ambient Air, *Analytical Chemistry*, *62* (19), 2084-2087, 1990.
- Kanda, Y., and M. Taira, Simultaneous Determination of Atmospheric Nitric Acid and Nitrous Acid By Reduction With Hydrazine and Ascorbic Acid With Chemiluminescence Detection, *Analyst*, *117* (5), 883-887, 1992.
- Kern, C., G. Balschbach, and S. Trick, personal communication, 2002.
- Kessler, C., Gasformige salpetrige Säure (HNO₂) in der belasteten Atmosphäre, PhD thesis, University of Cologne, 1984.
- Kessler, C., and U. Platt, Nitrous acid in polluted air masses - Sources and formation pathways, in *Physico-chemical behaviour of atmospheric pollutants*, edited by B. Versino, and G. Angeletti, D. Reidel, Varese, Italia, 1984.
- Keyser, L.F., S.B. Moore, and M.-T. Leu, Surface reaction and pore diffusion in flow tube reactors, *J. of Phys. Chem.*, *95*, 5496 - 5502, 1991.
- Killus, J.P., and G.Z. Whitten, Behavior of trace NO_x species in the nighttime urban atmosphere, *J. Geophys. Res.*, *90*, 2430-2432, 1985.
- Kirchner, U., V. Scheer, and R. Vogt, FTIR Spectroscopic Investigation of the Mechanism and Kinetics of the Heterogeneous Reactions of NO₂ and HNO₃ with Soot, *J. Phys. Chem. A*, *104*, 8908 - 8915, 2000.
- Kirchstetter, T.W., R.A. Harley, and D. Littlejohn, Measurement of Nitrous Acid in Motor Vehicle Exhaust, *Environmental Science & Technology*, *30* (9), 2843-2849, 1996.
- Kleffmann, J., Heterogene Umwandlung von Stickoxiden an sauren Oberflächen, PhD thesis, University of Wuppertal, Wuppertal, 1998.
- Kleffmann, J., K.H. Becker, and P. Wiesen, Heterogeneous NO₂ conversion processes on acid surfaces: possible atmospheric implications, *Atmos. Environ.*, *32*, 2721 - 2729, 1998.
- Kleffmann, J., J. Heland, R. Kurtenbach, J. Lörzer, and P. Wiesen, A new instrument for the Detection of Nitrous Acid (HONO), *Environ. Sci. & Pollut. Res.* (Special Issue 4), 48 - 54, 2002.
- Kleffmann, J., R. Kurtenbach, J. Lörzer, P. Wiesen, N. Kalthoff, B. Vogel, and H. Vogel, Measured and simulated vertical profiles of nitrous acid - Part I: Field measurements, *Atmos. Environ.*, *37*, 2949 - 2955, 2003.
- Kleffmann, J., R. Kurtenbach, and P. Wiesen, Surface catalysed conversion of NO₂ into HONO and N₂O: a new source of atmospheric N₂O?, in *Impact of Emissions from aircraft and Spacecraft upon the Atmosphere*, pp. 146-157, Porz-Wahnheide, Cologne, Germany, 1994.
- Kleinman, L., Y.-N. Lee, S.R. Springston, J.H. Lee, L. Nunnermacker, J. Weinstein-Lloyd, X. Zhou, and L. Newman, Peroxy radical concentration and ozone formation rate at a rural site in the southeastern United States, *J. Geophys. Res.*, *100* (D4), 7263-7274, 1995.
- Klepper, L., Nitric oxide (NO) and nitrogen dioxide (NO₂) emissions from herbicide-treated soybean plants, *Atmos. Environ.*, *13*, 537-542, 1979.
- Knoll, P., R. Singer, and W. Kiefer, Improving spectroscopic techniques by a scanning multichannel method, *Appl. Spectr.*, *44*, 776 - 782, 1990.
- Komiyama, H., and H. Inoue, Reaction and transport of nitrogen oxides in nitrous acid solutions, *J. Chem. Eng. Japan*, *11*, 25-32, 1978.
- Komiyama, H., and H. Inoue, Absorption of nitrogen oxides into water, *Chem. Eng. Sci.*, *35*, 154-161, 1980.
- Kotamarthi, V.R., J.S. Gaffney, N.A. Marley, and P.V. Doskey, Heterogeneous NO_x chemistry in the polluted PBL, *Atmospheric Environment*, *35* (26), 4489-4498, 2001.
- Koutrakis, P., C. Sioutas, S.T. Ferguson, J.M. Wolfson, J.D. Mulik, and R.M. Burton, Development and Evaluation of a Glass Honeycomb Denuder Filter Pack System to Collect Atmospheric Gases and Particles, *Environmental Science & Technology*, *27* (12), 2497-2501, 1993.
- Kraus, A., and A. Hofzumahaus, Field measurements of atmospheric photolysis frequencies for O₃, NO₂, HCHO, CH₃CHO, H₂O₂, and HONO by UV spectroradiometry, *Journal of Atmospheric Chemistry*, *31* (1-2), 161-180, 1998.
- Krieger, M.S., and R.A. Hites, Diffusion Denuder for the Collection of Semivolatile Organic Compounds, *Environmental Science & Technology*, *26* (8), 1551-1555, 1992.
- Kurtenbach, R., R. Ackermann, K.H. Becker, A. Geyer, J.A.G. Gomes, J.C. Lörzer, U. Platt, and P. Wiesen, Verification of the contribution of vehicular traffic to the total NMVOC emissions in Germany and the importance of the NO₃ chemistry in the city air, *J. Atmos. Chem.*, *42*, 395-411, 2002.

- Kurtenbach, R., K.H. Becker, J.A.G. Gomes, J. Kleffmann, J.C. Lorzer, M. Spittler, P. Wiesen, R. Ackermann, A. Geyer, and U. Platt, Investigations of emissions and heterogeneous formation of HONO in a road traffic tunnel, *Atmos. Environ.*, *35* (20), 3385-3394, 2001.
- Lammel, G., Formation of Nitrous Acid: Parameterization and Comparison with Observations, pp. 1 - 36, Max-Planck-Institut-für Meteorologie, Hamburg, 1999.
- Lammel, G., and J.N. Cape, Nitrous acid and nitrite in the atmosphere, *Chemical Society Reviews*, *25* (5), 361+, 1996.
- Lammel, G., and D. Perner, The atmospheric aerosol as a source of nitrous acid in the polluted atmosphere, *J. Aerosol Sci.*, *19*, 1199-1202, 1988.
- Langmuir, I., *J. Am. Chem. Soc.*, *40*, 1361, 1918.
- Lee, J.H., and I.N. Tang, Accommodation coefficient of gaseous NO₂ on water surfaces, *Atmos. Environ.*, *22*, 1147-1151, 1988.
- Lee, K., J. Xue, A.S. Geyh, H. Ozkaynak, B.P. Leaderer, C.J. Weschler, and J.D. Spengler, Nitrous acid, nitrogen dioxide, and ozone concentrations in residential environments, *Environmental Health Perspectives*, *110* (2), 145 - 150, 2002.
- Lee, Y.N., and S.E. Schwartz, Evaluation of the rate of uptake of nitrogen dioxide by atmospheric and surface liquid water, *J. Geophys. Res.*, *86*, 11,971-11,983, 1981a.
- Lee, Y.N., and S.E. Schwartz, Reaction Kinetics of Nitrogen Dioxide with liquid water at low partial pressure, *J. Phys. Chem.*, *85*, 840-848, 1981b.
- Leighton, P.A., Photochemistry of air pollution, *Academic Press, New York*, 1961.
- Lendzian, K.J., and J. Kahlert, Interactions between nitrogen dioxide and plant cuticles: Binding to cuticular structures, *Plant physiol. (Life Sci. Adv.)*, *7*, 197 - 207, 1988.
- Lennard-Jones, J.E., and A.F. Devonshire, *Proc. Roy. Soc.*, *A156* (6), 29, 1936.
- Lenner, M., Nitrogen dioxide in exhaust emission from motor vehicles, *Atmos. Environ.*, *27*, 1673 - 1690, 1987.
- Lenner, M., O. Lindqvist, and A. Rosen, The NO₂/NO_x ratio in emissions from gasoline-powered cars: High NO₂ percentage in idle engine measurements, *Atmos. Environ.*, *17*, 1395-1398, 1983.
- Lenschow, D., Reactive trace species in the boundary layer from a micrometeorological perspective, *J. Phys. Soc. Jpn.*, *60*, 472-480, 1981.
- Lenschow, D.H., R. Pearson, B.B. Stankov, and Vertikalfluá, Measurements of ozone vertical flux to ocean and forest, *J. Geophys. Res.*, *87*, 8833-8837, 1982.
- Leue, C., M. Wenig, T. Wagner, O. Klimm, U. Platt, and B. Jahne, Quantitative analysis of NO_x emissions from Global Ozone Monitoring Experiment satellite image sequences, *Journal of Geophysical Research-Atmospheres*, *106* (D6), 5493-5505, 2001.
- Levenberg, K., A method for the solution of certain non-linear problems in least squares, *Quart. Appl. Math.*, *2*, 164 -168, 1944.
- Levin, I., personal communication, , 2003.
- Levin, I., M. Born, M. Cuntz, U. Langendörfer, S. Mantsch, T. Naegler, M. Schmidt, A. Varlagin, S. Verclas, and D. Wagenbach, Observations of atmospheric variability and soil exhalation rate of Radon-222 at Russian forest site: Technical approach and deployment for boundary layer sites, *Tellus*, *54B*, 462 - 475, 2002.
- Levy, H., Photochemistry of minor constituents in the troposphere, *Planet. Space Sci.*, *21*, 575-591, 1973.
- Levy, H., and J.D. Mahlman, *Modeling Tropospheric N₂O*, 1980.
- Levy, H., J.D. Mahlman, and W.J. Moxim, A stratospheric source of reactive nitrogen in the unpolluted troposphere, *Geophys. Res. Let.*, *7*, 441 - 444, 1980.
- Levy, H., W.J. Moxim, and P.S. Kasibhatla, A global three- dimensional time- dependent lightning source of tropospheric NO_x, *J. Geophys. Res.*, *101*, 22911-22922, 1996.
- Li, S.-M., Equilibrium of particle nitrite with gas phase HONO: Tropospheric measurements in the high Arctic during polar sunrise, *J. Geophys. Res.*, *99* (D12), 25,469-25,478, 1994.
- Liu, S.C., J.R. McAfee, and R.J. Cicerone, Radon 222 and tropospheric vertical transport, *J. Geophys. Res.*, *89*, 7291-7297, 1984.
- Logan, J.A., Nitrogen Oxides in the troposphere: global and regional budgets, *J. Geophys. Res.*, *88* (C15), 10785 - 10807, 1983.
- Logan, J.I., M.J. Prather, S.C. Wofsy, and M.B. McElroy, Tropospheric Chemistry: A Global Perspective, *J. Geophys. Res.*, *86* (C8), 7210 - 7254, 1981.
- Longfellow, C., A. Ravishankara, and D. Hanson, Reactive and nonreactive uptake on hydrocarbon soot: HNO₃, O₃, and N₂O₅, *Journal of geophysical research - atmospheres*, *105* (D19), 24,345 - 24,350, 2000.
- Longfellow, C.A., T. Imamura, A.R. Ravishankara, and D.R. Hanson, HONO solubility and heterogeneous reactivity on sulfuric acid surfaces, *Journal of Physical Chemistry a*, *102* (19), 3323-3332, 1998.
- Lösch, J., Bestimmung von NO₂- und SO₂- Emissionen von Kraftfahrzeugen mittels DOAS-Tomographie, Diploma thesis, Universität Heidelberg, Heidelberg, 2001.

- Lovett, G.M., Atmospheric deposition of nutrients and pollutants in north america: an ecological perspective, *Ecol. Appl.*, 4, 629 - 650, 1994.
- Lu, X., J. Park, and M.C. Lin, Gas Phase Reactions of HONO with NO₂, O₃, and HCl: Ab Initio and TST Study, *J. Phys. Chem. A*, 104, 8730 - 8738, 2000.
- Mahrt, L., J. Sun, W. Blumen, T. Delany, and S. Oncley, Nocturnal boundary-layer regimes, *Boundary-Layer Meteorology*, 88 (2), 255 - 278, 1998.
- Marquardt, D.W., An algorithm for least squares estimation of non-linear parameters, *J. Soc. Indust. Appl. Math.*, 11, 431 - 441, 1963.
- McDonald-Buller, E.C., H.M. Liljestrang, and K. Sepehrnoori, Numerical modeling of dry deposition coupled to 22 photochemical reactions, *Atmos. Environ.*, 33 (10), 1491-1502, 1999.
- Mebel, A.M., M.C. Lin, and C.F. Melius, Rate constant of the HONO+HONO->H₂O+NO+NO₂ reaction from ab initio MO and TST calculations, *Journal of Physical Chemistry a*, 102 (10), 1803-1807, 1998.
- Meller, R., and G.K. Moortgat, Temperature dependence of the absorption cross sections of formaldehyde between 223 and 323 K in the wavelength range 225 - 375 nm, *JGR*, 201 (D6), 7089 - 7101, 2000.
- Mentel, T., D. Bleilebens, and A. Wahner, A Study of Nighttime Nitrogen Oxide Oxidation in a Large Reaction Chamber - the Fate of NO₂ N₂O₅ HNO₃, and O₃ at Different humidities, *Atmospheric Environment*, 30 (23), 4007 - 4020, 1996.
- Mertes, S., and A. Wahner, Uptake of nitrogen dioxide and nitrous acid on aqueous surfaces, *J. Phys. Chem.*, 99, 14000-14006, 1995.
- Middleton, J.T., J.B.K. jr., and H.W. Schwalm, Injury to herbaceous plants by smog or air pollution, *U.S.D.A. Plant Dis. Rep.*, 34, 245 - 252, 1950.
- Mihelcic, D., F. Holland, A. Hofzumahaus, L. Hoppe, S. Konrad, P. Müsgen, H.-W. Pätz, H.-J. Schäfer, T. Schmitz, A. Volz-Thomas, K. Bächmann, S. Schlomski, U. Platt, A. Geyer, B. Alicke, and G. Moortgat, Peroxy radicals during BERLIOZ at Pabstthum: Measurements, radical budgets and ozone production, *J. Geophys. Res.*, 108 (D4), 8254, doi:10.1029/2001JD001014, 2003.
- Mochida, M., and B.J. Finlayson-Pitts, FTIR studies of the reaction of gaseous NO with HNO₃ on porous glass: Implications for conversion of HNO₃ to photochemically active NO_x in the atmosphere, *Journal of Physical Chemistry*, 104 (43), 9705-9711, 2000.
- Morris, E.D., and H. Niki, Reaction of the nitrate radical with acetaldehyde and propylene, *J. Phys. Chem.*, 78, 1337-1338, 1974.
- Moussiopoulos, N., S. Papalexiou, G. Lammel, and T. Arvanitis, Simulation of nitrous acid formation taking into account heterogeneous pathways: application to the Milan metropolitan area, *Environmental Modelling & Software*, 15, 629 - 637, 2000.
- Muller, M., A. Kraus, and A. Hofzumahaus, Photolysis Frequencies Determined From Spectroradiometric Measurements of Solar Actinic Uv-Radiation - Comparison With Chemical Actinometer Measurements, *Geophysical Research Letters*, 22 (6), 679-682, 1995.
- Murray, F.W., On the Computation of Saturation Vapor Pressure, *J. Appl. Meteor.*, 6, pp. 204, 1966.
- Nash, T., Nitrous acid in the atmosphere and laboratory experiments on its photolysis, *Tellus*, 26, 175-179, 1974.
- Navas, M.J., A.M. Jimenez, and G. Galan, Air analysis: Determination of nitrogen compounds by chemiluminescence, *Atmos. Environ.*, 31, 3603 - 3608, 1997.
- Nazaroff, W.W., Radon transport from soil to air, *Reviews of Geophysics*, 30, 137-160, 1992.
- Nefel, A., A. Blatter, R. Hesterberg, and T. Staffelbach, Measurements of Concentration Gradients of HNO₂ and HNO₃ Over a Semi-Natural Ecosystem, *Atmos. Environ.*, 30 (17), 3017-3025, 1996.
- Nguyen, M.T., R. Sumathi, D. Sengupta, and J. Peeters, Theoretical analysis of reactions related to the HNO₂ energy surface: OH+NO and H+NO₂, *Chemical Physics*, 230 (1), 1-11, 1998.
- Nielsen, T., K. Plinegaard, A.H. Egelov, K. Granby, P. Hummelshoj, N.O. Jensen, and H. Skov, Atmospheric nitrogen compounds: occurrence, composition and deposition, *Sci. Total. Environ.*, 189/190, 459-465, 1996.
- Notholt, J., J. Hjorth, and F. Raes, Formation of HNO₂ on aerosol surfaces during foggy periods in the presence of NO and NO₂, *Atmos. Environ.*, 26A, 211-217, 1992.
- Pagsberg, P., E. Bjergbakke, E. Ratajczak, and A. Sillesen, Kinetics of the gas phase reaction OH+NO(+M)->HONO(+M) and the determination of the UV absorption cross sections of HONO, *Chemical Physics Letters*, 272 (5-6), 383-390, 1997.
- Parrish, D.D., and F.C. Fehsenfeld, Methods for gas-phase measurements of ozone, ozone precursors and aerosol precursors, *Atmospheric Environment*, 34 (12-14), 1921-1957, 2000.
- Parrish, D.D., M. Trainer, E.J. Williams, D.W. Fahey, G. Huebler, C.S. Eubank, S.C. Liu, P.C. Murphy, D.L. Albritton, and F.C. Fehsenfeld, Measurements of the NO_x-O₃ photostationary state at Niwot Ridge, Colorado, *J. Geophys. Res.*, 91, 5361-5370, 1986.
- Paulson, C.A., The mathematical presentation of wind speed and temperature profiles in the unstable atmospheric surface layer, *J. Appl. Meteorolog.*, 9, 857 - 861, 1970.

- Paulson, S.E., M.Y. Chung, and A.S. Hasson, OH radical formation from the gas-phase reaction of ozone with terminal alkenes and the relationship between structure and mechanism, *J. Phys. Chem. A*, *103* (41), 8125-8138, 1999.
- Paulson, S.E., and J.J. Orlando, The reactions of ozone with alkenes: an important source of HO_x in the boundary layer, *Geophys. Res. Lett.*, *23* (25), 3727-30, 1996.
- Paulson, S.E., A.D. Sen, L. Ping, J.D. Fenske, and M.J. Fox, Evidence for formation of OH radicals from the reaction of O₃ with alkenes in the gas phase, *Geophys. Res. Lett.*, *24* (24), 3193-6, 1997.
- Perner, D., D.H. Ehhalt, H.W. Paetz, U. Platt, E.P. Roeth, and A. Volz, OH radicals in the lower troposphere, *Geophys. Res. Lett.*, *3*, 466-468, 1976.
- Perner, D., C. Kessler, and U. Platt, *HNO₂, NO₂, and NO measurements in automobile engine exhaust by optical absorption*, 116-119 pp., 1985.
- Perner, D., and U. Platt, Detection of nitrous acid in the atmosphere by differential optical absorption, *Geophys. Res. Lett.*, *6*, 917-920, 1979.
- Perrino, C., A. Pietrodangelo, and A. Febo, An atmospheric stability index based on radon progeny measurements for the evaluation of primary urban pollution, *Atmos. Environ.*, *35* (31), 5235-5244, 2001.
- Perrino, C., F.D. Santis, and A. Febo, Criteria for the choice of a denuder sampling technique devoted to the measurement of atmospheric nitrous and nitric acids, *Atmos. Environ.*, *24 A*, 617-626, 1990.
- Pfeilsticker, K., C.E. Blom, R. Brandtjen, H. Fischer, N. Glatthor, A. Grendel, T. Gulde, M. Hüpfner, D. Perner, C. Piesch, U. Platt, W. Renger, J. Sessler, and M. Wirth, Aircraft-borne detection of stratospheric column amounts of O₃, NO₂, OCIO, ClNO₃, HNO₃, and aerosols around the arctic vortex (79°N to 39°N) during spring 1993. 1. observational data, *J. Geophys. Res.*, *102*, 10801-10814, 1997.
- Pfeilsticker, K., and U. Platt, Airborne measurements during the Arctic stratospheric experiment: Observation of O₃ and NO₂, *Geophys. Res. Lett.*, *21* (13), 1375-1378, 1994.
- Pitts, J.N., H.W. Biermann, A.M. Winer, and E.C. Tuazon, Spectroscopic identification and measurement of gaseous nitrous acid in dilute auto exhaust, *Atmos. Environ.*, *18*, 847-854, 1984a.
- Pitts, J.N., E. Sanhueza, R. Atkinson, W.P.L. Carter, A.M. Winer, G.W. Harris, and C.N. Plum, An investigation of the dark formation of nitrous acid in environmental chambers, *Int. J. Chem. Kinet.*, *XVI*, 919-939, 1984b.
- Pitts, J.N., E. Sanhueza, R. Atkinson, W.P.L. Carter, A.M. Winer, G.W. Harris, and C.N. Plum, An investigation of the dark formation of nitrous acid in environmental chambers, *Int. J. Chem. Kinet.*, *XVI*, 919-939, 1984c.
- Pitts, J.N., T.J. Wallington, H.W. Biermann, and A.M. Winer, Identification and measurement of nitrous acid in an indoor environment, *Atmos. Environ.*, *19*, 763-767, 1985.
- Pitts, J.N.j., H.W. Biermann, R. Atkinson, and A.M. Winer, Atmospheric implications of simultaneous nighttime measurements of NO₃ radicals and HONO, *Geophys. Res. Lett.*, *11*, 557 - 560, 1984d.
- Pitts, J.N.j., D. Grosjean, K.v. Cauwenberghe, J.P. Schmid, and D.R. Fitz, Photooxidation of aliphatic amines under simulated atmospheric conditions: Formation of nitrosamines, nitramines, amides and photochemical oxidant, *Env. Science & Technology*, *12* (8), 946 - 953, 1978.
- Platt, U., *The origin of nitrous and nitric acid in the atmosphere*, 299-319 pp., W. Jaeschke, Springer Verlag, 1986.
- Platt, U., Differential Optical Absorption Spectroscopy (DOAS), in *Monitoring by Spectroscopic Techniques*, M. W. Sigrist, J. Wiley, New York, 1994.
- Platt, U., and D. Perner, Direct measurements of atmospheric CH₂O, HNO₂, O₃, NO₂, and SO₂ by differential optical absorption in the near UV, *J. Geophys. Res.*, *85*, 7453-7458, 1980.
- Platt, U., D. Perner, G.W. Harris, A.M. Winer, and J.N. Pitts, Observations of nitrous acid in an urban atmosphere by differential optical absorption, *Nature*, *285*, 312-314, 1980.
- Platt, U., D. Perner, and H.W. Pätz, Simultaneous measurements of atmospheric CH₂O, O₃ and NO₂ by differential optical absorption, *J. Geophys. Res.*, *84*, 6329 - 6335, 1979.
- Preszler-Prince, A., J.L. Wade, V.H. Grassiana, P.D. Kleiberb, and M.A. Younga, Heterogeneous reactions of soot aerosols with nitrogen dioxide and nitric acid: atmospheric chamber and Knudsen cell studies, *Atmos. Environ.*, *36*, 5729 - 5740, 2002.
- Price, C., J. Penner, and M. Prather, NO_x from lightning. 1. Global distribution based on lightning physics, *Journal of Geophysical Research*, *102* (D5), 5929-41, 1997a.
- Price, C., J. Penner, and M. Prather, NO_x from lightning. 2. Constraints from the global atmospheric electric circuit, *Journal of Geophysical Research*, *102* (D5), 5943-51, 1997b.
- Prinn, R.G., R.F. Weiss, B.R. Miller, J. Huang, F.N. Alyea, D.M. Cunnold, P.J. Fraser, D.E. Hartley, and P.G. Simmonds, Atmospheric Trends and Lifetime of CH₃CCl₃ and Global OH Concentrations, *Science*, *269* (5221), 187-192, 1995.
- Ramazan, K.A., D. Syomin, and B.J. Finlayson-Pitts, Photoenhancement or photodepression of the hydrolysis of NO₂: Implications for the chemistry of polluted atmospheres, *in preparation*, 2003.

- Rao, K.S., and H.F. Snodgrass, Some parametrizations of the nocturnal boundary layer, *Bound.-Layer Meteor.*, *17*, 15-28, 1979.
- Rasmussen, T.R., M. Brauer, and S. Kjaergaard, Effects of Nitrous Acid Exposure On Human Mucous Membranes, *American Journal of Respiratory and Critical Care Medicine*, *151* (5), 1504-1511, 1995.
- Reichardt, H., Vollstaendige Darstellung der turbulenten Geschwindigkeitsverteilung in glatten Leitungen, *Z. Angew. Math. Mech.*, *31*, 208-219, 1951.
- Reisinger, A.R., Observations of HNO₂ in the polluted winter atmosphere: possible heterogeneous production on aerosols, *Atmospheric Environment*, *34*, 3864-3874, 2000.
- Ren, X., H. Harder, M. Martinez, R.L. Lesher, A. Oligier, T. Shirley, J. Adams, J.B. Simpas, and W.H. Brune, HO_x concentrations and OH reactivity observations in New York City during PMTACS-NY2001, *Atmos. Environ.*, *37*, 3627 – 3637, 2003.
- Ritz, D., M. Hausmann, and U. Platt, An improved open multi-path reflection cell for the measurement of NO₂ and NO₃, in *Optical Methods in Atmospheric Chemistry*, edited by H. Schiff, and U. Platt, pp. 200 - 211, Proc. SPIE, 1992.
- Rivera-Figueroa, A.M., A.L. Sumner, and B.J. Finlayson-Pitts, Laboratory studies of potential mechanisms of renoxification of tropospheric nitric acid, *Environmental Science & Technology*, *37* (3), 548-554, 2003.
- Rivett, A.C., D. Martin, G. Nickless, P.G. Simmonds, S.J. O'Doherty, D.J. Gray, and D.E. Shallcross, In situ gas chromatographic measurements of halocarbons in an urban environment, *Atmos. Environ.*, *37*, 2221 - 2235, 2003.
- Rodgers, M.O., and D.D. Davis, A UV-Photofragmentation/Laser-Induced Fluorescence Sensor for the Atmospheric Detection of HONO, *Environ. Sci. Technol.*, *23*, 1106-1112, 1989.
- Roedel, W., *Physik unserer Umwelt: Die Atmosphäre*, Springer Verlag, Berlin Heidelberg New York, 1994.
- Rondon, A., and E. Sanhueza, High HONO atmospheric concentrations during vegetation burning in the tropical savannah, *Tellus*, *41B*, 474-477, 1988.
- Rudich, Y., R. Talukdar, and A.R. Ravishankara, Reactive uptake of NO₃ on pure water and ionic solutions, *Journal of Geophysical Research*, *D101*, 21023 - 21031, 1996.
- Rudolf, T., Beschreibung und Charakterisierung einer Lang-Pfad-DOAS-Apparatur und eine Analyse des Auswerteverfahrens, Diploma thesis, Universität Heidelberg, Heidelberg, 1993.
- Russell, A.G., D.A. Winner, R.A. Herley, K.F. McCue, and G.R. Cass, Mathematical modeling and control of the dry deposition flux of nitrogen-containing air pollutants, *Environ. Sci. Technol.*, *27*, 2772-2782, 1993.
- Sakamaki, F., S. Hatakeyama, and H. Akimoto, Formation of nitrous acid and nitric oxide in the heterogeneous dark reaction of nitrogen dioxide and water vapor in a smog chamber, *Int. J. Chem. Kinet.*, *XV*, 1013-1029, 1983.
- Saliba, N.A., M. Mochida, and B.J. Finlayson-Pitts, Laboratory studies of sources of HONO in polluted urban atmospheres, *Geophysical Research Letters*, *27* (19), 3229-3232, 2000.
- Saliba, N.A., H. Yang, and B.J. Finlayson-Pitts, Reaction of gaseous nitric oxide with nitric acid on silica surfaces in the presence of water at room temperature, *Journal of Physical Chemistry*, *105* (45), 10339-10346, 2001.
- Sander, R., MOCCA and Mokka User Manual for Version 66, Mainz, 2001.
- Sander, S.P., R.R. Friedl, D.M. Golden, M.J. Kurylo, R.E. Huie, V.L. Orkin, G.K. Moortgat, A.R. Ravishankara, C.E. Kolb, M.J. Molina, and B.J. Finlayson-Pitts, Chemical Kinetics and Photochemical Data for Use in Atmospheric Studies - Eval. No. 14, NASA-JPL, Pasadena, CA, 2003.
- Schneider, W., G.K. Moortgat, G.S. Tyndall, and J.P. Burrows, Absorption cross-sections of NO₂ in the UV and visible region (299-700nm) at 298K, *J. Photochem. Photobiol.*, *40A*, 195 - 217, 1987.
- Schumann, U., Large-eddy simulation of turbulent diffusion with chemical reactions in the convective boundary layer, *Atmos. Environ.*, *23* (8), 1713-1727, 1989.
- Schurath, personal communication, , 2000.
- Schwartz, S.E., and W. White, *Kinetics of the reactive dissolution of the nitrogen oxides and oxyacides in aqueous solution*, Brookhaven Nat. Lab., 1981a.
- Schwartz, S.E., and W.H. White, Solubility equilibria of the nitrogen oxides and oxyacids in dilute aqueous solution, *Advances In Environmental Science And Engineering*, *4*, 1-45, 1981b.
- Seinfeld, J.H., and S.N. Pandis, *Atmospheric chemistry and physics: From air pollution to climate change*, John Wiley & Sons Inc., New York Chichester Weinheim Brisbane Singapore Toronto, 1998.
- Shaw, R.W., *The Atmosphere as Delivery Vehicle and Reaction Chamber for Acid Precipitation*, 33- 55 pp., J.L. Teasly, Butterworth, Stoneham / MA, 1984.
- Sjödin, A., Studies of the diurnal variation of nitrous acid in urban air, *Environ. Sci. Technol.*, *22*, 1086-1089, 1988.
- Sjödin, A., and M. Ferm, Measurement of nitrous acid in an urban area, *Atmos. Environ.*, *19*, 985-992, 1985.

- Spicer, C.W., D.V. Kenny, E. Chapman, K.M. Busness, and C.M. Berkowitz, Observation of dimethyl sulfide over the western North Atlantic Ocean using an airborne tandem mass spectrometer, *J. Geophys. Res.*, *101* (D22), 29137 - 29147, 1996.
- Spicer, C.W., D.V. Kenny, G.F. Ward, and I.H. Billick, Transformations, Lifetimes, and Sources of NO₂, HONO, and HNO₃ in Indoor Environments, *Journal of the Air & Waste Management Association*, *43* (11), 1479-1485, 1993.
- Spichtinger, N., M. Wenig, P. James, T. Wagner, U. Platt, and A. Stohl, Satellite detection of a continental-scale plume of nitrogen oxides from boreal forest fires, *Geophysical Research Letters*, *28* (24), 4579-4582, 2001.
- Spindler, G., E. Brüggemann, and H. Herrmann, Nitrous acid concentration measurements and estimation of dry deposition over grassland in Eastern Germany, in *EUROTRAC Symposium*, edited by P.M. Borrell, and P. Borrell, pp. 218-222, WIT, Boston, MA, 1998.
- Staffelbach, T., A. Neftel, A. Blatter, A. Gut, M. Fahrmi, J. Stählin, A. Prevot, A. Hering, M. Lehning, B. Neining, M. Bäumle, G.L. Kok, J. Dommen, M. Hutterli, and M. Anclin, Photochemical oxidant formation over southern Switzerland, 1. results from summer 1994, *J. Geophys. Res.*, *102* (D19), 23345 - 23362, 1997a.
- Staffelbach, T., A. Neftel, and L.W. Horowitz, Photochemical oxidant formation over southern Switzerland, 2. model results, *J. Geophys. Res.*, *102* (D19), 23363 - 23373, 1997b.
- Stedman, D.H., J. E.D. Morris, E.E. Daby, H. Niki, and B. Weinstock, The role of OH radicals in photochemical smog reactions, in *160th national meeting of the American Chemical Society*, Chicago, IL, 1970.
- Stockwell, R.W., and J.G. Calvert, The Near Ultraviolet Absorption Spectrum of Gaseous HONO and N₂O₃, *J. Photochem.*, *8*, 193 - 203, 1978.
- Stockwell, W.R., and J. Calvert, The mechanism of NO₃ and HONO formation in the nighttime chemistry of the urban atmosphere, *J. Geophys. Res.*, *88*, 6673-6682, 1983.
- Stockwell, W.R., F. Kirchner, M. Kuhn, and S. Seefeld, A new mechanism for regional atmospheric chemistry modeling, *J. Geophys. Res.*, *102* (D22), 25847 - 25879, 1997.
- Stuhl, F., and H. Niki, Flash Photochemical Study of the Reaction OH + NO + M Using Resonance Fluorescent Detection of OH, *J. Chem. Phys.*, *57* (9), 3677 - 3679, 1972.
- Stull, R.B., *An introduction to boundary layer meteorology*, Kluwer Academic Publishers, Dordrecht Boston London, 1988.
- Stutz, J., Charakterisierung von Photodiodenzeilen zur Messung stratosphärischer Spurenstoffe, Diploma thesis, University of Heidelberg, Heidelberg, 1991.
- Stutz, J., Messung der Konzentration troposphärischer Spurenstoffe mittels Differentieller Optischer Absorptionsspektroskopie: Eine neue Generation von Geräten und Algorithmen, PhD thesis, Universität Heidelberg, Heidelberg, 1996.
- Stutz, J., personal communication, 2004.
- Stutz, J., R. Ackermann, A. Geyer, E. Williams, and A. White, Vertical Profiles of Ozone and Nitrogen Oxides in the Nocturnal Boundary Layer: 1. Observations during the TEXAQS 2000 study, *submitted to J. Geophys. Res.*, 2004a.
- Stutz, J., B. Alicke, R. Ackermann, A. Geyer, S. Wang, A. White, E. Williams, C. Spicer, and J.D. Fast, Relative humidity dependence of HONO chemistry in urban areas, *J. Geophys. Res.*, 2004b.
- Stutz, J., B. Alicke, and A. Neftel, Nitrous acid formation in the urban atmosphere: Gradient measurements of NO₂ and HONO over grass in Milan, Italy, *J. Geophys. Res.*, *107* (D22), doi: 10.1029/2001JD000390, 2002.
- Stutz, J., and A. Geyer, Formation of HO_x radicals in the nocturnal boundary layer by chemical-transport mechanisms, *Geophys. Res. Lett.*, *submitted*, 2003.
- Stutz, J., E.S. Kim, U. Platt, P. Bruno, C. Perrino, and A. Febo, UV-visible absorption cross section of nitrous acid, *J. Geophys. Res.*, *105* (D11), 14858-14592, 2000.
- Stutz, J., and U. Platt, Problems in using diode arrays for open path DOAS measurements of atmospheric species, in *Proc. SPIE*, pp. 329 - 340, Optical Methods in the Atmospheric Chemistry, Berlin, 1992.
- Stutz, J., and U. Platt, Numerical analysis and estimation of the statistical error of differential optical absorption spectroscopy measurements with least-squares methods., *Appl. Optics*, *30*, 6041-6053, 1996.
- Stutz, J., and U. Platt, Improving long-path differential optical absorption spectroscopy with a quartz-fiber mode mixer, *Appl. Optics*, *36* (6), 1105-15, 1997.
- Sumner, A.L., and B.J. Finlayson-Pitts, Steps towards understanding heterogeneous chemistry in the troposphere: water uptake on environmental relevant surfaces, *in preparation*, 2003.
- Svensson, R., E. Ljungström, and O. Lindqvist, Kinetics of the reaction between nitrogen dioxide and water vapour, *Atmos. Environ.*, *21*, 1529-1539, 1987.
- Syomin, D., K.A. Ramazan, and B.J. Finlayson-Pitts, HONO reactions on clean and nitric acid doped glass surfaces, *in preparation*, 2002.
- Taylor, J.K., *Statistical techniques for data analysis*, Lewis Publishers, 1990.

- Taylor, N.N., C. Wagner-Riddle, G.W. Thurtell, and E.G. Beauchamp, Nitric oxide fluxes from an agricultural soil using a flux gradient method, *J. Geophys. Res.*, 104 (D10), 12213 - 12220, 1999.
- TenBrink, H.M., and H. Spoelstra, The dark decay of HONO in environmental (SMOG) chambers, *Atmospheric Environment*, 32 (2), 247-251, 1998.
- Thomas, J.M., and W.J. Thomas, *Principles and Practice of Heterogeneous Catalysis*, VCH Verlagsgesellschaft mbH, Weinheim New York Basel Cambridge Tokyo, 1997.
- Thompson, A.M., and D. Lenschow, Mean profiles of trace reactive species in the unpolluted marine surface layer, *J. Geophys. Res.*, 89 (D3), 4788-4796, 1984.
- Thompson, K.C., and P. Margey, Hydrogen bonded complexes between nitrogen dioxide, nitric acid, nitrous acid and water with SiH₃OH and Si(OH)₄, *Phys. Chem. Chem. Phys.*, 5, 2970 - 2975, 2003.
- Trick, S., Das Bildungspotential salpetriger Säure (HONO) an städtischen Oberflächen, Diploma thesis, Heidelberg, Heidelberg, 2000.
- Trick, S., U. Platt, K. Acker, W. Wiprecht, J. Kleffmann, J. Lörzer, and A. Febo, Determination of the effective HONO formation potential on asphalt surfaces, in *Annex II to WP2: Field Measurements in NITROCAT (NITrous acid and its influence on the Oxidation Capacity of the Atmosphere)*, pp. 91 - 113, European Union, 2003.
- Tuazon, E.C., A.M. Winer, R.A. Graham, and J. J.N. Pitts, Trace pollutants concentrations in a multiday smog episode in the California south coast air basin by long path length FT-IR spectroscopy, *Environ. Sci. Technol.*, 15 (1232 - 1237), 1978.
- Tuazon, E.C., A.M. Winer, R.A. Graham, and J. J.N. Pitts, Atmospheric measurements of trace pollutants by kilometer pathlength FT-IR spectroscopy, *Ad. Environ. Sci. Technol.*, 10, 259 - 300, 1980.
- Tyndall, G.S., J.J. Orlando, and J.G. Calvert, Upper Limit For the Rate Coefficient For the Reaction HO₂+NO₂->HONO+O₂, *Environmental Science & Technology*, 29 (1), 202-206, 1995.
- Vandaele, A.C., P.C. Simon, J.M. Guilmot, M. Carleer, and R. Colin, SO₂ Absorption Cross Section Measurement in the UV Using a Fourier Transform Spectrometer, *Journal of Geophysical Research-Atmospheres*, 99 (D12), 25599-25605, 1994.
- Vecera, Z., and P.K. Dasgupta, Measurement of Atmospheric Nitric and Nitrous Acids with a Wet Effluent Diffusion Denuder and Low-Pressure Ion Chromatography-Postcolumn Reaction Detection, *Anal. Chem.*, 63, 2210-2216, 1991.
- Veitel, H., Vertical profiles of NO₂ and HONO in the planetary boundary layer, PhD thesis, Universität Heidelberg, Heidelberg, 2002.
- Veitel, H., B. Kromer, M. Mössner, and U. Platt, New techniques for measurements of atmospheric vertical trace gas profiles using DOAS, *Environmental Science and Pollution Research*, submitted, 2002.
- Verver, G., A Modified K Model for Chemically Reactive Species in the Planetary Boundary Layer - Comment, *J. Geophys. Res.*, 99 (D9), 19021-19023, 1994.
- Vila-Guerau de Arellano, J., Bridging the Gap Between Atmospheric Physics and Chemistry in Studies of Small-Scale Turbulence, *Bull. Am. Met. Soc.*, 84 (1), 51-56, 2003.
- Vila-Guerau de Arellano, J., P.G. Duynkerke, and K.F. Zeller, Atmospheric surface layer similarity theory applied to chemically reactive species, *J. Geophys. Res.*, 100 (D1), 1397-1408, 1995.
- Vogel, B., H. Vogel, J. Kleffmann, and R. Kurtenbach, Measured and simulated vertical profiles of nitrous acid - Part II. Model simulations and indications for a photolytic source, *Atmos. Environ.*, 37, 2957 - 2966, 2003.
- Volkamer, R., Absorption von Sauerstoff im Herzberg I System und Anwendung auf Aromatenmessungen am European Photo Reaktor (EUPHORE), Diploma thesis, University of Heidelberg, Heidelberg, 1996.
- Wagner, T., C. Leue, M. Wenig, K. Pfeilsticker, and U. Platt, Spatial and temporal distribution of enhanced boundary layer BrO concentrations measured by the GOME instrument aboard ERS-2, *Journal of Geophysical Research-Atmospheres*, 106 (D20), 24225-24235, 2001.
- Wagner, T., C. Otten, and U. Platt, DOAS moonlight observation of atmospheric NO₃ and NO₂ in the arctic winter, *Geophys. Res. Lett.*, 27 (21), 3441-3444, 2000.
- Wagner, T., and U. Platt, Satellite mapping of enhanced BrO concentrations in the troposphere, *Nature*, 395, 486-490, 1998.
- Wagner, T., C. von Friedeburg, M. Wenig, C. Otten, and U. Platt, UV-visible observations of atmospheric O₄ absorptions using direct moonlight and zenith-scattered sunlight for clear-sky and cloudy sky conditions, *J. Geophys. Res.*, 107 (D20), pp. 4,424, 2002a.
- Wagner, T., F. Wittrock, A. Richter, M. Wenig, J.P. Burrows, and U. Platt, Continuous monitoring of the high and persistent chlorine activation during the Arctic winter 1999/2000 by the GOME instrument on ERS-2, *Journal of Geophysical Research-Atmospheres*, 107 (D20), 8267, 2002b.
- Wahner, A., T. Mentel, M. Sohn, and J. Stier, Heterogeneous reaction of N₂O₅ on sodium nitrate aerosol, *Journal of geophysical research - atmospheres*, 103 (D23), 31,103 - 31,112, 1998a.

- Wahner, A., T.F. Mentel, and M. Sohn, Gas-phase reaction of N_2O_5 with water vapor: Importance of heterogeneous hydrolysis of N_2O_5 and surface desorption of HNO_3 in a large Teflon chamber, *Geophys. Res. Lett.*, *25* (12), 2169-2172, 1998b.
- Wang, S., R. Ackermann, A. Geyer, J.C. Doran, W.J. Shaw, J.D. Fast, C.W. Spicer, and J. Stutz, Vertical Variation of nocturnal NO_x chemistry in the urban environment of Phoenix, in *AMS2003*, Long Beach, 2003.
- Wängberg, I., T. Etkorn, I. Barnes, U. Platt, and K.H. Becker, Absolute Determination of the Temperature Behavior of the $\text{NO}_2+\text{NO}_3+(\text{M})\leftrightarrow\text{N}_2\text{O}_5+(\text{M})$ Equilibrium, *Journal of Physical Chemistry*, *101* (50), 9694-9698, 1997.
- Wayne, L.G., and D.M. Yost, *J. Chem. Phys.*, *19* (41), 1951.
- Wayne, P., J. Robargea, T. Walkerb, R.B. McCullochc, and G. Murray, Atmospheric concentrations of ammonia and ammonium at an agricultural site in the southeast United States, *Atmos. Environ.*, *36*, 1661 - 1674, 2002.
- Weinstock, R., Carbon monoxide, residence time in the atmosphere, *Science*, *166*, 224 - 225, 1969.
- Wesely, M.L., and B.B. Hicks, A review of the current status of knowledge on dry deposition, *Atmos. Environ.*, *34* (12-14), 2261-2282, 2000.
- Westenberg, A.A., and N. DeHaas, Rate measurements on $\text{OH} + \text{NO} + \text{M}$ and $\text{OH} + \text{NO}_2 + \text{M}$, *J. Chem. Phys.*, *57* (12), 5375 - 5378, 1972.
- White, J.U., Long Optical Paths of Large Aperture, *J. Opt. Soc. Am.*, *32*, 1942.
- White, J.U., Very Long Optical Paths in Air, *J. Opt. Soc. Am.*, *66* (5), 1976.
- Wiesen, P., NITROCAT: NITrous acid and its influence on the Oxidation Capacity of the ATmosphere, European Union, 2003.
- Wiesen, P., J. Kleffmann, R. Kurtenbach, and K.H. Becker, Mechanistic Study of the Heterogeneous Conversion of NO_2 Into HONO and N_2O On Acid Surfaces, *Faraday Discussions* (100), 121-127, 1995.
- Wild, J., D. Kley, A. Rockel, P. Rockel, and H.J. Segschneider, Emission of NO from several higher plant species, *JGR*, *102*, 5919 - 5927, 1997.
- Wilkins, E.T., Air pollution aspects of the London fog of December 1952, *Quart. Jour. Roy. Met. Soc.*, *80*, 267 - 271, 1954.
- Winer, A.M., and H.W. Biermann, Long Pathlength Differential Optical Absorption Spectroscopy (DOAS) Measurements of Gaseous HONO, NO_2 and HCHO in the California South Coast Air Basin, *Research On Chemical Intermediates*, *20* (3-5), 423-445, 1994.
- Wingen, L.M., A.L. Sumner, D. Syomin, K.A. Ramazan, and B.J. Finlayson-Pitts, Heterogeneous formation of nitrous acid in laboratory systems, *in preparation*, 2003.
- Yang, Q., P.A. Mayewski, E. Lindner, S. Whitlow, and M. Twickler, Chemical species spatial distribution and relationship to elevation and snow accumulation rate over the Greenland Ice Sheet, *J. Geophys. Res.*, *101*, 18629-18637, 1996.
- Yoshizawa, A., A statistical investigation of shear turbulence: the Reynolds-stress transport equation, *J. Phys. Soc. Jpn.*, *51*, 658-666, 1982.
- Zabarnick, S., Kinetics of the Reaction $\text{OH}+\text{NO}+\text{M}\rightarrow\text{HONO}+\text{M}$ as a Function of Temperature and Pressure in the Presence of Argon, SF_6 , and N_2 Bath Gas, *Chemical Physics*, *171* (1-2), 265-273, 1993.
- Zeldovich, J., S.r. Quellen, NO_x , O/O_2 , and Energiegewinnung, The oxidation of nitrogen in combustion and explosions, *Acta Physicochim. U.R.S.S.*, *21*, 577-628, 1946.
- Zellweger, C., M. Ammann, U. Baltensperger, and P. Hofer, NO_y speciation with a combined wet effluent diffusion denuder-aerosol collector coupled to ion chromatography, *Atmos. Environ.*, *33*, 1131 - 1140, 1999.
- Zhang, R., M.-T. Leu, and L.F. Keyser, Heterogenous chemistry of HONO on liquid sulfuric acid: A new mechanism of chlorine activation on stratospheric sulfate aerosols, *J. Phys. Chem.*, *100*, 339 - 345, 1996.
- Zhou, X., H.J. Beine, R.E. Honrath, J.D. Fuentes, W. Simpson, P.B. Shepson, and J.W. Bottenheim, Snowpack photochemical production of HONO: a major source of OH in the Arctic boundary layer in springtime, *Geophys. Res. Letters*, *28* (21), 4087 - 4090, 2001.
- Zhou, X., K. Civerolo, H. Dai, G. Huang, J. Schwab, and K. Demerjian, Summertime nitrous acid chemistry in the atmospheric boundary layer at a rural site in New York State, *J. Geophys. Res.*, *107* (D21), doi:10.1029/2001JD001539, 2002a.
- Zhou, X., Y. He, G. Huang, T.D. Thornberry, M.A. Carroll, and S.B. Bertman, Photochemical production of nitrous acid on glass sample manifold surface, *Geophys. res. Letters*, *29*, doi. 14, 10.1029/2002GL015080, 2002b.
- Zhou, X., H. Qiao, G. Deng, and K. Civerolo, A Method for the Measurement of Atmospheric HONO based on DNPH Derivatization and HPLC Analysis, *Environ. Sci. Technol.*, *33*, 3672-3679, 1999.

Appendix

A. The HeCSI Model (Facsimile[©] Source Code)

```

*-----;
*-----;
*
* HONOTENT model (HeCSI)
* (= model to simulate HETereogeneous Chemistry
* and Surface Interactions in a smog chamber)
*
* VERSION 4.05 (January 09, 2004)
*
* Sebastian Trick, Andreas Geyer, Jochen Stutz
* UCLA and IUP HD
*
*-----;
*-----SETUP of Model-----;
*
ERRORTOL 1E-5; * Model parameter;
KMAX 3; * Model parameter;
*
*-----SETUP of Files-----;
*
COMPILE INSTANT
OPEN 10 "honotent\gas.dat"; * Output of gas data;
OPEN 11 "honotent\surf.dat"; * Output of surface data;
OPEN 12 "honotent\rate.dat"; * Output of reaction rate parameters;
OPEN 13 "honotent\leak.dat"; * Output of leakage data;
OPEN 14 "honotent\para.dat"; * Output of parameter data;
**
*-----;
*
*-----SETUP OF CHEMISTRY-----;
*
PARAMETER T; * Temperature [K];
PARAMETER S; * real area of the total surfaces [m2];
PARAMETER SR; * geometric area of reactive surface [m2];
PARAMETER SP; * geometric area of surface of the walls of tent [m2];
PARAMETER sm; * factor of arising of SR by sub-structures [ ];
PARAMETER V; * volume of tent [m3];
PARAMETER SV; * Surface-to-volume ratio of tent [1/m];
PARAMETER rH; * relative humidity [ ];
PARAMETER rH2; * corrected relative humidity [ ];
PARAMETER vHONO; * velocity of HONO [m/s];
PARAMETER vNO2; * velocity of NO2 [m/s];
PARAMETER vNO; * velocity of NO [m/s];
*
PARAMETER LEAK; * leakage frequency of tent [1/s];
PARAMETER r; * run time [s];
PARAMETER p; * 2nd run time [s];
*
PARAMETER gNO2; * uptake coeff NO2 [ ];
PARAMETER uNO2; * uptake freq. NO2 [1/s];
*
PARAMETER KUHONO; * uptake probability HONO [ ];
PARAMETER KOHONO; * outgassing probability HONO [ ];
PARAMETER uHONO; * uptake freq. HONO [1/s];
PARAMETER oHONO; * outgassing freq. HONO [1/s];
PARAMETER oNO; * outgassing freq. of NO [1/s];
*
PARAMETER NO2CONVP; * ratio HONO/HONOs at formation [ ];
PARAMETER NOCONVP; * ratio NO / NO2 formation from 2nd HONO reaction[ ];
*

```

```
PARAMETER THw;          *fractional coverage of surface by water [ ];
PARAMETER fact;        *fractional non - coverage of surface by water [ ];
PARAMETER kakd;        *ratio between water adsorption and desorption [cm3];
PARAMETER H2O;         * molecules of water in the gas phase [molec/cm3];
*
VARIABLE HONO;         * molecules of HONO in gas [molec/cm3];
VARIABLE HONOs;        * molecules of HONO at surface [molec/cm3];
VARIABLE HONOL;        * molecules of leaked HONO [molec/cm3];
VARIABLE NO2;          * molecules of NO2 in gas [molec/cm3];
VARIABLE NO2L;         * molecules of leaked NO2 [molec/cm3];
VARIABLE NO;           * molecules of NO in gas [molec/cm3];
VARIABLE NOL;          * molecules of leaked NO [molec/cm3];
VARIABLE HNO3s;        * molecules of HNO3 at surface [molec/cm3];
*
PARAMETER B1 B2 B3 B4 B5 B6 B7 B8 B9;          * reaction rates ;
*
*-----START PARAMETERS-----;
*
COMPILE INSTANT
*
*-----;
*
*measured starting values
*
T = 273.16 + 22
SR = 3.500
SP = 23.354 - SR
sm = 150.00
S = sm * SR + SP
V = 2.502
SV = S/V
*
vHONO = SQRT(8/3.14 * 1.38E-23 * T / 1.66E-27 / 47)
vNO2 = SQRT(8/3.14 * 1.38E-23 * T / 1.66E-27 / 46)
vNO = SQRT(8/3.14 * 1.38E-23 * T / 1.66E-27 / 30)
*
NO2 = 0.1*2.5e10
NO = 6.9*2.5e10
HONO = 1.7*2.5e10
rh = 0.07
rh2 = 0.07
*
leak = 1.3e-4
*
*-----;
*
*measured NO2 uptake determined independently
*
gNO2 = 1.2e-6
uNO2 = gNO2*vNO2/4*sv
*
*-----;
*
*best guess start parameters
*
kakd = 1.0e-16
KUHONO = 9.9e-5
KOHONO = 3.5e-7
ohono = KOHONO*vHONO/4*sv
*ohono = 3e-4*100
*
HONOs = 1.93e13
HNO3s = 3.21e11
*
no2convp = 0.13
*
oNO = leak*6.9*2.5e10
noconvp = 0.5+0.8*rh
*
*-----;
*
*running parameters
*
r = -10
p = 0
**
*-----;
*
```

```

*-----EQUATIONS-----;
*
COMPILE EQUATIONS
*
*-----;
*
*Calculation of actual rh
*
*rh = 0.05
*
IF (r-7056.5) 63 64 64
LABEL 63
rh = 0.07
JUMP 67
LABEL 64
IF (r-7056.5-14650.0) 65 65 66
LABEL 65
p = r-7056.5
rh = (9.122+0.0058*p-1.336E-7*p*p)/100
JUMP 67
LABEL 66
IF (r-40000) 71 71 72
LABEL 71
p = r-7056.5
rh = (15.353+48.243*exp(-(p-14650.0)/7047.6))/100
JUMP 67
LABEL 72
p = r-7056.5-14650.0
rh = (35.264*exp(-p*0.33e-4))/100
LABEL 67
*
*IF (rH-0.0901) 68 68 69
*LABEL 68
*rh2 = 0
*JUMP 70
*LABEL 69
*rh2 = rH
*LABEL 70
*
*-----;
*
*Calculate surface coverage by H2O and HONO adsorption and desorption
*
H2O = 6.1078*EXP(17.27*(T-273.16)/(T-35.86))/1.38E-23/T/10000*rH
THw = (kakt*H2O)/(1+kakt*H2O)
*
*fact = 1.0/(1+kakt*H2O)
fact = (1-(THw+0.010))
*uhono = fact*0.085*100
uhono = fact*KUHONO*vHONO/4*sv
*
*-----;
*
*Calculation of Chemistry
*
% leak:          HONO = HONOL
% leak:          NO2 = NO2L
% leak:          NO = NOL
*
*
B1 % uNO2:          NO2 =
  = 0.5 * B1 / sv*1e2 :      = HNO3s
  = 0.5 * B1 / sv*1e2 :      = HONOs
*   = 0.5 * B1 * (1-no2convp) / sv*1e2 :      = HONOs
*   = 0.5 * B1 * no2convp / sv*1e2 :      = HONO
*
B4 % uHONO:          HONO =
  = B4 / sv*1e2 :      = HONOs
B5 % ohono:          HONOs =
  = B5 * sv/1e2 :      = HONO
*
*
% oNO:              = NO
*
B6 % 0.9e-16 * rh :      HONOs + HNO3s =
  = B6 *sv/1e2 :      = NO + NO
*

```


B. The Chemical Mechanism of the RACM Model

[Stockwell et al., 1997]

Table 1. RACM Mechanism Species List

No.	Species	Definition	Carbon Number	Molecular Weight
<i>Stable Inorganic Compounds</i>				
Oxidants				
1	O ₃	ozone		48
2	H ₂ O ₂	hydrogen peroxide		34
Nitrogenous compounds				
3	NO	nitric oxide		30
4	NO ₂	nitrogen dioxide		46
5	NO ₃	nitrogen trioxide		62
6	N ₂ O ₅	dinitrogen pentoxide		108
7	HONO	nitrous acid		47
8	HNO ₃	nitric acid		63
9	HNO ₄	pernitric acid		79
Sulfur compounds				
10	SO ₂	sulfur dioxide		64
11	SULF	sulfuric acid		98
Carbon oxides				
12	CO	carbon monoxide	1	28
13	CO ₂	carbon dioxide	1	44
<i>Abundant Stable Species</i>				
14	N ₂	nitrogen		28
15	O ₂	oxygen		32
16	H ₂ O	water		18
17	H ₂	hydrogen		2
<i>Inorganic Short-Lived Intermediates</i>				
18	O ^{3P}	ground state oxygen atom, O(^{3P})		16
19	O ^{1D}	excited state oxygen atom, O(^{1D})		16
Odd hydrogen				
20	HO	hydroxy radical		17
21	HO ₂	hydroperoxy radical		33
<i>Stable Organic Compounds</i>				
Alkanes				
22	CH ₄	methane	1.0	16
23	ETH	ethane	2.0	30
24	HC3	alkanes, alcohols, esters, and alkynes with HO rate constant (298 K, 1 atm) less than $3.4 \times 10^{-12} \text{ cm}^3 \text{ s}^{-1}$	2.9	44
25	HCS	alkanes, alcohols, esters, and alkynes with HO rate constant (298 K, 1 atm) between 3.4×10^{-12} and $6.8 \times 10^{-12} \text{ cm}^3 \text{ s}^{-1}$	4.8	72
26	HC8	alkanes, alcohols, esters, and alkynes with HO rate constant (298 K, 1 atm) greater than $6.8 \times 10^{-12} \text{ cm}^3 \text{ s}^{-1}$	7.9	114
Alkenes				
27	ETE	ethene	2.0	28
28	OLT	terminal alkenes	3.8	42
29	OLI	internal alkenes	5.0	68
30	DIEN	butadiene and other anthropogenic dienes	4.0	54
Stable biogenic alkenes				
31	ISO	isoprene	5.0	68
32	API	α -pinene and other cyclic terpenes with one double bond	10.0	136
33	LIM	d-limonene and other cyclic diene-terpenes	10.0	136
Aromatics				
34	TOL	toluene and less reactive aromatics	7.1	92
35	XYL	xylene and more reactive aromatics	8.9	106
36	CSL	cresol and other hydroxy substituted aromatics	6.6	108
Carbonyls				
37	HCHO	formaldehyde	1.0	30
38	ALD	acetaldehyde and higher aldehydes	2.4	44
39	KET	ketones	3.5	72
40	GLY	glyoxal	2.0	58
41	MGLY	methylglyoxal and other α -carbonyl aldehydes	3.0	72
42	DCB	unsaturated dicarbonyls	4.2	87
43	MACR	methacrolein and other unsaturated monoaldehydes	4.0	70
44	UDD	unsaturated dihydroxy dicarbonyl	4.2	119
45	HKET	hydroxy ketone	3.0	74

Table 1. (continued)

No.	Specics	Definition	Carbon Number	Molecul Wcigh
Organic nitrogen				
46	ONIT	organic nitrate	4.0	119
47	PAN	peroxyacetyl nitrate and higher saturated PANs	2.0	121
48	TPAN	unsaturated PANs	4.0	147
Organic peroxides				
49	OP1	methyl hydrogen peroxide	1.0	48
50	OP2	higher organic peroxides	2.0	62
51	PAA	peroxyacetic acid and higher analogs	2.0	76
Organic acids				
52	ORA1	formic acid	1.0	46
53	ORA2	acetic acid and higher acids	2.0	60
<i>Organic Short-Lived Intermediates</i>				
Peroxy radicals from alkanes				
54	MO ₂	methyl peroxy radical	1.0	47
55	ETHP	peroxy radical formed from ETH	2.0	61
56	HC3P	peroxy radical formed from HC3	2.9	75
57	HC5P	peroxy radical formed from HC5	4.8	103
58	HC8P	peroxy radical formed from HC8	7.9	143
Peroxy radicals from alkenes				
59	ETEP	peroxy radicals formed from ETE	2.0	77
60	QLTP	peroxy radicals formed from QLT	3.8	91
61	OLIP	peroxy radicals formed from OLI	4.8	117
Peroxy radicals from biogenic alkenes				
62	ISOP	peroxy radicals formed from ISO and DIEN	5.0	117
63	APIP	peroxy radicals formed from API	10.0	185
64	LIMP	peroxy radicals formed from LIM	10.0	185
Radicals produced from aromatics				
65	PHO	phenoxy radical and similar radicals	6.6	107
66	ADDT	aromatic-HO adduct from TOL	7.1	109
67	ADDX	aromatic-HO adduct from XYL	8.9	123
68	ADDC	aromatic-HO adduct from CSL	6.6	125
69	TOLP	peroxy radicals formed from TOL	7.1	141
70	XYLP	peroxy radicals formed from XYL	8.9	155
71	CSLP	peroxy radicals formed from CSL	6.6	157
Peroxy radicals with carbonyl groups				
72	ACO ₃	acetyl peroxy and higher saturated acyl peroxy radicals	2.0	75
73	TCO ₃	unsaturated acyl peroxy radicals	4.0	115
74	KETP	peroxy radicals formed from KET	3.9	103
Other peroxy radicals				
75	OLNN	NO ₃ -alkene adduct reacting to form carbonitrates + HO ₂	3.0	136
76	OLND	NO ₃ -alkene adduct reacting via decomposition	3.0	136
77	XO ₂	accounts for additional NO to NO ₂ conversions

Table 2a. The RACM Mechanism: Photolysis Reactions

Reaction No.	Reaction	Photolysis Frequency, ^a s ⁻¹	Cross Section	Quantum Yield
(R1)	NO ₂ → O ³ P + NO	7.50 × 10 ⁻³	<i>DeMore et al.</i> [1994]	<i>DeMore et al.</i> [1994]
(R2)	O ₃ → O ¹ D + O ₂	1.62 × 10 ⁻⁵	<i>DeMore et al.</i> [1994]	<i>DeMore et al.</i> [1994]
(R3)	O ₃ → O ³ P + O ₂	4.17 × 10 ⁻⁴	<i>DeMore et al.</i> [1994]	total yield of O ¹ D and O ³ P assumed to be unity
(R4)	HONO → HO + NO	1.63 × 10 ⁻³	<i>DeMore et al.</i> [1994]	<i>DeMore et al.</i> [1994]
(R5)	HNO ₃ → HO + NO ₂	4.50 × 10 ⁻⁷	<i>DeMore et al.</i> [1994]	assumed to be unity
(R6)	HNO ₄ → 0.65 HO ₂ + 0.65 NO ₂ + 0.35 HO + 0.35 NO ₃	3.17 × 10 ⁻⁶	<i>DeMore et al.</i> [1994]	assumed to be unity
(R7)	NO ₃ → NO + O ₂	2.33 × 10 ⁻²	<i>Wayne et al.</i> [1991]	<i>Wayne et al.</i> [1991]
(R8)	NO ₃ → NO ₂ + O ³ P	1.87 × 10 ⁻¹	<i>Wayne et al.</i> [1991]	<i>Wayne et al.</i> [1991]
(R9)	H ₂ O ₂ → HO + HO	6.00 × 10 ⁻⁶	<i>DeMore et al.</i> [1994]	assumed to be unity
(R10)	HCHO → H ₂ + CO	3.50 × 10 ⁻⁵	wavelengths <300 nm: <i>Moortgat et al.</i> [1980] wavelengths >300 nm: <i>Cantrell et al.</i> [1990]	wavelengths <300 nm: <i>Atkinson et al.</i> [1994] ^b wavelengths >300 nm: <i>DeMore et al.</i> [1994] ^b
(R11)	HCHO → 2 HO ₂ + CO	2.17 × 10 ⁻⁵	same references as (R10)	same references as (R10) ^b
(R12)	ALD → MO ₂ + HO ₂ + CO	3.67 × 10 ⁻⁶	<i>Martinez et al.</i> [1992]	<i>Atkinson</i> [1994] ^b
(R13)	OP1 → HCHO + HO ₂ + HO	4.17 × 10 ⁻⁶	<i>DeMore et al.</i> [1994]	<i>DeMore et al.</i> [1994]
(R14)	OP2 → ALD + HO ₂ + HO	4.17 × 10 ⁻⁶	same as (R13)	same as (R13)
(R15)	PAA → MO ₂ + HO	1.57 × 10 ⁻⁶	H ₂ O ₂ cross sections scaled by 0.28; <i>Ciguere and Olmos</i> [1956]	assumed to be unity
(R16)	KET → ETHP + ACO ₃	6.67 × 10 ⁻⁷	<i>Martinez et al.</i> [1992]	<i>Atkinson</i> [1994]
(R17)	GLY → 0.13 HCHO + 1.87 CO + 0.87 H ₂	5.83 × 10 ⁻⁵	<i>Atkinson et al.</i> [1992b]	wavelengths <340: 0.0 wavelengths >340: 0.029 <i>Atkinson et al.</i> [1992b]
(R18)	GLY → 0.45 HCHO + 1.55 CO + 0.80 HO ₂ + 0.15 H ₂	2.00 × 10 ⁻⁵	<i>Atkinson et al.</i> [1992b]	wavelengths <340: 0.4 wavelengths >340: 0.0 <i>Atkinson et al.</i> [1992b]
(R19)	MGLY → CO + HO ₂ + ACO ₃	9.33 × 10 ⁻⁵	<i>Atkinson</i> [1994] and <i>Staffelbach et al.</i> [1995]	estimated from <i>Koch and Moortgat</i> [1996]
(R20)	DCB → TCO ₃ + HO ₂	4.33 × 10 ⁻⁴	<i>Stockwell et al.</i> [1990]	<i>Stockwell et al.</i> [1990]
(R21)	ONIT → 0.20 ALD + 0.80 KET + HO ₂ + NO ₂	2.17 × 10 ⁻⁶	assumed to be mixture of 20% n-propyl nitrate and 80% i-propyl nitrate; <i>Atkinson</i> [1994]	<i>Atkinson</i> [1994]
(R22)	MACR → CO + HCHO + HO ₂ + ACO ₃	1.33 × 10 ⁻⁶	<i>Gardner et al.</i> [1987]	<i>Gardner et al.</i> [1987]
(R23)	HKET → HCHO + HO ₂ + ACO ₃	6.67 × 10 ⁻⁷	same as (R16)	same as (R16)

^aTypical photolysis frequencies are given for solar zenith angle 40°, June 21, summer surface 40° northern latitude.

^bPressure dependences given by $\varphi(\lambda, P) = \varphi(\lambda, 1 \text{ atm}) / \{\varphi(\lambda, 1 \text{ atm}) + [1 - \varphi(\lambda, 1 \text{ atm})] \times P\}$, where P is in atmospheres.

Table 2b. The RACM Mechanism

Reaction No.	Reaction	A , $\text{cm}^3 \text{s}^{-1}$	E/R , K	k^a	Note
<i>Inorganic Reactions</i>					
(R24)	$\text{O}^3\text{P} + \text{O}_2 \rightarrow \text{O}_3$	Table 2f		1.50×10^{-14}	1
(R25)	$\text{O}^3\text{P} + \text{O}_3 \rightarrow 2 \text{O}_2$	8.00×10^{-12}	2060	7.96×10^{-15}	1
(R26)	$\text{O}^1\text{D} + \text{N}_2 \rightarrow \text{O}^3\text{P} + \text{N}_2$	1.80×10^{-11}	-110	2.60×10^{-11}	1
(R27)	$\text{O}^1\text{D} + \text{O}_2 \rightarrow \text{O}^3\text{P} + \text{O}_2$	3.20×10^{-11}	-70	4.05×10^{-11}	1
(R28)	$\text{O}^1\text{D} + \text{H}_2\text{O} \rightarrow \text{HO} + \text{HO}$	2.20×10^{-10}		2.20×10^{-10}	1
(R29)	$\text{O}_3 + \text{HO} \rightarrow \text{HO}_2 + \text{O}_2$	1.60×10^{-12}	940	6.83×10^{-14}	1
(R30)	$\text{O}_3 + \text{HO}_2 \rightarrow \text{HO} + 2 \text{O}_2$	1.10×10^{-14}	500	2.05×10^{-15}	1
(R31)	$\text{HO} + \text{HO}_2 \rightarrow \text{H}_2\text{O} + \text{O}_2$	4.80×10^{-11}	-250	1.11×10^{-10}	1
(R32)	$\text{H}_2\text{O}_2 + \text{HO} \rightarrow \text{HO}_2 + \text{H}_2\text{O}$	2.90×10^{-12}	160	1.70×10^{-12}	1
(R33)	$\text{HO}_2 + \text{HO}_2 \rightarrow \text{H}_2\text{O}_2 + \text{O}_2$	Table 2f		2.92×10^{-12}	1
(R34)	$\text{HO}_2 + \text{HO}_2 + \text{H}_2\text{O} \rightarrow \text{H}_2\text{O}_2 + \text{O}_2 + \text{H}_2\text{O}$	Table 2f		6.58×10^{-30}	1
(R35)	$\text{O}^3\text{P} + \text{NO} \rightarrow \text{NO}_2$	Table 2d		1.66×10^{-12}	1
(R36)	$\text{O}^3\text{P} + \text{NO}_2 \rightarrow \text{NO} + \text{O}_2$	6.50×10^{-12}	-120	9.72×10^{-12}	1
(R37)	$\text{O}^3\text{P} + \text{NO}_2 \rightarrow \text{NO}_2$	Table 2d		1.58×10^{-12}	1
(R38)	$\text{HO} + \text{NO} \rightarrow \text{HONO}$	Table 2d		4.87×10^{-12}	1
(R39)	$\text{HO} + \text{NO}_2 \rightarrow \text{HNO}_3$	Table 2d		1.15×10^{-11}	1
(R40)	$\text{HO} + \text{NO}_3 \rightarrow \text{NO}_2 + \text{HO}_2$	2.20×10^{-11}		2.20×10^{-11}	1
(R41)	$\text{HO}_2 + \text{NO} \rightarrow \text{NO}_2 + \text{HO}$	3.70×10^{-12}	-250	8.56×10^{-12}	1
(R42)	$\text{HO}_2 + \text{NO}_2 \rightarrow \text{HNO}_4$	Table 2d		1.39×10^{-12}	1
(R43)	$\text{HNO}_4 \rightarrow \text{HO}_2 + \text{NO}_2$	Table 2c		8.62×10^{-2}	1
(R44)	$\text{HO}_2 + \text{NO}_3 \rightarrow 0.3 \text{HNO}_3 + 0.7 \text{NO}_2 + 0.7 \text{HO} + \text{O}_2$	3.50×10^{-12}		3.50×10^{-12}	1,2
(R45)	$\text{HO} + \text{HONO} \rightarrow \text{NO}_2 + \text{H}_2\text{O}$	1.80×10^{-11}	390	4.86×10^{-12}	1
(R46)	$\text{HO} + \text{HNO}_3 \rightarrow \text{NO}_3 + \text{H}_2\text{O}$	Table 2f		1.47×10^{-13}	1
(R47)	$\text{HO} + \text{HNO}_4 \rightarrow \text{NO}_2 + \text{O}_2 + \text{H}_2\text{O}$	1.30×10^{-12}	-380	4.65×10^{-12}	1,3
(R48)	$\text{O}_3 + \text{NO} \rightarrow \text{NO}_2 + \text{O}_2$	2.00×10^{-12}	1400	1.82×10^{-14}	1
(R49)	$\text{O}_3 + \text{NO}_2 \rightarrow \text{NO}_3 + \text{O}_2$	1.20×10^{-13}	2450	3.23×10^{-17}	1
(R50)	$\text{NO} + \text{NO} + \text{O}_2 \rightarrow \text{NO}_2 + \text{NO}_2$	3.30×10^{-39}	-530	1.95×10^{-38}	4
(R51)	$\text{NO}_3 + \text{NO} \rightarrow \text{NO}_2 + \text{NO}_2$	1.50×10^{-11}	-170	2.65×10^{-11}	1
(R52)	$\text{NO}_3 + \text{NO}_2 \rightarrow \text{NO} + \text{NO}_2 + \text{O}_2$	4.50×10^{-14}	1260	6.56×10^{-16}	1
(R53)	$\text{NO}_3 + \text{NO}_2 \rightarrow \text{N}_2\text{O}_5$	Table 2d		1.27×10^{-12}	1
(R54)	$\text{N}_2\text{O}_5 \rightarrow \text{NO}_2 + \text{NO}_3$	Table 2e		4.36×10^{-2}	1
(R55)	$\text{NO}_3 + \text{NO}_3 \rightarrow \text{NO}_2 + \text{NO}_2 + \text{O}_2$	8.50×10^{-13}	2450	2.29×10^{-16}	1
(R56)	$\text{HO} + \text{H}_2 \rightarrow \text{H}_2\text{O} + \text{HO}_2$	5.50×10^{-12}	2000	6.69×10^{-15}	1
(R57)	$\text{HO} + \text{SO}_2 \rightarrow \text{SULF} + \text{HO}_2$	Table 2d		8.89×10^{-13}	1
(R58)	$\text{CO} + \text{HO} \rightarrow \text{HO}_2 + \text{CO}_2$	Table 2f		2.40×10^{-13}	1
<i>O³P + Organic Compounds</i>					
(R59)	$\text{ISO} + \text{O}^3\text{P} \rightarrow 0.86 \text{OLT} + 0.05 \text{HCHO} + 0.02 \text{HO} + 0.01 \text{CO} + 0.13 \text{DCB} + 0.28 \text{HO}_2 + 0.15 \text{XO}_2$	6.00×10^{-11}		6.00×10^{-11}	5
(R60)	$\text{MACR} + \text{O}^3\text{P} \rightarrow \text{ALD}$	1.59×10^{-11}	-13	1.66×10^{-11}	6
<i>HO + Organic Compounds</i>					
(R61)	$\text{CH}_4 + \text{HO} \rightarrow \text{MO}_2 + \text{H}_2\text{O}$	Table 2c		6.86×10^{-15}	7
(R62)	$\text{ETH} + \text{HO} \rightarrow \text{ETHP} + \text{H}_2\text{O}$	Table 2c		2.57×10^{-13}	7
(R63)	$\text{HC3} + \text{HO} \rightarrow 0.583 \text{HC3P} + 0.381 \text{HO}_2 + 0.335 \text{ALD} + 0.036 \text{ORA1} + 0.036 \text{CO} + 0.036 \text{GLY} + 0.036 \text{HO} + 0.010 \text{HCHO} + \text{H}_2\text{O}$	5.26×10^{-12}	260	2.20×10^{-12}	8
(R64)	$\text{HC5} + \text{HO} \rightarrow 0.75 \text{HC5P} + 0.25 \text{KET} + 0.25 \text{HO}_2 + \text{H}_2\text{O}$	8.02×10^{-12}	155	4.77×10^{-12}	8
(R65)	$\text{HC8} + \text{HO} \rightarrow 0.951 \text{HC8P} + 0.025 \text{ALD} + 0.024 \text{HKET} + 0.049 \text{HO}_2 + \text{H}_2\text{O}$	1.64×10^{-11}	125	1.08×10^{-11}	8
(R66)	$\text{ETE} + \text{HO} \rightarrow \text{ETEP}$	1.96×10^{-12}	-438	8.52×10^{-12}	7
(R67)	$\text{OLT} + \text{HO} \rightarrow \text{OLTP}$	5.72×10^{-12}	-500	3.06×10^{-11}	8
(R68)	$\text{OLI} + \text{HO} \rightarrow \text{OLIP}$	1.33×10^{-11}	-500	7.12×10^{-11}	8
(R69)	$\text{DIEN} + \text{HO} \rightarrow \text{ISOP}$	1.48×10^{-11}	-448	6.65×10^{-11}	7
(R70)	$\text{ISO} + \text{HO} \rightarrow \text{ISOP}$	2.54×10^{-11}	-410	1.01×10^{-10}	7
(R71)	$\text{API} + \text{HO} \rightarrow \text{APIP}$	1.21×10^{-11}	-444	5.37×10^{-11}	7
(R72)	$\text{LIM} + \text{HO} \rightarrow \text{LIMP}$	1.70×10^{-10}		1.71×10^{-10}	7
(R73)	$\text{TOL} + \text{HO} \rightarrow 0.90 \text{ADDT} + 0.10 \text{XO}_2 + 0.10 \text{HO}_2$	1.81×10^{-12}	-355	5.96×10^{-12}	7
(R74)	$\text{XYL} + \text{HO} \rightarrow 0.90 \text{ADDX} + 0.10 \text{XO}_2 + 0.10 \text{HO}_2$	7.30×10^{-12}	-355	2.40×10^{-11}	7, 10
(R75)	$\text{CSL} + \text{HO} \rightarrow 0.85 \text{ADDC} + 0.10 \text{PHO} + 0.05 \text{HO}_2 + 0.05 \text{XO}_2$	6.00×10^{-11}		6.00×10^{-11}	7, 11
(R76)	$\text{HCHO} + \text{HO} \rightarrow \text{HO}_2 + \text{CO} + \text{H}_2\text{O}$	1.00×10^{-11}		1.00×10^{-11}	1
(R77)	$\text{ALD} + \text{HO} \rightarrow \text{ACO}_3 + \text{H}_2\text{O}$	5.55×10^{-12}	-331	1.69×10^{-11}	7
(R78)	$\text{KET} + \text{HO} \rightarrow \text{KETP} + \text{H}_2\text{O}$	Table 2c		6.87×10^{-13}	7
(R79)	$\text{HKET} + \text{HO} \rightarrow \text{HO}_2 + \text{MGLY} + \text{H}_2\text{O}$	3.00×10^{-12}		3.00×10^{-12}	7
(R80)	$\text{GLY} + \text{HO} \rightarrow \text{HO}_2 + 2 \text{CO} + \text{H}_2\text{O}$	1.14×10^{-11}		1.14×10^{-11}	12
(R81)	$\text{MGLY} + \text{HO} \rightarrow \text{ACO}_3 + \text{CO} + \text{H}_2\text{O}$	1.72×10^{-11}		1.72×10^{-11}	7
(R82)	$\text{MACR} + \text{HO} \rightarrow 0.51 \text{TCO}_3 + 0.41 \text{HKET} + 0.08 \text{MGLY} + 0.41 \text{CO} + 0.08 \text{HCHO} + 0.49 \text{HO}_2 + 0.49 \text{XO}_2$	1.86×10^{-11}	-175	3.35×10^{-11}	7, 13
(R83)	$\text{DCB} + \text{HO} \rightarrow 0.50 \text{TCO}_3 + 0.50 \text{HO}_2 + 0.35 \text{UDD} + 0.15 \text{GLY} + 0.15 \text{MGLY}$	2.80×10^{-11}	-175	5.04×10^{-11}	14
(R84)	$\text{UDD} + \text{HO} \rightarrow 0.88 \text{ALD} + 0.12 \text{KET} + \text{HO}_2$	2.70×10^{-10}		2.70×10^{-10}	15
(R85)	$\text{OP1} + \text{HO} \rightarrow 0.65 \text{MO}_2 + 0.35 \text{HCHO} + 0.35 \text{HO}$	2.93×10^{-12}	-190	5.54×10^{-12}	7

Table 2b. (continued)

Reaction No.	Reaction	A , $\text{cm}^3 \text{s}^{-1}$	E/R , K	k^a	Note
(R86)	$\text{OP2} + \text{HO} \rightarrow 0.44 \text{ HC3P} + 0.08 \text{ ALD} + 0.41 \text{ KET} + 0.49 \text{ HO} + 0.07 \text{ XO}_2$	3.40×10^{-12}	-190	6.43×10^{-12}	16
(R87)	$\text{PAA} + \text{HO} \rightarrow 0.35 \text{ HCHO} + 0.65 \text{ ACO}_3 + 0.35 \text{ HO}_2 + 0.35 \text{ XO}_2$	2.93×10^{-12}	-190	5.54×10^{-12}	17
(R88)	$\text{PAN} + \text{HO} \rightarrow \text{HCHO} + \text{XO}_2 + \text{H}_2\text{O} + \text{NO}_3$	4.00×10^{-14}		4.00×10^{-14}	1, 18
(R89)	$\text{TPAN} + \text{HO} \rightarrow 0.60 \text{ HKET} + 0.40 \text{ HCHO} + 0.40 \text{ HO}_2 + \text{XO}_2 + 0.40 \text{ PAN} + 0.60 \text{ NO}_3$	3.25×10^{-13}	-500	1.74×10^{-12}	9, 19, 20
(R90)	$\text{ONIT} + \text{HO} \rightarrow \text{HC3P} + \text{NO}_2 + \text{H}_2\text{O}$	5.31×10^{-12}	260	2.22×10^{-12}	21
<i>NO₃ + Organic Compounds</i>					
(R91)	$\text{HCHO} + \text{NO}_3 \rightarrow \text{HO}_2 + \text{HNO}_3 + \text{CO}$	3.40×10^{-13}	1900	5.79×10^{-16}	1, 22
(R92)	$\text{ALD} + \text{NO}_3 \rightarrow \text{ACO}_3 + \text{HNO}_3$	1.40×10^{-12}	1900	2.38×10^{-15}	1
(R93)	$\text{GLY} + \text{NO}_3 \rightarrow \text{HNO}_3 + \text{HO}_2 + 2 \text{ CO}$	2.90×10^{-12}	1900	4.94×10^{-15}	22, 23
(R94)	$\text{MGLY} + \text{NO}_3 \rightarrow \text{HNO}_3 + \text{ACO}_3 + \text{CO}$	1.40×10^{-12}	1900	2.38×10^{-15}	24
(R95)	$\text{MACR} + \text{NO}_3 \rightarrow 0.20 \text{ TCO}_3 + 0.20 \text{ HNO}_3 + 0.80 \text{ OLNN} + 0.80 \text{ CO}$	8.27×10^{-15}	150	5.00×10^{-15}	25
(R96)	$\text{DCB} + \text{NO}_3 \rightarrow 0.50 \text{ TCO}_3 + 0.50 \text{ HO}_2 + 0.50 \text{ XO}_2 + 0.25 \text{ GLY} + 0.25 \text{ ALD} + 0.03 \text{ KET} + 0.25 \text{ MGLY} + 0.5 \text{ HNO}_3 + 0.5 \text{ NO}_2$	2.87×10^{-13}	1000	1.00×10^{-14}	14
(R97)	$\text{CSL} + \text{NO}_3 \rightarrow \text{HNO}_3 + \text{PHO}$	2.20×10^{-11}		2.20×10^{-11}	26
(R98)	$\text{ETE} + \text{NO}_3 \rightarrow 0.80 \text{ OLNN} + 0.20 \text{ OLND}$	Table 2c		2.05×10^{-16}	7
(R99)	$\text{OLT} + \text{NO}_3 \rightarrow 0.43 \text{ OLNN} + 0.57 \text{ OLND}$	1.79×10^{-13}	450	3.95×10^{-14}	8, 27
(R100)	$\text{OLI} + \text{NO}_3 \rightarrow 0.11 \text{ OLNN} + 0.89 \text{ OLND}$	8.64×10^{-13}	-450	3.91×10^{-12}	8, 27
(R101)	$\text{DIEN} + \text{NO}_3 \rightarrow 0.90 \text{ OLNN} + 0.10 \text{ OLND} + 0.90 \text{ MACR}$	1.0×10^{-13}		1.0×10^{-13}	28
(R102)	$\text{ISO} + \text{NO}_3 \rightarrow 0.90 \text{ OLNN} + 0.10 \text{ OLND} + 0.90 \text{ MACR}$	4.00×10^{-12}	446	8.96×10^{-13}	29
(R103)	$\text{API} + \text{NO}_3 \rightarrow 0.10 \text{ OLNN} + 0.90 \text{ OLND}$	1.19×10^{-12}	-490	6.16×10^{-12}	7
(R104)	$\text{LIM} + \text{NO}_3 \rightarrow 0.13 \text{ OLNN} + 0.87 \text{ OLND}$	1.22×10^{-11}		1.22×10^{-11}	7
(R105)	$\text{TPAN} + \text{NO}_3 \rightarrow 0.60 \text{ ONIT} + 0.60 \text{ NO}_3 + 0.40 \text{ PAN} + 0.40 \text{ HCHO} + 0.40 \text{ NO}_2 + \text{XO}_2$	2.20×10^{-14}	500	4.11×10^{-15}	9, 19, 30
<i>O₃ + Organic Compounds</i>					
(R106)	$\text{ETE} + \text{O}_3 \rightarrow \text{HCHO} + 0.43 \text{ CO} + 0.37 \text{ ORA1} + 0.26 \text{ HO}_2 + 0.13 \text{ H}_2 + 0.12 \text{ HO}$	9.14×10^{-15}	2580	1.59×10^{-18}	7
(R107)	$\text{OLT} + \text{O}_3 \rightarrow 0.61 \text{ HCHO} + 0.41 \text{ ALD} + 0.37 \text{ CO} + 0.14 \text{ ORA1} + 0.10 \text{ ORA2} + 0.25 \text{ HO}_2 + 0.40 \text{ HO} + 0.03 \text{ KET} + 0.03 \text{ KETP} + 0.06 \text{ CH}_4 + 0.05 \text{ H}_2 + 0.006 \text{ H}_2\text{O}_2 + 0.03 \text{ ETH} + 0.19 \text{ MO}_2 + 0.10 \text{ ETHP}$	4.33×10^{-15}	1800	1.03×10^{-17}	8, 31
(R108)	$\text{OLI} + \text{O}_3 \rightarrow 0.02 \text{ HCHO} + 0.99 \text{ ALD} + 0.16 \text{ KET} + 0.30 \text{ CO} + 0.011 \text{ H}_2\text{O}_2 + 0.14 \text{ ORA2} + 0.07 \text{ CH}_4 + 0.22 \text{ HO}_2 + 0.63 \text{ HO} + 0.23 \text{ MO}_2 + 0.12 \text{ KETP} + 0.06 \text{ ETH} + 0.18 \text{ ETHP}$	4.40×10^{-15}	845	2.58×10^{-16}	8, 31
(R109)	$\text{DIEN} + \text{O}_3 \rightarrow 0.90 \text{ HCHO} + 0.39 \text{ MACR} + 0.36 \text{ CO} + 0.15 \text{ ORA1} + 0.09 \text{ O}^3\text{P} + 0.30 \text{ HO}_2 + 0.35 \text{ OLT} + 0.28 \text{ HO} + 0.05 \text{ H}_2 + 0.15 \text{ ACO}_3 + 0.03 \text{ MO}_2 + 0.02 \text{ KETP} + 0.13 \text{ XO}_2 + 0.001 \text{ H}_2\text{O}_2$	1.34×10^{-14}	2283	6.33×10^{-18}	7
(R110)	$\text{ISO} + \text{O}_3 \rightarrow 0.90 \text{ HCHO} + 0.39 \text{ MACR} + 0.36 \text{ CO} + 0.15 \text{ ORA1} + 0.09 \text{ O}^3\text{P} + 0.30 \text{ HO}_2 + 0.35 \text{ OLT} + 0.28 \text{ HO} + 0.05 \text{ H}_2 + 0.15 \text{ ACO}_3 + 0.03 \text{ MO}_2 + 0.02 \text{ KETP} + 0.13 \text{ XO}_2 + 0.001 \text{ H}_2\text{O}_2$	7.86×10^{-15}	1913	1.28×10^{-17}	7
(R111)	$\text{API} + \text{O}_3 \rightarrow 0.65 \text{ ALD} + 0.53 \text{ KET} + 0.14 \text{ CO} + 0.20 \text{ ETHP} + 0.42 \text{ KETP} + 0.85 \text{ HO} + 0.10 \text{ HO}_2 + 0.02 \text{ H}_2\text{O}_2$	1.01×10^{-15}	736	8.66×10^{-17}	7
(R112)	$\text{LIM} + \text{O}_3 \rightarrow 0.04 \text{ HCHO} + 0.46 \text{ OLT} + 0.14 \text{ CO} + 0.16 \text{ ETHP} + 0.42 \text{ KETP} + 0.85 \text{ HO} + 0.10 \text{ HO}_2 + 0.02 \text{ H}_2\text{O}_2 + 0.79 \text{ MACR} + 0.01 \text{ ORA1} + 0.07 \text{ ORA2}$	2.00×10^{-16}		2.00×10^{-16}	7
(R113)	$\text{MACR} + \text{O}_3 \rightarrow 0.40 \text{ HCHO} + 0.60 \text{ MGLY} + 0.13 \text{ ORA2} + 0.54 \text{ CO} + 0.08 \text{ H}_2 + 0.22 \text{ ORA1} + 0.29 \text{ HO}_2 + 0.07 \text{ HO} + 0.13 \text{ OP2} + 0.13 \text{ ACO}_3$	1.36×10^{-15}	2112	1.14×10^{-18}	32
(R114)	$\text{DCB} + \text{O}_3 \rightarrow 0.21 \text{ HO} + 0.29 \text{ HO}_2 + 0.66 \text{ CO} + 0.50 \text{ GLY} + 0.28 \text{ ACO}_3 + 0.16 \text{ ALD} + 0.62 \text{ MGLY} + 0.11 \text{ PAA} + 0.11 \text{ ORA1} + 0.21 \text{ ORA2}$	2.00×10^{-18}		2.00×10^{-18}	14
(R115)	$\text{TPAN} + \text{O}_3 \rightarrow 0.70 \text{ HCHO} + 0.30 \text{ PAN} + 0.70 \text{ NO}_2 + 0.13 \text{ CO} + 0.04 \text{ H}_2 + 0.11 \text{ ORA1} + 0.08 \text{ HO}_2 + 0.036 \text{ HO} + 0.70 \text{ ACO}_3$	2.46×10^{-15}	1700	8.19×10^{-18}	9, 19, 33
<i>Reactions of Intermediates Produced by Aromatic Oxidation</i>					
(R116)	$\text{PHO} + \text{NO}_2 \rightarrow 0.10 \text{ CSL} + \text{ONIT}$	2.00×10^{-11}		2.00×10^{-11}	34
(R117)	$\text{PHO} + \text{HO}_2 \rightarrow \text{CSL}$	1.00×10^{-11}		1.00×10^{-11}	35
(R118)	$\text{ADDT} + \text{NO}_2 \rightarrow \text{CSL} + \text{HONO}$	3.60×10^{-11}		3.60×10^{-11}	7
(R119)	$\text{ADDT} + \text{O}_2 \rightarrow 0.98 \text{ TOLP} + 0.02 \text{ CSL} + 0.02 \text{ HO}_2$	1.66×10^{-17}	-1044	5.52×10^{-16}	7
(R120)	$\text{ADDT} + \text{O}_3 \rightarrow \text{CSL} + \text{HO}$	5.00×10^{-11}		5.00×10^{-11}	36
(R121)	$\text{ADDX} + \text{NO}_2 \rightarrow \text{CSL} + \text{HONO}$	3.60×10^{-11}		3.60×10^{-11}	37
(R122)	$\text{ADDX} + \text{O}_2 \rightarrow 0.98 \text{ XYLP} + 0.02 \text{ CSL} + 0.02 \text{ HO}_2$	1.66×10^{-17}	-1044	5.52×10^{-16}	37
(R123)	$\text{ADDX} + \text{O}_3 \rightarrow \text{CSL} + \text{HO}$	1.00×10^{-11}		1.00×10^{-11}	37
(R124)	$\text{ADDC} + \text{NO}_2 \rightarrow \text{CSL} + \text{HONO}$	3.60×10^{-11}		3.60×10^{-11}	37
(R125)	$\text{ADDC} + \text{O}_2 \rightarrow 0.98 \text{ CSLP} + 0.02 \text{ CSL} + 0.02 \text{ HO}_2$	1.66×10^{-17}	-1044	5.52×10^{-16}	37
(R126)	$\text{ADDC} + \text{O}_3 \rightarrow \text{CSL} + \text{HO}$	5.00×10^{-11}		5.00×10^{-11}	37
<i>Peroxyacynitrate Formation and Decomposition</i>					
(R127)	$\text{ACO}_3 + \text{NO}_2 \rightarrow \text{PAN}$	Table 2d		8.66×10^{-12}	1
(R128)	$\text{PAN} \rightarrow \text{ACO}_3 + \text{NO}_2$	Table 2e		4.63×10^{-4}	38
(R129)	$\text{TCO}_3 + \text{NO}_2 \rightarrow \text{TPAN}$	Table 2d		8.66×10^{-12}	38
(R130)	$\text{TPAN} \rightarrow \text{TCO}_3 + \text{NO}_2$	Table 2e		4.63×10^{-4}	38

Table 2b. (continued)

Reaction No.	Reaction	A , $\text{cm}^3 \text{s}^{-1}$	E/R , K	k^a	Note
<i>NO + Organic Peroxy Radicals</i>					
(R131)	$\text{MO}_2 + \text{NO} \rightarrow \text{HCHO} + \text{HO}_2 + \text{NO}_2$	4.2×10^{-12}	-180	7.68×10^{-12}	1
(R132)	$\text{ETHP} + \text{NO} \rightarrow \text{ALD} + \text{HO}_2 + \text{NO}_2$	8.7×10^{-12}		8.70×10^{-12}	1
(R133)	$\text{HC3P} + \text{NO} \rightarrow 0.047 \text{HCHO} + 0.233 \text{ALD} + 0.623 \text{KET} + 0.063 \text{GLY}$ $+ 0.742 \text{HO}_2 + 0.15 \text{MO}_2 + 0.048 \text{ETHP} + 0.048 \text{XO}_2 + 0.059 \text{ONIT}$ $+ 0.941 \text{NO}_2$	4.0×10^{-12}		4.00×10^{-12}	38
(R134)	$\text{HC5P} + \text{NO} \rightarrow 0.021 \text{HCHO} + 0.211 \text{ALD} + 0.722 \text{KET} + 0.599 \text{HO}_2$ $+ 0.031 \text{MO}_2 + 0.245 \text{ETHP} + 0.334 \text{XO}_2 + 0.124 \text{ONIT} + 0.876 \text{NO}_2$	4.0×10^{-12}		4.00×10^{-12}	38
(R135)	$\text{HC8P} + \text{NO} \rightarrow 0.15 \text{ALD} + 0.642 \text{KET} + 0.133 \text{ETHP} + 0.261 \text{ONIT}$ $+ 0.739 \text{NO}_2 + 0.606 \text{HO}_2 + 0.416 \text{XO}_2$	4.0×10^{-12}		4.00×10^{-12}	38
(R136)	$\text{ETEP} + \text{NO} \rightarrow 1.6 \text{HCHO} + \text{HO}_2 + \text{NO}_2 + 0.2 \text{ALD}$	9.0×10^{-12}		9.00×10^{-12}	7, 39
(R137)	$\text{OLT P} + \text{NO} \rightarrow 0.94 \text{ALD} + \text{HCHO} + \text{HO}_2 + \text{NO}_2 + 0.06 \text{KET}$	4.0×10^{-12}		4.00×10^{-12}	38
(R138)	$\text{OLIP} + \text{NO} \rightarrow \text{HO}_2 + 1.71 \text{ALD} + 0.29 \text{KET} + \text{NO}_2$	4.0×10^{-12}		4.00×10^{-12}	38
(R139)	$\text{ISOP} + \text{NO} \rightarrow 0.416 \text{MACR} + 0.354 \text{OLT} + 0.847 \text{HO}_2 + 0.606$ $\text{HCHO} + 0.153 \text{ONIT} + 0.847 \text{NO}_2$	4.0×10^{-12}		4.00×10^{-12}	38
(R140)	$\text{APIP} + \text{NO} \rightarrow 0.80 \text{HO}_2 + 0.80 \text{ALD} + 0.80 \text{KET} + 0.20 \text{ONIT} +$ 0.80NO_2	4.0×10^{-12}		4.0×10^{-12}	38
(R141)	$\text{LIMP} + \text{NO} \rightarrow 0.65 \text{HO}_2 + 0.40 \text{MACR} + 0.25 \text{OLI} + 0.25 \text{HCHO} +$ $0.35 \text{ONIT} + 0.65 \text{NO}_2$	4.0×10^{-12}		4.0×10^{-12}	38
(R142)	$\text{TOLP} + \text{NO} \rightarrow 0.95 \text{NO}_2 + 0.95 \text{HO}_2 + 0.65 \text{MGLY} + 1.20 \text{GLY} +$ $0.50 \text{DCB} + 0.05 \text{ONIT}$	4.0×10^{-12}		4.00×10^{-12}	38
(R143)	$\text{XYLP} + \text{NO} \rightarrow 0.95 \text{NO}_2 + 0.95 \text{HO}_2 + 0.60 \text{MGLY} + 0.35 \text{GLY} +$ $0.95 \text{DCB} + 0.05 \text{ONIT}$	4.0×10^{-12}		4.00×10^{-12}	38
(R144)	$\text{CSLP} + \text{NO} \rightarrow \text{GLY} + \text{MGLY} + \text{HO}_2 + \text{NO}_2$	4.0×10^{-12}		4.00×10^{-12}	38
(R145)	$\text{ACO}_3 + \text{NO} \rightarrow \text{MO}_2 + \text{NO}_2$	2.0×10^{-11}		2.00×10^{-11}	7, 39
(R146)	$\text{TCO}_3 + \text{NO} \rightarrow \text{ACO}_3 + \text{HCHO} + \text{NO}_2$	2.0×10^{-11}		2.00×10^{-11}	38
(R147)	$\text{KETP} + \text{NO} \rightarrow 0.54 \text{MGLY} + 0.46 \text{ALD} + 0.23 \text{ACO}_3 + 0.77 \text{HO}_2 +$ $0.16 \text{XO}_2 + \text{NO}_2$	4.0×10^{-12}		4.00×10^{-12}	38
(R148)	$\text{OLNN} + \text{NO} \rightarrow \text{HO}_2 + \text{ONIT} + \text{NO}_2$	4.0×10^{-12}		4.00×10^{-12}	38
(R149)	$\text{OLND} + \text{NO} \rightarrow 0.287 \text{HCHO} + 1.24 \text{ALD} + 0.464 \text{KET} + 2 \text{NO}_2$	4.0×10^{-12}		4.00×10^{-12}	38
<i>HO₂ + Organic Peroxy Radicals</i>					
(R150)	$\text{MO}_2 + \text{HO}_2 \rightarrow \text{OP1}$	3.8×10^{-13}	-800	5.57×10^{-12}	1
(R151)	$\text{ETHP} + \text{HO}_2 \rightarrow \text{OP2}$	7.5×10^{-13}	-700	7.86×10^{-12}	1
(R152)	$\text{HC3P} + \text{HO}_2 \rightarrow \text{OP2}$	1.66×10^{-13}	-1300	1.30×10^{-11}	38
(R153)	$\text{HC5P} + \text{HO}_2 \rightarrow \text{OP2}$	1.66×10^{-13}	-1300	1.30×10^{-11}	38
(R154)	$\text{HC8P} + \text{HO}_2 \rightarrow \text{OP2}$	1.66×10^{-13}	-1300	1.30×10^{-11}	38
(R155)	$\text{ETEP} + \text{HO}_2 \rightarrow \text{OP2}$	1.9×10^{-13}	-1300	1.50×10^{-11}	38, 40
(R156)	$\text{OLT P} + \text{HO}_2 \rightarrow \text{OP2}$	1.66×10^{-13}	-1300	1.30×10^{-11}	38
(R157)	$\text{OLIP} + \text{HO}_2 \rightarrow \text{OP2}$	1.66×10^{-13}	-1300	1.30×10^{-11}	38
(R158)	$\text{ISOP} + \text{HO}_2 \rightarrow \text{OP2}$	1.28×10^{-13}	-1300	1.00×10^{-11}	41
(R159)	$\text{APIP} + \text{HO}_2 \rightarrow \text{OP2}$	1.50×10^{-11}		1.50×10^{-11}	9
(R160)	$\text{LIMP} + \text{HO}_2 \rightarrow \text{OP2}$	1.50×10^{-11}		1.50×10^{-11}	9
(R161)	$\text{TOLP} + \text{HO}_2 \rightarrow \text{OP2}$	3.75×10^{-13}	-980	1.01×10^{-11}	38, 40
(R162)	$\text{XYLP} + \text{HO}_2 \rightarrow \text{OP2}$	3.75×10^{-13}	-980	1.01×10^{-11}	38, 40
(R163)	$\text{CSLP} + \text{HO}_2 \rightarrow \text{OP2}$	3.75×10^{-13}	-980	1.01×10^{-11}	38, 40
(R164)	$\text{ACO}_3 + \text{HO}_2 \rightarrow \text{PAA}$	1.15×10^{-12}	-550	7.28×10^{-12}	40
(R165)	$\text{ACO}_3 + \text{HO}_2 \rightarrow \text{ORA2} + \text{O}_3$	3.86×10^{-16}	-2640	2.72×10^{-12}	40
(R166)	$\text{TCO}_3 + \text{HO}_2 \rightarrow \text{OP2}$	1.15×10^{-12}	-550	7.28×10^{-12}	38
(R167)	$\text{TCO}_3 + \text{HO}_2 \rightarrow \text{ORA2} + \text{O}_3$	3.86×10^{-16}	-2640	2.72×10^{-12}	38
(R168)	$\text{KETP} + \text{HO}_2 \rightarrow \text{OP2}$	1.15×10^{-13}	-1300	9.02×10^{-12}	38, 40
(R169)	$\text{OLNN} + \text{HO}_2 \rightarrow \text{ONIT}$	1.66×10^{-13}	-1300	1.30×10^{-11}	38
(R170)	$\text{OLND} + \text{HO}_2 \rightarrow \text{ONIT}$	1.66×10^{-13}	-1300	1.30×10^{-11}	38
<i>Methyl Peroxy Radical + Organic Peroxy Radicals</i>					
(R171)	$\text{MO}_2 + \text{MO}_2 \rightarrow 1.33 \text{HCHO} + 0.66 \text{HO}_2$	9.1×10^{-14}	-416	3.68×10^{-13}	39
(R172)	$\text{ETHP} + \text{MO}_2 \rightarrow 0.75 \text{HCHO} + \text{HO}_2 + 0.75 \text{ALD}$	1.18×10^{-13}	-158	2.01×10^{-12}	38, 40
(R173)	$\text{HC3P} + \text{MO}_2 \rightarrow 0.81 \text{HCHO} + 0.992 \text{HO}_2 + 0.58 \text{ALD} + 0.018 \text{KET}$ $+ 0.007 \text{MO}_2 + 0.005 \text{MGLY} + 0.085 \text{XO}_2 + 0.119 \text{GLY}$	9.46×10^{-14}	-431	4.02×10^{-13}	38
(R174)	$\text{HC5P} + \text{MO}_2 \rightarrow 0.829 \text{HCHO} + 0.946 \text{HO}_2 + 0.523 \text{ALD} + 0.24 \text{KET}$ $+ 0.014 \text{ETHP} + 0.049 \text{MO}_2 + 0.245 \text{XO}_2$	1.00×10^{-13}	-467	4.79×10^{-13}	38
(R175)	$\text{HC8P} + \text{MO}_2 \rightarrow 0.753 \text{HCHO} + 0.993 \text{HO}_2 + 0.411 \text{ALD} + 0.419 \text{KET}$ $+ 0.322 \text{XO}_2 + 0.013 \text{ETHP}$	4.34×10^{-14}	-633	3.63×10^{-13}	38
(R176)	$\text{ETEP} + \text{MO}_2 \rightarrow 1.55 \text{HCHO} + \text{HO}_2 + 0.35 \text{ALD}$	1.71×10^{-13}	-708	1.84×10^{-12}	38
(R177)	$\text{OLT P} + \text{MO}_2 \rightarrow 1.25 \text{HCHO} + \text{HO}_2 + 0.669 \text{ALD} + 0.081 \text{KET}$	1.46×10^{-13}	-708	1.57×10^{-12}	38
(R178)	$\text{OLIP} + \text{MO}_2 \rightarrow 0.755 \text{HCHO} + \text{HO}_2 + 0.932 \text{ALD} + 0.313 \text{KET}$	9.18×10^{-14}	708	9.87×10^{-13}	38
(R179)	$\text{ISOP} + \text{MO}_2 \rightarrow 0.550 \text{MACR} + 0.370 \text{OLT} + \text{HO}_2 + 0.08 \text{OLI} +$ 1.09HCHO	1.36×10^{-13}	-708	1.46×10^{-12}	9
(R180)	$\text{APIP} + \text{MO}_2 \rightarrow \text{HCHO} + \text{ALD} + \text{KET} + 2 \text{HO}_2$	3.56×10^{-14}	-708	3.83×10^{-13}	9
(R181)	$\text{LIMP} + \text{MO}_2 \rightarrow 1.4 \text{HCHO} + 0.60 \text{MACR} + 0.40 \text{OLI} + 2 \text{HO}_2$	3.56×10^{-14}	-708	3.83×10^{-13}	9
(R182)	$\text{TOLP} + \text{MO}_2 \rightarrow \text{HCHO} + \text{HO}_2 + 0.35 \text{MGLY} + 0.65 \text{GLY} + \text{DCB}$	3.56×10^{-14}	-708	3.83×10^{-13}	38
(R183)	$\text{XYLP} + \text{MO}_2 \rightarrow \text{HCHO} + \text{HO}_2 + 0.63 \text{MGLY} + 0.37 \text{GLY} + \text{DCB}$	3.56×10^{-14}	-708	3.83×10^{-13}	38
(R184)	$\text{CSLP} + \text{MO}_2 \rightarrow \text{GLY} + \text{MGLY} + \text{HCHO} + 2 \text{HO}_2$	3.56×10^{-14}	-708	3.83×10^{-13}	38

Table 2b. (continued)

Reaction No.	Reaction	A , $\text{cm}^3 \text{s}^{-1}$	E/R , K	k^a	Note
(R185)	$\text{ACO}_3 + \text{MO}_2 \rightarrow \text{HCHO} + \text{HO}_2 + \text{MO}_2$	3.21×10^{-11}	440	7.33×10^{-12}	38
(R186)	$\text{ACO}_3 + \text{MO}_2 \rightarrow \text{HCHO} + \text{ORA2}$	2.68×10^{-16}	-2510	1.22×10^{-12}	38
(R187)	$\text{TCO}_3 + \text{MO}_2 \rightarrow 2 \text{HCHO} + \text{HO}_2 + \text{ACO}_3$	3.21×10^{-11}	440	7.33×10^{-12}	38
(R188)	$\text{TCO}_3 + \text{MO}_2 \rightarrow \text{HCHO} + \text{ORA2}$	2.68×10^{-16}	-2510	1.22×10^{-12}	38
(R189)	$\text{KETP} + \text{MO}_2 \rightarrow 0.75 \text{HCHO} + 0.88 \text{HO}_2 + 0.40 \text{MGLY} + 0.30 \text{ALD} + 0.30 \text{HKET} + 0.12 \text{ACO}_3 + 0.08 \text{XO}_2$	6.91×10^{-13}	508	3.80×10^{-12}	38
(R190)	$\text{OLNN} + \text{MO}_2 \rightarrow 0.75 \text{HCHO} + \text{HO}_2 + \text{ONIT}$	1.60×10^{-13}	-708	1.72×10^{-12}	38
(R191)	$\text{OLND} + \text{MO}_2 \rightarrow 0.96 \text{HCHO} + 0.5 \text{HO}_2 + 0.64 \text{ALD} + 0.149 \text{KET} + 0.5 \text{NO}_2 + 0.5 \text{ONIT}$	9.68×10^{-14}	-708	1.04×10^{-12}	38
<i>Acetyl Radical + Organic Peroxy Radicals</i>					
(R192)	$\text{ETHP} + \text{ACO}_3 \rightarrow \text{ALD} + 0.5 \text{HO}_2 + 0.5 \text{MO}_2 + 0.5 \text{ORA2}$	1.03×10^{-12}	-211	2.09×10^{-12}	38
(R193)	$\text{HC3P} + \text{ACO}_3 \rightarrow 0.724 \text{ALD} + 0.127 \text{KET} + 0.488 \text{HO}_2 + 0.508 \text{MO}_2 + 0.006 \text{ETHP} + 0.071 \text{XO}_2 + 0.091 \text{HCHO} + 0.10 \text{GLY} + 0.499 \text{ORA2} + 0.004 \text{MGLY}$	6.90×10^{-13}	-460	3.23×10^{-12}	38
(R194)	$\text{HC5P} + \text{ACO}_3 \rightarrow 0.677 \text{ALD} + 0.33 \text{KET} + 0.438 \text{HO}_2 + 0.554 \text{MO}_2 + 0.495 \text{ORA2} + 0.018 \text{ETHP} + 0.237 \text{XO}_2 + 0.076 \text{HCHO}$	5.59×10^{-13}	-522	3.22×10^{-12}	38
(R195)	$\text{HC8P} + \text{ACO}_3 \rightarrow 0.497 \text{ALD} + 0.581 \text{KET} + 0.489 \text{HO}_2 + 0.507 \text{MO}_2 + 0.495 \text{ORA2} + 0.015 \text{ETHP} + 0.318 \text{XO}_2$	2.47×10^{-13}	-683	2.44×10^{-12}	38
(R196)	$\text{ETEP} + \text{ACO}_3 \rightarrow 0.8 \text{HCHO} + 0.6 \text{ALD} + 0.5 \text{HO}_2 + 0.5 \text{MO}_2 + 0.5 \text{ORA2}$	9.48×10^{-13}	-765	1.24×10^{-11}	38
(R197)	$\text{OLTP} + \text{ACO}_3 \rightarrow 0.859 \text{ALD} + 0.501 \text{HCHO} + 0.501 \text{HO}_2 + 0.501 \text{MO}_2 + 0.499 \text{ORA2} + 0.141 \text{KET}$	8.11×10^{-13}	-765	1.06×10^{-11}	38
(R198)	$\text{OLIP} + \text{ACO}_3 \rightarrow 0.941 \text{ALD} + 0.569 \text{KET} + 0.51 \text{HO}_2 + 0.51 \text{MO}_2 + 0.49 \text{ORA2}$	5.09×10^{-13}	-765	6.63×10^{-12}	38
(R199)	$\text{ISOP} + \text{ACO}_3 \rightarrow 0.771 \text{MACR} + 0.229 \text{OLT} + 0.506 \text{HO}_2 + 0.494 \text{ORA2} + 0.340 \text{HCHO} + 0.506 \text{MO}_2$	7.60×10^{-13}	-765	9.90×10^{-13}	9
(R200)	$\text{APIP} + \text{ACO}_3 \rightarrow \text{ALD} + \text{KET} + \text{HO}_2 + \text{MO}_2$	7.40×10^{-13}	-765	9.63×10^{-12}	9
(R201)	$\text{LIMP} + \text{ACO}_3 \rightarrow 0.60 \text{MACR} + 0.40 \text{OLI} + 0.40 \text{HCHO} + \text{HO}_2 + \text{MO}_2$	7.40×10^{-13}	-765	9.63×10^{-12}	9
(R202)	$\text{TOLP} + \text{ACO}_3 \rightarrow \text{MO}_2 + \text{HO}_2 + 0.35 \text{MGLY} + 0.65 \text{GLY} + \text{DCB}$	7.40×10^{-13}	-765	9.63×10^{-12}	38
(R203)	$\text{XYLP} + \text{ACO}_3 \rightarrow \text{MO}_2 + \text{HO}_2 + 0.63 \text{MGLY} + 0.37 \text{GLY} + \text{DCB}$	7.40×10^{-13}	-765	9.63×10^{-12}	38
(R204)	$\text{CSLP} + \text{ACO}_3 \rightarrow \text{GLY} + \text{MGLY} + \text{MO}_2 + \text{HO}_2$	7.40×10^{-13}	-765	9.63×10^{-12}	38
(R205)	$\text{ACO}_3 + \text{ACO}_3 \rightarrow 2 \text{MO}_2$	2.80×10^{-12}	-530	1.66×10^{-11}	39
(R206)	$\text{TCO}_3 + \text{ACO}_3 \rightarrow \text{MO}_2 + \text{ACO}_3 + \text{HCHO}$	2.80×10^{-12}	-530	1.66×10^{-11}	38
(R207)	$\text{KETP} + \text{ACO}_3 \rightarrow 0.54 \text{MGLY} + 0.35 \text{ALD} + 0.11 \text{KET} + 0.12 \text{ACO}_3 + 0.38 \text{HO}_2 + 0.08 \text{XO}_2 + 0.5 \text{MO}_2 + 0.5 \text{ORA2}$	7.51×10^{-13}	-565	5.00×10^{-12}	38
(R208)	$\text{OLNN} + \text{ACO}_3 \rightarrow \text{ONIT} + 0.5 \text{ORA2} + 0.5 \text{MO}_2 + 0.50 \text{HO}_2$	8.85×10^{-13}	-765	1.15×10^{-11}	38
(R209)	$\text{OLND} + \text{ACO}_3 \rightarrow 0.207 \text{HCHO} + 0.65 \text{ALD} + 0.167 \text{KET} + 0.484 \text{ORA2} + 0.484 \text{ONIT} + 0.516 \text{NO}_2 + 0.516 \text{MO}_2$	5.37×10^{-13}	-765	7.00×10^{-12}	38
<i>NO₃-Alkene-Peroxyradical + NO₃-Alkene-Peroxyradical Reactions</i>					
(R210)	$\text{OLNN} + \text{OLNN} \rightarrow 2 \text{ONIT} + \text{HO}_2$	7.0×10^{-14}	-1000	2.00×10^{-12}	38
(R211)	$\text{OLNN} + \text{OLND} \rightarrow 0.202 \text{HCHO} + 0.64 \text{ALD} + 0.149 \text{KET} + 0.50 \text{HO}_2 + 1.50 \text{ONIT} + 0.50 \text{NO}_2$	4.25×10^{-14}	-1000	1.22×10^{-12}	38
(R212)	$\text{OLND} + \text{OLND} \rightarrow 0.504 \text{HCHO} + 1.21 \text{ALD} + 0.285 \text{KET} + \text{ONIT} + \text{NO}_2$	2.96×10^{-14}	-1000	8.50×10^{-13}	38
<i>NO₃ + Organic Peroxy Radicals</i>					
(R213)	$\text{MO}_2 + \text{NO}_3 \rightarrow \text{HCHO} + \text{HO}_2 + \text{NO}_2$	1.2×10^{-12}		1.20×10^{-12}	38
(R214)	$\text{ETHP} + \text{NO}_3 \rightarrow \text{ALD} + \text{HO}_2 + \text{NO}_2$	1.20×10^{-12}		1.20×10^{-12}	38
(R215)	$\text{HC3P} + \text{NO}_3 \rightarrow 0.048 \text{HCHO} + 0.243 \text{ALD} + 0.67 \text{KET} + 0.063 \text{GLY} + 0.792 \text{HO}_2 + 0.155 \text{MO}_2 + 0.053 \text{ETHP} + 0.051 \text{XO}_2 + \text{NO}_2$	1.20×10^{-12}		1.20×10^{-12}	38
(R216)	$\text{HC5P} + \text{NO}_3 \rightarrow 0.021 \text{HCHO} + 0.239 \text{ALD} + 0.828 \text{KET} + 0.699 \text{HO}_2 + 0.04 \text{MO}_2 + 0.262 \text{ETHP} + 0.391 \text{XO}_2 + \text{NO}_2$	1.20×10^{-12}		1.20×10^{-12}	38
(R217)	$\text{HC8P} + \text{NO}_3 \rightarrow 0.187 \text{ALD} + 0.88 \text{KET} + 0.845 \text{HO}_2 + 0.155 \text{ETHP} + 0.587 \text{XO}_2 + \text{NO}_2$	1.20×10^{-12}		1.20×10^{-12}	38
(R218)	$\text{ETEP} + \text{NO}_3 \rightarrow 1.6 \text{HCHO} + 0.2 \text{ALD} + \text{HO}_2 + \text{NO}_2$	1.20×10^{-12}		1.20×10^{-12}	38
(R219)	$\text{OLTP} + \text{NO}_3 \rightarrow \text{HCHO} + 0.94 \text{ALD} + 0.06 \text{KET} + \text{HO}_2 + \text{NO}_2$	1.20×10^{-12}		1.20×10^{-12}	38
(R220)	$\text{OLIP} + \text{NO}_3 \rightarrow 1.71 \text{ALD} + 0.29 \text{KET} + \text{HO}_2 + \text{NO}_2$	1.20×10^{-12}		1.20×10^{-12}	38
(R221)	$\text{ISOP} + \text{NO}_3 \rightarrow 0.60 \text{MACR} + 0.40 \text{OLT} + 0.686 \text{HCHO} + \text{HO}_2 + \text{NO}_2$	1.20×10^{-12}		1.20×10^{-12}	42
(R222)	$\text{APIP} + \text{NO}_3 \rightarrow \text{ALD} + \text{KET} + \text{HO}_2 + \text{NO}_2$	1.20×10^{-12}		1.20×10^{-12}	9
(R223)	$\text{LIMP} + \text{NO}_3 \rightarrow 0.60 \text{MACR} + 0.40 \text{OLI} + 0.40 \text{HCHO} + \text{HO}_2 + \text{NO}_2$	1.20×10^{-12}		1.20×10^{-12}	9
(R224)	$\text{TOLP} + \text{NO}_3 \rightarrow 0.70 \text{MGLY} + 1.30 \text{GLY} + 0.50 \text{DCB} + \text{HO}_2 + \text{NO}_2$	1.20×10^{-12}		1.20×10^{-12}	38
(R225)	$\text{XYLP} + \text{NO}_3 \rightarrow 1.26 \text{MGLY} + 0.74 \text{GLY} + \text{DCB} + \text{HO}_2 + \text{NO}_2$	1.20×10^{-12}		1.20×10^{-12}	38
(R226)	$\text{CSLP} + \text{NO}_3 \rightarrow \text{GLY} + \text{MGLY} + \text{HO}_2 + \text{NO}_2$	1.20×10^{-12}		1.20×10^{-12}	38
(R227)	$\text{ACO}_3 + \text{NO}_3 \rightarrow \text{MO}_2 + \text{NO}_2$	4.00×10^{-12}		4.00×10^{-12}	38
(R228)	$\text{TCO}_3 + \text{NO}_3 \rightarrow \text{HCHO} + \text{ACO}_3 + \text{NO}_2$	4.00×10^{-12}		4.00×10^{-12}	38
(R229)	$\text{KETP} + \text{NO}_3 \rightarrow 0.54 \text{MGLY} + 0.46 \text{ALD} + 0.77 \text{HO}_2 + 0.23 \text{ACO}_3 + 0.16 \text{XO}_2 + \text{NO}_2$	1.20×10^{-12}		1.20×10^{-12}	38
(R230)	$\text{OLNN} + \text{NO}_3 \rightarrow \text{ONIT} + \text{HO}_2 + \text{NO}_2$	1.20×10^{-12}		1.20×10^{-12}	38
(R231)	$\text{OLND} + \text{NO}_3 \rightarrow 0.28 \text{HCHO} + 1.24 \text{ALD} + 0.469 \text{KET} + 2 \text{NO}_2$	1.20×10^{-12}		1.20×10^{-12}	38

Table 2b. (continued)

Reaction No.	Reaction	A , $\text{cm}^3 \text{s}^{-1}$	E/R , K	k^a	Note
<i>Operator Reactions</i>					
(R232)	$\text{XO}_2 + \text{HO}_2 \rightarrow \text{OP2}$	1.66×10^{-15}	-1300	1.30×10^{-11}	38
(R233)	$\text{XO}_2 + \text{MO}_2 \rightarrow \text{HCHO} + \text{HO}_2$	5.99×10^{-15}	-1510	9.50×10^{-13}	38
(R234)	$\text{XO}_2 + \text{ACO}_3 \rightarrow \text{MO}_2$	3.40×10^{-14}	-1560	6.38×10^{-12}	38
(R235)	$\text{XO}_2 + \text{XO}_2 \rightarrow$	7.13×10^{-17}	-2950	1.42×10^{-12}	38
(R236)	$\text{XO}_2 + \text{NO} \rightarrow \text{NO}_2$	4.0×10^{-12}		4.00×10^{-12}	38
(R237)	$\text{XO}_2 + \text{NO}_3 \rightarrow \text{NO}_2$	1.20×10^{-12}		1.20×10^{-12}	38

Notes 1, *DeMore et al.* [1994]; 2, products estimated (see text); 3, products from *Uselman et al.* [1979]; 4, *Atkinson and Lloyd* [1984]; 5, *Paulson et al.*, [1992a]; 6, rate constant taken to be same as for iso-butene + O^3P [*Cvetanovic*, 1987]; 7, *Atkinson* [1994]; 8, rate constant and product distribution calculated for average U.S. emissions (see text); 9, *Kirchner and Stockwell* [1996b]; 10, E/R taken to be same as for the toluene + HO reaction; 11, taken as *m*-cresol; 12, O_2 -addition channel [*Atkinson*, 1994] is ignored for simplification (see text); 13, *Tuazon and Atkinson* [1990]; 14, rate constant from *Bierbach et al.* [1994]; 15, rate constant from *Wiesen et al.* [1995]; 16, rate constant estimated as for propyl hydroperoxide; 17, rate constant as for $\text{CH}_3\text{O}_2\text{H} + \text{HO}$; 18, rate constant is upper limit; 19, TPAN treated as methacrylic peroxy nitrate; 20, rate constant from *Grosjean et al.* [1993a], E/R from *Kirchner and Stockwell* [1996b], and products from *Grosjean et al.* [1993b]; 21, rate constant taken to be as HC3; decomposition is assumed; 22, E/R is treated as $\text{ALD} + \text{NO}_3$; 23, rate constant is assumed to be equal to $2 \times k(\text{ALD} + \text{NO}_3) - k(\text{ETH} + \text{NO}_3)$; 24, rate constant is treated as $\text{ALD} + \text{NO}_3$; 25, rate constant is taken to be as crotonaldehyde [*Atkinson*, 1994] and E/R and products from *Kirchner and Stockwell* [1996b]; 26, rate constant is estimated as the mean of a mixture of 50% methylphenol and 50% dimethylphenol [*Atkinson*, 1994]; 27, rate constant is uncertain because of large variation in rate constant for alkenes grouped into model species; 28, *Atkinson* [1991]; 29, rate constant is the mean of eight measurements, and products are described by *Kirchner and Stockwell* [1996b]; 30, rate constant taken to be 80% of estimated rate constant for methacrolein by *Kirchner and Stockwell* [1996b]; 31, rate constant and products estimated from *Atkinson* [1994]; 32, rate constant from *Atkinson* [1994], and the products were estimated from *Kirchner and Stockwell* [1996b]; 33, rate constant is from constant from *Grosjean et al.* [1993a], the yield of HCHO was from *Grosjean et al.* [1993b], and other products and E/R were estimated by *Kirchner and Stockwell* [1996b]; 34, rate constant taken to be same as $\text{CH}_3\text{O} + \text{NO}_2$; 35, rate constant taken to be same as $\text{C}_6\text{H}_5\text{CH}_2\text{O}_2 + \text{HO}_2$ [*Le Bras*, 1997]; 36, the difference between *Bierbach* [1994] and *Atkinson* [1994] was assumed (see text); 37, rate constant same as corresponding reaction for ADDT; 38, *Kirchner and Stockwell* [1996a]; 39, *Lightfoot et al.* [1992]; 40, *Le Bras* [1997]; 41, rate constant taken to be same as $\text{HO}_2 + \text{CH}_2=\text{CHCH}_2\text{O}$ [*Le Bras*, 1997]; 42, rate constant taken to be same as $\text{HCP} + \text{NO}_3$.

^aThe rate constants are for 298 K and 1 atm. The units for rate constants of first-order reactions are s^{-1} ; of second-order reactions, $\text{cm}^3 \text{s}^{-1}$; and for third-order reactions, $\text{cm}^6 \text{s}^{-1}$. For second-order reactions the rate constants are given by $k = A \exp\{(-E/R)/T\}$ unless indicated otherwise.

Table 2c. The RACM Chemical Mechanism: Reaction Rate Constants of the Form $k = T^2 C \exp(-D/T)$

Reaction No.	Reaction	C , $\text{K}^{-2} \text{cm}^3 \text{s}^{-1}$	D , K	Note
(R61)	$\text{CH}_4 + \text{HO} \rightarrow \text{MO}_2 + \text{H}_2\text{O}$	7.44×10^{-18}	1361	7
(R62)	$\text{ETH} + \text{HO} \rightarrow \text{ETHP} + \text{H}_2\text{O}$	1.51×10^{-17}	492	7
(R78)	$\text{KET} + \text{HO} \rightarrow \text{KETP} + \text{H}_2\text{O}$	5.68×10^{-18}	-92	7
(R98)	$\text{ETE} + \text{NO}_3 \rightarrow 0.80 \text{ OLNN} + 0.20 \text{ OLND}$	4.88×10^{-18}	2282	7

Note 7, *Atkinson* [1994].

Table 2d. The RACM Chemical Mechanism: Troe Reactions

Reaction No.	Reaction	k_0^{300} , $\text{cm}^6 \text{s}^{-1}$	n	k_∞^{300} , $\text{cm}^3 \text{s}^{-1}$	m	Note
(R35)	$\text{O}^3\text{P} + \text{NO} \rightarrow \text{NO}_2$	9.00×10^{-32}	1.5	3.00×10^{-11}	0.0	1
(R37)	$\text{O}^3\text{P} + \text{NO}_2 \rightarrow \text{NO}_3$	9.00×10^{-32}	2.0	2.20×10^{-11}	0.0	1
(R38)	$\text{HIO} + \text{NO} \rightarrow \text{HONO}$	7.00×10^{-31}	2.6	1.50×10^{-11}	0.5	1
(R39)	$\text{HO} + \text{NO}_2 \rightarrow \text{HNO}_3$	2.60×10^{-30}	3.2	2.40×10^{-11}	1.3	1
(R42)	$\text{HO}_2 + \text{NO}_2 \rightarrow \text{HNO}_4$	1.80×10^{-31}	3.2	4.70×10^{-12}	1.4	1
(R53)	$\text{NO}_3 + \text{NO}_2 \rightarrow \text{N}_2\text{O}_5$	2.20×10^{-30}	3.9	1.50×10^{-12}	0.7	1
(R57)	$\text{HO} + \text{SO}_2 \rightarrow \text{SULF} + \text{HO}_2$	3.00×10^{-31}	3.3	1.50×10^{-12}	0.0	1
(R127)	$\text{ACO}_3 + \text{NO}_2 \rightarrow \text{PAN}$	9.70×10^{-29}	5.6	9.30×10^{-12}	1.5	1
(R129)	$\text{TCO}_3 + \text{NO}_2 \rightarrow \text{TPAN}$	9.70×10^{-29}	5.6	9.30×10^{-12}	1.5	38

Here, k ($\text{cm}^3 \text{molecule}^{-1} \text{s}^{-1}$) = $\{k_0(T)[M]/(1 + k_0(T)[M]/k_\infty(T))\}0.6^{(1 + [\log_{10}(k_0(T)[M]/k_\infty(T))]^2)^{-1}}$ where: $k_0(T) = k_0^{300}(T/300)^{-n}$; $k_\infty(T) = k_\infty^{300}(T/300)^{-m}$; and $[M]$ is the concentration of air in molecules cm^{-3} [*DeMore et al.*, 1994]. Note 1, *DeMore et al.* [1994]; 38, *Kirchner and Stockwell* [1996a, 1997].

Table 2e. The RACM Chemical Mechanism: Troe Equilibrium Reactions

Reaction No.	Reaction	A	B	k_0^{300} , $\text{cm}^6 \text{s}^{-1}$	n	k_∞^{300} , $\text{cm}^3 \text{s}^{-1}$	m	Note
(R43)	$\text{HNO}_4 \rightarrow \text{HO}_2 + \text{NO}_2$	$4.76 \times 10^{+26}$	10900	1.80×10^{-31}	3.2	4.70×10^{-12}	1.4	1
(R54)	$\text{N}_2\text{O}_5 \rightarrow \text{NO}_2 + \text{NO}_3$	$3.70 \times 10^{+26}$	11000	2.20×10^{-30}	3.9	1.50×10^{-12}	0.7	1
(R128)	$\text{PAN} \rightarrow \text{ACU}_2 + \text{NO}_2$	$1.16 \times 10^{+28}$	13954	9.70×10^{-29}	5.6	9.30×10^{-12}	1.5	38
(R130)	$\text{TPAN} \rightarrow \text{TCO}_3 + \text{NO}_2$	$1.16 \times 10^{+28}$	13954	9.70×10^{-29}	5.6	9.30×10^{-12}	1.5	38

Here, k (s^{-1}) = $A \exp(-B/T) \times \{k_0(T)[M]/(1 + k_0(T)[M]/k_\infty(T))\}0.6^{(1 + [\log_{10}(k_0(T)[M]/k_\infty(T))]^2)^{-1}}$, where $k_0(T)$, $k_\infty(T)$, and $[M]$ are as defined for Table 2f [*DeMore et al.*, 1994]. Notes 1, *DeMore et al.* [1994]; 38, *Kirchner and Stockwell* [1996a].

Table 2f. The RACM Chemical Mechanism: Reactions With Special Rate Expressions

Reaction No.	Reaction	Rate Constant Expression ^a	Note
(R24)	$O^3P + O_2 \rightarrow O_3$	$[M] \times 6.0 \times 10^{-34} \times (T/300 \text{ K})^{-2.3}$	1
(R33)	$HO_2 + HO_2 \rightarrow H_2O_2 + O_2$	$2.3 \times 10^{-13} \times \exp(600/T) + 1.7 \times 10^{-33} \times [M] \times \exp(1000/T)$	1
(R34)	$HO_2 + HO_2 + H_2O \rightarrow H_2O_2 + O_2 + H_2O$	$3.22 \times 10^{-34} \times \exp(2800/T) + 2.38 \times 10^{-54} \times [M] \times \exp(3200/T)$	1
(R46)	$HO + HNO_3 \rightarrow NO_3 + H_2O$	$k = k_0 + k_3/(1 + k_3/k_2)$ $k_0 = 7.2 \times 10^{-15} \times \exp(785/T)$ $k_2 = 4.1 \times 10^{-16} \times \exp(1440/T)$ $k_3 = 1.9 \times 10^{-33} \times \exp(725/T) \times [M]$	1
(R58)	$CO + HO \rightarrow HO_2 + CO_2$	$1.5 \times 10^{-13} \times (1 + 2.439 \times 10^{-20} \times [M])$	1

Note 1, *DeMore et al.*, [1994].

^aThe units for second-order rate constants are $\text{cm}^3 \text{s}^{-1}$ and for third-order the units are $\text{cm}^6 \text{s}^{-1}$. For all of the above, $[M]$ is the concentration of air in molecules cm^{-3} .

Acknowledgements

The last years, when I was working at the IUP and doing my PhD, were really a great pleasure to me. It is fascinating to work together with friends and colleagues from all over the world, especially if they are that competent scientists and full of inquisitiveness. Besides, the most important matter of all was the spirit of friendship and cooperation everywhere in the field of atmospheric science. Among, the teamwork in the Heidelberg group was outstanding and the measurement campaigns and their results would never been achievable without.

I would like to mention some of these persons by name as those did the major support to me during my PhD. Without them, it would have never been possible to accomplish neither the experimental work, nor the scientific analysis, nor the final write-down of this thesis.

My first thank is to my supervisor Prof. Dr. Ulrich Platt, who first introduced me into the field of atmospheric physics and chemistry and inspired the interest for scientific work in me. He gave me the possibility to work in his group for several years, and supported me not only by its equipment and financially, but also by several arrangements, very helpful discussions and ideas pushing me right on my way. He also gave me plenty of rope during my PhD so that I could grow up in general but also with all the tasks performed in this thesis.

Thanks to my second referee Prof. Dr. U. Schurath for the extensive but also continuous discussions about HONO from on the beginning of my work in atmospheric science. He also kindly revised this thesis and even cancelled a conference to examine me.

Special thanks to Prof. Dr. Jochen Stutz, who offered me the possibility to join his group at UC Los Angeles for three months during my PhD. He spent plenty of time on intense discussions and without his incitation, I would neither had achieved this understanding of physical and chemical processes in the atmosphere, nor been able to perform the scientific analysis presented in this thesis. Thank you also, for intensive advising via very long phone-calls even when I was back in Germany.

Very special thanks to Dr. Andreas Geyer. Long time ago during my Staatsexamensarbeit already, he introduced me to experimental work as well as DOAS data analysis and atmospheric HONO chemistry. However, he continued this support even when he was a Post-Doc elsewhere in the world or had unfortunately left the field of science. He never gave up on explaining, supporting and encouraging even when I was awkwardly working on the technical equipment, data or models. He and his wife Claudia also managed everything well on the projects before I began my PhD and he paved the way for my trip to UCLA.

Thanks to Andreas Geyer, Roland von Glasow, Christoph Kern, Michael Long, Jochen Stutz and especially Yasmine Stutz for correcting the various drafts of this thesis for both: the scientific content as well as English language, ... This I think, was the hardest job during advising me, but now, this thesis is finished and its at least readable.

I am also very thankful to Andreas Geyer, Björn Alicke, Christoph Kern, Oliver Sebastian, Hans-Jörg Veitel, Christoph von Friedeburg, Rainer Volkamer, and Jutta Zingler for the lots of help the during the sweaty measurement campaigns. Without your help guys, I would never

been able to set up the instruments quickly and kept them running. However, you did a great job, so that I sometimes felt like on a holiday trip.

Additionally, thanks to all the remaining (so far not named) “Plattmaten” and “Klausologen”: Andre Butz, Marcel Dorf, Gerd Hönninger, Andreas Lotter, Kai-Uwe Mettendorf, Frank Weidner, Dr. Thomas Wagner, PD Dr. Klaus Pfeilsticker (my “smoking friend”), and Thomas Scholl (my office-roommate) for the great cooperation und the lots of fun we had while drinking coffee and beer during as well as after work.

Thanks to all my colleagues from elsewhere outside the IUP Heidelberg, who joined the numerous field campaigns or laboratory experiments (or even arranged them), provided their data, and gave me support by prosperous discussions of the results and further modeling studies. Among them special thanks to:

Karin Acker and Wolfgang Wieprecht from BTU Cottbus; Norbert Kalthoff, Prof. Dr. U. Kottmeier, Stefan Krauth, Heike Vogel, and especially Bernhard Vogel as well as Harald Saathoff from the IMK of the FZ Karlsruhe; Ralf Kurtenbach, Jutta Lörzer, Peter Wiesen and especially Jörg Kleffmann from the BUGH Wuppertal; Cinzia Perrino, Marco Giusto, Paolo Bruno and especially Antonio Febo from the CNR Rome; and finally Prof. Dr. Barbara Finlayson-Pitts from the UC Irvine.

Thanks to Dr. Ingeborg Levin for the loan and evaluation of the Radon-monitors, which were incessant for the analysis of the vertical profile data.

I also wish to thank everybody from the Instituts-Werkstatt of the IUP for the prompt execution (“till yesterday”) of the entire eccentric and sometimes poorly sophisticated modifications on the instrumental equipment.

The company of Hoffmann Meßtechnik especially Alex Hoffmann for the cooperation during the never-ending story of advancing the (DOAS) electronics.

The European Union for supporting this thesis within the 5th framework, project name: NITROCAT (NITRous acid and its influence on the Oxidation Capacity of the Atmosphere) - contract number EVK2-CT-1999-00025.

And last but not least of course the very special thanks to my parents and my brothers and sister. They encouraged my studying and doing this PhD thesis. And during all that long time, they supported me not only financial, but also helped me to find my own way in the world.

Hope, I didn't forget anybody, ...? ! Did I? My earnest apologies !